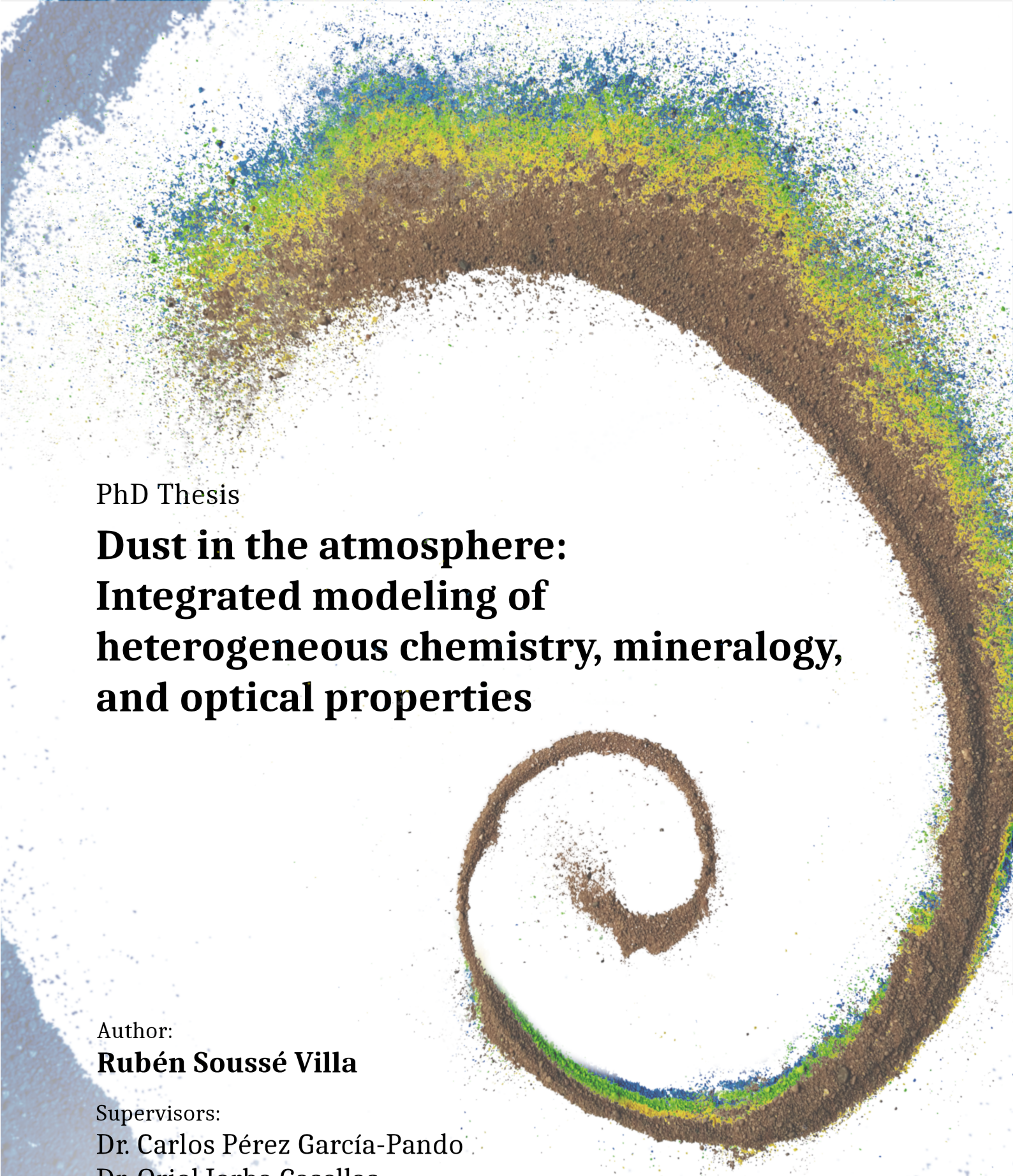

PhD Thesis

Dust in the atmosphere: Integrated modeling of heterogeneous chemistry, mineralogy, and optical properties

Author:
Rubén Soussé Villa

Supervisors:
Dr. Carlos Pérez García-Pando
Dr. Oriol Jorba Casellas

Tutor:
Dr. María Gonçalves Ageitos

Barcelona Supercomputing Center
Centro Nacional de Supercomputación

UNIVERSITAT POLITÈCNICA DE CATALUNYA
BARCELONATECH

This page is intentionally left in blank.

PhD Thesis

Dust in the atmosphere: Integrated modeling of heterogeneous chemistry, mineralogy, and optical properties.

Doctoral Program in Environmental Engineering
Department of Civil and Environmental Engineering
Universitat Politècnica de Catalunya

Author:
Rubén Soussé Villa

Supervisors:
Dr. Carlos Pérez García-Pando
Atmospheric Composition Group Team Leader, BSC
Dr. Oriol Jorba Casellas
Atmospheric Composition Group Team Leader, BSC

Tutor:
Dr. María Gonçalves Ageitos
Associate Professor, Project and Construction Engineering Department, UPC

Copyright © 2026
Reproduction of this publication in whole or in part must include the customary bibliographic citation, including author attribution, thesis title, etc.

This page is intentionally left in blank.

This PhD thesis was conducted at the Earth Sciences department of the Barcelona Supercomputing Center - Centro Nacional de Supercomputación (BSC-CNS)



The author acknowledges the financial support from the predoctoral programme AGAUR-FI Joan Oró (2025 FI-3 01106), funded by the Secretariat of Universities and Research of the Department of Research and Universities of the Generalitat of Catalonia and the European Social Plus Fund.





Further support was provided from the Horizon 2020 research and innovation programme through the ERC Consolidator Grant FRAGMENT (grant agreement No. 773051); the AXA Research Fund through the AXA Chair on Sand and Dust Storms at the Barcelona Supercomputing Center (BSC); the Spanish Ministerio de Economía y Competitividad (grants PID2022140365OB-I00 and PID2022140843OB-I00, funded by MICIU/AEI/10.13039/501100011033 and by ERDF, EU); and the Horizon Europe CERTAINTY project (CloudaERosol inTeractions their impActs IN The earth sYstem; grant agreement No. 101137680).







This page is intentionally left in blank.

To my parents, uncle,
and my other everyday family

This page is intentionally left in blank.

Acknowledgements

Over the five-year span of this project, several challenges along the way made me know myself better, especially in the lonely path that a PhD can be. However, this path also crossed those of other wonderful people. With most of them, our ways only got close briefly. With others, we walked side by side for longer. And with some of them we joined destinations. Their support helped me to reach this point. So here there are some words to all of them.

First of all, I want to thank my supervisors, Carlos and Oriol, who were almost the only people who knew (sometimes better than me) what I was working on. Thanks for your advice, patience, and tutoring during this long journey, and for getting close to me every time you had the time. I especially remember the personal support you gave me at the very beginning, when I needed it the most. Also thanks to my tutor Maria, for helping with the mineral data, the deadlines, and the bureaucracy of the University, but also for the fun moments outside the office. I also want to thank the people from the AC-Chem process group, for the interesting Friday discussions and suggestions, to Albert, for all the amazing technical help, and to Elisenda, for all the non-technical help, the snacks, the morning smiles, and the chitchat (especially when it rained).

Secondly, I want to thank my coworkers and now friends. Needless to write down their names; they know who they are, and the order never mattered. Thanks for walking side by side with me, each with its own direction, but always sharing — between *tupperwares* and coffee cups — humor, laughs, and frustrations. It was amazing to share with you this time of my life; You were a huge boost in the most difficult moments, and a huge joy in the best ones. Not to mention the beers... they also helped.

Thirdly, but no less important, I profoundly thank my "colivers" outside my workplace, with whom we crossed paths and shared our journeys and everyday lives for a long time. Isaura, Fran, Noe, Ane, and Sam, I could not be more grateful to have found such wonderful housemates and friends along my way. Thanks for the amazing and cozy times every home-working day, weekend, and every time I came home so late at night from the office. This gratefulness extends to my other "colivers" outside home. Those from Desenruna: Elena, Ada, Marti, Fulvi, Alba, Sarah *italiana*, Sarah *austríaca*, Judit, Nora, Paula,

Marcos, Simone, Antoine, Marta, Ferran, Dani, and so many others. For such enchanting moments shared among abundant tomatoes, exuberant fava beans, and dying lettuces, struggling together with me to turn our neighborhood and society into a better place. With you, every Saturday I experienced what I think comes closest to full happiness. Also thanks to all the plants that survived the harsh conditions when I could not take enough care of them because of the PhD: I think they gave me more joy than the other way around. I am also deeply grateful for joining my path and sharing such wonderful moments (and frustrations) with you Sara, Marco, Anna, and Gabriel (and Jai!). You have been more important in this journey than you can imagine. A huge thanks also to Alba, for pushing my steps along this lonely PhD road with your strength, and for such amazing times driving me across Catalunya, sharing trips, volunteer work, and co-living. And I do not want to forget Miriam. Thanks for all the years together and for your cosmic soul, which brought me back to Barcelona to start this project. Your amazing music accompanied me every single day of these 5 years.

Fourth, a heartfelt gratitude to the people of Vidàlia, always welcoming me when I needed to get out of Barcelona, and "abducting" me into their family as one of them, sharing joyful times, and wonderful *rurality*. Also thanks to the people of Cal Cases, who trusted me when I needed a laptop for a (very important) summer week.

Finally, thanks to my family, who gave me the opportunity and supported me to reach this point. To my mom, for having endured the most harsh circumstances for the people she loves. And especially thanks to Enric, for encouraging me, but also for always being such a pillar in our family, remaining available and next to us during the most extreme difficulties our family had to face. We have never thanked you enough.

Contents

Abstract v

Resum vii

Resumen ix

List of figures xx

List of tables xxvi

Acronyms xxvii

1 Introduction 1

1.1 Motivation . . . 1
1.2 Airborne mineral dust . . . 3
1.2.1 Sources, transport and deposition . . . 3
1.2.2 Mineralogical composition . . . 7
1.3 Dust heterogeneous chemistry . . . 8
1.3.1 Acid neutralization on aqueous particles by $NH_{3(g)}$ . . . 11
1.3.2 Acid neutralization on dust surfaces by alkaline minerals . . . 12
1.3.3 Other relevant reactions . . . 16
1.3.4 The role of dust acidity, temperature, and aerosol water content . . . 18
1.4 Impacts on air quality, health, and climate . . . 19
1.4.1 Air quality . . . 20
1.4.2 Health . . . 23
1.4.3 Ecosystems . . . 24
1.4.4 Aerosol acidity . . . 26
1.4.5 Climate . . . 27
1.5 Modeling of mineral dust heterogeneous chemistry and mineralogical representation . . . 31

2 Objectives and structure 37

2.1 Objectives, context and scope . . . 37
2.2 Structure . . . 39

3 Methodology **42**
3.1 The MONARCH atmospheric chemistry model . . . 42
3.1.1 Secondary inorganic aerosol formation: a hybrid heterogeneous chemical mechanism . . . 45
3.2 Dust soil-surface mineralogical datasets . . . 47
3.2.1 Land-based mineralogical datasets: Claquin et al. (1999) and Journet et al. (2014) . . . 48
3.2.2 Spaceborne retrievals of soil-surface mineralogy: the EMIT dataset 49
3.3 Processing of anthropogenic and other emission sources: the HERMES emission system . . . 51
3.4 Observational data for model evaluation . . . 53
3.5 Computing resources: Marenostrum 4 and Marenostrum 5 . . . 55

4 Model developments **57**
4.1 Aerosol size distribution . . . 57
4.2 Thermodynamic equilibrium model: ISORROPIA II . . . 59
4.3 Gas condensation schemes . . . 62
4.3.1 Irreversible condensation . . . 62
4.3.2 Reversible condensation . . . 67
4.4 Heterogeneous chemistry mechanisms . . . 68

5 Impacts of the dust heterogeneous chemistry mechanism **72**
5.1 Introduction . . . 72
5.2 Methods . . . 74
5.2.1 Modeling NO_3^- heterogeneous chemistry . . . 74
5.2.2 Sensitivity runs . . . 75
5.2.3 Experimental setup . . . 78
5.2.4 Model evaluation . . . 78
5.3 Results . . . 79
5.3.1 Spatial distributions . . . 79
5.3.1.1 Effects of omitting coarse NO_3^- formation . . . 80
5.3.1.2 Effects of assuming irreversible formation of coarse NO_3^- 82
5.3.1.3 Effects of accounting for reversible formation of coarse NO_3^- . . . 85
5.3.2 Evaluation with observations . . . 88
5.3.2.1 Nitrate species . . . 88
5.3.2.2 Ammonia species . . . 92
5.3.2.3 Sulfur species . . . 92

5.3.2.4 Fine and total particulate matter . . . 93
5.3.3 Nitrogen partitioning . . . 94
5.3.3.1 Partitioning between gas and particle phases . . . 94
5.3.3.2 Reduced and oxidized nitrogen . . . 96
5.3.4 Nitrate budgets . . . 99
5.4 Conclusions . . . 104

6 Impacts of the geographical representation of dust mineralogy 108
6.1 Introduction . . . 108
6.2 Methods . . . 110
6.2.1 EMIT spaceborne retrievals of soil-surface mineralogy . . . 110
6.2.2 Modeling dust mineralogy and heterogeneous chemistry . . . 111
6.2.3 Satellite-based constraints on modeled dust emissions . . . 113
6.2.4 Calculation of pH averages . . . 114
6.2.5 Simulations . . . 115
6.2.6 Model evaluation . . . 116
6.2.7 Regional assessment of high NO_3^- formation events . . . 117
6.3 Results . . . 118
6.3.1 Improvements in global $CaCO_3$ representation . . . 118
6.3.2 Impacts on NO_3^- and other SIA burdens . . . 120
6.3.3 Impacts on surface concentrations and aerosol acidity . . . 123
6.3.4 Evaluation and impact on regional extreme episodes . . . 125
6.4 Conclusions . . . 128

7 Impacts on aerosol optical properties 131
7.1 Introduction . . . 131
7.2 Methodology . . . 133
7.2.1 Modeling dust mineralogy and heterogeneous chemistry . . . 133
7.2.2 Calculation of optical properties . . . 135
7.2.3 Comparison of SSA with AERONET . . . 138
7.3 Results . . . 140
7.3.1 Effects of SIA formation on AOD and SSA . . . 140
7.3.2 Sensitivity to coarse aerosol formation . . . 144
7.3.3 Sensitivity to mineralogical variations . . . 147
7.4 Conclusions . . . 152

8 Achievements, conclusions and future work **154**
8.1 Achievements . . . 154
8.2 Conclusions . . . 156
8.3 Future work . . . 159

A Supplement of Chapter 5 **164**
A.1 Journet and Claquin mineral data . . . 164
A.2 Spatial distributions . . . 169
A.3 Supplementary evaluation results . . . 181
A.4 Budget tables . . . 187
A.5 Discussion of additional sensitivity experiments . . . 192
A.5.1 HYB_g0p1 . . . 192
A.5.2 DBCLL_duAlk . . . 192
A.5.3 DBCLL_ClaqAlk . . . 193
A.6 Evaluation of oxidized and reduced species . . . 194

B Supplement of Chapter 6 **195**
B.1 Satellite constraints of dust emissions . . . 195
B.2 $CaCO_3$ evaluation . . . 196
B.3 Burdens . . . 197
B.4 Methodology . . . 201
B.5 pH . . . 201
B.6 Statistical significance analysis and evaluation . . . 202
B.7 PM2.5 evaluation . . . 203
B.8 Experiment descriptions . . . 203
B.9 Domain definitions . . . 203

C Supplement of Chapter 7 **204**
C.1 Optical properties . . . 204
C.2 Refractive indexes . . . 205
C.3 Sensitivity to coarse SIA formation: Burdens . . . 206
C.4 Sensitivity to $CaCO_3$ geographical distribution . . . 208
C.4.1 Relative differences in AOD and SSA . . . 208
C.5 Sensitivity to the mineral atlas . . . 209
C.5.1 Differences in SIA burdens . . . 209
C.5.2 Relative differences in AOD and SSA . . . 210

References **213**

Abstract

Airborne mineral dust is one of the dominant aerosol components in the atmosphere and plays a central role in the Earth system through its interactions with atmospheric composition and radiation. Despite its importance, large uncertainties remain in its representation in atmospheric models, particularly concerning dust heterogeneous chemistry. These reactions between dust particles and gas species play a dominant role over dust affected regions in the formation of secondary inorganic aerosols (SIA) such as particulate nitrate (NO_3^-), ammonium (NH_4^+), and sulfate (SO_4^{2-}). Yet, they are still subject to strong simplifications and parameterizations in atmospheric models, which still show significant discrepancies in their representation.

This Thesis aims to advance the understanding of dust atmospheric chemical processes, their dependence on mineralogical composition, and their implications for aerosol optical properties. To this end, multiple dust heterogeneous chemistry mechanisms and mineralogical representations are implemented and systematically evaluated within the MONARCH atmospheric chemistry model. Their impacts on atmospheric composition, aerosol acidity, and optical properties are assessed and evaluated against observations. Notably, this work represents the first integration into an atmospheric chemistry model of observationally constrained maps of surface mineral composition of arid surfaces derived from the recently launched NASA's Earth Surface Mineral Dust Source Investigation (EMIT) spectrometer.

The evaluation of different dust heterogeneous chemistry mechanisms highlights the importance of representing reversible SIA formation in both fine and coarse particle modes, together with an accurate treatment of dust and sea-salt alkalinity. This combined approach is shown to be necessary to achieve consistent nitrogen (N) budgets and aerosol acidity, and to better reproduce observed atmospheric NO_3^- concentrations.

The comparison of different mineral atlases focuses on calcite ($CaCO_3$) as the primary contributor to dust alkalinity, demonstrating that EMIT provides the most consistent representation of the atmospheric $CaCO_3$ cycle. The use of source-resolved mineralogy compared to the common assumption of globally averaged dust mineral content, reveals strong geographical contrasts in $CaCO_3$ abundance, particularly between the Middle East and other major dusty regions such as the Sahara and East Asia. These differences in $CaCO_3$ lead to marked regional and size-dependent implications for aerosol acidity and SIA formation. Impacts on

particulate NO_3^- are found to be most pronounced during short-lived, intense formation events in regions affected by both dust and anthropogenic pollution, while NO_3^- global burdens and long-term trends are less sensitive to the $CaCO_3$ representation.

Aerosol optical properties are in general modestly impacted by the representation of dust chemistry and mineralogy, with fine-mode aerosols exerting a larger influence than coarse particles, though both remain secondary compared to strongly absorbing minerals such as iron (Fe) oxides. Limitations related to the representation of absorbing carbonaceous aerosols and the absence of cloud–aerosol interactions constrain the assessment of radiative effects.

Overall, this Thesis demonstrates that combining reversible dust heterogeneous chemistry with source-resolved mineralogical information from EMIT substantially improves the representation of dust–gas interactions and their impacts on atmospheric composition and aerosol optics. Remaining uncertainties highlight the need for continued development of mineralogical datasets and chemical parameterizations, as well as the inclusion of anthropogenic dust sources and additional reactive gas species. Further progress would also benefit from high-resolution modeling of small-scale dust events and from expanded observational coverage over dust-affected urban regions.

Resum

La pols mineral en suspensió és un dels principals aerosols de l'atmosfera i exerceix un paper central en el sistema terrestre mitjançant múltiples interaccions amb altres components atmosfèrics i amb la radiació. Malgrat la seva importància, la seva representació en models atmosfèrics continua associada a importants incerteses, especialment pel que fa a la seva química heterogènia. Aquest conjunt de reaccions entre partícules de pols i gasos és especialment rellevant en regions afectades per intrusions de pols, pel seu paper dominant en la formació d'aerosols inorgànics secundaris (SIA), com el nitrat (NO_3^-), l'amoni (NH_4^+) i el sulfat (SO_4^{2-}) particulats, i la seva modelització encara depèn d'importants simplificacions i parametritzacions que condueixen a discrepàncies notables entre models pel que fa als seus impactes atmosfèrics i climàtics.

Aquesta Tesi té com a objectiu avançar en la comprensió de la química atmosfèrica de la pols mineral, la seva dependència de la mineralogia i les seves implicacions per a les propietats òptiques dels aerosols. Amb aquesta finalitat, en aquesta Tesi s'implementen i s'avaluen sistemàticament múltiples mecanismes per representar la química heterogènia de la pols i la seva composició mineralògica dins del model de química atmosfèrica MONARCH, avaluant-ne els impactes sobre la composició atmosfèrica, l'acidesa dels aerosols i les propietats òptiques. Cal destacar que aquest treball constitueix la primera integració en un model atmosfèric de mapes mineralògics amb restriccions observacionals de superfícies àrides, a partir de les dades de l'espectròmetre Earth Surface Mineral Dust Source Investigation (EMIT) de la NASA.

L'estudi de diferents mecanismes de química heterogènia mostra que la representació de la formació reversible de SIA sobre partícules fines i gruixudes, conjuntament amb la representació de l'alcalinitat de la pols i de la sal marina, és necessària per aconseguir nivells consistents de nitrogen (N), d'acidesa, i reproduir els nivells de NO_3^- particulat observats.

La comparació de diferents atles mineralògics, centrada en la calcita ($CaCO_3$) com a principal contribuent a l'alcalinitat de la pols, indica que EMIT proporciona la representació més coherent del seu cicle atmosfèric. L'ús d'una mineralogia que resol geogràficament la composició de les fonts, enfront de l'assumpció habitual d'una mineralogia global mitjana, revela contrastos espacials marcats en l'abundància de $CaCO_3$, especialment en regions afectades per intrusions de pols, com l'Orient Mitjà, el Sàhara i l'Àsia Oriental, amb un impacte directe sobre l'acidesa dels aerosols i la formació de SIA. Els efectes són especialment rellevants

durant episodis intensos i de curta durada de formació de NO_3^-, mentre que els impactes globals i a llarg termini són més moderats.

Les implicacions òptiques associades a la química heterogènia i a la representació mineralògica de la pols són, en general, modestes, amb una contribució més important de les partícules fines que de les gruixudes, però que són secundàries en comparació amb el rol de minerals fortament absorbents com els òxids de ferro (Fe). Tanmateix, les limitacions en la representació d'aerosols carbonats absorbents i l'absència d'interaccions núvol–aerosol restringeixen l'avaluació dels efectes radiatius.

En conjunt, aquesta Tesi demostra que la combinació d'una representació reversible de la química heterogènia de la pols amb una mineralogia resolta geogràficament basada en EMIT millora substancialment la representació de les interaccions pols–gas i dels seus impactes químics i òptics. Les incerteses persistents posen de manifest la necessitat de continuar desenvolupant bases de dades mineralògiques i parametritzacions químiques, d'incorporar fonts de pols antropogèniques i gasos addicionals, així com de dur a terme simulacions d'alta resolució i ampliar la cobertura observacional sobre regions urbanes afectades per pols mineral.

Resumen

El polvo mineral en suspensión es uno de los principales aerosoles de la atmósfera y ejerce un papel central en el sistema terrestre mediante múltiples interacciones con otros componentes y con la radiación. A pesar de su importancia, su representación en los modelos atmosféricos está asociada a importantes incertidumbres, especialmente en lo que se refiere a su química heterogénea. Este conjunto de reacciones entre partículas y gases es especialmente importante en regiones afectadas por intrusiones de polvo, debido a su papel dominante en la formación de aerosoles inorgánicos secundarios (SIA) como el nitrato (NO_3^-), el amonio (NH_4^+) y el sulfato (SO_4^{2-}) particulados. Sin embargo, su modelización todavía depende de importantes simplificaciones y parametrizaciones que conducen a discrepancias notables entre modelos al reproducir sus impactos atmosféricos y climáticos.

La presente Tesis tiene como objetivo avanzar en la comprensión de la química atmosférica del polvo mineral, su dependencia de la mineralogía y sus implicaciones para las propiedades ópticas de los aerosoles. Con esta finalidad, en esta Tesis se implementan y evalúan sistemáticamente múltiples mecanismos para representar la química heterogénea y la composición mineralógica del polvo dentro del modelo de química atmosférica MONARCH, evaluando sus impactos sobre la composición, la acidez y las propiedades ópticas de los aerosoles. Cabe destacar que este trabajo constituye la primera integración en un modelo atmosférico de mapas mineralógicos de superficies áridas con restricciones observacionales a partir de los datos del espectrómetro Earth Surface Mineral Dust Source Investigation (EMIT) de la NASA.

El estudio de diferentes mecanismos de química heterogénea muestra que representar la formación reversible de SIA sobre partículas finas y gruesas, conjuntamente con la alcalinidad del polvo y de la sal marina, es necesario para conseguir niveles consistentes de nitrógeno (N) y acidez, y para reproducir los niveles de NO_3^- observados.

La comparación de distintos atlas mineralógicos, centrándose en la calcita ($CaCO_3$) como principal contribuyente a la alcalinidad del polvo, indica que EMIT proporciona la representación más coherente de su ciclo atmosférico. El uso de una mineralogía que resuelva geográficamente la composición de las fuentes, frente a la habitual representación de una mineralogía media global, revela marcados contrastes espaciales en la abundancia de $CaCO_3$, especialmente en regiones afectadas por intrusiones de polvo, como Oriente Medio, el Sáhara y Asia Oriental, con

un impacto directo sobre la acidez y la formación de SIA. Los efectos son especialmente relevantes durante episodios de formación de NO_3^- intensos y de corta duración, mientras que los impactos globales y a largo plazo son más moderados. Las implicaciones ópticas asociadas a la química heterogénea y a la representación mineralógica del polvo son, en general, modestas, con una mayor contribución de las partículas finas que de las gruesas, aunque ambas son secundarias en comparación con minerales fuertemente absorbentes como los óxidos de hierro (Fe). Sin embargo, las limitaciones en la representación de aerosoles carbonatados absorbentes y la ausencia de interacciones nube-aerosol restringen una evaluación completa de los efectos radiativos.

En conjunto, esta Tesis demuestra que combinar la representación reversible de la química heterogénea del polvo con una mineralogía resuelta geográficamente basada en EMIT mejora sustancialmente la representación de las interacciones polvo-gas, así como sus impactos químicos y ópticos. Las incertidumbres restantes ponen de manifiesto la necesidad de seguir desarrollando bases de datos mineralógicas y parametrizaciones químicas, de incorporar fuentes de polvo antropogénicas y gases adicionales, así como de realizar simulaciones de alta resolución y ampliar la cobertura observacional sobre regiones urbanas afectadas por polvo mineral.

List of Figures

1.1 Main atmospheric transport pathways of airborne mineral dust. Source: Querol et al. (2019) and Griffin (2007). 5

1.2 Schematic of the mineral dust lifecycle and its interaction with other atmospheric species, acting as a precursor agent of secondary inorganic aerosols, with important impacts on ecosystems, air quality, and climate. 9

1.3 Neutralization scenarios of acid and basic gas species in the presence or absence of NVCs dissolved from dust alkaline minerals. 11

1.4 Scheme of dust heterogeneous chemistry, considering the two possible scenarios of reversible and irreversible condensation of gas molecules into the particle phase. 13

1.5 Condensation of $HNO_{3(g)}$ onto dust mineral particles, pictured with a scanning electron microscope. *Reprinted from Atmospheric Environment, 38, B.J. Krueger, V.H. Grassian, J.P. Cowin, A. Laskin, Heterogeneous chemistry of individual mineral dust particles from different dust source regions: the importance of particle mineralogy, 6258, Copyright (2004), with permission from Elsevier.* 15

1.6 Distribution of SIA components as fractions of $PM_{2.5}$ and PM_{10} across countries and cities from the literature (pie charts). Colors on the map indicate PM_{20} dust surface concentration averaged for 2018 in $\mu g\ m^{-3}$. . 22

1.7 Representation of the uptake process of gas species in the aerosols liquid coating, and its parameterization through an uptake coefficient (γ) (adapted from Brasseur and Jacob (2017)). 34

2.1 Structure of this Thesis. Modeling tools and mineral datasets (left column), sensitivity analyses (central column), and developments (right column). The corresponding chapters are specified in red at the top of each section box. 40

3.1 The EMIT instrument (top right) and its scheme of data analysis procedure. 50

3.2 HERMES flowchart, from Guevara et al. (2020). 53

3.3 From left to right, the currently depricated Marenostrum 4 and the recently set Marenostrum 5 (Source: *BSC*). 55

4.1 Scheme of irreversible uptake of gas molecules into the particle phase. . . 64

4.2 Trigonometric fit of experimental data for $\gamma(HNO_3)$ on sea salt dependent on RH and particle size from Saul et al. (2006) and Liu et al. (2007). . . 66
4.3 Scheme of the heterogeneous chemistry reactions on dust and sea salt developed in this work. (a) Schemes for the fTEQ and HYB mechanisms. (b) Scheme for the DBCLL mechanism that includes the kinetic diffusion limitation of gas species. The legend for the line patterns is included in the center box. Numbers represent (1) fTEQ, (2) HYB and (3) DBCLL. At the bottom, the pathways for the processing of $SO_{2(g)}$ and $H_2SO_{4(g)}$ gases for each scheme are represented: $SO_{2(g)}$ is taken up by fine particles and the remaining gas is taken up by coarse particles. For $H_2SO_{4(g)}$, (a) the fTEQ and HYB mechanisms assume that it nucleates directly as fine SO_4^{2-}, while (b) the DBCLL mechanism assumes that 50% of its concentration nucleates, and the rest is divided by diffusion limitation between the fine and coarse modes, completely condensing on each of them. The uptake coefficients used for the uptake processes (solid arrows) are $\gamma_{1,2}$ for $HNO_{3(g)}$ uptake on dust and sea salt, and γ_3 for $SO_{2(g)}$ uptake on dust. Fine mode forms over dust particles with $0.2 < D < 2.5\mu m$, and coarse ones for $2.5 < D < 20\mu m$. 70
4.4 Scheme of the kinetic diffusion limitation methodology and the condensation-evaporation of gas species to and from the aerosol phase. . 71

5.1 Illustration of the mineral dust heterogeneous chemistry mechanisms implemented for fine ($0.2 < D < 2.5\mu m$) and coarse ($2.5 < D < 20\mu m$) particles. Fine dust aqueous coating is assumed to reach thermodynamic equilibrium (TEQ) with anthropogenic gas species to form fine particulate NO_3^- and NH_4^+. Conversely, coarse particulate NO_3^- and NH_4^+ are formed through either the reversible condensation (i.e. through TEQ) of $HNO_{3(g)}$ and $NH_{3(g)}$ after kinetic limitation or the irreversible uptake reaction (UPTK) of $HNO_{3(g)}$ on coarse dust particles, in this case only considering the formation of NO_3^- and not NH_4^+. 76
5.2 Surface concentration ($\mu g\ m^{-3}$) of $HNO_{3(g)}$, fine and coarse NO_3^- simulated by the different mechanisms, averaged for 2018. 81
5.3 Surface pH of the studied mechanisms for fine and coarse aerosol size modes, averaged for 2018. 82

5.4 Observational evaluation of gas and particulate species surface concentrations. Solid-black dots and crosses represent the monthly median and mean of the observations, respectively. Colored lines represent each configuration's monthly median over the observational points. Error bars are the observational interquartile 0.25 to 0.75 distance. Blue shading is the interquartile 0.25 - 0.75 distance for the DBCLL_du-ssAlk simulation. For the total NO_3^- modes, the available data from the European, Asian and North and Central American stations have been averaged together, despite data from Asia and North and Central America referring to total particle concentration, while data from Europe is limited strictly to particles with diameters up to 10 μm. 89

5.5 Atmospheric N average burdens (top) and accumulated depositions (bottom) in teragrams of N (TgN) for the different dust heterogeneous chemistry mechanisms. The corresponding fractions of the N-containing species simulated in MONARCH are shown in each bar plot. Total N deposition is reported at the top of each bar of the deposition chart. . . . 95

5.6 Average 2018 N budgets (a, b) and depositions (c, d) for the different dust heterogeneous chemistry mechanisms. Each plot shows oxidized (a, c) and reduced (b, d) mass for each mechanism (bars). They are compared with references from the literature (the final three bars on the right). 97

6.1 Illustration of the methodology to compare EMIT simulations using source-based (SB) versus globally averaged (AVG) mineral data. 116

6.2 Spatial distributions of modeled Ca^{2+} emissions (top), surface Ca^{2+}-to-dust mass fractions (middle), and comparison with airborne $CaCO_3$ observations (bottom) for the CLAQ, JOUR, and EMIT mineral datasets. All simulations use dust emissions constrained through the assimilation of satellite-retrieved dust optical depth. 119

6.3 Column loads for NO_3^-, NH_4^+, SO_4^{2-} and total SIA for fine ($D < 2.5\mu m$, coarse ($2.5 < D < 10\mu m$), and total ($D < 20\mu m$) size modes using EMIT source-based $CaCO_3$ distribution. 120

6.4 Absolute differences between EMIT source-based (SB) and globally averaged (AVG) $CaCO_3$ representations in column burdens of fine ($D < 2.5\mu m$), coarse ($2.5 < D < 10\mu m$), and PM20 (full size range up to 20 μm) species. Panels show (a1–c1) ionic Ca^{2+}, (a2–c2) particulate NO_3^-, (a3–c3) SO_4^{2-}, (a4–c4) NH_4^+, and (a5–c5) SIA (i.e. $NO_3^- + SO_4^{2-} + NH_4^+$). White gridcells indicate non statistically significant differences ($p<0.05$). 122

6.5 Surface-level impacts of $CaCO_3$ variability on Ca^{2+}, secondary aerosols, and pH. Absolute differences in surface concentrations between EMIT SB and AVG simulations for (a1–c1) Ca^{2+}, (a2–c2) NO_3^-, (a3–c3) SO_4^{2-}, (a4–c4) NH_4^+, (a5–c5) SIA, and (a6–c6) aerosol pH. 125

6.6 Comparison of simulated and observed total surface concentrations of NO_3^- and Ca^{2+} using the EMIT dataset. (a) Statistically-significant average annual differences in total NO_3^- between SB and AVG simulations. Evaluated stations are referenced as black circles, while red triangles indicate those stations where differences between SB and AVG runs are statistically significant ($p < 0.05$). (b) Monthly mean of total NO_3^- compared with global observations. Coloured shading and error bars represent the standard deviation of the model and observations, respectively. Evaluation is performed over stations marked as black dots in panel (a) map. (c) Spatial distribution of annual mean differences in coarse NO_3^- between SB and AVG simulations during the top 1 % and bottom 1 % of NO_3^- formation events. (d) Boxplots summarizing coarse NO_3^- differences across major regions for extreme (left) and high (right) formation percentiles. (e,f) Time series of the differences between the median concentrations for NO_3^- and Ca^{2+} with SB minus AVG simulations over East Asia. Fine (left) and coarse (right) modes are provided with 6-hourly temporal resolution. 127

7.1 Scheme of the optical properties analysis performed in this chapter. . . . 133

7.2 Scheme of the package for optical properties calculation. 136

7.3 Scheme of the mixture of bulk and condensable species assumed for the calculation of optical properties for coarse mode aerosols. 137

7.4 AeroNet stations used for the evaluation: Upward blue triangles are stations northeastern Africa, green left triangles for northwestern Africa, down orange triangles for the Sahel region, and red circles stations for Arabian Peninsula. 138

7.5 AOD for fine ($D < 2.5\mu m$), coarse ($2.5 < D < 10\mu m$) and total ($D < 20\mu m$) size modes using EMIT source-based $CaCO_3$ distribution with (*a1-a3*) all aerosol species, including dust, sea salt, BC, OM, and SIA. Difference in AOD compared to the previous case omitting (*b1-b3*) SIA species, and (*b1-b3*) particulate NO_3^-. 140

7.6 Aerosol size-resolved SSA using EMIT source-based $CaCO_3$ data with all condensed aerosol components (a1-a3), only SIA (b1-b3), and only NO_3^- (c1-c3) species. 142

7.7 SSA evaluation using the EMIT source-based methodology against stations close to dust emission areas, and filtered by the abundance of dust and condensable species. Results with only dust are evaluated in (a), with and without SIA species are shown in panels (b) and (c), respectively. Both cases are compared in (d). Correlations (r), mean square error (e), means ($mean$), and the number of stations (n) are shown the top of each panel. 143

7.8 Fine ($D < 2.5\mu m$), coarse ($2.5 < D < 10\mu m$), and total ($D < 20\mu m$) size AOD with all aerosols but coarse SIA using the EMIT source-based $CaCO_3$ (first row), and comparison with the DBCLL (*default*) mechanism (second row). 145

7.9 Fine ($D < 2.5\mu m$), coarse ($2.5 < D < 10\mu m$) and total ($D < 20\mu m$) size SSA with all aerosols but coarse SIA using the EMIT source-based $CaCO_3$ (first row), and comparison with the DBCLL (*default*) mechanism (second row). 146

7.10 Differences on aerosol optical depth (AOD) and single scattering albedo (SSA) response to mineral variability between the source-based (SB) and globally averaged (AVG) approximations. Panels *a1–a3* for AOD, and *c1-c3* for SSA, isolate the effect of $CaCO_3$ and its induced SIA formation, assuming identical distributions of additional minerals. Panels *b1-b3* for AOD, and *d1-d3* for SSA, include the additional contribution of mineralogical variations in Fe oxides. SB increases coarse-mode NO_3^- and Ca^{2+} over the Middle East, but decreases them over East Asia and the Sahara. Differences in fine-mode SIA slightly reduce overall SSA, whereas Fe-oxide variability dominates total SSA changes, lowering values over hematite-rich regions. 148

7.11 SSA evaluation using EMIT with different mineralogy distributions over stations close to dust emission areas, and filtered by the abundance of dust and condensable species. Results using EMIT source-based data (EMIT(SB)) are shown in panel (a), with globally-averaged data (EMIT(AVG)) in panel (b), and the comparison of both previous cases in panel (c). The global and regional correlations (r), the mean square error (e), the means, and the number of stations (n) are shown at the top of each panel. 149

7.12 Comparison of AOD results obtained with Journet et al. (2014) (JOUR, *a1* to *a3*) and Claquin et al. (1999) (CLAQ, *b1* to *b3*) source-based data, in comparison with results for AOD using EMIT. 150

7.13 Comparison of SSA results obtained with Journet et al. (2014) (JOUR, *a1* to *a3*) and Claquin et al. (1999) (CLAQ, *b1* to *b3*) source-based data, in comparison with results for SSA using EMIT. 150
7.14 SSA evaluation using source-based mineral data from the JOUR and CLAQ mineral datasets, and compared with EMIT, over stations close to dust emission areas, and filtered by the abundance of dust and condensable species. Results using JOUR and CLAQ data are shown in panels (a1) and (a2). Panels (c1) and (c2) compare JOUR and CLAQ with EMIT, respectively. The global and regional correlations (r), the mean square error (e), the means and the number of stations (n) are shown at the top of each panel. 151

A.1 Column loads ($mg\ m^{-2}$) of $HNO_{3(g)}$, fine and coarse particulate NO_3^- simulated by the different mechanisms, averaged for 2018. 170
A.2 Zonal average concentrations ($\mu g\ m^{-3}$) of $HNO_{3(g)}$, fine and coarse particulate NO_3^- simulated by the different mechanisms, averaged for 2018. . 171
A.3 Column loads ($mg\ m^{-2}$) of $HNO_{3(g)}$, fine and coarse particulate NO_3^- simulated by additional mechanisms, averaged for 2018. 172
A.4 Surface concentrations ($\mu g\ m^{-3}$) of $NH_{3(g)}$, fine and coarse particulate NH_4^+ simulated by the different mechanisms, averaged for 2018. 173
A.5 Column loads ($mg\ m^{-2}$) of $NH_{3(g)}$, fine and coarse particulate NH_4^+ simulated by different mechanisms, averaged for 2018. 174
A.6 Zonal average concentrations ($\mu g\ m^{-3}$) of $NH_{3(g)}$, fine and coarse particulate NH_4^+ simulated by the different mechanisms, averaged for 2018. . . 175
A.7 Surface concentration ($\mu g\ m^{-3}$) of $SO_{2(g)}$, fine and coarse particulate SO_4^{2-} simulated by the different mechanisms, averaged for 2018. 176
A.8 Column load ($mg\ m^{-2}$) of $SO_{2(g)}$, fine and coarse particulate SO_4^{2-} simulated by the different mechanisms, averaged for 2018. 177
A.9 Zonal average concentration ($\mu g\ m^{-3}$) of $SO_{2(g)}$, fine and coarse particulate SO_4^{2-} simulated by the different mechanisms, averaged for 2018. . . . 178
A.10 Dust average column load ($mg\ m^{-2}$) for 2018. 179
A.11 Sea salt average column load ($mg\ m^{-2}$) for 2018. 179

A.12 Yearly surface concentration evaluation for Asia, Europe and North-Central America continents. Species are in rows and continents in columns. Black solid dots and crosses represent observational mean and median, respectively. Error bars are the interquantile 0.25 to 0.75 distance. Coloured lines represent medians obtained from the most representative configurations. Blue shade is the interquantile 0.25 - 0.75 distance for the DBCLL_du-ssAlk simulation. Observational PM_{10} from EANET (Asia) and US-EPA-CASTNET (North America) refers to total particle concentration, while GHOST data (Europe) is limited to PM_{10}. (Continues in the next page) 181

A.12 (Continuation) Yearly surface concentration evaluation for Asia, Europe and North-Central America continents. Species are in rows and continents in columns. Black solid dots and crosses represent observational mean and median, respectively. Error bars are the interquantile 0.25 to 0.75 distance. Coloured lines represent medians obtained from the most representative configurations. Blue shade is the interquantile 0.25 - 0.75 distance for the DBCLL_du-ssAlk simulation. Observational PM_{10} from EANET (Asia) and US-EPA-CASTNET (North America) for SO_4^{2-} refers to total particle concentration, while GHOST data (Europe) is limited to PM_{10}. 182

A.13 Stations used in the observational evaluation for each species from the main text Fig.5.4 and Supplement Fig. A.12. 183

A.14 Observational evaluation of gas and particulate species of additional sensitivity experiments. Black solid dots and crosses represent monthly mean and median of observations, respectively. Colour lines represent each configuration's monthly median surface concentrations over observational points. Error bars are the observational interquantile 0.25 to 0.75 distance. For the Total NO_3 modes, data from Europe, Asia and North-Central America has been averaged, despite data from Asia and North-Central America refers to total particle concentration, while data from Europe is limited strictly to $10\mu m$ particle diameter. 184

A.15 Observational evaluation for oxidized ($HNO_{3(g)} + NO_3^-$, left) and reduced ($NH_{3(g)} + NH_4^+$, right) nitrogen species. 194

A.16 Stations employed for the observational evaluation of oxidized ($HNO_{3(g)} + NO_3^-$) and reduced ($NH_{3(g)} + NH_4^+$) nitrogen species. 194

B.1 Annual accumulated dust emissions (top row) and mean dust optical depth (bottom row) for the control (uncorrected) simulation, the analysis (assimilated) simulation, and their ratios. 195
B.2 Evaluation of assimilated dust optical depth against AERONET observations. Six-hourly correlation (top) and root mean square error (RMSE, bottom) of modeled versus AERONET dust optical depth for the control (left), analysis (center), and their difference (right). 196
B.3 Location and characteristics of observational $CaCO_3$ datasets. Geographical distribution, size range, and measured $CaCO_3$ content of the in situ observations used for model evaluationPerlwitz et al. (2015b). Observations span multiple campaigns and decades. 196
B.4 Relative average column differences for 2018 between source-based and globally averaged $CaCO_3$ representations (SB–AVG) for $CaCO_3$, SIA species, and SSA. White color gridcells refer to differences that are non-statistically significant ($p > 0.05$). 197
B.5 Average column differences for 2018 in precursor gases $HNO_{3(g)}$, $NH_{3(g)}$, and $SO_{2(g)}$ between source-based (SB) and globally averaged (AVG) simulations. 197
B.6 Average surface concentrations for 2018 of Ca^{2+}, NO_3^-, SO_4^{2-}, and NH_4^+ simulated using source-based EMIT mineralogy. 198
B.7 Average relative differences for 2018 in surface Ca^{2+}, NO_3^-, SO_4^{2-}, NH_4^+, and aerosol pH between EMIT source-based (EMIT(SB)) and globally averaged (EMIT(AVG)) mineral distributions. White color gridcells refer to differences that are non-statistically significant ($p > 0.05$). 199
B.8 pH from the arithmetic mean obtained with EMIT(SB) (a-c), calculating the temporal mean of instantaneous pH values for the studied period. . 201
B.9 pH from the proton activity mean obtained with EMIT(SB) (a-c) and differences with EMIT(AVG) (d-f), calculating the temporal mean of instantaneous activity values for the studied period. 201
B.10 Distribution of p-values for the differences in total NO_3^- between source-based and globally-averaged configurations. 202
B.11 Global evaluation of total NO_3^- monthly means against global observations over stations with statistically-significant differences ($p<0.05$), shown as red triangles in Fig. 6.6*a*. Coloured shading and error bars represent the standard deviation of the model and observations, respectively. 202

B.12 Global evaluation of PM2.5NO_3^- monthly means against global observations, with no restriction regarding the statistical significance. Coloured shading and error bars represent the standard deviation of the model and observations, respectively. 203

C.1 Refractive indexes for each species used for the calculation of aerosol optical properties in the offline package (Sect. 7.2.2). Solid red lines represent real imaginary index, and dotted blue ones do for the imaginary index. 205

C.2 Column loads of secondary inorganic aerosol (SIA) species when not accounting for coarse SIA formation. 206

C.3 Change in burdens of secondary inorganic aerosol (SIA) species when using EMIT source-based $CaCO_3$ distribution without and with coarse SIA formation (fTEQ-DBCLL). 207

C.4 Relative differences (%) in aerosol optical depth (AOD) and single scattering albedo (SSA) between source-based (SB) and globally average (AVG) approaches. As in Fig.7.10, differences isolating the effect of $CaCO_3$ and the resulting SIA species (*a1-a3* and *c1-c3* for AOD and SSA, respectively), and including additional mineralogical variations (*b1-b3* and *d1-d3* for AOD and SSA, respectively). *Total* refers to particles with $D < 20\mu m$. 208

C.5 Differences in secondary inorganic aerosol (SIA) column loads between simulations using $CaCO_3$ from Journet et al. (2014) (JOUR) and Claquin et al. (1999) (CLAQ) mineral datasets, and the case using EMIT $CaCO_3$. *Total* refers to particles with $D < 20\mu m$ 209

C.6 Differences in particulate nitrate column loads between simulations using $CaCO_3$ from Journet et al. (2014) (JOUR) and Claquin et al. (1999) (CLAQ) mineral datasets, and the case using EMIT $CaCO_3$. *Total* refers to particles with $D < 20\mu m$ 209

C.7 Relative change (%) in AOD when using source-based mineral data from alternative mineral atlases (JOUR and CLAQ) compared to EMIT. *Total* refers to particles with $D < 20\mu m$ 210

C.8 Relative change (%) in SSA when using source-based mineral data from alternative mineral atlases (JOUR and CLAQ) compared to EMIT. *Total* refers to particles with $D < 20\mu m$ 210

C.9 Differences in AOD derived from dust bulk minerals (i.e. no condensables included) between simulations using Journet et al. (2014) (JOUR) and Claquin et al. (1999) (CLAQ) mineral datasets, compared with the case using EMIT. *Total* refers to particles with $D < 20\mu m$ 211
C.10 Differences in SSA derived from dust bulk minerals (i.e. no condensables included) between simulations using Journet et al. (2014) (JOUR) and Claquin et al. (1999) (CLAQ) mineral datasets, compared with the case using EMIT. *Total* refers to particles with $D < 20\mu m$ 212

List of Tables

1.1 Neutralization reactions of $HNO_{3(g)}$ and $H_2SO_{4(g)}$ by $NH_{3(g)}$. 12
1.2 Reactions between dust alkaline minerals, and $HNO_{3(g)}$ and $H_2SO_{4(g)}$. . . 13
1.3 Reactions of NaCl from sea salt with $HNO_{3(g)}$ and $NH^+_{4(aq)}$. 16

3.1 Description of the three datasets implemented in MONARCH for this Thesis. 48
3.2 Total emissions (anthropogenic, biogenic and biomass burning) for 2018 used in this Thesis. 54

4.1 Density (ρ), volumetric diameter ($\varnothing$ vol.), geometric mean effective diameter ($\varnothing$ eff.), geometric mean effective diameter ranges ($\varnothing$ range), and $PM_{2.5}$ and PM_{10} fractions of each bin of the studied species. 58
4.2 ISORROPIA-II cases 61
4.3 Heterogeneous reactions implemented in MONARCH. Dust and sea salt particles are referred as *DU* and *SS*, respectively. 63
4.4 Sequence of reactions and calculations performed for each scheme (rows). In columns, the sequence order (tN) and the gas/aerosol size mode of each process is indicated. Dust and sea salt particles are referred as *DU* and *SS*, respectively, and condensation is abbreviated as *Cond.*. Fine mode is formed from reactions with dust and sea salt particles with $0.2 < D < 2.5\mu m$, and coarse ones with $2.5 < D < 20\mu m$ for dust and $2.5 < D < 30\mu m$ for sea salt. 69

5.1 The sensitivity experiments conducted in this study and the processes performed in each one of them (green boxes). *Fine TEQ* and *Coarse TEQ* refer to the respective calculations of the TEQ for the fine ($0.2 < D < 2.5\mu m$) and coarse modes of dust ($2.5 < D < 20\mu m$) and sea salt ($2.5 < D < 30\mu m$), referred to as *DU* and *SS*, respectively. *Coarse DU UPTK* and *Coarse SS UPTK* indicate the irreversible UPTK of $HNO_{3(g)}$ on coarse dust and sea salt, respectively. Alkalinity is denoted as *Alk.* and for the dust alkalinity column, the alkalinity derived from the Journet et al. (2014) and Claquin et al. (1999) simulations is indicated by J and C, respectively. 76

5.2 Correlation coefficients, bias (model - observations, $\mu g\ m^{-3}$), and root-mean-square error (RMSE, $\mu g\ m^{-3}$) of each configuration's median with respect to the median of the observations, corresponding to the time series shown in Fig. 5.4. 89

5.3 Results for fine ($D < 2.5\mu m$), coarse ($2.5 < D < 10\mu m$), and total ($D < 20\mu m$) particulate NO_3^- obtained using the heterogeneous chemistry mechanisms studied for 2018. Results from the literature references are reported in the second half of the table: the average of all the participating models in the intercomparison AeroCom phase III nitrate experiment for 2008 (*AeroCom*), specifying their standard deviation (*SD AeroCom*), results from the GMI model (*GMI*, using an HYB approach with UPTK reactions on dust and sea salt), and results from the EMAC model (*EMAC 2008*, using a similar approach to DBCLL_du-ssAlk). Also using the EMAC model, results obtained by the Karydis et al. (2016) study are reported as *EMAC 2005-2008*. Results from models using a similar approach to HYB_du-ssUPTK are reported as *IFS* for Rémy et al. (2022), *LMDz-INCA* for Hauglustaine et al. (2014), and *Met Office UM* for Jones et al. (2021). 100

A.1 Globally-averaged fractions (0 to 1) of the minerals attributed to each bin from the Claquin et al. (1999) mineral database. The respective references for the assumed solubility of each mineral are: References: 1. Assumed reactive because relatively soluble in acids (Webmineral 2008f). 2. Assumed reactive because relatively soluble in acids (Nutting 1941; 1932). 3. Assumed nonreactive because predominantly containing Al and Si (Yang 2008). 4. Assumed reactive because highly soluble (Usher et al. 2003, Krueger et al. 2004, Hodzic et al. 2006). 5. Assumed nonreactive because not soluble (Usher et al. 2003). 6. Assumed reactive because relatively soluble in acids (Blum 1994, Mindat.org b). 7. Assumed nonreactive because iron is not considered in ISORROPIA-II (National Center for Biotechnology Information 2024a, Weast 1980). 8. Assumed nonreactive because poorly soluble in water and soluble only in high acidity solutions (Zhang and Muhammed 1989, National Center for Biotechnology Information. PubChem Compound Database 2024a, Krueger et al. 2004, Hodzic et al. 2006). 165

A.2 The NVC content from globally-averaged mineralogy of Claquin et al. (1999) assumed for each size bin, derived from those minerals assumed to be soluble in water (Table A.1). The respective references for the ionic composition of each mineral and molar masses are: 1. Webmineral (2008f) 2. Nutting (1941; 1932) 3. Webmineral (2008a) 4. Webmineral (2008b) 5. Webmineral (2008e) 6. Webmineral (2008c), National Center for Biotechnology Information. PubChem Compound Database (2024a) 7. Webmineral (2008d), Hulett and Allen (1902) 166

A.3 Globally-averaged fractions (0 to 1) of the minerals attributed to each bin from the Journet et al. (2014) mineral database. The respective references for the assumed solubility of each mineral are: 1. Assumed reactive because relatively soluble in acids (Webmineral 2008f) 2. Assumed reactive because relatively soluble in acids (Nutting 1941; 1932) 3. Assumed nonreactive because predominantly containing Al and Si (Yang 2008). 4. Assumed nonreactive because not soluble in water (Britannica, The Editors of Encyclopaedia 2018, Mindat.org a). 5. Assumed nonreactive because not soluble (Huggett 2015, Schulze 2005, Bleam 2017). 6. Assumed reactive because relatively soluble in acids (Blum 1994, Mindat.org b). 7. Assumed nonreactive because not soluble (Usher et al. 2003). 8. Assumed reactive because highly soluble (Usher et al. 2003, Krueger et al. 2004, Hodzic et al. 2006). 9. Assumed nonreactive because iron is not considered in ISORROPIA-II (National Center for Biotechnology Information 2024a, Weast 1980). 10. Assumed nonreactive because not soluble, although lacking information if soluble in acids. (Essington et al. 2005, National Center for Biotechnology Information. PubChem Compound Database 2024b). 11. Assumed nonreactive because poorly soluble in water and soluble only in high acidity solutions (Zhang and Muhammed 1989, National Center for Biotechnology Information. PubChem Compound Database 2024a, Krueger et al. 2004, Hodzic et al. 2006). 12. Assumed nonreactive because non soluble (National Center for Biotechnology Information 2024b). 167

A.4 The NVC content from globally-averaged mineralogy of Journet et al. (2014) assumed for each size bin, derived from those minerals assumed to be soluble in water (Table A.3). The respective references for the ionic composition of each mineral and molar masses are: 1. Webmineral (2008f) 2. Nutting (1941; 1932) 3. Webmineral (2008a) 4. Webmineral (2008b) 5. Webmineral (2008e) 6. Webmineral (2008c), National Center for Biotechnology Information. PubChem Compound Database (2024a) 7. Webmineral (2008d), Hulett and Allen (1902) 168

A.6 Correlation coefficients, bias ($\mu g\ m^{-3}$) and root mean square error (rmse, $\mu g\ m^{-3}$) of additional sensitivity experiments. The evaluation corresponds to the configurations' median with respect to the median of observations, corresponding to the timeseries shown in Fig. A.14. 185

A.5 GHOST quality flags used for the observational evaluation. 186

A.7 Results for gas $HNO_{3(g)}$ obtained with the studied heterogeneous chemistry mechanisms. Results from the literature references are reported at the end of the table: The average of all the participating models in the intercomparison AeroCom phase III nitrate experiment for 2008 (*AeroCom*), specifying their standard deviation (*STD AeroCom*), results from the GMI model (*GMI*, using a similar HYB approach with UPTK reactions on dust and SS), and results from the EMAC model (*EMAC 2008*, using a similar approach to DBCLL_du-ssAlk). Also using the EMAC model, results obtained by the Karydis et al. (2016) study are reported as *EMAC 2005-2008*. Results from models using a similar approach to HYB_du-ssUPTK are reported as *IFS* for Rémy et al. (2022), *LMDz-INCA* for Hauglustaine et al. (2014) and *MetOffice UM* for Jones et al. (2021). 187

A.8 Results for gas $NH_{3(g)}$ obtained with the studied heterogeneous chemistry mechanisms. Results from the literature references are reported at the end of the table: The average of all the participating models in the intercomparison AeroCom phase III nitrate experiment for 2008 (*AeroCom*), specifying their standard deviation (*STD AeroCom*), results from the GMI model (*GMI*, using a similar HYB approach with UPTK reactions on dust and SS), and results from the EMAC model (*EMAC 2008*, using a similar approach to DBCLL_du-ssAlk). Also using the EMAC model, results obtained by the Karydis et al. (2016) study are reported as *EMAC 2005-2008*. Results from models using a similar approach to HYB_du-ssUPTK are reported as *IFS* for Rémy et al. (2022), *LMDz-INCA* for Hauglustaine et al. (2014) and *MetOffice UM* for Jones et al. (2021). 188

A.9 Results fine, coarse and total particulate NH_4^+ obtained with the studied heterogeneous chemistry mechanisms. Results from the literature references are reported at the end of the table: The average of all the participating models in the intercomparison AeroCom phase III nitrate experiment for 2008 (*AeroCom*), specifying their standard deviation (*STD AeroCom*), results from the GMI model (*GMI*, using a similar HYB approach with UPTK reactions on dust and SS), and results from the EMAC model (*EMAC 2008*, using a similar approach to DBCLL_du-ssAlk). Also using the EMAC model, results obtained by the Karydis et al. (2016) study are reported as *EMAC 2005-2008*. Results from models using a similar approach to HYB_du-ssUPTK are reported as *IFS* for Rémy et al. (2022), *LMDz-INCA* for Hauglustaine et al. (2014) and *MetOffice UM* for Jones et al. (2021). 189

A.10 Results for $SO_{2(g)}$, and fine, coarse and total particulate SO_4^{2-} obtained with the studied heterogeneous chemistry mechanisms. Results from the literature references are reported at the end of the table: The average of all the participating models in the intercomparison AeroCom phase III nitrate experiment for 2008 (*AeroCom*), specifying their standard deviation (*STD AeroCom*), results from the GMI model (*GMI*, using a similar HYB approach with UPTK reactions on dust and SS), and results from the EMAC model (*EMAC 2008*, using a similar approach to DBCLL_dussAlk). Also using the EMAC model, results obtained by the Karydis et al. (2016) study are reported as *EMAC 2005-2008*. Results from models using a similar approach to HYB_du-ssUPTK are reported as *IFS* for Rémy et al. (2022), *LMDz-INCA* for Hauglustaine et al. (2014) and *MetOffice UM* for Jones et al. (2021). 190

A.11 Nitrogen burdens (TgN) for each experiment and species. 191

B.1 Global budgets of fine ($D < 2.5\mu m$), coarse ($2.5 < D < 10\mu m$), and total ($D < 20\mu m$) NO_3^-, wet and dry deposition, production/loss, and atmospheric lifetime for all experiments (CLAQ(SB), JOUR(SB), EMIT(SB), EMIT(AVG)). Results are compared with the literature (Bian et al. 2017, Karydis et al. 2016, Rémy et al. 2022; 2024). 200

B.2 Summarized description of the performed mineralogical sensitivity experiments, with varied representations of $CaCO_3$ emission fractions —either source-based (SB) or globally averaged (AVG)— from the CLAQ, JOUR, and EMIT datasets. 203

B.3 Definition of geographical boundaries (latitude–longitude ranges) for analysis of nitrate formation events. 203

Acronyms

AeroCom AEROosol Comparisons between Observations and Models international initiative project

AeroNet AErosol RObotic NETwork of ground-based sun photometers

AOD Aerosol optical depth

AVG Globally-averaged calcite method

AWC Aerosol Water Content

BC Black carbon

BSC Barcelona Supercomputing Center

CAMS Copernicus Atmosphere Monitoring Service

CCN Cloud Condensation Nuclei

CLAQ Global mineralogy atlas from Claquin et al. (1999)

D Particle diameter

DBCLL Double-call method

DMS DiMethyl Sulfide

DMT Dynamic mass transfer calculation

DU Mineral dust aerosol

EMAC Global atmospheric multiphase chemistry–climate model, integrated by the Modular Earth Submodel System (MESSy) and the European Centre – Hamburg general circulation model (ECHAM5).

EMIT Earth Surface Mineral Dust Source Investigation imaging spectrometer aboard the International Space Station launched by NASA in 2022

fTEQ Partitioning of semivolatile inorganic species method neglecting coarse formation based on a Thermodynamic Equilibrium model

GHOST Globally Harmonised Observations in Space and Time dataset of measurements of atmospheric composition at the surface

GEOS-Chem Global 3-D model of atmospheric chemistry driven by meteorological input from the Goddard Earth Observing System (GEOS) of the NASA Global Modeling and Assimilation Office

HERMESv3 High Elective Resolution Modelling Emission System version 3

HERMESv3_GR HERMESv3 Global—Regional emission processing system

HPC High Performance Computing

HYB Hybrid method

IFS Integrated Forecasting System, used to produce the Copernicus Atmosphere Monitoring Service (CAMS) atmospheric composition forecasts

IFS-COMPO Extension of IFS to represent aerosols with the IFS(AER) model, as well as trace and greenhouses gases

IPCC Intergovernmental Panel on Climate Change

JOUR Global mineralogy atlas from Journet et al. (2014)

MONARCH Multiscale Online Nonhydrostatic AtmospheRe CHemistry model

NMMB Nonhydrostatic Multiscale Model on the B-grid

NMMB/BSC-CTM Nonhydrostatic Multiscale Model on the B-grid / Barcelona Supercomputing Center - Chemical Transport Model (former acronym of the MONARCH model)

NVCs Non-Volatile Cations in aerosols

OM Organic matter aerosol

$\boldsymbol{PM_{10}}$ Particulate matter with an aerodynamic diameter less than or equal to 10 μm

$\boldsymbol{PM_{2.5}}$ Particulate matter with an aerodynamic diameter less than or equal to 2.5 μm

$\boldsymbol{PM_{2.5-10}}$ Particulate matter with an aerodynamic diameter between 2.5 to 10 μm (representing the coarse fraction of PM10)

SB Source-based calcite method

SIA Secondary Inorganic Aerosol

SSA Single-scattering albedo

TEQ Thermodynamic equilibrium calculation

TOA Top of the atmosphere

UPTK First-order irreversible uptake calculation

VSWIR Visible to Short Wavelength Infrared

WHO World Health Organization

WMO World Meteorological Organization

1 Introduction

1.1 Motivation

The Earth's atmosphere is a complex mixture of gases and suspended particles that continuously interact with each other. These particles, known as *aerosols*, are composed of a wide range of solid and liquid materials and originate from both natural and anthropogenic sources, including volcanic eruptions, sea spray, wind-driven soil erosion, fossil fuel combustion, biomass burning, and agricultural and industrial activities.

On a global scale, sea salt and mineral dust are the most abundant atmospheric aerosols by mass (Textor et al. 2006, Kok et al. 2021). Mineral dust consists of windblown inorganic particles emitted from arid and semi-arid regions, such as deserts and other exposed sedimentary surfaces, and is composed primarily of silicates, carbonates, and iron (Fe) bearing minerals (Claquin et al. 1999, Querol et al. 2019, Kandler et al. 2007). Once emitted, dust particles can remain airborne for days to weeks and be transported over thousands of kilometers before deposition.

During transport, dust particles interact with multiple components of the Earth system, including solar radiation, clouds, and a wide range of atmospheric chemical species (Usher et al. 2003, Miller et al. 2014, Di Biagio et al. 2019, Kok et al. 2023). These interactions govern the role of dust in atmospheric chemistry, air quality, and climate. However, they are intrinsically complex and remain poorly quantified, partly due to persistent uncertainties in dust emissions, size distribution, particle shape, optical properties, and mineralogical composition (Perlwitz et al. 2015b, Li et al. 2024b, Obiso et al. 2024).

Among the many interactions involving dust, its chemical reactions with gas-phase species are among the least well constrained (Bian et al. 2017). These processes, referred to as *heterogeneous chemical reactions*, involve interactions between gases and solid or liquid particle surfaces (Usher et al. 2003). Dust heterogeneous chemistry is believed to be a dominant pathway for the formation of *secondary inorganic aerosols* (SIA), especially particulate nitrate (NO_3^-), and an important contributor to particu-

late ammonium (NH_4^+) and sulfate (SO_4^{2-}) at the global scale (Karydis et al. 2016). Through these pathways, dust can strongly influence gas–aerosol partitioning of acidic species and ammonia ($NH_{3(g)}$), with direct implications for air quality, nitrogen (N) deposition, and aerosol radiative effects, especially in regions affected by dust intrusions (Wang et al. 2015; 2017).

At the global scale, the large atmospheric burden of mineral dust implies that heterogeneous chemistry on dust surfaces may play a significant role in shaping atmospheric composition and climate. However, the complexity of dust interactions with atmospheric constituents, together with uncertainties in emissions, mineralogy, size partitioning, and total dust budgets, presents major obstacles for accurately representing these processes in atmospheric models (Kok et al. 2023, Milousis et al. 2025).

To manage this complexity while maintaining computational efficiency, models that include dust heterogeneous chemical reactions rely on substantial parameterizations and simplifications to describe both dust properties and gas–particle interactions (Usher et al. 2003, Bian et al. 2017). A common simplification is the neglect of regional variability in dust mineral composition (Claquin et al. 1999, Journet et al. 2014, Kandler et al. 2020), with dust often treated as a chemically homogeneous aerosol (Bian et al. 2017). Despite extensive efforts to improve heterogeneous chemistry schemes, models continue to diverge substantially in their predictions of secondary aerosol formation and associated gas-phase species (Fairlie et al. 2010, Hauglustaine et al. 2014, Paulot et al. 2016, Zakoura and Pandis 2018, Luo et al. 2019, Jones et al. 2021, Rémy et al. 2022, Wu et al. 2025), and frequently show significant biases when compared to observations (Bian et al. 2017, Wu et al. 2025).

Nevertheless, dust heterogeneous chemistry has been identified as a promising avenue to explain persistent discrepancies between modeled and observed atmospheric composition (Usher et al. 2003). Improving its representation has the potential to reduce biases in NO_3^-, NH_4^+, and SO_4^{2-} simulations, refine aerosol acidity estimates, and ultimately enhance predictions of air quality and aerosol–climate interactions (Karydis et al. 2021, Milousis et al. 2024, Li et al. 2024b, Milousis et al. 2025).

In this context, this Thesis aims to advance the representation of dust heterogeneous chemistry in atmospheric models by systematically investigating the combined roles of chemical parameterizations and dust mineralogical composition. By integrating multiple heterogeneous chemistry schemes within a global modeling framework and, for the first time, exploiting observationally constrained mineralogical information from recent spaceborne retrieved data, this work seeks to clarify how dust alkalinity, mineral composition, and size-resolved chemistry control SIA formation, aerosol acidity, and optical properties. Through detailed model–observation comparisons, this Thesis addresses key

sources of uncertainty in current models and provides a process-based foundation for improving the simulation of dust–chemistry interactions and their implications for air quality and climate.

1.2 Airborne mineral dust

1.2.1 Sources, transport and deposition

Aeolian mineral dust is windblown from arid and semi-arid surfaces, which represent approximately 33% of the Earth surface (Charlson and Heintzenberg 1995). As a consequence, mineral dust reaches approximately 40% of the total dry aerosol mass globally in the atmosphere, and between 70% and 80% if sea salt aerosol is not considered (Boucher et al. 2013, Kok et al. 2017; 2018, Adebiyi and Kok 2020), standing as one of the most abundant aerosols (Kok et al. 2018; 2023).

Dust emissions are dependent on the intrinsic characteristics of their sources, such as aridity, texture and soil particles size. However, additional variables linked to meteorology and land use are also relevant, such as soil vegetation cover, humidity and erosion rates (Shao et al. 2011, Klose et al. 2019, Kok et al. 2021).

Most of the dust is originally produced by wind erosion (i.e. *natural dust*), mainly originated in the Northern Hemisphere (90%). Its main source area is what is called the *dust belt*: A latitudinal range that extends from the Atlantic coast of North Africa in the Sahara to central Asia, and through the Middle East (Prospero et al. 2002, Ginoux et al. 2012, Kok et al. 2021, Gonçalves Ageitos et al. 2023), comprising the principal dust deserts, namely the Sahara, Sahel, Arabian, Taklamakan and Gobi (Huneeus et al. 2011, Ginoux et al. 2012, Shi et al. 2021). Additionally, other important dust sources have been identified beyond these regions, such as the Mojave desert in North America (González-Romero et al. 2024a), the Icelandic deserts (González-Romero et al. 2024b), and additional high-latitudinal (Bullard et al. 2016) and South Hemisphere sources from Australia (De Deckker 2019), Patagonia (Kim et al. 2024), and southern Africa (Cosentino et al. 2021). Kok et al. (2021) performed an estimation of the relative contribution of the different dust sources, with North African dust representing 55% of total dust emissions and 30% of atmospheric dust burden, while dsut from Asia accounts for 40% of total dust burden, with East Asia alone providing the 11% of global dust loading, close to the contribution of America, Australia, and southern Africa together (10%).

In addition to natural dust emissions, dust also originates from the wind erosion of anthropogenically-disturbed sources (e.g., cropland, pastures, urban areas, farmlands, and grasslands), and from resuspension of road dust by vehicle traction, all referred to as

anthropogenic and land-use dust. The dust fraction that originates from anthropogenic sources is estimated to account for approximately 25 to 29% of total emitted dust (Huang et al. 2015, Wang et al. 2022), although this percentage varies across regions. For instance, it is estimated that only 8% of Saharan dust has an anthropogenic origin, while this percentage increases to 75% for Australia, and it might represent 25% of the global dust load (Ginoux et al. 2012).

Overall, both natural and anthropogenic dust emissions depend on seasonality (Ginoux et al. 2012, Querol et al. 2019, Shi et al. 2021, Kok et al. 2021), on specific local drivers (i.e. topography Kok et al. (2021)), on soil characteristics (i.e. size Mahowald et al. (2014)) of each emission area (Shi et al. 2021, González-Romero et al. 2024a), and even on the epoch, with some recent studies proposing an increasing trend in dust emissions with respect to the pre-industrial period (Mahowald et al. 2010, Kok et al. 2023, Liu et al. 2024). For instance, dust emission fluxes could be changing with time due to the expansion of agricultural and pasture land, that reduce surface vegetation cover, enhancing dust particles suspension (Cowie et al. 2013, Ginoux et al. 2012, Kok et al. 2023), in addition to changes in precipitation patterns (Pendergrass et al. 2017), and land use such as mining, transport, and deforestation (Kok et al. 2023). The impact of anthropogenic climate change on dust loading is still very uncertain, with estimations widely ranging from -20% to +60% (Mahowald and Luo 2003, Mahowald et al. 2005, Mahowald 2007, Stanelle et al. 2014, Kok et al. 2023), due to complex feedback loops such as carbon fertilization that might enhance vegetation cover around desert areas (Mahowald 2007, Rodriguez-Caballero et al. 2022).

Due to the multiple factors affecting dust emissions, there is still significant uncertainty in its flux estimation in atmospheric models. For instance, Gliß et al. (2021) states that dust emissions range from 1200 to 3100 Tg/year, the global dust model intercomparison in AeroCom phase I project Huneeus et al. (2011) reports a median of 1440 Tg/year across models, with a 62% standard deviation, and Kok et al. (2021) significantly enhances the estimate to 3400-9100 Tg/year, considering dust particles up to 20 μm. These disagreements between atmospheric models, originated from discrepancies like dust size representation (Adebiyi and Kok 2020) or the emission mechanisms (Ginoux et al. 2001, Klose et al. 2021), have been a persistent handicap to accurately reproduce the atmospheric cycle of dust in models (Shao et al. 2011).

Dust particles can be classified into three categories that have diverse size ranges: clay, diameter (D) up to $2\mu m$, silt, D from 2 to $63\mu m$, and sand, D $\sim$75–$500\mu m$ (Shao et al. 1993, Kok et al. 2012). Once emitted, dust can last from days to weeks in the atmosphere (Fig. 1.1), with an estimated average annual lifetime of approximately 3 days (Kok et al. 2021, Gonçalves Ageitos et al. 2023). This lifetime is highly dependent

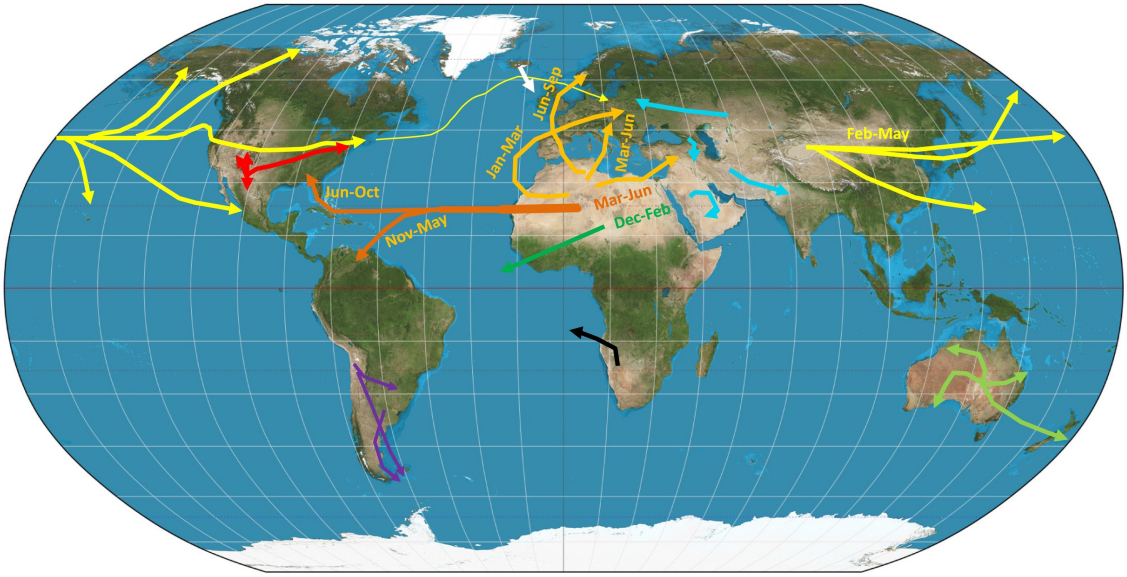

Figure 1.1: Main atmospheric transport pathways of airborne mineral dust. Source: Querol et al. (2019) and Griffin (2007).

on particle size, with fine dust (geometric $D < 2.5\mu m$) lasting longer in the atmosphere (Mahowald et al. 2014), while coarse (geometric D from 2.5 to $10\mu m$), super-coarse ($10 < D < 20\mu m$), and giant dust ($D > 20\mu m$) deposit much more faster (Kok et al. 2017, Adebiyi and Kok 2020, Adebiyi et al. 2023). Current estimates of the average annual dust atmospheric burden range from 14 to 28 Tg if accounting for dust below $D < 20\mu m$ (Shao et al. 2011, Adebiyi and Kok 2020, Gonçalves Ageitos et al. 2023). However, we have to consider the recent estimations of coarse and super-coarse dust missing from the atmosphere.

In fact, Adebiyi and Kok (2020) and Meng et al. (2022) indicate that most atmospheric models are missing over 75% of coarse dust, which might actually have longer lifetimes and traveling distances than those typically estimated in atmospheric models. This might lead to a 40% underestimation of total dust burden (Adebiyi and Kok 2020). Overall, approximately 50% of total dust burden is thought to belong to the coarse size dust, increasing up to to 85% if super-coarse dust is included. Together, coarse and super-coarse dust account for approximately 13 to 17 Tg of dust atmospheric burden, while fine dust estimates range from 1 to 15 Tg (Adebiyi and Kok 2020, Rémy et al. 2022, Adebiyi et al. 2023).

While suspended in the atmosphere, dust can travel thousands of kilometers and distribute around the globe (Shao 2001, Adebiyi et al. 2023). Its transport strongly depends on particle size: coarse dust generally remains closer to its emission sources than fine dust because of its shorter atmospheric residence time (Seinfeld and Pandis 2006, Shao 2008a;b). From these source regions, dust is often transported zonally by

tropical winds across the Atlantic, Pacific, and central Asia (Bristow et al. 2010, Shao et al. 2011, Ginoux et al. 2012, Liu et al. 2022b), and by mid- and high-latitude winds across the northern and southern hemispheres (Bullard et al. 2016, Kim et al. 2024). Along these transport pathways, dust frequently passes over industrialized and urban areas, where it mixes with anthropogenic pollutants and undergoes chemical reactions that modify air quality and atmospheric composition, as discussed in Section 1.3. Under humid conditions, mixing with anthropogenic pollutants such as NO_3^-, organic matter (OM), and SO_4^{2-} promotes the *hygroscopic growth* of dust: solid dust particles condense water vapor and other gas-phase species, forming a liquid coating around the solid core. This process increases particle size and mass, while effectively lowering their bulk density, thereby altering particle lifetime, hygroscopicity, as well as their chemical and optical properties (Usher et al. 2003, Krueger et al. 2003; 2004, Fountoukis and Nenes 2007, Crowley et al. 2010, Yang et al. 2018).

At the end of its atmospheric lifetime, deposited dust also affects biogeochemical cycles both on ocean and continental areas (Mahowald et al. 2014, Li et al. 2016, Bergas-Massó et al. 2023). Desert dust provides important amounts of metals and other elements to ecosystems, particularly Fe and phosphorous (P). These micronutrients are scarce in some areas, such as remote oceanic regions and the Amazon rain-forest. When deposited, they act as fertilizers that enhance the local N fixation and carbon dioxide (CO_2) uptake rates (Meskhidze et al. 2003, Bristow et al. 2010, Nenes et al. 2011). For instance, Bristow et al. (2010) estimated that 6.5 Tg of Fe and 0.12 Tg of P are emitted annually from the Bodélé Depression in Africa, mainly deposited in the Amazon and equatorial Atlantic ocean. Myriokefalitakis et al. (2022) estimated total Fe emissions coming from mineral dust to be between 48 and 59 Tg per year. However, not all this Fe is biologically available for ecosystems. Only dissolved Fe (dFe) acts as a fertilizer when deposited. The atmospheric burdens of dFe are estimated to be only 0.53 Tg, mainly produced from aerosol acidification processes (Myriokefalitakis et al. 2022). The deposition of Fe in the ocean leads to an enhancement of carbon (C) uptake by ocean microbiology, estimated in 4 ppm of CO_2 additionally absorbed by the global oceans during the 20th century (Mahowald et al. 2010). However, the deposition rates and the chemical pathways through which dFe interacts with oceanic biogeochemical cycles are still highly uncertain and dependent on climate change and socioeconomic evolution (Hamilton et al. 2023). Bergas-Massó et al. (2023) highlights the strong dependence of global dFe deposition rates on the Shared Socioeconomic Pathway (SSP), ranging from -35% for SSP 1-2.6 to +40% for SSP 3–7.0, althogh they estimate that - regardless of the socioeconomic evolution - dFe deposition is going to increase over the equatorial Pacific ocean and decrease over the Southern ocean during the next century. The conversion

rates of insoluble Fe from dust minerals (e.g. hematite) to bioavailable dFe strongly depend on various factors, such as sunlight, temperature, pH (see Section 1.4.4), and organic bonds present on dust aerosol (Zhu et al. 1993, Mexico et al. 2007, Hamer et al. 2003).

1.2.2 Mineralogical composition

Mineralogical composition of dust refers to the mixture and relative abundance of minerals that constitute airborne mineral dust particles. Airborne dust particles inherit the mineral composition of the surface soil they originated from, composed of weathered parent soil particles windblown from the surface (Gomes and Gillette 1993, Claquin et al. 1999, Journet et al. 2014, Karydis et al. 2016, Gonçalves Ageitos et al. 2023). Therefore, regional differences in geology and weathering potential (e.g. dry or wet locations) determine dust mineral composition (Scheuvens et al. 2013).

Northern African dust is subject to marked regional variations in mineralogy. For instance, while the northern Sahara desert is rich in limestones, carbonate soils (i.e. $CaCO_3$), quartz (SiO_2), illite, chlorite, palygorskite, and montmorillonite, the abundance of such minerals decreases towards the equator, with the Sahel Region being rich in kaolinite from feldspar hydrolysis (Caquineau et al. 2002) and hematite (Fe_2O_3) (Guerzoni and Chester 1996, Sokolik and Toon 1999, Claquin et al. 1999, Rad et al. 2012, Usher et al. 2003, Formenti et al. 2014). Comparatively, central Asia has high concentrations of quartz, illite, and chlorite (Gomes and Gillette 1993, Kandler et al. 2020). Diversity in mineralogy leads to differences in dust properties, such as the high hematite content of African dust providing a more red and yellow color compared to the more gray color of Asian dust (Usher et al. 2003).

Mineral concentrations are also dependent on particle size. For instance, phyllosilicates (illite, kaolinite, smectite, vermiculite and chlorite) are abundant in clays (therefore, in fine dust particles). Conversely, $CaCO_3$, feldspars, quartz and mica are more typical of silt and sand particles (i.e. coarse particles). Finally, Fe oxides (i.e. hematite and goethite) can be found in both categories (Claquin et al. 1999, Mashburn et al. 2006, Kandler et al. 2007, Chou et al. 2008, Formenti et al. 2011, Journet et al. 2014, Kandler et al. 2020, Gonçalves Ageitos et al. 2023). Smaller sizes lead to lower deposition rates, therefore clay particles tend to be more long-lived than sand, and away from emission locations dust is enriched with minerals typical of the clay mode (Pye 1987).

Despite the wide variety of minerals present in dust, the elemental composition of dust particles around the globe is quite similar: silicon (Si), alumninium (Al), Fe, and calcium (Ca), together with their oxides SiO_2, Al_2O_3, Fe_2O_3 and CaO, represent the principal chemical components of dust (Hans Wedepohl 1995, Usher et al. 2003). For

instance, it is estimated that the vast majority of windblown desert dust is composed by SiO_2 (30-60%) and Al_2O_3 (10-15%) (Goudie and Middleton 2001). The presence of other elements is more dependent on the location dust is sourced from. For instance, while it is estimated that the total illite, kaolinite, and smectite do not represent more than 12% globally, Middle East dust shows an average of 20% in illite content, and eastern Africa, western India and east Australia present maximums of 16% for kaolinite and 28% for smectite (Nickovic et al. 2012). Notably, $CaCO_3$, reaches 12% surface concentration over the Middle East, central Asia, northeastern Sahara, and southern Africa, while falling to 2-6% in other dust source regions (Nickovic et al. 2012, Gonçalves Ageitos et al. 2023).

Under humid conditions, some of these minerals and their oxides tend to dissolve in the aqueous coating formed around dust particles. Minerals such as $CaCO_3$ and dolomite ($CaMg(CO_3)_2$) - and also more scarce calcium oxide (CaO) and magnesium oxide (MgO) - are either highly soluble in water or in the presence of dissolved acids, and dissociate into inorganic cations, also referred as nonvolatile cations (NVCs) (Usher et al. 2003, Krueger et al. 2003, Fountoukis and Nenes 2007, Vasilakos et al. 2018). NVCs represent chemically active dust components, the most common being calcium (Ca^{2+}), potassium (K^+), magnesium (Mg^{2+}), and sodium (Na^+). They are typically more abundant in coarse dust particles than in the fine ones (Claquin et al. 1999, Seinfeld and Pandis 2006). Anions can also be found in the aqueous medium of dust and sea salt particles, such as chlorine (Cl^-) or SO_4^{2-}, coming from dissolved salts and other minerals (Seinfeld and Pandis 1998, Athanasopoulou et al. 2008, Karydis et al. 2016). In their ionic phase (i.e. dissolved in the aqueous medium), these elements can chemically interact with acidic gas species through heterogeneous chemical reactions.

1.3 Dust heterogeneous chemistry

During its transport in the atmosphere, aeolian dust can react with gas species through heterogeneous chemical reactions (Fig. 1.2). These reactions involve more than one matter phase (i.e. solid, liquid, and/or gas), and they take place on the surface of dust particles or in the aqueous medium of their liquid coatings (Hanisch and Crowley 2001, Jordan et al. 2003, Usher et al. 2003, Krueger et al. 2003; 2004). Examples of heterogeneous reactions include the condensation and evaporation of acidic gas species in and out of the liquid layer around particles or their solid surface, and also the direct chemical reaction of gas species with components of the particle's solid surface (Vlasenko et al. 2009, Fairlie et al. 2010, Hauglustaine et al. 2014, Karydis et al. 2016).

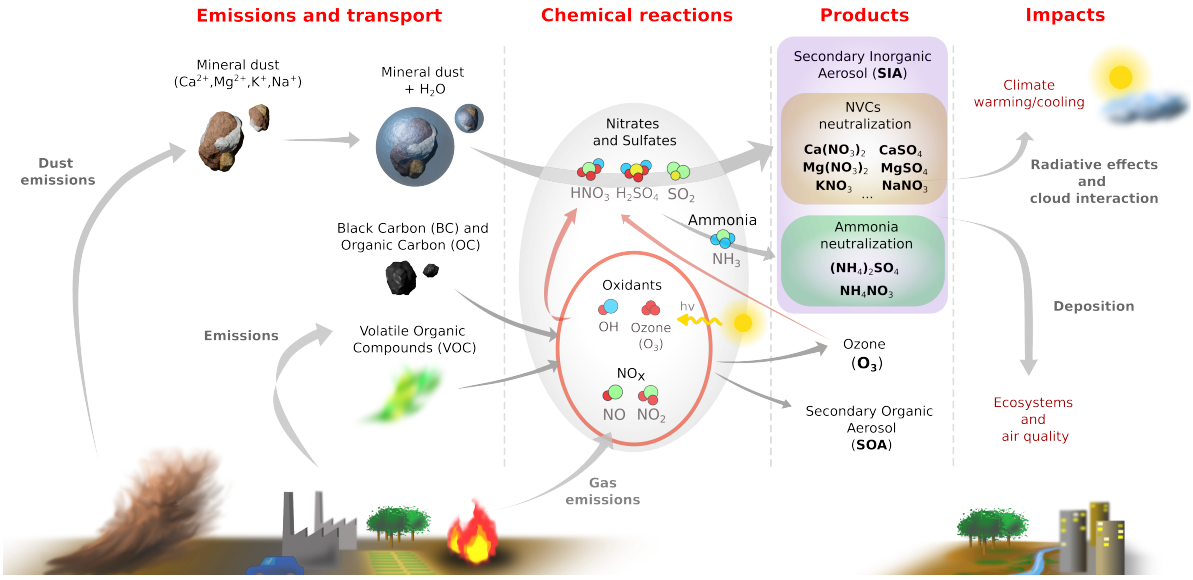

Figure 1.2: Schematic of the mineral dust lifecycle and its interaction with other atmospheric species, acting as a precursor agent of secondary inorganic aerosols, with important impacts on ecosystems, air quality, and climate.

These reactions ultimately translate into mass transfer between gas and aerosol phases, and they comprise complex microphysical and chemical processes thoroughly investigated by several experimental and theoretical studies (Fuchs and Sutugin 1970, Seinfeld and Pandis 1998, Jacob 2000, Vignati et al. 2004, Feng and Penner 2007, Prince et al. 2007, Jones et al. 2021). An attempt to describe them – reaching an agreement between the different research studies – is proposed by Kolb et al. (2010), which describes the sequence of processes leading to the mass exchange from gas to aerosol phase:

1. **Thermal accommodation** of gas molecules with the liquid or solid aerosol surface, transferring kinetic energy and reaching thermal equilibrium within an approximate timelapse of 10 seconds.

2. **Surface adsorption** of gas molecules (surface accommodation), retained in the liquid or solid surfaces for more time than the direct scattering (reflection) process lapse (10-12s), either by Van der Waals or hydrogen (H) bonds chemical weak forces (physisorption), or forming stronger chemical bonds through chemical reaction with surface species (chemisorption).

3. **Bulk absorption** of gas molecules after their surface accommodation (adsorption), transporting gas molecules into the aerosol's gas-liquid or gas-solid interface. This is described by the mass accommodation coefficient, representing the fraction between the number of molecules incorporated (dissolved) into the aerosol's solid (liquid) bulk and the total number of molecules colliding with the aerosol surface.

4. **Gas uptake** after surface or bulk accommodation, introducing surface reaction or bulk diffusion and - optionally - chemical reaction retaining the gas mass. The uptake coefficient may be defined as the ratio between the net mass loss from the gas phase (or mass increase in the condensed phase) and the number of gas molecules collisions with the aerosol surface. It must take into account the possible re-vaporization of gas molecules back to the gas phase, due to finite solubility of the gas species and/or the reversibility of surface or bulk chemical reactions.

In the case of dust, heterogeneous reactions have been found to importantly drive its chemical evolution in the atmosphere, with important implications for air quality and environment on regions affected by dust intrusions (Schwartz 1986, Dentener et al. 1996, Bauer et al. 2004; 2007, Karydis et al. 2016, Riemer et al. 2019).

Many gas species of both natural and anthropogenic sources have been observed to condense on aerosol surfaces and liquid coatings, especially low-volatility vapors like sulfuric acid ($H_2SO_{4(g)}$), nitric acid ($HNO_{3(g)}$), organic vapors, and basic gas species like $NH_{3(g)}$ (Jang et al. 2002, Guo et al. 2018). Compared with other gases, $HNO_{3(g)}$ and $H_2SO_{4(g)}$ tend to be more prone to condense and react on dust particles due to their relatively high acidity (low pH) and low volatility (Vlasenko et al. 2006, Crowley et al. 2010, Milousis et al. 2025).

Consequently, dust particles provide a reactive surface where dissolved ammonia ($NH_{3(aq)}$ or NH_4^+) and NVCs compete to neutralize condensed acidic species, primarily $H_2SO_{4(g)}$ and $HNO_{3(g)}$. The presence of NVCs modulates the neutralization pathways of the $NH_{3(g)}$-$HNO_{3(g)}$-$H_2SO_{4(g)}$-NVCs system (Fig. 1.3). For example, if NVCs are scarce or absent – insufficient to fully neutralize the condensed $HNO_{3(g)}$ and $H_2SO_{4(g)}$ – then $NH_{3(g)}$ has more available acids to react with. Conversely, if sufficient NVCs are present, a larger fraction of $NH_{3(g)}$ or NH_4^+ remain unreacted and is free to re-evaporate back into the gas phase.

The competition balance for the neutralization of acidic gas species by either NVCs or $NH_{3(g)}$ is particularly driven by environmental variables, such as relative humidity (RH) (Metzger et al. 2002, Fairlie et al. 2010, Liu and Abbatt 2021), temperature (Meng and Seinfeld 1996, Feng and Penner 2007, Guo et al. 2017, Uno et al. 2017a), and aerosol acidity (Nenes et al. 2020), which constrain the matter state of NO_3^- in the $NH_{3(g)}$-$HNO_{3(g)}$-$H_2SO_{4(g)}$-NVCs neutralization system. In particular, elevated RH enhances heterogeneous reactions by increasing aerosol water content (AWC), thereby promoting particle growth, and the uptake and dissociation of soluble gases (Liu and Abbatt 2021). Such is the case of $HNO_{3(g)}$ and $SO_{2(g)}$ uptake rates on mineral dust, which increase with RH (Fairlie et al. 2010) (see Section 1.5).

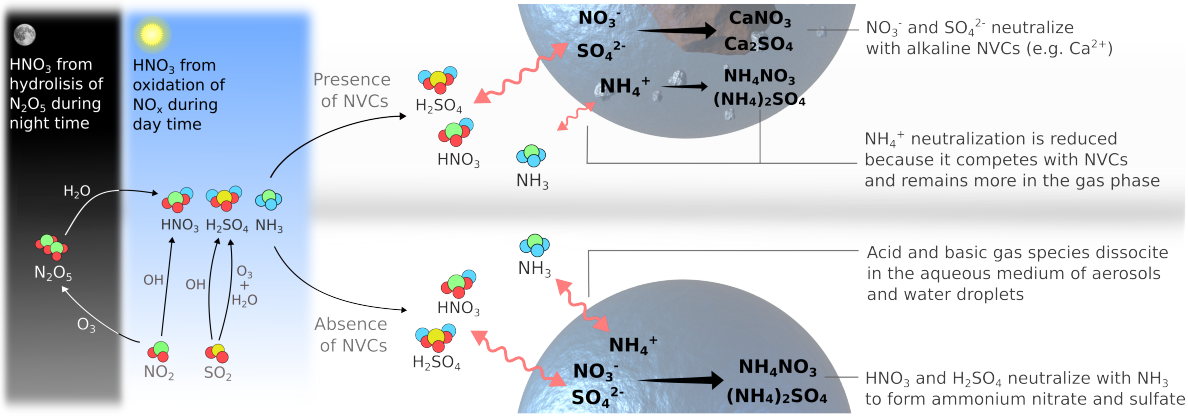

Figure 1.3: Neutralization scenarios of acid and basic gas species in the presence or absence of NVCs dissolved from dust alkaline minerals.

The following Sections 1.3.1 and 1.3.2 discuss these regimes in more detail.

1.3.1 Acid neutralization on aqueous particles by $NH_{3(g)}$

Dust particles provide surfaces that may act as condensation nuclei for water vapor, which forms aqueous layers where - similarly to cloud water droplets - gas species such as $NH_{3(g)}$, $HNO_{3(g)}$ and $H_2SO_{4(g)}$ can dissolve (Levin and Cotton 2009, Twohy et al. 2009). Once transferred into the aqueous phase, $NH_{3(g)}$ acts as a base that neutralizes with dissolved $HNO_{3(g)}$ and $H_2SO_{4(g)}$ acidic species, leading to the formation of ammonium nitrate (NH_4NO_3) and ammonium sulfate (e.g. NH_4HSO_4, $(NH_4)_2SO_4$, $(NH_4)_3H(SO_4)_2$) (Metzger et al. 2002, Usher et al. 2003, Guo et al. 2018, Liu et al. 2021). These products may crystallize or remain dissociated in the aqueous phase and are, throughout this Thesis, collectively included in the definition of particulate ammonium (NH_4^+) regardless of their specific salt form, as represented by the reactions in Table 1.1.

The products of the $NH_{3(g)}$-$HNO_{3(g)}$-$H_2SO_{4(g)}$ neutralization system predominantly form in aqueous fine particles, representing an important fraction of particulate matter (PM) with D below 2.5μm ($PM_{2.5}$) at the global level (Kanakidou et al. 2005, Liu et al. 2021). In the aqueous or deliquesced particle phase, NH_4^+ preferentially neutralizes H_2SO_4 rather than $HNO_{3(g)}$, because $H_2SO_{4(g)}$ produces low-volatility SO_4^{2-} species that do not readily partition back to the gas phase. This strong thermodynamic driving force makes SO_4^{2-} neutralization dominant over NO_3^- formation (Usher et al. 2003, Hauglustaine et al. 2014, Uno et al. 2020).

Importantly, the neutralization reactions described here generally require of humid conditions to take place (Guo et al. 2018, Liu et al. 2021). Under dry conditions, secondary formation pathways via synergetic clustering among $NH_{3(g)}$, $HNO_{3(g)}$ and

Table 1.1: Neutralization reactions of $HNO_{3(g)}$ and $H_2SO_{4(g)}$ by $NH_{3(g)}$.

(R1)	$HNO_{3(g)} + NH_{3(g)} \rightleftharpoons NH^+_{4(aq)} + NO^-_{3(aq)}$
(R2)	$H_2SO_{4(g)} + NH_{3(g)} \rightleftharpoons NH^+_{4(aq)} + SO^{2-}_{4(aq)}$
(R3)	$NH^+_{4(aq)} + NO^-_{3(aq)} \rightleftharpoons NH_4NO_{3(s)}$
(R4)	$NH^+_{4(aq)} + SO^{2-}_{4(aq)} \rightleftharpoons (NH_4)_2SO_{4(s)}$

$H_2SO_{4(g)}$ have also been observed, which might lead to new particle formation under cold and $NH_{3(g)}$-rich environments (Liu et al. 2018).

1.3.2 Acid neutralization on dust surfaces by alkaline minerals

Some salts present in dust minerals enhance dust *alkalinity*, or its capacity to neutralize acids (i.e. buffering capacity) (Muller 1994, Walters 2025). Common examples of such components are $CaCO_3$, magnesium carbonate ($MgCO_3$), potassium carbonate (K_2CO_3), and sodium carbonate (Na_2CO_3), hereafter referred as *alkaline minerals* (Usher et al. 2003). They dissociate into carbonate ($CO^{2-}_{3(aq)}$) bases and NVCs, either when reacting with acids in the gas or liquid phase, or in a lower rate by directly dissociating in the aqueous medium (Usher et al. 2003, Krueger et al. 2003, Fountoukis and Nenes 2007, Vasilakos et al. 2018). CO_3^{2-} products neutralize protons (H^+) - therefore acidity - contributing to the particle alkalinity, while NVCs neutralize oxidative radicals (Hauglustaine et al. 2014, Krueger et al. 2004)

Since the most commonly condensed acid gas species are $HNO_{3(g)}$ and $H_2SO_{4(g)}$ (Usher et al. 2003, Vlasenko et al. 2006, Crowley et al. 2010), they are the principal acids neutralized by alkaline minerals (Fig. 1.4). The neutralization of the dissolved anions from $HNO_{3(g)}$ and $H_2SO_{4(g)}$ with the NVCs from dust alkaline minerals produces particulate NO_3^- and SO_4^{2-} species, respectively (Li and Shao 2009, Bian et al. 2017). Their chemical composition depends on the composition of the NVCs from dust participating in the neutralization reactions, as shown in Table 1.2.

The products from NVC and acid neutralization in Table 1.2 crystallize in the following 9 mineral salts, which might precipitate and incorporate to the mineral dust bulk material: $Ca(NO_3)_2$, $CaSO_4$, $KHSO_4$, K_2SO_4, KNO_3, $MgSO_4$, $Mg(NO_3)_2$, $NaHSO_4$, Na_2SO_4, $NaNO_3$ (Karydis et al. 2016).

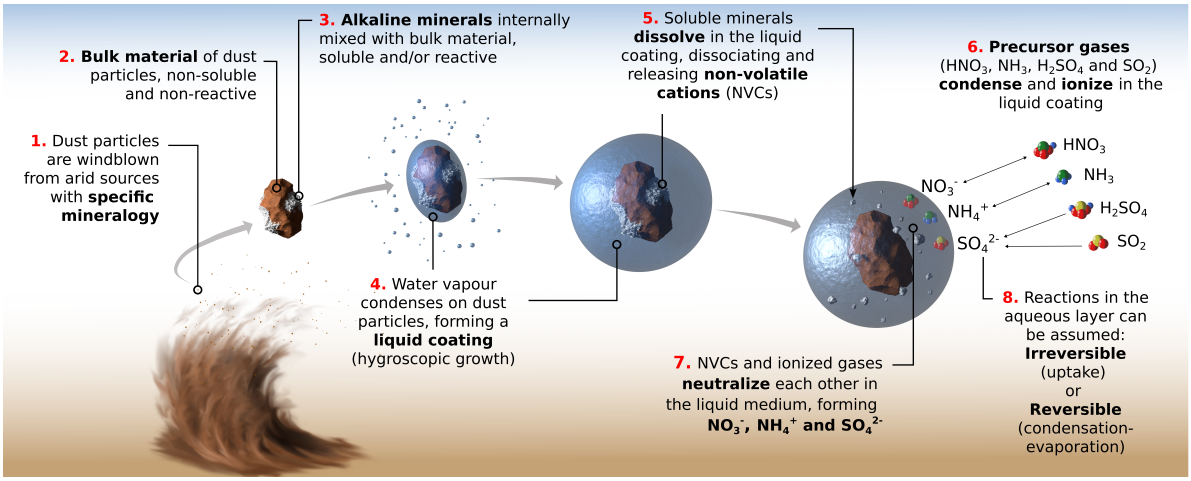

Figure 1.4: Scheme of dust heterogeneous chemistry, considering the two possible scenarios of reversible and irreversible condensation of gas molecules into the particle phase.

Table 1.2: Reactions between dust alkaline minerals, and $HNO_{3(g)}$ and $H_2SO_{4(g)}$.

(R1)	$CaCO_{3(s)} + 2HNO_{3(g)} + H_2O \rightleftharpoons Ca^{2+}_{(aq)} + 2NO^{-}_{3(aq)} + H_2O + CO_2$
(R2)	$MgCO_{3(s)} + 2HNO_{3(g)} + H_2O \rightleftharpoons Mg^{2+}_{(aq)} + 2NO^{-}_{3(aq)} + H_2O + CO_2$
(R3)	$K_2CO_{3(s)} + 2HNO_{3(g)} + H_2O \rightleftharpoons 2K^{+}_{(aq)} + 2NO^{-}_{3(aq)} + H_2O + CO_2$
(R4)	$Na_2CO_{3(s)} + 2HNO_{3(g)} + H_2O \rightleftharpoons 2Na^{+}_{(aq)} + 2NO^{-}_{3(aq)} + H_2O + CO_2$
(R5)	$CaCO_{3(s)} + H_2SO_{4(g)} + H_2O \rightleftharpoons Ca^{2+}_{(aq)} + SO^{2-}_{4(aq)} + H_2O + CO_2$
(R6)	$MgCO_{3(s)} + H_2SO_{4(g)} + H_2O \rightleftharpoons Mg^{2+}_{(aq)} + SO^{2-}_{4(aq)} + H_2O + CO_2$
(R7)	$K_2CO_{3(s)} + H_2SO_{4(g)} + H_2O \rightleftharpoons 2K^{+}_{(aq)} + SO^{2-}_{4(aq)} + H_2O + CO_2$
(R8)	$Na_2CO_{3(s)} + H_2SO_{4(g)} + H_2O \rightleftharpoons 2Na^{+}_{(aq)} + SO^{2-}_{4(aq)} + H_2O + CO_2$

Depending on their reversibility, Table 1.2 reactions can be:

Irreversible: Acidic gas vapors condense and react with alkaline species present in the solid surface of particles or in their liquid coating, and they do not re-evaporate back to the gas phase (Goodman 2000).

Reversible: Acidic gas vapors establish a condensation-evaporation equilibrium in-from the aqueous coating of dust particles, where they react with dust alkaline minerals (Song and Carmichael 2001, Usher et al. 2002; 2003, Krueger et al. 2003, Crowley et al. 2010, Yue et al. 2022).

Under dry conditions (absence of liquid coating), minerals remain in the solid phase and serve as active sites on the aerosol surface for reactions with gas species. In this scenario, heterogeneous reactions - often assumed to be irreversible (Fenter et al. 1995,

Crowley et al. 2010) - are limited to the available reaction sites exposed on the surfaces of the particles, reducing their reaction rates when surface reaction sites become progressively saturated after reacting with acids (Fenter et al. 1995, Goodman 2000, Hanisch and Crowley 2001, Underwood et al. 2001, Ammann et al. 2003, Vlasenko et al. 2009). This can be the case of dry dust particles that did not form a liquid coating around them, either because they are hydrophobic or because of very low ambient RH. However, the direct uptake of acidic gas species on the surface of particles may increase the hydrophilic potential of dust particles, leading to the formation of aqueous coatings around the particles (hygroscopic growth) (Usher et al. 2003, Krueger et al. 2003; 2004, Fountoukis and Nenes 2007, Li and Shao 2009), habilitating the reversible pathway.

Under humid conditions (Fig. 1.4), soluble alkaline minerals (e.g. MgO, K_2O, CaO, $CaCO_3$, and $MgCO_3$) dissociate into the particle's aqueous coating until its saturation, therefore substantially enhancing the neutralization capacity of dissolved acids (i.e. dust alkalinity). In this case, condensed acids can re-evaporate back to the gas phase, leading to sustained reaction rates once the condensation-evaporation equilibrium is reached (Usher et al. 2002; 2003, Fairlie et al. 2010, Karydis et al. 2016). Under such conditions, if dust particles are transported to environments poor in gas-phase acids, the condensation-evaporation equilibrium shifts towards the evaporation of condensed gas species back to the atmosphere, turning dust particles into important atmospheric transport means of acids (Dentener et al. 1996, Song and Carmichael 2001, Goodman et al. 2001, Usher et al. 2003, Liao et al. 2003, Hodzic et al. 2006, Vlasenko et al. 2006; 2009, Fairlie et al. 2010).

Insoluble minerals (R-Al_2O_3, TiO_2, and γ-Fe_2O_3) that are reactive with acids remain in the solid phase even under humid conditions, following a reaction pathway analogous to that under dry conditions (Usher et al. 2003). Ultimately, the simultaneous presence of soluble and insoluble reactive minerals on the dust surface combines both scenarios under humid conditions. Finally, other minerals insoluble and nonreactive with acidic species, such as quartz (SiO_2) and aluminum silicates, remain inert in the particles' bulk, as can be observed in Fig. 1.5 (Krueger et al. 2004, Yang et al. 2018). Alternatively, under acidic conditions, K^+, Fe^{2+} and other cations may be extracted from minerals such as illite (Muraleedharan et al. 2020).

In consequence, the rates of dust heterogeneous reactions is directly dependent on the availability of aerosol bulk active sites or NVC in the dust surfaces and liquid coatings, respectively, which are directly linked with the mineralogical composition of the dust particles, subject to the minerals' concentration and solubility (Metzger et al. 2006). Since the mineralogical content of dust is highly related to its source location, the

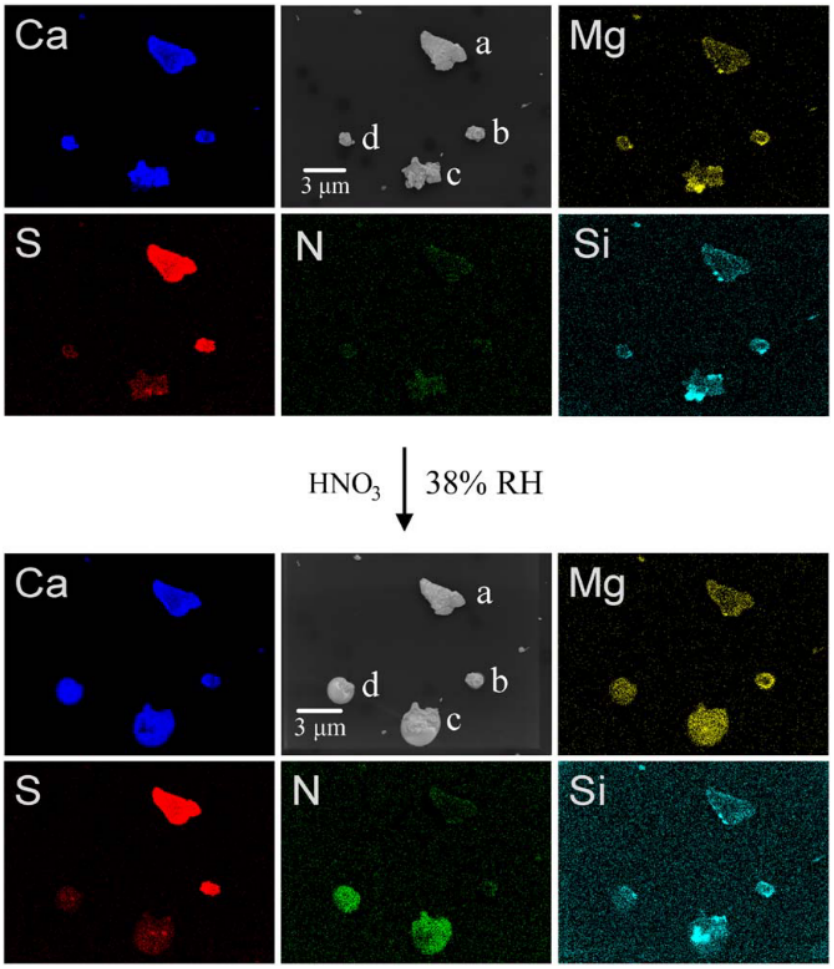

Figure 1.5: Condensation of $HNO_{3(g)}$ onto dust mineral particles, pictured with a scanning electron microscope.
Reprinted from Atmospheric Environment, 38, B.J. Krueger, V.H. Grassian, J.P. Cowin, A. Laskin, Heterogeneous chemistry of individual mineral dust particles from different dust source regions: the importance of particle mineralogy, 6258, Copyright (2004), with permission from Elsevier.

reaction rates of dust heterogeneous reactions are going to differ depending on the origin of airborne dust particles, also altering their impact on local air quality and climate.

Besides the origin of dust particles, their size distribution also determines the abundance of alkaline minerals; NVCs are generally more abundant in coarse particles rather than in fine ones (Seinfeld and Pandis 2006, Pan et al. 2009, Meier et al. 2009, Tian et al. 2014, Zhao et al. 2017). At the same time, the diffusivity of gas species towards the surface of dust is highly dependent on the particle size. This is an important factor influencing the heterogeneous reaction rates, as gas phase diffusion towards small particles is larger than that for large aerosol particles (Hobbs 2000, Pratte and Rossi 2006).

Beyond the above-mentioned alkaline minerals from dust, sea salt presents other

salts that may also participate in the formation of particulate NO_3^-, such as the sodium chloride (NaCl). Its reaction with acidic species, particularly $HNO_{3(g)}$, leads to the formation of sodium nitrate ($NaNO_3$) and hydrochloric acid ($HCl_{(g)}$) (Dasgupta et al. 2007).

Table 1.3: Reactions of NaCl from sea salt with $HNO_{3(g)}$ and $NH_{4(aq)}^+$.

(R1)	$NaCl_{(s)} + HNO_{3(g)} + H_2O \rightleftharpoons Na^+_{(aq)} + NO^-_{3(aq)} + HCl_{(g)} + H_2O$
(R2)	$NaCl_{(s)} + NH^+_{4(aq)} + H_2O \rightleftharpoons Na^+_{(aq)} + NH_4Cl_{(g)} + H_2O$

$HCl_{(g)}$ is released as a gas species that can either promote or deplete tropospheric ozone (O_3), depending on atmospheric conditions. However, its reaction rate is still not completely understood nowadays, with various studies presenting different quantifications and relationships with RH and particle size (Guimbaud et al. 2002, Saul et al. 2006, Pratte and Rossi 2006, Liu et al. 2007, Fagerli et al. 2015, Burkholder et al. 2020). Sea-salt may also neutralize NH_4^+ – primarily in the fine mode – through the reaction between NaCl and NH_4^+ to form ammonium chloride (NH_4Cl), leading to an increase of coarse particulate NO_3^- formation (Campbell et al. 2002). Table 1.3 summarizes the reactions of NaCl.

Since $HNO_{3(g)}$ and $H_2SO_{4(g)}$ are relevant gaseous pollutants with significant contribution from anthropogenic sources, their removal by dust heterogeneous reactions may have a strong impact on local air quality of dust-affected areas (Fig. 1.2), and it has important implications on dust particles' size, deposition rates, acidity, and optical properties (Schwartz 1986, Dentener et al. 1996, Usher et al. 2003, Bauer et al. 2004; 2007, Karydis et al. 2016, Bian et al. 2017, Wang et al. 2020, Milousis et al. 2025). Moreover, beyond affecting dust properties, these reactions can also serve as a means of transporting NO_3^- and SO_4^{2-} from polluting hotspots to cleaner regions (Rodríguez et al. 2011, Kim and Park 2012, Uno et al. 2017b, Wang et al. 2019, Ma et al. 2021). Because of these relevant effects on atmospheric chemistry, these reactions have caught the attention of atmospheric chemistry modeling studies in the recent years (see Section 1.5).

1.3.3 Other relevant reactions

NO_x species exert an important influence on dust heterogeneous chemistry (Fenter et al. 1995, Riemer et al. 2003). First, they control the production of $HNO_{3(g)}$ via daytime and nighttime oxidation (Fig. 1.3), leading to the subsequent heterogeneous formation of NO_3^-. Additionally, the uptake of NO_x on dust particles has been repeatedly observed in

experimental studies (Jordan et al. 2000, Song and Carmichael 2001, Underwood et al. 2001, Topping et al. 2004, Bates et al. 2004), suggesting that NO_x species can directly participate in dust heterogeneous reactions. For instance, $NO_{2(g)}$ uptake on dust surfaces can lead to its oxidation to $HNO_{3(g)}$, contributing to particulate NO_3^- formation. This reaction is enhanced by the presence of water on the surface of $CaCO_3$ particles (Al-Hosney and Grassian 2005, Li et al. 2010), although it represents a secondary route for $HNO_{3(g)}$ production compared to other production pathways (Jacob 2000, Underwood et al. 2001, Jordan et al. 2003, Seisel et al. 2005, Li et al. 2024b, Milousis et al. 2024).

For example, under typical atmospheric conditions (i.e. outside extreme dust events in industrial or urban areas), $N_2O_{5(g)}$ hydrolysis dominates particulate NO_3^- formation, exceeding the contribution from $NO_{2(g)}$ and $NO_{3(g)}$ oxidation on dust surfaces by two to three orders of magnitude (Jacob 2000, Liao et al. 2003). This is particularly pronounced in northern mid-latitudes and during local wintertime (Dentener and Crutzen 1993, Lamsal et al. 2010, Paulot et al. 2016).

Beyond N species, $SO_{2(g)}$ is another important gas taken up on mineral dust particles (Phadnis and Carmichael 2000, Usher et al. 2003). The 75% of tropospheric $SO_{2(g)}$ is emitted from anthropogenic sources, such as coal burning, while it secondarily emitted from volcanoes (Usher et al. 2003). $SO_{2(g)}$ is one of the main sources of secondary $SO_{4(aq)}^{2-}$ via its dissolution in the aqueous medium (Warneck and Williams 2012, Hoyle et al. 2016), and oxidation with OH, H_2O_2, O_3, and $NO_{2(g)}$ (Usher et al. 2002, Ullerstam et al. 2003, Li et al. 2010, Hoyle et al. 2016, Wang et al. 2021, Yang et al. 2024). If $H_2SO_{4(g)}$ forms in the gas phase, it rapidly condenses onto aqueous and preexisting particles due to its low vapor pressure, producing particulate SO_4^{2-} (Usher et al. 2002; 2003, Vet et al. 2014, Zhang et al. 2015, Tilgner et al. 2021).

In-cloud $SO_{2(g)}$ oxidation (i.e. in clouds and fog) accounts for approximately 60% of total particulate SO_4^{2-} formation, rather than through reactions on solid aerosols (Tilgner et al. 2021). Meanwhile, crustal $CaCO_3$ can oxidize $SO_{2(g)}$ under high humidity conditions (e.g. RH>40%) (Li et al. 2006, Yue et al. 2022), forming $CaSO_3$ (Gebel et al. 2000, Usher et al. 2002, Fairlie et al. 2010). This reaction is enhanced by the presence of condensed water and $CaSO_4$ particles (Li et al. 2006). The solubility of $SO_{2(g)}$ also increases with aerosol pH (Tilgner et al. 2021), accelerating its oxidation under low pH conditions (Faloona 2009, Paulot et al. 2017). Finally, dust metallic aerosols are observed to catalyze $SO_{2(g)}$ oxidation, with Fe^{3+} and Mn^{2+} identified as the key catalysts (Martin and Good 1991, Siefert et al. 1996, Usher et al. 2002, Alexander et al. 2009).

Despite its importance, still substantial uncertainties remain in models regarding the heterogeneous $SO_{2(g)}$ oxidation, both on water and solid aerosols (Faloona 2009), as well as regarding its deposition and mixing rates with other particles (Myhre et al. 2004).

Finally, OM is also believed to influence dust heterogeneous chemistry (Usher et al. 2003). As OM constitutes a significant fraction of $PM_{2.5}$, its role in atmospheric chemistry has attracted increasing attention (Denier van der Gon et al. 2015, Navarro-Barboza et al. 2024). Of particular relevance is the formation of organic coatings on mineral dust particles, such as acetic acid (Carlos-Cuellar et al. 2003), which can alter heterogeneous reactions by modifying the uptake rates of trace gases and other volatile organic compounds (VOCs) (Goss and Eisenreich 1996, Goss 2002a;b). Notably, these OM coatings are thought to inhibit the uptake of $NH_{3(g)}$ onto dust particles (Silvern et al. 2017, Bian et al. 2017).

1.3.4 The role of dust acidity, temperature, and aerosol water content

Dust pH is primarily driven by mineralogical composition, with alkaline salts reducing acidity (increasing pH). This initial pH influences and is modified by heterogeneous reactions between minerals and acidic or basic gas species.

In the absence of alkaline minerals, $NH_{3(g)}$ condensation increases dust pH, partially mitigating particle toxicity (Oakes et al. 2012, Fang et al. 2017, Karydis et al. 2021), and also affecting the formation of particulate NO_3^-, NH_4NO_3, $(NH_4)_2SO_4$, NH_4HSO_4, and $(NH_4)_3H(SO_4)_2$. On the contrary, when alkaline minerals are present, they provide cationic and surface-active sites that compete with $NH_{3(g)}$ to neutralize acidic gases, modulating gas-aerosol partitioning, $NH_{3(g)}$ condensation rates, and the overall aerosol pH.

Ultimately, aerosol acidity governs heterogeneous chemistry by modulating the partitioning of gas species into the aerosol phase: Low pH favors $HNO_{3(g)}$ to remain in the gas phase and NH_4^+ to form in the aerosol, while high pH promotes NO_3^- formation and leaves more $NH_{3(g)}$ as a gas (Weber et al. 2016). Specifically, pH regimes for NO_3^- formation are classified as (Nenes et al. 2020, Kakavas et al. 2021, IPCC 2021, Wang et al. 2025a):

- pH $<$ 1.5–2.0: NO_3^- mainly exists as $HNO_{3(g)}$, and $NH_{3(g)}$ condensation to NH_4^+ is largely favored.
- 1.5 $<$ pH $<$ 3.0: Transition regime of $HNO_{3(g)}$ and $NH_{3(g)}$ condensation to particulate NO_3^- and NH_4^+.
- pH $>$ 2.5–3.0: NO_3^- is predominantly particulate, with near-complete condensation of $HNO_{3(g)}$, while $NH_{3(g)}$ remains almost exclusively in the gas phase.

Additionally, AWC strongly modulates gas–aerosol partitioning dynamics. As AWC increases with RH, it favors the condensation of gaseous species, shifting gas–aerosol partitioning toward the particulate phase (Wang et al. 2025a). Elevated AWC also promotes the solubility of mineral components on dust particles (Usher et al. 2003) and broadens the pH transition regime between fully condensed and fully evaporated gas species (Nenes et al. 2020). In contrast, low AWC accentuates the critical pH thresholds that define the partitioning regimes of NO_3^- and NH_4^+, causing NO_3^- formation at intermediate pH to become largely insensitive to variations in $NH_{3(g)}$ and $HNO_{3(g)}$ concentrations (Nenes et al. 2020).

Finally, temperature exerts a significant influence on gas–aerosol partitioning by regulating the condensation and evaporation rates of $HNO_{3(g)}$ and $NH_{3(g)}$ (Meskhidze et al. 2003, Feng and Penner 2007, Uno et al. 2017a, Nenes et al. 2020, Wang et al. 2025a). Higher temperatures increase the volatility of these gas species and the dissociation of their neutralization products (i.e. NH_4NO_3), thereby shifting partitioning toward the gas phase at the expense of particulate NO_3^- and NH_4^+ (Uno et al. 2017a, Guo et al.; 2017). However, this a priori dependence on temperature is can be influenced by the presence of mineral dust and sea salt particles. Although higher temperatures are generally expected to evaporate fine-mode NO_3^- and enhance coarse-mode NO_3^- formation via increased availability of gaseous $HNO_{3(g)}$, experimental evidence indicates that this temperature-driven size redistribution is highly altered by the presence of sea salt and NVCs from dust (Matsumoto et al. 2012). More recently, Nenes et al. (2020) showed that high temperatures reduce the sensitivity of gas–aerosol partitioning to precursor gas concentrations, while mineral dust and sea salt can provide additional reactive surfaces that further modify this behavior. Overall, they showed that – similarly to low AWC – increasing temperatures broaden the insensitivity of aerosol formation to gas precursor concentrations, while the pH regimes mentioned shift toward the upper end.

1.4 Impacts on air quality, health, and climate

Mineral dust significantly affects air quality, human health, and ecosystems in regions impacted by dust intrusions. At the global scale, dust alters aerosol optical properties and associated radiative effects, both directly through interactions with radiation and indirectly through its influence on cloud formation. Beyond these physical impacts, heterogeneous reactions between mineral dust and trace gases modify particle properties, chemical reactivity, and atmospheric composition in affected regions (Guerzoni and Chester 1996, Wang et al. 2015, Karydis et al. 2016, Wang et al. 2017, Querol et al. 2019).

This section reviews the current understanding of the impacts of mineral dust and its heterogeneous chemistry.

1.4.1 Air quality

Heavily populated regions are frequently receptor areas of long-range transport of mineral dust (Park et al. 2005, Griffin 2007, Uno et al. 2009). The regions most affected by elevated atmospheric dust concentrations are typically located near, or downwind of, major dust source areas described in Section 1.2.

Asian dust originating from the Taklamakan and Gobi deserts frequently reaches densely populated regions of East Asia, but it can also be transported across the Pacific Ocean to North America, and occasionally further to Europe (Jaffe et al. 2003, Fairlie et al. 2010, Uno et al. 2009, Zhang et al. 2016, Wang et al. 2016; 2019).

Similarly, most dust emitted from North Africa (i.e. Sahara) is transported across West Africa, the Gulf of Guinea, and the Atlantic Ocean (McTainsh et al. 1997, Breuning-Madsen and Awadzi 2005, Anuforom 2007, Resch et al. 2008, Rodríguez et al. 2011, Prospero and Mayol-Bracero 2013). Saharan dust is regularly transported to Europe through the Mediterranean (Israelevich et al. 2012, Varga et al. 2013), with additional transport pathways toward the Middle East, East Asia (Tanaka et al. 2005), and even reaching the Arctic (Barkan and Alpert 2010).

As a result, some of the most densely populated and industrialized regions are affected by frequent or episodic dust events, especially East Asia (Wang et al. 2018a; 2019), southern Europe (Querol et al. 1998, Rodrıguez et al. 2001, Pey et al. 2013), and the Middle East (Engelbrecht et al. 2009), where dust intrusions are popularly referred to as *Kosa* in Asian countries, and *Calima* in Spain (Querol et al. 2019). For example, such events can lead to extreme PM_{10} concentrations, reaching up to 3000 μg m^{-3} in East Asia, and 2500 μg m^{-3} in southern Europe (Goudie 2014). Even in Australia, dust episodes have been registered to increase PM_{10} concentrations up to 900 μg m^{-3}, although their relative contribution to air pollution is in general secondary compared to anthropogenic sources in this region (Aragnou et al. 2021).

Because dust intrusions often affect industrialized and populated regions, the encountering of mineral dust with anthropogenic pollutants promotes heterogeneous chemical reactions on dust particle surfaces (see Section 1.3). These reactions modify dust chemical composition and influence gas-aerosol partitioning through the reactions summarized in Tables 1.1 and 1.2. The products of these reactions include SIA, mainly composed of particulate NO_3^-, SO_4^{2-}, and NH_4^+, by neutralizing acidic gas species with $NH_{3(g)}$ and NVCs from alkaline minerals (Fig. 1.3).

Therefore, heterogeneous reactions on dust play a critical role in SIA formation, which is a key contributor to air pollution. In fact, SIA represents a major fraction of $PM_{2.5}$ worldwide, particularly in urban environments (Amato et al. 2016, Masselot et al. 2022, Navarro-Barboza et al. 2024). Figure 1.6 illustrates their global distribution and highlights how particulate NO_3^-, SO_4^{2-}, and NH_4^+ often account for a substantial fraction of $PM_{2.5}$ mass. This figure also illustrates the frequent co-occurrence of high dust loads and SIA concentrations in regions such as East Asia, the western United States, Australia, South America, and southern Europe, again underscoring the significant influence of dust on SIA formation.

The atmospheric production and size distribution of SIA are controlled by the relative abundance of precursor gases (i.e. $HNO_{3(g)}$, $H_2SO_{4(g)}$, and $NH_{3(g)}$) and alkaline mineral components (Fig. 1.3). Fine-mode SIA predominantly forms through the neutralization of $H_2SO_{4(g)}$ and $HNO_{3(g)}$ by $NH_{3(g)}$, whereas reactions involving dust-derived NVCs, which are more abundant in coarse particles, shift SIA formation toward the coarse mode (Kanakidou et al. 2005, Jaffe et al. 2005, Amato et al. 2016). The former pathway dominates in regions with strong agricultural and traffic emissions, such as China, western United States, and northwestern Europe, where SO_4^{2-}, $HNO_{3(g)}$, and $NH_{3(g)}$ concentrations are high. In contrast, dust-driven coarse-mode SIA formation is particularly relevant in regions affected by dust intrusions, including East Asia and the Middle East (Jaffe et al. 2005, Pathak et al. 2009, Morgan et al. 2010, Highwood et al. 2012, Kakavas et al. 2021, Jones et al. 2021, Dang et al. 2023).

For example, Karydis et al. (2016) showed that coarse-mode NO_3^- formation is enhanced over densely populated regions that are simultaneously affected by dust intrusions and elevated $NO_{x(g)}$ emissions, such as southern Europe, the Arabian peninsula, central and eastern Asia, and southwestern United States. In contrast, other densely populated regions in Europe, China, and the eastern United States exhibit higher concentrations of fine-mode particulate NO_3^-, largely driven by local photochemical production from NO_x. The shift in NO_3^- size distribution is therefore largely attributed to the presence of mineral dust.

Heterogeneous chemistry on dust may also influence the future trends of SIA and their precursor gases. Increasing $NH_{3(g)}$ emissions from agricultural activities, manure management, and land use over the coming decades (van Vuuren et al. 2011), combined with stable or declining trends in NO_x and sulfate emissions, are expected to modify aerosol neutralization regimes. Current $NH_{3(g)}$ observed trends indicate stable or increasing concentrations across Asia, the United States, and Europe (between 0.05 and 0.1 $\mu g m^{-3} y^{-1}$) (Reche et al. 2022, Grange et al. 2023, Sun et al. 2025). Consequently, controlling $NH_{3(g)}$ emissions is likely to become a key strategy for mitigating $PM_{2.5}$

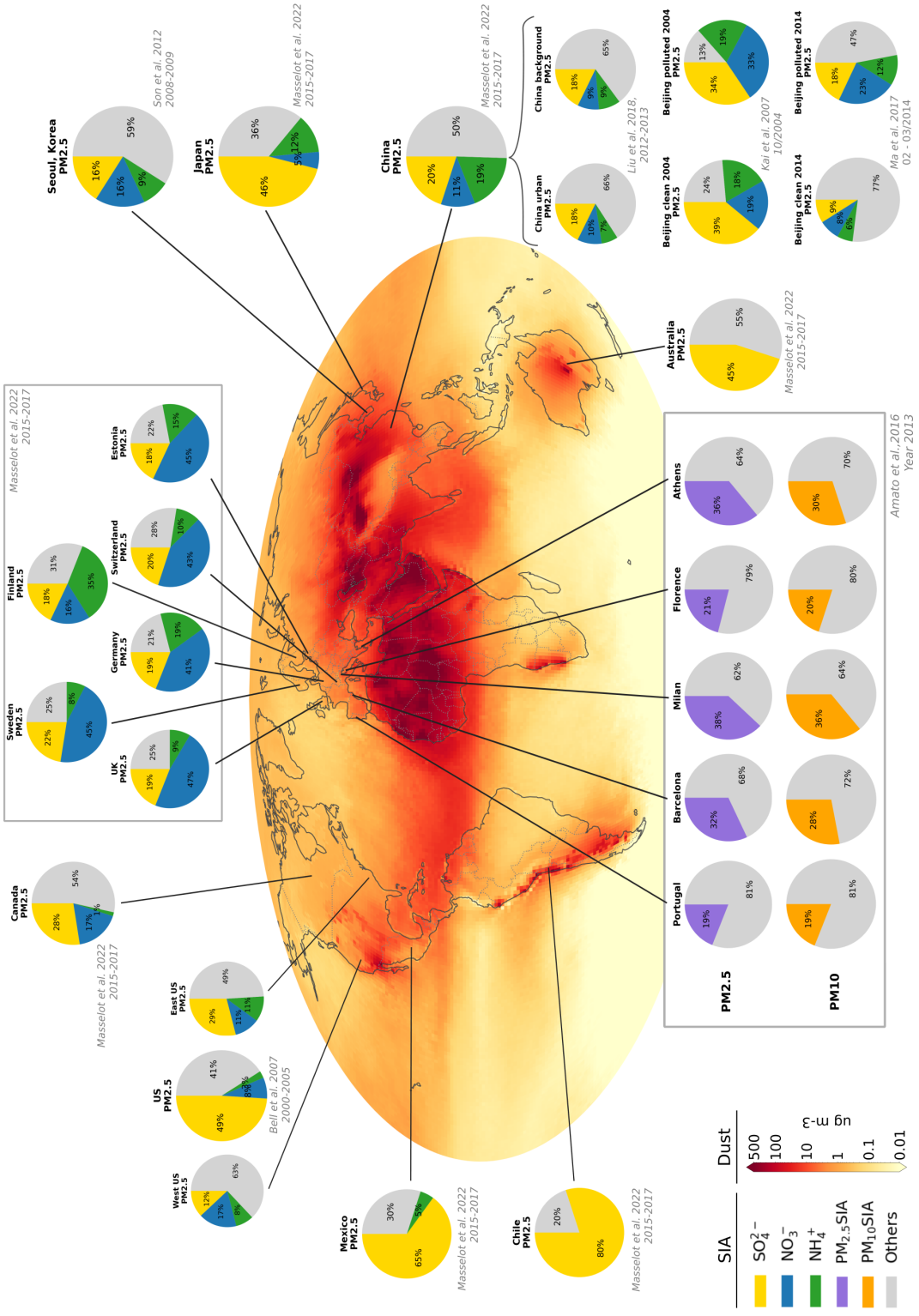

Figure 1.6: Distribution of SIA components as fractions of $PM_{2.5}$ and PM_{10} across countries and cities from the literature (pie charts). Colors on the map indicate PM_{20} dust surface concentration averaged for 2018 in $\mu g\ m^{-3}$.

pollution (Reche et al. 2022, Grange et al. 2023). In parallel, particulate SO_4^{2-} and NO_3^- concentrations have markedly declined in the last decades, in part due to a significant reduction in global $SO_{2(g)}$ emissions from stricter fossil fuel regulations and other implemented policies (Manktelow et al. 2007, Hand et al. 2013, Kyrö et al. 2014, Saleh 2020, Pye et al. 2020, Likus-Cieślik and Pietrzykowski 2021). Therefore, the lack of concurrent reductions in $NH_{3(g)}$, together with regionally steady NO_x concentrations, has shifted secondary aerosol production from SO_4^{2-} toward NO_3^- in some areas, particularly in East Asia (Lajtha and Jones 2013, Jonson et al. 2022, Pan et al. 2024, Lv et al. 2024, Huang et al. 2025).

Assessing the relative abundance and chemical composition of $PM_{2.5}$ precursors is therefore critical for anticipating future aerosol formation. For example, Clappier et al. (2021) showed that reducing $NH_{3(g)}$ emissions is most effective in regions where $NH_{3(g)}$ is not already in excess, whereas reducing NO_x emissions can, in some cases, enhance $PM_{2.5}$ formation by increasing atmospheric oxidative capacity and subsequent production of $HNO_3(g)$ and $H_2SO_{4(g)}$.

Overall, mineral dust remains a major source of uncertainty in determining the atmospheric burdens of SIA and anthropogenic pollutants in urban regions, with important implications for air quality assessments. SIA formation driven by dust heterogeneous chemistry is particularly relevant because it can increase regional $PM_{2.5}$ levels and modify aerosol size and chemical composition, which may lead to distinct health impacts (Masselot et al. 2022).

1.4.2 Health

In regions affected by dust outbreaks, populations are exposed to high atmospheric dust levels that, when inhaled, can harm human and animal health. The main effects of dust are respiratory diseases such as pneumonia, bronchitis, asthma, rhinitis, and emphysema, but also eye and skin irritations, and cardiovascular disorders have been reported (Kwon et al. 2002, Bennett et al. 2006, Mallone et al. 2011, Goudie 2014, Zhang et al. 2016, Querol et al. 2019). High dust concentrations have been linked to increased mortality in several European and Asian populations (Perez et al. 2008, Mallone et al. 2011, Zhang et al. 2016). Dust particle size strongly influences health impacts (Usher et al. 2003). Coarse particles typically deposit in the lower respiratory tract (i.e. thorax), while fine particles can penetrate deep into lung alveoli (Roy and Milton 2004). Different health impacts have been reported for various size ranges Zhang et al. (2016). While most studies agree that $PM_{2.5}$ (i.e. fine particles) poses a high risk for respiratory and cardiovascular diseases (Reiss et al. 2007, Cao et al. 2012, Liu et al. 2013, Lu et al. 2015, Lin et al. 2016, Zhao et al. 2019, Alari et al. 2025), $PM_{2.5-10}$ (i.e. coarse particles)

has also been shown to have health impacts on various populations (Chang et al. 2007, Perez et al. 2008, Lu et al. 2015, Alari et al. 2025).

Mineralogical and chemical composition of dust further modulates toxicity. Fibrous minerals (e.g. palygorskite) and quartz crystals can remain stuck in lung tissues, causing fibrosis, calcification, and silicosis (Parker and Rae 1998, Seaton and Cherrie 1998, Gomes and Silva 2021). Chemical composition is also critical as dust often contains transition metals (e.g. Fe, copper, lead, and zinc) (Perez et al. 2008, Lippmann et al. 2006) and other crustal elements (Cao et al. 2012), which can increase oxidative stress and particulate toxicity (Park et al. 2005, Cao et al. 2012, Son et al. 2012, Fang et al. 2017, Park et al. 2018, Fussell and Kelly 2021). Dust surfaces can additionally carry microbes, fungi (Kellogg and Griffin 2006, Griffin 2007), and condensed atmospheric gas species into the respiratory system (Grahame and Schlesinger 2005, Park et al. 2018, Fussell and Kelly 2021).

These condensed species are often SIA species, formed via heterogeneous reactions on dust surfaces. Particulate NO_3^- and SO_4^{2-} were initially considered as low-risk species due to their elevated solubility and natural occurrence (Schlesinger and Cassee 2003, Reiss et al. 2007), but in the last decades, rising evidence has linked exposure to them with increasing hospital admissions and mortality from respiratory and cardiovascular diseases (Son et al. 2012, Kim et al. 2012, Cao et al. 2012, Lin et al. 2016, Manisalidis et al. 2020, Zhang et al. 2021a, Konduracka and Rostoff 2022, Arfin et al. 2023). Particulate NH_4^+, although less studied, has also been shown to pose significant health risks, sometimes exceeding those of NO_3^-, SO_4^{2-}, or organic aerosols (Masselot et al. 2022). Controlling $NH_{3(g)}$ emissions as a precursor to particulate NH_4^+ is therefore an effective strategy to reduce $PM_{2.5}$-related health hazards (Pinder et al. 2007, Wu et al. 2016, Masselot et al. 2022).

Dust heterogeneous chemistry may decrease fine NH_4^+ formation while increasing coarse-mode NO_3^- and SO_4^{2-} via neutralization with NVCs. This process can mitigate health risks by reducing exposure to acidic gases, such as $H_2SO_{4(g)}$ and $HNO_{3(g)}$, which are otherwise harmful (Grahame and Schlesinger 2005, Son et al. 2012, Weber et al. 2016). Conversely, accumulation of OM on dust surfaces or reactions between metals and acid gases may increase the toxicological potential of dust particles (Reiss et al. 2007, Popovicheva et al. 2011, Oakes et al. 2012).

1.4.3 Ecosystems

While human health represents a primary concern of degraded air quality, atmospheric pollutants also affect natural ecosystems through deposition and chemical alteration of soils and waters. The deposition of oxidized and reduced N species ($HNO_{3(g)}$, NO_3^-,

$NH_{3(g)}$, and NH_4^+) drives environmental acidification and N saturation, with profound consequences for biodiversity and ecosystem carbon sequestration capacity (Grennfelt and Hultberg 1986, Dise et al. 2011, Swarbrick et al. 2019, Guo et al. 2022, Sartori et al. 2024). Due to its high solubility, deposited NO_3^- is rapidly assimilated by microorganisms or leached into aquatic systems, where elevated concentrations trigger eutrophication. This process often results in toxic algal blooms and subsequent anoxia, leading to mass mortality in fish populations (Pearce et al. 2003, de Vries et al. 2024). Furthermore, excessive NO_3^- loading induces critical stoichiometric C-N-P imbalances and alters light availability, which can suppress plant and microbial diversity (Pearce et al. 2003, van der Wal et al. 2005, Fernández-Martínez et al. 2020, Penuelas et al. 2020).

In terrestrial environments, NO_3^- contributes to soil acidification and direct toxicity, impairing vegetation growth and health. However, while traditionally viewed as a pollutant, recent research suggests that the impacts of NO_3^- are complex; shifts in microbial community structures have been observed, and its role in modulating the oxidation states of polluted environments is currently being investigated as a potential tool for ecosystem restoration (Wang et al. 2024a, Martín et al. 2024).

Both $NH_{3(g)}$ and NH_4^+ are central to the global N cycle (Liu et al. 2022a), and their condensation onto mineral dust significantly modulates their eventual deposition and ecological impact (Krupa 2003, Guo et al. 2018). On land, $NH_{3(g)}$ deposition can impair vegetation foliage, productivity, and resilience to pests, with severe consequences particularly for non-vascular plants, fungi, and lichens (Wolseley et al. 2006, Cape et al. 2009, Van Grinsven et al. 2013, Maas and Grennfelt 2016, UN 2021). These effects cumulatively decrease ecosystem biomass, biodiversity, and carbon sequestration capacity (Sheppard et al. 2011). In aquatic environments, $NH_{3(g)}$ induces eutrophication and species-specific toxicity, particularly in fish, where it disrupts homeostasis (Dise et al. 2011, de Vries et al. 2011, Bobbink and Hicks 2014, Edwards et al. 2024). This toxicity is generally more acute for $NH_{3(g)}$ than for NH_4^+ or NO_3^-, and its impact is more pronounced in freshwater systems compared to buffered marine environments (Camargo and Alonso 2006).

Conversely, the ecological influence of NH_4^+ is highly variable, dictated by local temperature and the abundance of limiting nutrients like phosphorus (Swarbrick et al. 2019). While NH_4^+ exposure can occasionally increase local biodiversity or vegetation coverage, it often suppresses fungal biomass and enzymatic activity, leading to the accumulation of surface organic carbon (Sheppard et al. 2011, Dias et al. 2014, Guo et al. 2022). In marine settings, NH_4^+ may either act as a nutrient to stimulate phytoplankton blooms or exhibit toxicity exceeding that of NO_3^-, depending on environmental conditions (Pearce

et al. 2003, Leoni et al. 2018, Swarbrick et al. 2019, Sartori et al. 2024). Critically, deposited $NH_{3(g)}$ and NH_4^+ undergo nitrification to NO_3^-, ultimately driving ecosystem acidification (Carey 2014, Sase 2020, Guo et al. 2022).

Given that global $NH_{3(g)}$ emissions—primarily from livestock and fertilizers—are projected to rise alongside food production, understanding their interaction with dust heterogeneous chemistry is essential for mitigating future N-driven environmental degradation (Guo et al. 2018, Zhang et al. 2018, Sutton and Howard 2018, Sutton et al. 2020, EEA 2020, Karydis et al. 2021, Deshpande et al. 2024).

As acidic and soluble species, SO_4^{2-} also have important detrimental impacts on ecosystems (Pöschl 2005, Seinfeld and Pandis 2006, Seinfeld 2015). While sulfur (S) is an essential plant nutrient (Zhao et al. 1999), excessive deposition as $SO_{2(g)}$ or SO_4^{2-} adversely affects roots and foliage, impairs stomatal function, and reduces plant growth (Tomlinson 1983, Marschner 2012, de Vries et al. 2014, Wei et al. 2017). Critically, deposited SO_4^{2-} binds to alkaline NVCs like Ca^{2+}, K^+, and Mg^{2+} from dust, accelerating soil acidification and base cation leaching, which hinders their uptake by plants, and has been linked to forest decline in the Northern Hemisphere (Feliciano et al. 2001, Menz and Seip 2004, de Vries et al. 2014, Likus-Cieślik and Pietrzykowski 2021). S deposition rates exhibit strong geographic variability; for instance, European environments show lower water acidity compared to the U.S. due to the neutralizing effect of Saharan Ca-rich dust and higher $NH_{3(g)}$ emissions (Lajtha and Jones 2013). Ultimately, the complex coupling of SO_4^{2-} with mineral dust, $NH_{3(g)}$, and NO_x underscores the necessity of representing heterogeneous chemistry to accurately predict environmental critical loads and ecosystem recovery (Likus-Cieślik and Pietrzykowski 2021).

1.4.4 Aerosol acidity

Beyond changes in pollutant concentrations, the chemical environment of the atmosphere plays a critical role in shaping aerosol properties. In particular, aerosol acidity governs multiphase reactions and modulates the formation, transformation, and toxicity of atmospheric particles.

The mineralogical origin of dust and the solubility of its constituent minerals, key determinants of particle alkalinity, together with the availability of acidic gas species along transport pathways, control the seasonal and regional evolution of dust pH and its associated health and environmental impacts (Fenter et al. 1995, Krueger et al. 2004, Karydis et al. 2016; 2021, Milousis et al. 2025).

In the anthropogenically polluted atmosphere of the Northern Hemisphere, particles generally exhibit lower pH during summer (Squizzato et al. 2013, Wang et al. 2019). Over Asia, aerosol acidity has increased (lower pH) over the past five decades, largely driven by

high $SO_{2(g)}$ emissions from China and India (Li et al. 2017). This long-term acidification of aerosols was partially offset by China's high emissions of $NH_{3(g)}$ and the buffering effect of alkaline dust intrusions from central Asia (Karydis et al. 2021). However, the last years have been characterized by a marked decrease in $SO_{2(g)}$ concentrations globally, and particularly over Asia, due to its thorough emission limitation (Wang et al. 2018b, Aas et al. 2019, Zhang et al. 2021b, Wang et al. 2025a). Over East Asia, reduced $SO_{2(g)}$ together with the neutralizing capacity of the still elevated $NH_{3(g)}$ concentrations and alkaline dust intrusions, leads to steady or increasing aerosol pH levels (Lv et al. 2024, Duan et al. 2025, Wang et al. 2025b).

Aerosol acidity influences the solubility of transition metals, with studies showing a marked increase in metal dissolution at pH values below 3 (Meskhidze et al. 2003, Nenes et al. 2011). Elevated concentrations of dissolved metals are associated with adverse health effects (Lippmann 2014, Kelly and Fussell 2016). In addition, aerosol pH affects particle hygroscopicity (Karydis et al. 2021) and contributes to acid rain (Pye et al. 2020), with important implications for water systems and ecosystems (see Section 1.4.5).

Aerosol acidity is also critical for the conversion of Fe and P into bioavailable forms. Acidic coatings have been shown to enhance Fe and P solubility by lowering dut pH (Meskhidze et al. 2003, Nenes et al. 2011, Lanzl et al. 2012, Stockdale et al. 2016, Kanakidou et al. 2018). Consequently, the bioavilability of these nutrients – and their impacts on ecosystems and human health – depends in part on heterogeneous reactions between mineral dust and acidic trace gases (Fang et al. 2017, Pye et al. 2020).

Overall, dust pH is partially regulated by coatings of inorganic acids and by neutralization through dust NVCs (see Section 1.3). Variations in aerosol acidity directly influence particle composition, solubility of trace metals, and oxidative potential, all of which affect human exposure and toxicity. These chemical characteristics provide a mechanistic link between atmospheric processes and observed health outcomes.

1.4.5 Climate

In addition to local and regional ecological impacts, dust influences the climate system through radiative forcing and interactions with clouds and biogeochemical cycles. Analyses of ice cores and ocean sediments (Rea 1994, Semeniuk and Dastoor 2020) revealed dust as a key driver of Earth's climate on time scales ranging from interannual to geological. Specific atmospheric processes, such as heterogeneous chemistry on particle surfaces, can modify dust optical properties and thus alter its net radiative effect.

Dust particles scatter and absorb shortwave (SW) and longwave (LW) radiation, processes collectively referred to as the dust *direct radiative effects* (Seinfeld and Pandis

2006). Particle size is a key factor governing dust–radiation interactions. In general, fine dust particles predominantly scatter SW radiation, leading to a cooling effect, whereas coarse dust more effectively absorbs LW radiation, producing a warming effect (Tsigaridis and Kanakidou 2018). Overall, dust is estimated to account for approximately 25% of total aerosol light absorption (Samset et al. 2018, Sand et al. 2021).

The shape and surface characteristics of dust particles are key factors controlling their direct radiative effects and, consequently, their radiative forcing, defined as the present-day net change in the Earth's radiative flux directly driven by dust particles relative to pre-industrial conditions (Hansen et al. 2005, Miller et al. 2014, Heald et al. 2014).

Although subject to substantial uncertainties, Mahowald et al. (2010) estimated the net dust radiative forcing over the 20th century to be $-0.14 \pm 0.11\,\mathrm{W\,m^{-2}}$. More recently, accounting for increases in dust emissions, Kok et al. (2023) estimated a value of $-0.2 \pm 0.5\,\mathrm{W\,m^{-2}}$. Both studies attribute the high uncertainties in these estimates largely to limited knowledge of dust optical properties, arising from poorly constrained dust mineralogical composition, emission patterns, and the radiative impacts of dust heterogeneous chemistry.

For instance, dust mineral composition can also influence its interaction with light (Usher et al. 2003, Riemer et al. 2019). Minerals such as goethite and hematite (Fe oxides) are considered strong absorbers of SW, while clays, quartz, $CaCO_3$ and phyllosilicates interact with LW (Sokolik and Toon 1999, Claquin et al. 1999, Moosmüller et al. 2012, Journet et al. 2014, Di Biagio et al. 2020).

The condensation of SIA, such as NO_3^- and SO_4^{2-}, within the particles' aqueous coatings significantly modulates the radiative forcing of mineral dust (Klingmüller et al. 2020, Zhang et al. 2020). While the cooling potential of SO_4^{2-} aerosols via SW scattering is well-established (Myhre et al. 2004, Bauer and Koch 2005), recent studies indicate that NO_3^- coatings similarly enhance the SW scattering cross-section of dust. This enhancement typically leads to a more pronounced net radiative cooling effect through the aerosol direct effect (Bauer et al. 2007, Xu and Penner 2012, Li et al. 2015, Milousis et al. 2025). However, the net climatic impact remains sensitive to the mixing state, as the presence of these non-absorbing coatings can also alter the internal light field of the particle, potentially enhancing the absorption of the underlying mineral core.

In the last decades, particulate NO_3^- has gained relevance because of the already sustained and projected important decreases in $SO_{2(g)}$ emissions for the next century. This, together with more slowly declining NO_x emissions (Zheng et al. 2018, EEA 2023, AAPCA 2025), and steady or rising $NH_{3(g)}$ emissions (Maas and Grennfelt 2016, UN 2021), are expected to increase particulate NO_3^- atmospheric concentrations (Tsimpidi

et al. 2007; 2008, Boucher et al. 2013, IPCC 2021, Jonson et al. 2022, Pan et al. 2024, Lv et al. 2024, Huang et al. 2025). Therefore, NO_3^- radiative effects are going to gain relevance in the next decades, potentially exceeding those from sulfate aerosols, and even reaching up to two-thirds of the anthropogenic optical depth globally (Bellouin et al. 2011, Hauglustaine et al. 2014).

The chemical interaction of mineral dust with NO_3^-, NH_4^+, and SO_4^{2-} species significantly alters the atmospheric burden and partitioning of these pollutants. By acting as a sink for these precursors, mineral dust effectively scavenges species that would otherwise form highly-scattering secondary aerosols. This reduction in the total column's scattering capacity can exert a net warming influence on the climate (Kok et al. 2023).

Simultaneously, these heterogeneous reactions fundamentally transform the physicochemical nature of the dust itself. The accumulation of inorganic coatings not only modifies the particles' complex refractive index and subsequent optical properties but also increases their hygroscopicity (Kelly et al. 2007). Such changes in hygroscopicity enhance the particles' ability to act as cloud condensation nuclei (CCN), potentially altering cloud lifetime and albedo, processes known as dust *indirect radiative effects* (Kok et al. 2018, IPCC 2021, Milousis et al. 2025).

In regions impacted by significant dust loading, these particles can promote cloud development (Levin and Cotton 2009, Twohy et al. 2009), with even the largest mineral grains functioning as giant CCN (Levin et al. 2005). Consequently, the presence of dust—and the degree to which it is coated by soluble species—can dictate the initial size distribution of cloud droplets (Milousis et al. 2025). The synergy between the mineral core and its soluble shell thus represents a primary mechanism through which dust influences cloud morphology and lifetime (IPCC 2021).

Beyond its role as CCN, mineral dust significantly modulates the properties and radiative interactions of existing cloud layers through *aerosol semi-direct effects* (Levin and Cotton 2009). These phenomena are primarily driven by the absorption of radiation by dust particles within or adjacent to cloud layers. When dust is interstitial to cloud droplets, the resulting localized heating increases the in-cloud temperature and reduces the internal RH. This thermodynamic shift induces the evaporation of water droplets, effectively reducing the overall cloud fraction and altering the cloud's radiative impact. Furthermore, below-cloud dust can increase local temperature and cause the upwelling of low-level clouds. Such perturbations influence the vertical growth, morphology, and thermal structure of these clouds, thereby modifying their interaction with radiation (Huang et al. 2006, Amiri-Farahani et al. 2017, Milousis et al. 2025).

Moreover, dust plays a critical role in the formation of cirrus and mixed-phase clouds by acting as ice nuclei particle (INP) (Levin et al. 2005, Chen et al. 2019). This ice-

nucleating efficiency is highly sensitive to the dust's specific mineralogy. For instance, K-feldspar, quartz, hematite, and illite are recognized as highly efficient promoters of immersion and deposition freezing. In contrast, minerals such as montmorillonite, $CaCO_3$, and gypsum are generally regarded as poor INPs, underscoring the necessity of representing mineral-specific surface properties in climate models (Zimmermann et al. 2008, Harrison et al. 2019).

Heterogeneous reactions fundamentally alter the hygroscopicity of mineral dust, driving a transition from hydrophobic to hydrophilic states. The accumulation of NO_3^- and SO_4^{2-} species lowers the critical supersaturation required for CCN activation, thereby potentially enhancing cloud formation and increasing cloud albedo in dust-impacted regions (Usher et al. 2002, Karydis et al. 2011, Milousis et al. 2025). Conversely, mineral dust provides an expansive surface area that scavenges anthropogenic CCN, such as SO_4^{2-} and organics, through uptake and coagulation. This process hinders the formation of new particles and cloud droplets, ultimately reducing cloud cover and total albedo (Klingmüller et al. 2020, Casquero-Vera et al. 2023). Klingmüller et al. (2020) estimated that this interaction between dust and pollutants results in a net warming of $+0.2 \pm 0.1$ W m^{-2} due to the suppression of aerosol radiative cooling.

Recent modeling efforts have further quantified these direct and indirect radiative forcing effects. On one side, early estimates by Liao and Seinfeld (2005) suggested that dust interactions with $SO_{2(g)}$ and $HNO_{3(g)}$ could currently reduce anthropogenic aerosol cooling by 0.5–1 W m^{-2}, potentially doubling by 2100. Later studies suggested that NO_3^- could induce a cooling direct radiative effect that ranges from -0.10 to -0.12 W m^{-2} (Bellouin et al. 2011, Xu and Penner 2012, Heald et al. 2014). In parallel, dust indirect effects alter atmospheric composition and the efficiency of cloud formation through both, the presence of the dust itself and its dust chemical transformations, indirectly modulating Earth's albedo and infrared transparency. Collectively, the direct and indirect radiative forcing of dust heterogeneous chemistry remains uncertain, with estimates of a net warming around $+0.10 \pm 0.15$ W m^{-2} (Bauer et al. 2007, Kok et al. 2023). This positive radiative forcing is largely a consequence of the removal of high-scattering anthropogenic aerosols, estimated to contribute a warming range of +0.12 to +0.20 W m^{-2} (Liao et al. 2004, Bauer and Koch 2005, Bauer et al. 2007, Kok et al. 2023). More recently, Milousis et al. (2025) estimated that NO_3^- direct effects exert a net cooling of -0.11 W m^{-2} – driven primarily by fine-mode scattering – while its indirect effects tell a different story; NO_3^- coatings enhance the scavenging of small anthropogenic particles, leading to a net warming of +0.17 W m^{-2} specifically attributed to NO_3^- (Milousis et al. 2025).

These findings underscore that the actual global radiative impact of dust is inextricably linked to its heterogeneous chemistry, with particulate NO_3^- playing a noticeable role in modulating the net climate response.

Finally, a significant source of uncertainty in aerosol modeling is the prescribed mixing state of dust with other atmospheric constituents. While the preceding discussion largely assumes dust to be *internally mixed*—where NO_3^-, SO_4^{2-}, and NH_4^+ form uniform coatings on the mineral core—these species can also exist as *externally mixed* populations. In the latter case, secondary inorganic species form independent particles through the neutralization of the $NH_{3(g)}$-$HNO_{3(g)}$-$H_2SO_{4(g)}$ system over non-mineral substrates, such as preexisting aqueous sulfate aerosols (Jacob 2000). The radiative implications of these mixing states are distinct; the optical cross-section and hygroscopicity of a coated dust particle differ fundamentally from those of an equivalent mass of separated inorganic aerosols and minerals (Bauer and Koch 2005). This complexity is further compounded by the presence of black carbon (BC), OM, and sea salt, which may coexist with dust in varying degrees of internal or external integration. Field observations underscore that the mixing state is neither static nor globally uniform; rather, it is highly variable and evolves dynamically during atmospheric transport (Huebert et al. 2003, Jacob et al. 2003, Trochkine et al. 2003).

1.5 Modeling of mineral dust heterogeneous chemistry and mineralogical representation

The integration of mineral dust heterogeneous chemistry into atmospheric models was pioneered by the seminal studies of Zhang et al. (1994) and Dentener et al. (1996). These foundational works respectively introduced the heterogeneous removal of $N_2O_{5(g)}$ and of $HNO_{3(g)}$, $SO_{2(g)}$, O_3, and HO_2 radicals onto dust surfaces within tropospheric chemistry models. Collectively, they established the first quantitative estimates regarding the significance of mineral dust in the global oxidative, N, and S atmospheric cycles (Zhang et al. 1994, Dentener et al. 1996, Tang et al. 2017).

These initial modeling studies catalyzed a rapid expansion of the field. In the subsequent years, a surge of research emerged to bridge the gap between experimental observations (Tabazadeh et al. 1998, Goodman 2000, de Reus et al. 2000, Underwood et al. 2001, Usher et al. 2002, Hanisch and Crowley 2003) and numerical simulations (Song and Carmichael 1999, Zhang and Carmichael 1999, Phadnis and Carmichael 2000, Song and Carmichael 2001). These efforts sought to elucidate gas-liquid-solid partitioning rates and the underlying mechanisms governing surface reactions (Pringle et al. 2010). Two referential reviews on this matter are Usher et al. (2003), which provide a comprehensive

theoretical and experimental investigation of the dynamics driving dust reactions, and Crowley et al. (2010; 2013), which compile heterogeneous reaction kinetics on different aerosol surfaces.

Over the last decades, representing mineral dust chemistry in atmospheric models has transitioned from a novelty to a standard requirement (Bian et al. 2017). Within this context, various approximations have been proposed to describe reactions involving both dust and sea salt, with a specific focus on the condensation of $HNO_{3(g)}$ to form particulate NO_3^-. However, the semi-volatile nature of $HNO_{3(g)}$ and other gas species introduces significant modeling challenges that are absent only in the case of $H_2SO_{4(g)}$, which exhibit lower volatility and higher reactivity upon condensation.

Consequently, a subset of methodologies has been developed to account for the reversible partitioning of species such as $HNO_{3(g)}$ and $NH_{3(g)}$. In contrast, species like $SO_{2(g)}$ and $H_2SO_{4(g)}$ are treated as irreversibly condensed (Karydis et al. 2016). As a result, the literature now reflects a spectrum of approaches for incorporating NO_3^- and other SIA formation, each adopting a different level of complexity to represent the multiphase chemical dynamics on dust particles.

The strategies for integrating mineral dust chemistry into atmospheric models can be categorized based on their treatment of the gas-aerosol partitioning:

1. **Dynamic Mass Transfer (DMT):** This approach explicitly calculates the kinetic flux between gas and aerosol phases (Meng and Seinfeld 1996, Lurmann et al. 1997, Song and Carmichael 2001, Feng and Penner 2007, Zaveri et al. 2008, Trump et al. 2015). While DMT accurately captures non-equilibrium processes across varying temperatures and humidities, its numerical stiffness makes it a computationally expensive methodology for atmospheric simulations (Feng and Penner 2007, Zaveri et al. 2008, Trump et al. 2015, Karydis et al. 2016).

2. **First-order irreversible uptake (UPTK):** To reduce computational costs, the mass transfer equations are often simplified into a first-order irreversible sink using an uptake coefficient (γ, Figure 1.7). This method, popularized by Bauer et al. (2004) and based on the formulation by Fuchs and Sutugin (1970), avoids integrating differential equations by ignoring equilibrium vapor pressures. However, it fails to account for the evaporation of semi-volatiles, the relative concentrations of reactants, and the temporal variation of the uptake rate due to their consumption (Jacob 2000, Feng and Penner 2007, Crowley et al. 2010; 2013). While Uno et al. (2017b;a) successfully applied UPTK in GEOS-Chem to reproduce seasonal NO_3^- variations, they reported slight underestimations in the coarse mode.

3. **Thermodynamic equilibrium (TEQ):** This paradigm assumes instantaneous equilibrium between gas/particle phases (Lurmann et al. 1997, Nenes et al. 1998, Feng and Penner 2007, Bauer et al. 2007, Hauglustaine et al. 2014, Paulot et al. 2016, Bian et al. 2017, Wu et al. 2025). While physically sound for fine particles—which equilibrate within minutes—it is often inappropriate for coarse particles that may take days to reach equilibrium (Seinfeld and Pandis 1998, Karydis et al. 2016).

   To address the tendency of bulk TEQ to underestimate fine NO_3^- (Wu et al. 2025), models often apply TEQ only to fine modes (fTEQ) (Watanabe et al. 2011, Schmidt et al. 2014) or use surface-area-weighted redistribution functions (Binkowski and Shankar 1995). However, the latter can lead to significant overpredictions of fine NO_3^- at the expense of the coarse mode (Karydis et al. 2011, Zakoura and Pandis 2018). Common thermodynamic models for these calculations include ISORROPIA-I/II (Nenes et al. 1998, Fountoukis and Nenes 2007) and EQSAM (Metzger et al. 2002).

4. **Hybrid approaches (HYB):** Currently the most prevalent strategy, the hybrid method applies fTEQ to fine modes and either UPTK or DMT to the coarse modes (Capaldo et al. 2000, Hodzic et al. 2006, Hauglustaine et al. 2014, Trump et al. 2015). This dual treatment leverages equilibrium efficiency where applicable while maintaining kinetic constraints for larger particles. Although HYB methods generally outperform bulk TEQ (Trump et al. 2015, Kakavas and Pandis 2020), global simulations often show a positive bias in surface NO_3^- (Hauglustaine et al. 2014, Paulot et al. 2016). This overestimation may stem from the irreversible nature of the UPTK component, which precludes the evaporation of species from dust surfaces (Soussé Villa et al. 2025).

5. **Double-call equilibrium (DBCLL):** A more recent refinement involves calculating TEQ twice: first for the fine mode and subsequently for the coarse mode (Pringle et al. 2010, Karydis et al. 2016). This approach constrains the mass available for each TEQ "call" through kinetic limitations or size-dependent weighting functions (Pandis et al. 1993, Vignati et al. 2004, Feng and Penner 2007). Specifically, Karydis et al. (2016) implemented a DBCLL constrained by diffusion kinetics, a mechanism that is explored in further detail in the Methodology section of this work.

While DMT and TEQ methods facilitate the simulation of reversible condensation-evaporation dynamics, the UPTK method remains limited to irreversible sinks based on

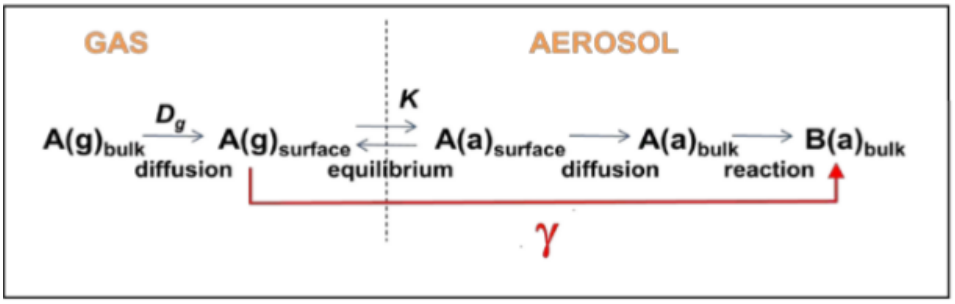

Figure 1.7: Representation of the uptake process of gas species in the aerosols liquid coating, and its parameterization through an uptake coefficient (γ) (adapted from Brasseur and Jacob (2017)).

gas-phase properties, particle's alkalinity, and environmental conditions (Fairlie et al. 2010, Paulot et al. 2016). Despite these diverse methodological approaches, significant discrepancies persist in predicting the tropospheric burden of oxidized ($HNO_{3(g)}$+NO_3^-) and reduced ($NH_{3(g)}$+NH_4^+) nitrogen (Fairlie et al. 2010, Hauglustaine et al. 2014, Paulot et al. 2016, Zakoura and Pandis 2018, Luo et al. 2019, Jones et al. 2021, Rémy et al. 2022, Wu et al. 2025).

The AeroCom phase III intercomparison exercise (Bian et al. 2017), an extensive intercomparison study of atmospheric models incorporating NO_3^- formation processes on dust and sea salt, highlights this lack of consensus. The average global NO_3^- burden was found to be 0.63 ± 0.56 Tg, a standard deviation nearly equal to the mean. Such variability, also reflected in NH_4^+ (0.32 ± 0.20 Tg), underscores a fundamental misrepresentation of N heterogeneous chemistry, particularly during long-range transport. These biases are generally attributed to three primary factors: 1) uncertainties in dust emission fluxes and size distributions (Adebiyi and Kok 2020, Kok et al. 2023, Wu et al. 2025); 2) inaccuracies in precursor (NO_x and $NH_{3(g)}$) emission inventories (Heald et al. 2012, Walker et al. 2012); and 3) knowledge gaps and the simplified treatment of surface-specific chemical processes (Sokolik et al. 2001, Usher et al. 2003, Heald et al. 2012, Walker et al. 2012, Bian et al. 2017, Wu et al. 2025).

Central to the chemical reactivity of dust is its mineralogical composition (Krueger et al. 2004, Karydis et al. 2021), particularly the presence of $CaCO_3$. Upon dissolution into the aqueous coating of a particle, $CaCO_3$ dissociates to provide soluble calcium cations (Ca^{2+}). These cations act as a primary alkaline buffer, neutralizing dissolved $HNO_{3(g)}$ in the aqueous medium to form stable particulate calcium nitrate ($Ca(NO_3)_2$), representing an important source of particulate NO_3^- (Fenter et al. 1995, Krueger et al. 2004, Hauglustaine et al. 2014).

The sensitivity of uptake coefficients to mineral content has been established across various dust types, including Saharan, Asian, and Arizona Test Dust (Usher et al. 2003,

Vlasenko et al. 2006, Liu et al. 2008, Wei 2010). Crucially, while regional models tend to assume a uniform mineralogy, global dust composition is highly heterogeneous (Claquin et al. 1999, Journet et al. 2014, Brodrick et al. 2025). Accounting for this heterogeneity is vital; for instance, Karydis et al. (2016) estimated that geographical heterogeneity in mineral distribution alone increases the global NO_3^- burden by 18%, while dust heterogeneous chemistry increases a 44% global NO_3^- burdens, with a disproportionate 53% increase in the coarse mode compared to 21% in the fine mode, supporting the paramount importance of heterogeneous processes in NO_3^- formation and their sensitivity to dust mineralogy.

Despite the projected future importance of NO_3^- in a context of decreasing $SO_{2(g)}$ emissions and $NH_{3(g)}$ increase (Bauer et al. 2007, Hauglustaine et al. 2014, IPCC 2021, EEA 2023, AAPCA 2025), most climate models continue to treat dust as a chemically homogeneous bulk mass (Sokolik et al. 2001, Usher et al. 2003, Nickovic et al. 2012, Bian et al. 2017). This omission leads to a systematic global overprediction of particulate NO_3^- (Myhre et al. 2006, Bian et al. 2009, Simpson et al. 2012, Hauglustaine et al. 2014).

Efforts to address these biases through grid refinement to capture the sharp gradients of NO_3^- precursor gases have yielded limited success (Zakoura and Pandis 2018). More promising results have emerged from models incorporating discrete mineralogy. For example, the EMAC global model utilizes TEQ calculations across 12 distinctly characterized dust mineral source regions. While regional biases remain, the transition from homogeneous to discrete mineralogy significantly improved model accuracy, highlighting the sensitivity to local crustal species and aerosol thermodynamic states (Karydis et al. 2016; 2021). Another example is the IFS-COMPO recent 49R1 version that integrates high-resolution mineralogical data from Journet et al. (2014). Although initial evaluations show better agreement with local observations, the model still lacks a comprehensive global validation for NO_3^- and exhibits persistent biases in the fine-to-coarse mass distribution (Rémy et al. 2024).

In summary, the transition toward source-based, mineral-specific modeling is essential for resolving long-standing discrepancies in atmospheric N cycles.

Despite the potential importance of mineralogical variability, its representation in atmospheric models has historically relied on a limited number of extrapolation-based soil atlases. The pioneering dataset of Claquin et al. (1999) provided the first global-scale description of dust mineral composition suitable for climate modeling and has since been widely used to assess dust radiative effects, aerosol–cloud interactions, and biogeochemical fluxes. Subsequent refinements by Journet et al. (2014) expanded the mineralogical

detail, notably distinguishing hematite and goethite. These datasets have been instrumental in advancing our understanding of mineral-specific dust radiative effects and remain a cornerstone of current Earth system modeling efforts (Riipinen et al. 2026). However, both mineralogical maps are ultimately constrained by sparse and unevenly distributed soil measurements, requiring strong empirical assumptions to extrapolate mineral fractions across arid and semi-arid regions. As a result, uncertainties remain substantial, particularly for key reactive minerals such as $CaCO_3$ and Fe_2O_3, whose abundance and size distribution critically regulate dust alkalinity, heterogeneous chemistry, and optical properties. Until recently, the absence of observationally constrained, spatially continuous mineralogical data has limited the ability of atmospheric models to rigorously assess how mineralogical variability influences gas–aerosol partitioning and SIA formation.

The recent launch of NASA's Earth Surface Mineral Dust Source Investigation (EMIT) spectrometer represents a major advance in this context. EMIT provides the first near-global, imaging spectroscopy-based maps of surface mineral composition over major dust-emitting regions, offering unprecedented spatial detail and observational grounding. Early modeling studies have already demonstrated the relevance of EMIT-derived mineralogy for constraining dust radiative effects and absorption, particularly through improved representation of Fe oxides (Li et al. 2025). However, to date, these datasets have not been systematically exploited to investigate dust heterogeneous chemistry and its implications for aerosol composition, acidity, and size-resolved SIA formation.

2

Objectives and structure

2.1 Objectives, context and scope

This Thesis investigates the role of dust heterogeneous chemical processes and dust mineralogical composition upon the partitioning of semi-volatile inorganic compounds. It presents a systematic exploration of multiple representations of heterogeneous chemistry and mineralogy implemented within the Multiscale Online Non-hydrostatic AtmospheRe CHemistry (MONARCH) atmospheric chemistry model. Notably, it features the first integration of the EMIT mineralogical dataset into a global atmospheric chemistry modeling framework to study dust-chemistry interactions. The outcomes of this Thesis aim at providing an up-to-date quantitative understanding of how dust mineralogy shapes atmospheric composition and aerosol optical properties at a global scale.

This aim is achieved by fulfilling the following objectives:

1. Implement a suite of dust heterogeneous chemistry mechanisms of varying complexity into a global model, including an explicit representation of regionally-varying mineral alkalinity.

2. Advance the current understanding of dust heterogeneous chemistry processes by assessing their impact upon the global burdens of semi-volatile inorganic compounds (i.e. NO_3^-, SO_4^{2-}, and NH_4^+) and their size distribution.

3. Quantify the implications of source-resolved mineral variability upon dust-gas interactions by comparing the effects of employing spatially-discrete dust mineralogy, against the commonly used assumption of homogeneous global dust composition.

4. Isolate the effect of dust mineralogical and chemical treatment on aerosol optical properties by investigating how different representations of these processes

influence aerosol optical depth (AOD) and single scattering albedo (SSA).

The outcomes of this investigations provide:

- A comprehensive assessment of the impacts that dust heterogeneous chemistry and mineralogical variability representations have on global atmospheric composition.
- Advanced understanding of the processes driving SIA formation on fine and coarse particles at a global-scale, and recommendations on how to integrate them in atmospheric models.
- Assessment on different representations of dust mineralogy in atmospheric models, evaluating their significance for inorganic aerosol heterogeneous chemistry and aerosol acidity.
- Insights into how dust mineralogy and its derived SIA influence aerosol optical properties.
- A benchmark framework for estimating the present-day direct radiative effect of dust and aerosols in future studies.

The present PhD Thesis was conducted under the umbrella of the ERC Consolidator Grant entitled FRontiers in dust minerAloGical coMposition and its Effects upoN climate (FRAGMENT) led by Dr. Carlos Pérez García-Pando. FRAGMENT aimed at fundamentally advancing the treatment of dust mineralogy by fulfilling several objectives: 1) It contributed new fundamental understanding to reduce the large uncertainties in the emitted dust particle size distribution (PSD) by evaluating and extending current theoretical paradigms, based on an unprecedented ensemble of coordinated measurement campaigns and laboratory analyses. This included addressing both experimentally and theoretically the size-resolved mineralogy of dust at emission and its relationship with the parent soil; 2) Precise knowledge of dust mineral content requires more detailed and widespread measurements of soil mineralogy. FRAGMENT evaluated and used airborne and spaceborne hyperspectral imaging to improve global atlases of soil mineralogy for dust modeling. In this sense FRAGMENT has been intimately linked to the EMIT NASA project; 3) While the impact of dust mineralogy upon climate is potentially large, the interconnection of mechanisms has been neglected in the few models that represent mineral variations. FRAGMENT generated integrated and quantitative knowledge regarding the effects of dust mineral composition based on modeling experiments constrained with the theoretical innovations, field measurements and new soil

mineralogical map. This Thesis is specifically linked to the third objective of FRAGMENT.

This Thesis was also performed in the context of the EMIT mission (Green and Thompson 2020, Brodrick et al. 2025), in which Dr. Pérez García-Pando is part of the Science Team. In a context of uncertain compositional knowledge of the Earth's mineral dust source regions, mostly derived from extrapolated mineral datasets (Claquin et al. 1999, Journet et al. 2014), EMIT provides empirical spectroscopically-derived surface mineral composition, updating the prescribed boundary conditions for models. The EMIT mission operates from the International Space Station since May 2022, using visible to short wavelength infrared imaging spectroscopy to determine the mineral composition of the arid land dust source regions of the Earth. This Thesis represent the first integration of EMIT data in an atmospheric chemistry model to constrain the mineralogy of dust sources and further understand its effects upon dust chemistry and climate.

2.2 Structure

This manuscript is organized into 8 chapters, following the chronological sequence of the developments and investigations performed during this PhD, particularly from Chapter 4 to 7. Figure 2.1 summarizes the structure and workflow of this Thesis.

Chapter 1 introduces the motivation for this Thesis and summarizes the state of the art in atmospheric mineral dust and its impacts upon air quality and climate. It reviews the life cycle of mineral dust, from sources to depositions, and highlights its interactions with atmospheric chemistry and the Earth radiative balance. The current treatment of dust heterogeneous chemistry in atmospheric models is also discussed.

Chapter 2 presents the objectives and scope of the thesis.

Chapter 3 presents the main methods and datasets that served as the foundation for the research conducted throughout the thesis. It introduces the numerical modeling tools (3.1), the dust mineralogical datasets (3.2), the emission scheme (3.3), and the observations used for the evaluation of the results (3.4).

Chapter 4 comprehensively describes the model developments performed during this PhD. We incorporate varying levels of dust heterogeneous chemistry complexity into the MONARCH model, which allows for assessing the sensitivity to critical processes. Main developments within MONARCH include modifications to the aerosol size distribution representation (4.1), the coupling of the ISORROPIA-II thermodynamic equilibrium model (4.2), the implementation of different gas-aerosol partitioning mechanisms (4.3),

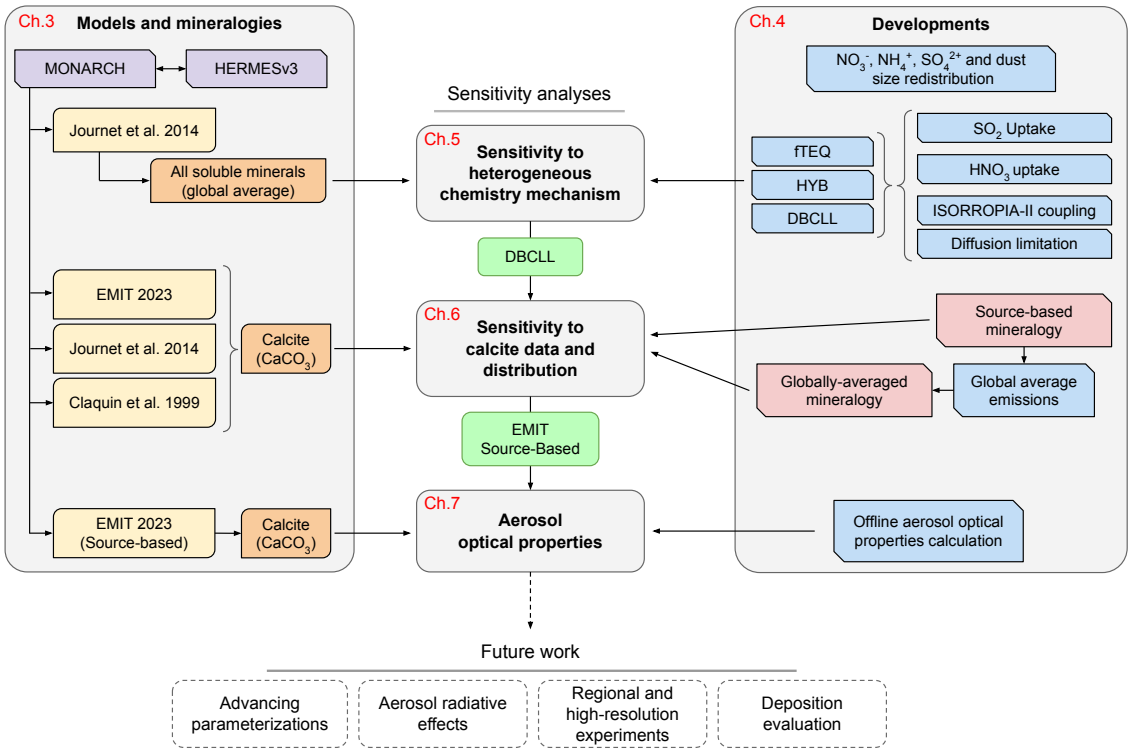

Figure 2.1: Structure of this Thesis. Modeling tools and mineral datasets (left column), sensitivity analyses (central column), and developments (right column). The corresponding chapters are specified in red at the top of each section box.

and dust heterogeneous chemistry schemes (4.4). These developments are explored in the subsequent chapters through multiple sensitivity studies.

Chapter 5 presents the published study that investigates key processes in NO_3^- formation in the presence of dust and evaluates their representation in models. Our analyses address the condensation pathways of gas species onto dust (irreversible and reversible), the influence of NO_3^- representation on species burdens, lifetimes, and size distribution, and the role of alkalinity.

Chapter 6 presents the submitted study where we use novel spaceborne imaging spectroscopy of arid surfaces from NASA's EMIT, together with a global chemistry configuration of MONARCH model constrained by satellite-inverted dust emissions, to quantify how real-world variability in $CaCO_3$ alters aerosol chemistry and acidity.

Chapter 7 examines the influence of dust heterogeneous chemistry processes investigated in this Thesis on aerosol optical properties (AOD and SSA), assessing the sensitivity of these optical properties to different representations of dust mineralogy, SIA formation pathways, and size distribution.

Finally, Chapter 8 summarizes the main findings of the investigation presented in this

Thesis and outlines directions for future research to further advance our understanding of the impacts of airborne dust on air quality, atmospheric chemistry and climate.

3

Methodology

This Chapter presents the baseline tools used across this Thesis, including the numerical atmospheric model (Section 3.1), the implemented mineral datasets (Section 3.2), the emission processing system (Section 3.3), the observational data used in the evaluation (Section 3.4), and the computational resources (Section 3.5).

The technical developments conducted in this Thesis are specifically described in Chapter 4, which evolve the atmospheric model described here to achieve the objectives of the research.

3.1 The MONARCH atmospheric chemistry model

The present Thesis makes use of the Multiscale Online Non-hydrostatic AtmospheRe CHemistry model (MONARCH; https://earth.bsc.es/gitlab/es/monarch), which is under continuous development at the Earth Sciences department of the Barcelona Supercomputing Center (Pérez et al. 2011, Jorba et al. 2012, Badia et al. 2017, Klose et al. 2021, Gonçalves Ageitos et al. 2023, Navarro-Barboza et al. 2024). It simulates the atmospheric life cycle of aerosol and gas-phase species through an online coupling with the Nonhydrostatic Multiscale Model on the B-grid (NMMB) (Janjic and Gall 2012). NMMB allows running both global and regional atmospheric simulations with embedded telescoping nests. The Arakawa B grid is used in the horizontal direction and the Lorenz hybrid pressure-sigma coordinate in the vertical direction. MONARCH global simulations use a regular latitude-longitude grid with polar filtering and a rotated longitude-latitude grid is adopted for regional applications. The NMMB numerical schemes are based on principles described in Janjic and Gall (2012). The physical parameterizations used in the model include (1) a surface layer scheme based on the Monin-Obuknov similarity theory (Monin and Obukhov 1954) combined with a viscous sublayer on continental and water surfaces (Zilitinkevich 1965, Janjic 1984; 1996), (2) the Mellor–Yamada–Janjic (MYJ) planetary boundary layer and the free troposphere

turbulence scheme (Janjić 2001), (3) the Unified NCEP-NCAR-AFWA Noah land surface model (Ek et al. 2003) to compute the surface heat and moisture fluxes, (4) the 1D Rapid Radiative Transfer Model for Global circulation Models (RRTMG) (Iacono et al. 2008) for the calculation shortwave and longwave radiative fluxes, (5) the Ferrier microphysics scheme (Ferrier et al. 2002) for grid-scale clouds, and (6) the Betts–Miller–Janjic convective clouds scheme (Betts and Miller 1986, Emanuel and Živković Rothman 1999, Janjić 2000). The same advection and vertical mixing schemes formulated in NMMB are used for both meteorological and chemistry species for consistency.

MONARCH includes a gas-phase module combined with a hybrid sectional–bulk multi-component mass-based aerosol module. The gas-phase chemistry is based on the Carbon Bond 2005 (CB05) chemical mechanism extended with Cl chemistry (Yarwood et al. 2005, Whitten et al. 2010) designed to describe urban to remote tropospheric conditions. The photolysis rates are computed using the Fast-J scheme (Wild et al. 2000) accounting for aerosols, clouds, and absorbers such as O_3. A resistance approach is adopted for dry deposition (Wesely 1989) and in-cloud and below-cloud scavenging and wet deposition follows Byun (1999) and Foley et al. (2010). Short-lived radical species are not advected in the model.

The aerosol representation in MONARCH considers 8 main components, namely dust, sea salt, BC, OM (both primary and secondary), SO_4^{2-}, NH_4^+, NO_3^- and unspeciated aerosol mass. Mineral dust and sea salt are described with a sectional size distribution of 8 bins spanning from $0.2\mu m$ to $20\mu m$ and $30\mu m$ in diameter, respectively. All the other aerosol components are represented by a fine mode, except NO_3^-, represented with both fine and coarse modes to consider the condensation of $HNO_{3(g)}$ on coarse particles.

BC is represented in two primary modes: hydrophobic and hydrophilic, with 80% of its emitted mass initially classified as hydrophobic. During atmospheric transport, an aging process with an e-folding time of 1.2 days facilitates the transition of mass from the hydrophobic to the hydrophilic mode (Chin et al. 2002). Secondary organic aerosol (SOA) formation can be solved in MONARCH with a two-product scheme from Tsigaridis and Kanakidou (2007), or a simple nonvolatile parameterized scheme based on Pai et al. (2019) (Tsigaridis and Kanakidou 2007, Hodzic and Jimenez 2011, Pai et al. 2019). For this work, organic aerosols (OA) are represented using the simplified scheme of Pai et al. (2019), which assumes fixed SOA yields calibrated to align with more complex volatility-based approaches. Various SOA precursors from biogenic, pyrogenic, and anthropogenic origin emission sources are accounted for by Pai et al. (2019) scheme. Combustion emissions are scaled to estimate the precursors coming from combustion and

fossil fuels sources. SOA particles are formed from gas phase precursors using a first-order rate constant. For primary organic aerosols (POA), a dual-mode representation — hydrophobic and hydrophilic — is adopted, similar to BC. In this scheme, 50% of the emitted mass is classified as hydrophobic, with an aging e-folding time of 1.15 days transitioning it to the hydrophilic mode, with specific OM/OC ratios for the hydrophilic and hydrophobic modes. Originally designed for global models, this approach has also demonstrated strong performance at regional scales (Navarro-Barboza et al. 2024).

The S chemistry is calculated through a simplified gas–aqueous–aerosol mechanism that accounts for the oxidation of $SO_{2(g)}$ and dimethyl sulfide (DMS) to $H_2SO_{4(g)}$. At the end of each chemistry integration time step, the remaining $H_2SO_{4(g)}$ that has not formed aqueous sulfate is assumed to fully nucleate into fine particulate SO_4^{2-} (Spada 2015).

The heterogeneous hydrolysis of $N_2O_{5(g)}$ on aqueous sulfate particles is included to account for additional $HNO_{3(g)}$ formation, following the formulation of Riemer et al. (2003). The model does not include the transformation of $NO_{2(g)}$ to $HNO_{3(g)}$ on aerosol particles due to its relatively low significance (Jacob 2000, Jordan et al. 2003, Liao et al. 2003, Li et al. 2024b). By default, the SIA formation is solved using a HYB method as described in detail below (Section 3.1.1).

Finally, MONARCH includes meteorology-driven emission modules for key species. Emissions of biogenic non-methane volatile organic compounds (NMVOC) and $NO_{(g)}$ are calculated from the Model of Emissions of Gases and Aerosols from Nature (MEGAN) v2.04 (Guenther et al. 2006). Several sea salt source functions are available in the model (Spada et al. 2013); here we use the Jaeglé et al. (2011) formulation. Similarly, different parameterizations for dust emissions are available ranging from more simplified to more physics-based descriptions (Klose et al. 2021). Following Gonçalves Ageitos et al. (2023), the G01-UST scheme based on Ginoux et al. (2001) described in Klose et al. (2021) is used in this Thesis. Dust emission is limited to areas presenting a frequency of occurrence of dust optical depth above 0.2, identified using maps created from Moderate Resolution Imaging Spectroradiometer (MODIS) Deep Blue retrievals (Hsu et al. 2004, Ginoux et al. 2012). Surface roughness influence on dust emission is parameterized based on Raupach et al. (1993), whose vegetation cover is determined using surface reflectance from Landsat and MODIS monthly data (Raupach et al. 1993, Guerschman et al. 2015). By default, dust was be treated as a uniform bulk species in MONARCH. However, mineral dust composition has been recently incorporated in the model (Gonçalves Ageitos et al. 2023) to trace the transport and chemistry of the minerals included in the mineralogical datasets described in Section 3.2.

For the evaluation and development of the model's dust cycle, the reader is referred to Klose et al. (2021) and Gonçalves Ageitos et al. (2023), and for sea salt to Spada et al. (2013).

Beyond meteorology-driven emissions, MONARCH also ingests anthropogenic and other pertinent emissions preprocessed with the HERMES system, as described in Section 3.3.

3.1.1 Secondary inorganic aerosol formation: a hybrid heterogeneous chemical mechanism

To form secondary NO_3^-–NH_4^+-SO_4^{2-} aerosols through heterogeneous chemistry, the default version of MONARCH - prior to the developments performed in this Thesis (Chapter 4) - implements an HYB mechanism in the same manner as other atmospheric models (see Section 1.5).

On fine particles, the gas-aerosol partitioning of semivolatile inorganic aerosols is modeled using the TEQ module EQuilibrium Simplified Aerosol Model version v03d (EQSAM v03d; Metzger et al. 2002). EQSAM is a computationally efficient gas/aerosol partitioning model designed for global and regional atmospheric modeling. Through the parameterization of non-ideal solution properties, based on the relationship between activity coefficients and RH, it avoids the computationally-expensive iterative calculation of activity coefficients employed in other thermodynamic models to solve the nonlinear equilibrium equation systems. Originally designed to handle the partitioning of NH_4^+-SO_4^{2-}-NO_3^--H_2O system excluding solids, it was extended with respect to sea salt (i.e. HCl and Cl^-/Na^+) and a simplified treatment of solids/hysteresis in version v03d, the one used in MONARCH. EQSAMv03d gas/aerosol partitioning calculation follows these steps:

1. Assuming that the water activity equals to RH, the molality of the solution consequently depends solely on the water mass. For salt solutes of binary and multicomponent solutions, the molality is obtained from the total water content of the mixture, calculated based on the ZSR-relation mixing rule (Zdanovskii 1948, Stokes and Robinson 1966). This relationship equals the water activity of the mixture to that of each single-solute solution, proved as an accurate assumption in atmospheric models.

2. Three concentration domains are defined subject to the relative concentrations of acid-base species (Nenes et al. 1998). These domains assume that gas/aerosol equilibrium occurs with SO_4^{2-} residing completely in the aerosol phase, due to

the low vapor pressure of $H_2SO_{4(g)}$. Based on the acid-base ratios, SO_4^{2-} can be partially or totally neutralized, so each domain defines a specific aerosol type. An advantage of this methodology is the reduced species needed to be considered in each domain, increasing the computational efficiency by reducing the total nimber of equilibrium reactions.

3. Liquid/solid partitioning is calculated via subdomains, defined based on RH being below/above the RH of deliquescence (RHD) and the mutual deliquescence RH (MDRH) of the single and mixture of solutes, respectively, calculated for the species considered at the given domain and ambient temperature (Nenes et al. 1998). If RH is higher than the RHD and MDRH, species are only in the aqueous medium and gas/liquid equilibrium is calculated. If RH is below some species' RHD, gas-solid equilibrium is assumed instead.

4. Activity coefficients are determined by the specific subdomain. If a given salt crystallize, its activity is 1, while if deliquesced, its activity coefficient is calculated for the given RH through an empirical relationship (Metzger 2000).

5. The mixture's equilibrium constant and the solution molalities are calculated based on the derived activity and stoichiometric coefficients parameterized for each solute salts and RH. From them, the gas-liquid-solid concentrations at equilibrium are calculated from the total and solid/aqueous partition of each species, after considering the neutralization rates between acid-alkaline species.

One of the main limitations of EQSAMv03d is that it neglects the presence of dust-related NVCs (i.e. Ca^{2+}, K^+, Mg^{2+}) when calculating equilibrium concentrations, only considering those elemental constituents from sea salt (i.e. Cl^-/Na^+). As a result, the model does not capture the potential influence of mineral dust on aerosol thermodynamics. For example, in the case of $CaCO_3$, EQSAMv03b does not account for the specific formation of $Ca(NO_3)_2$ or calcium sulfate ($CaSO_4$). Instead, it only treats Na^+ and Cl^- ions and computes total particulate NO_3^-, NH_4^+, and SO_4^{2-} without considering their neutralization by crustal species. Consequently, the model cannot quantify the alkalinity consumed during particulate NO_3^- formation. However, as seen in Section 1.3, incorporating crustal species into thermodynamic equilibrium calculation is therefore an important feature for atmospheric modeling, particularly in regions affected by mineral dust (Ansari and Pandis 2000, Fountoukis and Nenes 2007).

To account for secondary NO_3^- aerosol on coarse dust and sea salt particles, MONARCH follows the HYB approach through an UPTK reaction of $HNO_{3(g)}$. As

a first-order reaction (Schwartz 1986), it uses the uptake rate (K) defined by Jacob (2000):

$$K = \left(\frac{r}{D_g} + \frac{4}{v\gamma} \right)^{-1} \cdot S \tag{3.1}$$

where r is the aerosol bin radius, D_g the gas-phase diffusion coefficient, v the mean molecular speed, S the aerosol specific surface area, and γ the uptake coefficient, defined as the ratio of the number of gas molecules reacting with the particle's surface over the fraction of molecules being absorbed by the given surface (i.e. the accommodation coefficient) (Phadnis and Carmichael 2000, Guimbaud et al. 2002).

A γ constant value of 0.1 is assumed for dust (Hanisch and Crowley 2001, Vlasenko et al. 2006), and 0.01 is used for sea salt (Tolocka et al. 2004).

The production of SIA is therefore limited to fine SO_4^{2-}-NH_4^+-NO_3^- (through fTEQ) and coarse NO_3^- (through UPTK) traced in separate bins (Table 4.1).

3.2 Dust soil-surface mineralogical datasets

Alkalinity refers to the ability of a substance to neutralize acids and maintain a stable pH level (see Section 1.3.2). Both dust and sea salt particles contain NVCs that contribute to the overall alkalinity of the aerosol, thereby neutralizing gas acidic species such as $HNO_{3(g)}$ and $H_2SO_{4(g)}$.

To investigate the importance of representing dust alkalinity and its influence on aerosol heterogeneous chemistry, this Thesis relies on three different dust soil-surface mineralogical datasets (Table 3.1). Using multiple atlases allows us to assess the uncertainty arising from our limited knowledge of the soil mineralogy of dust sources.

This section introduces the three mineralogical datasets, summarizing their main characteristics and limitations. The land-based mineral atlases typically used in atmospheric models prior to this Thesis, namely the datasets of Claquin et al. (1999) and Journet et al. (2014), are presented in Section 3.2.1. The novel space-borne mineralogical data from the NASA's Earth Surface Mineral Dust Source Investigation (EMIT) mission is described in Section 3.2.2, detailing its geographical and spectral coverage, the mineral characterization, and the parametrizations used for the retrieval of surface mineralogy.

This PhD comprises the first implementation of space-based mineral observations into an atmospheric chemistry model, assessing the relevance of accounting for more realistic soil mineral content for atmospheric composition. Compared to the previous implementations of land-based mineralogical atlases based on widely extended soil types extrapolations (e.g. Gonçalves Ageitos et al. 2023), the implementation of geographically-

discrete mineral data present important upgrades that are discussed in Chapter 6 and Chapter 7.

Table 3.1: Description of the three datasets implemented in MONARCH for this Thesis.

Mineral dataset	Minerals	Based on	Resolution	References
CLAQ	quartz, feldspar, illite, smectite, kaolinite, calcite, gypsum, hematite	Land sampling and soil type generalization	$0.0833^{o}\times0.0833^{o}$	Claquin et al. (1999)
JOUR	quartz, feldspar, illite, smectite, kaolinite, calcite, gypsum, hematite, chlorite, vermiculite, mica, goethite	Land sampling and soil type generalization	$0.0833^{o}\times0.0833^{o}$	Journet et al. (2014)
EMIT	quartz, feldspar, illite, smectite, kaolinite, calcite, gypsum, hematite, chlorite, vermiculite, goethite, montmorillonite, hematite and goethite (Fe oxides)	Spaceborne retrieval	$0.5^{o}\times0.5^{o}$	Brodrick et al. (2025)

3.2.1 Land-based mineralogical datasets: Claquin et al. (1999) and Journet et al. (2014)

Global-scale soil mineralogy counts on a very limited set of soil descriptions. These, moreover, are specially scarce over arid areas, therefore constraining the mineral characterization of dust sources. Furthermore, information about the size distribution of emitted minerals is also very limited.

Claquin et al. (1999) (CLAQ) represents the first attempt to develop a global soil mineralogical map. After some modifications by Nickovic et al. (2012), it is still nowadays a reference atlas. It defines 8 mineral species: Quartz, feldspar, illite, smectite, kaolinite, calcite, gypsum, and hematite. Afterwards, Journet et al. (2014) (JOUR), developed an additional dataset, adding 4 more minerals to the CLAQ one (12 minerals): Chlorite, vermiculite, mica, and goethite. The minerals included by each dataset are shown in Tables 3.1, and their percentages in Tables A.1 and A.3.

Both CLAQ and JOUR provide soil-mineralogical maps by assigning a mean mineral composition to each soil type, therefore assuming that the same mineral composition is shared across all regions with the same soil type. They also provide the size distribution of their correspondent mineralogy, classified in clay ($D < 2\mu m$) and silt (D from 2 to 63 μm) size modes. They report just some discrepancies regarding the presence of some minerals in one or both size modes.

However, the limited availability of soil composition samples limits the geographic mineral characterization in both maps. For instance, CLAQ relies on 239 soil analyses to characterize 80% of the 25 soil types it assumes across arid and semi-arid areas, while JOUR uses more than 700 soil mineral characterizations to describe 55% of the

220 soil units it is based on, extending the characterization coverage to additional regions not covered by CLAQ. These limitations, along with some gaps in the soil mineral characterization, oblige both studies to make several assumptions to provide geographically resolved surface mineralogy maps: Extrapolating mineral composition of major soil groups to non-characterized minor soil types or assuming empirical relationships between soil texture, color and mineral composition, among others (Perlwitz et al. 2015a, Li et al. 2024a, Gonçalves Ageitos et al. 2023). Eventually, CLAQ and JOUR achieve mid latitudinal surface resolutions of $\sim$ 10 km and $\sim$ 1 km respectively, remarking the limitations derived from the mentioned assumptions. More technical details about CLAQ and JOUR data and limitations can be found in Gonçalves Ageitos et al. (2023).

As noted earlier, MONARCH already incorporates modules to trace the transport of emitted dust minerals included in CLAQ and JOUR datasets using flexible configurations (Gonçalves Ageitos et al. 2023). The implemented maps for CLAQ and JOUR in MONARCH are mapped at $0.0833^{o}\times$ 0.0833^{o} horizontal resolution, and they are available at Zenodo (Gonçalves Ageitos et al. (2023), https://doi.org/10.5281/zenodo.8091828).

3.2.2 Spaceborne retrievals of soil-surface mineralogy: the EMIT dataset

A central innovation of this Thesis, particularly implemented in Chapters 6 and 7, is the first use of high-resolution, observationally constrained soil-surface $CaCO_3$ data from the EMIT imaging spectrometer (Brodrick et al. 2025) to inform atmospheric chemistry modeling (Fig. 3.1).

As detailed in the previous Section 3.2.1, prior efforts to characterize global dust mineralogy have relied on extrapolated soil datasets, such as the CLAQ and JOUR mineralogical atlases. These atlases assign mean mineral compositions to broad soil types and extrapolate sparse soil sample measurements to uncharacterized dust source areas based on soil classification schemes and empirical rules (see Section 3.2.1). Both lack direct spatial observations, leading to major uncertainties in dust composition modeling (Perlwitz et al. 2015a, Li et al. 2024a, Gonçalves Ageitos et al. 2023).

By contrast, the EMIT imaging spectrometer, launched by NASA in 2022, provides the first near-global, high-resolution retrievals of soil mineralogy across arid and semi-arid regions. EMIT is mounted on the International Space Station and is designed to identify minerals through their distinctive absorption features visible in sunlight reflected from the surface. It measures between 380 and 2500 nm (VSWIR) at 7.5 nm spectral sampling and 60-meter spatial sampling between $\pm 51.6^{o}$ latitude. Each scene undergoes calibration to units of spectrally resolved radiance. Radiative transfer models are then

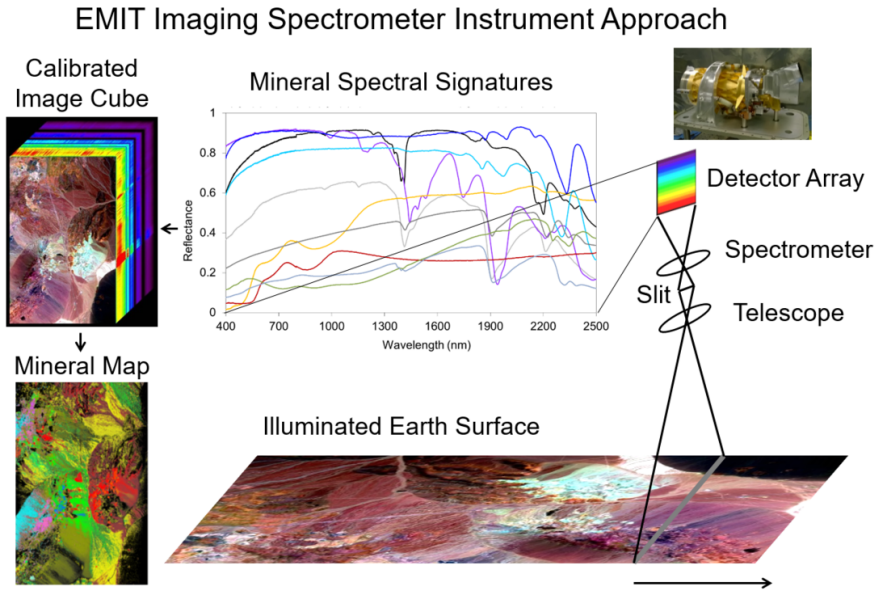

Figure 3.1: The EMIT instrument (top right) and its scheme of data analysis procedure.

used to infer the surface reflectance component of each spectrum (Thompson et al. 2024). Feature matching routines identify and measure the depth of mineral absorption features using the Tetracorder system (Clark et al. 2024) to produce mineral maps over bare soil and rock surfaces. EMIT maps hundreds of different mineral signatures, but it focuses on 10 mineral classes: quartz, feldspar, illite, smectite, kaolinite, calcite, gypsum, hematite, chlorite, vermiculite, goethite, montmorillonite, and hematite+geothite (Fe oxides, Fe_2O_3).

In this Thesis, we use the recently released EMIT mineral abundance maps (version 2) to obtain the soil-surface mineral mass fractions at 0.5^{o} spatial resolution (Brodrick et al. 2025). These abundance maps are produced using the calibrated VSWIR reflectance spectra interpreted through a Hapke-style model of the soil surface coupled with the Tetracorder spectral-matching algorithm (Clark et al. 2024). Key mineral groups are directly mapped while quartz+feldspar abundances are inferred indirectly due to the absence of diagnostic absorption features in the VSWIR range. Additional details on the spectrometer design and the full methodology for producing the mineral atlases are provided in prior documents (Okin et al. 2025, Brodrick et al. 2023). The publicly available EMIT soil mineral atlases are archived at NASA's Distributed Active Archive Center (DAAC) (Brodrick et al. 2025).

In this Thesis (Chapters 6 and 7), we focus primarily on $CaCO_3$ variations due to its central role in atmospheric dust heterogeneous chemistry. In Chapter 7 we also account for Fe_2O_3 (hematite and goethite), which are key to determining the optical properties and radiative impact of dust aerosols.

While EMIT provides bulk mass fractions for these and other minerals summed across the full soil particle size distribution, the dust emission parameterizations used in atmospheric models require mineralogical information resolved by soil particle size—specifically, the clay ($D < 2\mu m$) and silt ($2 < D < 50\mu m$) fractions that dominate the emitted dust. In contrast to the CLAQ and JOUR datasets, which directly provide mineral abundances within these size classes, EMIT requires the application of additional assumptions to partition its bulk values into clay- and silt-resolved fractions.

To estimate the clay and silt content of $CaCO_3$ from the total EMIT-derived abundance, we apply observationally constrained size-resolved ratios consistent with those used in JOUR (Journet et al. 2014). For Fe_2O_3, we assume that both hematite and goethite present the same fraction across all soil particle sizes due to internal mixing with other minerals (Panta et al. 2023).

This full-size disaggregation of the EMIT bulk mineralogy allows for a consistent and physically based representation of mineral-resolved particle size distributions at emission, in line with the treatment used for CLAQ and JOUR. The resulting estimates form the basis for all size-resolved mineral tracers simulated in our atmospheric model.

3.3 Processing of anthropogenic and other emission sources: the HERMES emission system

Beyond meteorology-driven emissions described in Section 3.1, atmospheric chemistry modeling also requires input from anthropogenic emissions and other relevant sources, such as ocean and biomass burning emissions. To this end, MONARCH employs the High-Elective Resolution modeling Emission System version 3 (HERMESv3; Guevara et al. 2019; 2020) to compile and preprocess emissions from various sources.

Developed and maintained at BSC, HERMESv3 is an open source, parallel, and standalone multiscale emission modeling framework that consists of two independent modules that can be either combined or executed separately: (i) the global—regional module (HERMESv3_GR; Guevara et al. 2019) and (ii) the bottom—up module (HERMESv3_BU; Guevara et al. 2020).

HERMESv3_GR is used in this Thesis. HERMESv3_GR can apply user-defined vertical, temporal, and speciation profiles of pollutant emissions to one or multiple different up-to-date emission inventories, allowing the user to set the combinations of existing emission inventories and apply country-specific scaling factors and masks both at regional and global scales.

The processing and remapping of emission inventories provides results compatible with different chemical mechanisms (Seemann et al. 2024) and user-defined grids

(Navarro-Barboza et al. 2024). Consequently, the HERMES output file can be directly read by atmospheric models, significantly simplifying the emission inputs, representing a highly useful tool for atmospheric modeling. Figure 3.2 shows the flowchart of HERMES, that follows three steps to produce the processed emission inventories:

1. Preprocessing: The original emission inventories are transformed into files with a standard format to work within HERMES (e.g. standard $kg \cdot m^2 \cdot s^1$ unit).

2. Preparing the configuration files: The emission configuration file is used to define the destination grid and select the species and pollutants across the various emission inventories and sectors employed. These specifications will serve to create the output emission files. The emission inventories and sectors are combined using temporal, vertical, speciation profiles, and country-specific factors, all defined in separate files. The HERMES configuration file contains the requirements and conventions of the output file defined by the user.

3. Running: HERMES calculates the spatial regridding from the source grid to the destination grid, the vertical emission distribution, the temporal disaggregation, and the speciation mapping to each emission inventory and sector combination specified in the emission configuration file. Adding up all the combinations, HERMES generates the output emission files in netCDF format according to the HERMES configuration file and readable by the atmospheric chemistry model.

In this Thesis, three main emissions inventories are processed by HERMESv3_GR to provide anthropogenic, ocean, and biomass burning emissions to MONARCH. The Copernicus Global Anthropogenic emission inventory CAMS-GLOB-ANT_v4.2 (Soulie et al. 2024), developed under the Copernicus Atmosphere Monitoring Service (CAMS), is used. Covering the period 2000-2023, it is based on the Emissions Database for Global Atmospheric Research (EDGARv4.3.2) available until 2015, the global emissions provided by the Community Emissions Data System (CEDS) version 1 used for the extrapolation of the emissions up to 2023, the temporal profiles from the CAMS-GLOB-TEMPO dataset (Guevara et al. 2021), and the ship emissions from the CAMS-GLOB-SHIP dataset. Description and treatment of each of these inventories is found in Soulie et al. (2024). CAMS-GLOB-ANT_v4.2 has a resolution of $0.1^{o} \times 0.1^{o}$, and includes the emissions for regulatory air pollutants and greenhouse gases for 17 emission sectors.

For DMS natural oceanic emissions, the emission inventory CAMS-GLOB-OCE_v3.1 (Lana et al. 2011, Denier van der Gon et al. 2023) is employed, which reports averaged DMS emissions for the 2000-2019 period at 0.5^{o} x 0.5^{o} resolution. Based on available data on concentrations in ocean water and meteorological information, a flux

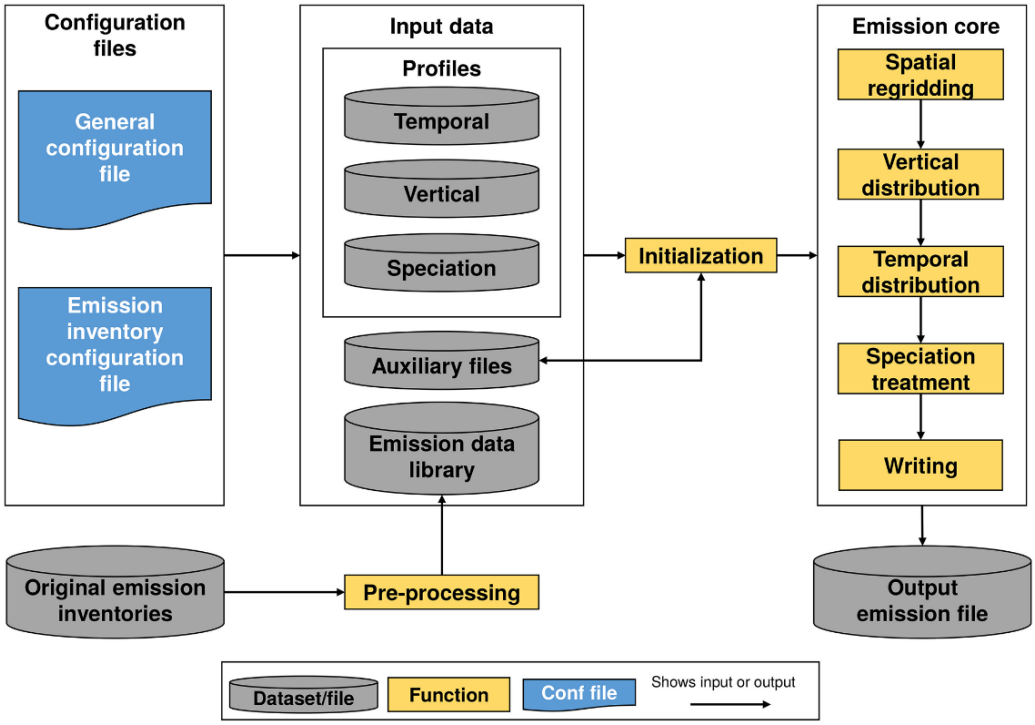

Figure 3.2: HERMES flowchart, from Guevara et al. (2020).

formula based on Henry's law is used to derive the emission fluxes. DMS concentration in ocean water by (Lana et al. 2011) and sea surface temperature and wind speeds from the ERA5 reanalysis are used to create multi-year data sets (Denier van der Gon et al. 2023).

Finally, biomass burning emissions from forests, grasslands, and fires of agricultural waste are obtained from the CAMS Global Fire Assimilation System (GFAS) v1.2 (Kaiser et al. 2012) emission inventory. Based on satellite retrievals from the NASA Moderate Resolution Imaging Spectroradiometers (MODIS) on Terra and Aqua satellites, they report daily estimates of emissions from 40 pyrogenic species, with a resolution of 0.1º x 0.1º and temporal coverage from 2003 to the present (Kaiser et al. 2012).

Table 3.2 summarizes the total emissions (anthropogenic, biogenic and biomass burning) resulting from the global simulations performed in this Thesis.

3.4 Observational data for model evaluation

The Globally Harmonised Observations in Space and Time (GHOST) dataset (Bowdalo et al. 2024), an initiative of the BSC's Earth Department dedicated to the harmonization of publicly available global surface observations, is used throughout the Thesis to evaluate the model runs against measurements.

Table 3.2: Total emissions (anthropogenic, biogenic and biomass burning) for 2018 used in this Thesis.

Species	**Emission (Tg y^{-1})**
NO	75.93
NO_2	17.86
HONO	0.51
NH_3	61.81
NO_x	93.8
SO_2	104.40
$PM_{2.5}SO_4$	0.53

GHOST represents one of the biggest collections of harmonised measurements of atmospheric composition at the surface from 1970 to 2023. Over 227 different components from 38 reporting networks, are compiled, parsed, and standardised. The components processed include gaseous species, total and speciated particulate matter, and aerosol optical properties. GHOST provides its own quality assurance associated with measurements data and metadata.

For gas and aerosol NO_3^-, NH_4^+, and $SO_{2(g)}$ and SO_4^{2-} species, GHOST includes datasets from the Clean Air Status and Trends Network (US-EPA-CASTNET), the US EPA Air Quality System (US-EPA-AQS), and the Canada National Air Pollution Surveillance Program (NAPS) for North and Central America; the East Asia Acid Deposition Monitoring Network (EANET) for Asia; and the EBAS and the European Environmental Agency Air Quality (EEA AQ eReporting) for Europe. Figure A.13 in the Supplement shows the stations used for each of the species analyzed.

These observations are filtered for rural and background sites only, in order to exclude stations near emission sources not representative of the background conditions depicted by the model resolution, which describes the long-range transport of NO_3^-, NH_4^+ and SO_4^{2-} formation. However, information on the station type was not available for the EANET and US-EPA-CASTNET data. For these networks, all stations were used, a factor that has to be accounted for when evaluating the results.

Regarding $PM_{2.5}$ and PM_{10}, GHOST includes data from the CHILE-SINCA network for Chile, the Beijing Municipal Ecological and Environmental Monitoring Center (BJMEMC), the China National Environmental Monitoring Centre (CNEMC), WMO World Data Center for Aerosols (EBAS-WMO-WDCA) for Europe, the Japan National Institute for Environmental Studies (NIES), the Ministerio de Transición Ecológica (MITECO) for Spain, the UK AIR network for United Kingdom, and the global AirNow DOS network (US-EPA-AirNow-DOS). For these networks, the station type was not included as a criteria to include it in the evaluation. The quality flags for the selected stations are summarized in Supl. Table A.5.

Finally GHOST also includes aerosol optical properties from the AErosol RObotic NETwork (AERONET; https://aeronet.gsfc.nasa.gov/new_web/) of ground-based sun photometers. Climatological data from 2000 to 2020 is used to constrain the optical properties of the model.

Model results presented in Chapters 5, 6 and 7 are evaluated against observations in terms of correlation coefficient (corr), mean bias (bias) and root mean square error (rmse), formulated as follows:

$$corr = \frac{\sum_{i=1}^{N}(S_i - \bar{S})(O_i - \bar{O})}{\sqrt{\sum_{i=1}^{N}(S_i - \bar{S})^2}\sqrt{\sum_{i=1}^{N}(O_i - \bar{O})^2}} \tag{3.2}$$

$$bias = \frac{\sum_{i=1}^{N}(S_i - O_i)}{N} \tag{3.3}$$

$$rmse = \sqrt{\frac{\sum_{i=1}^{N}(S_i - O_i)^2}{N}} \tag{3.4}$$

Where S are the simulation results, O the observational data, and N the number of observations.

3.5 Computing resources: Marenostrum 4 and Marenostrum 5

Designed to exploit intensive parallelism, the high computational demands of the simulation runs for this Thesis using MONARCH and HERMES were met by the MareNostrum 4 and MareNostrum 5 supercomputer resources (Fig. 3.3), hosted by the Barcelona Supercomputing Center - Centro Nacional de Supercomputación (BSC-CNS).



Figure 3.3: From left to right, the currently depricated Marenostrum 4 and the recently set Marenostrum 5 (Source: *BSC*).

MareNostrum 4 had a peak performance capacity of 13.7 Petaflop/s, it was decommissioned in April 2024 and replaced by its 5th generation, MareNostrum5. MareNostrum 4 consisted of 3400 general-purpose Lenovo nodes in 48 racks, equipped with next-generation Intel Xeon processors and a central memory of 390 Terabytes, along with clusters of different technologies. MareNostrum 4 was connected to the RedIris and Geant networks.

MareNostrum 5 (Banchelli et al. 2026) is a pre-exascale EuroHPC supercomputer, built using Bull Sequana XH3000 and Lenovo ThinkSystem architectures. It has a peak computational power of 314 Petaflop/s (almost 23 times its predecessor's top performance) and consists of four specialized partitions designed to meet diverse HPC user needs: 1) General Purpose Partition: Uses Intel Sapphire Rapids with 6408 standard nodes and 72 HBM nodes, delivering 45 PFlops. 2) Accelerated Partition: Features Intel Sapphire Rapids CPUs and Nvidia Hopper GPUs, with 1120 nodes (each equipped with 4 GPUs), reaching 230 PFlops. 3) General Purpose - Next Generation Partition: Built on Nvidia GRACE CPU technology. 4) Accelerated - Next Generation Partition (details yet to be fully defined).

The system includes high-performance storage with 248 PB of SSD/Flash and HDD capacity, supporting 1.2 TB/s write and 1.6 TB/s read speeds. Additionally, a long-term archive based on tapes provides 402 PB of extra storage. IBM Storage Scale and Archive handle parallel file system operations and data management.

To run MONARCH, we used the workflow manager Autosubmit (Manubens-Gil et al. 2016) together with the MONARCH-specific extension Auto-MONARCH, developed within the Earth Sciences department at BSC. This combination facilitates the easy management of model runs as well as pre- and post-processing on HPC platforms. The specific model configuration and workflow setup were tuned to leverage MareNostrum 4 and Marenostrum 5 resources.

4

Model developments

In this Thesis, by integrating mechanisms of varying complexity within the global model MONARCH (Section 3.1) we investigate the primary chemical pathways responsible for NO_3^- formation and other SIA species on preexisting particles, with a particular focus on coarse dust particles.

The original mechanism available in MONARCH presented some relevant obstacles on the way to pursue the last three of the four objectives aimed in this Thesis. Namely, a limited representation of dust alkaline minerals, a simplified irreversible formation of NO_3^- on coarse particles, no representation of SO_4^{2-} and NH_4^+ aerosols coarse fraction, and neglecting the role of NVCs on SIA formation. Such limitations motivated the first objective of this Thesis and the developments described in this chapter.

Here we detail the enhancements implemented in MONARCH to partially or fully address the array of reactions of interest, with a primary focus on maintaining a balance between complexity, accuracy, and computational efficiency in the resulting solution.

4.1 Aerosol size distribution

The size representation of aerosols in MONARCH considers 8 size bins from $0.2 < D < 20\mu m$ for dust, and from $0.2 < D < 30\mu m$ for sea salt. Originally, all the other aerosol components, namely BC, OM (both primary and secondary), SO_4^{2-}, NH_4^+, NO_3^- and unspeciated aerosol mass, were represented by a fine mode ($0.2 < D < 2.5\mu m$), except NO_3^-, represented with both fine and coarse ($2.5 < D < 30\mu m$) modes to consider the condensation of $HNO_{3(g)}$ on coarse particles via the HYB mechanism.

To trace the formation of fine and coarse NH_4^+ and SO_4^{2-} under moist conditions – the primary regime where these formation pathways occur (Usher et al. 2003, Jordan et al. 2003) – an additional hydrophilic bin for the coarse mode of these species is added to the default MONARCH size parametrization, as detailed in Table 4.1. These new bins, together with the preexisting coarse bin for NO_3^-, account for the total mass of NO_3^-, NH_4^+, and SO_4^{2-} formed on both dust and sea salt particles indiscriminately.

Table 4.1 reports the bin volumetric and effective diameters, density, and their fractional contribution to $PM_{2.5}$ and PM_{10}.

Table 4.1: Density (ρ), volumetric diameter (⌀ vol.), geometric mean effective diameter (⌀ eff.), geometric mean effective diameter ranges (⌀ range), and $PM_{2.5}$ and PM_{10} fractions of each bin of the studied species.

Dust						
Property	ρ	⌀ vol.	⌀ eff.	⌀ range	PM2.5	PM10
Units	kg m-3	µm	µm	µm	frac.	frac.
Bin 1	2500	0.3	0.3	0.20–0.36	1	1
Bin 2	2500	0.5	0.5	0.36–0.60	1	1
Bin 3	2500	0.94	0.9	0.60–1.20	1	1
Bin 4	2500	1.6	1.56	1.20–2.00	1	1
Bin 5	2650	2.72	2.64	2.00–3.60	0.38	1
Bin 6	2650	4.58	4.48	3.60–6.00	0	1
Bin 7	2650	7.86	7.6	6.00–12.00	0	0.87
Bin 8	2650	14.48	14.22	12.00–20.00	0	0

Sea salt						
Property	ρ	⌀ vol.	⌀ eff.	⌀ range	PM2.5	PM10
Units	kg m-3	µm	µm	µm	frac.	frac.
Bin 1	2160	0.3	0.28	0.20–0.36	1	1
Bin 2	2160	0.5	0.48	0.36–0.60	1	1
Bin 3	2160	0.94	0.9	0.60–1.20	1	1
Bin 4	2160	1.62	1.58	1.20–2.00	1	1
Bin 5	2160	2.8	2.72	2.00–3.60	0.32	1
Bin 6	2160	4.74	4.64	3.60–6.00	0	1
Bin 7	2160	8.6	8.26	6.00–12.00	0	0.75
Bin 8	2160	18.46	17.28	12.00–30.00	0	0

NO_3^-						
Property	ρ	⌀ vol.	⌀ eff.	⌀ range	PM2.5	PM10
Units	kg m-3	µm	µm	µm	frac.	frac.
Bin 1	1700	0.7	0.48	0.01–2.00	1	1
Bin 2	2380	4.46	3.58	2.00–20.00	0.2	0.8

NH_4^+						
Property	ρ	⌀ vol.	⌀ eff.	⌀ range	PM2.5	PM10
Units	kg m-3	µm	µm	µm	frac.	frac.
Bin 1	1700	0.7	0.48	0.01–2.00	1	1
Bin 2	2380	4.46	3.58	2.00–20.00	0.2	0.8

SO_4^{2-}						
Property	ρ	⌀ vol.	⌀ eff.	⌀ range	PM2.5	PM10
Units	kg m-3	µm	µm	µm	frac.	frac.
Bin 1	1700	0.7	0.48	0.01–2.00	1	1
Bin 2	2380	4.46	3.58	2.00–20.00	0.2	0.8

4.2 Thermodynamic equilibrium model: ISORROPIA II

The gas-aerosol partitioning of semivolatile inorganic aerosols in previous studies with MONARCH was based on the the EQSAM v03d thermodynamic equilibrium model. However, as described in Section 3.1.1, one of the limitations of this version is the lack of information on NVCs from mineral dust species for the neutralization of acidic gas species.

Such a limitation motivated the implementation for this Thesis of ISORROPIA II v1 (Fountoukis and Nenes 2007) as a more comprehensive thermodynamic equilibrium model to investigate the sensitivity of the partitioning of semivolatile inorganic compounds to NVCs. While a more recent version of ISORROPIA-II exists (v2.3), which improves aerosol pH estimations at near-pH-neutral conditions (Song et al. 2018), global-scale simulations have shown only minor differences when compared to ISORROPIA-II v1 (Milousis et al. 2024).

ISORROPIA-I (Nenes et al. 1998) calculates concentrations at thermodynamic equilibrium following a similar methodology to EQSAM, namely constraining the number of equilibrium equations to be solved in terms of the ratio of basic species (i.e. NH_4^+ and NVC) over the SO_4^{2-} present in the mixture. Based on their ratios, a domain is determined and a correspondent tabulated subset of solid, liquid and gas species is selected. The equilibrium reactions of this subset of species are solved numerically, with the option to use precalculated tables of activity coefficients to speed up calculations, and taking into account mutual deliquescence relative humidity (MDRH) of multicomponent solutions (Fountoukis and Nenes 2007).

However, as EQSAM, ISORROPIA-I does not incorporate the thermodynamics of crustal species. Instead, the second version of ISORROPIA, ISORROPIA-II (Fountoukis and Nenes 2007, Mellon 2009), incorporates the specific treatment of NVC present in dust and sea salt, namely Ca^{2+}, K^+, and Mg^{2+}. The inclusion of the thermodynamics of the 3 additional crustal NVC species leads to include 10 additional salts in the solid phase. The species included in ISORROPIA-II are $NH_{3(g)}$, $HNO_{3(g)}$, $HCl_{(g)}$, $H_2O_{(g)}$ for the gas phase, NH_4^+, Na^+, H^+, Cl^-, NO_3^-, SO_4^{2-}, $HNO_{3(g)}$, $NH_{3(g)}$, $HCl_{(g)}$, HSO_4^-, OH, H_2O, Ca^{2+}, K^+, Mg^{2+} for the liquid phase, and $(NH_4)_2SO_4$, NH_4HSO_4, $(NH_4)_3H(SO_4)_2$, NH_4NO_3, NH_4Cl, $NaCl$, $NaNO_3$, $NaHSO_4$, Na_2SO_4, $CaSO_4$, $Ca(NO_3)_2$, $CaCl_2$, K_2SO_4, $KHSO_4$, KNO_3, KCl, $MgSO_4$, $Mg(NO_3)_2$, $MgCl_2$ for the solid phase.

Among them, the concentrations of $NH_{3(g)}$, Na^+, Ca^{2+}, K^+, Mg^{2+}, $HNO_{3(g)}$, $HCl_{(g)}$, and $H_2SO_{4(g)}$ – as relevant species determining the reactions and products from thermodynamic equilibrium – are used to compute the following three ratios (R_i, in molar

units):

- **SO_4^{2-} Ratio (R_{so4})**: Represents the degree of SO_4^{2-} neutralization by NH_4^+.
- **Crustal species and Na^+ ratio (R_{crna})**: Accounts for both NH_4^+, crustal and sea salt cations in relation to SO_4^{2-}.
- **Crustal species ratio (R_{cr})**: Reflects the contribution of crustal cations to aerosol neutralization.

These rations are defined as:

$$R_{so4} = \frac{[NH_4^+] + [Na^+] + [Ca^{2+}] + [Mg^{2+}] + [K^+]}{[SO_4^{2-}]} \tag{4.1}$$

$$R_{crna} = \frac{[Na^+] + [Ca^{2+}] + [Mg^{2+}] + [K^+]}{[SO_4^{2-}]} \tag{4.2}$$

$$R_{cr} = \frac{[Ca^{2+}] + [Mg^{2+}] + [K^+]}{[SO_4^{2-}]} \tag{4.3}$$

The available species, together with the relative values of R_{so4}, R_{crna}, and R_{cr} ratios, determine 15 different cases, which serve to characterize 5 different compositional regimes (Table 4.2 in this manuscript, and Table 3 in Fountoukis and Nenes (2007)). Each case constrains the subsystem of equations to be solved and species present in the medium, and each regime addresses a specific subset of relevant species and equilibrium equations, determining compositional regimes and the available species for each one of them. Efficiency is further improved by retrieving species' activity coefficients from look-up tables (Fountoukis and Nenes 2007, Milousis et al. 2024).

Finally, for each compositional regime, as in EQSAM, subdomains are determined depending on the ambient RH and T, and the RHD and MDRH of the species present in the solution. The calculation of activity coefficients in ISORROPIA-II incorporates also a temperature dependence, which is not included neither in EQSAMv0.3 nor in the previous version of ISORROPIA.

For each case in Table 4.2, ISORROPIA-II can assume either stable conditions, where compounds can precipitate into solids, or metastable conditions, where compounds remain as supersaturated liquid solutions (Pringle et al. 2010).

The medium acidity is determined by ISORROPIA-II from the concentrations of acidic/basic gaseous species ($HNO_{3(g)}$, $NH_{3(g)}$, $H_2SO_{4(g)}$), particle (NH_4^+, SO_4^{2-}, NO_3^-), and crustal and sea salt ions (K^+, Ca^{2+}, Mg^{2+}, Na^+, Cl^-), which are inputs to ISORROPIA-II. After TEQ is calculated with these species, the resulting pH is provided by the thermodynamic model.

Table 4.2: ISORROPIA-II cases

Case	Species missing	Ratios thresholds	Conditions	Regime
1	Ca,K,Mg,Na,Cl,NO_3^-=0	2.0 $\leq$ NH_4^+/SO_4^{2-}	SO_4^{2-} POOR	3
2		1.0 $\leq$ NH_4^+/SO_4^{2-} <2.0	SO_4^{2-} RICH (NO ACID)	2
3		NH_4^+/SO_4^{2-} <1.0	SO_4^{2-} RICH (FREE ACID)	1
4	Ca,K,Mg,Na,Cl=0	2.0 $\leq$ NH_4^+/SO_4^{2-}	SO_4^{2-} POOR	3
5		1.0 $\leq$ NH_4^+/SO_4^{2-} <2.0	SO_4^{2-} RICH (NO ACID)	2
6		NH_4^+/SO_4^{2-} <1.0	SO_4^{2-} RICH (FREE ACID)	1
7	Ca,K,Mg=0	2.0 $\leq$ $(Na^+ + NH_4^+)/SO_4^{2-}$ & $Na^+/SO_4^{2-} \leq 2.0$	SO_4^{2-} POOR ; Na^+ POOR	3
8		2.0$\leq$ $(Na^+ + NH_4^+)/SO_4^{2-}$ & 2.0$\leq$ Na^+/SO_4^{2-}	SO_4^{2-} POOR ; Na^+ RICH	4
9		1.0$\leq$ $(Na^+ + NH_4^+)/SO_4^{2-}$ <2.0	SO_4^{2-} RICH (NO ACID)	2
10		$(Na^+ + NH_4^+)/SO_4^{2-}$ <1.0	SO_4^{2-} RICH (FREE ACID)	1
11	All present	2.0 $\leq$ R_{so4} & R_{crna} <2.0	SO_4^{2-} POOR and (DUST + Na^+) POOR	3
12		$R_{so4} \geq 2.0$ & $R_{crna} \geq 2.0$	SO_4^{2-} POOR, (DUST + Na^+) RICH, and DUST POOR	4
13		R_{cr} >2.0	SO_4^{2-} POOR, (DUST + Na^+) RICH, DUST RICH	5
14		1.0 $\leq$ R_{so4} <2.0	SO_4^{2-} RICH (NO ACID)	2
15		R_{so4} <1.0	SO_4^{2-} SUPER RICH (FREE ACID):	1

Finally, ISORROPIA-II makes the following assumptions to simplify and reduce the computational cost of calculating thermodynamic equilibrium concentrations:

- It assumes that all $H_2SO_{4(g)}$ is completely dissociated in the aqueous media, and always reside in the aerosol mode (liquid or solid phase). This is also true for Na^+ and NVC from crustal species, which are assumed to always reside in the aerosol phase.

- Some species, when formed, are assumed to be always liquid (e.g. $MgSO_4$) or always solid (e.g. $CaSO_4$).

- The SO_4^{2-} concentration ratio is used to set some species as minor species, which are assumed to not perturb the equilibrium of their precursor reactions. Also aqueous OH is assumed as minor species.

- The MDRH of mixtures containing crustal species is the same as mixtures not containing them, since the modification of MDRH by crustal species is not known, and its effect on aerosol water is expected to be small compared with other species.

- Solutions with cations from crustal NVC exceeding the anions are assumed to have a neutral acidity (pH=7).

- Organic anions' effect on aerosol acidity and water activity is neglected, therefore they are not considered in calculations.

- The DRH values, its temperature dependence and equilibrium constants of $Ca(NO_3)_2$ and $Mg(NO_3)_2$ salts correspond to their most hydrated forms.

- ISORROPIA-II does not consider the multiple hydration states of salts, nor the formation of double salts.

4.3 Gas condensation schemes

The dust heterogeneous chemistry mechanisms implemented in this Thesis are aimed to investigate the primary chemical pathways responsible for NO_3^- formation on preexisting particles, with a particular focus on coarse dust particles. By integrating mechanisms of varying complexity within the global model MONARCH (Fig. 2.1), we represented a wide variety of chemical reactions on dust and sea salt. Table 4.3 lists the irreversible and reversible heterogeneous reactions considered in our analysis.

In this Section, we detail the enhancements implemented in MONARCH to address partially or fully the array of reactions of interest, with a primary focus on maintaining a balance between complexity, accuracy, and computational efficiency in the resulting solution.

By combining the condensation schemes described in this section, various mechanisms are developed, as described in the next Section 4.4. Subsequently, sensitivity tests suppressing dust or sea salt mineralogy, or neglecting the coarse hydrophilic bins added in the aerosol size representation (Section 4.1) are performed in Chapter 5, in order to assess the relative contribution of each factor.

4.3.1 Irreversible condensation

A widely adopted method to simulate NO_3^- and SO_4^{2-} formation on coarse particles involves incorporating irreversible heterogeneous reactions of gas species on dust and sea salt through a first-order uptake parameterization (see Section 1.5). Specifically, the uptake of $HNO_{3(g)}$ on coarse particles is commonly assumed to drive coarse NO_3^- formation (Jacob 2000, Bauer et al. 2004, Hodzic et al. 2006, Feng and Penner 2007, Fairlie et al. 2010, Hauglustaine et al. 2014, Paulot et al. 2016, Jones et al. 2021), while the uptake of $SO_{2(g)}$ is known to lead to the formation of coarse SO_4^{2-} (Phadnis and Carmichael 2000, Song and Carmichael 2001, Usher et al. 2002, Prince et al. 2007, Fairlie et al. 2010, Li et al. 2012, Liu and Abbatt 2021, Yue et al. 2022) (Fig. 4.1).

The uptake coefficients (γ) for these reactions are assumed constant by most models. For example, the $\gamma = 0.1$ is assumed for $HNO_{3(g)}$ uptake on dust (Dentener et al. 1996, Hanisch and Crowley 2001; 2003, Bauer et al. 2004, Hodzic et al. 2006, Wei 2010). This value was also considered in the default version of MONARCH.

However, recent studies have shown that using this value tends to overestimate NO_3^- formation (Vlasenko et al. 2006, Mashburn et al. 2006, Fairlie et al. 2010). This

Table 4.3: Heterogeneous reactions implemented in MONARCH. Dust and sea salt particles are referred as *DU* and *SS*, respectively.

Irreversible reactions			
	Reaction	Process	Notes
(R1)	$DU_{(aer)} + H_2SO_{4(g)} \rightarrow SO^{2-}_{4(aq)}$	condensation	1
(R2)	$SS_{(aer)} + H_2SO_{4(g)} \rightarrow SO^{2-}_{4(aq)}$	condensation	1
(R3)	$DU_{(aer)} + SO_{2(g)} \rightarrow SO_{4(aer)}$	UPTK (γ_1)	2
(R4)	$CaCO_{3(aer)} + 2HNO_{3(g)} \rightarrow Ca(NO_3)_{2(aer)} + H_2O + CO_2$	UPTK (γ_2)	3, 4
(R5)	$SS_{(aer)} + HNO_{3(g)} \rightarrow NaNO_{3(aer)} + HCl_{(g)}$	UPTK (γ_3)	4, 5

Gas-particle equilibrium reactions			
	Reaction	Process	Notes
(R6)	$HNO_{3(g)} + NH_{3(g)} \rightleftharpoons NH^{+}_{4(aq)} + NO^{-}_{3(aq)}$	TEQ	6
(R7)	$H_2SO_{4(g)} + NH_{3(g)} \rightleftharpoons NH^{+}_{4(aq)} + SO^{2-}_{4(aq)}$	TEQ	6, 7
(R8)	$CaCO_{3(aq)} + 2HNO_{3(g)} \rightleftharpoons Ca^{2+}_{(aq)} + 2NO^{-}_{3(aq)} + H_2O + CO_2$	TEQ	4, 8
(R9)	$MgCO_{3(aq)} + 2HNO_{3(g)} \rightleftharpoons Mg^{2+}_{(aq)} + 2NO^{-}_{3(aq)} + H_2O + CO_2$	TEQ	4, 8
(R10)	$K_2CO_{3(aq)} + 2HNO_{3(g)} \rightleftharpoons 2K^{+}_{(aq)} + 2NO^{-}_{3(aq)} + H_2O + CO_2$	TEQ	4, 8
(R11)	$Na_2CO_{3(aq)} + 2HNO_{3(g)} \rightleftharpoons 2Na^{+}_{(aq)} + 2NO^{-}_{3(aq)} + H_2O + CO_2$	TEQ	4, 8
(R12)	$NaCl_{(aq)} + HNO_{3(g)} \rightleftharpoons Na^{+}_{(aq)} + NO^{-}_{3(aq)} + HCl_{(g)}$	TEQ	4, 9

1. Sulfuric acid ($H_2SO_{4(g)}$) is assumed to completely condense on fine and coarse dust and sea salt, transferring mass to the respective size mode. The condensation reaction does not depend on dust and sea salt alkalinity, but solely on their specific surface area based on Pringle et al. (2010).

2. Sulfur dioxide ($SO_{2(g)}$) uptake coefficient on dust (γ_1) is a function of RH as defined in Fairlie et al. (2010) and based on experimental studies performed on $CaCO_3$ particles by Prince et al. (2007). However, to account for $SO_{2(g)}$ oxidation by deliquesced O_3 and NO_2, the UPTK reaction of $SO_{2(g)}$ is performed even in the absence of alkalinity. That is why this reaction is considered to happen over $DU_{(aer)}$ and not only over $CaCO_{3(aq)}$, although it assumes same dust alkalinity as in $HNO_{3(g)}$ uptake (R4).

3. $HNO_{3(g)}$ uptake coefficient on $CaCO_{3(aq)}$ (γ_2) is a function of RH as defined by Fairlie et al. (2010) based on experimental studies performed on $CaCO_3$ particles by Liu et al. (2008). $CaCO_{3(aq)}$ concentration is used instead of $DU_{(aer)}$ concentration because the uptake coefficient is scaled for alkalinity, as shown in Eq. 4.4.

4. $CaCO_{3(aq)}$, $MgCO_{3(aq)}$, $K_2CO_{3(aq)}$, $Na_2CO_{3(aq)}$ and $NaCl_{(aq)}$ refers to the NVC content derived from the $dust_{(aer)}$ and $seasalt_{(aer)}$ concentrations using fractions from Gonçalves Ageitos et al. (2023) for dust and from Seinfeld and Pandis (2006) for sea salt (Sections 3.2 and 5.2.1).

5. $HNO_{3(g)}$ uptake coefficient on sea salt (γ_3) is based on the experimental study Liu et al. (2007), that reports $HNO_{3(g)}$ uptake kinetics for different RH and sea salt particles sizes. The average value $\gamma_3 = 0.05$ for particles from 2.5 to 10 μm (coarse mode) is assumed, considering ambient RH=80%.

6. Neutralization of $HNO_{3(g)}$ and $H_2SO_{4(g)}$ by $NH_{3(g)}$ is calculated through TEQ with ISORROPIA-II. It is assumed to happen in the fine mode for all mechanisms, and additionally in the coarse mode over coarse particles in those mechanisms considering coarse NO_3^- and NH_4^+ formation (Myhre et al. 2006, Usher et al. 2003, Uno et al. 2020). All reactants and products are assumed to remain in the aqueous phase (metastable assumption).

7. The result of the neutralization of $H_2SO_{4(g)}$ can be $(NH_4)_2SO_{4(aer)}$, $NH_4HSO_{4(aer)}$ or $(NH_4)_3H(SO_4)_{2(aer)}$ if solid results were assumed (Liu et al. 2022c), but under metastable assumption only aqueous ions of SO_4^{2-} are considered.

8. Ca^{2+}, Mg^{2+}, K^+ and Na^+ (NVC) dissolved from carbonates present in the bulk of dust particles react with $HNO_{3(g)}$ in the liquid coating of dust aerosols (Usher et al. 2003, Krueger et al. 2004, Fountoukis and Nenes 2007, Hauglustaine et al. 2014). Dust NVC content (i.e. alkalinity) is dependent on particle size and globally averaged from Journet et al. (2014) mineral data.

9. NaCl from sea salt particles dissolves and reacts with $HNO_{3(g)}$ in the liquid coating of sea salt particles (Myhre et al. 2006). Sea-salt also presents other NVC that are included in reactions R8-11, which are assumed globally homogeneous from Seinfeld and Pandis (2006) and Karydis et al. (2016).

suggests that the uptake coefficient for $HNO_{3(g)}$ should be lower and that it is highly influenced by RH (Goodman 2000, Krueger et al. 2003, Vlasenko et al. 2006; 2009,

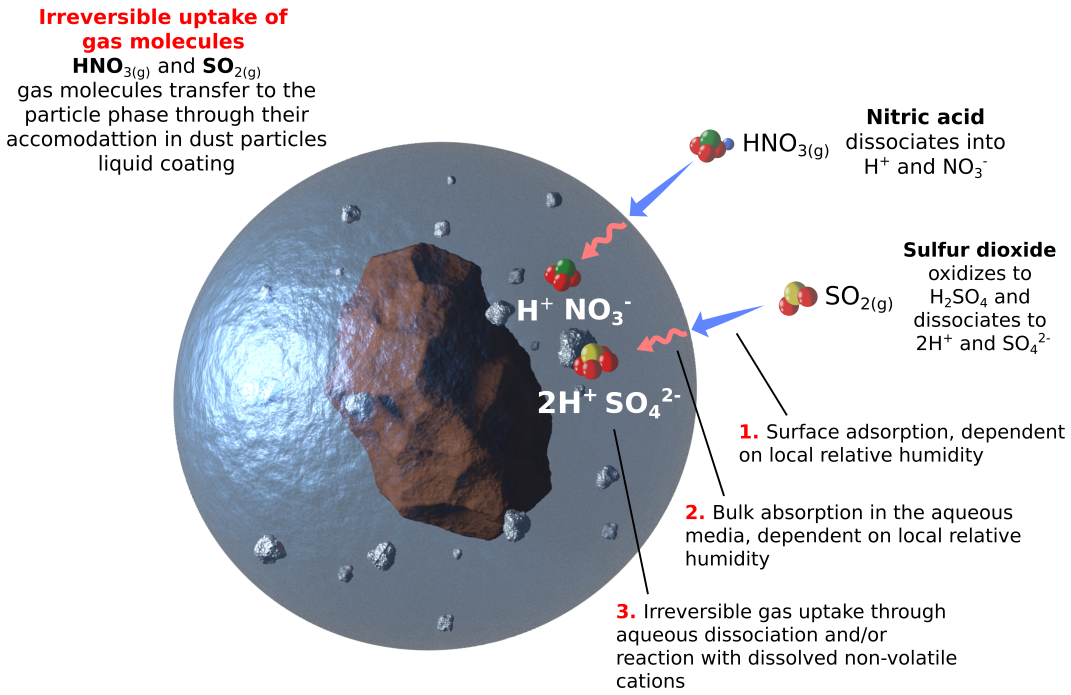

Figure 4.1: Scheme of irreversible uptake of gas molecules into the particle phase.

Fairlie et al. 2010, Wei 2010) and dust alkalinity (Goodman 2000, Hanisch and Crowley 2001, Krueger et al. 2004, Liu et al. 2007, Prince et al. 2007, Wei 2010, Crowley et al. 2010). Recent studies increasingly implement γ as a function of RH and employ different parameterizations of this function to account for dust alkalinity (Simpson et al. 2012, Hauglustaine et al. 2014, Paulot et al. 2016, Jones et al. 2021).

For this Thesis, we extended the chemical mechanism of MONARCH to incorporate pathways for the formation of coarse NO_3^- and SO_4^{2-} aerosols (Fig. 4.3). This extension involved refining irreversible heterogeneous parameterizations within the model, specifically the uptake of $HNO_{3(g)}$ on dust and sea salt particles (R4-5 in Table 4.3), as well as the uptake of $SO_{2(g)}$ on dust particles (R3 in Table 4.3).

Our implementation incorporates dependencies of γ on RH and the alkalinity of dust (Vlasenko et al. 2006; 2009, Liu et al. 2007; 2008, Crowley et al. 2010, Fairlie et al. 2010, Wei 2010). The γ dependency on RH is modeled akin to a Brunauer–Emmett–Teller (BET) isotherm, which characterizes water adsorption on dust particles (Vlasenko et al. 2006). We employed a modified BET function to formulate γ, extending it to account for dust alkalinity. This formulation is represented by the following equation:

$$\gamma = Sc \cdot \frac{|c_1 \cdot RH|}{(1 - RH)|1 + c_2 \cdot RH|} \tag{4.4}$$

where RH is the relative humidity (ranging from 0 to 1), c_1 and c_2 denote the water adsorption scaling factors (Vlasenko et al. 2006), and Sc is a factor dependent on dust

alkalinity. For the uptake of $HNO_{3(g)}$ on dust (R4 in Table 4.3), typical values assumed for c_1 and c_2 are 8.0 and 7.0, respectively (Li et al. 2012, Paulot et al. 2016, Wang et al. 2017). For Sc, however, literature reports varying values based on dust alkalinity assumptions, ranging from Sc=0.033 for the industrially-standardized Arizona Test Dust (Möhler et al. 2006, Herich et al. 2009, Suman et al. 2024) to $Sc = 0.018$ for China Loess samples with 39% $CaCO_3$ content (Krueger et al. 2004, Wei 2010).

We adopt the uptake RH functions for both $HNO_{3(g)}$ and $SO_{2(g)}$ on dust from Fairlie et al. (2010). To fit experimental data from Song et al. (2007) and the RH function reported by Fairlie et al. (2010), for $\gamma(HNO_3)$ (Reaction R4 in Table 4.3) we determine c_1=$3.84 \cdot 10^{-4}$ and c_2= 0.56. Additionally, Fairlie et al. (2010) assumes a NVC content of 3.0% of Ca^{2+} and 0.6% of Mg^{2+}, which differs from the NVC values used in the present study. Therefore, we use the alkalinity scaling factor Sc to normalize the Fairlie et al. (2010) function accordingly. Specifically, values for Sc are defined as the ratio of Ca^{2+} and Mg^{2+} percentages used in our study relative to those assumed by Fairlie et al. (2010). For instance, Sc values result in $Sc = 1.80$ and $Sc = 1.52$ for the two average alkalinity values derived from Journet et al. (2014) and Claquin et al. (1999) used in our experiments, respectively (see Section 5.2.1). Note that Sc is zero if no alkalinity is considered, and that a constant value of $\gamma(HNO_3) = Sc \cdot 1.05 \cdot 10^{-3}$ is used for RH higher than 80%.

Similarly, we determined the $\gamma(SO_2)$ on dust (R3 in Table 4.3) fitting Eq. 4.4 to experimental data from Prince et al. (2007) and the RH function from Fairlie et al. (2010), yielding values of $c_1 = 2.7 \cdot 10^{-6}$ and $c_2 = -1.06$. The same Sc values as used for $\gamma(HNO_3)$ are applied for $\gamma(SO_2)$: $Sc = 1.80$ and $Sc = 1.52$. However, if alkalinity is not considered, Sc is set to 1.0 (and not zero, as the case for $\gamma(HNO_3)$) to account for the oxidation of $SO_{2(g)}$ by deliquesced O_3 and NO_2 (Usher et al. 2002, Prince et al. 2007, Yu et al. 2017, Li et al. 2024b). For RH above 90%, $\gamma(SO_2)$ remains constant at $\gamma(SO_2) = Sc \cdot 5.0 \cdot 10^{-4}$ after Fairlie et al. (2010).

For the $HNO_{3(g)}$ uptake on sea salt (R5 in Table 4.3), we adopted the $\gamma(HNO_3)$ size-dependent values of Liu et al. (2007), which provide experimental estimates of this factor for different particle sizes and RH. However, a clear uptake function on these parameters has not been found in the literature. Therefore, for this Thesis the RH dependency of $\gamma(HNO_3)$ for sea salt is not generally considered. Instead, we used average values of uptake rates for $HNO_{3(g)}$ on sea salt particles based on the experimental Liu et al. (2007) study assuming 80% RH: $\gamma(HNO_3) = 0.15$ for fine sea salt particles (in the D range from 0.2 to 2.5μm) and $\gamma(HNO_3) = 0.05$ for coarse ones (D from 2.5 to 30μm).

While larger values have been reported by Guimbaud et al. (2002), we opted for the above-mentioned rates as they align with more widely accepted ranges found in the literature (Saul et al. 2006, Pratte and Rossi 2006, Liu et al. 2007, Fagerli et al. 2015). Using higher values could potentially overestimate the uptake on sea salt particles.

Additionally, to try to reach a consensus among experimental studies, we characterized the simultaneous dependence of sea salt $\gamma(HNO_3)$ on RH and particle size (Fig. 4.2), based on a larger set of experimental values from Liu et al. (2007) and Saul et al. (2006).

This experimental data can be fitted using the following trigonometric function:

$$\gamma_{(HNO_3)} = \max(0,\ 0.16\sin(1.86\,D_{SS}) - 0.13\cos(5.14\,RH) - 0.05) \tag{4.5}$$

Where D_{SS} is the diameter in μm of sea salt particles, and RH is the relative humidity (from 0 to 1). The parameterization is applied only for combinations of RH and particle D yielding positive values of γ. Otherwise the coefficient is assumed to be zero. Also note from Fig. 4.2 the scarce experimental values that such a parameterization relies on, highly limiting the extend of its applicability and accuracy.

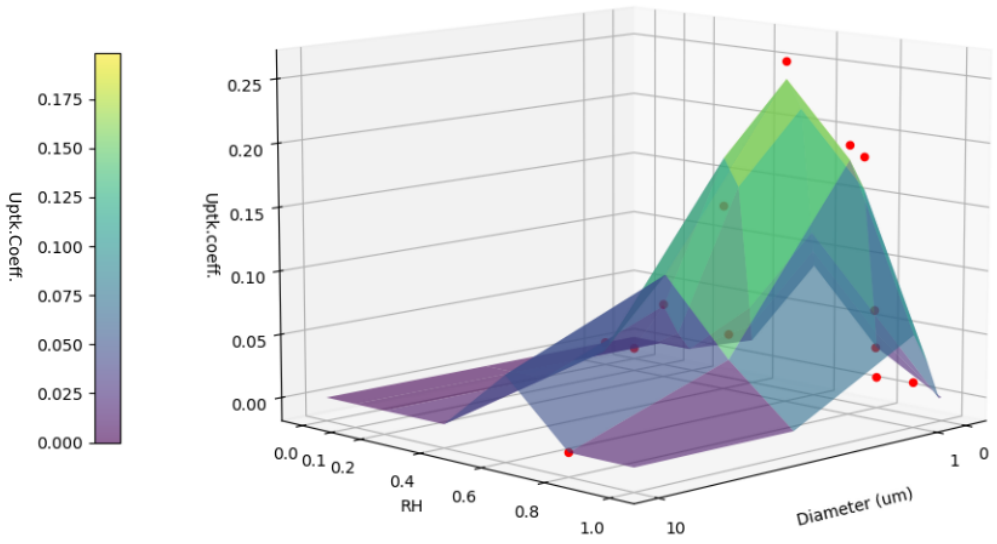

Figure 4.2: Trigonometric fit of experimental data for $\gamma(HNO_3)$ on sea salt dependent on RH and particle size from Saul et al. (2006) and Liu et al. (2007).

The condensation of $H_2SO_{4(g)}$ (R1-2 in Table 4.3) on dust and sea salt is another relevant source of SO_4^{2-} introduced in our model. Due to the extremely low volatility of $H_2SO_{4(g)}$ at atmospheric temperatures, its condensation onto existing particles is assumed as irreversible and complete. This process accounts for a direct mass transfer from the gas to the aerosol phase (Zaveri et al. 2008, Hauglustaine et al. 2014). The amount of $H_2SO_{4(g)}$ that condenses in the fine and coarse modes is determined using

kinetic diffusive coefficients calculated as described in Section 4.4. Consequently, particulate SO_4^{2-} forms through three main pathways: (1) aqueous-phase oxidation of $SO_{2(g)}$ and DMS in the fine mode; (2) direct uptake of $SO_{2(g)}$ onto preexisting dust and sea salt particles in both fine and coarse modes (Prince et al. 2007, Fairlie et al. 2010); and (3) condensation of kinetically limited $H_2SO_{4(g)}$ vapor into each particle mode, assuming that its low volatility prevents it from remaining in the gas phase (Pringle et al. 2010).

Note that the NO_2 oxidation on dust surfaces is not included in the model because of its relatively low relevance compared with other reactions. For instance, Jacob (2000) estimates the reaction probability after uptake of NO_2 onto dust to be in the order of $1 \cdot 10^{-4}$ (Liao et al. 2003), Underwood et al. (2001) estimates it to be on average $4.4 \cdot 10^{-5}$ and $2.0 \cdot 10^{-4}$, and Zhu et al. (2010) to be $2.1 \cdot 10^{-6}$. In most of the cases, the reaction rate of NO_2 is below the estimated average rates for $HNO_{3(g)}$ and $N_2O_{5(g)}$, this last one ranging from $6 \cdot 10^{-4}$ to 0.1 (Fairlie et al. 2010, Zhu et al. 2010).

4.3.2 Reversible condensation

In this Thesis, we adopt the ISORROPIA-II v1 (Fountoukis and Nenes 2007) TEQ model (Section 4.2) to investigate the sensitivity of the partitioning of semivolatile inorganic compounds to the NVC content.

We use the metastable solution of ISORROPIA-II, assuming all the resulting particulate compounds from the TEQ computation remain in the liquid phase. Previous studies comparing stable and metastable methodologies with ISORROPIA-II have reported only marginal differences in global NO_3^- budgets between both modes. At global scales, these differences noted slightly higher pH values (0.5) and NO_3^- formation (2%) when using the metastable assumption (Karydis et al. 2016; 2021, Milousis et al. 2024), although these differences are reported to be more important (<2 pH units and <60% NO_3^- concentrations) close to regions with low RH and high concentration of crustal species, or their downwind areas. However, given the global scale scope of the present study, we used the metastable assumption since it allows for full traceability of total aerosol NO_3^-, NH_4^+ and SO_4^{2-} formation (reactions R6-12 in Table 4.3).

We also adopt the temperature and pressure applicability range for ISORROPIA-II proposed by Sulprizio (2022), which highlights potential instabilities in reactions occurring below 250ºK and 200hPa. Consequently, ISORROPIA-II computations are limited to model gridcells with temperature and pressure values above these thresholds.

4.4 Heterogeneous chemistry mechanisms

Since in atmospheric conditions $HNO_{3(g)}$ and $NH_{3(g)}$ exhibit higher volatility compared to $H_2SO_{4(g)}$, their condensation onto liquid coatings around particles is a reversible process and should not be assumed as irreversible uptake reactions (Usher et al. 2003). As explained in Section 1.5, different approaches have been proposed in the literature to incorporate the condensation-evaporation of $HNO_{3(g)}$ and $NH_{3(g)}$ across the entire aerosol size range, aiming to mitigate the computationally expensive cost of solving the dynamic mass transfer equations.

The assumption of TEQ between gas and aerosol phases for fine and coarse particles provides a practical approximation to account for the potential evaporation of already dissolved molecules in their respective liquid coatings. Such mechanism assumes that TEQ is reached within each model time-step (on the order of few minutes). This assumption is reasonable for fine particles, since for example fine NH_4NO_3 with $D < 1\mu m$ generally reaches gas-vapor equilibrium on the order of minutes under typical atmospheric conditions (Wexler and Seinfeld 1990, Dassios and Pandis 1999). However, broad TEQ assumption is less appropriate for processes on coarse particles, where achieving equilibrium can take minutes to hours (Feng and Penner 2007).

To overcome this limitation, different approaches have been proposed in the literature to incorporate the condensation–evaporation of $HNO_{3(g)}$ and $NH_{3(g)}$ on particles while minimizing computational costs. In this Thesis, the MONARCH model has been developed to incorporate such methods.

The three main mechanisms studied are:

(1) A simple scheme neglecting coarse NO_3^- and NH_4^+ formation, so assuming that TEQ is reached solely in the fine mode (fTEQ).

(2) The hybrid method (HYB) (Hodzic et al. 2006, Feng and Penner 2007), that solves first the partitioning over fine particles using a TEQ calculation as in fTEQ, and then employs a first-order irreversible uptake reaction (UPTK, Section 4.3.1) reaction for condensation over coarse particles.

(3) A more refined approach that treats the formation of coarse NO_3^- as a reversible process through the combination of a double call of the TEQ calculation (DBCLL), one for the fine and one for the coarse mode, together with a kinetic limitation of the gas species involved in the partitioning (Pringle et al. 2010).

The processes included in each of these three mechanisms are described in Table 4.4. They are also illustrated in Fig. 4.3, and evaluated in Chapter 5. We detail them more comprehensively below.

Table 4.4: Sequence of reactions and calculations performed for each scheme (rows). In columns, the sequence order (tN) and the gas/aerosol size mode of each process is indicated. Dust and sea salt particles are referred as *DU* and *SS*, respectively, and condensation is abbreviated as *Cond.*. Fine mode is formed from reactions with dust and sea salt particles with $0.2 < D < 2.5\mu m$, and coarse ones with $2.5 < D < 20\mu m$ for dust and $2.5 < D < 30\mu m$ for sea salt.

Mechanism	**t0: Fine SO_4**	**t1: Fine DU**	**t2: Coarse DU**	**t3: Gas HNO_3, NH_3 and H_2SO_4**	**t4: Fine DU & SS**	**t5: Coarse DU**	**t6: Coarse SS**	**t7: Fine / Coarse SO_4**
fTEQ	Cond. ($\times$1.0 H_2SO_4)	UPTK (SO_2)	UPTK (SO_2)	-	TEQ (HNO_3 & NH_3)	-	-	-
HYB	Cond. ($\times$1.0 H_2SO_4)	UPTK (SO_2)	UPTK (SO_2)	-	TEQ (HNO_3 & NH_3)	UPTK (HNO_3)	UPTK (HNO_3)	-
DBCLL	Cond. ($\times$0.5 H_2SO_4)	UPTK (SO_2)	UPTK (SO_2)	DIFFLIM	TEQ (HNO_3 & NH_3)	TEQ (HNO_3 & NH_3)		Cond. H_2SO_4

The fTEQ approach (Fig. 4.3a) solves the partitioning of semivolatile inorganic species with ISORROPIA-II exclusively within the fine mode to assess the effect of neglecting coarse NO_3^- and NH_4^+ formation on atmospheric composition. This mechanism solves the $HNO_{3(g)}$-$NH_{3(g)}$-$H_2SO_{4(g)}$ neutralization (R6-7 in Table 4.3), accounting for alkalinity effects (R8-12 in Table 4.3) if fine dust and sea salt are considered in the mixture. Since $H_2SO_{4(g)}$ and SO_4^{2-} influence the ambient pH, they are always involved in any TEQ calculation. As described in Section 3.1, aqueous SO_4^{2-} formation is first solved through the oxidation of $SO_{2(g)}$ and DMS. Then, only 50% of the remaining $H_2SO_{4(g)}$ is assumed to directly nucleate as fine SO_4^{2-} through the aqueous phase chemistry, while the rest condenses into fine SO_4^{2-} through reactions R1 and R2 in Table 4.3. Under this assumption, the fTEQ eventually attributes all SO_4^{2-} to the fine mode, attempting at acknowledging the role of nucleation as a particle formation pathway, treating it in a simplified way considering the scope of our current study, the absence of a detailed microphysics scheme in the model, and the inherent uncertainty in $H_2SO_{4(g)}$ nucleation modeling (Kulmala et al. 1998, Vehkamäki et al. 2002, Kuang et al. 2008). This simplified approach follows similar methodologies implemented in other mass-based models (Chin et al. 2000, Rémy et al. 2019) Finally, while fTEQ serves in our study as a sensitivity test to assess the impact of neglecting coarse NO_3^- and NH_4^+ formation, the fTEQ approach may be appropriate in environments where coarse particles are sparse or in applications focusing primarily on fine particle formation (Bian et al. 2017).

Conversely, the HYB mechanism (Fig. 4.3*a*) is a commonly employed strategy in atmospheric chemistry models to represent NO_3^- formation on coarse particles. It

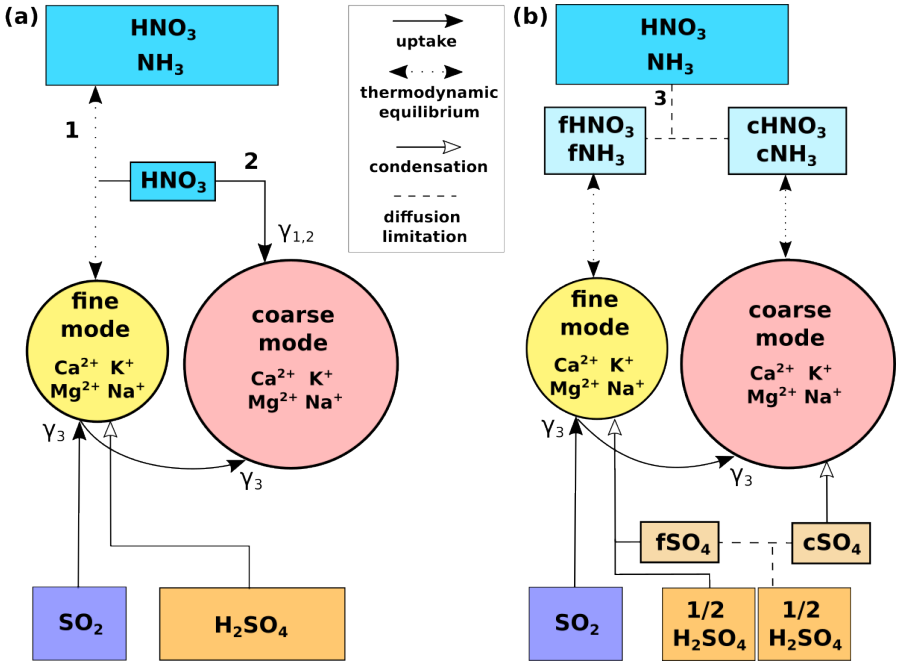

Figure 4.3: Scheme of the heterogeneous chemistry reactions on dust and sea salt developed in this work. (a) Schemes for the fTEQ and HYB mechanisms. (b) Scheme for the DBCLL mechanism that includes the kinetic diffusion limitation of gas species. The legend for the line patterns is included in the center box. Numbers represent (1) fTEQ, (2) HYB and (3) DBCLL. At the bottom, the pathways for the processing of $SO_{2(g)}$ and $H_2SO_{4(g)}$ gases for each scheme are represented: $SO_{2(g)}$ is taken up by fine particles and the remaining gas is taken up by coarse particles. For $H_2SO_{4(g)}$, (a) the fTEQ and HYB mechanisms assume that it nucleates directly as fine SO_4^{2-}, while (b) the DBCLL mechanism assumes that 50% of its concentration nucleates, and the rest is divided by diffusion limitation between the fine and coarse modes, completely condensing on each of them. The uptake coefficients used for the uptake processes (solid arrows) are $\gamma_{1,2}$ for $HNO_{3(g)}$ uptake on dust and sea salt, and γ_3 for $SO_{2(g)}$ uptake on dust. Fine mode forms over dust particles with $0.2 < D < 2.5\mu m$, and coarse ones for $2.5 < D < 20\mu m$.

solves NO_3^- formation through a sequential implementation of 1) fTEQ reaction between $HNO_{3(g)}$ and $NH_{3(g)}$ considering internal mixing with fine dust and sea salt modes (R6-12 in Table 4.3), and 2) an irreversible first-order UPTK reaction of the remaining $HNO_{3(g)}$ on the coarse modes of dust and sea salt, excluding its evaporation back to the gas phase (R4 and R5 in Table 4.3). The UPTK reaction of $HNO_{3(g)}$ follows the implementation detailed in Section 4.3.1, and SO_4^{2-} is treated in an analogous manner to the fTEQ mechanism.

Finally, the DBCLL mechanism (Fig. 4.3*b*), inspired in Pringle et al. (2010) and previously used in (Myriokefalitakis et al. 2022), treats coarse NO_3^- and NH_4^+ formation as a reversible condensation-evaporation process (Fig. 4.4). Firstly, the DBCLL methodology involves the calculation of kinetic diffusion limitation coefficients (DIFFLIM) for both the fine and coarse size modes of each of the condensing gas species, which restricts

the amount of gas available to condense on each mode (Table 4.4). DIFFLIM has been implemented based on the formulation by Vignati et al. (2004) for $H_2SO_{4(g)}$, and its extension to other gases by Pringle et al. (2010). Following DIFFLIM, sequential TEQ calculations are conducted over fine and coarse modes (double call of the TEQ model, reactions R8-12 in Table 4.3), using the DIFFLIM size-specific calculated coefficients to limit the availability of gas condensing on each mode.

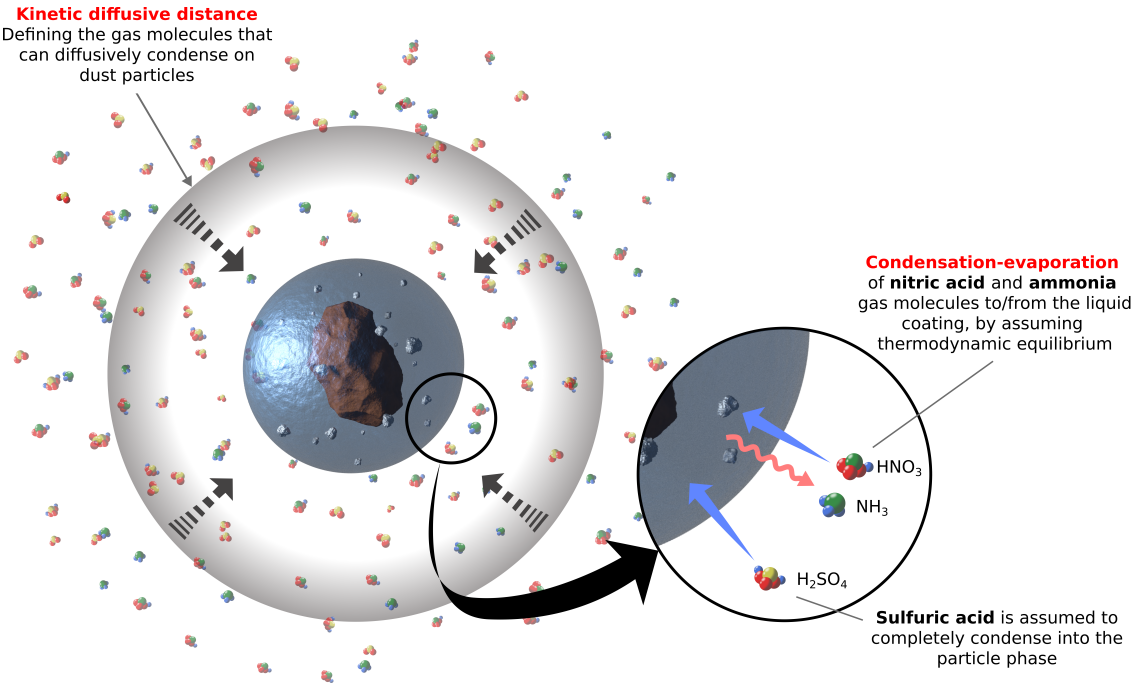

Figure 4.4: Scheme of the kinetic diffusion limitation methodology and the condensation-evaporation of gas species to and from the aerosol phase.

Regarding the SO_4^{2-} treatment in DBCLL, a similar approach to fTEQ is employed, but the DIFFLIM coefficients calculated for $H_2SO_{4(g)}$ are used to condense the remaining $H_2SO_{4(g)}$ available — after accounting for the 50% nucleation fraction via aqueous chemistry — into the fine and coarse modes of SO_4^{2-} (reactions R1 and R2 in Table 4.3 and Fig. 4.3*b*).

5

Impacts of the dust heterogeneous chemistry mechanism

Published as:

Soussé Villa, R., Jorba, O., Gonçalves Ageitos, M., Bowdalo, D., Guevara, M., and Pérez García-Pando, C.: A comprehensive global modeling assessment of nitrate heterogeneous formation on desert dust, Atmospheric Chemistry and Physics, 25, 4719–4753, doi.org/10.5194/acp-25-4719-2025, 2025

5.1 Introduction

As detailed in Chapter 1 (Section 1.2), dust heterogeneous chemistry has a relevant role over both, dusty regions and at a global level. Therefore, it proofs important to accurately represent them in atmospheric models for present and future air quality control (Myhre et al. 2006).

Section 1.5 summarizes the recent efforts made by atmospheric chemistry and Earth models to include dust heterogeneous reactions. There, we underscore that for the sake of computational efficiency, such efforts have been focused on simplifying heterogeneous reactions to ease their incorporation into models. The most important developed assumptions have been: The instant thermodynamic equilibrium calculation (TEQ) between gas and aerosol phases for the bulk aerosol mass (Lurmann et al. 1997), simplifying the dynamic condensation-evaporation processes with a first-order irreversible uptake reaction (UPTK) (Jacob 2000, Bauer et al. 2004, Feng and Penner 2007, Fairlie et al. 2010), combining the TEQ calculation on the fine mode with the UPTK on the coarse mode (hybrid, HYB) (Capaldo et al. 2000, Hodzic et al. 2006, Hauglustaine et al. 2014, Trump et al. 2015), and the double call of the TEQ for fine and coarse aerosol modes

separately (DBCLL), either after kinetically limiting the gas condensing on each bin or mode (Pringle et al. 2010) or redistributing the condensed mass from the bulk TEQ using kinetic coefficients (i.e. DIFFLIM) (Karydis et al. 2016).

Despite these efforts, atmospheric models still struggle to reproduce observational data of particulate NO_3^- and NH_4^+ (Fairlie et al. 2010, Hauglustaine et al. 2014, Paulot et al. 2016, Zakoura and Pandis 2018, Luo et al. 2019, Jones et al. 2021, Rémy et al. 2022).

For instance, the AeroCom phase III nitrate experiment (Bian et al. 2017) intercompares global NO_3^- budgets from nine global models for the year 2008, highlighting the substantial disagreements among models. For instance, the intermodel average NO_3^- atmospheric burden is 0.63 Tg, with a standard deviation of 0.56 Tg, nearly 90% of the mean value. Similar variability is observed for NH_4^+ (0.32 ± 0.20 Tg). The study also underscores the general inaccuracy of current models in reproducing observations of NO_3^- concentrations after long-range transport of precursor species, indicating that N heterogeneous chemistry processes on dust and sea salt are often misrepresented in models. Other studies, such as Hauglustaine et al. (2014), (Karydis et al. 2016), and Rémy et al. (2022) provide a qualitative view of current estimates of particulate NO_3^- formation in the atmosphere and the role of representing key processes in models, despite results from the literature being representative for different study periods.

The scope of the present chapter is to understand the role of dust in NO_3^- formation through a systematic investigation of the underlying processes governing dust heterogeneous chemistry. To achieve this goal, we incorporate a variety of mechanisms of different complexities into a global model. This enables a comprehensive analysis of the partitioning between gas and aerosol phases, the suitability of irreversible and reversible parameterizations for the condensation of gas species on dust, and the role of explicit representation of alkalinity. While our primary emphasis is on the heterogeneous chemistry on dust surfaces, we also account for NO_3^- formation on sea salt and its alkalinity.

This chapter is structured as follows. Section 5.2 introduces the sensitivity runs performed with the implemented mechanisms (5.2.2), this experimental setup (5.2.3), and the datasets used for evaluation (5.2.4). Section 5.3 presents an analysis of the global simulations and their evaluation against observational data. This last section includes a comparison of the spatial distributions and an examination of the total N burden and gas/aerosol partitioning. Additionally, we discuss the budgets of reduced and oxidized N species, depositions, production/loss rates, and lifetimes. Our results are contextualized with findings from previous studies, providing a comprehensive understanding of the results. Section 5.4 provides a summary of our key findings.

5.2 Methods

5.2.1 Modeling NO_3^- heterogeneous chemistry

The MONARCH model is employed to comprehensively assess the role of mineral dust on NO_3^- heterogeneous formation. The advances implemented in MONARCH (see Section 3.1.1 and Chapter 4) are exploited here through different model configurations, which incorporate the mechanisms described in Section 4.4 with additionally modified factors to study, among other parameters, the sensitivity of the model to the representation of dust and sea salt alkalinity. Table 4.3 lists the set of reactions under investigation in our analysis.

In this work, dust and sea-salt alkalinity have been assumed to be globally-homogeneous, deriving average values from global mineralogical datasets for dust and from literature values for sea salt, in order to investigate the importance of representing dust alkalinity in atmospheric models.

The globally-averaged dust mineralogy from JOUR and CLAQ soil mineralogical datasets are derived from 5-year long MONARCH simulations that explicitly track dust mineral species (Gonçalves Ageitos et al. 2023). We relied on two different MONARCH experiments detailed in Gonçalves Ageitos et al. (2023), which utilized the CLAQ and JOUR data, respectively (see Section 3.2.1). The simulation based on CLAQ accounts for eight distinct minerals, including quartz, feldspar, illite, smectite, kaolinite, calcite, gypsum, and hematite (supplementary Table A.1). Whereas, the simulations based on JOUR for twelve minerals, also including these minerals as well as chlorite, vermiculite, mica, and goethite (supplementary Table A.3).

In this study, we assume size-dependent but globally homogeneous values for dust mineralogy, and consequently dust alkalinity and NVC, to focus on understanding heterogeneous reaction parameterizations. We also adopt an upper bound for the minerals' solubility and reactivity with gas species based, on Hanisch and Crowley (2001).

Moreover,

Based on the global average mineral mass fraction for each dust size bin and the elemental chemical composition associated to each mineral, we estimate the average NVC content per dust size bin at each time step following Eq. 5.1:

$$NVC_{i,j} = \left(\sum_k fNVC_{k,j} \cdot M_{i,k} \right) \cdot DU_i \tag{5.1}$$

where the NVC concentration for each element j (i.e., Ca^{2+}, Mg^{2+}, K^+, Na^+) and size bin i ($NVC_{i,j}$) at a given location is derived by considering the molar fraction of each element j in each mineral k ($fNVC_{k,j}$), the global average mass fraction of each mineral

and size bin ($M_{i,k}$), and the bin's dust concentration at the specified location (DU_i). $NVC_{i,j}$ then serves as input to the TEQ calculation. As mentioned, we assume an upper limit of minerals' potential solubility, considering only minerals soluble in water or acids that may at least partly dissolve in the liquid coating of the particles (Usher et al. 2003). Only NVC reacting with the gas species in ISORROPIA-II are used (Ca^{2+}, Mg^{2+}, K^+, SO_4^{2-}, Cl^- or Na^+) for the calculation (see Section 4.2).

After including all the minerals from the datasets, accounting for their respective solubility, the dust NVC global average content results in: 5.17% Ca^{2+}, 0.79% Na^+, 2.37% K^+, 1.32% Mg^{2+} for the JOUR dataset, and 3.68% Ca^{2+}, 0.87% Na^+, 3.15% K^+, 1.75% Mg^{2+} for CLAQ. The resulting size-resolved NVC percentages for each dust bin are reported in the supplementary Tables A.2 and A.4.

As a reference, these values are within the range reported by Karydis et al. (2016) (5.36±3.69% Ca^{2+}, 2.46±1.90% Na^+, 2.08±1.34% K^+, 1.96±2.20% Mg^{2+}). Comparatively, the JOUR dataset results in a higher proportion of Ca^{2+} than CLAQ, while similar fractions for Na^+ and K^+ are reported.

Regarding sea salt, we use a global average composition from Seinfeld and Pandis (2006), with 55% Cl^-, 30.6% Na^+, 7.7% SO_4^{2-}, 3.7% Mg^{2+}, 1.2% Ca^{2+}, and 1.1% K^+.

5.2.2 Sensitivity runs

The sensitivity experiments in this work aim at assessing the performance of the mechanisms described in Section 4.4 and illustrated in Fig. 5.1, alongside with the sensitivity to the representation of fine ($0.2 < D < 2.5\mu m$) and coarse ($2.5 < D < 30\mu m$) dust alkalinity.

Overall, eleven different runs (Table 5.1) are analyzed to test different degrees of complexity and sensitivity to parameterizations when simulating heterogeneous chemistry of dust, such as the hypothesis on reversibility on NO_3^- formation, and the role that dust (and sea salt) alkalinity play in the partitioning of gas and aerosol species. Unless stated to the contrary, all the experiments employ dust alkalinity derived from the average of the Journet et al. (2014) simulation, as explained in Section 5.2.1.

Three initial run sets are conducted neglecting coarse NO_3^- formation, serving as a comparison reference for following experiments including coarse NO_3^-. The noHC run assumes that there is no formation of NO_3^-, NH_4^+ or SO_4^{2-} aerosol through heterogeneous chemistry on any aerosol particle, serving as a baseline to estimate the burden of gas condensing in particles in other configurations and the influence of particle formation on N deposition rates. Additionally, two sensitivity experiments with fTEQ are included to discuss the impact of ignoring the partitioning of semivolatile inorganic species on

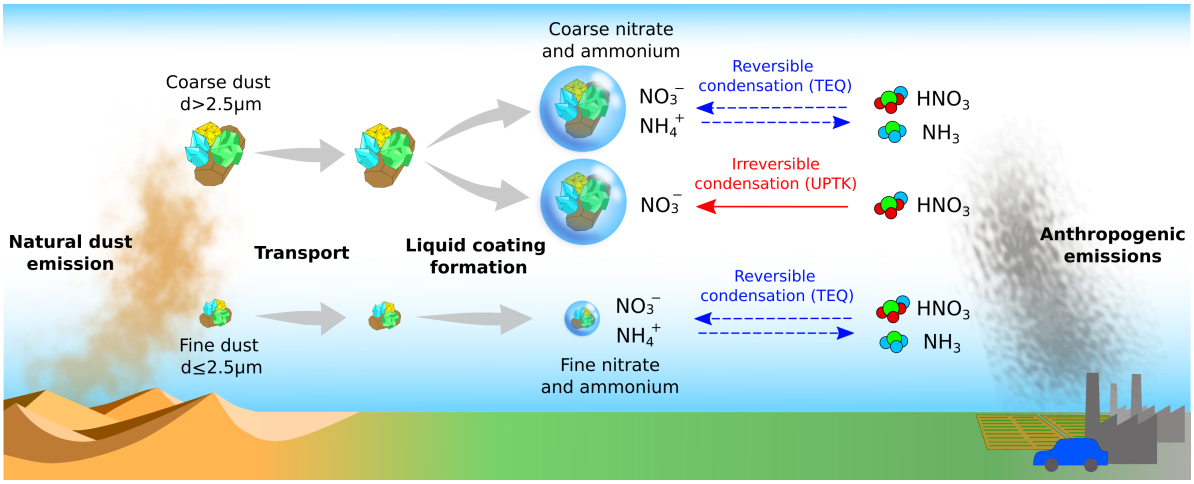

Figure 5.1: Illustration of the mineral dust heterogeneous chemistry mechanisms implemented for fine ($0.2 < D < 2.5\mu m$) and coarse ($2.5 < D < 20\mu m$) particles. Fine dust aqueous coating is assumed to reach thermodynamic equilibrium (TEQ) with anthropogenic gas species to form fine particulate NO_3^- and NH_4^+. Conversely, coarse particulate NO_3^- and NH_4^+ are formed through either the reversible condensation (i.e. through TEQ) of $HNO_{3(g)}$ and $NH_{3(g)}$ after kinetic limitation or the irreversible uptake reaction (UPTK) of $HNO_{3(g)}$ on coarse dust particles, in this case only considering the formation of NO_3^- and not NH_4^+.

Experiment	Fine TEQ	Coarse TEQ	Coarse DU UPTK	Coarse SS UPTK	DIFFLIM	DU Alk.	SS Alk.
noHC							
fTEQ_noAlk	■						
fTEQ_du-ssAlk	■					J	■
HYB_duUPTK	■		■			J	
HYB_du-ssUPTK	■		■	■		J	■
HYB_DL	■		■	■	■	J	■
HYB_g0p1	■		■	■		J	■
DBCLL_noAlk	■	■			■		
DBCLL_duAlk	■	■			■	J	
DBCLL_du-ssAlk	■	■			■	J	■
DBCLL_ClaqAlk	■	■			■	C	■

Table 5.1: The sensitivity experiments conducted in this study and the processes performed in each one of them (green boxes). *Fine TEQ* and *Coarse TEQ* refer to the respective calculations of the TEQ for the fine ($0.2 < D < 2.5\mu m$) and coarse modes of dust ($2.5 < D < 20\mu m$) and sea salt ($2.5 < D < 30\mu m$), referred to as *DU* and *SS*, respectively. *Coarse DU UPTK* and *Coarse SS UPTK* indicate the irreversible UPTK of $HNO_{3(g)}$ on coarse dust and sea salt, respectively. Alkalinity is denoted as *Alk.* and for the dust alkalinity column, the alkalinity derived from the Journet et al. (2014) and Claquin et al. (1999) simulations is indicated by *J* and *C*, respectively.

coarse particles: fTEQ_noAlk neglects the presence of dust or sea salt in the aerosol mixture (R6-7 in Table 4.3), while fTEQ_du-ssAlk considers TEQ between gas and NVC in the fine modes of dust and sea salt particles (R6-12 in Table 4.3).

Next, we addressed the condensation of NO_3^- across the entire particle size range

with runs employing the HYB and DBCLL mechanisms.

We conducted two sensitivity runs with the HYB mechanism to explore the impact of implementing the $HNO_{3(g)}$ UPTK reaction on coarse dust only (HYB_duUPTK, reaction R4 from Table 4.3)) and on both coarse dust and sea salt (HYB_du-ssUPTK, reactions R4 and R5), comparing their results to assess the relative contributions of dust and sea salt in heterogeneous chemistry under the assumption of $HNO_{3(g)}$ irreversible UPTK on the coarse mode.

In the HYB approach, all $HNO_{3(g)}$ and $NH_{3(g)}$ concentrations are initially available to condense in the fine mode through TEQ reactions. Only the remaining $HNO_{3(g)}$ after the TEQ calculation is considered for UPTK reactions in the coarse mode. Note that this assumption neglects coarse NH_4^+ formation, and may also potentially lead to a misrepresentation of fine and coarse NO_3^-, such as the underproduction of fine and overproduction of coarse NO_3^- (Feng and Penner 2007, Hauglustaine et al. 2014, Bian et al. 2017, Jones et al. 2021). To address this potential limitation, an additional simulation (HYB_DL) was conducted using the calculation of kinetic limitations to distribute the $HNO_{3(g)}$ and $NH_{3(g)}$ gas that is available to diffuse in the fine and coarse modes (DIFFLIM, Section 4.4), calculating the condensation in fine particles through TEQ, and the $HNO_{3(g)}$ that can form coarse NO_3^- through UPTK reactions.

Furthermore, to assess the influence of the UPTK coefficient of $HNO_{3(g)}$ on the results, instead of using a RH function (see Section 4.3.1) we also conducted a simulation setting $\gamma(HNO_3) = 0.1$ for dust (HYB_g0p1), following experimental findings (Fenter et al. 1995, Hanisch and Crowley 2001; 2003) and various modeling studies (Dentener et al. 1996, Liao et al. 2003, Bauer et al. 2004, Hodzic et al. 2006, Bauer et al. 2007, Feng and Penner 2007).

Finally, we conducted four sensitivity simulations using the DBCLL mechanism, which accounts for reversible heterogeneous SIA chemistry both on fine and coarse modes. These simulations evaluate the influence of alkalinity, including the DBCLL_noAlk run that excludes both dust and sea salt NVC content (reactions R6-7, Table 4.3), the DBCLL_duAlk run accounting for dust alkalinity only (reactions R8-11), and the DBCLL_du-ssAlk run accounting for both dust and sea salt alkalinity (reactions R8-12). Additionally, since all three cases use dust alkalinity from the average of the Journet et al. (2014) simulation, an additional simulation was performed using the average dust data from Claquin et al. (1999) simulations (DBCLL_Claq), instead of Journet et al. (2014), to assess the effect of the specific mineralogy used.

Note that most of the sensitivity runs employ the JOUR global average, if not stated otherwise (see Table 5.1). Values for CLAQ are used solely in one sensitivity test.

5.2.3 Experimental setup

Simulations were run on a global domain at a spatial resolution of 1.4 º longitude by 1.0 º latitude, utilizing 48 hybrid pressure-sigma vertical layers up to 5hPa. The dynamics timestep was set to 180s and results were stored every 6 hours. The analysis period is the year 2018 after a spin-up period of half a year to initialize the concentration fields. Meteorological variables were initialized from the ERA5 reanalysis (Hersbach et al. 2023) every 24h to keep the modeled circulation close to observations. A meteorological spin-up of 12h was used in each daily cycle before solving the chemistry. The initial state of the chemistry fields are those prognostically calculated by MONARCH the day before.

In addition to the meteorology-driven online emissions (e.g. dust and sea salt, described in Section 3.1), the HERMESv3_GR (Guevara et al. 2019) (see Section 3.3) is employed to process both anthropogenic and biomass burning primary emissions. For anthropogenic sources, we use the global inventory CAMS-GLOB-ANT_v4.2 (Soulie et al. 2024) for 2016, with updated temporal profiles that provide gridded monthly, day-of-the-year, day-of-the-week and hourly weight factors for the temporal disaggregation of emitted fluxes (Guevara et al. 2021). For biomass burning emissions, we used data from the GFASv1.2 (Kaiser et al. 2012) inventory, that accounts for forest, grassland, and agricultural waste fires derived from satellite products. Oceanic natural emissions of DMS are provided by CAMS-GLOB-OCE_v3.1 (Lana et al. 2011, Denier van der Gon et al. 2023).

Table 3.2 summarizes the total emissions (anthropogenic, biogenic, and biomass burning) used in this work. The annual emitted mass of the main anthropogenic aerosol precursors is 104.4 Tg for $SO_{2(g)}$, 93.8 Tg for $NO_{x(g)}$, and 61.8 Tg for $NH_{3(g)}$.

5.2.4 Model evaluation

The model results are evaluated against surface observational datasets from several networks sourced from the GHOST project (Bowdalo et al. 2024), described in Section 3.4.

Figure A.13 in the Supplement shows the stations used for each of the species analyzed. For aerosol NO_3^-, NH_4^+, and SO_4^{2-} species, and their precursor gases, GHOST includes datasets from the Clean Air Status and Trends Network (US-EPA-CASTNET), the US EPA Air Quality System (US-EPA-AQS), and the Canada National Air Pollution Surveillance Program (NAPS) for North and Central America; the East Asia Acid Deposition Monitoring Network (EANET) for Asia; and the EBAS and the European Environmental Agency Air Quality (EEA AQ eReporting) for Europe. Evaluation is performed for $PM_{2.5}$ aerosol observations, ranging from 0 to 2.5 μm, and "Total" aerosol

observations, referring to total particle concentration for Asia, and North and Central America, while limited to 10 μm for European sites.

Only ural and background sites are selected, in order to exclude stations close to emission sources that might not be representative of the background conditions represented under the employed model resolution. This filtering aims at evaluating the long-range transport and formation of NO_3^-, NH_4^+, and SO_4^{2-}. However, this constrain is not applied to stations from the EANET and US-EPA-CASTNET networks, due to missing information on the station types for these datasets. In their case all stations were used, a limitation worth to be considered for the evaluation of the model outcomes.

Regarding $PM_{2.5}$ and PM_{10} (2.5-10 μm), GHOST includes data from the CHILE-SINCA network for Chile, the Beijing Municipal Ecological and Environmental Monitoring Center (BJMEMC), the China National Environmental Monitoring Centre (CNEMC), the WMO World Data Center for Aerosols (EBAS-WMO-WDCA) for Europe, the Japan National Institute for Environmental Studies (NIES), the Ministerio de Transición Ecológica (MITECO) for Spain, the UK AIR network for the United Kingdom, and the global AirNow DOS network (US-EPA-AirNow-DOS). For these networks, the station type was not included as a criterion for inclusion in the evaluation. The statistical metrics used in the evaluation are outlined in the Section 3.4 and the quality flags for the selected stations in supplementary Table A.5.

Additionally, we compare our model results with the budgets reported in the literature (Hauglustaine et al. 2014, Bian et al. 2017, Rémy et al. 2022). Namely, the AeroCom phase III nitrate experiment (Bian et al. 2017), devoting here a particular discussion on the results shown there from the GMI (Bian et al. 2009) and EMAC (Karydis et al. 2016) models, which introduce approaches that are of interest to our work. Complementarily, results from Hauglustaine et al. (2014) and Rémy et al. (2022) are also reported. Since results from the literature are provided for different years, some of the differences may be attributed to changes in emissions and environmental conditions. For instance, the AeroCom experiment simulates 2008 while the present study simulates year 2018. So, emission of precursor gases are different due to not only the different emission schemes used, but to the impact of different emission policies implemented globally since 2008.

5.3 Results

5.3.1 Spatial distributions

The spatial distribution of NO_3^- species exhibits significant variability depending on the assumed formation mechanisms. Here, we analyze the results of the main sensitivity runs, arranged in order of increasing complexity as detailed in Section 5.2.2. These

simulations range from a basic scenario that considers only fine SIA formation (i.e., fTEQ) while excluding dust and sea salt alkalinity, to a comprehensive approach that incorporates reversible NO_3^- formation in both fine and coarse modes (i.e. HYB and DBCLL) with full alkalinity.

Spatial distributions of surface concentration, column load and zonal average concentration for all sensitivity simulations (see Table 5.1) are averaged for 2018 and presented for $HNO_{3(g)}$ and particulate NO_3^- (Fig. 5.2, and supplementary Figures A.1, and A.2), $NH_{3(g)}$ and NH_4^+ (supplementary Figures A.4, A.5, and A.6), and $SO_{2(g)}$ and SO_4^{2-} (supplementary Figures A.7, A.8, and A.9). To facilitate readability, the analysis of the HYB_g0p1, DBCLL_duAlk and DBCLL_ClaqAlk runs is provided in supplementary Section A.5.

5.3.1.1 Effects of omitting coarse NO_3^- formation

In the fTEQ_noAlk sensitivity run, fine particulate NO_3^- primarily forms in regions with significant anthropogenic pollution— areas where emissions of $NO_{x(g)}$, $NH_{3(g)}$, and $SO_{2(g)}$ are dominant—such as northern China, India, Europe and eastern North America. In these regions, NO_3^- reaches annual average concentrations of 2 to 10 $\mu g\ m^{-3}$ (Fig. 5.2*e*). At the surface, NH_4^+ is mostly associated with fine NO_3^-, presenting concentrations between 1 and 3 $\mu g\ m^{-3}$ (supplementary Figures 5.2*e* and A.1). At higher altitudes, fine NH_4^+ also forms in the presence of dust and sea salt, resulting in column burdens ranging from 1 to 3 $mg\ m^{-2}$ (supplementary Fig. A.5 and Fig. A.8). This occurs because NH_4^+ neutralizes particulate SO_4^{2-}, which forms when $H_2SO_{4(g)}$ and $SO_{2(g)}$ condense on fine dust and sea salt particles.

The omission of dust and sea salt alkalinity leads to globally low pH values. Over oceanic and dusty regions, aerosol pH typically ranges from 1 to 2, while in industrialized regions, such as Europe and Asia, pH values can reach up to 5 (Fig. 5.3*a*).

Aerosol pH increases significantly when dust and sea salt NVC are included in the fTEQ_du-ssAlk run (Fig. 5.3*b*). This effect is especially pronounced over the open ocean, where pH increases from 1 to 5, and over dust source regions such as the Sahara desert, where pH increases from 1 to 9.

Column burdens of $HNO_{3(g)}$ are notably affected by the elevated pH, decreasing by approximately 5 $mg\ m^{-2}$ across the Northern Hemisphere compared to the fTEQ_noAlk scenario (supplementary Fig. A.1*d*, *g*). This decline predominantly happens in the upper troposphere (above 500hPa, supplementary Fig. A.2*d*, *g*) where concentrations decrease by about 0.5 $\mu g\ m^{-3}$. Conversely, column burdens of fine NO_3^- increase substantially, by more than 5 $mg\ m^{-2}$ over dusty regions such as the Saharan desert and Middle

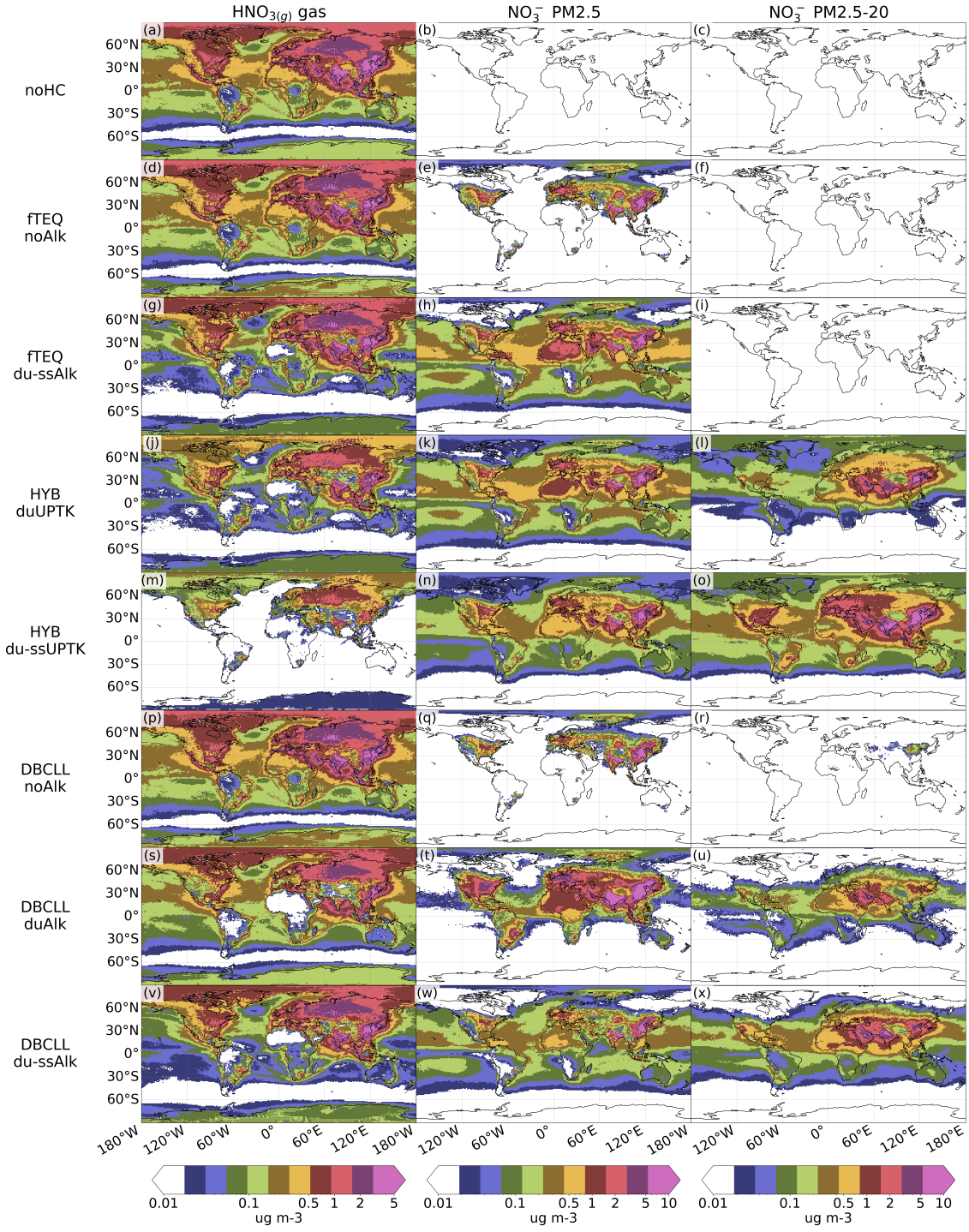

Figure 5.2: Surface concentration ($\mu g\ m^{-3}$) of $HNO_{3(g)}$, fine and coarse NO_3^- simulated by the different mechanisms, averaged for 2018.

East (supplementary Fig. A.1*e*, *h*). In remote oceanic regions, fine NO_3^- column burdens increase by approximately 1 $mg\ m^{-2}$, with transoceanic transport at low latitudes showing column loads ranging from 4 to 7 $mg\ m^{-2}$ (supplementary Fig. A.1*h*).

At the surface, the inclusion of dust and sea salt alkalinity has a minimal impact

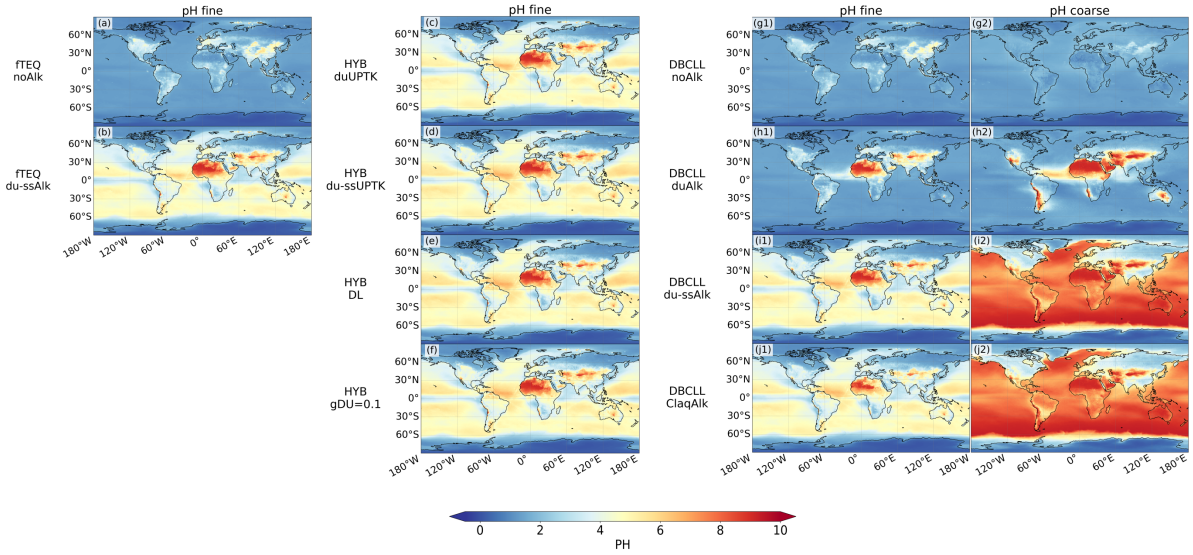

Figure 5.3: Surface pH of the studied mechanisms for fine and coarse aerosol size modes, averaged for 2018.

on continental $HNO_{3(g)}$ concentrations (Fig. 5.2*d*, *g*). Surface fine NO_3^- concentrations of about 0.5 $\mu g\ m^{-3}$ are present across the equatorial belt, with higher values, up to 2 $\mu g\ m^{-3}$, over remote dusty regions. However, no significant increase in fine NO_3^- concentrations is simulated in polluted areas such as Europe and Asia (Fig. 5.2*e*, *h* and supplementary Fig. A.2*e*, *h*).

These results suggest that the condensation of $HNO_{3(g)}$ on dust and sea salt happens mostly during long-range transport, representing a key driver of NO_3^- formation in this scenario. They also indicate that incorporating reactions R8-12 increases fine NO_3^- concentrations, with the majority forming on dust rather than on sea salt. This is attributed to the relatively higher alkalinity of dust compared to sea salt, as derived from the Journet et al. (2014) dataset (see Sect. 5.2.1).

5.3.1.2 Effects of assuming irreversible formation of coarse NO_3^-

The HYB methods exclude the possibility of coarse NO_3^- evaporating back to the gas phase, which may lead to positive biases in global NO_3^- burdens.

In the HYB_duUPTK sensitivity run, coarse NO_3^- forms exclusively on dust, redistributing the available $HNO_{3(g)}$ towards coarse NO_3^- production in regions affected by dust, such as the Middle East and East Asia. Coarse NO_3^- column loads average between 0.5 and 4.0 $mg\ m^{-2}$ across the Northern Hemisphere, with peaks reaching 10-20 $mg\ m^{-2}$ (supplementary Fig. A.1 *l*). Notably, this impact is less pronounced in the Saharan dust belt, where limited $HNO_{3(g)}$ availability constrains coarse NO_3^- formation. The production of coarse NO_3^- is accompanied by a modest reduction in fine NO_3^- column loads over

dusty regions (around 1 $mg\ m^{-2}$) compared to that in the fTEQ_du-ssAlk simulation, driven by the availability of $HNO_{3(g)}$ for fine NO_3^- formation.

The uptake of $HNO_{3(g)}$ significantly influences the long-range transport of NO_3^-, showcasing notable transatlantic and transpacific transport (supplementary Fig. A.1). This transport predominantly occurs below 800hPa, with concentrations around $1\mu g\ m^{-3}$, although lower concentrations of coarse NO_3^- are also discernible at altitudes up to 400hPa (supplementary Fig. A.2). At the surface, coarse NO_3^- concentrations also increase, ranging from 2 to 10 $\mu g\ m^{-3}$ over regions such as China, India, and the Middle East (Fig. 5.2*l*).

The HYB_du-ssUPTK run investigates the role of sea salt by enabling both Reactions R4 and R5 from Table 4.3.

The uptake of $HNO_{3(g)}$ on sea salt enhances the formation of coarse NO_3^- over the open ocean and those coastal areas affected by sea salt outbreaks (supplementary Fig. A.11). Surface concentrations in Europe and North America reach 1-2 $\mu g\ m^{-3}$, with regions exceeding 5 $\mu g\ m^{-3}$ significantly expanding (Fig. 5.2*o*). Coarse NO_3^- also becomes notable over western Siberia, eastern South America, southern Africa (0.5-1 $\mu g\ m^{-3}$), and over remote oceanic regions (0.2 $\mu g\ m^{-3}$). Its presence extends to high altitudes in the Southern Hemisphere (Fig. A.2*o*). Long-range transport of coarse NO_3^- is enhanced over oceans, with column burdens increasing by approximately 3.5 $mg\ m^{-2}$ (supplementary Fig. A.1*o*) compared to those in the HYB_duUPTK case. This increase is attributed to greater depletion of $HNO_{3(g)}$ through irreversible uptake over dust and sea salt (supplementary Fig. A.1*m*), resulting in lower $HNO_{3(g)}$ concentrations in the atmosphere compared to the other simulations.

Results obtained by increasing the value of $\gamma(HNO_3)$ in the HYB_g0p1 scenario (supplementary Section A.5 and Fig. A.3) provide insights into the nature of the coarse NO_3^- transoceanic transport. While the inclusion of UPTK on sea salt enhances long-range transport, the HYB_g0p1 run shows a slight increase in coarse NO_3^- compared to HYB_du-ssUPTK, particularly over the Sahara and across the Atlantic and Pacific oceans. Although these differences are not major, they suggest that the availability of $HNO_{3(g)}$ may act as a limiting factor for coarse NO_3^- formation.

To further explore this phenomenon, we used the HYB_DL run, which is equivalent to the HYB_du-ssUPTK run but constrains the available gas using the DIFFLIM calculation (see Section 5.2.2). This approach results in coarse NO_3^- column burdens just below those obtained in HYB_g0p1. The similarity between HYB_DL and HYB_du-ssUPTK can be attributed to two possible factors: 1) HYB_DL conserves more $HNO_{3(g)}$ for reactions on coarse dust during long-range transport via Reactions (R4) and (R5) (Table 4.3) or 2) there is an intrinsic overestimation of the uptake coefficients, leading to

similar coarse NO_3^- formation rates regardless of the $HNO_{3(g)}$ available. This is further discussed in Section 5.3.2.

Overall, results show that the HYB mechanisms preferentially condense $HNO_{3(g)}$ via TEQ in the fine mode and over sea salt through R5 in the coarse mode, rather than over coarse dust through R4, as noted here and also assessed in subsequent sections.

A comparison of the spatial distributions obtained by the EMEP, INCA and GMI models in Bian et al. (2017), which employ HYB approaches similar to our HYB_du-ssUPTK run, reveals comparable trends. All models show significant formation of total NO_3^- (fine and coarse) over polluted regions, although our results, ranging from 10 to 25 $mg\ m^{-2}$, generally exceed the column loads reported by AeroCom models, which range from 7 to 16 $mg\ m^{-2}$ (supplementary Fig. A.1*n*, *o*). AeroCom models do not show such a pronounced transport of coarse NO_3^- across the North Atlantic as it is observed in our study, with column burdens of 0.2-0.5 $mg\ m^{-2}$ compared to 4 $mg\ m^{-2}$ in our results. Section 5.3.4 further investigates the excessive formation of particulate NO_3^- in the HYB mechanism in terms of the total N budget.

A closer comparison with Hauglustaine et al. (2014), using the LMDz-INCA model with UPTK reactions on dust and sea salt, shows strong agreement with our HYB_duUPTK run but not with HYB_du-ssUPTK. For instance, concentrations of total NO_3^- over polluted areas in Hauglustaine et al. (2014) align with HYB_duUPTK in both geographical distribution and magnitude (14-20 $mg\ m^{-2}$ in HYB_duUPTK vs. 10-20 $mg\ m^{-2}$ in Hauglustaine et al. (2014), Fig. A.1*l*). Similarly, Hauglustaine et al. (2014) simulate fine NO_3^- transport downwind of the Sahara and coarse NO_3^- across the North Atlantic, with column burdens around 1-2 $mg\ m^{-2}$, slightly below our HYB_duUPTK results of 1-5 $mg\ m^{-2}$. This preferential similarity of Hauglustaine et al. (2014) to HYB_duUPTK rather than HYB_du-ssUPTK may be attributed to the $HNO_{3(g)}$ UPTK coefficient for sea salt employed in Hauglustaine et al. (2014). For this reaction, instead of a constant value as used in HYB_du-ssUPTK, Hauglustaine et al. (2014) use a function of RH ranging from $1 \cdot 10^{-3}$ to 0.1, leading to lower NO_3^- formation over sea salt in their model. This comparison suggests a potential overestimation of the UPTK coefficient for $HNO_{3(g)}$ on sea salt in the HYB_du-ssUPTK simulation. This conclusion is further discussed in the observational evaluation (Section 5.3.2) and in the budget analysis (Section 5.3.4). As a final remark, it is important to note that, similar to the findings of Hauglustaine et al. (2014), the HYB_duUPTK simulations overestimate particulate NO_3^- concentrations compared to observational data, as discussed in Section 5.3.2.

To further investigate the source of the coarse NO_3^- overestimation in the HYB_du-ssUPTK simulation, we compare our spatial distributions with those from Jones et al. (2021), which employ a similar HYB mechanism using the Met Office Unified Model (UM). In Jones et al. (2021), fine NO_3^- formation is computed using adaptations from Hauglustaine et al. (2014), specifically by testing different accommodation coefficients for $HNO_{3(g)}$ onto preexisting NH_4NO_3 aerosols - although this adjustment has minimal impact on coarse NO_3^- concentrations. Coarse NO_3^- is formed through the uptake of $HNO_{3(g)}$, with coefficients sourced from Fairlie et al. (2010) for dust and Burkholder et al. (2020) for sea salt. Despite using different uptake coefficients for $HNO_{3(g)}$ on sea salt, the resulting coarse NO_3^- distribution is broadly comparable to that of the HYB_du-ssUPTK simulation. However, key differences emerge between the two models. Compared to the Jones et al. (2021) model, HYB_du-ssUPTK exhibits a stronger tendency for coarse NO_3^- formation over polluted areas such as Europe, eastern North America, and Asia (8-20 $mg\ m^{-2}$ in HYB_du-ssUPTK vs. 4 $mg\ m^{-2}$ in Jones et al. (2021)), as well as over oceanic regions (1.5-3.0 vs. 0.4-2.0 $mg\ m^{-2}$), rather than over sub-Saharan areas. Remarkably, significant North Atlantic transport of coarse NO_3^- (2.0-4.0 $mg\ m^{-2}$) is only present in our simulation and is absent in Jones et al. (2021). The global budget comparison in Section 5.3.4 and Table 5.3 further highlights the fact thatJones et al. (2021) report significantly lower global NO_3^- burdens compared to our HYB runs, including HYB_duUPTK. This suggests that the HYB mechanisms in our simulations may produce coarse NO_3^- excessively, as both the burdens and distributions of coarse NO_3^- in Jones et al. (2021) are consistently lower, despite also accounting for sea salt in NO_3^- formation. Nevertheless, several alternative explanations could account for the differences between the models. These include differences in the fine NO_3^- formation mechanism, variations in the study period (2018 in our study vs. a 20-year average in Jones et al. (2021)), and differing parameterizations of $HNO_{3(g)}$ uptake on sea salt.

Overall, the comparison of spatial distributions between our HYB mechanisms and those reported in the literature supports the initial hypothesis that the assumption of irreversible $HNO_{3(g)}$ uptake, and potentially the uptake coefficients used, may contribute to the overestimation of NO_3^- formation. This issue is examined in greater detail in Sections 5.3.2 and 5.3.4.

5.3.1.3 Effects of accounting for reversible formation of coarse NO_3^-

The DBCLL simulations (described in Section 5.2.2, and Tables 4.4 and 5.1) assess the impact of reversible chemistry and the role of dust and sea salt NVC in NO_3^- partitioning.

The DBCLL_noAlk run produces spatial distributions of $HNO_{3(g)}$ and fine NO_3^- similar to those in the fTEQ_noAlk run. $HNO_{3(g)}$ remains predominantly in the gas phase

across the Northern Hemisphere (supplementary Fig. A.1*p*), while fine NO_3^- primarily associates with fine NH_4^+ over regions lacking dust or sea salt influence, such as parts of China, India, Europe and eastern North America (Fig. 5.2*q*). Minimal concentrations of fine NO_3^- are simulated at higher altitudes (Fig. A.2*q*), although fine NH_4^+ coexists with SO_4^{2-} particles at elevated levels, as observed in the fTEQ_du-ssAlk case. In contrast, coarse NO_3^- is nearly absent in DBCLL_noAlk, with only minimal surface concentrations over northern China (0.4 $\mu g\ m^{-3}$), and no clear correlation with dust and sea salt presence (Fig. 5.2*r*). Coarse NH_4^+ formation is similarly limited, with slight presence over the Persian Gulf and the Sahara (0.02-0.1 $mg\ m^{-2}$), primarily in anthropologically polluted regions where it forms alongside coarse SO_4^{2-} (0.2 $mg\ m^{-2}$) (Fig. A.5*r* and Fig. A.8*r*). The simultaneous formation of coarse NH_4^+ and SO_4^{2-} particles is attributed to diffusion limitation, where $NH_{3(g)}$ preferentially neutralizes coarse SO_4^{2-} particles.

The differences between fTEQ_noAlk and DBCLL_noAlk illustrate the impact of diffusion limitation before the partitioning of semivolatile species. While fine NO_3^- formation remains consistent between both runs, the assumption of allowing all acidic species to partition into the fine mode in fTEQ_noAlk leads to enhanced fine particle production and long-range transport—an effect not observed in DBCLL_noAlk. Consistently, the pH in the fine mode closely mirrors that in fTEQ_noAlk, while the pH of particles in the coarse mode indicates even greater acidity (Fig. 5.3*f1* and *f2*)).

Including dust and sea salt alkalinity in DBCLL_du-ssAlk produces an important increase in the pH over arid regions and oceanic regions—from 1 to 5-6 in the fine mode and above 7 in the coarse mode—compared to DBCLL_noAlk (Fig. 5.3*h1* and *h2*). Relative to DBCLL_du-Alk (dust alkalinity only, see supplementary A.5), DBCLL_du-ssAlk redistributes the NO_3^- partitioning toward the coarse mode: fine NO_3^- concentrations approximately halve across regions, while coarse NO_3^- surface concentrations and column loads roughly double over dusty regions but not over the ocean (Fig. 5.2*w*, *x* and Fig. A.1*w*, *x*). This shift leads to enhanced transatlantic and transpacific transport, with column loads of 2-4 $mg\ m^{-2}$, surface concentrations of 0.4 $\mu g\ m^{-3}$, and zonal averages of 0.5-1.0 $\mu g\ m^{-3}$. Over continental regions with dust concentrations, coarse NO_3^- reaches column loads of 4-5 $mg\ m^{-2}$, and surface concentrations of 0.5-1.0 $\mu g\ m^{-3}$. Additionally, $HNO_{3(g)}$ surface concentrations increase from 0.1 to 1.0 $\mu g\ m^{-3}$ in the heavily polluted areas (Fig. 5.2*s*, *v*). The enhancement of coarse NO_3^- formation is attributed to sea salt crustal species (see Section 3.2), with Cl^- and SO_4^{2-} suppressing fine NO_3^- formation and leaving more $HNO_{3(g)}$ available for transport and subsequent coarse NO_3^- formation over dusty regions.

Including sea salt alkalinity reduces fine NH_4^+ loads over Europe and eastern North America from 3 to 1 $mg\ m^{-2}$ and slightly lowers values over Asia (2-3 $mg\ m^{-2}$). Con-

versely, coarse NH_4^+ increases over Europe and eastern North America (0.1-0.2 $mg\ m^{-2}$), Asia (up to 1.0 $mg\ m^{-2}$), and transoceanic regions (0.1 $mg\ m^{-2}$) (supplementary Fig. A.5x). This redistribution mirrors the particulate NO_3^- patterns, highlighting the strong coupling between these species when TEQ is applied to both fine and coarse partitioning. These results emphasize the sensitivity of NO_3^- formation to sea salt alkalinity, particularly due to NVCs like Na^+.

Compared to the HYB_du-ssUPTK run, DBCLL_du-ssAlk shows lower coarse NO_3^- concentrations and shifts coarse NO_3^- formation toward dusty rather than anthropologically polluted areas. For example, over Europe, surface concentrations in DBCLL_du-ssAlk do not exceed 0.5 $\mu g\ m^{-3}$, while HYB_du-ssUPTK reports 1-2 $\mu g\ m^{-3}$ (Fig. 5.2x).

Overall, regardless of the mechanism used, the results demonstrate the high sensitivity of NO_3^- formation to dust and sea salt alkalinity (reactions R8 to R12, Table 4.3), significantly altering NO_3^- spatial distribution. Conversely, implementing the DIFFLIM calculation in the DBCLL mechanism has a limited impact, as shown by the comparison between fTEQ_noAlk and DBCLL_noAlk.

We now compare the results from DBCLL_du-ssAlk with those from the EMAC model (Karydis et al. 2016), which similarly employs TEQ for the bulk gas and aerosol mass, followed by DIFFLIM. Additionally, EMAC makes use of globally heterogeneous dust alkalinity based on 12 mineralogy source data points. Results from the EMAC model are reported in Bian et al. (2017) for 2018 and in Karydis et al. (2016) for the period 2004-2008 (Table 5.3 and supplementary Section A.4). Surface distributions of aerosol NO_3^- are closely aligned in both models over Europe and North America, with average surface concentrations ranging from 1 to 3$\mu g\ m^{-3}$. However, DBCLL_du-ssAlk shows higher concentrations over Asia, India, and the Middle East compared to EMAC (5-10$\mu g\ m^{-3}$ vs. 6-15$\mu g\ m^{-3}$, respectively). Additionally, our results show some variations over secondary areas compared to those of Karydis et al. (2016). EMAC reports biases, such as underestimating coarse NO_3^- over southern Europe and central-eastern Asia, attributed to excessive SO_4^{2-} condensation on dust—a limitation mitigated in our study due to lower SO_4^{2-} levels (supplementary Fig. A.7). Additionally, while EMAC overestimates fine NO_3^- over the Arctic, this is not observed in our results due to the RH and temperature restrictions applied in ISORROPIA-II (see Section 4.3.2). Over central Africa, EMAC overpredicts coarse NO_3^- due to excessive $HNO_{3(g)}$ from biomass burning coupled with low $H_2SO_{4(g)}$ concentrations, from where Karydis et al. (2016) suggested that an HYB approach could reduce the bias. Our DBCLL_du-ssAlk and HYB runs report lower concentrations, although still potentially overestimated due to too-low $HNO_{3(g)}$ levels. Total particulate SO_4^{2-} and NH_4^+ are in close agreement in

both EMAC and the DBCLL_du-ssAlk run (supplementary Figures A.4*w*, *x* and A.7*w*, *x*), with only slightly higher formation of coarse NH_4^+ over the Indian subcontinent in MONARCH compared to EMAC.

5.3.2 Evaluation with observations

To assess the performance of each sensitivity run, we compare simulated surface concentrations of key species involved in NO_3^- formation with observational data, as described in Section 5.2.4. This evaluation includes analyses of both statistics and time series of monthly mean values, focusing on how effectively each modeled mechanism captures observed NO_3^- variability on a global scale. Globally averaged results are shown in Fig. 5.4, while region-specific evaluations for Europe, Asia, and central North America are presented in Fig. A.12 in the supplementary Section A.3. It is important to note that the number of stations and spatial coverage vary significantly by species, as illustrated in supplementary Fig. A.13. Consequently, certain evaluation metrics may not fully reflect global model performance, and could instead represent accuracy in data-rich regions.

Correlation coefficients (Corr), bias and root-mean-square error (RMSE) metrics for the different sensitivity simulations, defined as equations 3.2, 3.3, and 3.4, are reported in Table 5.2.

A detailed evaluation of the HYB_g0p1, DBCLL_duAlk and DBCLL_ClaqAlk simulations is available in supplementary Section A.5. Additionally, a similar evaluation for total reduced and oxidized N species is presented in supplementary Section A.6, and discussed in Section 5.3.3.2.

5.3.2.1 Nitrate species

Over the evaluated stations (supplementary Fig. A.13), fine particulate NO_3^- ($PM_{2.5}NO_3$) is consistently formed by all mechanisms through TEQ, with the exception of the DBCLL scheme, which incorporates the DIFFLIM coefficients to limit its formation. Consequently, while the fTEQ and HYB mechanisms produce higher $PM_{2.5}NO_3$ from October to April (0.5-1.0 $\mu g\ m^{-3}$) than the DBCLL, which approximately halves these values. This discrepancy is more pronounced over North and Central America than in Europe, although both regions exhibit similar seasonal patterns. From April to October, differences among mechanisms diminish, except in the HYB_du-ssUPTK, which significantly overestimates $PM_{2.5}NO_3$ during these months.

Notably, the runs considering the effects of dust and sea salt alkalinity in the partitioning process significantly reduce the $PM_{2.5}NO_3$ model underestimation (negative bias), especially during February.

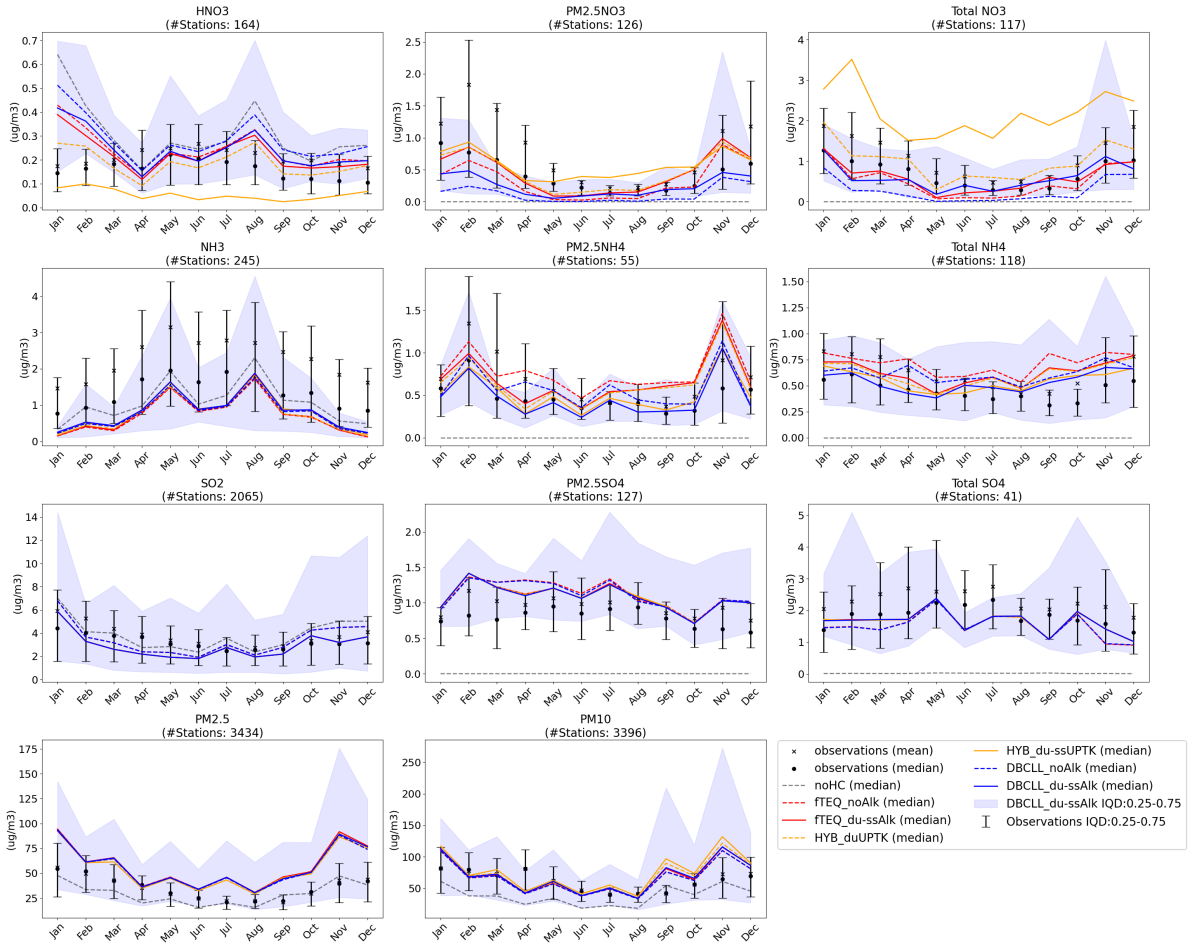

Figure 5.4: Observational evaluation of gas and particulate species surface concentrations. Solid-black dots and crosses represent the monthly median and mean of the observations, respectively. Colored lines represent each configuration's monthly median over the observational points. Error bars are the observational interquartile 0.25 to 0.75 distance. Blue shading is the interquartile 0.25 - 0.75 distance for the DBCLL_du-ssAlk simulation. For the total NO_3^- modes, the available data from the European, Asian and North and Central American stations have been averaged together, despite data from Asia and North and Central America referring to total particle concentration, while data from Europe is limited strictly to particles with diameters up to 10 μm.

Table 5.2: Correlation coefficients, bias (model - observations, $\mu g\ m^{-3}$), and root-mean-square error (RMSE, $\mu g\ m^{-3}$) of each configuration's median with respect to the median of the observations, corresponding to the time series shown in Fig. 5.4.

	$HNO_{3(g)}$			$PM_{2.5}NO_3^-$			Total NO_3^-		
	Corr.	**Bias**	**RMSE**	**Corr.**	**Bias**	**RMSE**	**Corr.**	**Bias**	**RMSE**
noHC	0.03	0.15	0.20	0.00	-0.43	0.49	0.00	-0.70	0.77
fTEQ_noAlk	0.15	0.08	0.12	0.70	-0.10	0.23	0.91	-0.19	0.25
fTEQ_du-ssAlk	0.23	0.07	0.10	0.76	0.02	0.20	0.88	-0.09	0.19
HYB_duUPTK	0.23	0.03	0.06	0.80	0.04	0.18	0.90	0.29	0.36
HYB_du-ssUPTK	0.06	-0.10	0.11	0.77	0.14	0.21	0.66	1.50	1.56
DBCLL_noAlk	0.06	0.13	0.16	0.68	-0.31	0.36	0.86	-0.43	0.46
DBCLL_du-ssAlk	0.16	0.08	0.12	0.82	-0.18	0.24	0.78	-0.10	0.23

	NH_3			$PM_{2.5}NH_4$			Total NH_4		
	Corr.	**Bias**	**RMSE**	**Corr.**	**Bias**	**RMSE**	**Corr.**	**Bias**	**RMSE**
noHC	0.80	-0.29	0.44	0.00	-0.48	0.51	0.00	-0.45	0.46
fTEQ_noAlk	0.88	-0.65	0.69	0.64	0.29	0.35	0.41	0.26	0.28

Table 5.2 continued from previous page

fTEQ_du-ssAlk	0.87	-0.62	0.67	0.59	0.18	0.28	0.51	0.17	0.20
HYB_duUPTK	0.87	-0.61	0.66	0.56	0.16	0.27	0.48	0.15	0.18
HYB_du-ssUPTK	0.86	-0.55	0.60	0.70	0.03	0.16	0.54	0.10	0.13
DBCLL_noAlk	0.86	-0.58	0.62	0.66	0.10	0.20	0.51	0.16	0.18
DBCLL_du-ssAlk	0.85	-0.53	0.59	0.70	-0.02	0.17	0.47	0.08	0.12

	SO_2			$PM_{2.5}SO_4$			Total SO_4		
	Corr.	**Bias**	**RMSE**	**Corr.**	**Bias**	**RMSE**	**Corr.**	**Bias**	**RMSE**
noHC	0.61	0.65	1.24	0.59	-0.79	0.80	0.62	-1.91	1.93
fTEQ_noAlk	0.59	0.23	1.12	0.61	0.33	0.36	0.51	-0.47	0.58
fTEQ_du-ssAlk	0.63	-0.30	0.91	0.57	0.30	0.33	0.60	-0.38	0.49
HYB_duUPTK	0.63	-0.29	0.91	0.57	0.29	0.33	0.59	-0.38	0.50
HYB_du-ssUPTK	0.63	-0.29	0.91	0.57	0.29	0.33	0.60	-0.38	0.49
DBCLL_noAlk	0.59	0.23	1.12	0.58	0.32	0.36	0.49	-0.47	0.59
DBCLL_du-ssAlk	0.63	-0.29	0.91	0.56	0.29	0.32	0.69	-0.52	0.67

	$PM_{2.5}$			PM_{10}		
	Corr.	**Bias**	**RMSE**	**Corr.**	**Bias**	**RMSE**
noHC	0.75	-5.62	9.55	0.40	-23.16	28.42
fTEQ_noAlk	0.76	20.91	24.98	0.46	5.14	22.49
fTEQ_du-ssAlk	0.74	21.75	26.16	0.44	7.16	24.38
HYB_duUPTK	0.74	21.05	25.32	0.40	10.16	27.41
HYB_du-ssUPTK	0.76	19.59	23.91	0.36	13.92	30.45
DBCLL_noAlk	0.76	20.59	24.74	0.46	4.98	22.50
DBCLL_du-ssAlk	0.75	21.02	25.22	0.43	8.09	24.80

Greater variability among experiments emerges when evaluating $HNO_{3(g)}$ and total NO_3^-, with more observational data available over North and Central America than Europe or Asia. This variability is highly influenced by how each mechanism models coarse NO_3^- formation, especially over Asia (supplementary Fig. A.12). For example, the HYB runs, which rely on irreversible uptake reactions, consistently overestimate total NO_3^- across all regions. In contrast, the DBCLL runs, which assume reversible partitioning, align better with observations.

From the HYB simulations, the HYB_duUPTK run demonstrates strong correlation coefficients for both fine and total NO_3^- concentrations (0.8 and 0.9, respectively, Table 5.2). The seasonal variability in this run closely resembles that of the fTEQ_noAlk and fTEQ_du-ssAlk experiments, which fully neglect coarse NO_3^- formation. This similarity suggests a limited number of sites significantly affected by coarse NO_3^- formation, while highlighting the relevant role of the TEQ calculation in the fine mode. Despite showing a systematic positive bias compared to observations (0.03, 0.04, and 0.29 $\mu g\ m^{-3}$ for $HNO_{3(g)}$, fine NO_3^-, and total NO_3^-, respectively), HYB_duUPTK maintains consistency across continents. However, it notably overestimates total NO_3^- over Asia in November and over Europe from May to September (supplementary Fig. A.12), likely due to dust events affecting the monitoring sites.

Including the UPTK reactions on sea salt in the HYB_du-ssUPTK run exacerbates this overestimation due to excessive $HNO_{3(g)}$ condensation into coarse NO_3^-. Specifically, the correlation for total NO_3^- drops from 0.9 to 0.66, $HNO_{3(g)}$ concentrations are underestimated (bias of -0.10 $\mu g\ m^{-3}$), and total NO_3^- surface concentrations are overestimated by 1.50 $\mu g\ m^{-3}$—the highest bias among all sensitivity runs (Table 5.2). This overestimation is most pronounced over Asia (3-5 $\mu g\ m^{-3}$ vs. 1 $\mu g\ m^{-3}$) and North and

Central America (1.5-2.5 $\mu g\ m^{-3}$ vs. 1.0 $\mu g\ m^{-3}$). Discrepancies in European sites are more pronounced during summer and fall.

To evaluate whether this overestimation results from unlimited $HNO_{3(g)}$, we examined the HYB_g0p1 and HYB_DL configurations (see supplementary Section A.5). Increasing the uptake coefficient $\gamma(HNO_3)$ in HYB_g0p1 further enhances the overestimation of total NO_3^- by an additional 30%, suggesting that $HNO_{3(g)}$ availability is not the limiting factor. Similarly, HYB_DL shows only a marginal reduction in total NO_3^- bias (from 1.5 to 1.3 $\mu g\ m^{-3}$), reinforcing the conclusion that the overestimation stems from the overly high $\gamma(HNO_3)$ values for sea salt particles, as previously discussed in Section 5.3.1.2. This highlights the need to refine HYB schemes.

Conversely, DBCLL mechanisms markedly reduce surface concentration biases. Without alkalinity, the total NO_3^- bias shifts from 0.29 to -0.43 $\mu g\ m^{-3}$ between the HYB and DBCLL runs. Incorporating dust and sea salt NVCs further improves the bias, reducing it from 1.5 to -0.1 $\mu g\ m^{-3}$ between the HYB_du-ssUPTK and DBCLL_du-ssAlk runs (Table 5.2). Both DBCLL_noAlk and DBCLL_du-ssAlk consistently achieve high correlation coefficients (approximatelly 0.8).

However, the DBCLL_noAlk run tends to underestimate total NO_3^-(bias of -0.43$\mu g\ m^{-3}$) and overestimates $HNO_{3(g)}$ (bias of +0.13 $\mu g\ m^{-3}$), failing to capture its seasonal cycle (correlations of 0.06). Surprisingly, the fTEQ runs outperform DBCLL_noAlk despite neglecting coarse NO_3^- formation.

Including dust and sea salt alkalinity in DBCLL_du-ssAlk substantially improves these biases. Enhanced condensation of $HNO_{3(g)}$ into both fine and coarse NO_3^- (Fig. 5.4) yields a reduced bias in total NO_3^- (-0.10 $\mu g\ m^{-3}$) and a strong seasonal agreement, with correlation coefficients of 0.82 and 0.78 for fine and total NO_3^-, respectively. These results, combined with lower biases, outperform the DBCLL_duAlk run, which excludes sea salt alkalinity (supplementary Section A.5 and Table A.6).

The evaluation of the DBCLL experiments highlights the paramount importance of accounting for NO_3^- formation on both dust and sea salt to accurately represent $HNO_{3(g)}$ and particulate NO_3^- concentrations.

The sensitivity of model performance to the dust NVC representation is further assessed using the DBCLL_Claq run, which applies an average dust alkalinity based on Claquin et al. (1999) instead of on Journet et al. (2014) (see Sect. 5.2.1). Results show limited differences between mineral atlases, with the correlation and bias for total NO_3^- just slightly improved in DBCLL_Claq, at 0.81 and -0.09 $\mu g\ m^{-3}$, respectively (supplementary Section A.5 and Table A.6). The time series from Fig. 5.4, compared to Fig. A.14, also shows comparably similar results when using DBCLL with the Claquin et al. (1999) or Journet et al. (2014) mineral datasets. Overall, based on the limited

number of observation sites used in our evaluation, the impact of dust NVC representation on surface NO_3^- concentrations does not appear to be significant at the observational points.

5.3.2.2 Ammonia species

Results for $NH_{3(g)}$ and particulate NH_4^+ are generally more consistent across all mechanisms compared to NO_3^- outcomes. This consistency is expected, as all sensitivity runs use the same condensation pathway for the conversion of $NH_{3(g)}$ to fine NH_4^+ through reactions R6 and R7 (Table 4.3). All mechanisms effectively capture the seasonal cycle of both $NH_{3(g)}$ and fine NH_4^+. Correlation coefficients for $NH_{3(g)}$ range from 0.85 to 0.88, while those for fine NH_4^+ range from 0.59 to 0.70. However, model performance is slightly weaker for total NH_4^+, with correlations between 0.41 and 0.54.

Including dust and sea salt alkalinity in the DBCLL_du-ssAlk and DBCLL_Claq runs yield the lowest errors for NH_4^+. RMSEs are 0.17 $\mu g\ m^{-3}$ for fine and 0.12 $\mu g\ m^{-3}$ for total concentrations, with corresponding biases of -0.02 $\mu g\ m^{-3}$ and 0.08 $\mu g\ m^{-3}$ (Tables 5.2 and A.6). These results highlight the significant sensitivity of NH_4^+ predictions to the treatment of dust and sea salt NVCs; Including or omitting NVC representation notably affects the biases across different schemes. Unlike NO_3^-, increased particle alkalinity reduces the condensation of $NH_{3(g)}$, thereby limiting NH_4^+ formation. This effect helps mitigate biases when compared to observational data.

Overall, biases for both fine and total NH_4^+ remain relatively low in most experiments, ranging from -0.02 to 0.29 $\mu g\ m^{-3}$. Lower correlation scores for NH_4^+ compared to NO_3^- might be caused by potential inaccuracies in the strongly seasonal emission cycle of $NH_{3(g)}$.

5.3.2.3 Sulfur species

Results for $SO_{2(g)}$ and particulate SO_4^{2-} are consistent across all sensitivity simulations. This consistency is expected since SO_4^{2-} formation is independent of the pathways used for coarse NO_3^- formation; In all cases, particulate SO_4^{2-} is produced from $SO_{2(g)}$ and $H_2SO_{4(g)}$ in a similar manner (see Section 4.4). Differences arise solely from variations in the treatment of the $\gamma(SO_2)$ coefficient when accounting for dust alkalinity, which introduces slight differences in SO_4^{2-} formation. Overall, the model slightly underestimates both $SO_{2(g)}$ and total SO_4^{2-}, particularly at European monitoring sites (average bias of -0.43). In contrast, global fine SO_4^{2-} is marginally overestimated (average bias of 0.30 $\mu g\ m^{-3}$, Table 5.2 and supplementary Fig. A.12), mainly driven by observations from central North American sites. Temporal correlation coefficients average around 0.6, with slightly lower values for total SO_4^{2-}. For $SO_{2(g)}$, the slight mismatch with

observational data primarily stems from the European evaluation, which presents a consistent negative bias compared to observations of -0.5 $\mu g\ m^{-3}$ throughout the period studied (supplementary Fig. A.12). Fine and total SO_4^{2-} concentrations also show generally good agreement with observations. The underestimation of SO_4^{2-} concentrations, and the comparatively lower correlations may be attributed to the combined effect of the S emission inventories employed in our runs and the SO_4^{2-} formation scheme. For instance, reevaluating the $SO_{2(g)}$ uptake coefficient, and the aqueous nucleation parameterization, could provide valuable insights. The current implementation uses the uptake coefficient function from Fairlie et al. (2010), but alternative formulations have been suggested in the literature, such as the uptake coefficient values proposed by Phadnis and Carmichael (2000) for $SO_{2(g)}$ uptake on dust, and those by Song and Carmichael (2001) for uptake on sea salt, as reported in Li et al. (2012). Exploring these alternatives may help improve the model's representation of S species.

5.3.2.4 Fine and total particulate matter

Results for $PM_{2.5}$ and PM_{10} are consistent across the different sensitivity runs (Fig. 5.4), indicating that the total mass is more influenced by components other than SIA species.

Globally, the seasonal cycles of $PM_{2.5}$ are reproduced well across all sensitivity runs, with correlation coefficients consistently around 0.75, although its annual mean concentrations are overestimated in average by 20 $\mu g\ m^{-3}$ (Table 5.2). In contrast, PM_{10} concentrations over Asia show good agreement with observations. the fact that $PM_{2.5}$ is overestimated but PM_{10} meets observations indicates that the model underestimates coarse PM, especially at monitoring sites in mainland China (supplementary Figures A.12 and A.13). It is important to note that regions with significant $PM_{2.5}$ overestimation do not overlap with the limited sites where chemical composition measurements are available—locations where the model accurately represents total particulate NO_3^- and NH_4^+ (supplementary Fig. A.12). Our results suggest that the absence of anthropogenic coarse dust emissions in the CAMS emission inventory may hinder the formation of coarse SIA species, including NO_3^-. The formation of coarse NO_3^- is critical for scavenging $HNO_{3(g)}$, suppressing the formation of fine particulate NO_3^- by providing surfaces for heterogeneous reactions. The significant influence of typically neglected anthropogenic coarse PM emissions on NO_3^- formation has been emphasized in previous studies (e.g. Zhai et al. (2023)), highlighting the need for improved emission inventories to better capture the interactions between coarse particles and N species.

In contrast, $PM_{2.5}$ model results over Europe and North and Central America are well aligned with observations (Fig. A.12). The evaluation of PM_{10} across simulations

shows just slightly worsened RMSEs (ranging from 22.49 to 30.45 $\mu g\ m^{-3}$) and correlation coefficients (from 0.36 to 0.46) compared to $PM_{2.5}$ (RMSEs from 24.74 to 26.16 $\mu g\ m^{-3}$, and correlations from 0.74 to 0.76, Table 5.2). This is attributed to the PM_{10} surface concentration underestimations over North and Central America, especially from April to September, which do not seem to be caused by the underestimation of any SIA species studied in this work. Over Europe, our results are in agreement with those reported by Jones et al. (2021).

5.3.3 Nitrogen partitioning

In this section, we explore the impact of coarse particulate NO_3^- formation on the overall partitioning of atmospheric N between the gas and particle phases (Section 5.3.3.1). Additionally, we analyze how this formation influences the distribution of N between its oxidized and reduced forms (Section 5.3.3.2). The observational evaluation of surface concentrations for total reduced and oxidized N is presented in supplementary A.6.

5.3.3.1 Partitioning between gas and particle phases

The partitioning of atmospheric N species in gas and aerosol phases varies according to the underlying chemical assumptions. We analyze the average atmospheric burden and deposition of N species in the MONARCH model across sensitivity runs (Fig. 5.5 and supplementary Table A.11).

The simulation labeled as noHC, excluding heterogeneous chemistry involving NO_3^-, serves as the baseline for understanding the distribution of N species in the gas phase. Under this configuration, the dominant N species are $HNO_{3(g)}$, peroxyacetly NO_3^- (PAN), $NH_{3(g)}$, and NO_x, with burdens of 1.06, 0.8, 0.71, and 0.38 TgN, respectively. The longer atmospheric lifetimes of $HNO_{3(g)}$ and PAN result from their chemical stability compared to more reactive NO_x species. Notably, $N_2O_{5(g)}$ plays a key role in nighttime $HNO_{3(g)}$ production via heterogeneous hydrolysis (Riemer et al. 2003) (Fig. 1.3).

Total N burden is highly sensitive to the NO_3^- formation mechanism. Schemes promoting efficient coarse-mode NO_3^- formation significantly reduce N burdens.

For example, assuming irreversible condensation of $HNO_{3(g)}$ onto coarse particles of dust only (HYB_duUPTK), and onto both dust and sea salt (HYB_du-ssUPTK), reduces N load by 32% and 40%, respectively. In HYB_duUPTK, 0.13 TgN partitions into fine and coarse NO_3^- on dust. Including sea salt (HYB_du-ssUPTK) further increases consumption of $HNO_{3(g)}$ and coarse NO_3^- formation leading to a total NO_3^- burden 0.27 TgN, while the fine NO_3^- burden remains unchanged at 0.12 TgN (supplementary Table A.11).

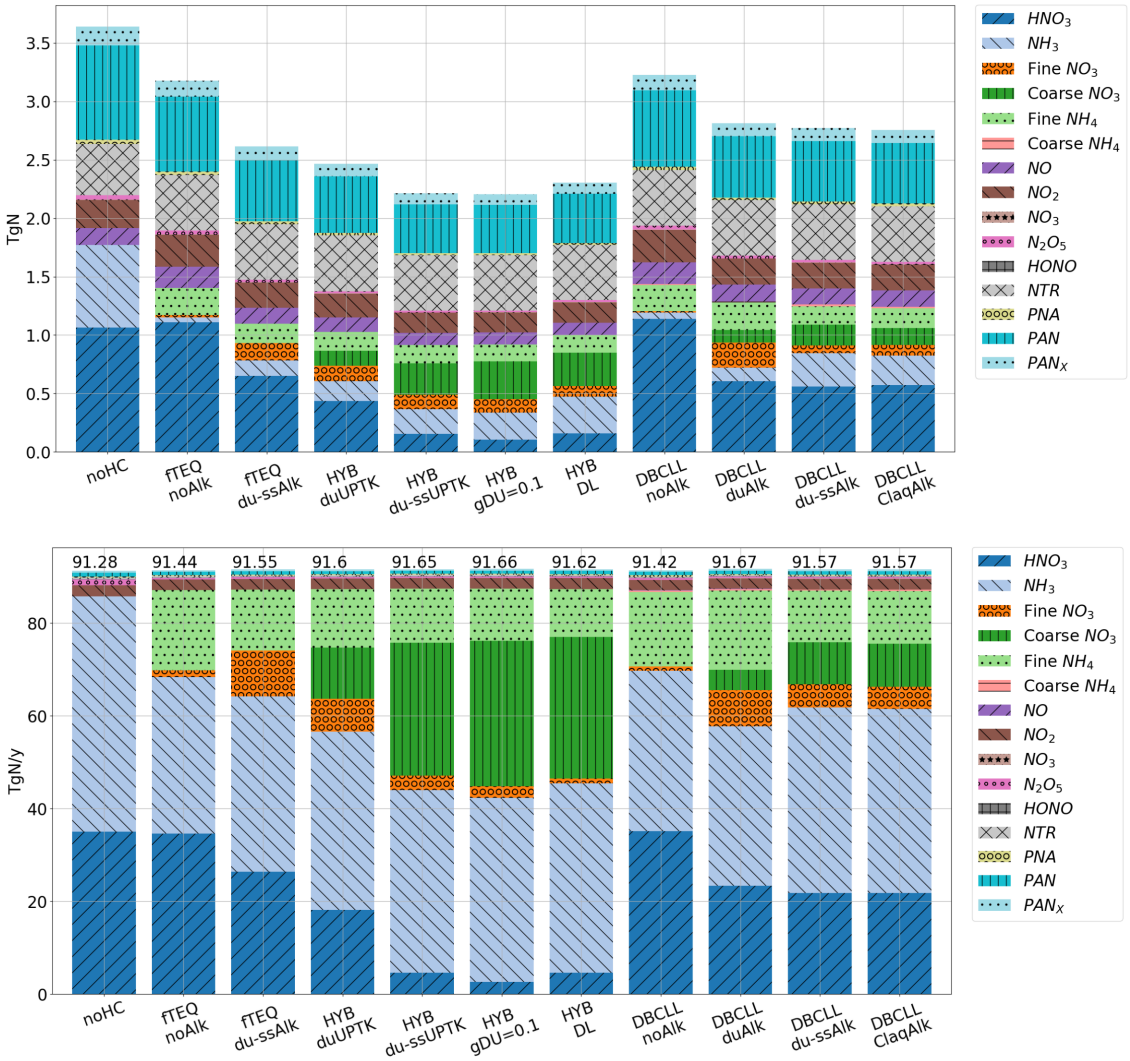

Figure 5.5: Atmospheric N average burdens (top) and accumulated depositions (bottom) in teragrams of N (TgN) for the different dust heterogeneous chemistry mechanisms. The corresponding fractions of the N-containing species simulated in MONARCH are shown in each bar plot. Total N deposition is reported at the top of each bar of the deposition chart.

Comparing HYB runs to fTEQ_du-ssAlk reveals that dust and sea salt uptake reduces $HNO_{3(g)}$ burdens by 0.21 TgN (dust) and 0.50 TgN (dust + sea salt) relative to fTEQ-only partitioning. This is driven by the irreversible uptake of $HNO_{3(g)}$ in the coarse mode. Consequently, the deposition rate of NO_3^- increases from 80 to 140 Tg yr^{-1}, and its atmospheric lifetime decreases from 2.6 to 2.3 days (Table 5.3). The combined UPTK on dust and sea salt nearly depletes $HNO_{3(g)}$, leaving only 0.15 TgN, which contributes to the overestimation of surface NO_3^- (Sections 5.3.1 and 5.3.2).

Irreversible condensation also reduces the $NO_{(g)}$, $NO_{2(g)}$, and $N_2O_{5(g)}$ burdens to 0.11, 0.17, and 0.01 TgN, respectively, due to enhanced $N_2O_{5(g)}$ hydrolysis on increased particle surfaces. This reduction can be attributed to increased NO_3^- particle formation

and, consequently, the availability of surfaces where hydrolysis of $N_2O_{5(g)}$ can take place. Ultimately, this leads to more $HNO_{3(g)}$ available for partitioning into the particle phase.

Conversely, N loads increase when reversible condensation of $HNO_{3(g)}$ and $NH_{3(g)}$ is considered in the fTEQ and DBCLL sensitivity simulations. A larger proportion of N remains in the gas phase compared to HYB schemes. Notably, neglecting dust and sea salt alkalinity (fTEQ_noAlk, DBCLL_noAlk) slightly increases $HNO_{3(g)}$ burdens (from 1.11 to 1.14 TgN) and elevates $NO_{(g)}$ and $NO_{2(g)}$ by 0.29% and 0.12%, respectively.

When dust and sea salt alkalinity are considered (fTEQ_du-ssAlk, DBCLL_duAlk, DBCLL_du-ssAlk), $HNO_{3(g)}$ burdens decrease by 40–50%, enhancing particulate NO_3^- formation. This shift towards the aerosol phase results from the reaction of NVC from dust and sea salt with $HNO_{3(g)}$. In these cases, the $NO_{(g)}$, $NO_{2(g)}$, and $N_2O_{5(g)}$ budgets decrease by approximately 20% compared to analogous mechanisms without alkalinity, driven by the more efficient $N_2O_{5(g)}$ aqueous dissociation due to the increased particle presence. Sea salt alkalinity alters the partitioning of aerosol NO_3^- from fine (-72%) towards coarse mode (+63%) when comparing DBCLL_duAlk and DBCLL_du-ssAlk, resulting in burdens of 0.06 (fine) and 0.18 TgN (coarse) (Fig. 5.5). This surge in coarse NO_3^- formation with dust and sea salt alkalinity causes a 26% decrease in the total NO_3^- burden and a 14% increase in deposition rates compared to the DBCLL_duAlk case, mainly driven by the enhanced wet deposition of coarse NO_3^- from 11.0 to 27.5 Tg yr^{-1} (Table 5.3). This can be attributed to the higher deposition efficiency of sea salt particles due their larger size ranges and abundances near the surface. Consequently, the presence of sea salt decreases the atmospheric lifetime of particulate NO_3^- from 4.9 to 3.1 days, contrasting with scenarios that consider only dust alkalinity.

Additionally, sea salt NVCs (e.g., Na^+) inhibit $NH_{3(g)}$ condensation into NH_4^+, reducing NH_4^+ burdens from 0.31 to 0.22 Tg (Table A.9).

5.3.3.2 Reduced and oxidized nitrogen

Figure 5.6 presents the annual averaged burdens and depositions of oxidized ($HNO_{3(g)}$ and NO_3^-) and reduced ($NH_{3(g)}$ and NH_4^+) N for each sensitivity run. These results are compared with global estimates from the AeroCom phase III nitrate experiment (Bian et al. 2017), which offers a comprehensive range of budgets derived from different global aerosol models employing mechanisms similar to those analyzed in our study. As additional references, the results from the EMAC model (Karydis et al. 2016) and the LMDz-INCA model (Hauglustaine et al. 2014) are shown separately from the average of AeroCom in Fig. 5.6 due to their similarities to the DBCLL and HYB mechanisms, respectively.

The HYB mechanisms yield an annual average burden of oxidized N of 0.55 TgN, slightly below the AeroCom multimodel mean but in close agreement with that of Hauglustaine et al. (2014). Compared to the fTEQ and DBCLL mechanisms that account for dust and sea salt alkalinity, which show higher oxidized N burdens (0.6–0.8 TgN), the HYB mechanisms fall on the lower end of the distribution. This reduction is primarily due to the efficient deposition of particulate NO_3^- and the limited atmospheric presence of $HNO_{3(g)}$ under the assumption of irreversible uptake, as discussed in Sections 5.3.2 and 5.3.3.1.

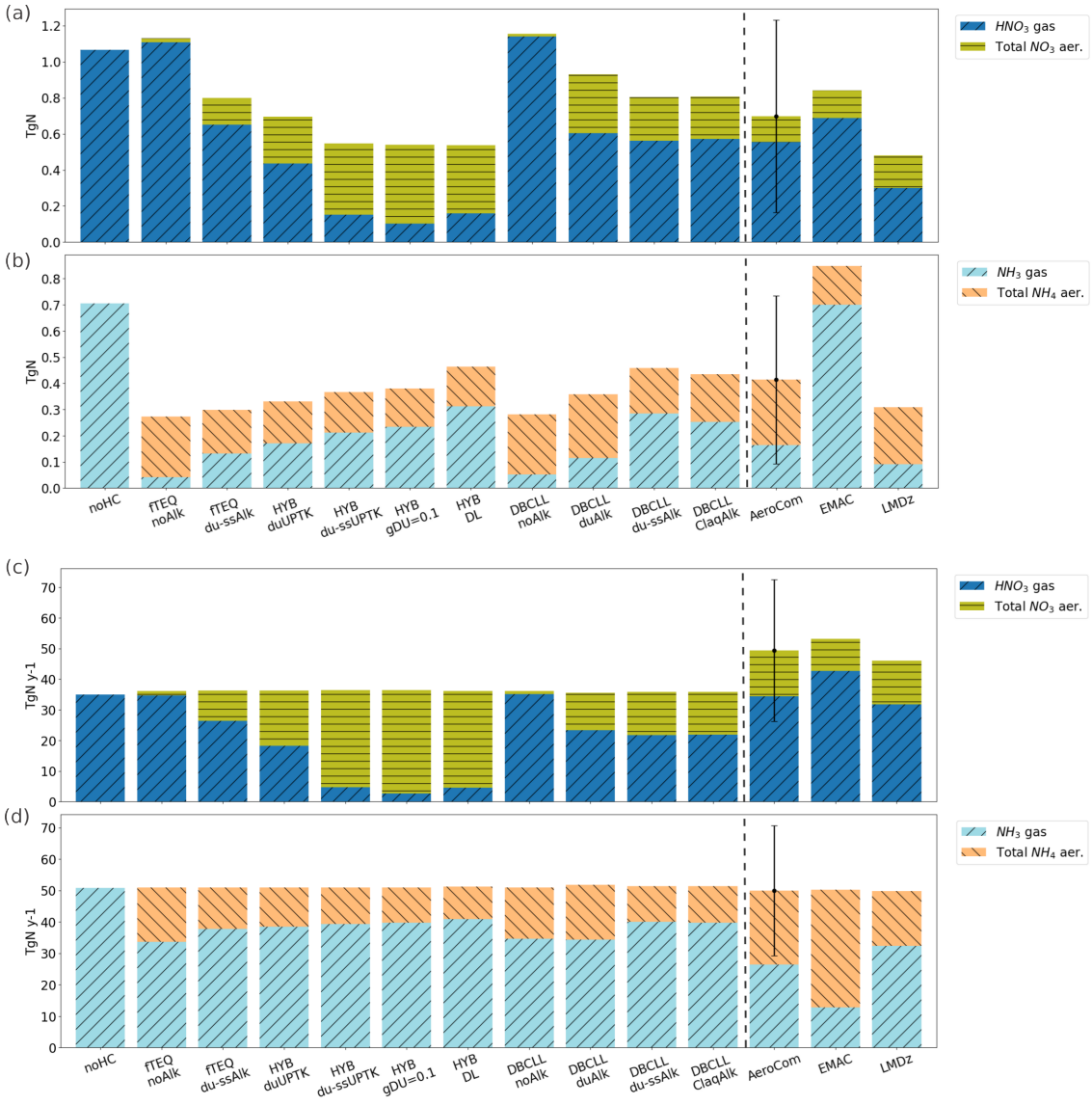

Figure 5.6: Average 2018 N budgets (a, b) and depositions (c, d) for the different dust heterogeneous chemistry mechanisms. Each plot shows oxidized (a, c) and reduced (b, d) mass for each mechanism (bars). They are compared with references from the literature (the final three bars on the right).

For reduced N species, the HYB mechanisms produce an average burden of approx-

imately 0.3 TgN, aligning well with the AeroCom mean. However, HYB configurations yield lower particulate NH_4^+ burdens (0.15 TgN, supplementary Table A.9) and higher $NH_{3(g)}$ levels in the gas phase compared to the Hauglustaine et al. (2014) mechanism and others. Among HYB cases, $NH_{3(g)}$ budgets show an inverse relationship with $HNO_{3(g)}$, indicating that $HNO_{3(g)}$ acts as a limiting factor for the $NH_{3(g)}$ neutralization in the fine mode. Given that most $HNO_{3(g)}$ is consumed by the UPTK reactions in the HYB mechanism, these results suggest that the NH_4^+ mass formed with this configuration is mainly a product of $NH_{3(g)}$ neutralization with SO_4^{2-} through the fTEQ calculation.

The fTEQ and DBCLL mechanisms exhibit a high sensitivity in the partitioning of oxidized and reduced N to alkalinity, regardless of whether coarse NO_3^- formation is considered. When dust and sea salt alkalinity are neglected (fTEQ_noAlk and DBCLL_noAlk), oxidized N burdens rise significantly, to 1.1 TgN, primarily due to the accumulation of unreacted $HNO_{3(g)}$, which slightly exceeds the burden in the noHC run (1.05 TgN). This is attributed to the sensitivity of $N_2O_{5(g)}$ hydrolysis to aerosol loading. Conversely, reduced N burdens in these schemes remain relatively low compared to other mechanisms due to the high consumption of $NH_{3(g)}$ by neutralization of $HNO_{3(g)}$, which acts as an important sink of reduced N as particulate NH_4^+. The introduction of dust and sea salt NVCs into the reactions decreases oxidized N by an enhanced consumption of $HNO_{3(g)}$ to form NO_3^-. Furthermore, reduced N concentrations increase as a consequence of the lower availability of $HNO_{3(g)}$ to neutralize $NH_{3(g)}$. This phenomenon is similarly observed in simulations including TEQ calculations over fine (fTEQ_du-ssAlk) and over both fine and coarse modes (DBCLL_duAlk and DBCLL_du-ssAlk). Comparatively, the presence of dust and sea salt alkalinity decreases the oxidized N burdens by approximately 27% compared to analogous simulations neglecting NVCs. However, contrasting the results between DBCLL_duAlk and DBCLL_du-ssAlk shows that while the presence of sea salt NVCs further enhances the consumption of $HNO_{3(g)}$ by 20%, it concurrently reduces NO_3^- burdens by 5%. This is likely due to sea salt contributing to increase Cl^- and SO_4^{2-} (see Section 5.2.1), which hinders the formation of particulate NO_3^- in the fine mode and leaves more $HNO_{3(g)}$ available to form coarse NO_3^- over dust. This is consistent with the spatial distributions discussed in Section 5.3.1.3 and the N budgets presented in Section 5.3.3.1 and Fig. 5.5.

Alkalinity from dust and sea salt components leads to higher reduced N budgets due to enhanced basic conditions (high pH, as shown in Fig. 5.3). This environment inhibits $NH_{3(g)}$ condensation over dust and sea salt particles, thereby increasing the $NH_{3(g)}$ atmospheric lifetime (Table A.8) and allowing it to mix with SO_4^{2-} from polluted areas, as can be seen in the spatial correlation between particulate SO_4^{2-} and NH_4^+ (see discussion in Section 5.3.1 and supplementary Figures A.4 and A.7). Consequently,

alkalinity facilitates the formation of NH_4^+ through the neutralization of $NH_{3(g)}$ with $H_2SO_{4(g)}$, contrasting with the neutralization process involving $HNO_{3(g)}$ observed in the DBCLL_noAlk simulation.

Overall, the DBCLL_du-ssAlk run aligns with the average of AeroCom in both oxidized and reduced partitions, although its reduced phase falls below EMAC levels. This discrepancy can be attributed to EMAC showing very low deposition rates of $NH_{3(g)}$ (see supplementary Table A.8), which enhances its atmospheric burden.

The observational evaluation of both reduced and oxidized species, along with the monitoring stations used, can be found in the supplementary Section A.6. Overall, a general good agreement with observations is obtained. Oxidized N species exhibit low biases in all mechanisms except HYB_du-ssUPTK, which overestimates observations throughout the studied period, supporting the conclusion that UPTK coefficients used are excessively efficient. Reduced N species, while slightly underestimated, remain well within the observational variability range.

5.3.4 Nitrate budgets

The NO_3^- budgets from the sensitivity runs are summarized in Table 5.3, including burdens, wet and dry deposition, productivities, and lifetime of fine, coarse and total NO_3^-. Comparative data from previous studies (Bian et al. 2017, Karydis et al. 2016, Rémy et al. 2022, Hauglustaine et al. 2014, Jones et al. 2021) are also included. Analogous information on $HNO_{3(g)}$, $NH_{3(g)}$, NH_4^+, and SO_4^{2-} can be found in supplementary Section A.4 (Tables A.7 to A.10).

The sensitivity runs conducted in this study yield a wide range of total NO_3^- burdens, ranging from 0.09 to 1.93 Tg. Experiments neglecting coarse NO_3^- and the role of NVCs fall on the lower end of this spectrum, while the HYB schemes consistently report higher burdens. The coarse-to-fine ratio decreases in the mechanisms that neglect NVCs partly or completely in the NO_3^- partitioning, and HYB runs consistently simulate the highest coarse burdens (0.57 to 1.43 Tg). Compared to the reported values in the literature, total NO_3^- on both the HYB (1.15 to 1.93 Tg) and DBCLL (1.04 to 1.44 Tg) schemes considering NVCs fall within the upper range of the Aerocom total NO_3^- burden (Bian et al. 2017) and above specific global models such as IFS (Rémy et al. 2022) or Met Office UM (Jones et al. 2021). Similar differences are found in total annual depositions with ranges that span a factor of 2 among schemes. For wet deposition, DBCLL mechanisms show values ranging from 37 to 45 Tg yr^{-1}, within the lower half of the range found in the literature (45±30 Tg yr^{-1} for AeroCom to 75 Tg yr^{-1} for IFS), while HYB consistently simulates higher estimates even beyond

the reported values (63 to 120 Tg). This feature is also seen in the dry deposition. Consequently, the lifetimes of total NO_3^- shown in Table 5.3 range from 2.3 to 2.6 days for the HYB schemes, systematically estimating the lowest lifetimes. Conversely, models introducing reversible partitioning provide longer lifetimes (2.6 to 4.9 days). To better understand the possible reasons for such a wide range of estimates, in the next paragraphs we analyze some of our sensitivity runs compared to similar systems in the literature.

Table 5.3: Results for fine ($D < 2.5\mu m$), coarse ($2.5 < D < 10\mu m$), and total ($D < 20\mu m$) particulate NO_3^- obtained using the heterogeneous chemistry mechanisms studied for 2018. Results from the literature references are reported in the second half of the table: the average of all the participating models in the intercomparison AeroCom phase III nitrate experiment for 2008 (*AeroCom*), specifying their standard deviation (*SD AeroCom*), results from the GMI model (*GMI*, using an HYB approach with UPTK reactions on dust and sea salt), and results from the EMAC model (*EMAC 2008*, using a similar approach to DBCLL_du-ssAlk). Also using the EMAC model, results obtained by the Karydis et al. (2016) study are reported as *EMAC 2005-2008*. Results from models using a similar approach to HYB_du-ssUPTK are reported as *IFS* for Rémy et al. (2022), *LMDz-INCA* for Hauglustaine et al. (2014), and *Met Office UM* for Jones et al. (2021).

NO_3^-	Burden (Tg)			Wet Dep. (Tg y-1)			Dry Dep. (Tg y-1)			Total Dep. (Tg y-1)			Production (Tg y-1)			Lifetime (days)		
Experiment	Fine	Coarse	**Total**	Fine	Coarse	**Total**	Fine	Coarse	**Total**	Fine	Coarse	**Total**	Fine	Coarse	**Total**	Fine	Coarse	**Total**
fTEQ_noAlk	0.09	-	**0.09**	4.6	-	**4.6**	2.0	-	**2.0**	6.6	-	**6.6**	6.6	-	**6.6**	2.6	0.0	**2.6**
fTEQ_du-ssAlk	0.66	-	**0.66**	36.1	-	**36.1**	7.4	-	**7.4**	43.5	-	**43.5**	43.6	-	**43.6**	2.7	0.0	**2.7**
HYB_duUPTK	0.58	0.57	**1.15**	25.8	37.9	**63.7**	5.4	11.1	**16.5**	31.2	49.0	**80.2**	31.3	48.9	**80.2**	3.4	2.1	**2.6**
HYB_du-ssUPTK	0.55	1.20	**1.75**	10.7	103.4	**114.1**	2.9	23.6	**26.5**	13.6	127.0	**140.6**	13.6	126.9	**140.5**	7.4	1.7	**2.3**
HYB_gdust=0.1	0.50	1.43	**1.93**	8.4	111.9	**120.4**	2.3	27.0	**29.3**	10.7	138.9	**149.7**	10.8	138.9	**149.6**	8.5	1.9	**2.4**
HYB_DL	0.41	1.26	**1.68**	2.8	109.7	**112.6**	1.4	25.7	**27.1**	4.2	135.4	**139.6**	4.2	135.3	**139.5**	17.8	1.7	**2.2**
DBCLL_noAlk	0.06	0.00	**0.06**	2.5	0.0	**2.6**	1.6	0.1	**1.7**	4.1	0.1	**4.2**	4.2	0.1	**4.3**	2.6	2.8	**2.6**
DBCLL_duAlk	0.96	0.47	**1.44**	26.5	11.0	**37.5**	8.3	8.2	**16.5**	34.8	19.3	**54.0**	34.7	19.2	**53.9**	5.1	4.5	**4.9**
DBCLL_du-ssAlk	0.28	0.78	**1.07**	18.2	27.5	**45.7**	4.0	12.6	**16.5**	22.2	40.1	**62.3**	22.3	40.0	**62.2**	2.3	3.6	**3.1**
DBCLL_ClaqAlk	0.41	0.63	**1.04**	17.4	27.8	**45.2**	3.8	12.9	**16.7**	21.2	40.7	**61.9**	21.3	40.6	**61.9**	3.5	2.8	**3.1**
AeroCom	-	-	**0.63**	-	-	**45.9**	-	-	**20.7**	-	-	**66.6**	-	-	**60.6**	-	-	**5.0**
SD AeroCom	-	-	**±0.56**	-	-	**±30.7**	-	-	**±19.5**	-	-	**±50.2**	-	-	**±45.9**	-	-	**±2.3**
GMI	-	-	**0.97**	-	-	**43.3**	-	-	**14.8**	-	-	**58.1**	-	-	**59.3**	-	-	**6.0**
EMAC 2008[1]	-	-	**0.67**	-	-	**0.0**	-	-	**46.3**	-	-	**46.3**	-	-	**-**	-	-	**-**
EMAC 2005-2008[2]	-	-	**0.44**	-	-	**-**	-	-	**-**	-	-	**-**	-	-	**-**	-	-	**-**
IFS[3]	0.47	0.35	**0.82**	35.9	39.6	**75.5**	4.6	23.8	**28.4**	40.5	63.4	**103.9**	40.5	63.4	**103.6**	4.2	2.1	**3.0**
LMDz-INCA	0.22	0.58	**0.80**	-	-	**56.1**	-	-	**7.4**	-	-	**63.5**	14.1	49.5	**63.6**	-	-	**4.6**
Met Office UM[4]	0.49	0.40	**0.89**	-	-	**63.3**	-	-	**39.4**	-	-	**102.8**	27.9	73.5	**101.4**	6.2	2.0	**3.2**

[1] From Bian et al. (2017).
[2] From Karydis et al. (2016).
[3] Fine NO_3^- reported from neutralization of $HNO_{3(g)}$, $NH_{3(g)}$ and SO_4^{2-}. Coarse NO_3^- from heterogeneous chemistry. (Rémy et al. 2022).
[4] Jones et al. (2021) performs two sensitivity tests to the accommodation coefficient used for NO_3^- formation in the fine mode: *FAST* with 0.193 and *SLOW* with 0.001. Here, results from the *FAST* test are reported on the basis that they present similar fine NO_3^- formation rates to our average fine NO_3^- results.

The assumption of irreversibility of $HNO_{3(g)}$ condensation onto dust and sea salt particles (HYB_du-ssUPTK run) produces the largest increase in coarse NO_3^- formation, exceeding values reported in the literature. For instance, the HYB_du-ssUPTK model reports a total NO_3^- burden of 1.75 Tg, which is higher than the AeroCom range (0.63 ± 0.56 Tg) and than values from models such as EMAC in AeroCom (Bian et al. 2017), as well as findings from Bian et al. (2017), Jones et al. (2021), Rémy et al. (2022) and Hauglustaine et al. (2014) (0.67, 0.89, 0.82, and 0.80 Tg, respectively). Interestingly,

the results surpass those from three AeroCom models (EMEP, INCA, and GMI) using a similar HYB approach with UPTK reactions on dust and sea salt, which range from 0.26 to 0.95 Tg of total NO_3^- (see Bian et al. (2017)). Multiple reasons could explain the excessive NO_3^- formation found in this comparison. For instance, Hauglustaine et al. (2014) employ a similar HYB implementation and UPTK coefficients for dust as the HYB_du-ssUPTK run, although a different parametrization for the $HNO_{3(g)}$ UPTK on sea salt. Despite Hauglustaine et al. (2014) also overestimating particulate NO_3^- with a global normalized mean bias of +68%, the HYB_du-ssUPTK simulation still reports higher burdens for NO_3^- (0.80 vs. 1.75 Tg) and lower burdens for $HNO_{3(g)}$ (1.35 vs. 0.69 Tg, Table A.7). Our study also presents lower NO_x emissions than those in Hauglustaine et al. (2014), which would imply a reduced availability of precursor gases that would typically result in lower NO_3^- formation (40.8 vs. 46.0 TgN, Table 3.2). Additionally, the run neglecting the uptake on sea salt (HYB_duUPTK) reports values closer to observations (Section 5.3.2) and to the budgets in the literature.

This suggests that the high coefficients used for $HNO_{3(g)}$ UPTK on sea salt may be excessively efficient. This conclusion is consistent with analyses discussed in Sections 5.3.1.2, 5.3.2, and 5.3.3. In comparison, other systems (Hauglustaine et al. 2014, Jones et al. 2021, Rémy et al. 2022) typically employ much lower UPTK coefficients for sea salt compared to our implementation.

Therefore, a function for the uptake coefficient on sea salt dependent on RH and on sea salt particle size should be considered in future work, following the same approach as for dust (Eq. 4.4). However, such a function has not clearly been determined in the literature. While Hauglustaine et al. (2014) assume a BET isotherm for the $HNO_{3(g)}$ UPTK on sea salt similar to the UPTK on dust (Fairlie et al. 2010), it remains unclear if this approach is as suitable for sea salt as it is for dust. To our best knowledge, the most appropriate alternative to the assumption of averaged UPTK coefficients for sea salt would be to fit a function to the experimental values reported by Liu et al. (2007), which provides uptake coefficient dependencies with RH and particle size. However, several discrepancies between Liu et al. (2007) and previous studies still remain unresolved (Tolocka et al. 2004, Saul et al. 2006), presenting difficulties in reaching a common agreement on a $HNO_{3(g)}$ UPTK coefficient function on sea salt. Alternatively, in Equation 4.5 (Section 4.3.1) we provide a potential uptake coefficient function based on the cited experimental data treating uptake reactions of $HNO_{3(g)}$ on sea salt.

Beyond the excessive NO_3^- formation driven by the UPTK on sea salt, the sole implementation of $HNO_{3(g)}$ UPTK on dust (HYB_duUPTK run) still slightly exceeds

particulate NO_3^- burdens and deposition rates reported by the references (Table 5.3). This is also observed when compared to observational surface concentrations (see Section 5.3.2), suggesting that the sole UPTK on dust results in excessive NO_3^- formation. Given that previous studies have consistently shown non-negligible $HNO_{3(g)}$ uptake on sea salt (Myhre et al. 2006, Athanasopoulou et al. 2008), these biases could be explained by 1) an excessive UPTK coefficient employed for $HNO_{3(g)}$ UPTK on dust, 2) the inherent inappropriateness of the irreversible condensation assumption of gas species on particles to simulate particulate NO_3^- formation, or 3) the different atmospheric lifetimes of coarse particles among different systems. Regarding possible issues in the UPTK parameterization on dust adopted in our study, the inclusion of the scaling factor for alkalinity added to the dust uptake coefficients (Sc in Eq. 4.4) could contribute to excessively high UPTK rates. This alkalinity scaling factor is based on the NVC fractions provided by Fairlie et al. (2010), namely Ca^{2+} and Mg^{2+} (see Section 4.3.1). Since our study includes additional NVCs (i.e. K^+ and Na^+), this estimation might not be representative and could result in excessive condensation. However, additional information on the NVC content in Fairlie et al. (2010) is missing to refine our approach. Concerning the possible inappropriateness of the irreversible condensation assumption, indeed models implementing such an approach with similar UPTK coefficients tend to overestimate particulate NO_3^- formation (Hauglustaine et al. 2014, Jones et al. 2021, Rémy et al. 2022). This might point to the assumption of reversible evaporation-condensation of gas species or to the inclusion of alkalinity consumption as necessary implementations to improve the results.

Lastly, a longer lifetime of coarse particles such as dust or sea salt could contribute to the enhancement of NO_3^- production regardless of the mechanism adopted. Spada et al. (2013) compared different sea salt emission schemes in the MONARCH model and reported lifetimes ranging from 4 to 12 days, including results from the literature. These findings highlight significant differences in emission, transport, and deposition schemes among global models, which are not negligible. Such differences could explain part of the variations identified in our analysis. For instance, if a model assumes a longer lifetime for coarse particles, it would result in a prolonged period during which $HNO_{3(g)}$ can condense onto these particles, thus increasing the overall burden of particulate NO_3^-. Understanding and standardizing these lifetimes could be crucial to achieve more consistent and accurate predictions of NO_3^- aerosol formation across different modeling frameworks.

Linking with the limitations of irreversible approaches, we finally analyze the DBCLL runs to illustrate the paramount role of alkalinity in NO_3^- formation. Neglecting NVC

in the partitioning (DBCLL_noAlk) results in negligible NO_3^- formation, with a burden of just 0.06 Tg in the fine mode (Table 5.3). In contrast, only considering dust alkalinity (DBCLL_duAlk) significantly increases the burden of both fine and coarse modes to 0.96 and 0.47 Tg, respectively, which exceeds the estimates reported in other works (Hauglustaine et al. 2014, Jones et al. 2021, Rémy et al. 2022).

Additionally accounting for sea salt alkalinity (reaction R12 from Table 4.3), the DBCLL_du-ssAlk run shifts particulate NO_3^- formation from the fine towards the coarse mode, increasing coarse burdens from 0.47 Tg in DBCLL_duAlk to 0.78 Tg. Consequently, this leads to higher total NO_3^- deposition rates, rising from 54 to 62 Tg yr^{-1}. Including both dust and sea salt alkalinity results in a notable agreement for total NO_3^- (1.07 Tg) and $HNO_{3(g)}$ (2.53 Tg) burdens with the values reported in the literature. This improvement highlights the importance of considering both dust and sea salt alkalinity when accurately modeling NO_3^- formation and deposition rates in atmospheric chemistry simulations.

Some differences emerge when comparing the NO_3^- size distribution to references that report fine and coarse NO_3^- budgets. Specifically, the fine NO_3^- burden tends to be on the lower end of the references range (0.28 Tg vs. 0.39 Tg on average), while the coarse NO_3^- burden is on the higher end (0.78 Tg vs. 0.54 Tg on average), although the relatively high variability between the references in both modes should be considered. Despite these variations, accounting for alkalinity significantly improves the agreement of NO_3^- lifetime (3.1 days) compared to AeroCom (5.0±2.3 days), Rémy et al. (2022) (3.0 days), and Jones et al. (2021) (3.2 days).

To delve into the differences observed between simulations employing constant dust alkalinity derived from Journet et al. (2014) (DBCLL_du-ssAlk) and that from Claquin et al. (1999) (DBCLL_ClaqAlk, discussed in supplementary Section A.5) as shown in Table 5.3, it becomes evident that DBCLL_ClaqAlk results in a noticeable shift towards fine NO_3^- formation (from 0.28 Tg to 0.40 Tg), with fine NO_3^- increasing its lifetime (from 2.3 to 3.5 days) and coarse NO_3^- decreasing it (from 3.6 to 2.8 days). Also, we observe a slightly higher burden of $HNO_{3(g)}$ (from 2.53 Tg to 2.58 Tg) and a lower burden of $NH_{3(g)}$ (from 0.35 Tg to 0.31 Tg) (see supplementary Tables A.7 and A.8). This can be attributed to the lower fractions of Mg^{2+} and K^+ in the fine mode derived from Journet et al. (2014), despite higher Ca^{2+} content (5.73%) compared to that of Claquin et al. (1999) (3.68%). Both datasets present more similar fractions of Ca^{2+} for the coarse mode (4.61% vs. 3.74%) (see supplementary Tables A.2 and A.4). This underscores the important role that NVCs play in heterogeneous chemistry. The comparison between DBCLL_du-ssAlk and DBCLL_ClaqAlk provides a quantification of the impact that mineral distributions among dust sources have on gas–aerosol

partitioning, especially in the formation of particulate NO_3^-. It also highlights the importance of advancing in the representation of mineralogical dust composition at the global-scale and its regional variability.

Finally, we compare the outcomes from the DBCLL_du-ssAlk simulation with those reported by the EMAC model, which employs a similar approach to the DBCLL mechanism and also accounts for dust and sea salt alkalinity (see Section 5.3.1.3). The analysis is performed against two studies where EMAC budgets were reported: the AeroCom intercomparison NO_3^- experiment (Bian et al. 2017) and Karydis et al. (2016) (Table 5.3). It is notable that the total NO_3^- burden (1.07 Tg) in DBCLL_du-ssAlk exceeds both the EMAC results from AeroCom (0.67 Tg) and Karydis et al. (2016) (0.44 Tg), although our findings show reasonable agreement with observations, especially over Asia (see Section 5.3.2). Regarding the total budget of $HNO_{3(g)}$ (2.53 Tg), despite our result closely matches the AeroCom experiment average (2.50±1.83 Tg, Table A.7), it is below the values reported by EMAC in this experiment (3.10 Tg) while significantly exceeding results from Karydis et al. (2016) (1.65 Tg). These outcomes reveal intrinsic differences in the rates of $HNO_{3(g)}$ condensation on dust and sea salt between both models. Conversely, the $NH_{3(g)}$ burden (0.35 Tg) in our simulation falls below those reported by both studies (0.85 and 0.82 Tg, respectively), potentially due to the high formation of particulate NO_3^- over dust and sea salt NVCs in our study. Nevertheless, the resulting burdens for NH_4^+ align with both references (0.22 vs. 0.19 and 0.17 Tg for EMAC in AeroCom and Karydis et al. (2016), respectively). Various factors could explain the differences observed between EMAC and the DBCLL_du-ssAlk simulation: the different simulated periods between our study, and those of Karydis et al. (2016) and AeroCom (2018 vs. 2005-2008 average and 2008, respectively), the varying NVC contents assumed for dust and sea salt between DBCLL_du-ssAlk and EMAC (Section 5.3.1.3), and the intrinsic differences in the heterogeneous chemistry mechanisms employed in both models (DIFFLIM and DBCLL in MONARCH and bulk TEQ followed by DIFFLIM in EMAC). Despite their conceptual equivalence, our results demonstrate that these mechanisms may yield different outcomes.

5.4 Conclusions

In this study, we conducted a comprehensive exploration of the processes driving NO_3^- formation on fine ($D < 2.5\mu m$) and coarse ($2.5 < D < 10\mu m$) particles at a

global-scale using the MONARCH atmospheric model. Our sensitivity simulations incorporated state-of-the-art dust heterogeneous chemistry mechanisms, including reversible condensation-evaporation through thermodynamic equilibrium (TEQ) and irreversible uptake reactions (UPTK) between gas and aerosol phases. Three mechanisms for particulate NO_3^- formation were implemented: (1) fTEQ, which considers the formation of fine NO_3^- through reversible TEQ reactions and does not include coarse NO_3^- formation; (2) HYB, where fine NO_3^- forms via TEQ with a subsequent irreversible uptake of $HNO_{3(g)}$ on coarse particles; and (3) DBCLL, which allows for both fine and coarse NO_3^- formation through reversible TEQ processes with kinetic gas limitation.

Key assumptions such as uptake coefficients, reversible partitioning, and the inclusion of dust and sea salt alkalinity were thoroughly assessed. Global average dust alkalinity was sourced from previous dust mineralogy simulations (Gonçalves Ageitos et al. 2023) using the Journet et al. (2014) and Claquin et al. (1999) mineral atlases, while globally homogeneous sea salt alkalinity values are derived from Seinfeld and Pandis (2006). We evaluated annual cycle surface concentrations against observations for various atmospheric species and compared global spatial distributions and budgets with the existing literature. Additionally, we investigated the partitioning of N species and assessed the impact of dust and sea salt heterogeneous chemistry on total N budgets.

Neglecting coarse NO_3^- formation (fTEQ_du-ssAlk run) results in budgets and distributions of fine NO_3^- that closely match observational surface concentrations of total NO_3^- (-0.09 $\mu g\ m^{-3}$ bias, 0.88 correlation). This good agreement suggests that observational stations are dominated by fine NO_3^- concentrations or that fine NO_3^- formation is overestimated in this run. Since this mechanism aligns with references forming both fine and coarse NO_3^- (Hauglustaine et al. 2014, Bian et al. 2017, Rémy et al. 2019), it likely compensates for the lack of coarse NO_3^- formation through the instantaneous TEQ of gas species in the fine mode, thus not accurately reflecting the size distribution of particles.

The formation of coarse NO_3^- through the irreversible uptake of $HNO_{3(g)}$ on coarse particles (HYB methodologies) is highly sensitive to whether the $HNO_{3(g)}$ uptake is assumed to occur solely on dust or on both dust and sea salt particles. The uptake solely on dust (HYB_duUPTK run) closely reproduces fine and total particulate NO_3^- seasonality (correlations of 0.8 and 0.9, respectively), although it slightly overestimates observations (+0.29 $\mu g\ m^{-3}$ bias), particularly over Asia, and overestimates NO_3^- budgets compared to the literature (1.15 vs. 0.74 Tg on average). An excessively efficient $HNO_{3(g)}$ uptake on dust particles could explain such performance, which could be improved through more accurate scaling factors adopted for alkalinity. However, the lack of information in the literature poses a challenge when implementing such adjustments.

The introduction of the $HNO_{3(g)}$ uptake on sea salt (HYB_du-ssUPTK run) further increases the formation of coarse NO_3^-, exceeding the reported burdens in the literature (1.75 vs. 0.74 Tg from the references' average) and highly overestimating observational surface concentrations (+1.50 $\mu g\ m^{-3}$ bias). Moreover, some deviations with respect to references are observed in the latitude and magnitude of the transatlantic transport of coarse NO_3^- formed during long-range transport of dust and sea salt. These findings indicate the need for a revision of the $HNO_{3(g)}$ uptake coefficients on sea salt. A potential alternative could involve its implementation as a function of RH and particle size, aligning it with experimental data from Liu et al. (2007), although discrepancies compared to earlier experimental studies present difficulties in determining consistent uptake coefficients for sea salt.

The reversible condensation-evaporation of gas species on both fine and coarse modes of dust and sea salt (DBCLL mechanism) highlight the paramount importance of accounting for alkalinity to derive consistent results both globally and across continents. Remarkably, the DBCLL_du-ssAlk run, which accounts for dust and sea salt alkalinity, effectively captures monthly global concentrations of fine and total NO_3^-, with correlations of 0.82 and 0.78 and concentrations that are slightly underestimated with -0.18 and -0.10 $\mu g\ m^{-3}$ bias, respectively. These good results extend to particulate NH_4^+ for both fine and total fractions (-0.02 and 0.08 $\mu g\ m^{-3}$ bias, respectively). Compared to observations, the consistent excessive formation of total $PM_{2.5}$ (+20 $\mu g\ m^{-3}$ bias) over Asia across the experiments may be explained by the absence of anthropogenic coarse dust emissions in the CAMS inventory employed. This omission leads to the overestimation of fine particulate matter formation, compensating for the misrepresentation of coarse particulate matter.

Including both dust and sea salt alkalinity in the DBCLL mechanism significantly raises global pH levels, which enhances particulate NO_3^- formation by 94% in comparison to the same mechanism with no alkalinity. This incorporation also reduces NO_x budgets and lowers the reduced N burden due to an increase in NH_4^+ formation. Moreover, the sole inclusion of sea salt alkalinity is identified as being responsible for substantially shifting the size partitioning of particulate NO_3^- from fine (-72%) to coarse (+63%), along with the rise in wet deposition of particulate NO_3^- due to the high scavenging rate of sea salt particles, overall reducing the total aerosol NO_3^- atmospheric lifetime from 4.9 to 3.1 days.

Comparison with references reveals that while surface concentrations in the DBCLL_du-ssAlk simulation align well with observations, its global burden (1.07 Tg) sits at the upper limit of AeroCom's reported range (0.63±0.56 Tg) and slightly exceeds the average reported by other studies (0.74 Tg). Fundamental differences between the

models, such as the alkalinity factors, intrinsic differences in the heterogeneous chemistry, aerosol representation, and transport processes can partly explain the wide range of results reported in the literature. Overall, the DBCLL_du-ssAlk scheme demonstrates the best accuracy compared to the other configurations tested, as evidenced by its closer alignment with observations.

A comparison between runs adopting the two different dust alkalinity fractions derived from averaging simulations using the Journet et al. (2014) and Claquin et al. (1999) soil mineralogy datasets as described in Gonçalves Ageitos et al. (2023) reveals that assumptions regarding the dust composition are crucial, particularly influencing the particulate NO_3^- size distribution. A decrease from 5.17% to 3.71% in ionic Ca^{2+} fractions, along with slight increases in Na^+, K^+ and Mg^{2+} between the Journet et al. (2014) and Claquin et al. (1999) mineral datasets leads to a +35% increase in fine and -21% decrease in coarse NO_3^- formation. This high sensitivity is especially attributed to the lower $CaCO_3$ content and its different size distribution in the Claquin et al. (1999) database compared to that of Journet et al. (2014).

It is important to note that our computational cost analysis reveals highly similar processing times across the sensitivity runs, with a standard variation of only 5%. This is within the estimated variability in the supercomputing resources utilized for the present work. Consequently, the computational cost does not indicate a clear advantage in efficiency for any of the methodologies assessed.

This study establishes a crucial benchmark for future investigations into the impact of incorporating regional variations in dust alkalinity, as derived from Claquin et al. (1999), Journet et al. (2014), and the upcoming spectroscopically based EMIT surface mineralogical dataset (Green et al. 2018, Thompson et al. 2024, Brodrick et al. 2025), on the formation of particulate NO_3^- and atmospheric composition. The findings also evaluate the significance of dust and sea salt alkalinity in inorganic aerosol heterogeneous chemistry, providing insights into the optimal representation of dust alkalinity in atmospheric models. Ultimately, these results aim to enhance the capability of atmospheric and climate models to simulate the formation of aerosol NO_3^-, NH_4^+, and SO_4^{2-}, potentially improving our ability to estimate the radiative effects of these species in climate projections.

6

Impacts of the geographical representation of dust mineralogy

Adapted from the manuscript submitted to Nature Comms.:
Rubén Soussé Villa, Oriol Jorba, María Gonçalves Ageitos et al. Space-borne spectroscopy links dust source composition to atmospheric acidity and nitrate, 27 January 2026, PREPRINT (Version 1) available at Research Square [https://doi.org/10.21203/rs.3.rs-8678680/v1]

6.1 Introduction

In Chapter 1 we introduced the paramount role of mineral dust for global atmospheric chemistry, principally via gas-aerosol heterogeneous reactions, often misrepresented in atmospheric models (Section 1.5). In Chapter 5 we systematically explore different implementations of dust heterogeneous reactions with the MONARCH model (Section 3.1). Our findings reveal the importance of accounting for reversible formation of fine and coarse SIA, accompanied by a rigorous representation of dust mineralogical content, to accurately reproduce atmospheric composition at a global level.

In fact, one of the main uncertainties to implement dust heterogeneous chemistry in models has traditionally been the limited quantitative understanding of the global chemical composition of dust (Adebiyi and Kok 2020), as detailed in Section 1.5.

Since airborne dust provides reactive surfaces where $HNO_{3(g)}$ and $H_2SO_{4(g)}$ condense, the neutralization rate of these species strongly depends on the abundance of basic species on the dust surface and its liquid coating. In Section 1.3 we introduced how NVCs compete on dust surfaces with condensed $NH_{3(g)}$ to react with acidic gas species to form SIA, especially particulate NO_3^-, SO_4^{2-} and NH_4^+. These reactions influence

gas-aerosol partitioning, altering aerosol composition and modulating aerosol pH (Usher et al. 2003, Karydis et al. 2016; 2021), with important consequences for climate and air quality (Section 1.4).

$CaCO_3$ plays a leading role in the neutralization of dissolved $HNO_{3(g)}$, forming $Ca(NO_3)_2$ from dissolved Ca^{2+}, as detailed in Section 1.3.2. Due to its prevalence and solubility compared to other minerals containing NVCs – such as K^+ or Mg^{2+} (Fenter et al. 1995, Krueger et al. 2004) – the amount and spatial distribution of $CaCO_3$ in dust modulates the neutralization rates and the gas-aerosol partitioning of other gas species that are precursors of SIA (i.e. $NH_{3(g)}$, $SO_{2(g)}$, and $H_2SO_{4(g)}$). Ultimately, the $CaCO_3$ dust fraction substantially shapes aerosol chemistry and acidity, together with the atmospheric composition and bioavailability of Fe within dust (Usher et al. 2003, Krueger et al. 2003, Li and Shao 2009, Karydis et al. 2021, Bergas-Massó et al. 2023).

Despite its pivotal role in heterogeneous chemistry, most atmospheric models either neglect NVCs altogether or assume a highly simplified, globally uniform NVC fraction across all dust sources (Feng and Penner 2007, Hauglustaine et al. 2014, Paulot et al. 2016, Jones et al. 2021, Soussé Villa et al. 2025), as summarized in Section 1.5. Such coarse parameterizations ignore the strong spatial variability in soil mineralogy revealed by field surveys and remote sensing, which show that for instance the dust $CaCO_3$ content varies substantially among arid regions (Claquin et al. 1999, Journet et al. 2014).

The recent launch of the NASA's EMIT mission, an imaging spectrometer aboard the International Space Station, provides the first global, high-resolution, observationally constrained maps of surface mineral composition across all major dust-emitting regions (Okin et al. 2025, Brodrick et al. 2025). EMIT's hyperspectral retrievals of $CaCO_3$ and other key minerals enable a step change in representing dust composition, offering the first opportunity to test how directly-observed spatial variations in dust alkalinity influence atmospheric chemistry and radiative behavior on a global scale. A comprehensive description of EMIT can be found in Section 3.2.2.

In this chapter comprises the first implementation of EMIT-derived surface mineralogy to quantify the atmospheric implications of source-resolved mineral variability. We first incorporate EMIT $CaCO_3$ into the MONARCH atmospheric chemistry model (Section 3.1), constraining dust emissions with satellite-inverted observations. From the investigation performed in Chapter 5, the treatment of heterogeneous chemistry used in the present chapter comprises the reversible fine and coarse SIA formation through the calculation of thermodynamic equilibrium (i.e. double call mechanism, DBCLL).

The resulting simulations are evaluated against airborne observations of $CaCO_3$ content to benchmark EMIT's realism relative to existing global datasets (Claquin et al.

1999, Journet et al. 2014). This framework provides a state-of-the-art representation of dust–NO_3^- interactions and enables us to isolate the effects of realistic $CaCO_3$ distributions on SIA formation and aerosol acidity. We show to what extent accounting for spatial variability in dust mineralogy leads to regional shifts in NO_3^- production and aerosol pH, affecting air quality, NO_3^- pollution extremes, and the climatic influence of mineral dust.

This chapter is structured as follows:

Section 6.2 describes the methodology, including mineral data 6.2.1, the model framework 6.2.2, the constrain on dust emissions 6.2.3, the calculation of dust acidity 6.2.4, the sensitivity simulations performed 6.2.5, the evaluation methodology 6.2.6, and the methodology followed to select extreme episodes of particulate NO_3^- formation 6.2.7.

Section 6.3 presents the results for simulated $CaCO_3$ concentrations 6.3.1, for the resulting NO_3^- column loads 6.3.2, surface concentrations and aerosol acidity 6.3.3, and the observational evaluation and assessment on extreme formation episodes of particulate NO_3^- 6.3.4.

6.2 Methods

6.2.1 EMIT spaceborne retrievals of soil-surface mineralogy

This chapter represents the first incorporation of observationally constrained $CaCO_3$ data from the EMIT imaging spectrometer (Brodrick et al. 2025) into an atmospheric chemistry model.

EMIT is comprehensively described in Section 3.2.2. In this section, some contextual information and a summary the main characteristics of this dataset are provided.

As detailed in Section 3.2.1, pre-EMIT mineral atlases such as Claquin et al. (1999) (CLAQ) and Journet et al. (2014) (JOUR) are based on mean mineral compositions of soil types, extrapolating sparse soil sample measurements to globally characterize dust source areas via soil classification schemes and empirical rules. Consequently, both CLAQ and JOUR are susceptible of major uncertainties in dust composition modeling (Perlwitz et al. 2015a, Li et al. 2024a, Gonçalves Ageitos et al. 2023).

The EMIT mineralogical atlas represents the first empirical, near-global, high-resolution retrieval of soil mineralogy based on satellite-retrieved observations of arid and semi-arid regions between $\pm 51.6^{\circ}$ latitude. Launched in 2022 onboard the International Space Station, EMIT identifies the distinctive absorption features of reflected sunlight from surface minerals employing radiative transfer models (Thompson et al. 2024).

Its spectral coverage ranges from the UV to the infrared at 7.5 nm spectral resolution. The spatial sampling reaches 60-meter resolution, which serve to derive mineral abundances at 0.5º resolution via the reflectance spectra (Brodrick et al. 2025) interpreted through a Hapke-style model coupled with the Tetracorder spectral-matching algorithm (Clark et al. 2024).

We use the EMIT version 2 mineral abundance map of $CaCO_3$, which is relevant for this study. However, EMIT can map hundreds of mineral species, with an especial focus on: quartz, feldspar, illite, smectite, kaolinite, calcite, gypsum, hematite, chlorite, vermiculite, goethite, montmorillonite, hematite+goethite (Fe oxides).

In this chapter we constrain the dust mineral representation to $CaCO_3$ due to its primordial chemical role in dust heterogeneous reactions. Clay and silt content of $CaCO_3$ are derived from size-resolved observational ratios from JOUR (Journet et al. 2014, Gonçalves Ageitos et al. 2023).

6.2.2 Modeling dust mineralogy and heterogeneous chemistry

To investigate the influence of dust mineralogy on heterogeneous atmospheric chemistry, we employ the MONARCH model (Pérez et al. 2011, Jorba et al. 2012, Spada et al. 2013, Spada 2015, Klose et al. 2021, Navarro-Barboza et al. 2024), comprehensively described in Section 3.1. The developments incorporated for this Thesis are also explained in Chapter 4.

In this chapter, dust heterogeneous chemistry is implemented with the double call (DBCLL) mechanism, comprehensively described in Section 4.4, and evaluated in Chapter 5. The DBCLL method calculates gas–aerosol partitioning of $HNO_{3(g)}$, $NH_{3(g)}$, and $H_2SO_{4(g)}$ with the ISORROPIA-II model assuming metastable conditions (Usher et al. 2003, Krueger et al. 2003, Hodzic et al. 2006, Adebiyi and Kok 2020). The partitioning depends upon pH, humidity, and Ca^{2+} from $CaCO_3$ dust content. We treat $CaCO_3$ as the dominant dust-derived contributor to the pool of NVCs involved in dust heterogeneous chemistry, owing to its comparatively high solubility and its strong buffering capacity under atmospherically relevant humid conditions. Accordingly, we assume that $CaCO_3$ completely dissociates into Ca^{2+} and CO_3^{2-} within the liquid coatings of dust particles (Usher et al. 2003).

The dissolved Ca^{2+} is treated as the only dust-sourced NVC participating in heterogeneous neutralization reactions, together with additional ions originating from sea salt (i.e. Na^+, Cl^-, and SO_4^{2-}). This formulation allows us to directly isolate and quantify the contribution of $CaCO_3$ to dust heterogeneous chemistry.

While other dust mineral species such as clays (e.g., illite, smectite), and feldspars may also contain mineral calcium (Ca), together with Na and K, their contribution is

expected to be negligible due to their very low solubility and slow dissolution kinetics, which are incompatible with the typically short atmospheric residence time of dust particles (hours to days) (Guo et al. 2023, Usher et al. 2003). In particular, Ca in feldspars is largely structurally bound and not readily exchangeable or reactive under atmospheric conditions. Gypsum ($CaSO_4$), although more soluble than most silicate minerals, is excluded because its abundance in mineral dust is generally very low and because it does not contribute net alkalinity to the aerosol aqueous phase. Dissolution of $CaSO_4$ releases Ca^{2+} together with SO_4^{2-}, and therefore may not enhance the neutralization capacity of dust compared to NO_3^-.

Consequently, these sources are excluded from our estimate of reactive Ca^{2+} or additional NVCs susceptible to participate in heterogeneous reactions (e.g. K^+ and Mg^{2+}), and we restrict our analysis to Ca^{2+} originating from $CaCO_3$.

To derive size-resolved Ca^{2+} concentrations from modeled $CaCO_3$, we apply the following conversion based on their relative molar masses:

$$[Ca^{2+}] = \frac{Mw_{(Ca)}}{Mw_{(CaCO_3)}}[CaCO_3] = \frac{40.08}{100.09}[CaCO_3] \approx 0.4[CaCO_3] \tag{6.1}$$

This formulation is used consistently across all size bins and mineral datasets considered in this study.

Particulate SO_4^{2-} forms through three main pathways: (1) aqueous-phase oxidation of $SO_{2(g)}$ and DMS in the fine mode; (2) direct uptake of $SO_{2(g)}$ onto preexisting dust and sea salt particles in both fine and coarse modes, modulated by the Ca^{2+} content (Prince et al. 2007, Fairlie et al. 2010, Soussé Villa et al. 2025); and (3) condensation of kinetically limited $H_2SO_{4(g)}$ vapor into each particle mode, assuming that its low volatility prevents it from remaining in the gas phase (Pringle et al. 2010).

The thermodynamic equilibrium model determines various reactivity scenarios based on the relative abundance of acid and basic species present at each gridcell and timestep. The available non-neutralized cations and anions in the liquid medium determine the aerosol pH, which drives the condensation/evaporation rates of gas/aerosol species. For instance, low pH values (acidic conditions) — like those caused by elevated $H_2SO_{4(g)}$ condensation rates — shift the $NH_{3(g)}$-NH_4^+-$HNO_{3(g)}$-NO_3^- neutralization system towards $HNO_{3(g)}$ gas and NH_4^+ aerosol, while high pH (alkaline conditions) enhances the formation of NO_3^- aerosol and leaves more $NH_{3(g)}$ in the gas phase (Weber et al. 2016). Consequently, as more comprehensively explained in Section 1.3.4, aerosol pH plays a pivotal role for particulate NO_3^- formation, together with AWC and temperature. For instance, previous studies have proposed that pH values above 2.5-3.0 substantially enhance NO_3^- synthesis, while almost completely disabling it when pH is below 1.5-2.0

units (Nenes et al. 2020, Kakavas et al. 2021). If dust minerals are present, they contribute with alkalinity and NVCs to the aerosol liquid medium, enhancing NO_3^- and SO_4^{2-} formation from the condensation of acidic gas species to the aerosol phase.

Sea-salt is assumed to provide a globally homogeneous ionic composition of 55% Cl^-, 30.6% Na^+, 7.7% SO_4^{2-}, 3.7% Mg^{2+}, 1.2% Ca^{2+}, and 1.1% K^+ for all size bins, based on (Seinfeld and Pandis 2006).

6.2.3 Satellite-based constraints on modeled dust emissions

The wide variability in estimated dust flux across modeling studies arises from uncertainties in dust emission parameterizations, soil and surface properties, meteorological forcing, and model configuration. This variability poses a particular challenge for modeling dust mineralogy, since the emitted mineral composition is directly scaled by the magnitude, timing, and location of dust emissions. As a result, errors in dust emissions propagate linearly into simulated atmospheric mineral abundances, potentially biasing the representation of chemically and radiatively active components such as $CaCO_3$ and Fe oxides.

To mitigate this source of uncertainty, we constrain dust emissions using satellite-derived dust optical depth (DOD) through an offline ensemble-based inversion framework. This approach is based on a modified Local Ensemble Transform Kalman Filter (LETKF), in which dust emissions are treated as the control variable and adjusted retrospectively to minimize discrepancies between simulated and observed DOD (Escribano et al. 2023).

The inversion assimilates dust-filtered aerosol optical depth retrievals from the SNPP-VIIRS Deep Blue product (Sayer et al. 2019, Hsu et al. 2019). The observational operator is the full MONARCH dust model, which links emissions to DOD through explicit simulation of transport and removal. Under the working assumption that uncertainties in simulated DOD are dominated by errors in dust emissions rather than by transport, deposition, or optical properties, the assimilation attributes the bulk of model–observation mismatches to emission errors.

Uncertainty in dust emissions is represented through a 100-member ensemble, constructed by perturbing emissions in both space and time. Spatial perturbations are generated using correlated Gaussian noise with characteristic length scales comparable to major dust source regions, allowing the inversion to correct emissions at regional scales. Temporal perturbations are designed to explicitly resolve the lagged influence of emissions on atmospheric DOD, by perturbing emissions over contiguous multi-day windows and allowing their impact to propagate forward in time. This ensemble design enables the LETKF to attribute DOD mismatches to the appropriate emission periods

while accounting for the finite atmospheric residence time of dust aerosols (order of days).

The MONARCH dust module includes several dust emission parameterizations (Pérez et al. 2011, Klose et al. 2021). In this study, we employ the G01-UST scheme (Klose et al. 2021) as the prior emission configuration before assimilation. This scheme combines a topography-based dust source function (Ginoux et al. 2001) with a physically based dust flux formulation (Gillette and Passi 1988) driven by friction velocity, and includes dependencies on soil moisture (Fécan et al. 1999), and surface roughness from vegetation and non-erodible elements (Marticorena and Bergametti 1995). The satellite-constrained emission fields derived from the inversion are subsequently used as input for the mineralogical simulations presented in this study.

6.2.4 Calculation of pH averages

Aerosol pH is diagnosed from 6-hourly instantaneous values of the proton concentration ($[H^+]$) as:

$$pH = -log_{10}(a_{H+}) \approx -log_{10}([H^+]) \tag{6.2}$$

Were a_{H+} is the activity of protons in the solution, assumed to be equivalent to the $[H^+]$ outputs from the ISORROPIA-II thermodynamic model.

As noted in previous studies (Wang et al. 2024b), the methodology used to compute temporal averages of pH can have a significant influence on the resulting values. Because pH is a logarithmic quantity, different averaging approaches implicitly weight acidic and less acidic conditions differently. To date, no consensus has emerged regarding a preferred averaging strategy for aerosol pH (Pye et al. 2020, Karydis et al. 2021, Rémy et al. 2024, Wang et al. 2024b). We therefore report pH statistics using the two most commonly applied approaches in the literature.

The first approach computes the arithmetic mean of instantaneous pH values:

$$\bar{pH} = \frac{1}{N}\sum_{i}^{N} pH_i \tag{6.3}$$

The second approach computes pH from the mean proton activity (i.e. proton concentration), which gives greater weight to more acidic conditions:

$$\bar{pH} = -log_{10}(\frac{1}{N}\sum_{i}^{N} 10^{-pH_i}) \tag{6.4}$$

These two averaging methods yield systematically different pH distributions and can lead to quantitatively different estimates of pH differences between sensitivity simulations.

Finally, pH is diagnosed only under humid conditions, considering exclusively grid points and times for which aerosol liquid water is present and RH exceeds 10%. As a result, differences reported between the SB and AVG simulations reflect changes in aerosol acidity only during periods when aqueous-phase chemistry is active.

6.2.5 Simulations

To assess the influence of dust mineralogical variability on atmospheric composition, we conducted a series of global simulations using the MONARCH atmospheric chemistry model. Each experiment differs only in the specification of mineralogy in emitted dust, allowing the effects of mineralogical assumptions to be isolated from those of emission magnitude or meteorology. The only dust mineral considered to participate in gas-aerosol heterogeneous reactions is $CaCO_3$, providing Ca^{2+}.

We employed the different mineralogical datasets to prescribe the spatial and size-dependent distribution of minerals at the dust source regions. For each dataset, the model was run using a source-based (SB) configuration, which retains the full spatial variability of minerals at emission. In the case of EMIT, an additional globally averaged (AVG) configuration was performed, in which the size-resolved $CaCO_3$ fractions at emission were replaced by their global mean values from the EMIT–SB run.

This experimental design (Fig 6.1) enables direct quantification of how spatially resolved versus spatially uniform $CaCO_3$ distributions affect SIA formation and aerosol acidity.

All experiments share identical meteorology and dust emission timing, ensuring that differences among simulations reflect only the representation of $CaCO_3$ and its associated alkalinity. A summary of the simulations is provided in supplementary Table B.2.

Simulations were conducted on a global domain for the year 2018, after a half-year spin-up. The spatial resolution is 1.4^{o} longitude by 1.0^{o} latitude, with 48 hybrid pressure-sigma vertical layers up to 5hPa. The ERA5 reanalysis datasets (Hersbach et al. 2023) are used to initialize meteorology, and meteorological variables are restored every 24h to minimize their bias with observations. Dynamics were computed in 180s timesteps, and model outputs are produced every 6 hours.

For anthropogenic emissions, the HERMESv3_GR (Guevara et al. 2019) is utilized to process emissions from anthropogenic and biomass-burning sources. In this study, we employed HERMES with the CAMS-GLOB-ANT_v4.2 inventory (Soulie et al. 2024) for anthropogenic emissions with updated temporal profiles (Guevara et al. 2021), while

GFASv1.2 was used for fire emissions (Kaiser et al. 2012). Finally, DMS emissions from oceanic sources are obtained from CAMS-GLOB-OCE v3.1 (Lana et al. 2011, Denier van der Gon et al. 2023).

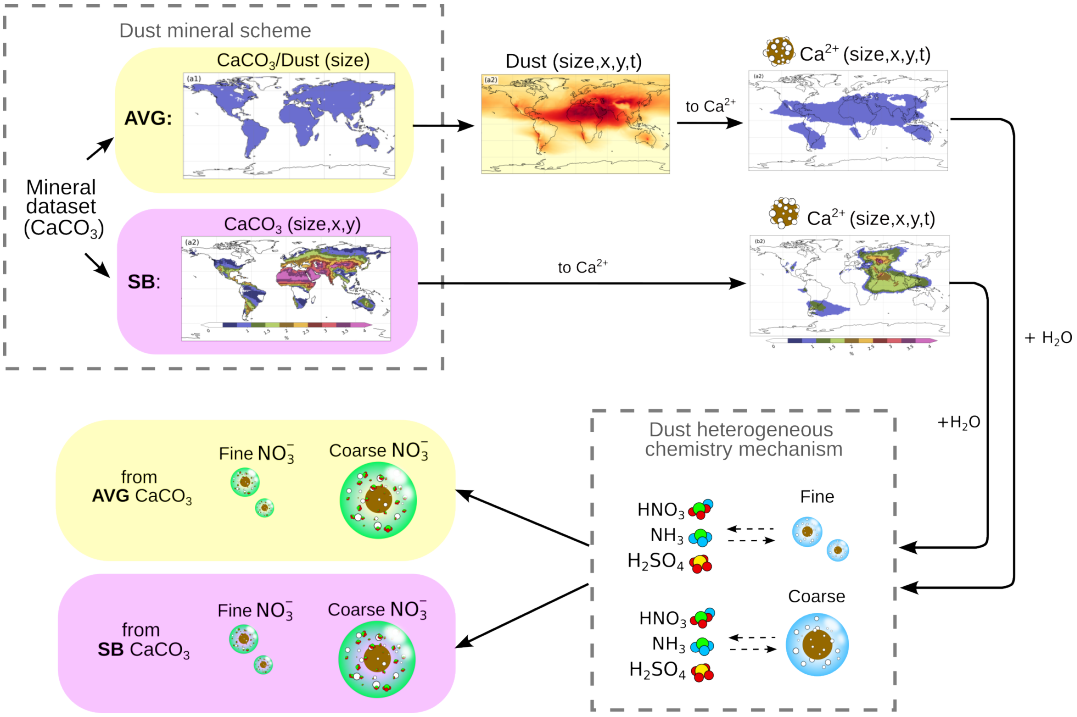

Figure 6.1: Illustration of the methodology to compare EMIT simulations using source-based (SB) versus globally averaged (AVG) mineral data.

For reference, in supplementary Table B.1, particulate NO_3^- budgets with all simulations are compared with the literature results (Bian et al. 2017, Rémy et al. 2019; 2022; 2024).

6.2.6 Model evaluation

The modeled $CaCO_3$ mass fractions were evaluated against a compilation of in situ measurements of surface concentrations and deposition from long-term observational datasets spanning the late 1960s to the present day (Perlwitz et al. 2015b) (supplementary Fig. B.3). Model–observation pairs were collocated in time, space, and particle size. Given that the variability of dust mineralogy at specific locations is expected to be small over decadal timescales, the dataset was considered representative of regional mineralogical patterns at climatological scales. To account for seasonal variations, we considered the reported months in the observations to compare them with the corresponding monthly means from the model. Uncertainties associated with comparing high-frequency observations to monthly means were estimated as in (Perlwitz et al. 2015a). Spatial collocation used the model value at the nearest grid cell for fixed stations and an average

along the modeled trajectory for shipborne measurements. Size collocation accounted for mineralogical variability across particle diameters and included only the size ranges reported in the observations up to 20 μm—the upper limit of the MONARCH model's size distribution. Observations covering larger size ranges are shown for completeness but were excluded from the calculation of the normalized mean bias, normalized RMSE, and Pearson correlation coefficients.

Surface concentrations of NO_3^- were evaluated against monthly-mean observations from the GHOST project (Section 3.4), a publicly available repository of harmonized global surface observations initiative of the BSC's Earth Department (Bowdalo et al. 2024). The selected stations (Fig. 6.6) belong to rural and background locations to avoid data close to anthropogenic emission sources, since these might not be properly represented due to the global model resolution not capturing local emission plumes and small-scale topography. The quality flags used for the selected stations are described in supplementary Table A.5. Particulate NO_3^- is evaluated solely over those stations located in areas with statistically-significant ($p<0.05$) differences between sensitivity runs.

6.2.7 Regional assessment of high NO_3^- formation events

We analyzed the implications of $CaCO_3$ variability on surface concentrations of particulate NO_3^-, focusing on continental regions. To highlight potential air-quality impacts, the analysis was restricted to periods of high coarse-mode NO_3^- formation. Oceanic grid cells were excluded using a sea mask to minimize sea salt influence.

High-formation events were identified statistically for EMIT using Equation 6.5. At each grid cell, the 6-hourly time series of coarse-mode NO_3^- surface concentrations from the SB and AVG simulations (C_{SB} and C_{AVG}, respectively) were differenced in time. Differences (ΔC) exceeding the 99th percentile or falling below the 1st percentile were classified as extreme positive or negative events:

$$\Delta C = \frac{\sum_{t=0}^{T} \left(C_{SB}(t) - C_{AVG}(t)\right)}{N_t} \begin{cases} C_{SB}(t) - C_{AVG}(t) > p99(C_{SB}(t) - C_{AVG}(t)) \\ C_{SB}(t) - C_{AVG}(t) < p01(C_{SB}(t) - C_{AVG}(t)) \end{cases} \tag{6.5}$$

Different regional domains are defined in this analysis, which separate areas with distinct dust–pollution interactions, as listed in supplementary Table B.3. For each region, the temporal mean of these differences were computed to characterize systematic shifts between the SB and AVG approaches, minimizing the influence of isolated outliers. The geographical distributions of the resulting mean differences were used to assess the

spatial extent and intensity of coarse NO_3^- formation anomalies, that have the 6-hourly temporal resolution of the used timeseries.

6.3 Results

6.3.1 Improvements in global $CaCO_3$ representation

Accurate representation of $CaCO_3$ content in airborne dust is essential for simulating particulate NO_3^- formation, yet it has long been limited by sparse and uneven observational constraints. Existing global mineralogy atlases—such as those by CLAQ and JOUR —relied on soil measurements that are few in number and unevenly distributed, often extrapolated across broad regions based on generalized soil classifications. The most comprehensive of these, the JOUR dataset, is derived from fewer than 700 soil samples, representing just 55% of FAO soil units, leaving many key arid dust-producing regions underrepresented or absent (Gonçalves Ageitos et al. 2023).

To overcome these limitations, we implemented the new global mineralogy dataset from NASA's EMIT mission (Brodrick et al. 2025), comprehensively explained in Sections 3.2.2 and 6.2.1. Via spaceborne spectroscopic observation of surface mineralogy, EMIT enables direct retrieval of $CaCO_3$ and other minerals abundance at high spatial resolution across all major dust source regions.

We incorporated EMIT, together with the CLAQ and JOUR mineralogical datasets, into the MONARCH atmospheric chemistry model (Section 3.1) constraining the model's dust source function through assimilation of DOD from SNPP-VIIRS (Sayer et al. 2019, Hsu et al. 2019, Escribano et al. 2022) (Section 6.2.3). After assimilation, substantial regional and temporal adjustments occur in the estimated emissions (supplementary Fig. B.1), yielding spatially and temporally consistent dust fluxes that more accurately capture observed DOD variability. The impact of these corrections on the DOD was evaluated by comparing simulated DOD against independent AERONET sunphotometer observations, which show a marked improvement in model skill relative to simulations using uncorrected emissions (supplementary Fig. B.2), both increasing the correlation and reducing the RMSE temporally and spatially. These optimized emission fields provide a more realistic basis for representing atmospheric dust mineralogy and for simulating dust–nitrogen interactions.

Figure 6.2 illustrates the spatial distribution of modeled Ca^{2+} emissions, the Ca^{2+}-to-dust surface mass fraction, and the evaluation against airborne measurements of $CaCO_3$ content. Results are presented for identical experiments varying exclusively the mineralogical source data, that is JOUR, CLAQ, and EMIT. All three datasets produce peak Ca^{2+} emissions over the global dust belt, with prominent sources in the

Sahara, Middle East, and central Asia. However, notable differences emerge in the spatial detail and magnitude of $CaCO_3$ representation. CLAQ yields relatively low $CaCO_3$ fractions, while JOUR identifies regions with moderate $CaCO_3$ enrichment. The broader, less localized features in both representations may reflect the limitations of extrapolating sparse soil data to large FAO units. EMIT, in contrast, shows fine-scale variability and localized high-$CaCO_3$ hotspots, with high values in the Middle East and East Asian sources, while highlighting low-$CaCO_3$ areas such as portions of the Sahara and Australia, inducing low Ca^{2+} dust fractions over these regions (*a2-c2*).

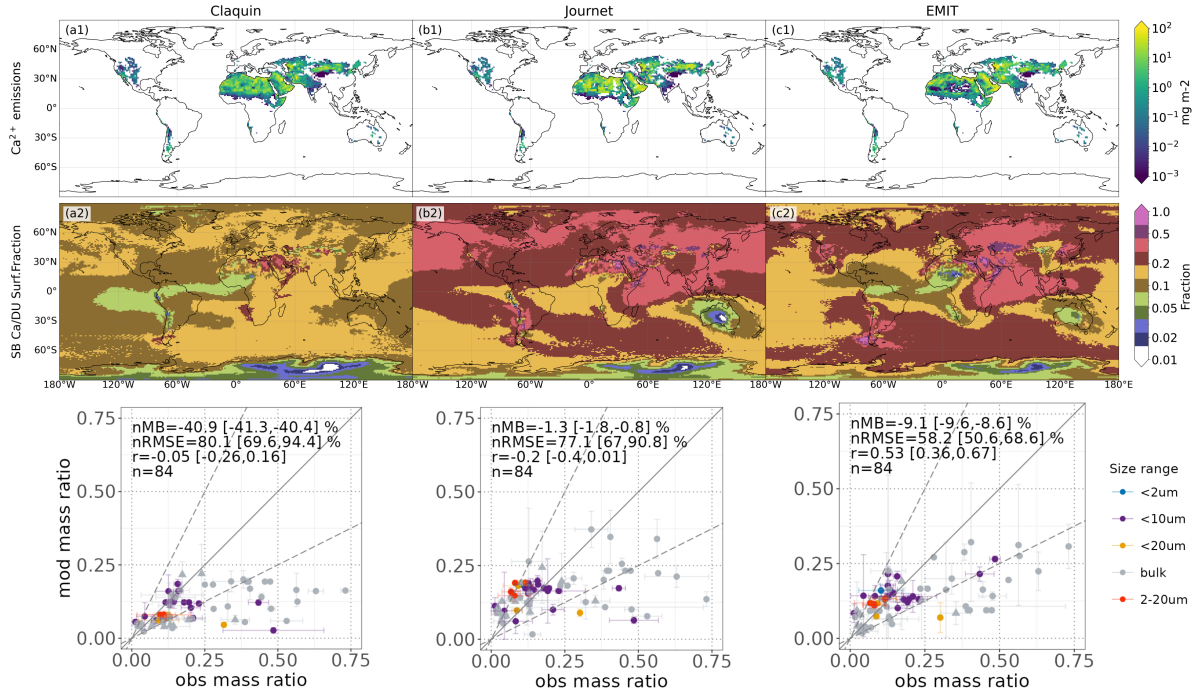

Figure 6.2: Spatial distributions of modeled Ca^{2+} emissions (top), surface Ca^{2+}-to-dust mass fractions (middle), and comparison with airborne $CaCO_3$ observations (bottom) for the CLAQ, JOUR, and EMIT mineral datasets. All simulations use dust emissions constrained through the assimilation of satellite-retrieved dust optical depth.

The bottom panels compare modeled and observed $CaCO_3$ mass fractions across available atmospheric measurements, covering a range of particle sizes and locations (see Section 6.2.6 and supplementary Fig. B.3), in all cases benefiting from constrained dust emissions through DOD assimilated data. CLAQ and JOUR perform poorly in capturing variability (r = -0.05 and -0.20, respectively). EMIT, by contrast, achieves the best overall agreement with observations, lowering the error (normalized RMSE) to 58.2%, and scoring a correlation of 0.53.

These results demonstrate that, compared to JOUR and CLAQ, the spatially realistic soil $CaCO_3$ distributions retrieved with EMIT markedly improve the agreement with atmospheric measurements of airborne $CaCO_3$. Consequently, we adopted EMIT as the

baseline mineralogy dataset for all subsequent simulations and sensitivity experiments examining the role of SB versus AVG $CaCO_3$ representations. In the SB configuration, the heterogeneous $CaCO_3$ soil fractions are preserved for each size bin, whereas the AVG configuration replaces this heterogeneity with a simplified, globally uniform $CaCO_3$ fraction for each size bin (Section 6.2).

6.3.2 Impacts on NO_3^- and other SIA burdens

In this section we start by presenting the column loads of SIA species (Fig. 6.3) obtained with the DBCLL mechanism using the EMIT SB $CaCO_3$ data.

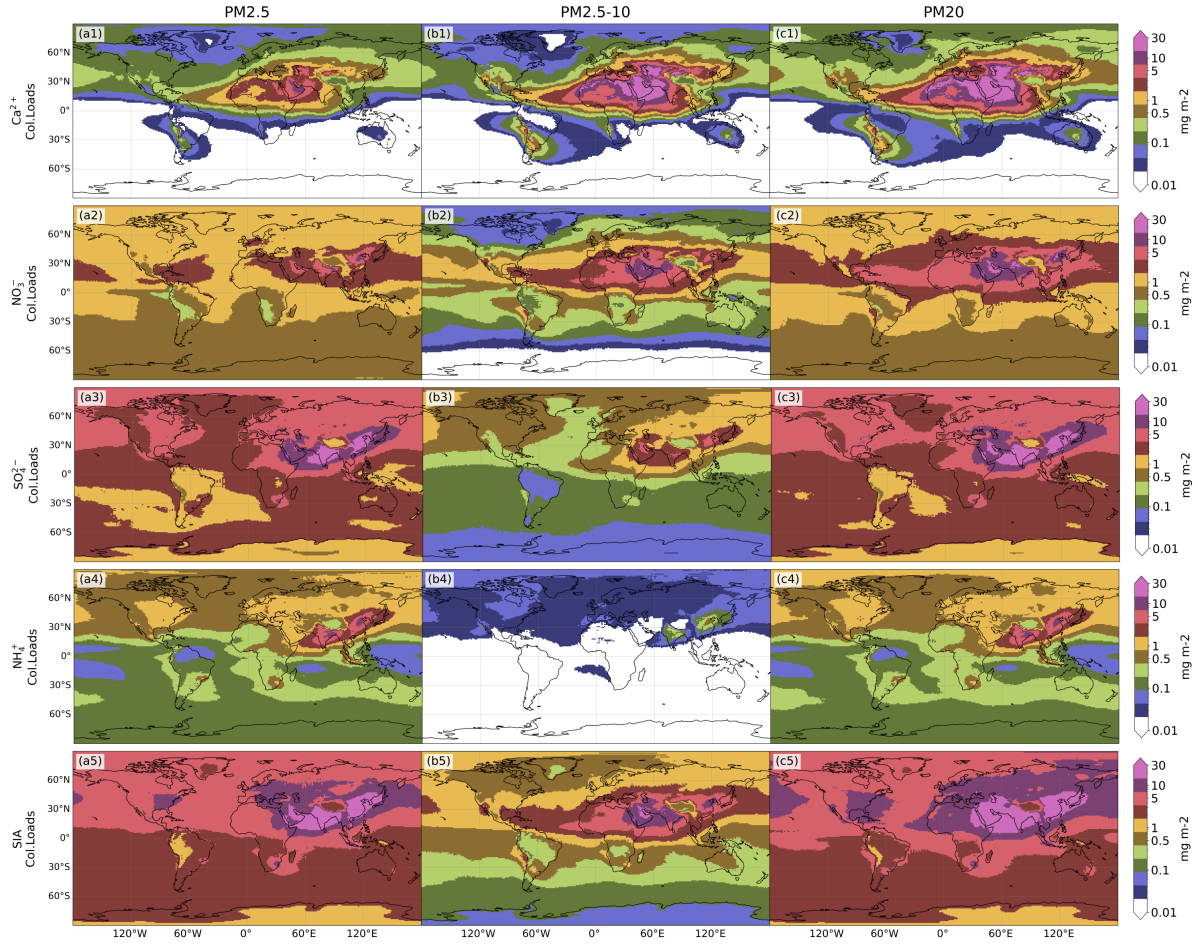

Figure 6.3: Column loads for NO_3^-, NH_4^+, SO_4^{2-} and total SIA for fine ($D < 2.5\mu m$, coarse ($2.5 < D < 10\mu m$), and total ($D < 20\mu m$) size modes using EMIT source-based $CaCO_3$ distribution.

The largest total NO_3^- burdens occur over East Asia and the Middle East (Fig. 6.3), where dust and anthropogenic emissions coincide to favor NO_3^- formation. Coarse NO_3^- ($2.5 < D < 10\mu m$) dominates over dusty regions such as the Middle East, whereas

fine NO_3^- ($D < 2.5\mu m$) accounts for most of the global burden (supplementary Table B.1).

The geographical availability of NVCs and $NH_{3(g)}$, and their coincidence with SIA formation, provides some hints on the neutralization regime dominant over each region. The most representative region governed by NVC-driven SIA formation is the Middle East: abundant NO_3^- ($\sim$10 $mg\ m^{-2}$) and SO_4^{2-} formation, particularly in the coarse mode ($2.5 < D < 10\mu m$), aligns with high Ca^{2+} dust fractions (more than 50%, Fig. 6.2*c2*) and relatively low $NH_{3(g)}$ availability, resulting in low NH_4^+ concentrations (*b2*) and SIA composed by coarse $CaSO_4$ and $Ca(NO_3)_2$. The former coincides with the intensified uptake of $SO_{2(g)}$ over dust particles, modulated by the elevated dust content in $CaCO_3$.

Conversely, an increased contribution from $NH_{3(g)}$ neutralization is found over East Asia and India, where the simultaneous high loads of NO_3^-, SO_4^{2-}, and NH_4^+, especially in the fine mode, along with moderate Ca^{2+} fractions (less than 30% of total dust, Fig. 6.2*c2*), indicates that SIA is partially composed by fine NH_4^+ salts (i.e. NH_4NO_3, $(NH_4)_2SO_4$), mixed with fine and coarse $CaSO_4$ and $Ca(NO_3)_2$.

A final paradigmatic case is the Sahara desert, where the presence of high NO_3^- (5 $mg\ m^{-2}$, Fig. 6.3*c2*), but low concentrations of other SIA species, and moderate Ca^{2+} loads (less than 10%, Fig. 6.2*c2*), suggest that locally-emitted Ca^{2+} is the limiting factor for particulate NO_3^- formation, whose elevated loads might also be the result of the interaction with of Ca^{2+} transported from high emission areas in the east and north of the Sahara (Fig. 6.2*c1*).

With the improved $CaCO_3$ representation in place, we next evaluate how EMIT-SB heterogeneity versus AVG $CaCO_3$ distributions (Section 6.2.5) influence SIA formation, while in both cases constraining dust emissions through DOD assimilation (Section 6.2.3). Figure 6.4 presents the absolute differences in global column burdens of fine, coarse, and total Ca^{2+}, and SIA, between SB and AVG simulations (relative differences are displayed in supplementary Fig. B.4). Differences in NO_3^- burdens largely mirror spatial variations in total Ca^{2+} loading between experiments. Over East Asia and the Sahara, the SB simulation yields lower NO_3^- columns than the AVG simulation (reductions up to 2 $mg\ m^{-2}$, or 20%) coinciding with reduced Ca^{2+} concentrations (reductions up to 10 $mg\ m^{-2}$ in East Asia and 30 $mg\ m^{-2}$ in the Sahara, or up to 150%). In contrast, over the Middle East, SB enhances both fine and coarse NO_3^- (by 0.5-1 $mg\ m^{-2}$, +10-20%), in line with higher Ca^{2+} loads (up to +7 $mg\ m^{-2}$ in the fine and +60 $mg\ m^{-2}$ in the coarse size, increase of 110%). These results confirm the strong control exerted by $CaCO_3$ on heterogeneous acid–base reactions that form NO_3^-.

On a global scale, SB increases total NO_3^- by roughly 10% across remote regions such as the polar oceans and the Indian Ocean, driven by enhanced fine-mode NO_3^- formation. These increases reflect improved spatial alignment between $CaCO_3$ availability and temporally varying dust emissions, captured by the EMIT mineralogy combined with DOD-constrained emission fields.

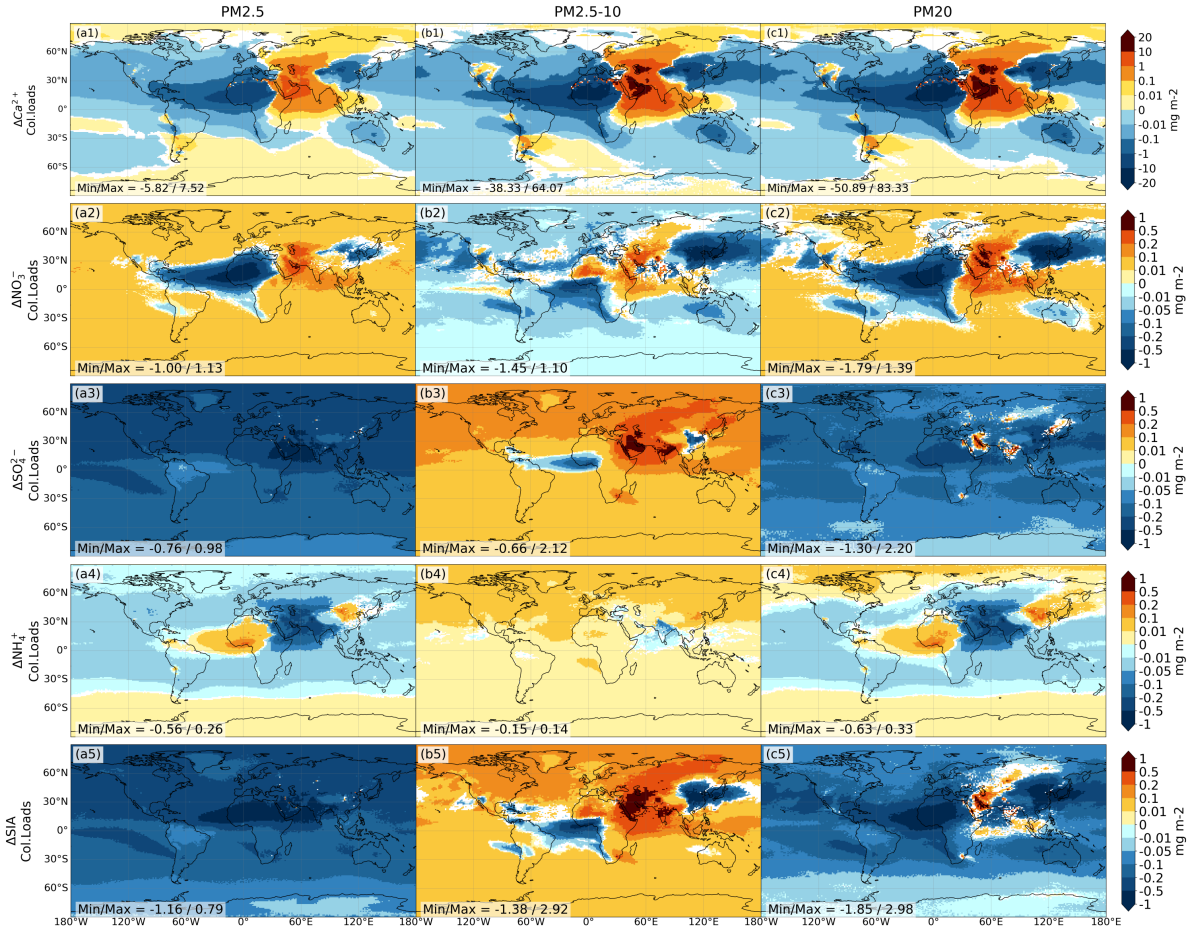

Figure 6.4: Absolute differences between EMIT source-based (SB) and globally averaged (AVG) $CaCO_3$ representations in column burdens of fine ($D < 2.5\mu m$), coarse ($2.5 < D < 10\mu m$), and PM20 (full size range up to 20 μm) species. Panels show (a1–c1) ionic Ca^{2+}, (a2–c2) particulate NO_3^-, (a3–c3) SO_4^{2-}, (a4–c4) NH_4^+, and (a5–c5) SIA (i.e. NO_3^- + SO_4^{2-} + NH_4^+). White gridcells indicate non statistically significant differences ($p<0.05$).

A visible exception to the otherwise direct Ca^{2+}–NO_3^- relationship emerges over the central Sahara. In this region, coarse NO_3^- increases under SB conditions (by 0.2–0.5 $mg\ m^{-2}$) despite lower SB Ca^{2+} burdens (10 $mg\ m^{-2}$). This apparent decoupling is driven by the low $HNO_{3(g)}$ burden characteristic of the central Sahara. Under these $HNO_{3(g)}$-limited conditions, the AVG simulation introduces more Ca^{2+} in both the fine and coarse modes; however, the key difference lies in the fine mode. Because AVG contains substantially more fine-mode Ca^{2+}, it rapidly consumes the scarce $HNO_{3(g)}$ to

form fine NO_3^-, leaving little acid available for coarse NO_3^- production. In contrast, the SB simulation carries less Ca^{2+} overall, but its lower fine-mode Ca^{2+} burden does not exhaust the limited $HNO_{3(g)}$ pool (supplementary Fig. B.5). As a result, more gas-phase $HNO_{3(g)}$ remains available to partition to coarse particles, yielding higher coarse NO_3^- under SB than under AVG despite the reduced total Ca^{2+} load.

Over Europe, the Indian subcontinent, and the northern and central Atlantic, coarse NO_3^- concentrations are either non statistically significant or they show pronounced heterogeneity despite relatively uniform coarse Ca^{2+} fields. This likely reflects spatially varying $HNO_{3(g)}$ and $H_2SO_{4(g)}$ precursor sources, competition with particulate SO_4^{2-} to react with NVC, and the influence of complex topography and long-range NO_3^- transport. In western North America, localized Ca^{2+} hotspots found in the SB simulation (up to 1 $mg\ m^{-2}$, +20%) coincide with enhanced NO_3^- formation (up to 0.2 $mg\ m^{-2}$, +10%).

A marked shift is also observed in particulate SO_4^{2-}. The SB simulation shows globally lower fine-mode SO_4^{2-} burdens (-0.2 to -0.8 $mg\ m^{-2}$, -10 to -20%), and regionally reduced coarse-mode SO_4^{2-} downwind of the Sahara and East Asia (-0.6 $mg\ m^{-2}$, from -10 to -50%). These differences align with Ca^{2+} reductions (-20 to -38 $mg\ m^{-2}$), and reflect the modulation of $SO_{2(g)}$ uptake by dust alkalinity. Because the SB methodology presents higher concentrations of Ca^{2+} in coarse particles near to $SO_{2(g)}$ emission areas (e.g. Middle East), SB enhances coarse-mode uptake of $SO_{2(g)}$ and depletes this precursor gas just after emission. Consequently, the SB run leaves low $SO_{2(g)}$ available for fine-mode SO_4^{2-} formation, suppressing SO_4^{2-} production in the smaller size range. In contrast, evenly-distributed Ca^{2+} concentrations in the AVG run causes lower consumption rates of $SO_{2(g)}$ close to emission areas, leaving it free to form globally higher fields of fine SO_4^{2-}.

The influence of these processes on the gas-phase NO_3^- and NH_4^+ precursors is shown in supplementary Fig. B.5. Differences in NO_3^- and NH_4^+ closely correspond with changes in $HNO_{3(g)}$ and $NH_{3(g)}$ between SB and AVG simulations, reflecting shifts in gas–aerosol partitioning driven by dust alkalinity. In contrast, concentrations of $N_2O_{5(g)}$, which hydrolyzes on SIA particle surfaces (Section 6.2), remain largely unchanged, indicating that the overall nocturnal N budget is less sensitive to $CaCO_3$ distribution than daytime NO_3^- formation.

6.3.3 Impacts on surface concentrations and aerosol acidity

Surface-level absolute differences between SB and AVG Ca^{2+} representations (Fig. 6.5) closely mirror those in column burdens (Fig. 6.4). The corresponding surface concentrations of individual species (Ca^{2+}, NO_3^-, SO_4^{2-}, NH_4^+, and total SIA) for the SB

simulation are provided in supplementary Fig. B.6, and the surface relative differences with respect to the AVG simulation are shown in supplementary Fig. B.7. The SB configuration produces a distinct bipolar pattern in surface Ca^{2+} concentrations, with increases of up to +10 and +80 $\mu g\ m^{-3}$ in the fine and coarse modes, respectively, over the Middle East, and decreases of –5 $\mu g\ m^{-3}$ and –20 $\mu g\ m^{-3}$ over the Sahara and East Asia. The only notable deviation between surface and column differences occurs over northern East Asia, where SB yields higher near-surface Ca^{2+} (up to +5 $\mu g\ m^{-3}$) not reflected in column totals, consistent with regional boundary-layer trapping of dust.

These spatial patterns propagate to SIA. Fine and coarse NO_3^- surface differences align with Ca^{2+} anomalies, reaching +1.7 $\mu g\ m^{-3}$ over the Middle East and –0.5 $\mu g\ m^{-3}$ over the Sahara and East Asia (Fig. 6.5 *a2*-*c2*). The largest surface–column discrepancy occurs for fine SO_4^{2-}: although column burdens are globally lower with SB, surface concentrations increase locally over eastern Europe, the Red Sea, the Persian Gulf, and northern and eastern Asia (up to +0.1 $\mu g\ m^{-3}$, Fig. 6.5 *a3*). This reflects the enhanced near-surface uptake of $SO_{2(g)}$ where SB predicts higher Ca^{2+}, reinforcing the role of dust alkalinity in modulating heterogeneous SO_4^{2-} production.

Total SIA at the surface is enhanced under SB in the Middle East, northeastern Asia, eastern Europe, East Asia, and the Indian Ocean (by 1.0–7.6 $\mu g\ m^{-3}$), primarily reflecting changes in SO_4^{2-} (Fig. 6.5 *c3* and *c5*). Coarse-mode SIA also increases almost globally, but over Australia and central Atlantic, supported by both NO_3^- and SO_4^{2-} contributions.

Surface aerosol acidity shows a pronounced sensitivity to the spatial distribution of $CaCO_3$, underscoring the central role of mineral dust alkalinity in controlling global aerosol pH (Fig. 6.5 *a6* to *c6*). The SB configuration produces systematically more basic aerosols in regions of enhanced Ca^{2+}, with pH increases of up to +3 units over the Middle East, eastern Africa, and some localized hotspots over northern Africa. In contrast, the averaged $CaCO_3$ field under the AVG configuration yields higher pH over and downwind of the Sahara (up to +4 units), East Asia (up to +2 units), and in coarse particles across remote regions (up to +2 units). Local annual mean differences span –4 to +3 pH units, revealing that $CaCO_3$ variability alone can shift aerosol acidity by more than one order of magnitude in H^+ ion concentration. pH values resulting from the SB configuration are provided in supplementary Fig. B.8, showing slightly more acidic but broadly consistent patterns compared with previous studies (Karydis et al. 2021).

It is worth noting that the reported pH averages are based on the arithmetic mean of instantaneous pH values (Eq. 6.3, see Section 6.2.4). For comparison, supplementary Fig. B.9 presents results obtained based on the H^+ activity mean (Eq. 6.4), which yields substantially higher (more basic) pH levels. Under this alternative averaging method,

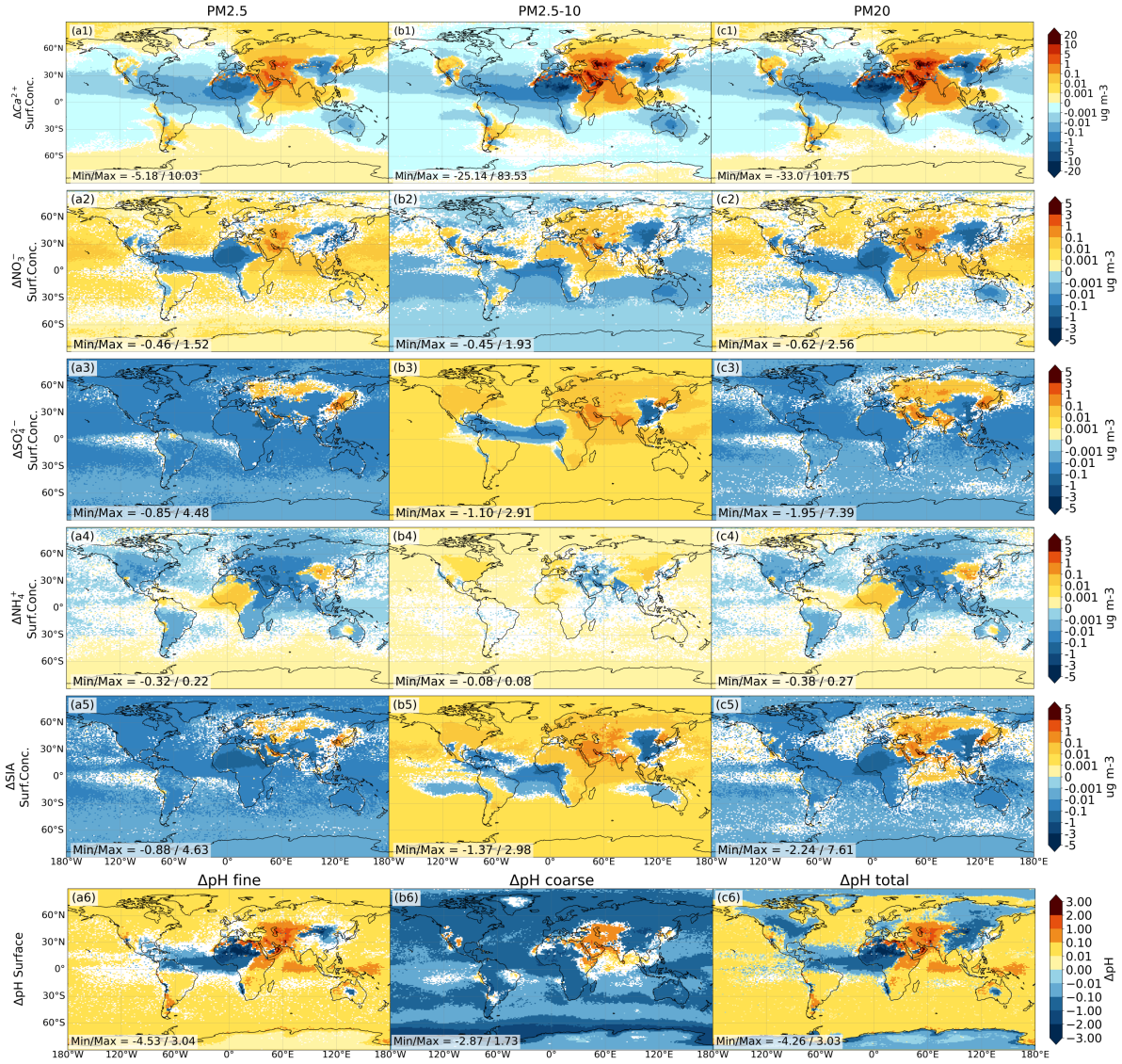

Figure 6.5: Surface-level impacts of $CaCO_3$ variability on Ca^{2+}, secondary aerosols, and pH. Absolute differences in surface concentrations between EMIT SB and AVG simulations for (a1–c1) Ca^{2+}, (a2–c2) NO_3^-, (a3–c3) SO_4^{2-}, (a4–c4) NH_4^+, (a5–c5) SIA, and (a6–c6) aerosol pH.

SB–AVG differences exhibit similar spatial patterns to Fig. 6.5, but with increased variability (–7.3 to +3.7 units). Note that the sensitivity of the acidity results to the methodology chosen to average pH values has also been previously reported (Wang et al. 2024b), highlighting the importance of accounting for the pH calculation approach to ensure reproducibility across studies.

6.3.4 Evaluation and impact on regional extreme episodes

We evaluated the impact of the dust $CaCO_3$ representation on simulated NO_3^- aerosols by comparing surface NO_3^- concentrations from the SB and AVG simulations against

available global observations (Fig. 6.6). To assess both overall model performance and sensitivity to dust heterogeneous chemistry, we distinguish between climatological mean behavior and episodic NO_3^- formation events (Section 6.2.7), for which dust–acid interactions are expected to be most relevant.

At the global scale, monthly mean total NO_3^- concentrations exhibit substantial variability across stations (Fig. 6.6*b*). Both SB and AVG simulations reproduce the observed seasonal cycle and magnitude of NO_3^- reasonably well, and differences between the two configurations remain modest. SB slightly increases the global mean bias relative to AVG (0.29 vs. 0.20 $\mu g\ m^{-3}$), while yielding a higher monthly correlation with observations (r = 0.55 vs. 0.48). However, consistent with the statistical analysis of differences in total NO_3^- (supplementary Fig. B.10), the two configurations are statistically indistinguishable at many observational locations (black dots in Fig. 6.6*a*). Evaluating NO_3^- exclusively over stations where differences are significant—marked as red triangles in Fig. 6.6*a*–reveals improvements in correlation with the SB configuration compared to AVG (supplementary Fig. B.11), despite results still not being statistically significant.

This limited separation in mean evaluation metrics is largely explained by the spatial distribution of the observational network. As shown in Fig. 6.6*a*, the majority of NO_3^- monitoring stations are located in regions where desert dust heterogeneous chemistry is weak, intermittent, or infrequent, such as the eastern United States and much of Europe. In these regions, differences between SB and AVG simulations are small and rarely statistically significant, limiting the sensitivity of mean-state evaluation metrics to dust mineralogical variability. Consistent with this interpretation, supplementary Fig. B.12 further shows that SB and AVG simulations exhibit very similar performance when evaluated using monthly mean $PM_{2.5}$ NO_3^- concentrations across the full observational dataset.

To isolate the impact of dust mineralogy under conditions where dust–acid interactions are most active, we therefore examined NO_3^- variability during extreme NO_3^- formation events (Section 6.2.7). Focusing on the top 1% of coarse-mode NO_3^- formation episodes (Fig. 6.6*c*–*d*), differences between SB and AVG simulations amplify markedly and exhibit pronounced regional heterogeneity. SB produces substantially higher extreme coarse NO_3^- concentrations over northwestern Asia (+5 $\mu g\ m^{-3}$) and the Middle East (+2.5–5 $\mu g\ m^{-3}$), reflecting localized $CaCO_3$-rich dust sources resolved by EMIT. In contrast, the AVG configuration enhances extremes over East and Southeast Asia (+7.5–10 $\mu g\ m^{-3}$), where the assumption of spatially uniform $CaCO_3$ overestimates dust alkalinity and promotes excessive reaction with$HNO_{3(g)}$.

These contrasting responses indicate that the spatial distribution of $CaCO_3$ exerts a first-order control on the location and intensity of extreme NO_3^- events, even when

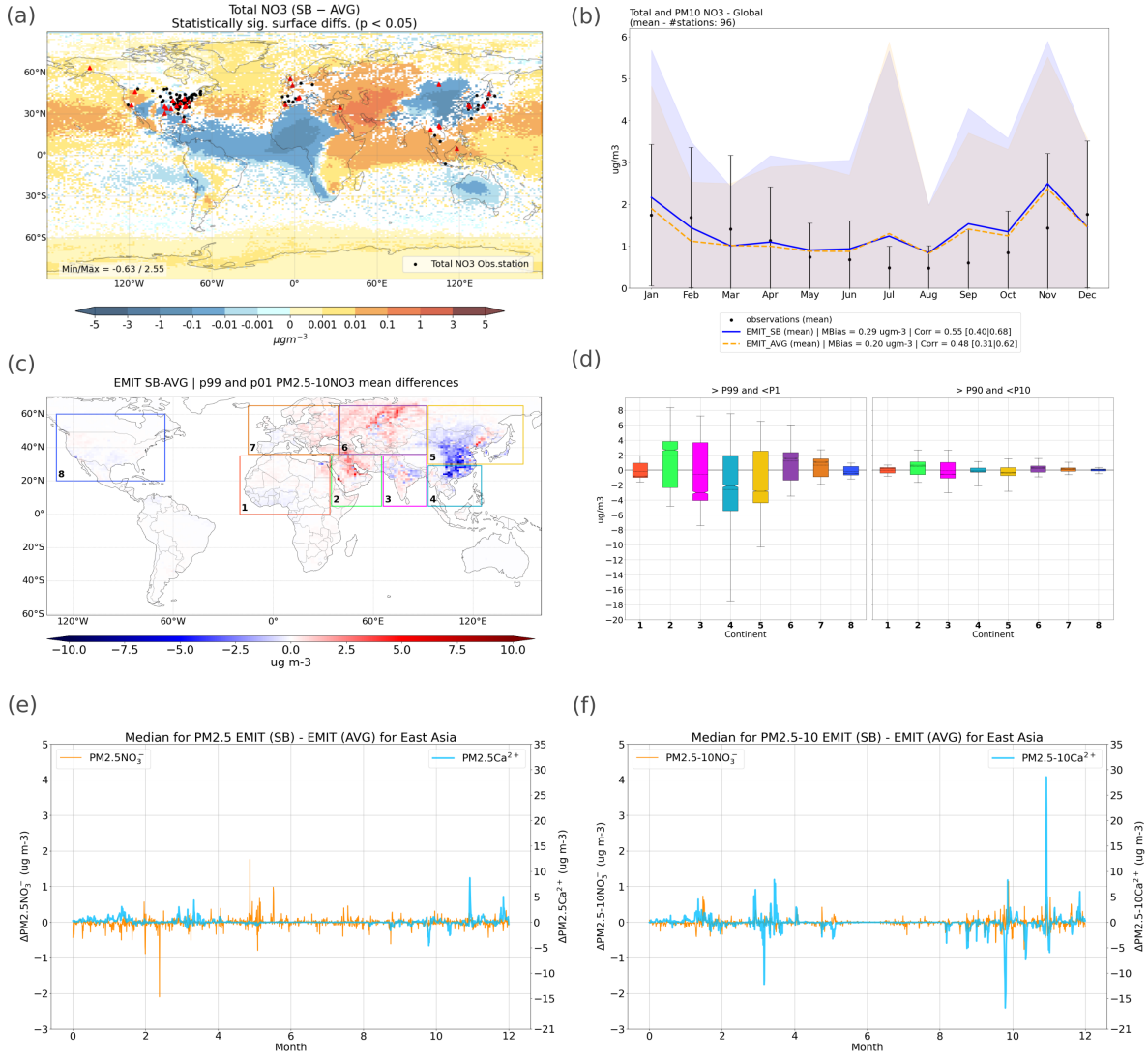

Figure 6.6: Comparison of simulated and observed total surface concentrations of NO_3^- and Ca^{2+} using the EMIT dataset. (a) Statistically-significant average annual differences in total NO_3^- between SB and AVG simulations. Evaluated stations are referenced as black circles, while red triangles indicate those stations where differences between SB and AVG runs are statistically significant ($p < 0.05$). (b) Monthly mean of total NO_3^- compared with global observations. Coloured shading and error bars represent the standard deviation of the model and observations, respectively. Evaluation is performed over stations marked as black dots in panel (a) map. (c) Spatial distribution of annual mean differences in coarse NO_3^- between SB and AVG simulations during the top 1 % and bottom 1 % of NO_3^- formation events. (d) Boxplots summarizing coarse NO_3^- differences across major regions for extreme (left) and high (right) formation percentiles. (e,f) Time series of the differences between the median concentrations for NO_3^- and Ca^{2+} with SB minus AVG simulations over East Asia. Fine (left) and coarse (right) modes are provided with 6-hourly temporal resolution.

long-term mean concentrations remain similar. The divergence between SB and AVG diminishes when broader percentile ranges are considered (90th–10th, right panel of Fig. 6.6*d*), confirming that mineralogical heterogeneity primarily affects the tails of the

NO_3^- distribution rather than its climatological mean. These opposing patterns show that the spatial distribution of $CaCO_3$ is significant for predicting the local occurrence of extreme coarse NO_3^- formation events, particularly over highly populated areas affected by dust intrusions.

Time series of Ca^{2+} and NO_3^- over East Asian stations further illustrate this behavior (Fig. 6.6*e–f*). Differences between SB and AVG simulations are small for much of the year but intensify sharply during episodic dust intrusions. Peaks in coarse Ca^{2+} coincide with enhanced coarse NO_3^- formation, confirming that injections of $CaCO_3$-rich dust act as transient chemical sinks for gaseous $HNO_{3(g)}$ and sources of particulate $Ca(NO_3)_2$. These events occur preferentially in spring and autumn, when strong dust transport overlaps with elevated anthropogenic acid availability. Fine-mode NO_3^- exhibits less synchronized responses, consistent with its dominant control by gas–particle $NH_{3(g)}$–$HNO_{3(g)}$ equilibrium rather than direct dust interactions.

6.4 Conclusions

This study demonstrates that incorporating source-resolved dust mineralogy — constrained by EMIT imaging spectroscopy and paired with satellite-inverted dust emissions — substantially refines the spatial and chemical context in which dust–acid interactions operate. By resolving fine-scale, observationally supported variability in $CaCO_3$ abundance, the EMIT-based representation improves agreement with airborne measurements, reorganizes the regional partitioning of SIA, and reveals a strong sensitivity of aerosol acidity to dust alkalinity.

A first implication is that regional variations in $CaCO_3$ fractions across dust source regions have a significant impact upon local aerosol chemistry and air quality — an influence that is largely obscured when $CaCO_3$ fractions are assumed to be globally uniform. The source-based configuration shifts NO_3^- formation toward regions and seasons where $CaCO_3$-rich dust coincides with $HNO_{3(g)}$ availability, enhancing coarse NO_3^- formation in the Middle East and suppressing it over East Asia and parts of the Sahara. Notably, these redistributions occur with only modest changes to the global NO_3^- burden, underscoring that regional chemistry and episodic extremes, rather than global means, govern many air-quality and deposition-relevant outcomes.

A second implication concerns aerosol acidity. Differences of up to –4 to +3 pH units between source-based and globally-averaged configurations indicate that dust alkalinity exerts a first-order control on aerosol pH at continental scales. Because pH regulates gas–aerosol partitioning and multiphase reaction kinetics, this sensitivity likely propagates beyond the NO_3^-–SO_4^{2-}–NH_4^+ system considered here. Processes such as elemental

dissolution (e.g. Fe, Mn, P), and nutrient delivery, heterogeneous oxidation pathways for $SO_{2(g)}$, $NO_{2(g)}$ and organics, and hygroscopic growth and activation as CCN/INP are all expected to respond to shifts in acidity, linking mineral composition to cloud microphysics, oxidant budgets, and biogeochemical cycles.

A third implication is temporal. The influence of mineralogical heterogeneity is strongly amplified during extreme events. Divergence between source-based and globally averaged configurations is greatest during the upper tail of coarse-NO_3^- formation, when $CaCO_3$-rich dust outbreaks coincide with elevated $HNO_{3(g)}$. Accurately capturing these episodes—which are disproportionately important for air quality and deposition—requires realistic mineral heterogeneity rather than uniform assumptions. By contrast, monthly mean NO_3^- concentrations show weaker sensitivity, partly reflecting the limited availability of long-term monitoring stations in dust-affected regions.

While this work focuses on the chemical impacts of dust mineralogy on SIA burden and aerosol acidity, several limitations of this study point toward important directions for future work.

First, heterogeneous chemistry involving dust is restricted here to mineral dust emitted from arid and semi-arid source regions. While this approach captures the dominant global source of alkaline mineral aerosol, it does not account for dust generated in urban or industrial environments, such as resuspended road dust. These anthropogenic dust sources may exhibit distinct mineralogical compositions and emission patterns (Canals-Angerri et al. 2025), and can contribute to heterogeneous chemistry in densely populated regions. Extending source-resolved mineralogical frameworks to include urban and industrial dust represents an important next step for improving regional air-quality assessments.

Second, uncertainties may remain in the satellite-derived $CaCO_3$ distribution used to constrain dust mineralogy. EMIT identifies $CaCO_3$ through its diagnostic spectral features, which are most robust where $CaCO_3$ constitutes a substantial fraction of the surface mineral assemblage. At low $CaCO_3$ abundances, spectral signatures may be muted or masked by more abundant clay minerals within the instrument's spectral window, potentially limiting sensitivity to diffuse or background $CaCO_3$. As a result, EMIT-based maps likely emphasize regions where $CaCO_3$ is most chemically relevant for dust–acid interactions, while underrepresenting weaker contributions elsewhere.

Our findings highlight the broad influence that dust $CaCO_3$ representation has on atmospheric composition and aerosol acidity. Repercussions for accurately representing air quality might be important, especially in regions simultaneously affected by episodic dust intrusions and anthropogenic pollution, leading to short-lived particulate NO_3^- formation episodes. However, our results also suggest the need of additional observations

close to such regions, and the additional inclusion of anthropogenic dust, to further constrain the impacts of dust mineral representation on atmospheric composition, and particularly on SIA formation.

7

Impacts on aerosol optical properties

7.1 Introduction

In the recent years, increasing research efforts have focused on constraining uncertainties in the dust radiative effect and in clarifying whether mineral dust acts as a net warming or cooling agent in the climate system (Boucher et al. 2013, Di Biagio et al. 2020).

The direct dust radiative effect is controlled by both its atmospheric burden and its optical properties, which depend on particle size, shape, and chemical/mineralogical composition (Section 1.4.5). These dependencies are commonly expressed through AOD and SSA, which together describe the magnitude of aerosol extinction, and its partitioning between scattering and absorption (Gliß et al. 2021, Obiso et al. 2024); AOD quantifies the total attenuation of radiation by aerosols along the atmospheric column, while SSA represents the fraction of extinction attributable to scattering (Gliß et al. 2021). Consequently, high SSA values indicate predominantly scattering aerosol populations, whereas lower values reflect a stronger absorbing contribution. Accurate representation of both AOD and SSA is therefore essential for quantifying aerosol radiative effects, as scattering primarily promotes atmospheric cooling, while absorption enhances atmospheric heating (Milousis et al. 2025). More information on the definition of AOD and SSA can be found in supplementary Section C.1.

Both AOD (i.e. extinction) and SSA depend strongly on particle D and radiation wavelength (λ). When particles are much smaller than the wavelength ($D \ll \lambda$), extinction efficiency is low, whereas it increases as particle D approaches λ, and typically peaks when $D \approx \lambda$ (Adebiyi et al. 2023). For larger particles, extinction efficiency gradually decreases. Consequently, coarse ($2.5 < D < 10\ \mu m$) and super-coarse ($D > 10\ \mu m$) dust dominate AOD at longwave λ, with scattering and absorption contributing at similar magnitudes. In contrast, at shortwave λ, AOD is primarily controlled by fine ($D < 2.5\ \mu m$) and accumulation ($0.1 < D < 2.5\ \mu m$) mode particles (Friedlander 2000,

Seinfeld and Pandis 2006, Adebiyi et al. 2023), whose sizes are more comparable to the incident radiation, while fine dust contributes only marginally to longwave extinction (Adebiyi et al. 2023).

The SSA of dust tends towards unity for fine particles and decreases for coarser sizes, as absorption becomes increasingly important due to the presence of absorbing species such as Fe oxides, reducing SSA (Ryder 2021, Adebiyi et al. 2023). Despite substantial uncertainties associated with mineralogical composition (Claquin et al. 1999, Journet et al. 2014, Schuster et al. 2016), shortwave absorption by dust is estimated to account for only about 5% of total shortwave extinction (Adebiyi et al. 2023).

Beyond particle size, dust optical properties depend upon its mineralogy, size sorting, and chemical processing during transport (Section 1.4.5), in part through the condensation of gaseous species (Section 1.3). Namely, heterogeneous reactions on dust surfaces can substantially modify particle composition and, consequently, their interaction with radiation (Milousis et al. 2025).

While minerals on dust bulk — especially Fe oxides — are primary absorbing components in the shortwave, heterogeneous reactions can generate SIA species that enhance scattering. These processes are especially relevant in regions where dust plumes interact with anthropogenic pollution (Klingmüller et al. 2020, Zhang et al. 2020, Lu et al. 2023). The formation of SO_4^{2-}, NO_3^-, and NH_4^+ on dust particles alters their optical properties and can affect the direct radiative effect of dust (Kok et al. 2023, Milousis et al. 2025).

In addition to their direct optical influence, dust–SIA interactions can indirectly modify aerosol optical properties by altering gas-phase chemistry. Dust acts as an efficient sink for acidic precursor gases (Wang et al. 2015, Krueger et al. 2004), thereby limiting the formation of other secondary aerosols and modifying aerosol partitioning and abundance. These feedbacks can influence atmospheric radiative properties (Usher et al. 2003).

Because SIA formation rates depend strongly on dust mineralogy, regional variations in mineral composition can produce geographically heterogeneous optical responses (Usher et al. 2003, Karydis et al. 2021, Soussé Villa et al. 2025, Milousis et al. 2025). Among SIA components, particulate SO_4^{2-} is a well-established scattering aerosol with a net cooling effect (Myhre et al. 2004, Bauer and Koch 2005). Particulate NO_3^- is an additional contributor to aerosol scattering at short wavelengths, with potentially important implications for aerosol optical properties (Bauer et al. 2007, Xu and Penner 2012, Li et al. 2015, Milousis et al. 2025). Its relative contribution is expected to increase in the coming decades, as $SO_{2(g)}$ emissions decline more rapidly than NO_x emissions (Tsimpidi et al. 2007; 2008, Boucher et al. 2013). Under specific future emission scenarios, NO_3^- aerosols have been projected to account for a substantial fraction of

anthropogenic AOD, potentially exceeding that of SO_4^{2-} in some regions and seasons (Bellouin et al. 2011, Hauglustaine et al. 2014).

This chapter examines how heterogeneous formation of SIA on dust particles affects AOD and SSA (Fig. 7.1). We assess the sensitivity of these optical properties to different representations of dust heterogeneous chemistry and mineralogy in atmospheric models, building on the chemical analyses presented in Chapters 5 and 6. Section 7.2 presents the methodology. Section 7.3.1 presents baseline AOD and SSA results using EMIT mineral data and reversible condensation on both fine and coarse dust modes. Subsequent sections evaluate the sensitivity of optical properties to alternative modeling assumptions, including the neglect of coarse SIA formation (Section 7.3.2), and the mineral representation choice (Section 7.3.3), including different mineral datasets and the representation of $CaCO_3$ geographical distribution. Finally, Section 7.4 summarizes the main findings.

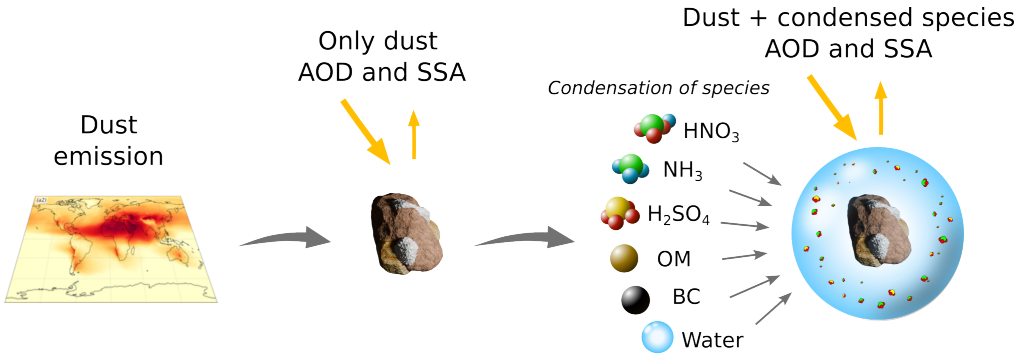

Figure 7.1: Scheme of the optical properties analysis performed in this chapter.

7.2 Methodology

7.2.1 Modeling dust mineralogy and heterogeneous chemistry

The MONARCH model, described in Section 3.1.1 with the developments performed in Chapter 4, is used to investigate the sensitivity of mineral dust optical properties to the introduction of dust heterogeneous chemistry variety mechanisms studied.

The baseline mechanism for simulating SIA formation on dust particles employs the double call mechanism (DBCLL, see Section 4.3) together with source-based (SB) mineralogical data from the EMIT dataset (Section 3.2.2 and Chapter 6). The DBCLL methodology assumes instantaneous aerosol-gas thermodynamic equilibrium for each dust size bin after constraining the fraction of precursor gases that are kinetically available for condensation in that size range. Thermodynamic equilibrium calculations are then performed sequentially for the fine and coarse size modes of dust (see Section 4.4).

The DBCLL configuration is used as the reference case for all subsequent sensitivity experiments in this chapter, aimed at assessing the sensitivity of aerosol optical properties to alternative representations of dust heterogeneous chemistry. The three additional sensitivity simulations performed are:

1. SIA formation is constrained to the fine dust ($D < 2.5\mu m$) mode only (fTEQ).
2. Pre-EMIT mineralogical datasets from Journet et al. (2014) (JOUR) and Claquin et al. (1999) (CLAQ) are used in place of EMIT.
3. A globally averaged $CaCO_3$ distribution derived from EMIT (AVG) is assumed instead of the SB representation.

As in Chapter 6, only Ca^{2+} from $CaCO_3$ is assumed to participate in dust heterogeneous reactions in all the sensitivity experiments. This assumption isolates the role of $CaCO_3$ on SIA formation and is justified by its dominant role as the primary alkaline mineral neutralizing acidic gas species on dust particles (Section 1.3.2).

In contrast to Chapter 6, where mineral tracking was limited to $CaCO_3$, the present analysis includes all mineral species available in each dataset (EMIT, JOUR, and CLAQ; see Table 3.1) for the calculation of dust optical properties. Under the EMIT dataset, this includes quartz, feldspar, illite, smectite, kaolinite, calcite, gypsum, hematite, chlorite, vermiculite, goethite, montmorillonite, as well as mixed Fe-oxide phases. Each mineral species is explicitly traced and represented across eight dust size bins spanning D from 0.2 to $20\mu m$. The contribution of individual minerals to the aerosol optical mixture is described in Section 7.2.2.

Following the methodology from the previous chapter, dust emissions are also constrained here using assimilated DOD data from the SNPP-VIIRS Deep Blue product combined with a modified Local Ensemble Transform Kalman Filter (Escribano et al. 2023) (see Section 6.2.3).

All simulations are conducted over a global domain at 1.4° longitude by 1.0° latitude resolution, with 48 hybrid pressure–sigma vertical layers extending up to 5 hPa. The simulated period is the year 2018, preceded by a six-month spin-up, and model output is archived at 6-hourly intervals.

Meteorological fields are from ERA5 reanalysis data (Hersbach et al. 2023) and restored daily with observations. Chemical transport and reactions are computed using a 180s time step. Anthropogenic emissions are processed with the HERMESv3_GR preprocessor using the CAMS-GLOB-ANT_v4.2 inventory (Soulie et al. 2024, Guevara et al. 2021), fire emissions are taken from GFASv1.2 (Kaiser et al. 2012), and oceanic DMS emissions from CAMS-GLOB-OCE v3.1 (Lana et al. 2011, Denier van der Gon et al. 2023).

7.2.2 Calculation of optical properties

AOD and SSA are used to characterize the sensitivity of aerosol optical properties to the representation of dust heterogeneous chemistry (see supplementary Section C.2). Both factors are diagnosed offline (Fig. 7.2), accounting for visible wavelengths of the solar spectrum throughout 12 radiation size bins. The calculation proceeds by first distributing the mass of the simulated aerosol species into the radiation bins, and subsequently retrieving the corresponding optical properties from a pre-calculated generic optical look-up table. Aerosol–radiation interactions are not treated interactively in the online model simulations; instead, the radiative transfer configuration is held identical across all experiments. This design choice avoids radiative feedbacks on meteorology and chemistry, allowing differences in aerosol chemistry, AOD, and SSA to be interpreted purely as direct responses to changes in dust composition and SIA formation. Consequently, the results presented here characterize changes in aerosol optical properties as first-order proxies for potential radiative implications, rather than fully coupled radiative effects.

The aerosol species contributing to total aerosol optical properties included dust (described below), sea salt, OM, BC, and particulate NO_3^-, SO_4^{2-} and NH_4^+. Each species is mapped onto the 12 radiation bins considered, which span particle D from 0.01 to 144μm. Dry mass of dust and sea salt is distributed in these radiation bins covering diameters from 0.2 to 20μm (dust) and from 0.2 to 40μm (sea salt). Depending on local RH, sea salt can extend up to 144μm due to hygroscopic growth. Other aerosol species are represented either as bulk tracers (i.e. OM and BC) or distributed over fine and coarse size bins (i.e. SIA). The mass associated with each radiation bin is computed assuming log-normal size distributions. Hygroscopic growth is applied to hydrophilic species based on local RH, and aerosol liquid water is treated as a separate species and added to the total column mass loading.

The final aerosol mixture is constructed separately for the fine ($D < 2.5\mu m$) and coarse ($2.5 < D < 10\mu m$) modes. In the fine mode, all species are assumed to be internally mixed spherical particles, with mixing performed using volume-weighted refractive indices to determine the effective optical properties of the mixture Obiso et al. (2024). In the coarse mode, dust and sea salt form a host material that is internally mixed via volume weighting, while OM, BC, SO_4^{2-}, NO_3^-, and NH_4^+ are treated as inclusions within this host (Fig. 7.3). Because the host material dominates the particle volume, the interaction between host and inclusions is represented using a Maxwell Garnett mixing approximation Markel (2016), Obiso et al. (2024).

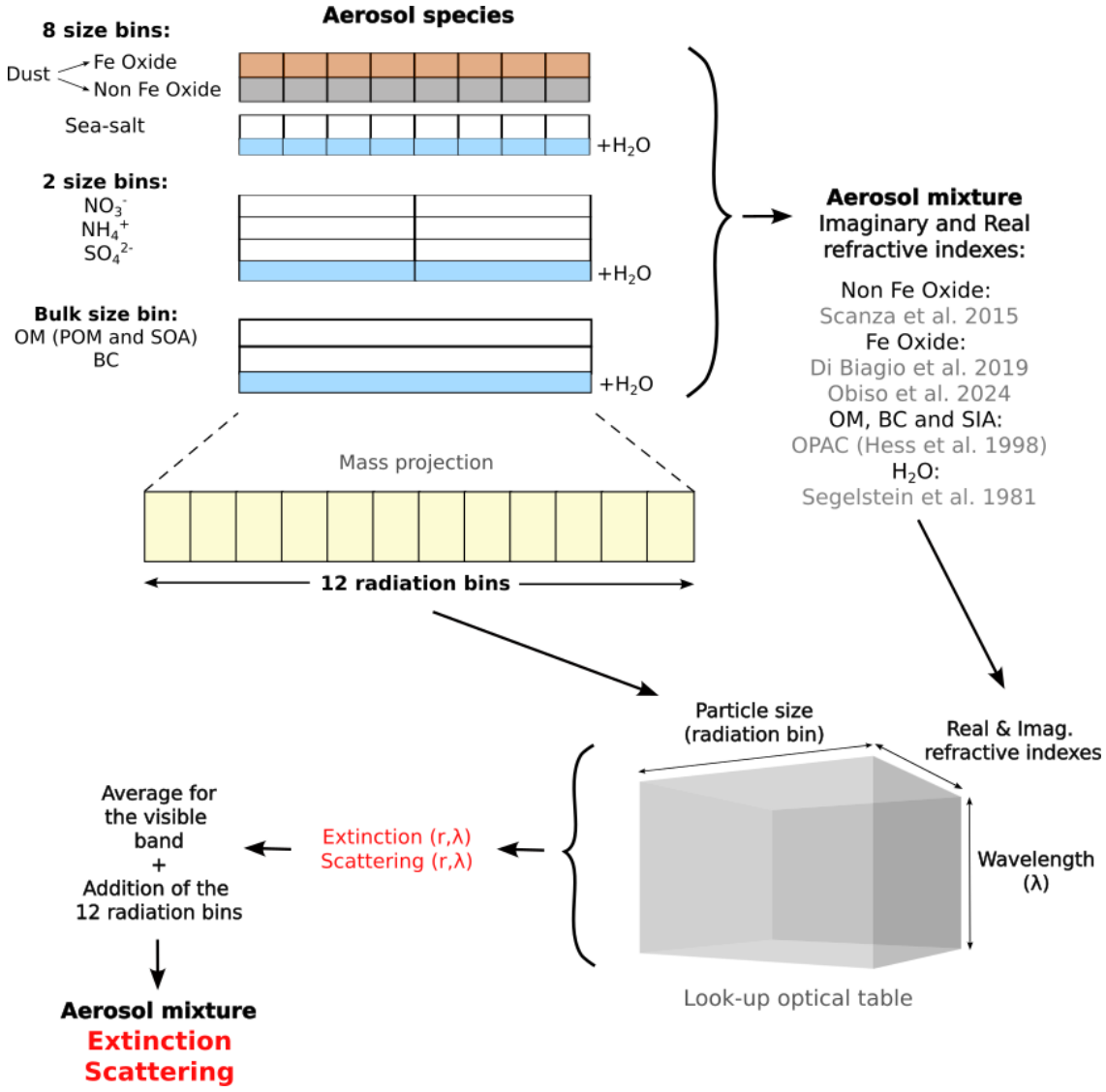

Figure 7.2: Scheme of the package for optical properties calculation.

Dust is represented as a mixture of two internally mixed materials: a weakly absorbing non-Fe mineral host (Scanza et al. 2015), and radiatively active Fe oxides (goethite and hematite) (Sokolik and Toon 1999, Balkanski et al. 2007, Moosmüller et al. 2012). The refractive index of the non-Fe mineral host is computed from the mineral-specific indices provided by Scanza et al. (2015), weighted by the simulated mineral fractions (Gonçalves Ageitos et al. 2023). Refractive indices for Fe oxides are calculated following the methodology of Obiso et al. (2024), using laboratory measurements from Di Biagio et al. (2019). For OM, BC, SIA, and water, physical properties and refractive indices are taken from OPAC (Hess et al. 1998) and Segelstein (1981), respectively.

The calculated real and imaginary refractive indexes used in this study are reported in supplementary Fig. C.1. SIA species (particulate NO_3^-, NH_4^+ and SO_4^{2-}) are considered to share identical optical properties, and the aerosol size classification conforms

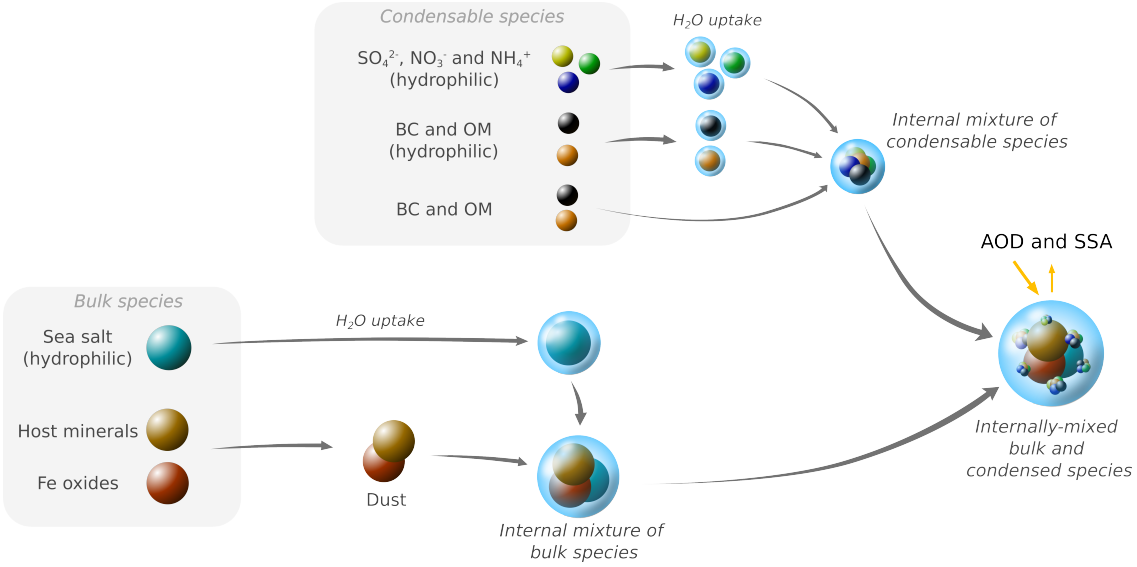

Figure 7.3: Scheme of the mixture of bulk and condensable species assumed for the calculation of optical properties for coarse mode aerosols.

"PM2.5" for particles with $D < 2.5\mu m$, "PM2.5-10" for particles with $2.5 < D < 10\mu m$, and "Total" for particles with $D < 20\mu m$.

Optical properties of the resulting aerosol mixtures are obtained from a look-up table containing pre-computed intensive optical properties—extinction, scattering, and asymmetry factor—derived from Mie theory. The table is defined as a function of particle size (12 radiation bins), wavelength (0.3–1.0μm), and complex refractive index for a set of representative aerosol mixtures.

Once the aerosol mixture and its complex refractive index are determined, optical properties are retrieved from the look-up table by selecting the closest tabulated refractive index. Optical properties are bi-linearly interpolated in wavelength and subsequently averaged over the visible spectral range (0.4–0.7μm). Contributions from all radiation bins are then summed to obtain total-column aerosol optical properties, or aggregated separately for fine and coarse modes to derive size-resolved SSA.

When specified, constant Fe oxide content is assumed in the sensitivity experiments designed to isolate the influence of SIA variability on SSA (the global average EMIT-based content), with globally averaged mass fractions of ∼3% for goethite and ∼2% for hematite.

7.2.3 Comparison of SSA with AERONET

Modeled SSA is evaluated against climatological retrievals from AERONET stations for the period 2000-2020 (https://aeronet.gsfc.nasa.gov/new_web/). The spatial distribution of the selected stations is shown in Fig. 7.4. To evaluate modeled aerosol optical properties, we use dust-dominated SSA retrievals from AERONET Version 3 (Sinyuk et al. 2020), following the filtering methodology described in Obiso et al. (2024). Hourly AERONET inversion products are screened to isolate scenes where mineral dust is the dominant aerosol component, and monthly climatologies of SSA are generated for the period 2000–2020 at the four almucantar wavelengths (0.440, 0.675, 0.870, and 1.020μm). Only Level 2.0 inversion products are used, which require a minimum AOD at 440nm of 0.4 to ensure low inversion uncertainty (Holben et al. 2006).

Dust-dominated scenes are identified using a combination of size-based and spectral absorption filters. First, the contribution of fine-mode aerosols is minimized by imposing a threshold on the fine-volume fraction, requiring it to be below 0.1, which exploits the characteristic dominance of coarse particles in mineral dust size distributions (Dubovik et al. 2002). While this filter removes most fine anthropogenic aerosols, coarse sea salt and small amounts of absorbing carbonaceous and non-absorbing particles may still contaminate the retrievals.

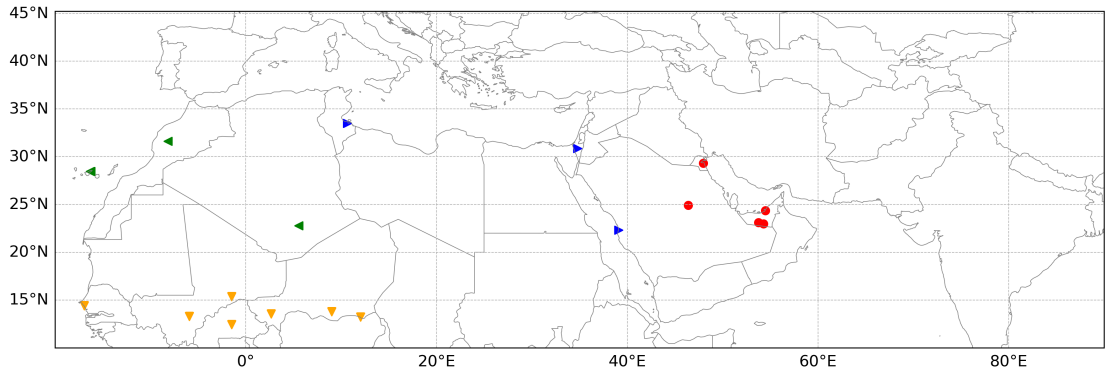

Figure 7.4: AeroNet stations used for the evaluation: Upward blue triangles are stations north-eastern Africa, green left triangles for northwestern Africa, down orange triangles for the Sahel region, and red circles stations for Arabian Peninsula.

To further discriminate dust from other aerosol types, spectral SSA constraints are applied. Mineral dust is unique among tropospheric aerosols in exhibiting an increase in SSA between 0.440 and 0.675μm, due to its coarse size and the preferential absorption of Fe oxides at UV and short-visible wavelengths. Therefore, only retrievals showing a

positive SSA slope across the UV–VIS range are retained (Ginoux et al. 2010). This criterion effectively excludes to a large extent fine anthropogenic aerosols, biomass-burning smoke, and sea salt, which typically exhibit flat or decreasing SSA with wavelength.

Finally, to reduce residual contamination by absorbing carbonaceous species, a threshold is imposed on the imaginary part of the refractive index at red–near-infrared wavelengths. Following Schuster et al. (2016), the mean imaginary refractive index over 0.675, 0.870, and $1.020\mu m$ is required to be below 0.0042. This condition exploits the fact that BC is the only aerosol species with significant absorption at these wavelengths, while mineral dust exhibits very weak absorption. The chosen threshold minimizes overlap between dust-dominated and carbonaceous aerosol retrievals, allowing only 5% overlap between their respective refractive-index distributions.

After filtering, climatological seasonal means of SSA and DOD are computed using only stations providing at least 80 valid hourly measurements per month for at least one month during the 2000–2020 period. This threshold represents a compromise between reducing sampling uncertainty and retaining sufficient spatial coverage. Monthly SSA values are calculated as DOD-weighted averages, and spectrally averaged over the model shortwave band (0.30–$0.77\mu m$) using the same procedure applied to model output, ensuring methodological consistency.

Despite the strict filtering, it is important to note that the resulting AERONET dust SSA does not represent a purely mineral-dust optical property. Fine pollution particles may remain internally mixed with dust, and the AERONET inversion assumes a single homogeneous refractive index for both fine and coarse modes. This assumption can partially redistribute absorption by fine particles into the coarse mode, thereby influencing the retrieved SSA. Consequently, the filtered AERONET SSA should be interpreted as a dust-dominated reference, rather than an idealized representation of externally mixed, chemically inert dust.

The filtering applied to the model output is therefore not intended to reproduce the observational selection exactly, but to approximate it in a physically consistent manner. First, to enable a meaningful comparison with the dust-dominated AERONET SSA, model grid cells and times are retained only when dust AOD accounts for more than 50% of total AOD, and BC and OM contribute less than 3% and 30% of total AOD, respectively. This selection removes scenes dominated by strongly absorbing fine aerosols. Second, we retain scenes with more than 10% of SIA contribution to AOD, to understand the sensitivity of SSA to the influence of mineralogy-driven SIA formation episodes. As such, the model filtering does not aim to isolate purely mineral dust, but rather to reproduce aerosol mixtures comparable to those captured by the observational dust-dominated sample. Under this framework, AERONET dust SSA is

used as a physically meaningful benchmark to assess the sensitivity of modeled dust optical properties to SIA formation, rather than as a strict reference for optically pure mineral dust.

7.3 Results

7.3.1 Effects of SIA formation on AOD and SSA

In this section we relate the SIA burdens in the baseline configuration shown in Fig. 6.3 (Chapter 6) with the resulting AOD and SSA distributions, analyzing the individual optical contributions of SIA species with a especial focus on particulate NO_3^-. Finally, we evaluate SSA against AERONET observations.

Total AOD is highest over the Middle East, East Asia, the Indian subcontinent, and the Sahara (0.2–0.8; Fig. 7.5*a1–a3*), consistent with previous modeling studies (Rémy et al. 2024). Consistent with the burdens in Fig. 6.3, the SIA-induced AOD enhancement (Fig. 7.5*b1–b3*) is most pronounced over regions where NVC-driven neutralization is active—notably the Middle East, East Asia, and India—where SIA increases AOD by up to ∼0.3, accounting for 40–49% of local AOD.

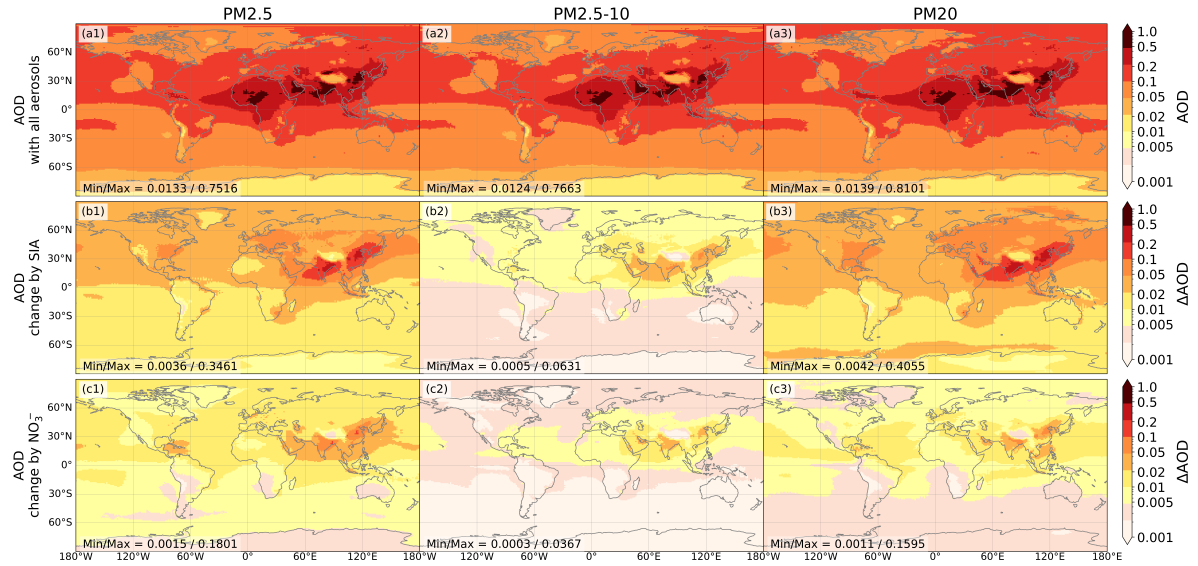

Figure 7.5: AOD for fine ($D < 2.5\mu m$), coarse ($2.5 < D < 10\mu m$) and total ($D < 20\mu m$) size modes using EMIT source-based $CaCO_3$ distribution with (*a1-a3*) all aerosol species, including dust, sea salt, BC, OM, and SIA. Difference in AOD compared to the previous case omitting (*b1-b3*) SIA species, and (*b1-b3*) particulate NO_3^-.

Among SIA species, SO_4^{2-} is the dominant contributor to the SIA-driven AOD enhancement, mainly through its fine-mode fraction. In particular, strong fine-mode SO_4^{2-} burdens over the Indian subcontinent and East Asia (Fig. 6.3*c1*) coincide with

the largest SIA-induced increases in total AOD (Fig. 7.5*b3*), consistent with the high visible extinction efficiency of fine SO_4^{2-} aerosols.

In comparison, particulate NO_3^- exerts a more modest influence on total AOD (Fig. 7.5*c1–c3*). Its contribution becomes regionally relevant primarily where fine-mode NO_3^- formation is substantial, notably over East Asia and the Indian subcontinent, where fine NO_3^- increases local AOD by up to ∼0.13, corresponding to about 17% of total AOD. Coarse-mode NO_3^- contributes more weakly and in a geographically confined manner, enhancing AOD mainly over the Arabian Peninsula (up to 0.05; ∼5%) and the Sahara (up to 0.02; ∼3%). These magnitudes are consistent with previous estimates indicating that NO_3^- typically contributes on the order of one quarter of the SO_4^{2-} contribution to total AOD (Bian et al. 2017), and therefore remains secondary to SO_4^{2-} in dust-influenced regions.

A key outcome of the AOD analysis is the clear dominance of fine-mode SIA over coarse-mode SIA in controlling total AOD, despite the larger mass abundance of coarse particles in several dust-affected regions. This reflects the much higher visible-band extinction efficiency of fine aerosols, as represented in the offline optical calculation framework (Section 7.2). Consequently, accurately simulating the size partitioning of SIA formed through dust heterogeneous chemistry is essential for robust regional AOD estimates.

In contrast to AOD, SSA remains generally high across most regions, indicating that column-integrated aerosol mixtures are predominantly scattering (Fig. 7.6*a1–a3*). Nevertheless, the updated SSA fields reveal clear spatial variability rather than uniform behavior. The highest SSA values are found over remote continental and oceanic regions, frequently exceeding 0.99, whereas lower SSA values occur over southern Africa and Australia (0.79–0.95), as well as over parts of South America, western North America, the Sahel, the central Atlantic, and eastern Siberia (0.90–0.95).

These reduced SSA values reflect an enhanced contribution of absorbing aerosol components, such as BC and absorbing OM, typically associated with biomass-burning emissions. In several of these regions, lower SSA also coincides with reduced SIA column loads (Fig. 6.3), limiting the presence of strongly scattering SIA and enhancing the relative importance of absorption.

The SIA-induced SSA perturbations (Fig. 7.6*b1–b3*) show that the largest SSA increases—reaching up to ∼0.05—occur preferentially over regions characterized by more absorbing background (low AOD) aerosol mixtures, including southern Africa, Australia, and parts of South and North America. These enhancements are dominated by the fine aerosol fraction (Fig. 7.6*b1*), whereas the coarse mode contributes only weakly (Fig. 7.6*b2*). This indicates that fine-mode SIA plays a primary role in modifying SSA.

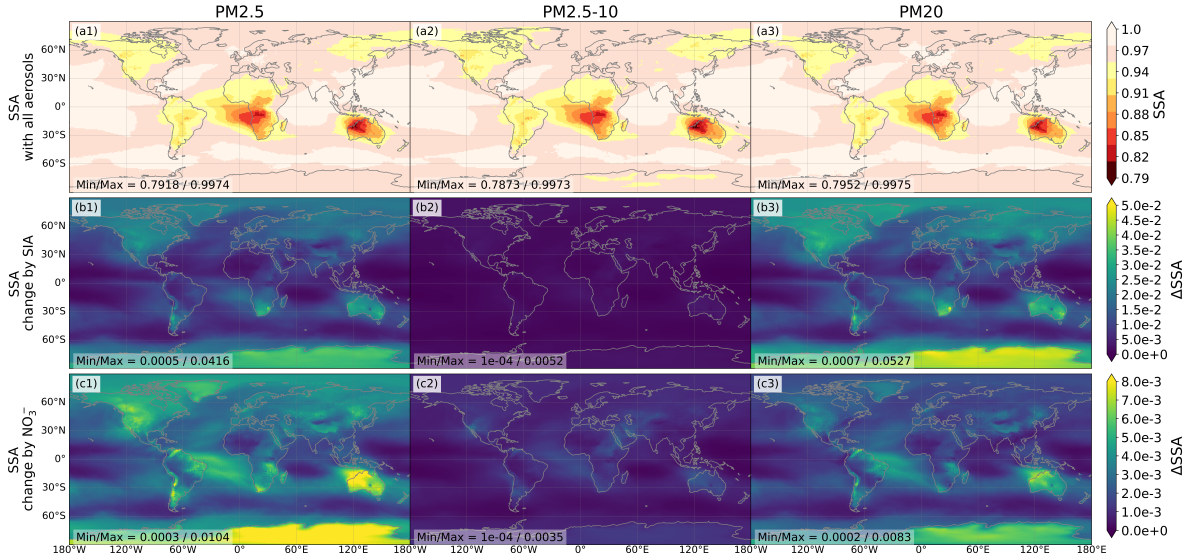

Figure 7.6: Aerosol size-resolved SSA using EMIT source-based $CaCO_3$ data with all condensed aerosol components (a1-a3), only SIA (b1-b3), and only NO_3^- (c1-c3) species.

The NO_3^--specific contribution to SSA (Fig. 7.6*c1–c3*) follows a similar but weaker spatial pattern, with maximum SSA increases of up to ∼0.01. This confirms that particulate NO_3^- contributes to enhanced aerosol scattering but remains secondary to the combined effect of all SIA species.

Overall, these patterns indicate that SSA is particularly sensitive to the addition of scattering material in absorption-dominated regimes, where modest increases in fine-mode SIA substantially enhance aerosol reflectivity. In contrast, over regions already characterized by highly scattering aerosol mixtures—such as remote oceanic and continental environments—the additional formation of SIA produces only limited SSA changes, as the scattering regime is already close to saturation.

The evaluation of SSA against dust-dominated AERONET retrievals (Fig. 7.7) shows that including the condensation of SIA species over dust improves the spatial agreement with observations relative to the simulation without SIA formation (correlation of 0.50 versus 0.42; Fig. 7.7*b* vs. *c*). This improvement indicates that accounting for chemically aged dust enhances the model's ability to reproduce observed regional variability in SSA. The comparison further highlights a non-negligible SIA contribution to total SSA, which locally reaches up to 0.02 units (Fig. 7.7*d*) over stations in the Arabian Peninsula and northeastern Africa. These enhancements are primarily driven by elevated fine-mode SO_4^{2-}, followed by NO_3^-, consistent with the SSA spatial patterns shown in Fig. 7.6.

Despite the improved correlation, SSA remains systematically overestimated across most regions. At first glance, this positive bias could be attributed to excessive modeled concentrations of scattering SIA species, as suggested by the overestimation of

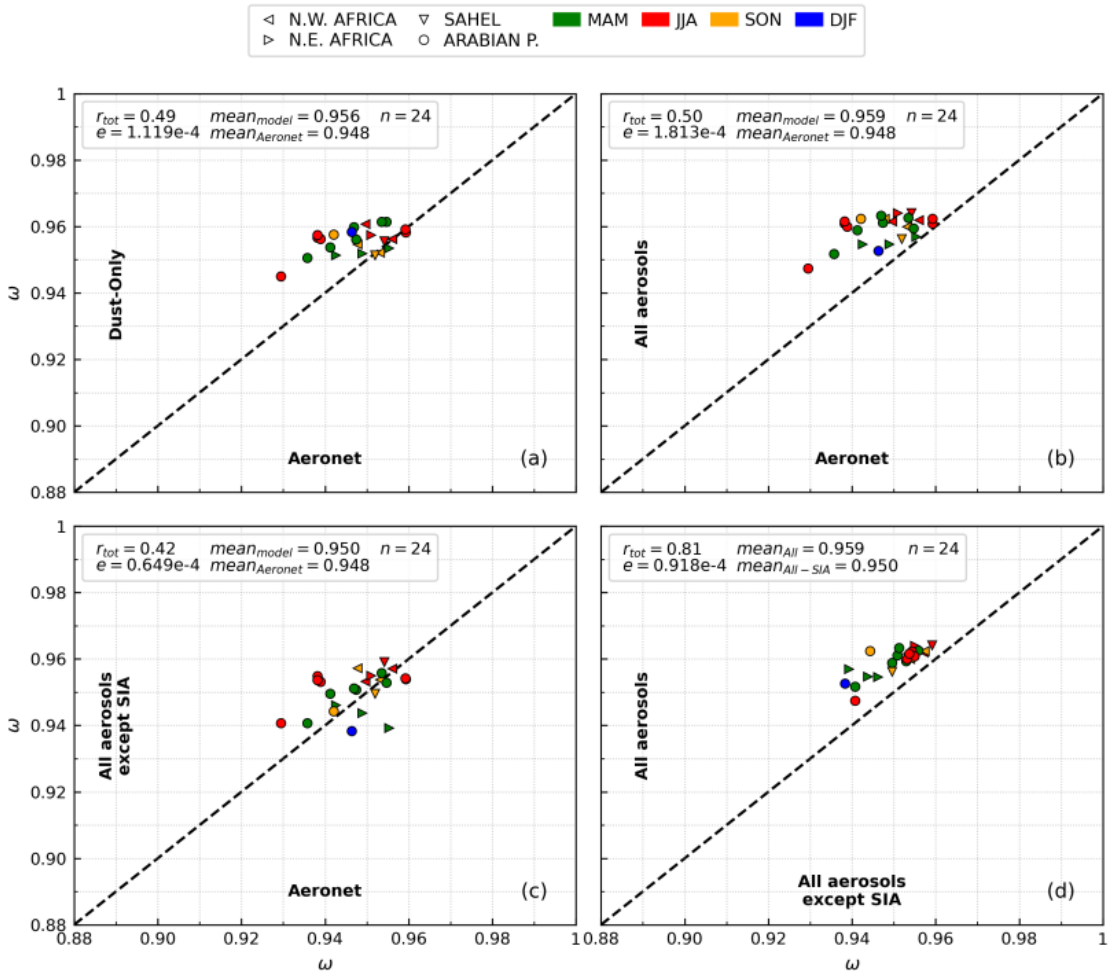

Figure 7.7: SSA evaluation using the EMIT source-based methodology against stations close to dust emission areas, and filtered by the abundance of dust and condensable species. Results with only dust are evaluated in (a), with and without SIA species are shown in panels (b) and (c), respectively. Both cases are compared in (d). Correlations (r), mean square error (e), means ($mean$), and the number of stations (n) are shown the top of each panel.

surface NO_3^- reported in Chapter 6 (Fig. 6.6*b* and supplementary Fig. B.11). However, evaluating a dust-only configuration—excluding BC, OM, SIA, and sea salt (Fig. 7.7*a*)—reveals a similarly strong SSA overestimation. Moreover, both the dust-only and full-condensation scenarios achieve comparable correlations with observations (0.49 and 0.50, respectively), while the inclusion of SIA increases mean SSA by only about 0.003 units.

This behavior indicates that the SSA bias cannot be explained solely by excessive scattering from SIA. Rather, it points to a combined effect of overestimated scattering components and an underrepresentation of absorbing aerosols, particularly BC and OM, or mineral particles with $D > 20\mu m$ that are not represented by the model. In the dust-only case, the absence of absorbing species or coarser dust leads to unrealistically high

SSA values. Adding BC and OM partially compensates for this bias, reducing the mean square error from 1.81×10^{-4} to 0.65×10^{-4} (Fig. 7.7*a* and *c*). However, the subsequent inclusion of scattering SIA restores SSA to levels comparable to the dust-only case, yielding a mean square error again close to 1.81×10^{-4} (Fig. 7.7*b*). This sequence suggests that the overall SSA overestimation arises from the interplay between underestimated absorption by carbonaceous species or coarser dust and excessive scattering associated with SIA formation.

Regional patterns further support this interpretation. Over the Sahel—where modeled contributions from BC, OM, and SIA are small—SSA shows little sensitivity to aerosol composition (Fig. 7.7*a* versus *b*). In contrast, over the Arabian Peninsula and northeastern Africa, where dust interacts more frequently with anthropogenic and industrial emissions, SSA varies markedly between scenarios. In these regions, dust alone cannot reproduce observed SSA values, leading to overestimation. The likely underrepresentation of absorbing aerosols, combined with elevated modeled SIA concentrations, contributes to the excessive SSA bias in these areas.

Overall, the SSA evaluation highlights both the sensitivity of dust optical properties to chemical aging by condensable species, and the limitations inherent in comparing modeled SSA with dust-dominated AERONET retrievals. While including SIA formation improves the spatial coherence of SSA patterns, remaining biases underscore the importance of accurately representing absorbing aerosol components and acknowledge that AERONET dust SSA represents a dust-dominated—but not purely mineral—reference. These results emphasize that realistic simulations of aerosol optical properties require a balanced representation of both scattering and absorbing species within chemically mixed dust–pollution systems.

7.3.2 Sensitivity to coarse aerosol formation

Neglecting the formation of coarse SIA is a simplification that can be adopted to avoid numerical and thermodynamic inconsistencies in condensation–evaporation calculations over coarse particles (Schmidt et al. 2014, Bian et al. 2017). As shown in Chapter 5, this approximation substantially alters SIA burdens and their size partitioning, with potential direct implications for AOD and SSA. In this section, we quantify these impacts by comparing simulations in which SIA formation is restricted to fine-mode thermodynamic equilibrium (fTEQ; Section 4.4) with the baseline DBCLL configuration, which allows kinetically limited SIA formation in both fine and coarse modes (Section 7.3.1). Note that all simulations apply dust emission corrections based on satellite-derived DOD (Section 6.2.3).

Restricting SIA formation to the fine mode induces a pronounced redistribution of aerosol mass from coarse to fine sizes. As shown in Section 5.3.1.1 and supplementary Fig. C.3, suppressing coarse SIA formation substantially enhances fine-mode SIA production. This effect is particularly strong for particulate NO_3^-, as preventing the formation of coarse NO_3^- leaves larger amounts of $HNO_{3(g)}$ available to condense onto fine particles. An important regional exception is the Middle East, where both fine and coarse NO_3^- burdens decrease under the fTEQ approximation (supplementary Fig. C.3*a1* and *b1*). In this region, enhanced fine-mode SO_4^{2-} formation leads to aerosol acidification (supplementary Fig. C.3*a2*), inhibiting NO_3^- partitioning in both size modes. Overall, the increase in fine SIA does not compensate for the loss of coarse SIA, resulting in a net reduction of total SIA burdens (supplementary Fig. C.3*c4*).

These changes in SIA burdens translate into perturbations in AOD (Fig. 7.8). Enhanced fine-mode SIA formation increases fine-mode AOD (Fig. 7.8*b1*), particularly over central Europe, the Indian subcontinent, the eastern Arabian Peninsula, and East Asia, with local increases of up to 0.03. More moderate fine-mode AOD enhancements (0.005–0.010) are also observed along equatorial transport pathways downwind of the Sahara, over the Mediterranean, eastern Europe, and parts of central Asia and the Pacific. These increases are dominated by fine NO_3^-, together with equatorial enhancements in fine SO_4^{2-} (supplementary Fig. C.3*a1* and *a2*).

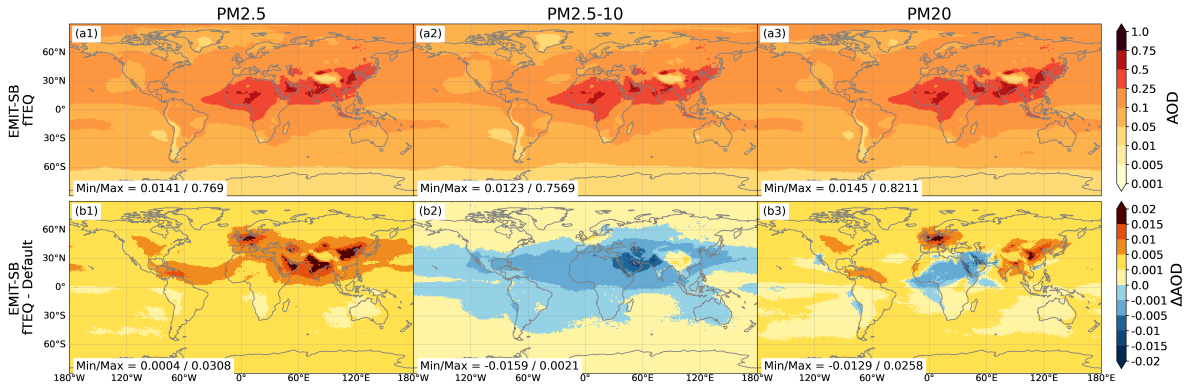

Figure 7.8: Fine ($D < 2.5\mu m$), coarse ($2.5 < D < 10\mu m$), and total ($D < 20\mu m$) size AOD with all aerosols but coarse SIA using the EMIT source-based $CaCO_3$ (first row), and comparison with the DBCLL (*default*) mechanism (second row).

In contrast, neglecting coarse SIA formation leads to a systematic reduction in coarse-mode AOD (Fig. 7.8*b2*), most pronounced over the Middle East, but also evident over and downwind of the Sahara, the Indian Ocean, and East Asia. These reductions directly reflect the loss of coarse NO_3^-, with local decreases in coarse NO_3^- burdens of up to 19 $mg\ m^{-2}$ (supplementary Fig. C.3*b1*). As a result of these opposing fine- and coarse-mode responses, the net impact on total AOD is regionally heterogeneous (Fig. 7.8*b3*). Total

AOD decreases over the Sahara and Middle East by 0.005–0.013 (up to ∼2% of local AOD), while it increases over Europe, the Himalaya Plateau, the Indian subcontinent, and East Asia by 0.005–0.026 (8–16%).

The corresponding SSA response (Fig. 7.9) mirrors to some extent the spatial structure observed for AOD. Suppressing coarse SIA formation redistributes scattering from the coarse to the fine mode, reducing coarse-mode SSA by approximately 1×10^{-3} over regions such as the Middle East, the Mediterranean, Sub-Saharan Africa, Australia, and the western coasts of the Americas (Fig. 7.9*b2*). Fine-mode SSA increases globally by up to 5×10^{-3}, particularly over polar regions and downwind of major dust sources (Fig. 7.9*b1*). The net effect on total SSA (Fig. 7.9*b3*) is spatially polarized, with increases of order 5×10^{-3} over the Arctic, Antarctic, Australia, and South America, and slight decreases ($\sim 5 \times 10^{-4}$) over the Arabian Peninsula and the Sahara. As for AOD, these responses in total SSA are primarily driven by regional differences in NO_3^- formation between the fTEQ and DBCLL approaches (supplementary Fig. C.3*a1* and *a4*).

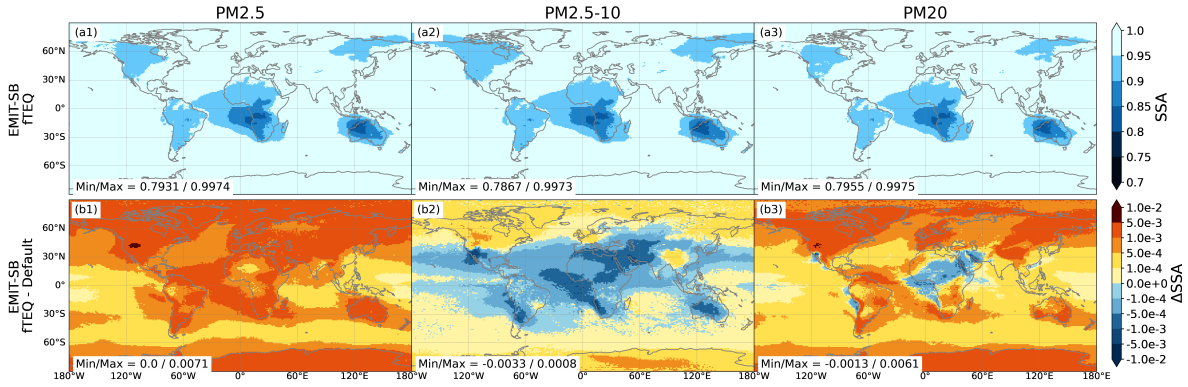

Figure 7.9: Fine ($D < 2.5\mu m$), coarse ($2.5 < D < 10\mu m$) and total ($D < 20\mu m$) size SSA with all aerosols but coarse SIA using the EMIT source-based $CaCO_3$ (first row), and comparison with the DBCLL (*default*) mechanism (second row).

Overall, these results demonstrate the dominant role of fine-mode SIA in controlling both AOD and SSA, owing to the higher extinction efficiency of fine particles. They also highlight the potential regional biases introduced by neglecting coarse SIA formation in atmospheric models, either through artificial redistribution of aerosol mass toward the fine mode or through changes in aerosol acidity that suppress NO_3^- formation, particularly over the Middle East. At the global scale, however, the magnitude of these effects remains limited, with differences below 3% for AOD and 0.1% for SSA. Consequently, the size representation of SIA formation exerts only a minor influence on global mean aerosol optical properties, but can become regionally significant, especially during in-

tense dust–pollution interaction events, and over sensitive regions such as the Middle East and polar regions.

7.3.3 Sensitivity to mineralogical variations

Dust mineralogy controls aerosol optical properties through two distinct pathways: (i) by modulating the production and size partitioning of scattering SIA via the abundance and distribution of reactive $CaCO_3$, and (ii) by directly altering absorption through variations in intrinsically absorbing minerals, particularly Fe oxides (hematite and goethite). Here we synthesize both effects by first quantifying the sensitivity to *mineral distributions* within a given atlas (SB versus AVG mineralogy using EMIT), and then placing the sensitivity to *alternative atlases* (JOUR and CLAQ) in that context.

SB versus AVG mineralogy with EMIT: Separating $CaCO_3$–SIA and Fe-oxide effects

We first compare optical properties obtained with the realistic SB EMIT mineralogy against a simplified AVG EMIT assumption. Figure 7.10 isolates the optical impacts of (i) $CaCO_3$ differences and their induced SIA formation (panels *a1–a3* and *c1–c3*), and (ii) the additional contribution of mineralogical variability in Fe oxides (panels *b1–b3* and *d1–d3*). As discussed in Section 6.3.2, differences in SIA burdens between SB and AVG yield globally lower fine Ca^{2+} and fine-mode SIA burdens with the SB configuration (Fig. 6.3), driven primarily by reductions in fine particulate SO_4^{2-}. This reflects enhanced uptake of $SO_{2(g)}$ in the coarse mode under the SB mineralogy, which reduces the availability of SO_4^{2-} precursors for fine-mode formation. This decrease in fine scattering aerosol translates into a net reduction of total AOD (Fig. 7.10*a3*), especially over the Sahara, the Middle East, and India (up to -1×10^{-2}, ∼1.5% of local AOD; supplementary Fig. C.4*a3*). Relative AOD reductions can be larger (up to ∼3%) over regions with low background aerosol loadings (e.g., the Himalaya Plateau and central Asia), where small absolute changes produce larger fractional responses..

In contrast, coarse-mode SIA differences on AOD between SB and AVG are more spatially polarized (Fig. 7.10*a2*) and closely follow regional shifts in Ca^{2+} and particulate NO_3^- (Fig. 6.2 and Fig. 6.3). However, these coarse changes have a comparatively weak imprint on total AOD, consistent with the dominant contribution of fine particles to visible light extinction in our offline optical calculations. Overall, these results indicate that, within EMIT, the primary $CaCO_3$-driven optical signal arises through changes in fine-mode SIA (particularly SO_4^{2-}), whereas regional variations in coarse SIA burdens play a secondary role in shaping AOD.

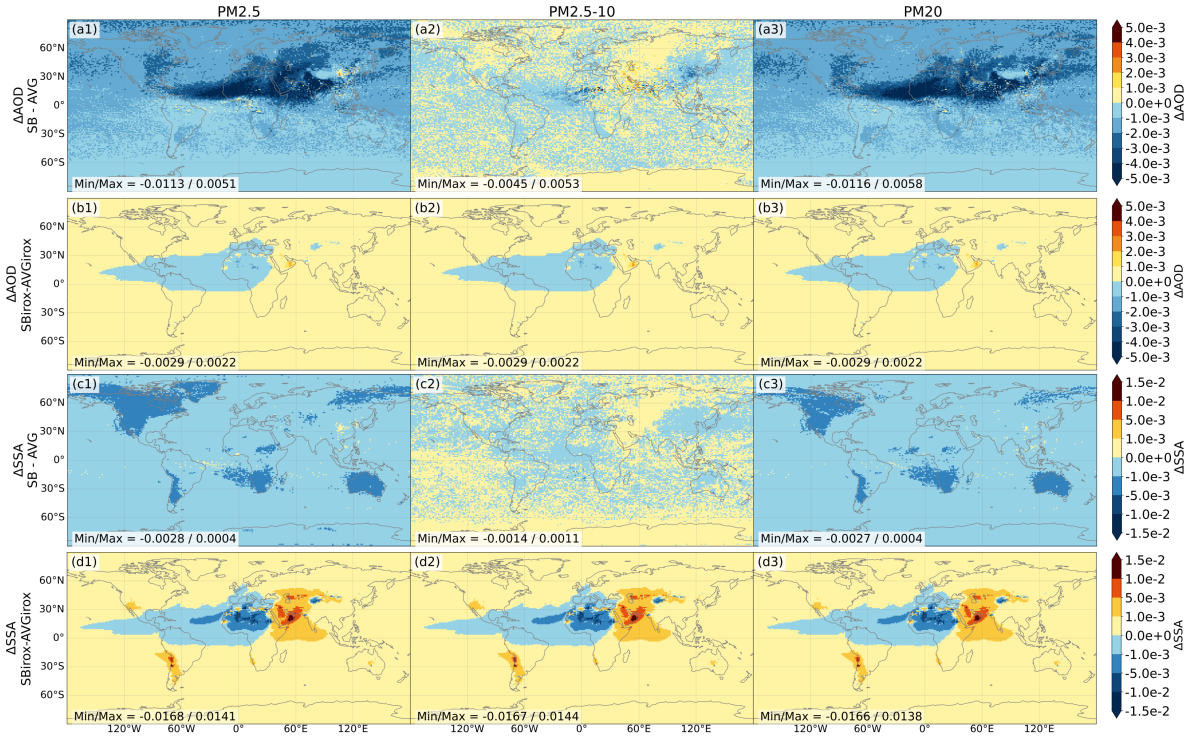

Figure 7.10: Differences on aerosol optical depth (AOD) and single scattering albedo (SSA) response to mineral variability between the source-based (SB) and globally averaged (AVG) approximations. Panels *a1–a3* for AOD, and *c1-c3* for SSA, isolate the effect of $CaCO_3$ and its induced SIA formation, assuming identical distributions of additional minerals. Panels *b1-b3* for AOD, and *d1-d3* for SSA, include the additional contribution of mineralogical variations in Fe oxides. SB increases coarse-mode NO_3^- and Ca^{2+} over the Middle East, but decreases them over East Asia and the Sahara. Differences in fine-mode SIA slightly reduce overall SSA, whereas Fe-oxide variability dominates total SSA changes, lowering values over hematite-rich regions.

For SSA, the contrast between $CaCO_3$-driven SIA changes and Fe-oxide-driven absorption changes is even clearer. The SIA-related SSA perturbations under SB versus AVG are small (Fig. 7.10*c1–c3*), typically within $\pm 3 \times 10^{-3}$ (0.3%, supplementary Fig. C.4*c1–c3*). Fine-mode and total SSA decrease slightly under SB, consistent with reduced fine scattering from lower fine SIA burdens (Fig. 6.3*a5*). Although coarse-mode SSA increases locally where SB enhances $CaCO_3$ and associated coatings (e.g., parts of the Middle East and northern Africa), the bulk SSA response largely follows the fine-mode trend, again reflecting the higher optical leverage of the fine fraction.

By contrast, introducing mineralogical variability in Fe oxides produces SSA changes an order of magnitude larger (Fig. 7.10*d1–d3*), reaching $\pm 1.5 \times 10^{-2}$ ($\sim$1.5%, supplementary Fig. C.4*d1–d3*). SSA decreases over hematite- and goethite-rich regions (notably the Sahara/Sahel and parts of East Asia), while it increases over comparatively Fe-poor sources such as the Middle East. This demonstrates that, for SSA, the dominant sensi-

tivity to mineralogical variations arises from changes in intrinsic dust absorption driven by Fe oxides, while $CaCO_3$-driven SIA variability acts mainly as a secondary modifier of scattering through coatings and mixing state. Conversely, the opposite effect is observed for AOD (Fig. 7.10*b1* – *b3*), that tends to converge between both mineral distributions with the introduction of Fe oxides.

The SSA evaluation against AERONET further indicates that the treatment of $CaCO_3$ distribution can affect agreement with observations (Fig. 7.11). Using SB $CaCO_3$ improves the overall correlation ($r_{tot} = 0.50$) compared with the AVG configuration ($r_{tot} = 0.30$), while both cases retain a systematic positive bias. The comparison between SB and AVG (Fig. 7.11*c*) shows that SB tends to produce slightly higher SSA, with local differences reaching 0.02, particularly over the Arabian Peninsula observations, where SIA burdens—and especially particulate NO_3^-— particularly differ between the two configurations (Fig. 6.3). These results support the view that $CaCO_3$-driven SIA formation can modulate dust optical properties and their evaluation, but primarily as a second-order effect superimposed on the stronger mineral-absorption control.

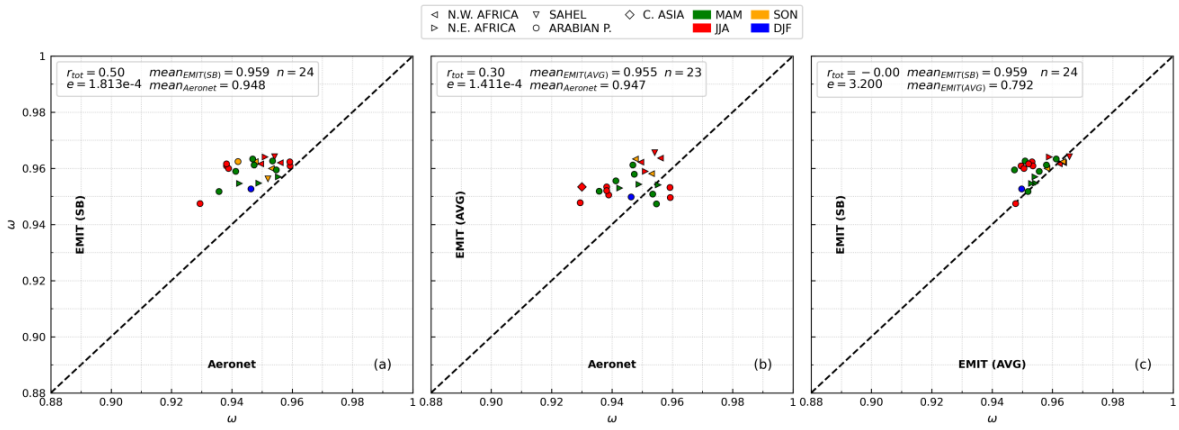

Figure 7.11: SSA evaluation using EMIT with different mineralogy distributions over stations close to dust emission areas, and filtered by the abundance of dust and condensable species. Results using EMIT source-based data (EMIT(SB)) are shown in panel (a), with globally-averaged data (EMIT(AVG)) in panel (b), and the comparison of both previous cases in panel (c). The global and regional correlations (r), the mean square error (e), the means, and the number of stations (n) are shown at the top of each panel.

Alternative mineral atlases (JOUR and CLAQ): context and limited added value for SIA-driven optics

We next compare EMIT against the two widely used extrapolation-based atlases of JOUR and CLAQ, using the same DBCLL mechanism and DOD-constrained dust emissions (Section 6.2.3) in both cases. Figures 7.12 and 7.13 summarize differences in AOD and SSA relative to EMIT, respectively.

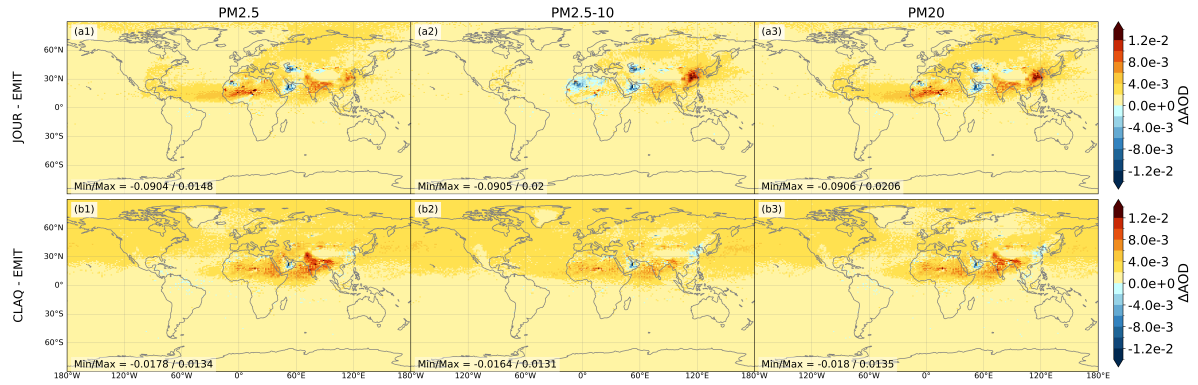

Figure 7.12: Comparison of AOD results obtained with Journet et al. (2014) (JOUR, *a1* to *a3*) and Claquin et al. (1999) (CLAQ, *b1* to *b3*) source-based data, in comparison with results for AOD using EMIT.

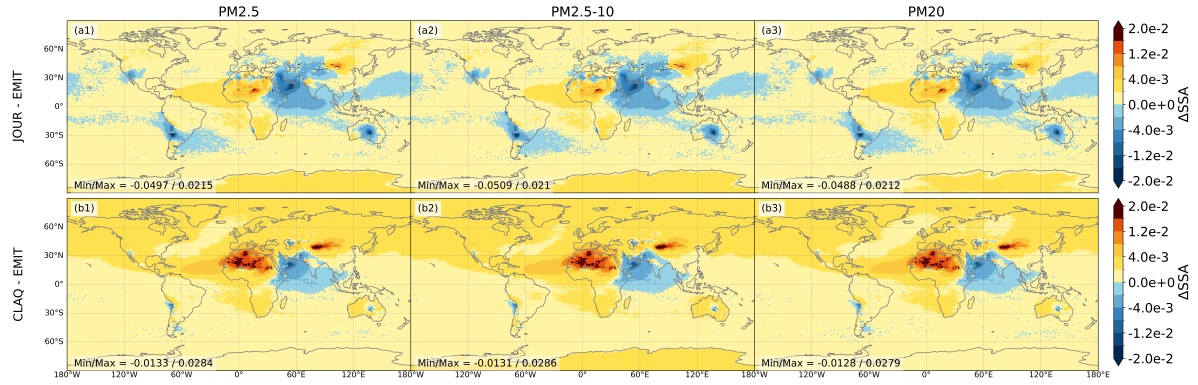

Figure 7.13: Comparison of SSA results obtained with Journet et al. (2014) (JOUR, *a1* to *a3*) and Claquin et al. (1999) (CLAQ, *b1* to *b3*) source-based data, in comparison with results for SSA using EMIT.

Relative to EMIT, both JOUR and CLAQ generally shift SIA toward the fine mode (supplementary Fig. C.5), increasing fine burdens (up to +2 $mg\ m^{-2}$ over dusty regions) and decreasing coarse burdens (down to $-5\ mg\ m^{-2}$), with localized exceptions (e.g., East Asia with JOUR and parts of the Sahara outflow with CLAQ). These differences are mainly driven by changes in $CaCO_3$ emissions and size partitioning between datasets (Fig. 6.2), and they primarily manifest through changes in particulate NO_3^- (supplementary Fig. C.6). As expected from Section 7.3.2, enhanced fine SIA tends to increase total AOD, and both JOUR and CLAQ broadly amplify AOD by ∼3% (supplementary Fig. C.7), although with regionally heterogeneous signals (Fig. 7.12).

For SSA, JOUR and CLAQ produce more polarized responses than for AOD (Fig. 7.13). Importantly, regions with increased fine SIA do not systematically show increased SSA (supplementary Figs. C.5 and C.10). Instead, SSA changes reflect the competition between added scattering from fine SIA and altered dust absorption from

mineralogical differences—again implicating Fe-bearing minerals as a leading driver. Thus, while JOUR/CLAQ-driven SIA shifts can modulate AOD and contribute to SSA changes, the dominant factor shaping SSA differences across atlases is the mineralogical control of absorption rather than $CaCO_3$-driven SIA variability.

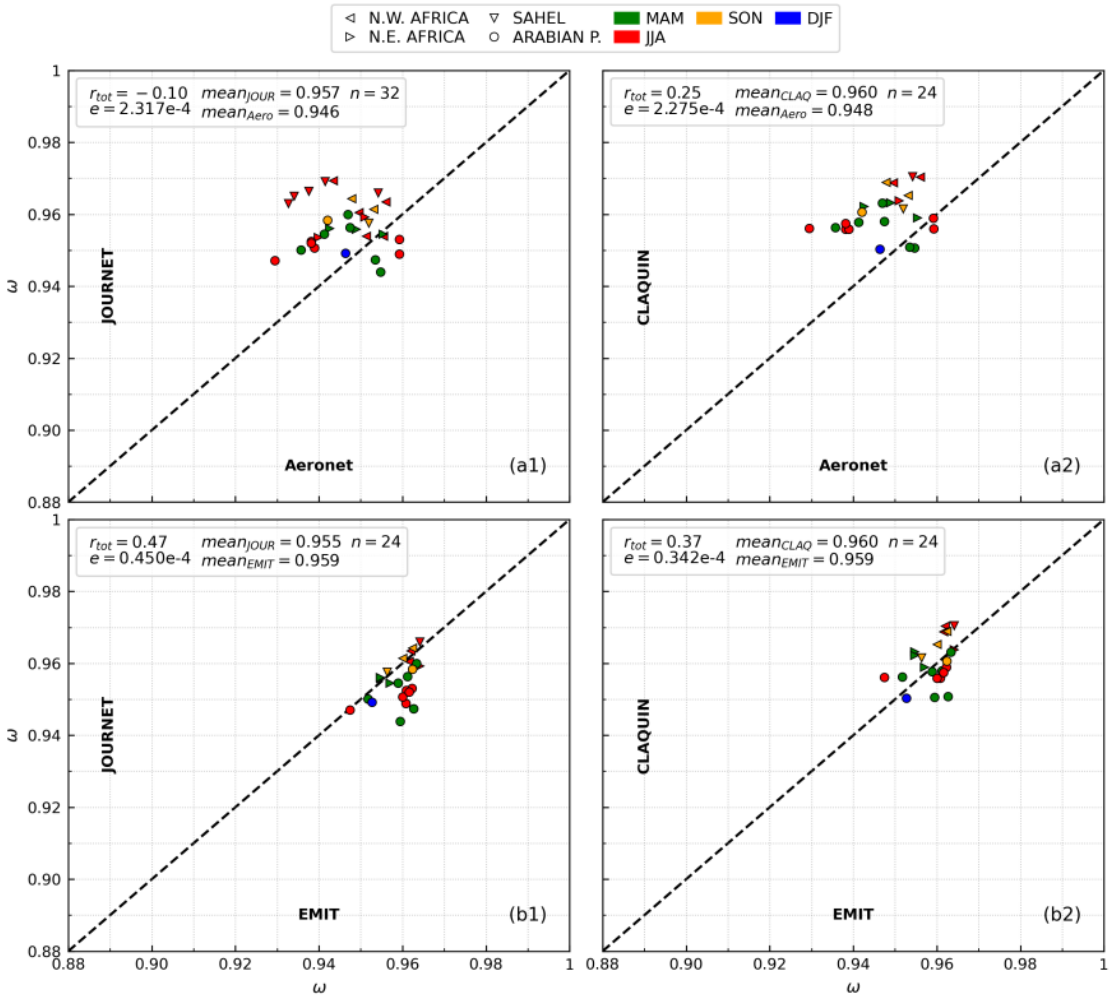

Figure 7.14: SSA evaluation using source-based mineral data from the JOUR and CLAQ mineral datasets, and compared with EMIT, over stations close to dust emission areas, and filtered by the abundance of dust and condensable species. Results using JOUR and CLAQ data are shown in panels (a1) and (a2). Panels (c1) and (c2) compare JOUR and CLAQ with EMIT, respectively. The global and regional correlations (r), the mean square error (e), the means and the number of stations (n) are shown at the top of each panel.

The AERONET-based SSA evaluation (Fig. 7.14) shows that JOUR and CLAQ also overestimate SSA, with more dispersed and regionally inconsistent deviations than EMIT. EMIT yields the most robust agreement with observations (Fig. 7.7), whereas JOUR and CLAQ tend to increase dispersion even when mean biases are slightly reduced. This behavior is consistent with the conclusion that atlas-to-atlas mineralogical differences introduce additional variability in absorption that is difficult to explain

through SIA formation alone.

7.4 Conclusions

This chapter quantifies how dust heterogeneous chemistry and mineralogy jointly shape aerosol optical properties, focusing on AOD and SSA. Using the EMIT source-based mineral dataset as baseline, we represent dust–gas interactions and SIA formation through a kinetically limited, size-resolved equilibrium approach applied to both fine and coarse modes (double-call method; DBCLL). We then assess the sensitivity of AOD and SSA to (i) neglecting coarse-mode SIA formation (fine-only thermodynamic equilibrium; fTEQ), and (ii) mineralogical assumptions, including the simplification from source-based to globally averaged mineral distributions and alternative mineral atlases. Model results are interpreted using the simulated spatial patterns of SIA, AOD and SSA, and are evaluated against dust-dominated AERONET SSA retrievals for 2000–2020.

The baseline simulation produces widespread fine-mode SIA across the Northern Hemisphere, while coarse-mode SIA remains concentrated near major dust sources and polluted outflow regions. The resulting total AOD peaks over the Middle East, East Asia, the Indian subcontinent, and the Sahara (0.2–0.8). In these regions, SIA formed through dust heterogeneous chemistry can account for a substantial fraction of AOD, locally enhancing AOD by up to ∼0.3 (40–49% of total AOD). This AOD response is dominated by fine-mode SIA and, within SIA, by SO_4^{2-}; NO_3^- contributes more modestly overall and becomes regionally important primarily where fine-mode NO_3^- formation is strong. A key implication is that the optical impact of dust chemistry depends strongly on the simulated size partitioning of SIA, because fine particles exert a primordial control on optical extinction.

SSA exhibits a different sensitivity than AOD. While dust source regions largely retain high SSA values, localized reductions occur where absorbing components (e.g., dust mineral absorption and carbonaceous aerosols) are more influential. The evaluation against AERONET shows that including SIA condensation improves the correlation with observed dust-dominated SSA (0.50 versus 0.42 without SIA), indicating that dust chemical aging and associated coatings measurably increase modeled scattering. However, the simulations still show an overall positive SSA bias, consistent with a combination of (i) overly scattering aerosol mixtures (e.g., excessive SIA), and/or (ii) insufficient absorption from OM, BC, and/or coarser dust particles in dust-influenced scenes. Importantly, AERONET "dust SSA" retrievals, despite stringent filtering, likely retain some residual fine pollution and internal mixing effects; therefore, they provide a

physically meaningful dust-dominated benchmark rather than a strictly pure-dust reference. Under this framework, the improved agreement when including SIA supports the conclusion that dust coatings are an important contributor to observed dust-dominated SSA, even if they cannot be isolated perfectly in either observations or model.

Neglecting coarse SIA formation with fTEQ strongly redistributes SIA toward the fine mode by leaving additional $HNO_{3(g)}$ available for fine-mode condensation. This shift produces regionally heterogeneous optical effects: fine-mode AOD increases (up to 0.03) over Europe, the Indian subcontinent, and East Asia, whereas total AOD decreases over the Sahara and the Middle East (up to -0.013; $\sim$2% locally) where enhanced SO_4^{2-}-driven acidification can suppress NO_3^- formation. SSA responses are comparatively small (global changes $\lesssim$0.1%) but show coherent regional structure, indicating that coarse-mode treatments can matter for regional optics and for extreme events, even if global-mean impacts remain limited.

Mineralogical variations introduce a clear separation between scattering- and absorption-controlled responses. Changes in $CaCO_3$ distribution primarily affect optics indirectly, by modulating SIA formation and its size partitioning. Within EMIT, using source-based versus globally averaged $CaCO_3$ produces modest but systematic changes in AOD (order 10^{-2}; $\sim$1–2%) and SSA (order 10^{-3}; $\sim$0.3%), consistent with changes in fine-mode SO_4^{2-} and overall scattering efficiency. In contrast, variations in absorbing Fe oxides (hematite and goethite) dominate SSA sensitivity, producing changes an order of magnitude larger (up to $\pm 1.5 \times 10^{-2}$) and driving pronounced regional "darkening" over Fe-rich sources. Thus, while $CaCO_3$-driven SIA coatings act as a secondary modifier of scattering and mixing state, the leading control on SSA differences across mineralogical configurations is the representation of Fe-bearing minerals and their absorption.

Overall, this chapter shows that (i) dust heterogeneous chemistry can enhance regional AOD through the formation of fine scattering SIA, (ii) SSA is sensitive to dust chemical aging but is more strongly controlled by absorbing mineralogy, particularly Fe oxides, and (iii) correctly representing size partitioning (fine versus coarse) is essential to interpret both AOD and SSA responses. While the optical impacts documented here are primarily direct-radiative, they likely underestimate the full climatic importance of dust chemical aging, because SIA coatings also modify hygroscopicity, CCN activity, and aerosol–cloud interactions. Extending this framework to quantify impacts on CCN and clouds is therefore a key priority for future work.

8

Achievements, conclusions and future work

8.1 Achievements

Mineral dust is one of the main aerosol components in the atmosphere. Through its multiple interactions with atmospheric species and radiation, dust exerts a determinant influence on our planet's atmospheric composition and climate. However, many of these interactions remain poorly understood, and their representation in atmospheric models often relies on simplistic approximations. As a result, mineral dust remains a large source of uncertainty in estimates of air quality, aerosol radiative forcing and, ultimately, in climate projections.

Dust *heterogeneous chemistry* has gained increasing attention because it provides an efficient pathway for the formation of secondary inorganic aerosols (SIA) through interactions between mineral dust and gas-phase species that are largely of anthropogenic origin. These reactions are thought to have a dominant role on atmospheric particulate nitrate (NO_3^-) formation, and to represent an important source of particulate ammonium (NH_4^+) and sulfate (SO_4^{2-}) in dust-influenced environments. NO_3^-, NH_4^+, and SO_4^{2-} strongly affect air quality and ecosystems, and their net climatic effects remain an active area of research. Despite their relevance, most atmospheric chemistry models still employ simplified parameterizations of these processes, largely due to their computational cost, the limited experimental constraints available to support robust schemes, and persistent uncertainty in the mineralogical composition of dust. Consequently, models frequently disagree with each other and with observations in the predicted products of dust heterogeneous chemistry and their impacts on atmospheric composition and climate.

To advance the understanding of dust heterogeneous chemistry and improve its representation in atmospheric models, this Thesis systematically investigates the implementation of multiple dust chemical mechanisms and mineralogical representations in

a state of the art atmospheric chemistry model, the Multiscale Online Non-hydrostatic AtmospheRe CHemistry (MONARCH) system. Our investigation explores how these implementations influence atmospheric composition, aerosol acidity, and optical properties, and evaluates model performance against observations. Notably, this Thesis represents one of the first global-scale implementations of the Earth Surface Mineral Dust Source Investigation (EMIT)-derived mineralogical constraints within an atmospheric chemistry model, and the first, to our knowledge, to explicitly exploit these observations to investigate dust heterogeneous chemistry and its implications for secondary aerosol formation and aerosol optical properties.

Specifically, the four objectives introduced in Section 2.1 have been achieved as follows:

- We implemented a series of representative dust heterogeneous chemistry mechanisms of varying complexity into a global atmospheric model, explicitly including different representations of mineral alkalinity.

- This novel framework enabled a comprehensive assessment of the sensitivity of global NO_3^-, NH_4^+, and SO_4^{2-} burdens on gas-aerosol partitioning processes. These results provide a benchmark for future investigations into the role of regional variations in dust alkalinity in atmospheric chemistry.

- By integrating high-resolution mineralogical constraints from EMIT with satellite-inverted dust emission fluxes, we quantified the influence of dust alkalinity representation on aerosol acidity and SIA burdens. The results show that resolving fine-scale heterogeneity in alkaline mineral content – with a special focus on calcite ($CaCO_3$) – is important for accurately simulating dust-acid interactions and for improving the spatial distribution of NO_3^-, NH_4^+, and SO_4^{2-} at the global scale.

- By disentangling the optical contributions of SIA and iron (Fe) oxides, we isolated the effects of mineralogical and chemical treatments of mineral dust on aerosol optical properties. We identify a response that separates into scattering- versus absorption-driven components: while absorbing minerals dominate the variability in single scattering albedo (SSA) and radiative impacts, $CaCO_3$-driven SIA changes act mainly as a secondary modifier through mixing state and scattering.

The main findings of the studies presented in this Thesis are summarized in Section 8.2, followed by recommendations for future research on dust mineralogical and chemical composition in Section 8.3.

8.2 Conclusions

Chapter 5 investigates how different parameterizations of dust heterogeneous chemistry modulate global particulate NO_3^- formation. We evaluate the implications of key assumptions, including size-dependent pathways (fine and/or coarse), equilibrium-based versus kinetically-defined irreversible condensation, uncertainties in gas uptake coefficients, and mineralogical constraints on dust alkalinity.

The analysis shows that neglecting coarse NO_3^- (diameter between 2.5 and 10μm) formation systematically overestimates fine-mode NO_3^- (diameter below 2.5μm), despite in some cases matching total NO_3^- observations. Conversely, incorporating coarse NO_3^- formation using irreversible uptake of nitric acid ($HNO_{3(g)}$) on dust and sea salt leads to strong NO_3^- overestimation. Agreement improves only when uptake coefficients are parameterized with experimentally supported dependencies on relative humidity and alkalinity for both dust and sea salt. This highlights the need to represent environmental controls on heterogeneous uptake more explicitly in global models, and suggests a promising direction for future parameterization development.

The most consistent agreement with literature estimates and observations is obtained with the *double-call* mechanism. This configuration couples reversible condensation–evaporation of relevant gases in both fine and coarse modes with kinetic limitations, while explicitly accounting for dust and sea salt alkalinity. It captures both fine and coarse NO_3^- observations and yields NO_3^-, NH_4^+, and SO_4^{2-} burdens consistent with established literature ranges. This method is therefore adopted as the baseline configuration in subsequent chapters.

Sensitivity experiments further demonstrate that, beyond the choice of mechanism, dust and sea salt alkalinity exert a decisive control on NO_3^- partitioning, aerosol pH, deposition fluxes, and atmospheric lifetime. In particular, accounting for the coupled availability of reactive mineral species on both dust and sea salt is essential to reproduce global NO_3^- dynamics.

Overall, this chapter underscores the importance of explicitly representing heterogeneous processes in both size modes, and of accounting for dust and sea salt alkalinity to capture secondary aerosol formation, especially coarse NO_3^-, providing a robust benchmark for future model development.

Chapter 6 extends the investigation of Chapter 5 by integrating EMIT spaceborne imaging spectroscopy into MONARCH to quantify how variability in dust alkalinity ($CaCO_3$ fraction) alters aerosol chemistry and aerosol acidity. The MONARCH

model was expanded to include mineral-resolved dust composition supporting multiple soil mineralogical datasets, including the pre-EMIT atlases from Claquin et al. (1999) and Journet et al. (2014), and the new EMIT-derived soil mineralogy. Using a size-resolved double-call equilibrium approach, we conducted sensitivity experiments on the specification of mineralogy in emitted dust considering the use of geographically-varying data against its simplification to a homogeneous global average. To prevent dust emission uncertainties from propagating into our mineralogical analysis, we constrained global dust fluxes using a satellite-informed inversion framework, which optimizes the magnitude and location of dust emissions against observed dust optical depth.

Factors such as the global atmospheric burdens of $CaCO_3$ and SIA, aerosol acidity, and the occurrence of extreme events of particulate NO_3^- formation are studied to assess the repercussions of the different mineralogical assumptions.

Results show that integrating source-resolved dust mineralogy constrained by EMIT and satellite-inverted emissions yields the closest agreement with $CaCO_3$ observations among the tested mineralogy representations. Additionally, resolving observationally supported mineral variability produces large geographical differences in $CaCO_3$: $CaCO_3$ loads increase by roughly 40–100% over the Middle East and parts of West and East Asia, while decreasing by up to ∼150% over the Sahara, Sahel, and parts of East Asia.

These regional differences in $CaCO_3$ substantially modulate size-dependent SIA formation. Through $CaCO_3$–regulated uptake of sulfur dioxide ($SO_{2(g)}$), the source-based configuration shifts particulate SO_4^{2-} formation from the fine mode toward the coarse mode. At the same time, particulate NO_3^- increases in both size modes where $CaCO_3$ and $HNO_{3(g)}$ co-occur (e.g., the Middle East), but decreases over East Asia and the Sahara where nearby dust sources are less $CaCO_3$-rich in the source-based approach. Importantly, these redistributions occur with only modest changes in global NO_3^- burden, emphasizing that regional extremes and episodic events, rather than global means, may control air-quality and deposition outcomes.

Aerosol acidity exhibits a strong sensitivity to $CaCO_3$ representation, with pH differences of up to –4 to +3 units between source-based and globally averaged configurations. Because pH regulates gas–aerosol partitioning, trace elements dissolution, and heterogeneous oxidation kinetics, this sensitivity provides a mechanistic link between mineral composition and broader biogeochemical cycles and cloud-relevant processes.

The small-scale and temporal responses on SIA formation dynamics are further explored through the analysis of global extreme NO_3^- formation events. Our outcomes show that source-based $CaCO_3$ predicts more intense and frequent coarse NO_3^- formation episodes over the Middle East, western North Asia, and Europe, compared to assuming globally-averaged $CaCO_3$. On the contrary, this last methodology substantially enhances extreme coarse NO_3^- formation over East and Southeast Asia. Choosing a realistic $CaCO_3$ representation is therefore an important factor in the predictability of short-lived and intense coarse NO_3^- pollution episodes in regions where $CaCO_3$ and $HNO_{3(g)}$ coincide. While the impacts on large-scale mean NO_3^- patterns are comparatively modest, source-based $CaCO_3$ generally outperforms the globally averaged configuration in correlation with observations. Both configurations nonetheless show similar tendencies toward slight underestimation of fine NO_3^- and overestimation of coarse NO_3^- over the evaluated stations, with differences remaining below statistically significant levels in the present evaluation.

Despite these advances, several limitations motivate future research. While our framework captures dominant arid sources, it excludes anthropogenic dust (e.g., resuspended road dust), which has distinct mineralogy and may affect densely populated regions. In addition, while EMIT provides strong constraints in $CaCO_3$-rich areas, retrieval uncertainties may be larger in regions with diffuse or low $CaCO_3$ abundance. Incorporating anthropogenic dust sources and further validating spaceborne-derived mineral maps against ground-based mineralogical observations remain priorities for improving regional assessments. Finally, longer-term observations over dust affected areas would enhance the characterization of global impacts of the dust mineralogy representation.

Chapter 7 quantifies the joint influence of mineralogical composition and heterogeneous chemistry on aerosol optical properties, focusing on aerosol optical depth (AOD) and SSA. Using the EMIT source-based mineral dataset, dust–gas interactions and SIA formation are simulated with a size-resolved double-call equilibrium approach. Sensitivity experiments evaluate the effects of neglecting coarse-mode SIA formation, of simplifying mineral distributions from source-based to globally averaged, and of employing alternative pre-EMIT mineral atlases. Model performance is further assessed against a 20-year record of dust-dominated AERONET SSA retrievals.

Results show that dust heterogeneous chemistry can modestly enhance regional AOD over major dust-influenced regions (including the Sahara, the Middle East,

and East Asia). The enhancement is dominated by fine-mode SO_4^{2-}, confirming that the optical impact of dust chemistry depends strongly on size partitioning, since fine particles disproportionately control visible extinction. Including SIA coatings improves the correlation with AERONET dust SSA (from 0.42 to 0.50), although a persistent positive bias indicates that the model may still overestimate scattering and/or underestimate absorbing components (i.e. organic matter, black carbon, or coarser dust) in dust-influenced scenes.

A clear functional separation emerges between the roles of $CaCO_3$ and Fe oxides. $CaCO_3$ acts mainly as an indirect optical modifier by regulating alkalinity and hence the formation of scattering SIA coatings. In contrast, the dominant control on SSA variability is the representation of Fe-bearing minerals: variations in hematite and goethite produce SSA changes an order of magnitude larger than those driven by $CaCO_3$–SIA interactions. In addition, neglecting coarse-mode chemistry artificially redistributes NO_3^- toward the fine mode, distorting regional AOD patterns.

Overall, heterogeneous chemistry is a regional driver of AOD through the formation of fine scattering aerosols, whereas accurate Fe-oxide speciation remains the primary requirement for reproducing dust absorption and SSA. Because these processes also modify dust hygroscopicity and mixing state, extending this framework to quantify impacts on cloud condensation nuclei (CCN) and aerosol–cloud interactions is identified as a critical priority for future research.

8.3 Future work

The results presented in this Thesis identify key pathways where further research can reduce existing uncertainties and improve the mechanistic representation of dust heterogeneous chemistry within atmospheric models.

Dust mineralogical representation: Our results suggest that remaining uncertainties in the EMIT-retrieved $CaCO_3$ product could still be reduced, potentially improving upon the already substantial performance gains relative to pre-EMIT mineral atlases. It would also be valuable to investigate the potential chemical role of additional alkaline minerals beyond $CaCO_3$, such as dolomite ($CaMg(CO_3)_2$)). Although some of these minerals have low solubility, under specific conditions they may supply non-volatile cations (e.g., magnesium and potassium) that may influence gas–aerosol partitioning.

Anthropogenic dust sources: Dust sources in this work are limited to desert dust produced by wind erosion in arid and semi-arid regions. Despite they represent the major global sources of dust, the presence of urban and industrial dust at the regional level is likely important. These anthropogenic sources are currently absent from our framework, yet they may contain chemically active minerals and interact efficiently with co-emitted anthropogenic gases in densely populated environments. Incorporating such sources may improve air-quality assessments, especially in regions weakly affected by desert dust.

Constraining dust emitted flux: We constrained dust emissions through assimilation of satellite-inferred dust optical depth, motivated by the fact that emission uncertainty is a major contributor to dust model error. However, this approach does not explicitly address uncertainties in other processes such as transport and deposition, which may be partially compensated by the emission correction. Although improving these processes may yield more modest gains than correcting emissions, it would increase physical consistency and strengthen the robustness of the conclusions.

Heterogeneous chemistry and aerosol acidity: Dust heterogeneous chemistry extends beyond the formation of SIA. For instance, previous studies have shown the existence of heterogeneous reactions between dust particles and organic species. Also, the presence of oxidants such as nitrogen oxides (NO_x) and ozone (O_3) in the liquid coatings of dust might be relevant to represent the dynamics of heterogeneous reactions. In this Thesis we constrained the representation of dust heterogeneous reactions to inorganic gas species, well-known for their paramount importance for secondary aerosol formation and consequential air-quality implications. Solely the role of oxidants in the oxidation of $SO_{2(g)}$ is implicit in the empirical uptake coefficient used for this species. Nevertheless, a more complete representation of dust heterogeneous chemistry would benefit from specifically representing oxidant species, extending the chemical implications beyond inorganic aerosols. Another relevant topic of research is the accurate description of dust alkalinity titration and its associated buffering capacity, as the rate of mineral base consumption is a primary determinant of aerosol acidity, NO_3^- partitioning, and the subsequent chemical aging of dust during long-range transport. Beyond dust heterogeneous chemistry, sea salt chemistry also deserves further research to reduce current uncertainties in the uptake coefficients and its role in aerosol acidity.

Advancing model parameterizations: Future studies should advance towards more explicit mechanistic representation of aerosol heterogeneous chemistry in models. Currently, the structural simplifications required to mitigate the high computational burden of processes such as multiphase chemistry limit the accuracy of models. The implementation of the dynamic mass transfer approach to solve gas-aerosol partitioning serves as a good example of a physically superior yet computationally non-viable methodology for current global-scale simulations. A strategic frontier for incorporating this complexity without compromising efficiency lies in the development of process-level emulators. An option could be leveraging machine learning solutions to approximate expensive chemical solvers, allowing models to integrate high-fidelity thermodynamic and kinetic knowledge with negligible computational overhead, effectively bridging the gap between detailed box-model physics and global-scale simulations.

In addition to improving individual parameterizations, future studies should adopt ensemble-based uncertainty quantification approaches that jointly perturb mineralogical composition, uptake coefficients, and emission fluxes. Such ensembles would allow attribution of uncertainty in aerosol optical properties and chemistry to specific processes and guide observational priorities more efficiently than single-sensitivity experiments.

Regional and high-resolution experiments: Higher-resolution simulations are needed to better assess the impacts of dust heterogeneous chemistry on short-lived and localized NO_3^- formation events, particularly over sensitive regions such as East Asia. Regional experiments would provide insights into mechanisms driving extremes and improve predictability.

Extending these simulations to air-quality–oriented metrics, such as exceedances of particulate matter with diameter below $2.5\mu m$ ($PM_{2.5}$) and population exposure, would further clarify the relevance of dust heterogeneous chemistry for regulatory assessments, particularly in regions where dust–pollution interactions drive episodic NO_3^- pollution events.

Wet deposition evaluation: Future work should evaluate wet deposition of SIA. At the resolution used here ($1.4^\circ \times 1^\circ$), many precipitation processes are parameterized rather than explicitly resolved, which introduces uncertainty in wet removal and species lifetime. High-resolution simulations of targeted precipitation episodes, together with dedicated observational constraints, are needed to refine wet deposition and better constrain SIA lifetimes.

Optical properties and radiative forcing: Future research should prioritize the refinement of Fe oxide speciation within global models, specifically distinguishing between the mass fractions and mixing states of hematite and goethite. Because these minerals possess distinct spectral absorption profiles, transitioning from total Fe mass to mineral-specific concentrations is essential for reducing uncertainties in the simulated SSA.

An important limitation of the current framework is the implicit assumption regarding aerosol mixing state in the optical calculations. The radiative effects of dust depend not only on mineral composition and secondary aerosol mass, but also on whether absorbing minerals and SIA are internally or externally mixed. Future work should explicitly explore alternative mixing-state assumptions for dust–SIA systems, including core–shell versus externally mixed representations, and assess their impact on SSA, absorption enhancement, and radiative forcing. Such developments would help reconcile discrepancies between modeled and observed SSA and improve the physical realism of aerosol optical calculations.

While this Thesis focuses on aerosol optical properties, translating these changes into direct radiative forcing was beyond its scope. Future studies should explicitly quantify direct radiative forcing responses to mineralogical variability and dust heterogeneous chemistry, including the competing roles of enhanced scattering by SIA and increased absorption by Fe oxides. Such analyses are essential to place the chemical sensitivities identified here into a climate-relevant context.

Cloud interactions and radiative forcing: SIA formation and aerosol acidity modify dust hygroscopicity, size distribution, and mixing state, which can alter dust activity as CCN and its influence on cloud microphysics. Although these pathways may be critical for total dust radiative forcing, they are not addressed here. Future work should extend this framework to quantify how source-resolved dust mineralogy affects CCN activation, cloud albedo and lifetime, and ultimately the total radiative forcing of dust–pollution–cloud interactions.

Experimental and observational constraints: While this Thesis advances the representation of dust–gas interactions, significant uncertainties persist due to the scarcity of targeted experimental and observational constraints. Future progress requires a multi-scale strategy encompassing the following:

- **Laboratory and kinetic characterization:** Targeted laboratory studies are required to further characterize the interplay between mineralogical composition, particle surface acidity, and solubility. Specifically, additional studies are needed to constrain uptake coefficients (γ) for ammonia ($NH_{3(g)}$),

$SO_{2(g)}$, and sulfuric acid ($H_2SO_{4(g)}$) on mineral dust and sea salt substrates. A primary objective should be the refinement of $HNO_{3(g)}$ uptake parameterizations on sea salt, which remains poorly constrained in current global models.

- **In-situ observations and field campaigns:** Robust model evaluation is currently hindered by the scarcity of simultaneous in-situ observations of gas-phase precursors and their particulate counterparts (notably $HNO_{3(g)}$, $NH_{3(g)}$, and size-resolved NO_3^-, NH_4^+, and SO_4^{2-} particulate matter). Expanding intensive field campaigns and incorporating observations of dry and wet deposition will be essential for further advancing our current understanding of heterogeneous chemical processes and their incorporation in atmospheric models.
- **Exploitation of novel remote sensing products:** The integration of high-resolution mineralogical maps – building upon the refinements from EMIT imaging spectroscopy – should be combined with advanced column retrievals. This includes leveraging improved *AERONET* intensive properties and emerging spaceborne lidar datasets from the *EarthCare* mission. Furthermore, the systematic exploitation of satellite products—such as *CrIS* for $NH_{3(g)}$, *TROPOMI* for nitrogen dioxide ($NO_{2(g)}$), and *VIIRS* for AOD—alongside ground-based lidars from networks such as *EARLINET*, should provide the necessary spatial constraints to refine model parameterizations across diverse dust-affected regions.

Overall, advancing the representation of dust heterogeneous chemistry will require coordinated progress in mineralogical characterization, chemical parameterization, optical modeling, and observational constraints. This Thesis provides a process-based foundation upon which such integrated developments can be built, with the aim of improving atmospheric modeling in the current context of rapidly evolving air quality conditions and climate change.

A

Supplement of Chapter 5

A.1 Journet and Claquin mineral data

Mineral	Bin 1	Bin 2	Bin 3	Bin 4	Bin 5	Bin 6	Bin 7	Bin 8	Soluble in water?	Soluble in acids?	Assumed reactive?	Notes/ References
Illite	1.1E-04	5.4E-04	4.0E-03	1.2E-02	2.9E-02	4.2E-02	7.2E-02	1.9E-02	no	yes	yes	1
Montmorillonite	6.4E-05	3.0E-04	2.3E-03	6.5E-03	1.7E-02	2.4E-02	4.1E-02	1.1E-02	-	yes	yes	2
Kaolinite	7.6E-05	3.6E-04	2.7E-03	7.8E-03	2.0E-02	2.8E-02	4.8E-02	1.3E-02	no	yes	no	3
Calcite	1.3E-05	6.3E-05	4.7E-04	1.4E-03	5.2E-03	1.2E-02	2.7E-02	8.0E-03	yes	yes	yes	4
Quartz	2.0E-05	9.7E-05	7.3E-04	2.1E-03	2.4E-02	8.0E-02	2.1E-01	6.7E-02	no	no	no	5
Feldspar	8.1E-06	3.9E-05	2.9E-04	8.3E-04	8.5E-03	2.8E-02	7.3E-02	2.3E-02	no	yes	yes	6
Iron Oxide	4.6E-06	2.2E-05	1.6E-04	4.7E-04	1.6E-03	3.3E-03	7.3E-03	2.2E-03	-	-	no	7
Gypsum	3.4E-06	1.6E-05	1.2E-04	3.5E-04	1.3E-03	2.8E-03	6.3E-03	1.9E-03	poor	yes	no	8
Total	3.0E-04	1.4E-03	1.1E-02	3.1E-02	1.1E-01	2.2E-01	4.9E-01	1.4E-01				

Table A.1: Globally-averaged fractions (0 to 1) of the minerals attributed to each bin from the Claquin et al. (1999) mineral database. The respective references for the assumed solubility of each mineral are: References:
1. Assumed reactive because relatively soluble in acids (Webmineral 2008f).
2. Assumed reactive because relatively soluble in acids (Nutting 1941; 1932).
3. Assumed nonreactive because predominantly containing Al and Si (Yang 2008).
4. Assumed reactive because highly soluble (Usher et al. 2003, Krueger et al. 2004, Hodzic et al. 2006).
5. Assumed nonreactive because not soluble (Usher et al. 2003).
6. Assumed reactive because relatively soluble in acids (Blum 1994, Mindat.org b).
7. Assumed nonreactive because iron is not considered in ISORROPIA-II (National Center for Biotechnology Information 2024a, Weast 1980).
8. Assumed nonreactive because poorly soluble in water and soluble only in high acidity solutions (Zhang and Muhammed 1989, National Center for Biotechnology Information. PubChem Compound Database 2024a, Krueger et al. 2004, Hodzic et al. 2006).

Mineral	Mineral Mw (g/mol)	Soluble element	Element Mw (g/mol)	Element fraction	Bin 1	Bin 2	Bin 3	Bin 4	Total fine	Bin 5	Bin 6	Bin 7	Bin 8	Total coarse	Total	References
Illite	389.340	K	39.10	0.10	3.76%	3.76%	3.76%	3.76%	3.76%	2.78%	1.92%	1.49%	1.31%	1.88%	2.92%	1
	389.340	Mg	24.31	0.06	2.34%	2.34%	2.34%	2.34%	2.34%	1.73%	1.19%	0.93%	0.82%	1.17%	1.82%	1
Montmorillonite	549.070	Ca	40.08	0.07	1.54%	1.54%	1.54%	1.54%	1.54%	1.14%	0.78%	0.61%	0.54%	0.77%	1.20%	2
	549.070	Na	22.99	0.04	0.88%	0.88%	0.88%	0.88%	0.88%	0.65%	0.45%	0.35%	0.31%	0.44%	0.69%	2
Feldspar																
- 1/3 Albite	263.020	Na (1/3)	22.99	0.03	0.07%	0.07%	0.07%	0.07%	0.07%	0.21%	0.33%	0.39%	0.42%	0.34%	0.19%	3
- 1/3 Anorthite	277.410	Ca (1/3)	40.08	0.04	0.12%	0.12%	0.12%	0.12%	0.12%	0.35%	0.55%	0.65%	0.70%	0.56%	0.31%	4
- 1/3 Orthoclase	278.330	K (1/3)	39.10	0.04	0.11%	0.11%	0.11%	0.11%	0.11%	0.34%	0.54%	0.63%	0.68%	0.55%	0.31%	5
Calcite	100.090	Ca	40.08	0.40	1.76%	1.76%	1.76%	1.76%	1.76%	1.95%	2.11%	2.19%	2.22%	2.12%	1.92%	6
Gypsum	172.200	Ca	40.08	0.23	0.26%	0.26%	0.26%	0.26%	0.26%	0.28%	0.30%	0.30%	0.31%	0.30%	0.28%	7
Total Ca					3.68%	3.68%	3.68%	3.68%	**3.68%**	3.71%	3.74%	3.76%	3.76%	**3.74%**	**3.71%**	
Total Na					0.95%	0.95%	0.95%	0.95%	**0.95%**	0.86%	0.78%	0.75%	0.73%	**0.78%**	**0.87%**	
Total K					3.87%	3.87%	3.87%	3.87%	**3.87%**	3.12%	2.45%	2.13%	1.99%	**2.42%**	**3.15%**	
Total Mg					2.34%	2.34%	2.34%	2.34%	**2.34%**	1.73%	1.19%	0.93%	0.82%	**1.17%**	**1.75%**	

Table A.2: The NVC content from globally-averaged mineralogy of Claquin et al. (1999) assumed for each size bin, derived from those minerals assumed to be soluble in water (Table A.1). The respective references for the ionic composition of each mineral and molar masses are:
1. Webmineral (2008f)
2. Nutting (1941; 1932)
3. Webmineral (2008a)
4. Webmineral (2008b)
5. Webmineral (2008e)
6. Webmineral (2008c), National Center for Biotechnology Information. PubChem Compound Database (2024a)
7. Webmineral (2008d), Hulett and Allen (1902)

Mineral	Bin 1	Bin 2	Bin 3	Bin 4	Bin 5	Bin 6	Bin 7	Bin 8	Soluble in water?	Soluble in acids?	Assumed reactive?	Notes/ References
Illite	8.5E-5	4.1E-4	3.1E-3	8.8E-3	2.2E-2	3.2E-2	5.5E-2	1.4E-2	no	yes	yes	1
Montmorillonite	6.2E-5	3.0E-4	2.2E-3	6.4E-3	1.6E-2	2.3E-2	4.0E-2	1.0E-2	-	yes	yes	2
Kaolinite	7.8E-5	3.7E-4	2.8E-3	8.0E-3	2.0E-2	2.9E-2	5.0E-2	1.3E-2	no	yes	no	3
Chlorite	1.2E-5	5.6E-5	4.2E-4	1.2E-3	4.8E-3	1.1E-2	2.6E-2	7.9E-3	no	-	no	4
Vermiculite	7.9E-6	3.8E-5	2.8E-4	8.1E-4	2.1E-3	2.9E-3	5.1E-3	1.3E-3	no	no	no	5
Feldspar	3.4E-6	1.6E-5	1.2E-4	3.5E-4	6.3E-3	2.2E-2	6.0E-2	1.9E-2	no	yes	yes	6
Quartz	1.2E-5	5.8E-5	4.4E-4	1.3E-3	1.9E-2	6.6E-2	1.8E-1	5.6E-2	no	no	no	7
Calcite	3.1E-5	1.5E-4	1.1E-3	3.2E-3	1.0E-2	1.9E-2	3.9E-2	1.1E-2	yes	yes	yes	8
Hematite	3.5E-6	1.7E-5	1.3E-4	3.6E-4	9.2E-4	1.3E-3	2.3E-3	5.9E-4	no	yes	no	9
Goethite	6.2E-6	2.9E-5	2.2E-4	6.3E-4	1.8E-3	3.1E-3	6.2E-3	1.8E-3	no	-	no	10
Gypsum	4.7E-7	2.2E-6	1.7E-5	4.8E-5	1.4E-4	2.5E-4	5.2E-4	1.5E-4	poor	yes	no	11
Mica	0.0E+0	0.0E+0	0.0E+0	0.0E+0	2.7E-3	1.0E-2	2.8E-2	9.0E-3	no	no	no	12
Total	3.0E-4	1.4E-3	1.1E-2	3.1E-2	1.1E-1	2.2E-1	4.9E-1	1.5E-1				

Table A.3: Globally-averaged fractions (0 to 1) of the minerals attributed to each bin from the Journet et al. (2014) mineral database. The respective references for the assumed solubility of each mineral are:
1. Assumed reactive because relatively soluble in acids (Webmineral 2008f)
2. Assumed reactive because relatively soluble in acids (Nutting 1941; 1932)
3. Assumed nonreactive because predominantly containing Al and Si (Yang 2008).
4. Assumed nonreactive because not soluble in water (Britannica, The Editors of Encyclopaedia 2018, Mindat.org a).
5. Assumed nonreactive because not soluble (Huggett 2015, Schulze 2005, Bleam 2017).
6. Assumed reactive because relatively soluble in acids (Blum 1994, Mindat.org b).
7. Assumed nonreactive because not soluble (Usher et al. 2003).
8. Assumed reactive because highly soluble (Usher et al. 2003, Krueger et al. 2004, Hodzic et al. 2006).
9. Assumed nonreactive because iron is not considered in ISORROPIA-II (National Center for Biotechnology Information 2024a, Weast 1980).
10. Assumed nonreactive because not soluble, although lacking information if soluble in acids. (Essington et al. 2005, National Center for Biotechnology Information. PubChem Compound Database 2024b).
11. Assumed nonreactive because poorly soluble in water and soluble only in high acidity solutions (Zhang and Muhammed 1989, National Center for Biotechnology Information. PubChem Compound Database 2024a, Krueger et al. 2004, Hodzic et al. 2006).
12. Assumed nonreactive because non soluble (National Center for Biotechnology Information 2024b).

Mineral	Mineral Mw (g/mol)	Soluble element	Element Mw (g/mol)	Element fraction	Bin 1	Bin 2	Bin 3	Bin 4	Total fine	Bin 5	Bin 6	Bin 7	Bin 8	Total coarse	Total	References
Illite	389.34	K	39.10	0.10	2.84%	2.84%	2.84%	2.84%	2.84%	2.10%	1.45%	1.13%	0.99%	1.41%	2.20%	1
	389.34	Mg	24.31	0.06	1.76%	1.76%	1.76%	1.76%	1.76%	1.30%	0.90%	0.70%	0.62%	0.88%	1.37%	1
Montmorillonite	549.07	Ca	40.08	0.07	1.50%	1.50%	1.50%	1.50%	1.50%	1.11%	0.76%	0.59%	0.52%	0.75%	1.16%	2
	549.07	Na	22.99	0.04	0.86%	0.86%	0.86%	0.86%	0.86%	0.63%	0.44%	0.34%	0.30%	0.43%	0.67%	2
Feldspar																
- 1/3 Albite	263.02	Na (1/3)	22.99	0.03	0.03%	0.03%	0.03%	0.03%	0.03%	0.16%	0.27%	0.32%	0.35%	0.27%	0.14%	3
- 1/3 Anorthite	277.41	Ca (1/3)	40.08	0.04	0.05%	0.05%	0.05%	0.05%	0.05%	0.26%	0.44%	0.53%	0.57%	0.45%	0.23%	4
- 1/3 Orthoclase	278.33	K (1/3)	39.10	0.04	0.05%	0.05%	0.05%	0.05%	0.05%	0.25%	0.43%	0.52%	0.56%	0.44%	0.22%	5
Calcite	100.09	Ca	40.08	0.40	4.15%	4.15%	4.15%	4.15%	4.15%	3.76%	3.41%	3.23%	3.16%	3.39%	3.81%	6
Gypsum	172.20	Ca	40.08	0.23	0.04%	0.04%	0.04%	0.04%	0.04%	0.03%	0.03%	0.02%	0.02%	0.03%	0.03%	7
Total Ca					5.73%	5.73%	5.73%	5.73%	**5.73%**	5.15%	4.64%	4.39%	4.28%	**4.61%**	**5.17%**	
Total Na					0.89%	0.89%	0.89%	0.89%	**0.89%**	0.79%	0.71%	0.66%	0.65%	**0.70%**	**0.79%**	
Total K					2.88%	2.88%	2.88%	2.88%	**2.88%**	2.35%	1.88%	1.64%	1.55%	**1.85%**	**2.37%**	
Total Mg					1.76%	1.76%	1.76%	1.76%	**1.76%**	1.30%	0.90%	0.70%	0.62%	**0.88%**	**1.32%**	

Table A.4: The NVC content from globally-averaged mineralogy of Journet et al. (2014) assumed for each size bin, derived from those minerals assumed to be soluble in water (Table A.3). The respective references for the ionic composition of each mineral and molar masses are:

1. Webmineral (2008f)
2. Nutting (1941; 1932)
3. Webmineral (2008a)
4. Webmineral (2008b)
5. Webmineral (2008e)
6. Webmineral (2008c), National Center for Biotechnology Information. PubChem Compound Database (2024a)
7. Webmineral (2008d), Hulett and Allen (1902)

A.2 Spatial distributions

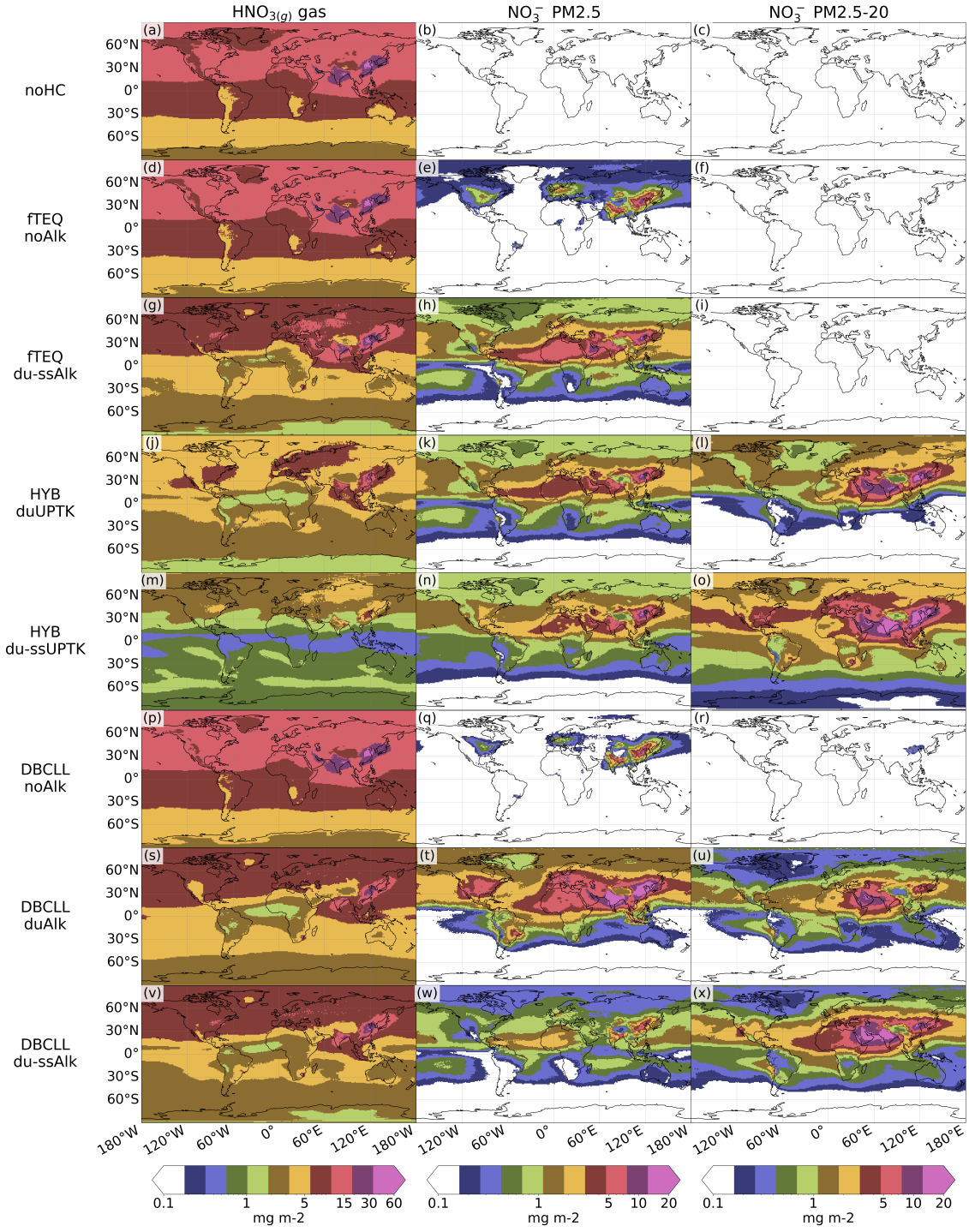

Figure A.1: Column loads ($mg\ m^{-2}$) of $HNO_{3(g)}$, fine and coarse particulate NO_3^- simulated by the different mechanisms, averaged for 2018.

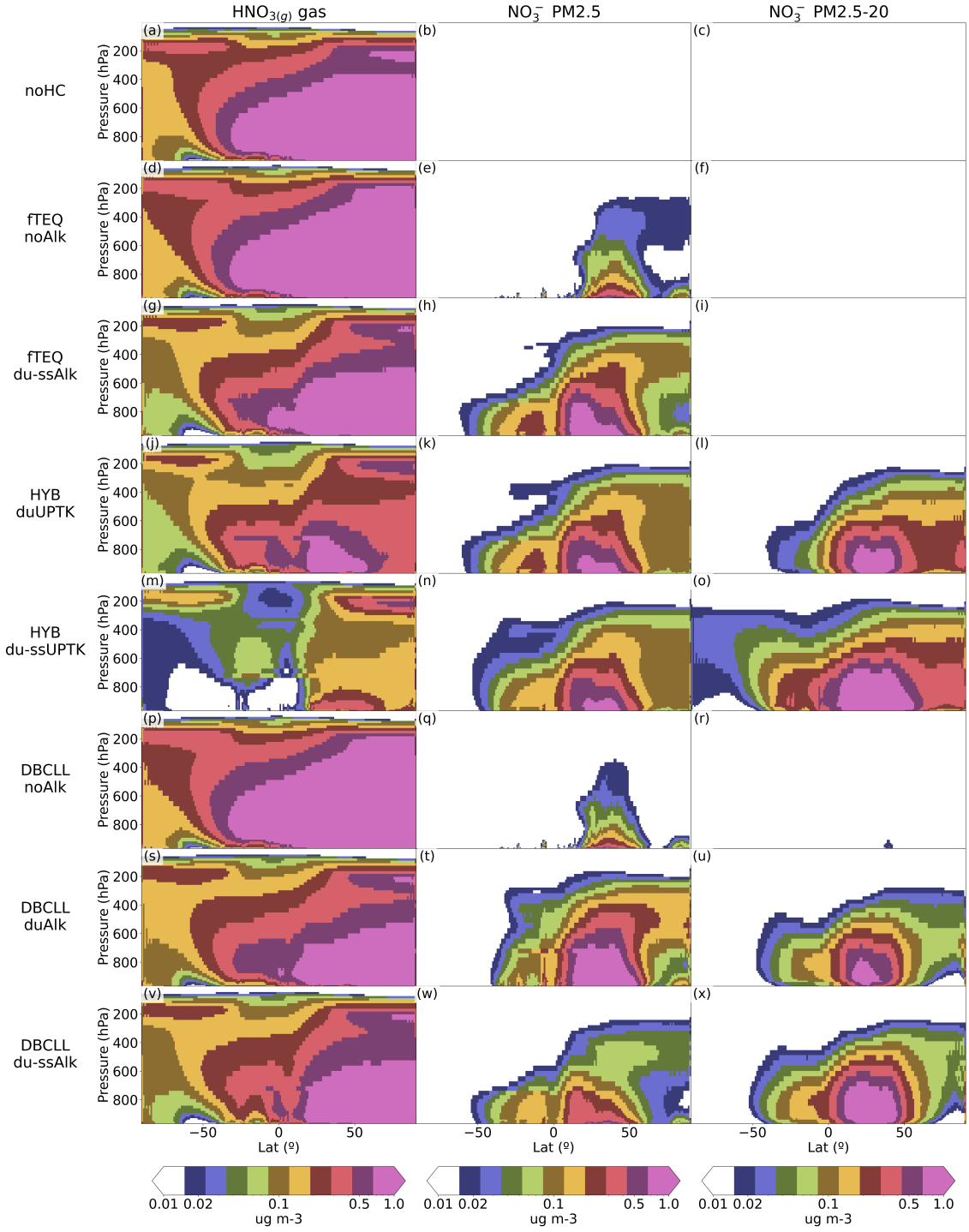

Figure A.2: Zonal average concentrations ($\mu g\ m^{-3}$) of $HNO_{3(g)}$, fine and coarse particulate NO_3^- simulated by the different mechanisms, averaged for 2018.

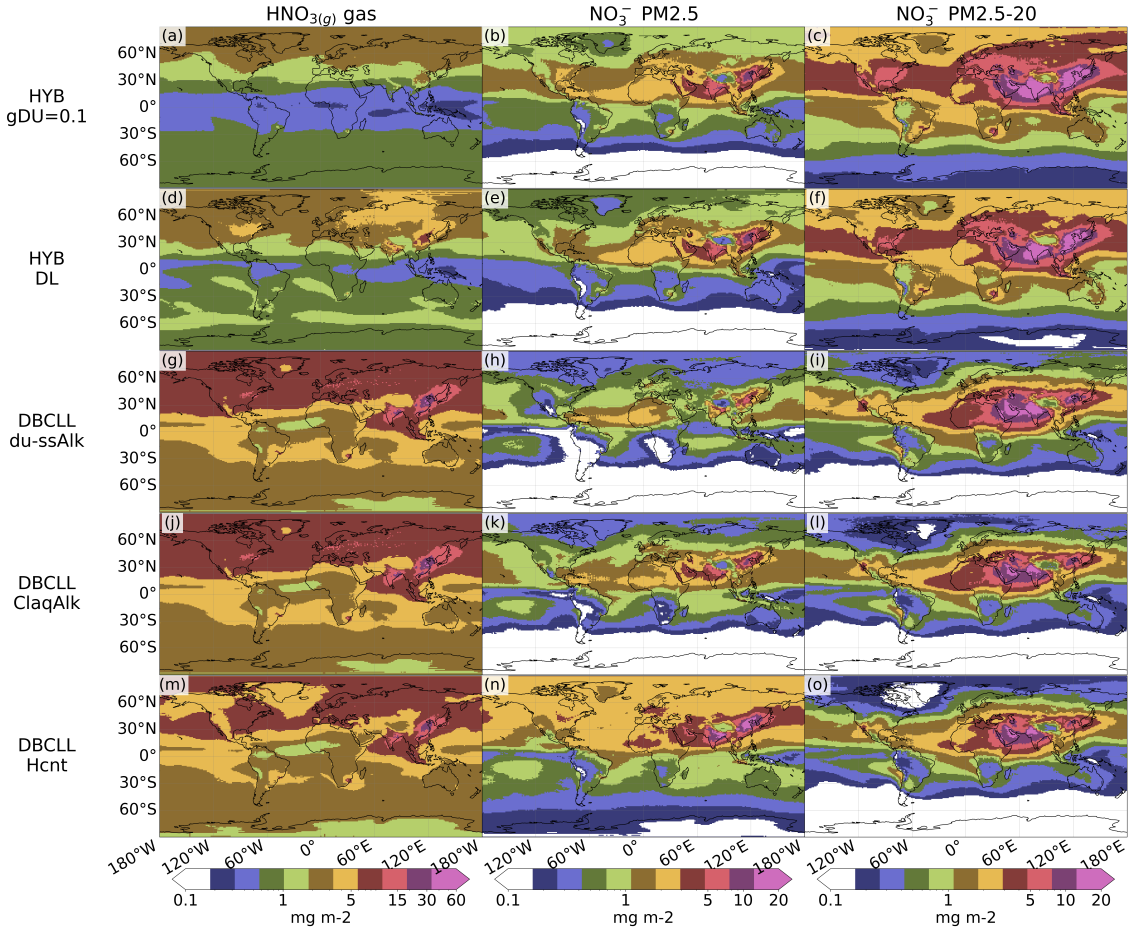

Figure A.3: Column loads ($mg\ m^{-2}$) of $HNO_{3(g)}$, fine and coarse particulate NO_3^- simulated by additional mechanisms, averaged for 2018.

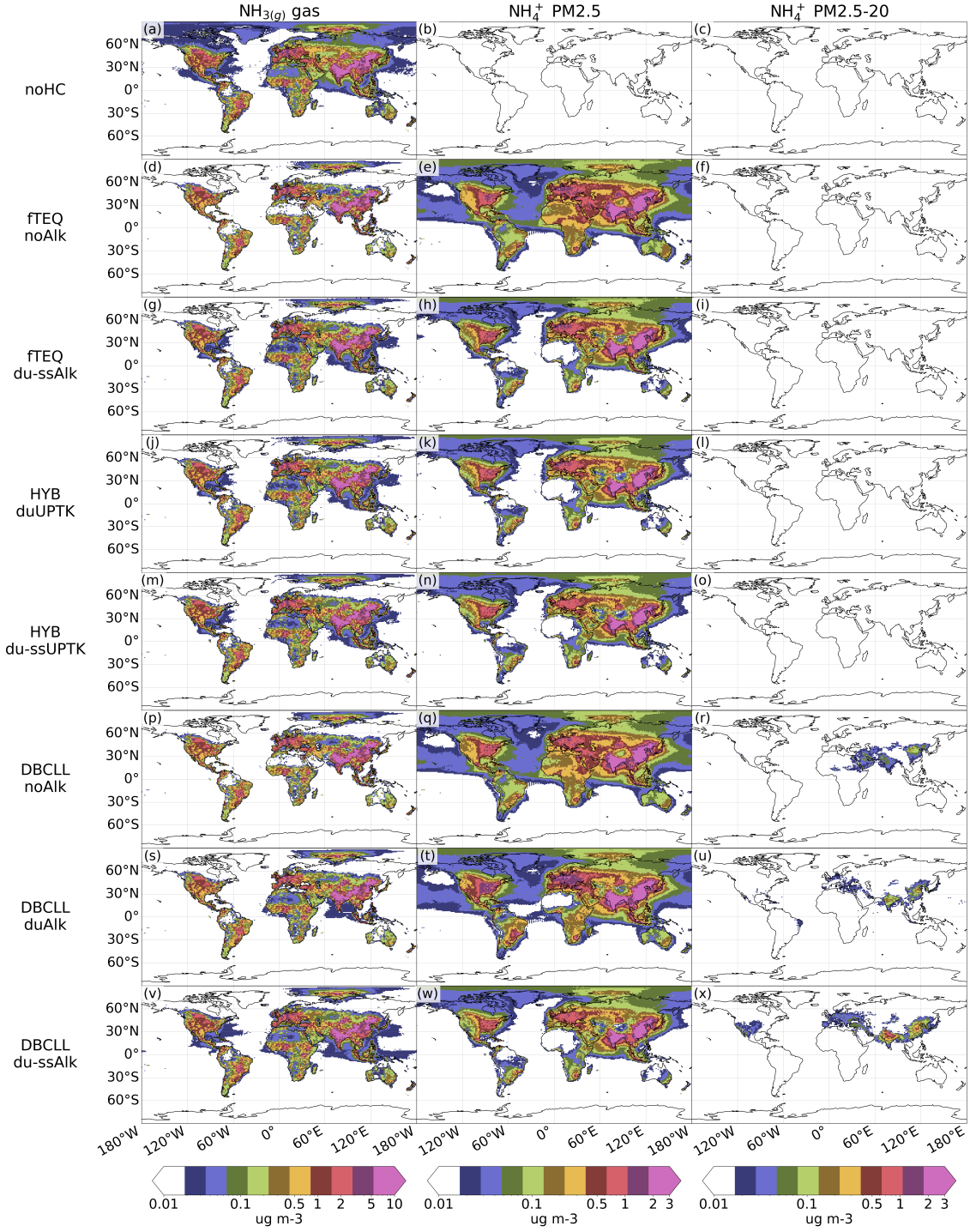

Figure A.4: Surface concentrations ($\mu g\ m^{-3}$) of $NH_{3(g)}$, fine and coarse particulate NH_4^+ simulated by the different mechanisms, averaged for 2018.

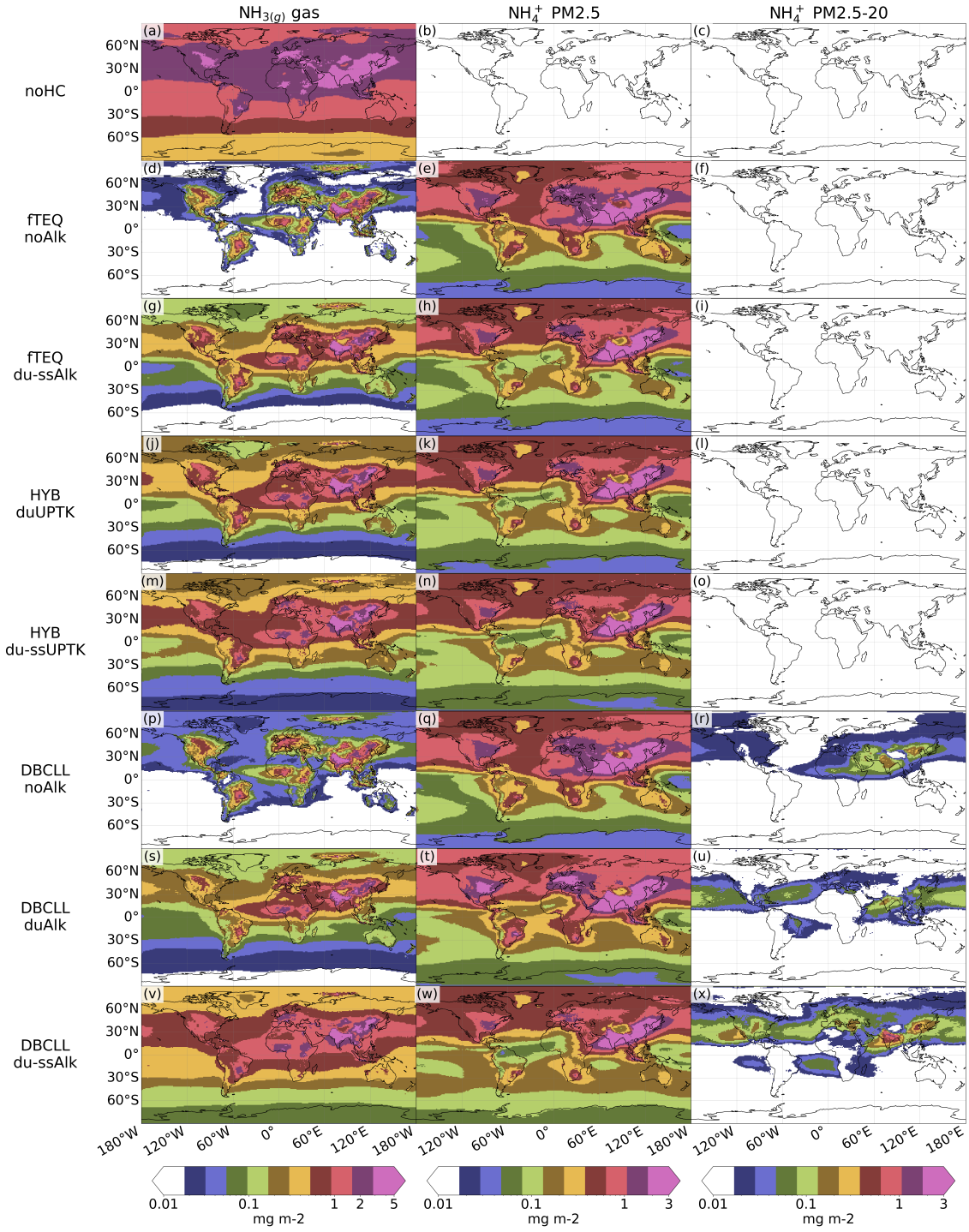

Figure A.5: Column loads ($mg\ m^{-2}$) of $NH_{3(g)}$, fine and coarse particulate NH_4^+ simulated by different mechanisms, averaged for 2018.

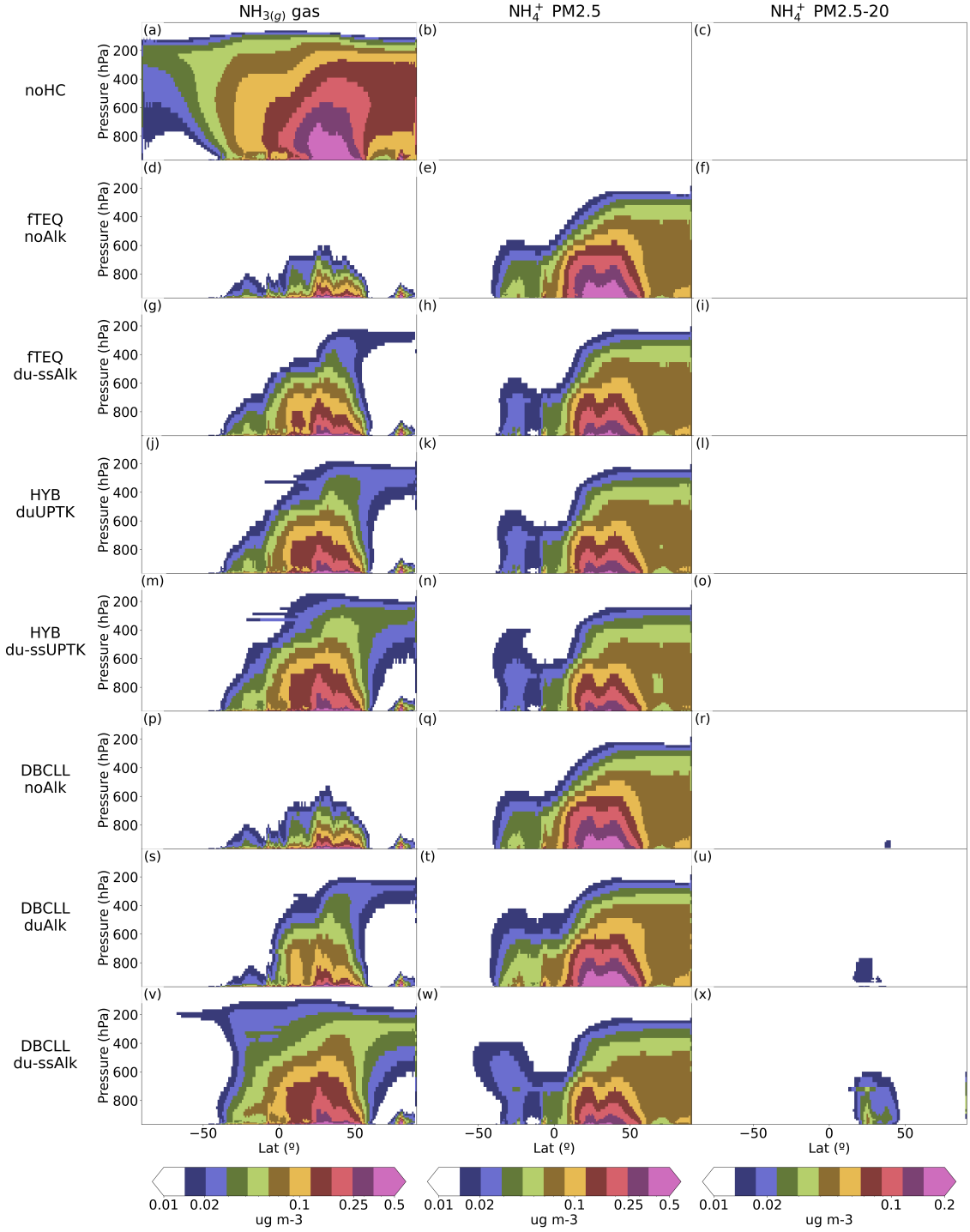

Figure A.6: Zonal average concentrations ($\mu g\ m^{-3}$) of $NH_{3(g)}$, fine and coarse particulate NH_4^+ simulated by the different mechanisms, averaged for 2018.

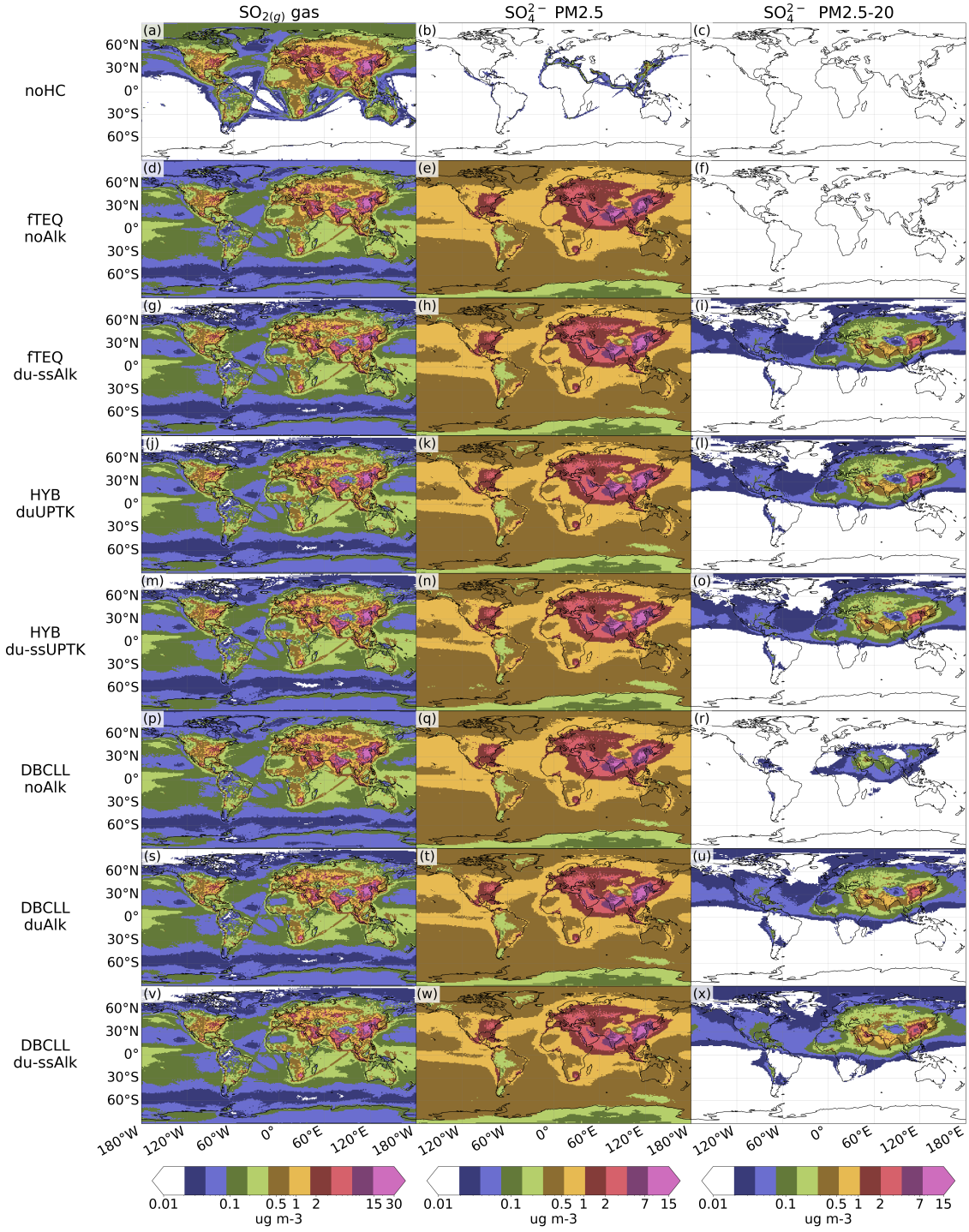

Figure A.7: Surface concentration ($\mu g\ m^{-3}$) of $SO_{2(g)}$, fine and coarse particulate SO_4^{2-} simulated by the different mechanisms, averaged for 2018.

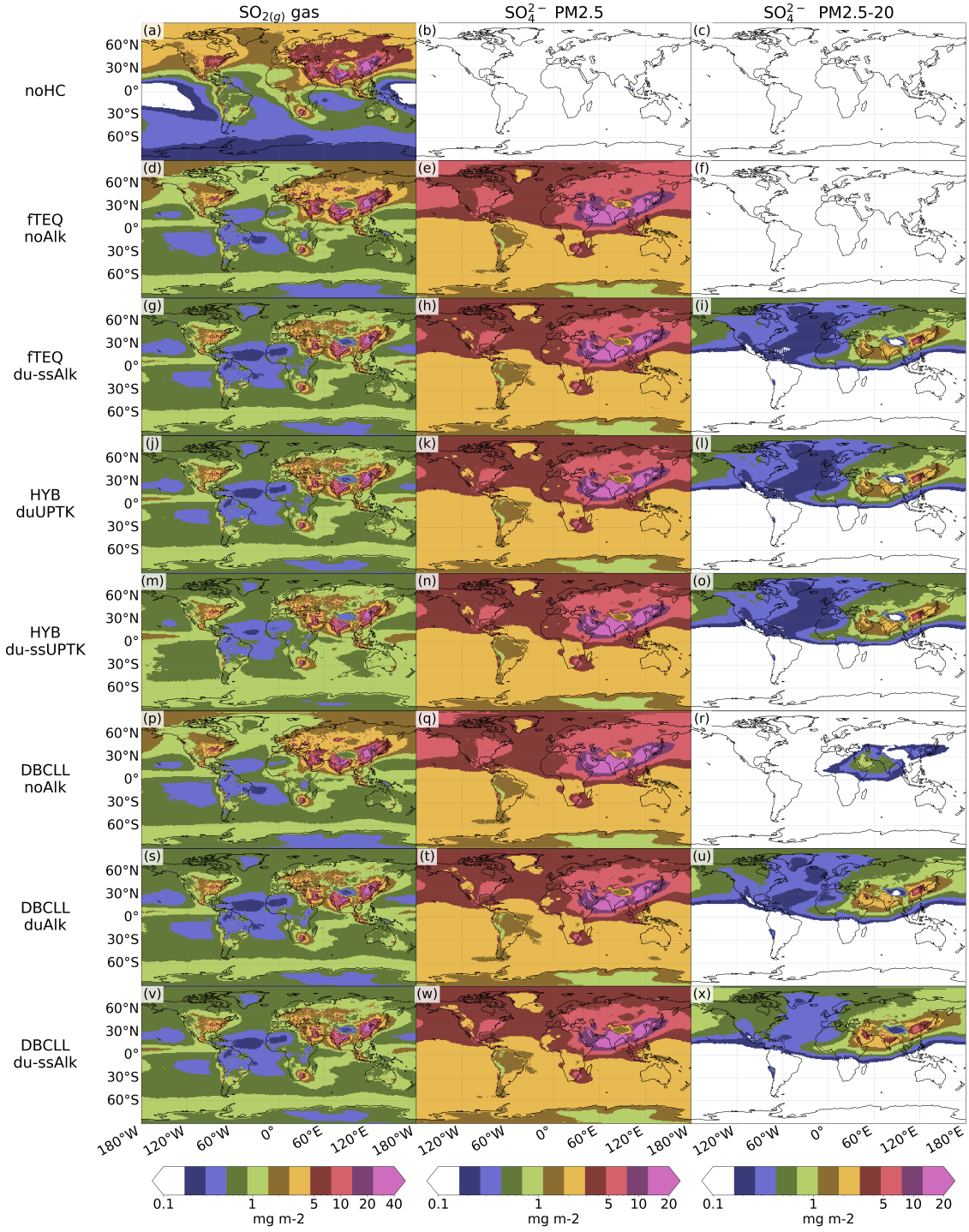

Figure A.8: Column load ($mg\ m^{-2}$) of $SO_{2(g)}$, fine and coarse particulate SO_4^{2-} simulated by the different mechanisms, averaged for 2018.

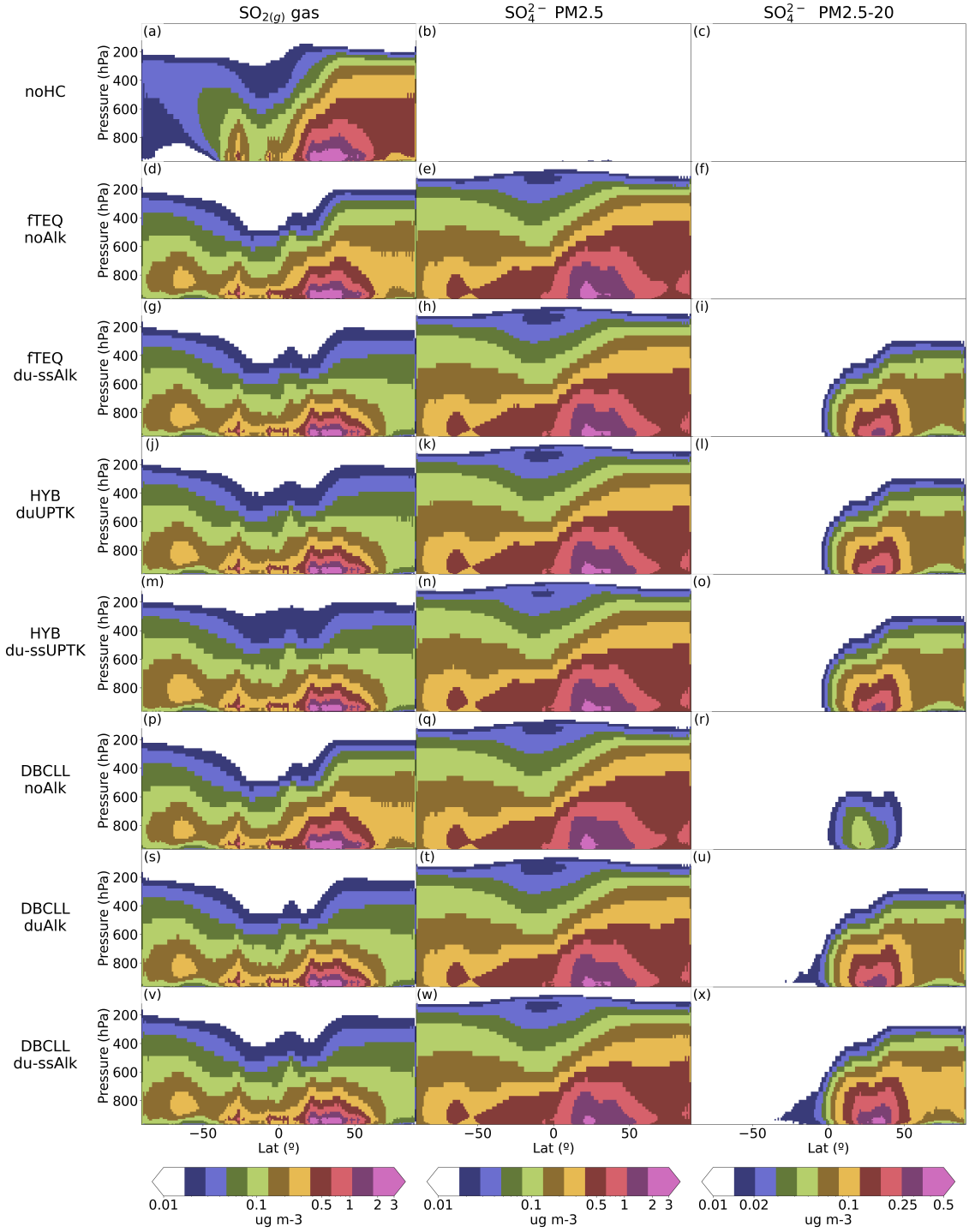

Figure A.9: Zonal average concentration ($\mu g\ m^{-3}$) of $SO_{2(g)}$, fine and coarse particulate SO_4^{2-} simulated by the different mechanisms, averaged for 2018.

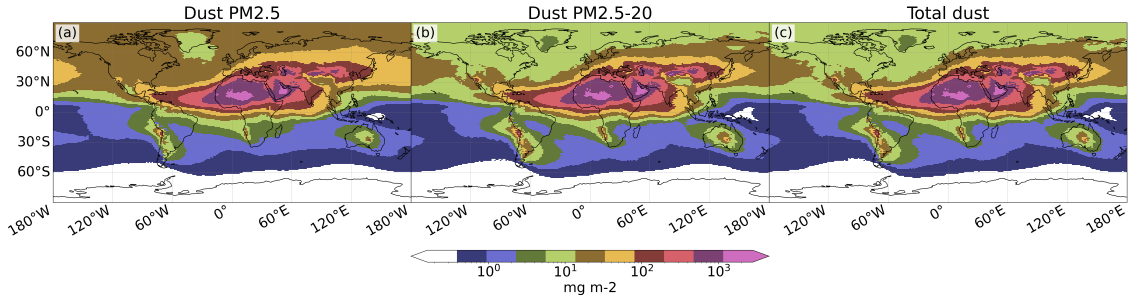

Figure A.10: Dust average column load ($mg\ m^{-2}$) for 2018.

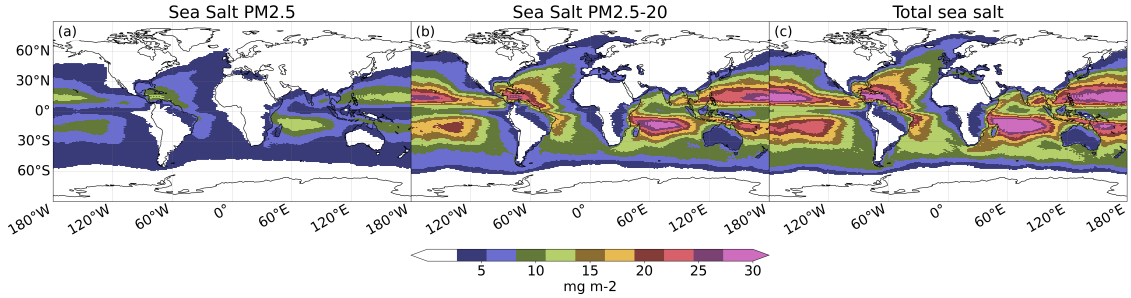

Figure A.11: Sea salt average column load ($mg\ m^{-2}$) for 2018.

A.3 Supplementary evaluation results

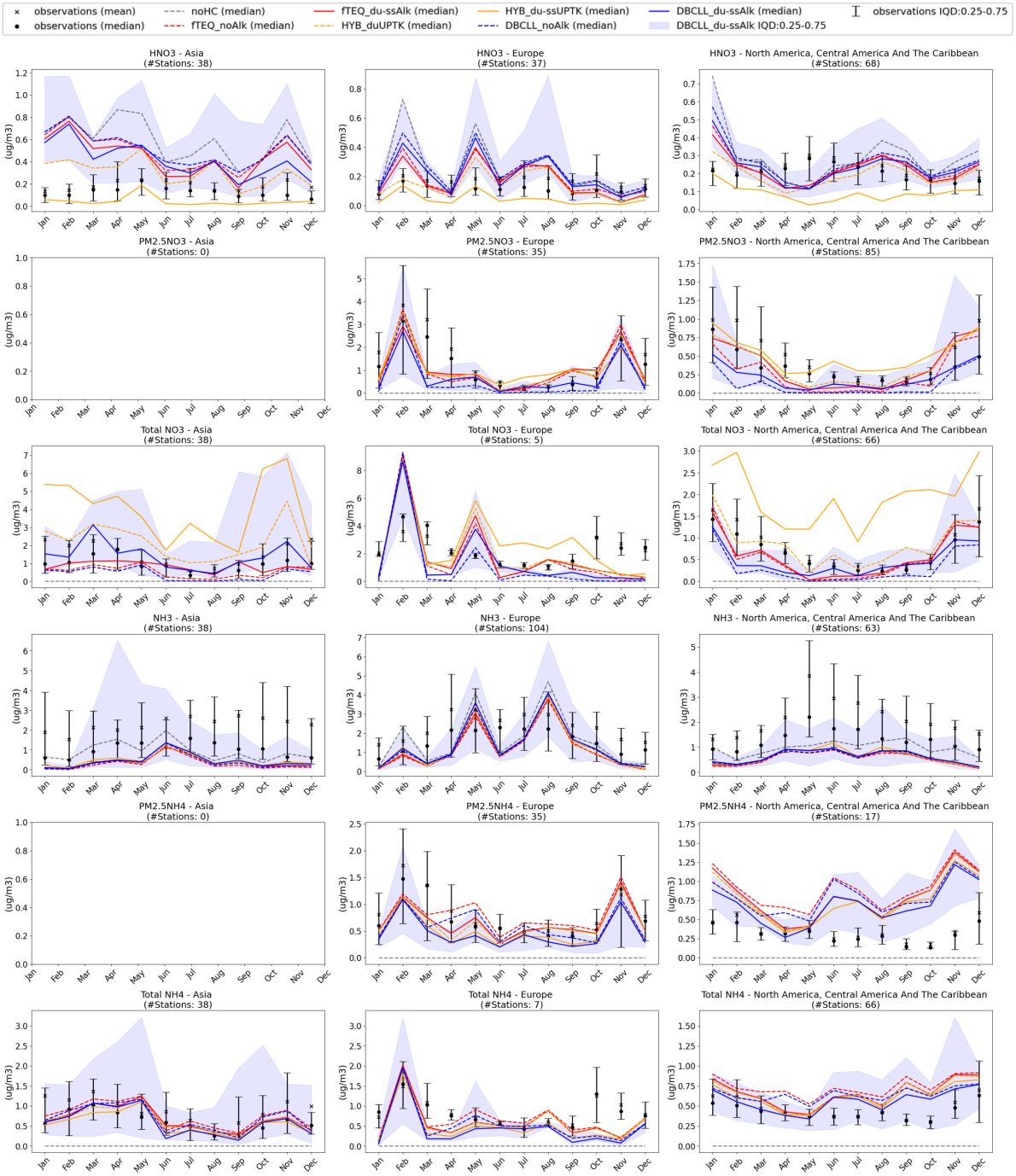

Figure A.12: Yearly surface concentration evaluation for Asia, Europe and North-Central America continents. Species are in rows and continents in columns. Black solid dots and crosses represent observational mean and median, respectively. Error bars are the interquantile 0.25 to 0.75 distance. Coloured lines represent medians obtained from the most representative configurations. Blue shade is the interquantile 0.25 - 0.75 distance for the DBCLL_du-ssAlk simulation. Observational PM_{10} from EANET (Asia) and US-EPA-CASTNET (North America) refers to total particle concentration, while GHOST data (Europe) is limited to PM_{10}. (Continues in the next page)

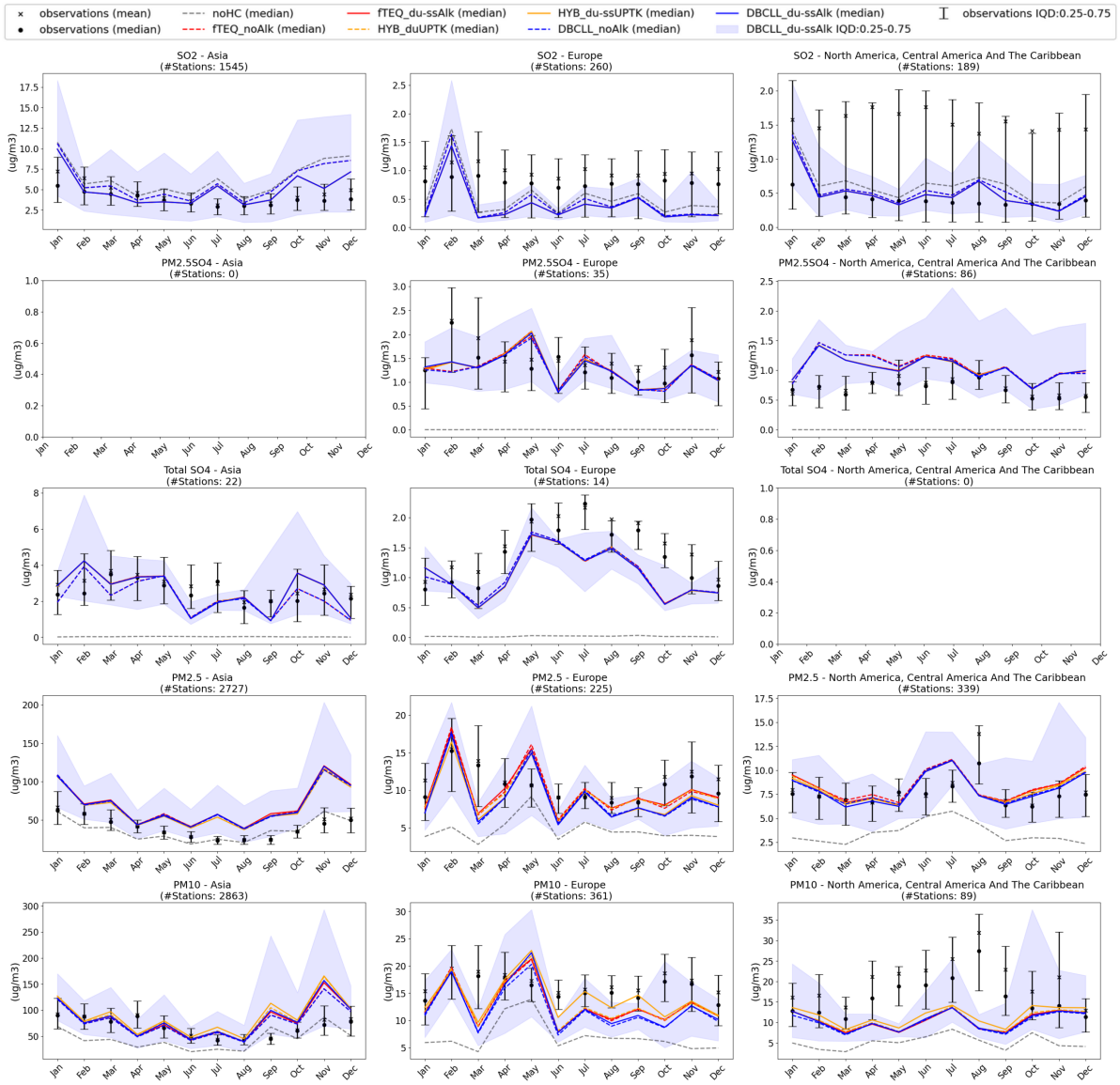

Figure A.12: (Continuation) Yearly surface concentration evaluation for Asia, Europe and North-Central America continents. Species are in rows and continents in columns. Black solid dots and crosses represent observational mean and median, respectively. Error bars are the interquantile 0.25 to 0.75 distance. Coloured lines represent medians obtained from the most representative configurations. Blue shade is the interquantile 0.25 - 0.75 distance for the DBCLL_du-ssAlk simulation. Observational PM_{10} from EANET (Asia) and US-EPA-CASTNET (North America) for SO_4^{2-} refers to total particle concentration, while GHOST data (Europe) is limited to PM_{10}.

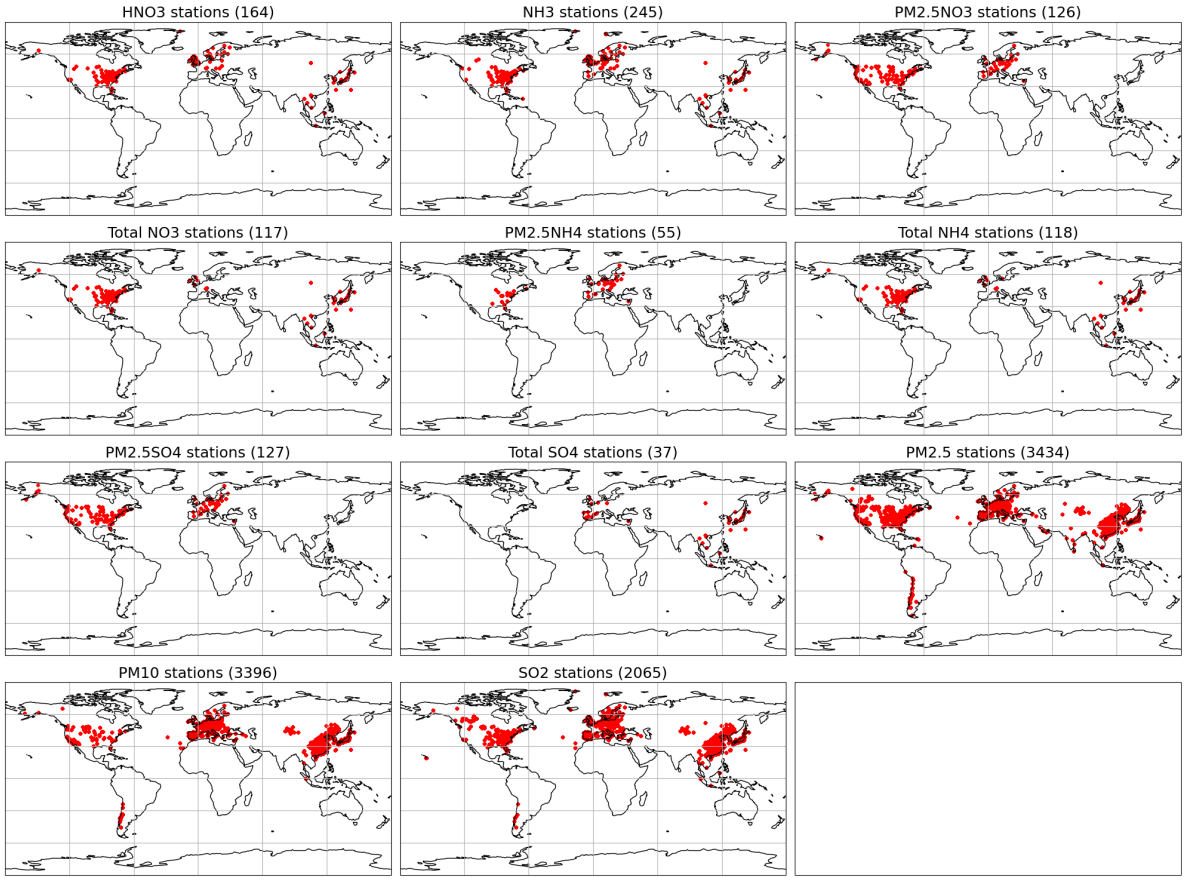

Figure A.13: Stations used in the observational evaluation for each species from the main text Fig.5.4 and Supplement Fig. A.12.

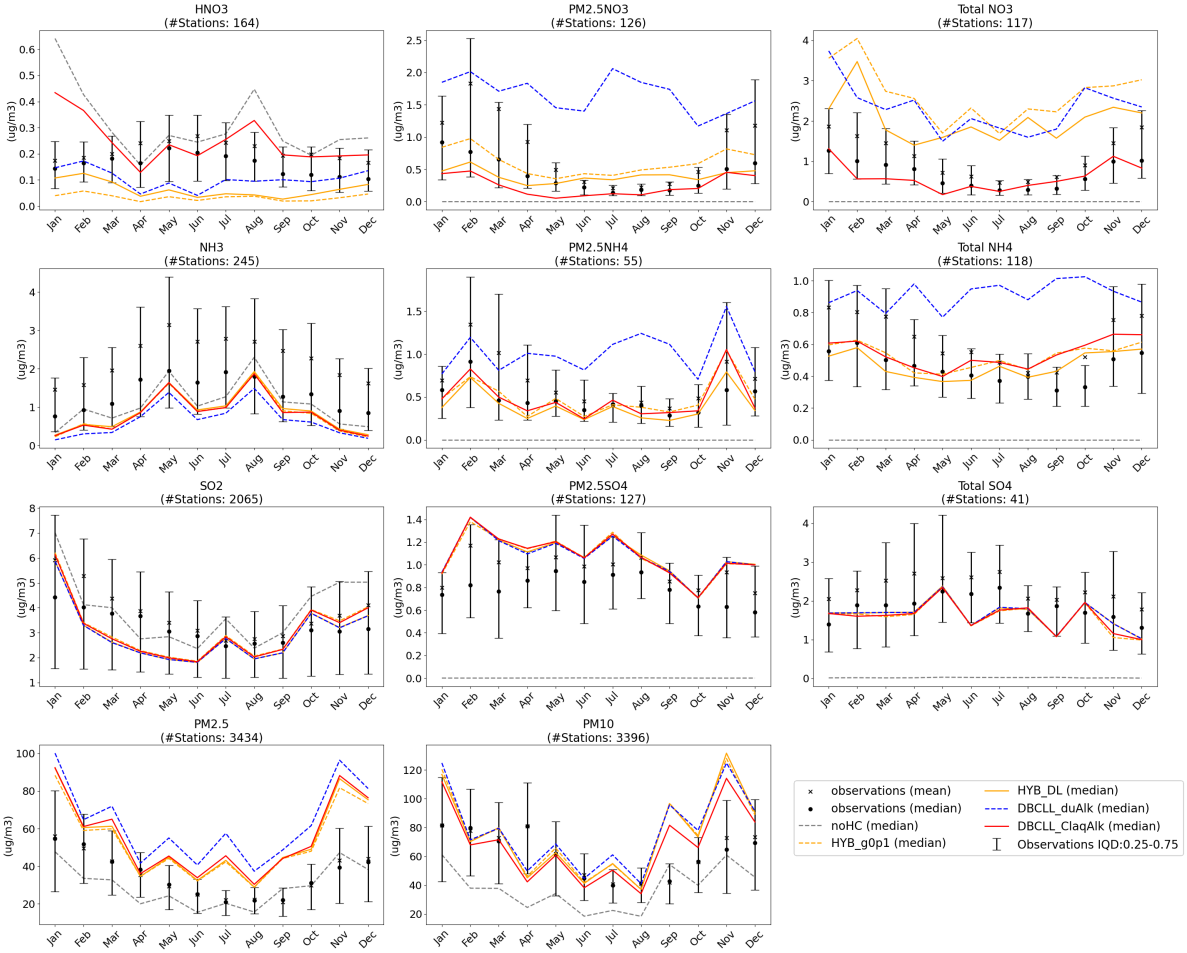

Figure A.14: Observational evaluation of gas and particulate species of additional sensitivity experiments. Black solid dots and crosses represent monthly mean and median of observations, respectively. Colour lines represent each configuration's monthly median surface concentrations over observational points. Error bars are the observational interquantile 0.25 to 0.75 distance. For the Total NO_3 modes, data from Europe, Asia and North-Central America has been averaged, despite data from Asia and North-Central America refers to total particle concentration, while data from Europe is limited strictly to $10\mu m$ particle diameter.

Table A.6: Correlation coefficients, bias ($\mu g\ m^{-3}$) and root mean square error (rmse, $\mu g\ m^{-3}$) of additional sensitivity experiments. The evaluation corresponds to the configurations' median with respect to the median of observations, corresponding to the timeseries shown in Fig. A.14.

	HNO3			**PM2.5NO3**			**Total NO3**		
	corr	**bias**	**rmse**	**corr**	**bias**	**rmse**	**corr**	**bias**	**rmse**
noHC	0.03	0.15	0.20	0.00	-0.43	0.49	0.00	-0.70	0.77
HYB_g0p1	0.05	-0.13	0.13	0.83	0.18	0.23	0.81	1.96	2.01
HYB_DL	-0.08	-0.10	0.11	0.61	-0.03	0.21	0.53	1.32	1.40
DBCLL_duAlk	-0.34	-0.05	0.08	0.21	1.24	1.28	0.80	1.61	1.65
DBCLL_ClaqAlk	0.14	0.09	0.12	0.82	-0.18	0.24	0.81	-0.09	0.22

	NH3			**PM2.5NH4**			**Total NH4**		
	corr	**bias**	**rmse**	**corr**	**bias**	**rmse**	**corr**	**bias**	**rmse**
noHC	0.80	-0.29	0.44	0.00	-0.48	0.51	0.00	-0.45	0.46
HYB_g0p1	0.85	-0.53	0.59	0.64	0.01	0.16	0.47	0.07	0.11
HYB_DL	0.85	-0.49	0.56	0.77	-0.09	0.14	0.50	0.02	0.09
DBCLL_duAlk	0.88	-0.71	0.73	0.27	0.53	0.58	-0.46	0.46	0.48
DBCLL_ClaqAlk	0.85	-0.53	0.59	0.70	-0.01	0.16	0.50	0.09	0.12

	SO2			**PM2.5SO4**			**Total SO4**		
	corr	**bias**	**rmse**	**corr**	**bias**	**rmse**	**corr**	**bias**	**rmse**
noHC	0.61	0.65	1.24	0.59	-0.79	0.80	0.62	-1.91	1.93
HYB_g0p1	0.62	-0.12	0.94	0.59	0.29	0.32	0.53	-0.42	0.54
HYB_DL	0.63	-0.29	0.91	0.57	0.29	0.33	0.60	-0.39	0.50
DBCLL_duAlk	0.63	-0.29	0.91	0.55	0.29	0.32	0.59	-0.38	0.49
DBCLL_ClaqAlk	0.62	-0.16	0.94	0.57	0.29	0.33	0.55	-0.41	0.52

	PM2.5			**PM10**		
	corr	**bias**	**rmse**	**corr**	**bias**	**rmse**
noHC	0.75	-5.62	9.55	0.40	-23.16	28.42
HYB_g0p1	0.76	18.02	21.95	0.38	14.27	29.96
HYB_DL	0.76	19.44	23.81	0.36	13.87	30.41
DBCLL_duAlk	0.71	28.07	31.58	0.38	16.47	30.10
DBCLL_ClaqAlk	0.76	20.75	24.88	0.43	7.45	24.20

Table A.5: GHOST quality flags used for the observational evaluation.

Code	Flag	Description
0	Missing Measurement	i.e. NaN.
1	Infinite Value	Value is infinite – occurs when data values are outside of the range that *float32* data type can handle (-3.4×10^{38} to +3.4×10^{38}).
2	Negative Measurement	Measurement is negative in absolute terms.
6	Invalid Data Provider Flags - GHOST Decreed	Measurements are associated with data quality flags given by the data provider which have been decreed by the GHOST project architects as being associated with substantial uncertainty/bias.
8	No Valid Data to Average	After screening by key QA flags, no valid data remains to average in the temporal window.
20	Erroneous Primary Sampling	The primary sampling is not appropriate to prepare the specific parameter for subsequent measurement.
21	Erroneous Sample Preparation	The sample preparation is not appropriate to prepare the specific parameter for subsequent measurement.
22	Erroneous Measurement Methodology	The measurement methodology used is not known to be able to measure the specific parameter.
72	Below Preferential Lower Limit of Detection	Measurement is below or equal to the preferential lower limit of detection.
75	Above Preferential Upper Limit of Detection	Measurement is above or equal to the preferential upper limit of detection.
82	Insufficient Measurement Resolution - Preferential	The preferential resolution for the measurement is coarser than a set limit (variable by measured parameter).
83	Insufficient Measurement Resolution - Empirical	The resolution of the measurement is analysed month by month. If the minimum difference between observations is coarser than a set limit (variable by measured parameter), measurements are flagged.
110	Data Outlier - Exceeds Scientifically Decreed Lower/Upper Limit	The measured value is below or greater than scientifically feasible lower/upper limits (variable by parameter).
111	Data Outlier - Monthly Median Exceeds Scientifically Decreed Upper Limit	The median of the measurements in a month is greater than a scientifically feasible limit (variable by parameter).
112	Data Outlier - Network Decreed	Data has been reported to be an outlier through data flags by the network data reporters (and not manually checked and verified as valid).
113	Data Outlier - Manually Decreed	Data has been found and decreed manually to be an outlier.
115	Probable Data Outlier - Monthly Adjusted Boxplot	Measured value exceeds adjusted boxplot outer fence (lower or upper) of monthly data, therefore is a probable data outlier.
132	Systematic Inconsistent Monthly Distributions - 4/6 Months >= Zone 6	4 out of 6 months' distributions are classed as Zone 6 or higher, suggesting there are potentially systematic reasons for the inconsistent distributions across the 6 months.
133	Systematic Inconsistent Monthly Distributions - 8/12 Months >= Zone 6	8 out of 12 months' distributions are classed as Zone 6 or higher, suggesting there are potentially systematic reasons for the inconsistent distributions across the 12 months.

A.4 Budget tables

Table A.7: Results for gas $HNO_{3(g)}$ obtained with the studied heterogeneous chemistry mechanisms. Results from the literature references are reported at the end of the table: The average of all the participating models in the intercomparison AeroCom phase III nitrate experiment for 2008 (*AeroCom*), specifying their standard deviation (*STD AeroCom*), results from the GMI model (*GMI*, using a similar HYB approach with UPTK reactions on dust and SS), and results from the EMAC model (*EMAC 2008*, using a similar approach to DBCLL_du-ssAlk). Also using the EMAC model, results obtained by the Karydis et al. (2016) study are reported as *EMAC 2005-2008*. Results from models using a similar approach to HYB_du-ssUPTK are reported as *IFS* for Rémy et al. (2022), *LMDz-INCA* for Hauglustaine et al. (2014) and *MetOffice UM* for Jones et al. (2021).

$HNO_{3(g)}$	Burden (Tg)	Wet Dep. (Tg y-1)	Dry Dep. (Tg y-1)	Total Dep. (Tg y-1)	Production (Tg y-1)	Lifetime (days)
noHC	4.79	47.1	110.4	157.5	158.3	5.5
fTEQ_noAlk	4.99	48.6	107.3	155.9	156.7	5.8
fTEQ_du-ssAlk	2.93	41.4	77.4	118.8	119.3	4.5
HYB_duUPTK	1.96	29.9	52.0	81.9	82.4	4.4
HYB_du-ssUPTK	0.69	7.2	13.7	20.9	21.4	5.9
HYB_gDU=0.1	0.46	5.9	5.9	11.8	12.2	7.1
HYB_DL	0.72	6.7	14.0	20.7	21.2	6.2
DBCLL_noAlk	5.13	49.1	109.1	158.2	159.0	5.9
DBCLL_duAlk	2.72	45.4	59.9	105.3	105.7	4.7
DBCLL_du-ssAlk	2.53	36.1	61.9	98.0	98.6	4.7
DBCLL_ClaqAlk	2.58	36.2	62.1	98.3	98.9	4.8
AeroCom	**2.50**	**108.7**	**45.8**	**154.5**	**179.0**	**4.6**
STD AeroCom	**±1.83**	**±39.8**	**±13.0**	**±52.8**	**±89.9**	**±1.6**
GMI	**2.50**	**108.7**	**45.8**	**154.5**	**110.0**	**3.5**
EMAC 2008[1]	**3.10**	**136.0**	**56.1**	**192.1**	-	-
EMAC 2005-2008[2]	**1.65**	-	-	-	-	-
IFS	-	-	-	-	-	-
LMDz-INCA	**1.35**	**76.6**	**66.0**	**142.6**	**218.3**	**2.3**
MetOffice UM[3]	**2.16**	**67.1**	**27.0**	**94.1**	**242.1**	**3.2**

[1] From Bian et al. (2017).
[2] From Karydis et al. (2016).
[3] Jones et al. (2021) performs two sensitivity tests to the accommodation coefficient used for NO_3^- formation in the fine mode: *FAST* with 0.193 and *SLOW* with 0.001. Here, results from the *FAST* test are reported on the basis that they present similar fine NO_3^- formation rates to our average fine NO_3^- results.

Table A.8: Results for gas $NH_{3(g)}$ obtained with the studied heterogeneous chemistry mechanisms. Results from the literature references are reported at the end of the table: The average of all the participating models in the intercomparison AeroCom phase III nitrate experiment for 2008 (*AeroCom*), specifying their standard deviation (*STD AeroCom*), results from the GMI model (*GMI*, using a similar HYB approach with UPTK reactions on dust and SS), and results from the EMAC model (*EMAC 2008*, using a similar approach to DBCLL_du-ssAlk). Also using the EMAC model, results obtained by the Karydis et al. (2016) study are reported as *EMAC 2005-2008*. Results from models using a similar approach to HYB_du-ssUPTK are reported as *IFS* for Rémy et al. (2022), *LMDz-INCA* for Hauglustaine et al. (2014) and *MetOffice UM* for Jones et al. (2021).

$NH_{3(g)}$	**Emissions (Tg y-1)**	**Burden (Tg)**	**Wet Dep. (Tg y-1)**	**Dry Dep. (Tg y-1)**	**Total Dep. (Tg y-1)**	**Loss (Tg y-1)**	**Lifetime (days)**
noHC	61.8	0.86	7.1	54.5	61.7	0.0	5.1
fTEQ_noAlk	61.8	0.05	1.3	39.6	40.9	-20.9	0.3
fTEQ_du-ssAlk	61.8	0.16	1.8	44.2	45.9	-15.9	0.9
HYB_duUPTK	61.8	0.21	1.9	44.7	46.6	-15.1	1.2
HYB_du-ssUPTK	61.8	0.26	2.2	45.6	47.8	-14.0	1.5
HYB_gDU=0.1	61.8	0.28	2.2	46.0	48.3	-13.5	1.7
HYB_DL	61.8	0.38	2.9	46.7	49.6	-12.1	2.2
DBCLL_noAlk	61.8	0.06	1.6	40.4	42.0	-19.8	0.4
DBCLL_duAlk	61.8	0.14	1.8	39.8	41.7	-20.2	0.8
DBCLL_du-ssAlk	61.8	0.35	2.8	45.9	48.6	-13.2	2.0
DBCLL_ClaqAlk	61.8	0.31	2.7	45.5	48.2	-13.6	1.8
AeroCom	**62.9**	**0.20**	**13.4**	**18.7**	**32.1**	**-32.1**	**0.7**
STD AeroCom	**±3.9**	**±0.20**	**±5.1**	**±5.1**	**±10.2**	**±12.0**	**±0.3**
GMI	**60.4**	**0.85**	**1.1**	**8.7**	**9.8**	**-50.1**	**5.2**
EMAC 2008[1]	**59.3**	**0.85**	**0.0**	**15.5**	**15.5**	**-**	**-**
EMAC 2005-2008[2]	**-**	**0.82**	**-**	**-**	**-**	**-**	**-**
IFS	**-**	**-**	**-**	**-**	**-**	**-**	**-**
LMDz-INCA	**61.3**	**0.11**	**13.4**	**25.9**	**39.3**	**-21.2**	**0.6**
MetOffice UM[3]	**64.7**	**0.05**	**6.9**	**21.1**	**28.0**	**-36.8**	**0.3**

[1] From Bian et al. (2017).
[2] From Karydis et al. (2016).
[3] Jones et al. (2021) performs two sensitivity tests to the accommodation coefficient used for NO_3^- formation in the fine mode: *FAST* with 0.193 and *SLOW* with 0.001. Here, results from the *FAST* test are reported on the basis that they present similar fine NO_3^- formation rates to our average fine NO_3^- results.

Table A.9: Results fine, coarse and total particulate NH_4^+ obtained with the studied heterogeneous chemistry mechanisms. Results from the literature references are reported at the end of the table: The average of all the participating models in the intercomparison AeroCom phase III nitrate experiment for 2008 (*AeroCom*), specifying their standard deviation (*STD AeroCom*), results from the GMI model (*GMI*, using a similar HYB approach with UPTK reactions on dust and SS), and results from the EMAC model (*EMAC 2008*, using a similar approach to DBCLL_du-ssAlk). Also using the EMAC model, results obtained by the Karydis et al. (2016) study are reported as *EMAC 2005-2008*. Results from models using a similar approach to HYB_du-ssUPTK are reported as *IFS* for Rémy et al. (2022), *LMDz-INCA* for Hauglustaine et al. (2014) and *MetOffice UM* for Jones et al. (2021).

NH_4^+	Burden (Tg)			Wet Dep. (Tg y-1)			Dry Dep. (Tg y-1)			Total Dep. (Tg y-1)			Production (Tg y-1)			Lifetime (days)		
Experiment	Fine	Coarse	**Total**	Fine	Coarse	**Total**	Fine	Coarse	**Total**	Fine	Coarse	**Total**	Fine	Coarse	**Total**	Fine	Coarse	**Total**
fTEQ_noAlk	0.30	0.00	**0.30**	19.2	0.0	**19.2**	3.0	0.0	**3.0**	22.2	0.0	**22.2**	22.2	0.0	**22.2**	2.5	0.0	**2.5**
fTEQ_du-ssAlk	0.21	0.00	**0.21**	14.9	0.0	**14.9**	2.0	0.0	**2.0**	16.9	0.0	**16.9**	16.9	0.0	**16.9**	2.3	0.0	**2.3**
HYB_duUPTK	0.21	0.00	**0.21**	14.3	0.0	**14.3**	1.9	0.0	**1.9**	16.2	0.0	**16.2**	16.2	0.0	**16.2**	2.3	0.0	**2.3**
HYB_du-ssUPTK	0.20	0.00	**0.20**	13.2	0.0	**13.2**	1.7	0.0	**1.7**	15.0	0.0	**15.0**	15.0	0.0	**15.0**	2.4	0.0	**2.4**
HYB_gDU=0.1	0.19	0.00	**0.19**	12.9	0.0	**12.9**	1.6	0.0	**1.6**	14.5	0.0	**14.5**	14.5	0.0	**14.5**	2.4	0.0	**2.4**
HYB_DL	0.19	0.00	**0.19**	11.7	0.0	**11.7**	1.6	0.0	**1.6**	13.3	0.0	**13.3**	13.3	0.0	**13.3**	2.7	0.0	**2.7**
DBCLL_noAlk	0.29	0.01	**0.30**	17.8	0.3	**18.1**	2.8	0.2	**2.9**	20.5	0.5	**21.0**	20.5	0.5	**21.0**	2.6	3.1	**2.6**
DBCLL_duAlk	0.30	0.01	**0.31**	18.9	0.3	**19.2**	3.1	0.2	**3.3**	22.1	0.4	**22.5**	22.1	0.4	**22.5**	2.5	4.1	**2.5**
DBCLL_du-ssAlk	0.20	0.02	**0.22**	12.6	0.2	**12.7**	1.8	0.1	**1.9**	14.3	0.3	**14.6**	14.3	0.3	**14.6**	2.6	10.8	**2.8**
DBCLL_ClaqAlk	0.22	0.02	**0.23**	12.9	0.2	**13.1**	1.8	0.2	**2.0**	14.7	0.4	**15.1**	14.7	0.4	**15.1**	2.7	7.7	**2.8**
AeroCom	-	-	**0.32**	-	-	**24.4**	-	-	**5.8**	-	-	**30.2**	-	-	**30.4**	-	-	**4.3**
STD AeroCom	-	-	**±0.20**	-	-	**±10.0**	-	-	**±5.8**	-	-	**±15.8**	-	-	**±4.3**	-	-	**±2.6**
GMI	-	-	**0.48**	-	-	**50.7**	-	-	**1.9**	-	-	**52.6**	-	-	**53.0**	-	-	**3.4**
EMAC 2008[1]	-	-	**0.19**	-	-	**44.5**	-	-	**3.6**	-	-	**48.1**	-	-	**-**	-	-	**-**
EMAC 2005-2008[2]	-	-	**0.17**	-	-	**-**	-	-	**-**	-	-	**-**	-	-	**-**	-	-	**-**
IFS[3]	-	-	**0.15**	-	-	**17.4**	-	-	**1.4**	-	-	**18.8**	-	-	**18.6**	-	-	**2.9**
LMDz-INCA	-	-	**0.28**	-	-	**19.2**	-	-	**3.2**	-	-	**22.4**	-	-	**22.4**	-	-	**4.5**
MetOffice UM[4]	-	-	**0.54**	-	-	**32.1**	-	-	**7.4**	-	-	**32.1**	-	-	**39.2**	-	-	**5.0**

[1] From Bian et al. (2017).
[2] From Karydis et al. (2016).
[3] Fine NO_3^- reported from neutralization of $HNO_{3(g)}$, $NH_{3(g)}$ and $H_2SO_{4(g)}$. Coarse NO_3^- from heterogeneous chemistry (Rémy et al. 2022).
[4] Jones et al. (2021) performs two sensitivity tests to the accommodation coefficient used for NO_3^- formation in the fine mode: *FAST* with 0.193 and *SLOW* with 0.001. Here, results from the *FAST* test are reported on the basis that they present similar fine NO_3^- formation rates to our average fine NO_3^- results

Table A.10: Results for $SO_{2(g)}$, and fine, coarse and total particulate SO_4^{2-} obtained with the studied heterogeneous chemistry mechanisms. Results from the literature references are reported at the end of the table: The average of all the participating models in the intercomparison AeroCom phase III nitrate experiment for 2008 (*AeroCom*), specifying their standard deviation (*STD AeroCom*), results from the GMI model (*GMI*, using a similar HYB approach with UPTK reactions on dust and SS), and results from the EMAC model (*EMAC 2008*, using a similar approach to DBCLL_du-ssAlk). Also using the EMAC model, results obtained by the Karydis et al. (2016) study are reported as *EMAC 2005-2008*. Results from models using a similar approach to HYB_du-ssUPTK are reported as *IFS* for Rémy et al. (2022), *LMDz-INCA* for Hauglustaine et al. (2014) and *MetOffice UM* for Jones et al. (2021).

SO_4^{2-}	SO4 Emissions (Tg y-1)		SO2 Emissions (Tg y-1)	SO4 Burden (Tg)			SO4 Wet Dep. (Tg y-1)			SO4 Dry Dep. (Tg y-1)			SO4 Total Dep. (Tg y-1)			SO4 Production (Tg y-1)			SO4 Lifetime (days)		
Experiment	Fine	Coarse	**Total**	Fine	Coarse	**Total**	Fine	Coarse	**Total**	Fine	Coarse	**Total**	Fine	Coarse	**Total**	Fine	Coarse	**Total**	Fine	Coarse	**Total**
noHC	0.5	0.0	**104.4**	4.4E-3	0.00	**0.00**	0.5	0.0	**0.5**	0.1	0.0	**0.1**	0.5	0.0	**0.5**	0.0	0.0	**0.0**	3.1	0.0	**3.0**
fTEQ_noAlk	0.5	0.0	**104.4**	1.98	0.00	**1.98**	126.9	0.0	**126.9**	13.5	0.0	**13.5**	140.5	0.0	**140.5**	139.9	0.0	**139.9**	2.6	0.9	**2.6**
fTEQ_du-ssAlk	0.5	0.0	**104.4**	1.82	0.14	**1.96**	116.7	6.9	**123.6**	13.0	3.5	**16.5**	129.7	10.4	**140.1**	129.1	10.4	**139.5**	2.6	2.4	**2.6**
HYB_duUPTK	0.5	0.0	**104.4**	1.82	0.14	**1.96**	116.5	7.0	**123.5**	13.0	3.5	**16.4**	129.4	10.5	**139.9**	128.9	10.5	**139.3**	2.6	2.4	**2.6**
HYB_du-ssUPTK	0.5	0.0	**104.4**	1.85	0.14	**1.98**	116.4	7.1	**123.5**	12.9	3.5	**16.4**	129.3	10.6	**139.9**	128.7	10.6	**139.3**	2.6	2.4	**2.6**
HYB_gDU=0.1	0.5	0.0	**104.4**	1.87	0.12	**1.99**	117.8	6.1	**124.0**	12.7	2.9	**15.7**	130.6	9.1	**139.7**	130.0	9.0	**139.1**	2.6	2.4	**2.6**
HYB_DL	0.5	0.0	**104.4**	1.85	0.14	**1.99**	116.4	7.1	**123.5**	12.9	3.5	**16.4**	129.3	10.6	**139.9**	128.7	10.6	**139.3**	2.6	2.4	**2.6**
DBCLL_noAlk	0.5	0.0	**104.4**	1.94	0.04	**1.98**	124.4	2.0	**126.4**	13.2	0.9	**14.0**	137.6	2.9	**140.5**	137.0	2.9	**139.9**	2.6	2.5	**2.6**
DBCLL_duAlk	0.5	0.0	**104.4**	1.78	0.16	**1.94**	114.8	8.4	**123.1**	12.7	4.1	**16.8**	127.5	12.4	**139.9**	126.9	12.4	**139.3**	2.6	2.4	**2.5**
DBCLL_du-ssAlk	0.5	0.0	**104.4**	1.76	0.20	**1.96**	114.9	8.3	**123.2**	12.7	4.1	**16.8**	127.6	12.4	**140.0**	127.1	12.3	**139.4**	2.5	3.0	**2.6**
DBCLL_ClaqAlk	0.5	0.0	**104.4**	1.84	0.13	**1.97**	117.0	6.9	**123.8**	12.8	3.3	**16.1**	129.8	10.1	**139.9**	129.2	10.1	**139.3**	2.6	2.4	**2.6**
AeroCom	-	-	**122.0**	-	-	**1.80**	-	-	**140.0**	-	-	**14.3**	-	-	**154.3**	-	-	**151.0**	-	-	**4.5**
STD AeroCom	-	-	**±12.0**	-	-	**±0.81**	-	-	**±65.3**	-	-	**±163.3**	-	-	**±228.6**	-	-	**±56.0**	-	-	**±1.9**
GMI	-	-	**122.0**	-	-	**3.30**	-	-	**140.0**	-	-	**14.3**	-	-	**154.3**	-	-	**151.0**	-	-	**4.5**
EMAC 2008[1]	-	-	**138.0**	-	-	**1.90**	-	-	**302.0**	-	-	**504.0**	-	-	**806.0**	-	-	**187.0**	-	-	**0.9**
EMAC 2005-2008[2]	-	-	-	-	-	**1.78**	-	-	-	-	-	-	-	-	-	-	-	-	-	-	-
IFS[3]	-	-	**70.3**	-	-	**0.367**	-	-	**39.7**	-	-	**1.9**	-	-	**39.7**	-	-	**41.4**	-	-	**3.2**
LMDz-INCA	-	-	-	-	-	**1.26**	-	-	-	-	-	-	-	-	-	-	-	-	-	-	-
MetOffice UM[4]	-	-	-	-	-	-	-	-	-	-	-	-	-	-	-	-	-	-	-	-	-

[1] From Bian et al. (2017).
[2] From Karydis et al. (2016).
[3] Fine NO_3^- reported from neutralization of $HNO_{3(g)}$, $NH_{3(g)}$ and $H_2SO_{4(g)}$. Coarse NO_3^- from heterogeneous chemistry (Rémy et al. 2022).
[4] Jones et al. (2021) performs two sensitivity tests to the accommodation coefficient used for NO_3^- formation in the fine mode: *FAST* with 0.193 and *SLOW* with 0.001. Here, results from the *FAST* test are reported on the basis that they present similar fine NO_3^- formation rates to our average fine NO_3^- results

Table A.11: Nitrogen burdens (TgN) for each experiment and species.

Nitrogen burdens	noHC	fTEQ noAlk	fTEQ du-ssAlk	HYB duUPTK	HYB du-ssUPTK	HYB gDU=0.1	HYB DL	DBCLL noAlk	DBCLL duAlk	DBCLL du-ssAlk	DBCLL ClaqAlk
$HNO_{3(g)}$	1.06	1.11	0.65	0.44	0.15	0.1	0.16	1.14	0.6	0.56	0.57
$NH_{3(g)}$	0.71	0.04	0.13	0.17	0.21	0.23	0.31	0.05	0.11	0.28	0.25
$NO_{(g)}$	0.14	0.18	0.14	0.13	0.11	0.1	0.11	0.19	0.14	0.14	0.14
$NO_{2(g)}$	0.24	0.27	0.22	0.2	0.17	0.17	0.17	0.28	0.22	0.22	0.22
$N_2O_{5(g)}$	0.04	0.03	0.02	0.02	0.01	0.01	0.01	0.03	0.02	0.02	0.02
$NTR_{(g)}$	0.44	0.47	0.48	0.48	0.47	0.47	0.47	0.47	0.47	0.48	0.48
$PNA_{(g)}$	0.04	0.03	0.02	0.02	0.02	0.02	0.02	0.03	0.02	0.02	0.02
$PAN_{(g)}$	0.8	0.64	0.53	0.49	0.42	0.41	0.42	0.65	0.52	0.52	0.52
$PAN_{x(g)}$	0.16	0.13	0.11	0.11	0.09	0.09	0.09	0.14	0.11	0.11	0.11
$PM_{2.5}NO_{3(aer)}$	0	0.02	0.15	0.13	0.12	0.11	0.09	0.01	0.22	0.06	0.09
$PM_{2.5–10}NO_{3(aer)}$	0	0	0	0.13	0.27	0.32	0.29	0	0.11	0.18	0.14
$PM_{2.5}NH_{4(aer)}$	0	0.23	0.17	0.16	0.15	0.15	0.15	0.22	0.24	0.16	0.17
$PM_{2.5–10}NH_{4(aer)}$	0	0	0	0	0	0	0	0.01	0.01	0.01	0.01
$NO_{(g)} + NO_{2(g)} + NO_{3(g)}$	**0.39**	**0.46**	**0.36**	**0.33**	**0.28**	**0.28**	**0.28**	**0.47**	**0.37**	**0.36**	**0.36**
$NTR_{(g)} + PNA_{(g)} + PAN_{(g)} + PAN_{x(g)}$	**1.44**	**1.28**	**1.14**	**1.09**	**1.01**	**0.99**	**1**	**1.29**	**1.13**	**1.13**	**1.13**
Aerosol $NO_3^- + NH_4^+$	**0**	**0.25**	**0.31**	**0.42**	**0.55**	**0.58**	**0.53**	**0.24**	**0.57**	**0.41**	**0.42**
Total nitrogen	**3.63**	**3.15**	**2.62**	**2.48**	**2.19**	**2.18**	**2.29**	**3.22**	**2.79**	**2.76**	**2.74**

A.5 Discussion of additional sensitivity experiments

A.5.1 HYB_g0p1

To assess the sensitivity to more efficient coarse NO_3^- production rates on dust (reactions R1-R4 in Table 4.3), we perform the HYB_g0p1 run, that employs a constant value for γ_{dust} of 0.1, rather than utilizing the RH-dependent function proposed by (Fairlie et al. 2010). This experiment is also intended to elucidate the relative role of the dust over SS. , the γ_{dust} values used in both HYB_duUPTK and HYB_du-ssUPTK runs are well below the value used for γ_{SS} and other studies in the literature (Hauglustaine et al. 2014, Rémy et al. 2022). Results indicate an increase in coarse NO_3^- formation in regions rich in dust (Fig. A.3), such as the Sahara desert, the Persian Gulf and East Asia. Furthermore, a slight enhancement in the transport of coarse NO_3^- across northern latitudes is observed, despite lower dust concentrations in that region. This can be attributed to the predominant production of coarse NO_3^- on dust across continental Eurasia, followed by its long-range transport at high altitudes to North America.

Among the mechanisms analyzed, HYB_g0p1 shows the most efficient depletion of $HNO_{3(g)}$, achieved by using a constant value of $\gamma = 0.1$ instead of the RH-dependent dust uptake coefficient from Fairlie et al. (2010). In this scenario, $HNO_{3(g)}$ is further reduced to 0.46 TgN, accompanied by an increase in coarse NO_3^- formation up to 1.93 Tg. Furthermore, the deposition rates rise from 140 to 149 Tg/y, as shown in Table 5.3 in the main text.

A.5.2 DBCLL_duAlk

The DBCLL_duAlk configuration only accounts for dust alkalinity in the DBCLL mechanism. It shows that the sole presence of dust, compared to the case with no alkalinity in the DBCLL_noAlk configuration, significantly increases pH values (i.e. more basic) over the Sahara and continental Asia to a range of 6 to 8 pH units. Thereby, dust enhances the formation of both fine and coarse NO_3^- as well as coarse SO_4^{2-} in these regions. Additionally, fine NO_3^- formation is amplified in polluted areas, with surface concentrations rising beyond 5 $\mu g\ m^{-3}$ (an increase of 2-5 $\mu g\ m^{-3}$ relative to DBCLL_noAlk). This enhanced formation extends to regions rich in coarse dust, such as the Persian Gulf (surface concentrations of 1-3 $\mu g\ m^{-3}$) and central/downwind areas of the Saharan desert (surface concentrations of 0.2-0.5 $\mu g\ m^{-3}$ and loads of 2.0 $mg\ m^{-2}$), as shown in Fig. A.3. Over these areas, DBCLL_duAlk nearly depletes $HNO_{3(g)}$ gas (remaining surface concentrations of 0.01 to 0.05 $\mu g\ m^{-3}$). At high altitudes, both fine and coarse NO_3^- are distributed across the Atlantic and Pacific oceans with column loads of 1-2 $mg\ m^{-2}$, resembling the transoceanic patterns also observed in the HYB

mechanisms. Conversely, compared to the DBCLL_noAlk run, fine NH_4^+ increases over Europe and North-Central America (by at least 1 $mg\ m^{-2}$), while it decreases over dusty areas (by 1.0 to 2.0 $mg\ m^{-2}$). This pattern is consistent with the comparison between the fTEQ_noAlk and the fTEQ_du-ssAlk runs. Concurrently, coarse NH_4^+ formation increases significantly in transoceanic areas, reaching 0.08-0.1 $mg\ m^{-2}$ alongside coarse NO_3^- particles, although its formation is halted over dusty regions (i.e. Middle East and Sahara). This inhibition can be attributed to the increased alkalinity of dust, which neutralizes $HNO_{3(g)}$ and limits the condensation of $NH_{3(g)}$. Lastly, the introduction of dust alkalinity strongly enhances the formation of coarse SO_4^{2-}, both over polluted regions (5 $mg\ m^{-2}$) and remote areas (0.2-1.0 $mg\ m^{-2}$). The enhanced production of coarse particles (principally coarse NO_3^-) provides additional surface area for $H_2SO_{4(g)}$ to condense on.

When compared with observations, DBCLL_duAlk results in opposite results to DBCLL_noAlk: $HNO_{3(g)}$ is underestimated with respect to observations from March to September by -0.1$\mu g\ m^{-3}$, while both fine and total particulate NO_3^- are overestimated with respect to observations by 1.5 and 2 $\mu g\ m^{-3}$ respectively (see Fig. A.14).

Comparing the obtained NO_3^- burdens and size distributions with those reported by Rémy et al. (2022), Hauglustaine et al. (2014), and Jones et al. (2021) (Table A.7), we observe that the total NO_3^- values are notably high when only dust alkalinity is considered. This discrepancy can be attributed to excessive fine NO_3^- formation, as already noted in the observational evaluation. This indicates that while the DBCLL_duAl approach improves the representation of alkalinity effects compared to the irreversible mechanisms, it still tends to overestimate the fine mode NO_3^-, suggesting a need for further refinement in the parameterization of NVC effects to achieve more accurate NO_3^- aerosol predictions. Moreover, deposition rates of total NO_3^- (54.01 Tg/y) fall below those reported by all the consulted references, suggesting that DBCLL_duAlk might form too much fine NO_3^- (with lower deposition rates) and misses coarse NO_3^- formation (with higher deposition rates).

A.5.3 DBCLL_ClaqAlk

The DBCLL_ClaqAlk employs the average alkalinity of dust from Claquin et al. (1999) instead of Journet et al. (2014) with the DBCLL mechanism, and it shows significant differences in specific arid regions compared with DBCLL_du-ssAlk. Notably, with DBCLL_ClaqAlk the load of NO_3^- substantially increases over the Middle East and northern India, while a slight reduction is observed over northern Africa. These changes are significant enough to impact the long-range transport of both fine and coarse NO_3^- across

the northern hemisphere. Coarse NO_3^- decreases by about 1-2 $mg\ m^{-2}$ over and downwind of dusty areas, while fine NO_3^- increases by 2-5 $mg\ m^{-2}$ along the equatorial belt and over polluted regions. Similar differences are found in particulate NH_4^+, although with an order of magnitude lower. Notably, $HNO_{3(g)}$ distributions report negligible differences between both runs. The lower alkalinity derived from the Claquin et al. (1999) dataset accounts for these differences, primarily affecting the formation of NO_3^- during long-range transport of dust.

A.6 Evaluation of oxidized and reduced species

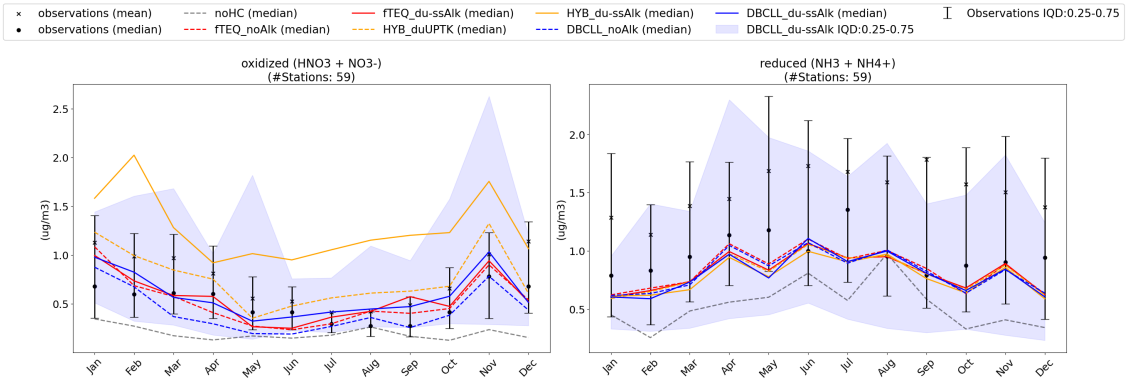

Figure A.15: Observational evaluation for oxidized ($HNO_{3(g)} + NO_3^-$, left) and reduced ($NH_{3(g)} + NH_4^+$, right) nitrogen species.



Figure A.16: Stations employed for the observational evaluation of oxidized ($HNO_{3(g)} + NO_3^-$) and reduced ($NH_{3(g)} + NH_4^+$) nitrogen species.

B

Supplement of Chapter 6

B.1 Satellite constraints of dust emissions

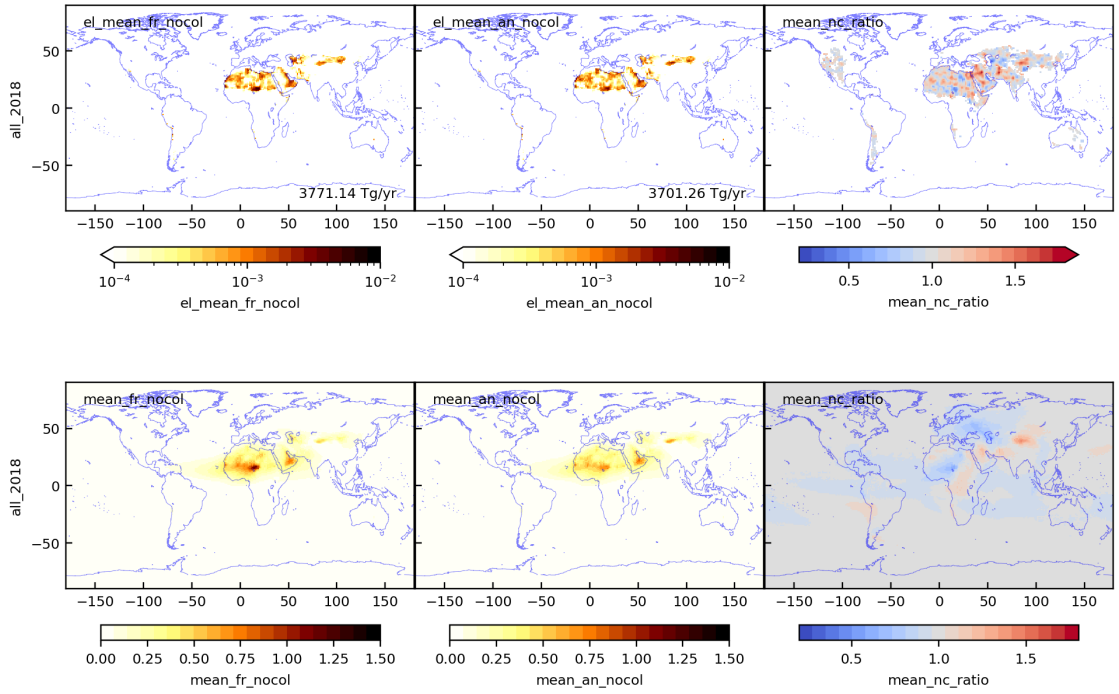

Figure B.1: Annual accumulated dust emissions (top row) and mean dust optical depth (bottom row) for the control (uncorrected) simulation, the analysis (assimilated) simulation, and their ratios.

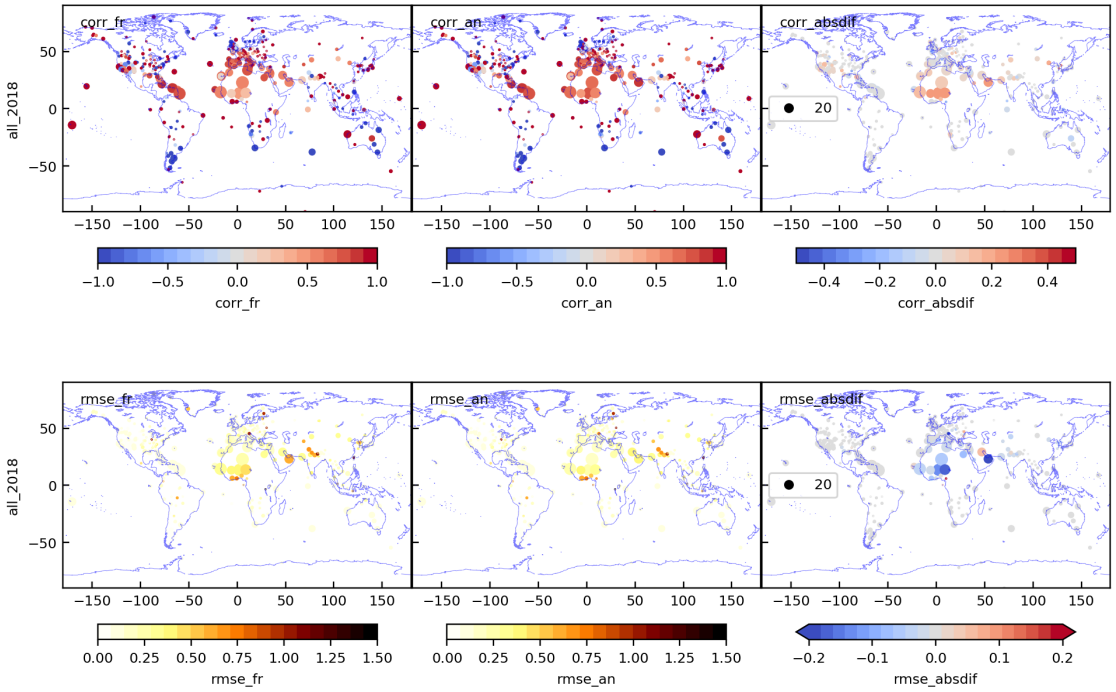

Figure B.2: Evaluation of assimilated dust optical depth against AERONET observations. Six-hourly correlation (top) and root mean square error (RMSE, bottom) of modeled versus AERONET dust optical depth for the control (left), analysis (center), and their difference (right).

B.2 $CaCO_3$ evaluation

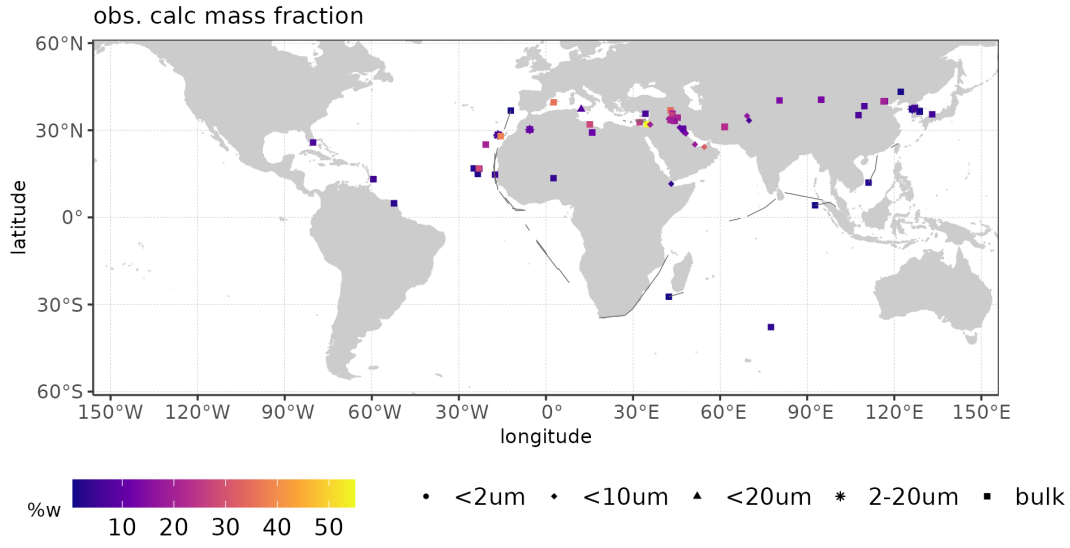

Figure B.3: Location and characteristics of observational $CaCO_3$ datasets. Geographical distribution, size range, and measured $CaCO_3$ content of the in situ observations used for model evaluationPerlwitz et al. (2015b). Observations span multiple campaigns and decades.

B.3 Burdens

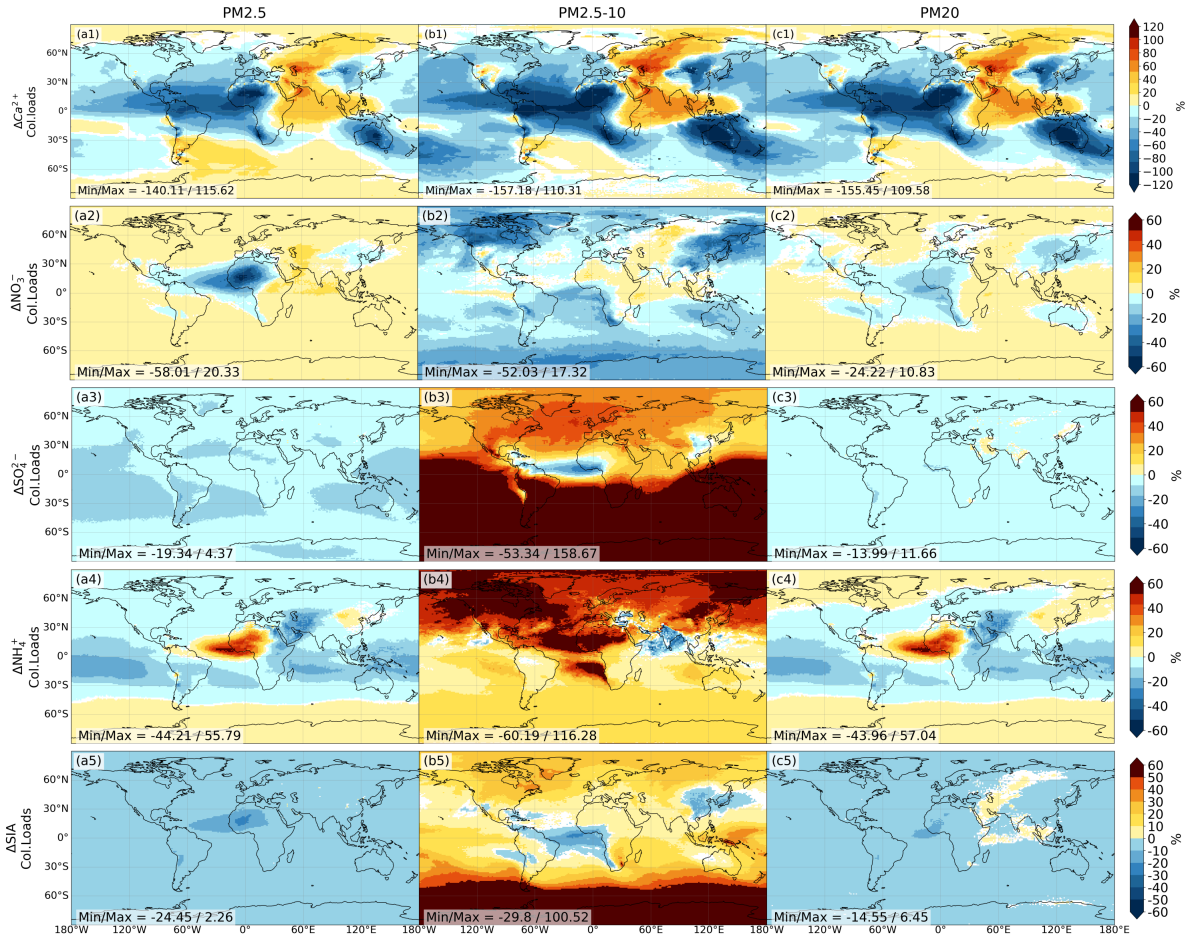

Figure B.4: Relative average column differences for 2018 between source-based and globally averaged $CaCO_3$ representations (SB–AVG) for $CaCO_3$, SIA species, and SSA. White color gridcells refer to differences that are non-statistically significant ($p > 0.05$).

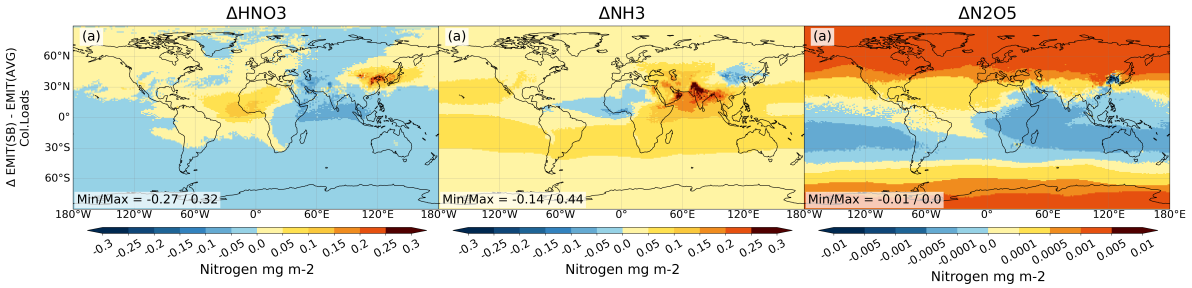

Figure B.5: Average column differences for 2018 in precursor gases $HNO_{3(g)}$, $NH_{3(g)}$, and $SO_{2(g)}$ between source-based (SB) and globally averaged (AVG) simulations.

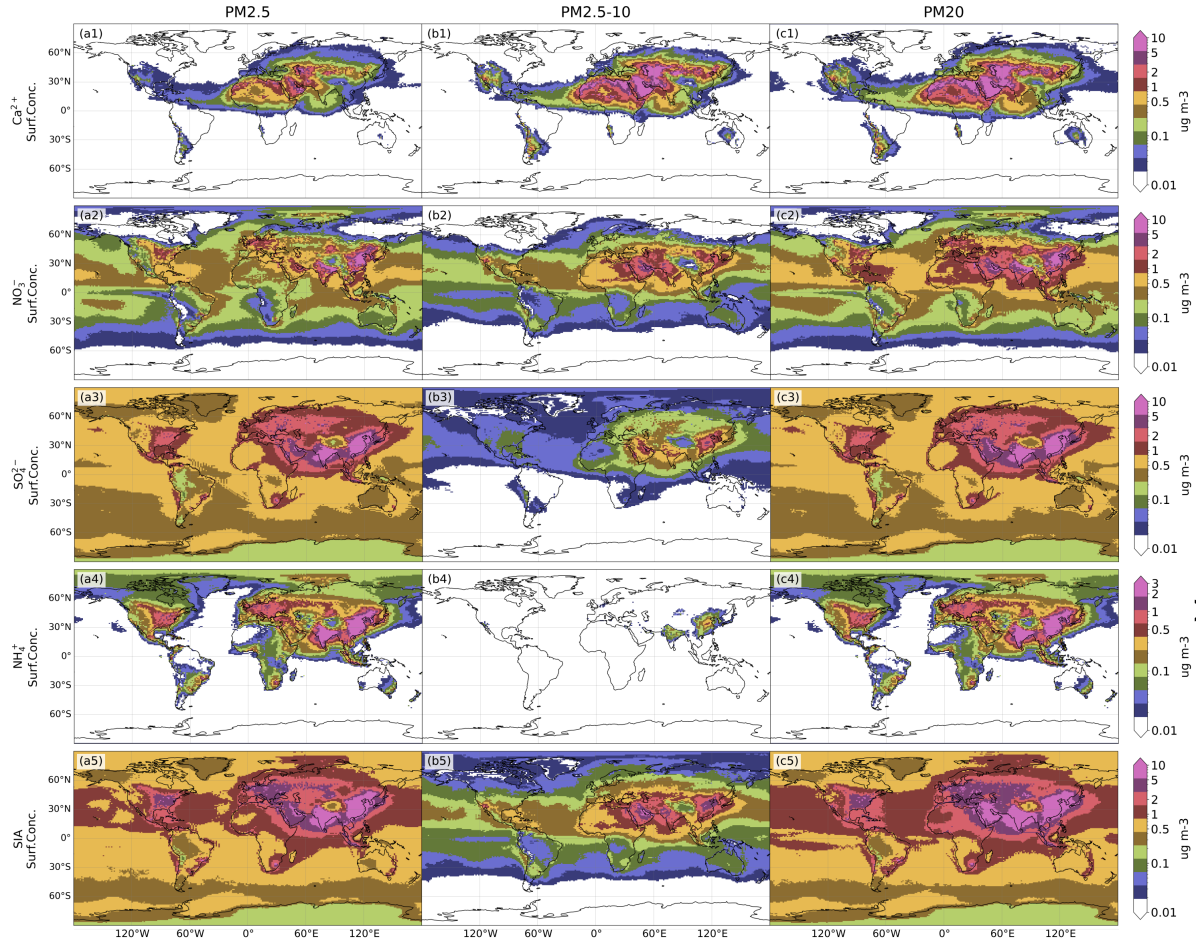

Figure B.6: Average surface concentrations for 2018 of Ca^{2+}, NO_3^-, SO_4^{2-}, and NH_4^+ simulated using source-based EMIT mineralogy.

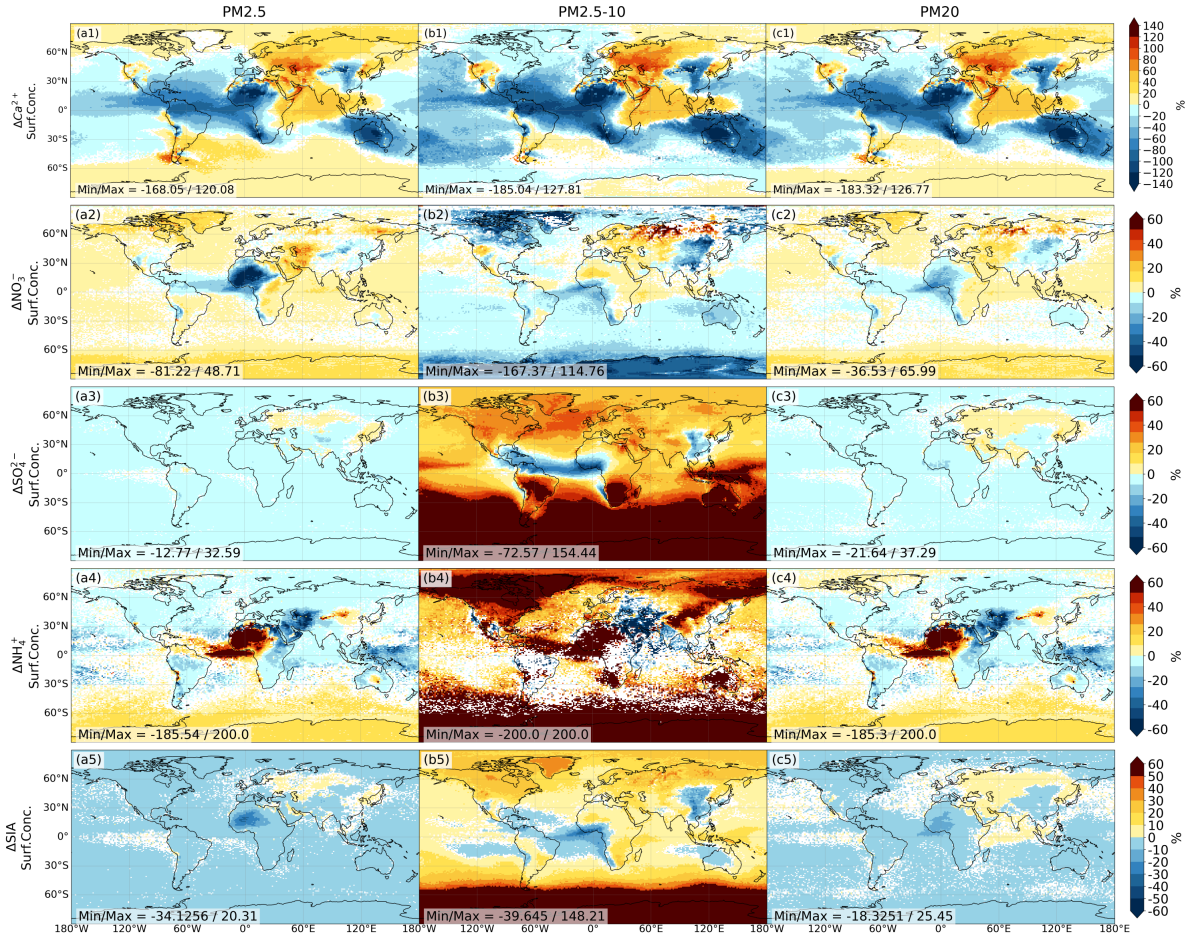

Figure B.7: Average relative differences for 2018 in surface Ca^{2+}, NO_3^-, SO_4^{2-}, NH_4^+, and aerosol pH between EMIT source-based (EMIT(SB)) and globally averaged (EMIT(AVG)) mineral distributions. White color gridcells refer to differences that are non-statistically significant ($p > 0.05$).

Table B.1: Global budgets of fine ($D < 2.5\mu m$), coarse ($2.5 < D < 10\mu m$), and total ($D < 20\mu m$) NO_3^-, wet and dry deposition, production/loss, and atmospheric lifetime for all experiments (CLAQ(SB), JOUR(SB), EMIT(SB), EMIT(AVG)). Results are compared with the literature (Bian et al. 2017, Karydis et al. 2016, Rémy et al. 2022; 2024).

Particulate Nitrate	**Burden (Tg y-1)**			**Wet Dep. (Tg y-1)**			**Dry Dep. (Tg y-1)**			**Total Dep. (Tg y-1)**			**Prod/Loss (Tg y-1)**			**Lifetime (days)**		
Experiment	Fine	Coarse	**Total**	Fine	Coarse	**Total**	Fine	Coarse	**Total**	Fine	Coarse	**Total**	Fine	Coarse	**Total**	Fine	Coarse	**Total**
CLAQ(SB)	0.52	0.44	**0.96**	10.15	12.19	**22.34**	2.11	5.33	**7.44**	12.26	17.52	**29.78**	12.59	17.45	**30.04**	7.6	4.6	**5.9**
JOUR(SB)	0.58	0.46	**1.04**	20.88	24.51	**45.39**	4.36	11.64	**16.01**	25.25	36.15	**61.40**	25.60	36.07	**61.67**	4.2	2.3	**3.1**
EMIT(SB)	0.56	0.45	**1.01**	20.96	24.21	**45.17**	4.35	11.93	**16.28**	25.31	36.14	**61.45**	25.65	36.06	**61.71**	4.0	2.3	**3.0**
EMIT(AVG)	0.56	0.46	**1.02**	20.53	24.76	**45.29**	4.31	11.87	**16.18**	24.84	36.63	**61.46**	25.18	36.55	**61.73**	4.1	2.3	**3.0**
AeroCom	0.00	0.00	**0.63**	0.00	0.00	**45.90**	0.00	0.00	**20.70**	0.00	0.00	**66.60**	0.00	0.00	**60.60**	0.0	0.0	**5.0**
STD AeroCom	0.00	0.00	**0.56**	0.00	0.00	**30.68**	0.00	0.00	**19.54**	0.00	0.00	**50.22**	0.00	0.00	**45.91**	0.0	0.0	**2.3**
Karydis et al., 2016			**0.45**															
Rémy et al., 2022	0.47	0.35	**0.82**	35.90	39.60	**75.50**	4.60	23.80	**28.40**	40.50	63.40	**103.90**	40.50	63.40	**103.90**	4.2	2.1	**3.2**
Rémy et al., 2024	0.35	0.27	**0.62**	18.16	13.29	**31.44**	2.79	23.91	**26.70**	20.95	37.20	**58.15**	20.81	37.20	**58.01**	6.2	2.6	**4.4**

B.4 Methodology

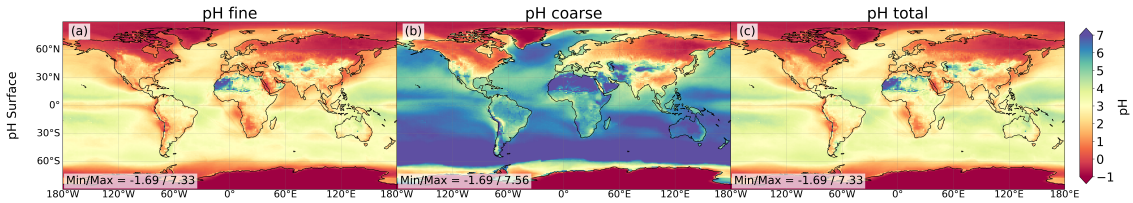

Figure B.8: pH from the arithmetic mean obtained with EMIT(SB) (a-c), calculating the temporal mean of instantaneous pH values for the studied period.

B.5 pH

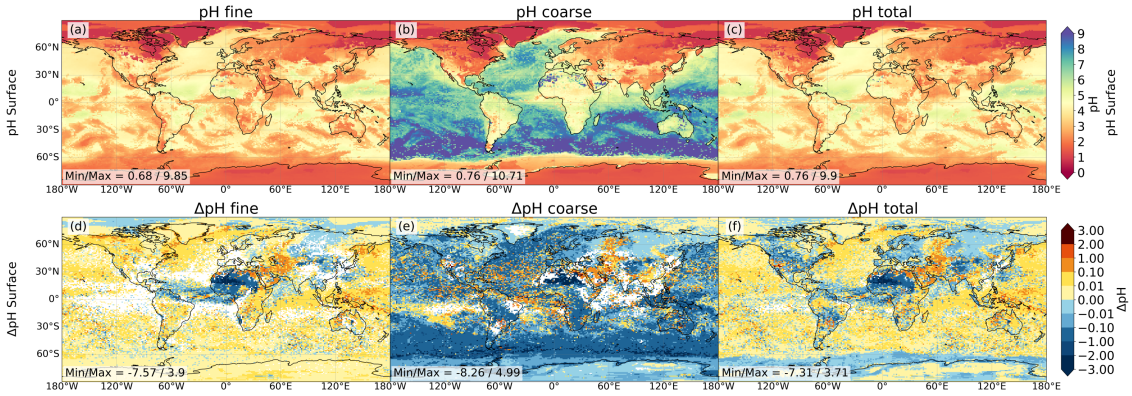

Figure B.9: pH from the proton activity mean obtained with EMIT(SB) (a-c) and differences with EMIT(AVG) (d-f), calculating the temporal mean of instantaneous activity values for the studied period.

B.6 Statistical significance analysis and evaluation

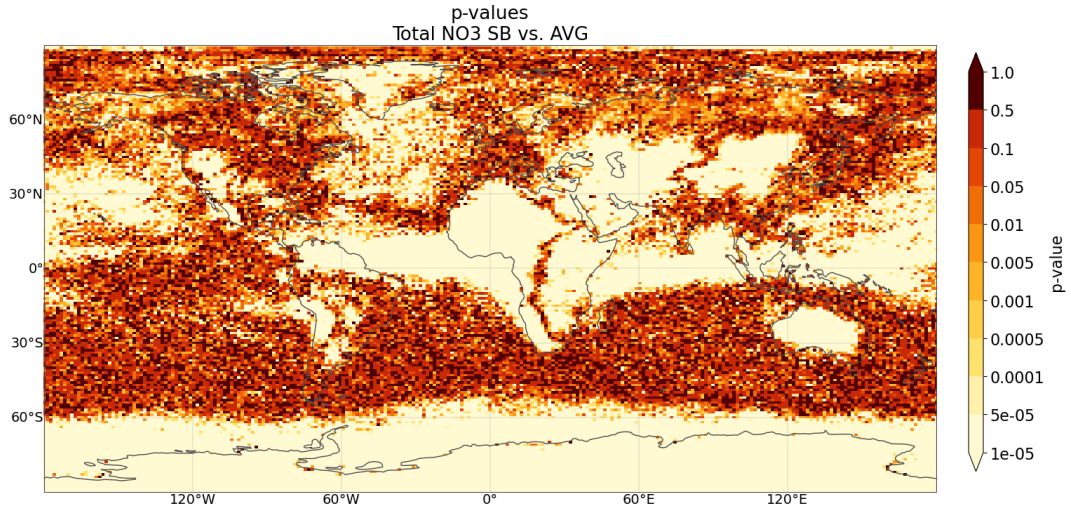

Figure B.10: Distribution of p-values for the differences in total NO_3^- between source-based and globally-averaged configurations.

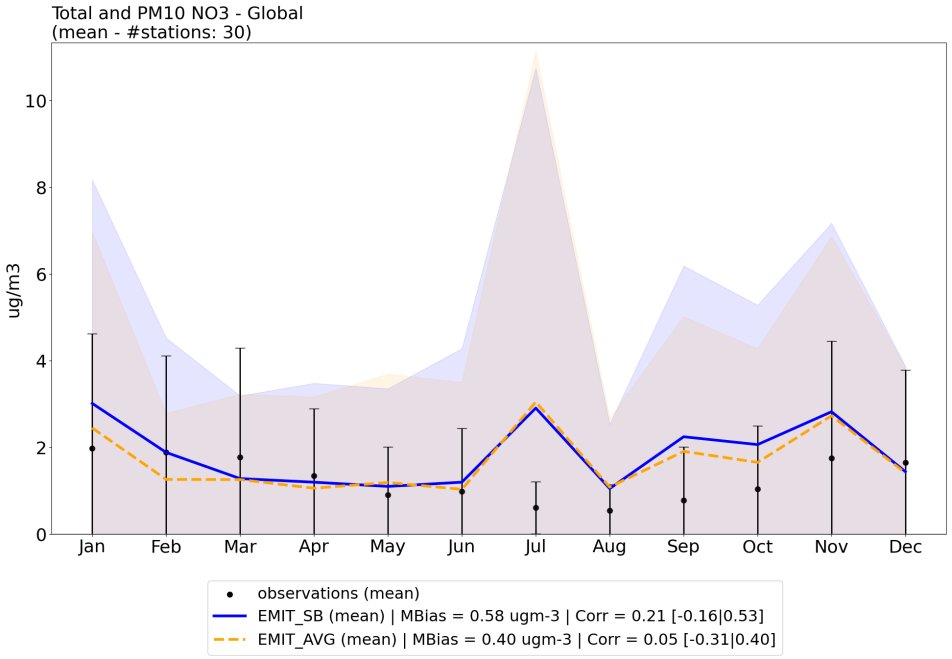

Figure B.11: Global evaluation of total NO_3^- monthly means against global observations over stations with statistically-significant differences ($p<0.05$), shown as red triangles in Fig. 6.6*a*. Coloured shading and error bars represent the standard deviation of the model and observations, respectively.

B.7 PM2.5 evaluation

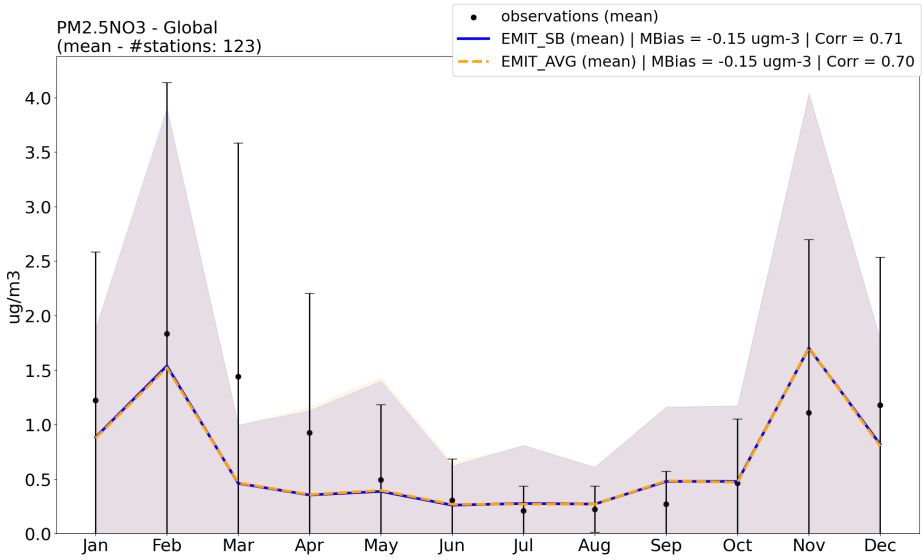

Figure B.12: Global evaluation of $PM2.5NO_3^-$ monthly means against global observations, with no restriction regarding the statistical significance. Coloured shading and error bars represent the standard deviation of the model and observations, respectively.

B.8 Experiment descriptions

Table B.2: Summarized description of the performed mineralogical sensitivity experiments, with varied representations of $CaCO_3$ emission fractions —either source-based (SB) or globally averaged (AVG)— from the CLAQ, JOUR, and EMIT datasets.

Experiment	Description
CLAQ(SB)	$CaCO_3$ emission fluxes is obtained from the size-dependent and geographically discrete $CaCO_3$ dust fractions from the CLAQ dataset.
JOUR(SB)	$CaCO_3$ emission fluxes is obtained from the size-dependent and geographically discrete $CaCO_3$ dust fractions from the JOUR dataset.
EMIT(SB)	$CaCO_3$ emission fluxes is obtained from size-dependent and geographically discrete $CaCO_3$ dust fractions from the EMIT L3-2024 mineral data.
EMIT(AVG)	$CaCO_3$ dust fractions are globally averaged from the $CaCO_3$ average fraction at emission of EMIT(SB).

B.9 Domain definitions

Table B.3: Definition of geographical boundaries (latitude–longitude ranges) for analysis of nitrate formation events.

Region	Latitudes, Longitudes
North Africa and Sahel	(0 to 35), (-20 to 34)
Middle East	(5 to 35), (35 to 65)
India	(5 to 35), (66 to 92)
Southeast Asia	(5 to 35), (93 to 125)
East Asia	(36 to 65), (80 to 140)
West Asia	(36 to 65), (40 to 79)
Europe	(36 to 65), (-15 to 39)
North America	(20 to 60), (-130 to -70)

C

Supplement of Chapter 7

C.1 Optical properties

The light transmission factor (T) throughout an atmospheric column is defined by the Beer-Lambert Law as:

$$T(\lambda, z) = e^{-AOD(\lambda,z)} \tag{C.1}$$

here $AOD(\lambda, z)$ measures the extinction of light along the optical path by aerosols, and it is defined as:

$$AOD(\lambda, z) = \int_{z}^{\infty} \beta_{ext}(\lambda) dz \tag{C.2}$$

Where β_{ext} (0-1) is the extinction coefficient, and comprises the scattering (β_{scat}) and absorption (β_{abs}) coefficients by aerosols along the vertical atmospheric path (Brasseur and Jacob 2017).

These coefficients serve to define the SSA of aerosols (ω) as the fraction of the light scattered over the extinguished one (Brasseur and Jacob 2017):

$$\omega(\lambda) = \frac{\beta_{scat}(\lambda)}{\beta_{ext}(\lambda)} = \frac{\beta_{scat}(\lambda)}{\beta_{scat}(\lambda) + \beta_{abs}(\lambda)} \tag{C.3}$$

C.2 Refractive indexes

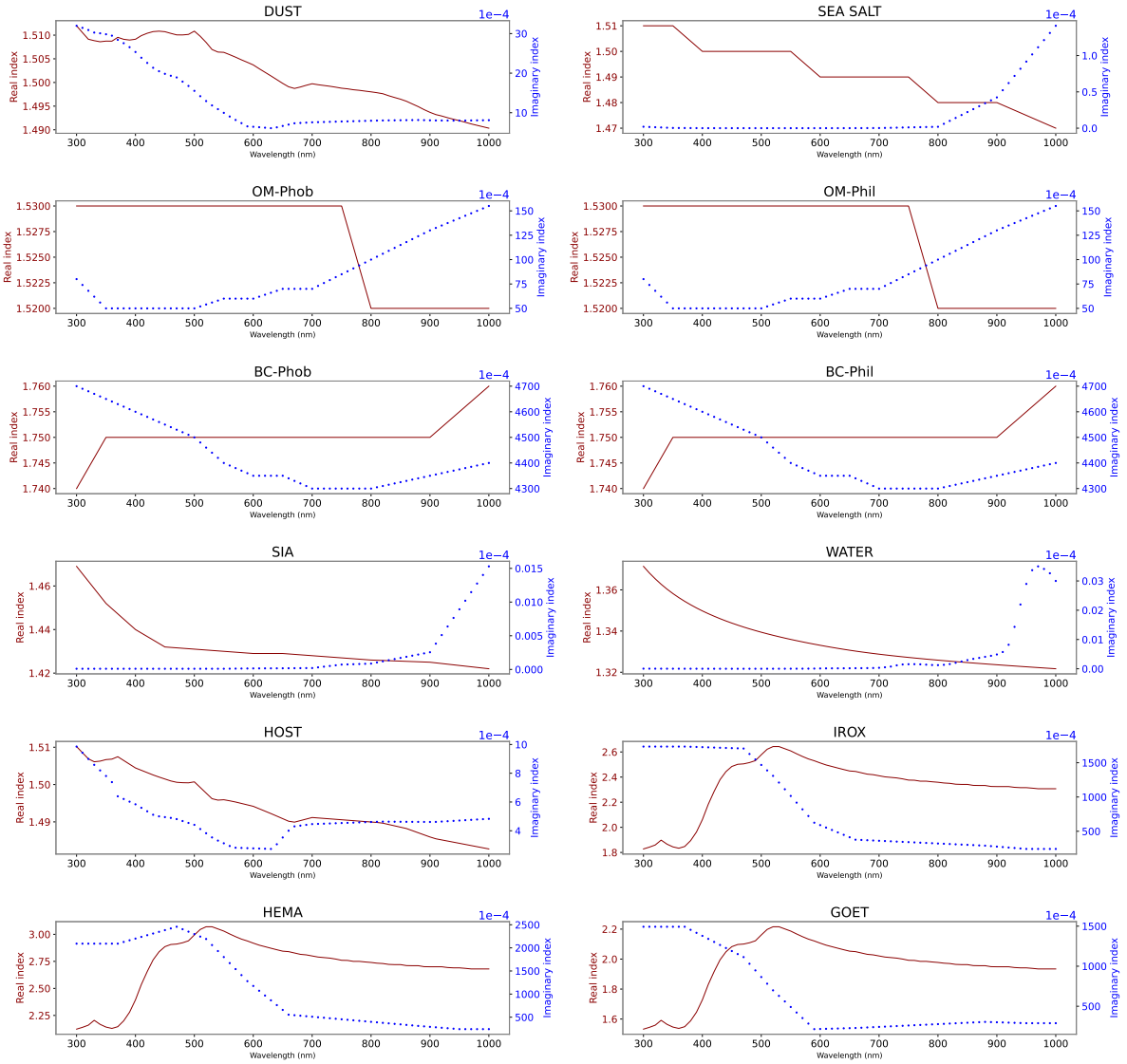

Figure C.1: Refractive indexes for each species used for the calculation of aerosol optical properties in the offline package (Sect. 7.2.2). Solid red lines represent real imaginary index, and dotted blue ones do for the imaginary index.

C.3 Sensitivity to coarse SIA formation: Burdens

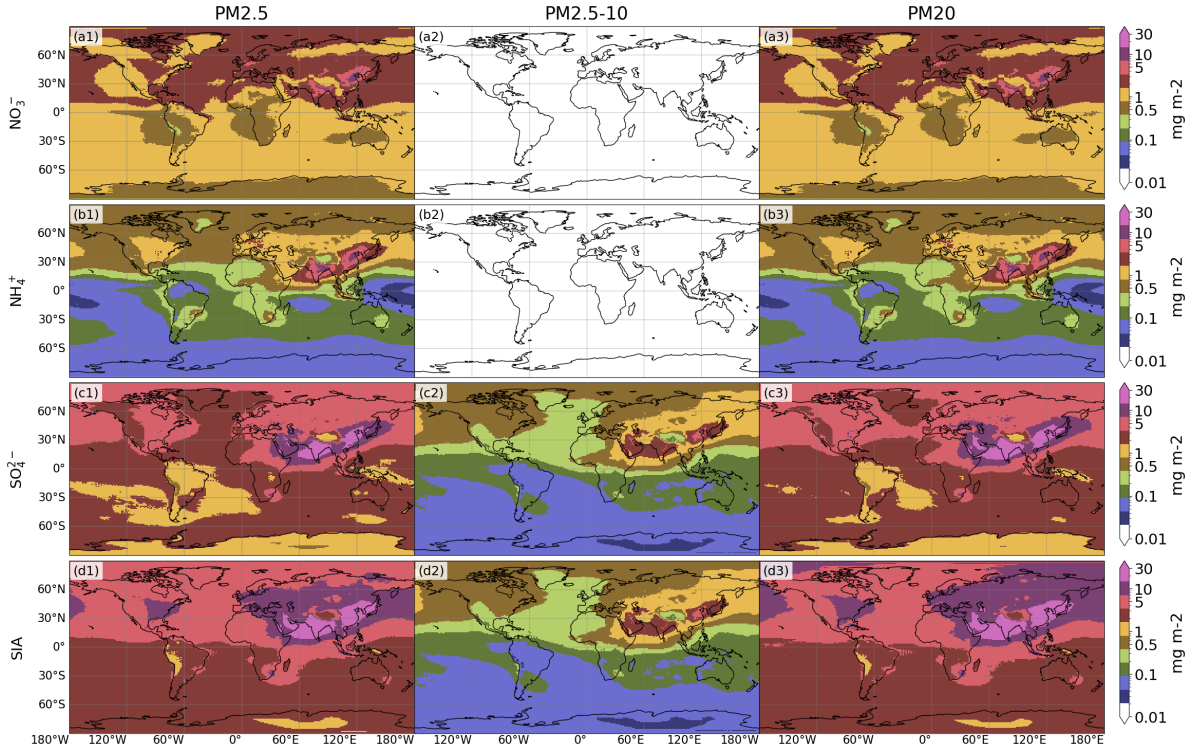

Figure C.2: Column loads of secondary inorganic aerosol (SIA) species when not accounting for coarse SIA formation.

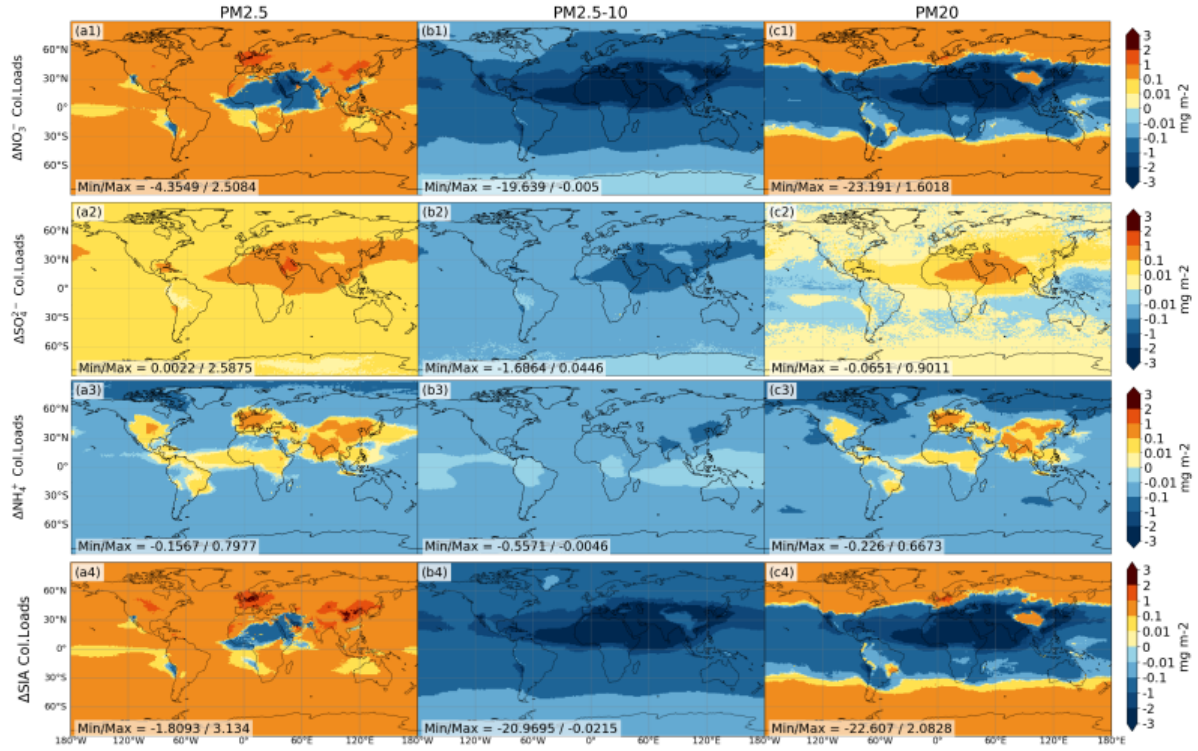

Figure C.3: Change in burdens of secondary inorganic aerosol (SIA) species when using EMIT source-based $CaCO_3$ distribution without and with coarse SIA formation (fTEQ-DBCLL).

C.4 Sensitivity to $CaCO_3$ geographical distribution

C.4.1 Relative differences in AOD and SSA

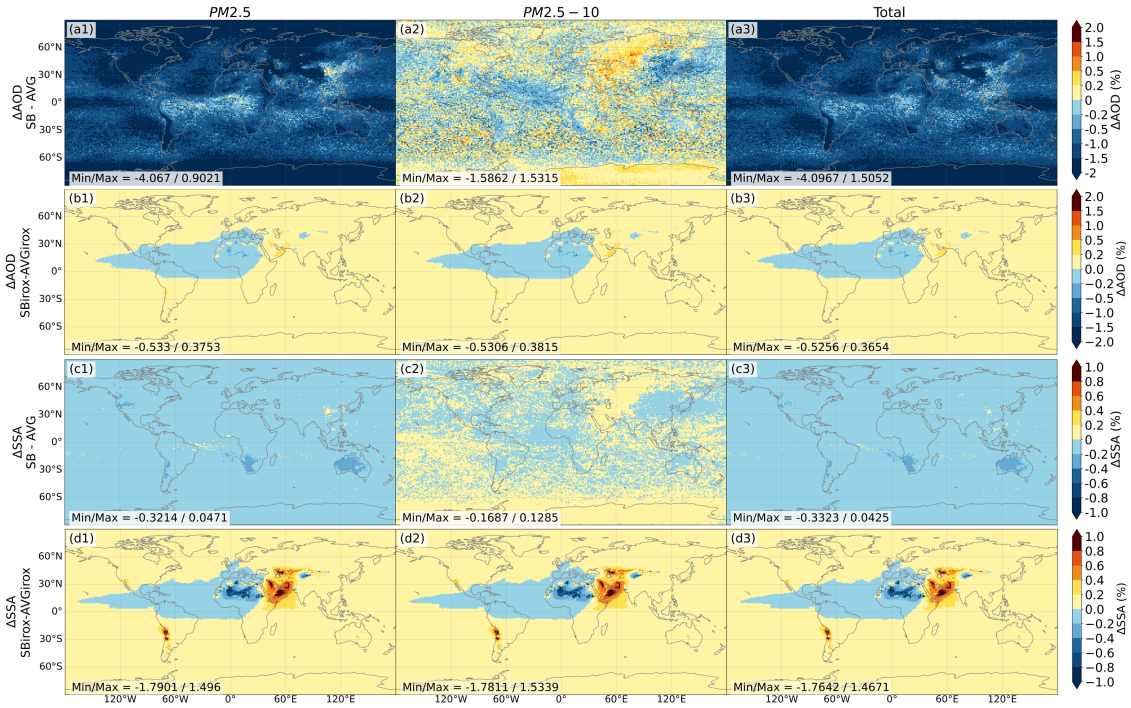

Figure C.4: Relative differences (%) in aerosol optical depth (AOD) and single scattering albedo (SSA) between source-based (SB) and globally average (AVG) approaches. As in Fig.7.10, differences isolating the effect of $CaCO_3$ and the resulting SIA species (*a1-a3* and *c1-c3* for AOD and SSA, respectively), and including additional mineralogical variations (*b1-b3* and *d1-d3* for AOD and SSA, respectively). *Total* refers to particles with $D < 20\mu m$.

C.5 Sensitivity to the mineral atlas

C.5.1 Differences in SIA burdens

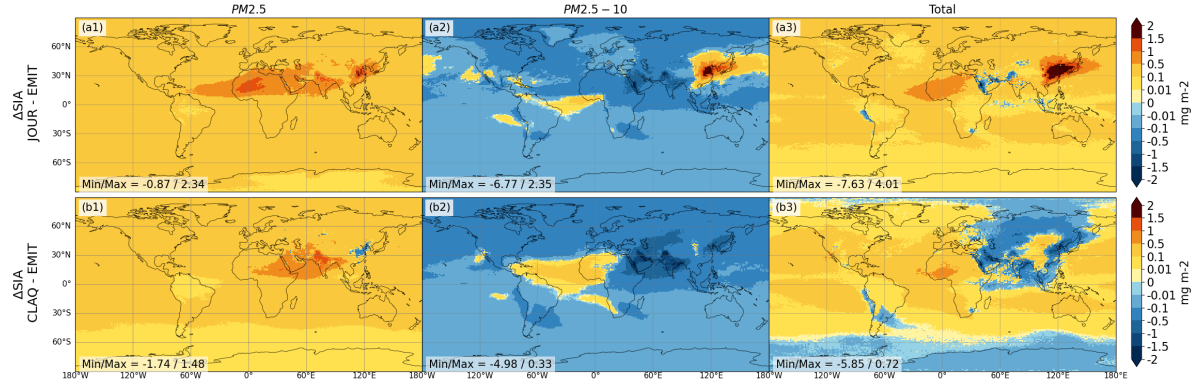

Figure C.5: Differences in secondary inorganic aerosol (SIA) column loads between simulations using $CaCO_3$ from Journet et al. (2014) (JOUR) and Claquin et al. (1999) (CLAQ) mineral datasets, and the case using EMIT $CaCO_3$. *Total* refers to particles with $D < 20\mu m$

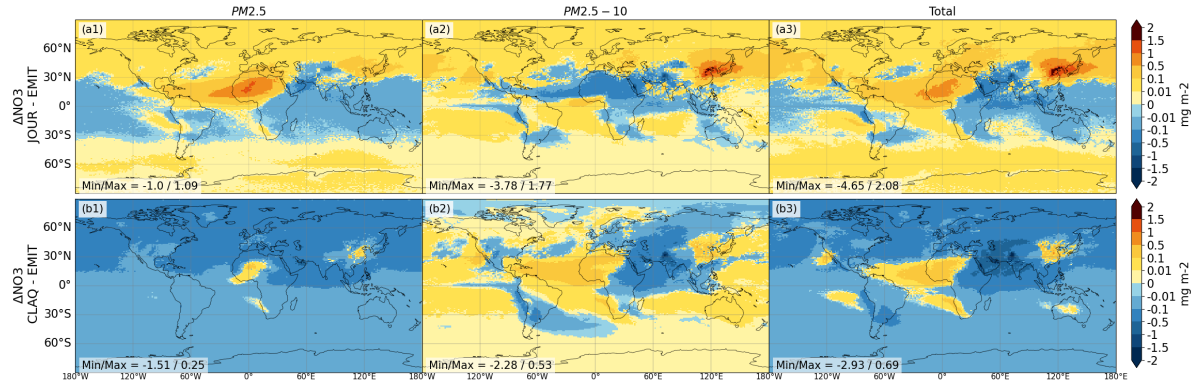

Figure C.6: Differences in particulate nitrate column loads between simulations using $CaCO_3$ from Journet et al. (2014) (JOUR) and Claquin et al. (1999) (CLAQ) mineral datasets, and the case using EMIT $CaCO_3$. *Total* refers to particles with $D < 20\mu m$

C.5.2 Relative differences in AOD and SSA

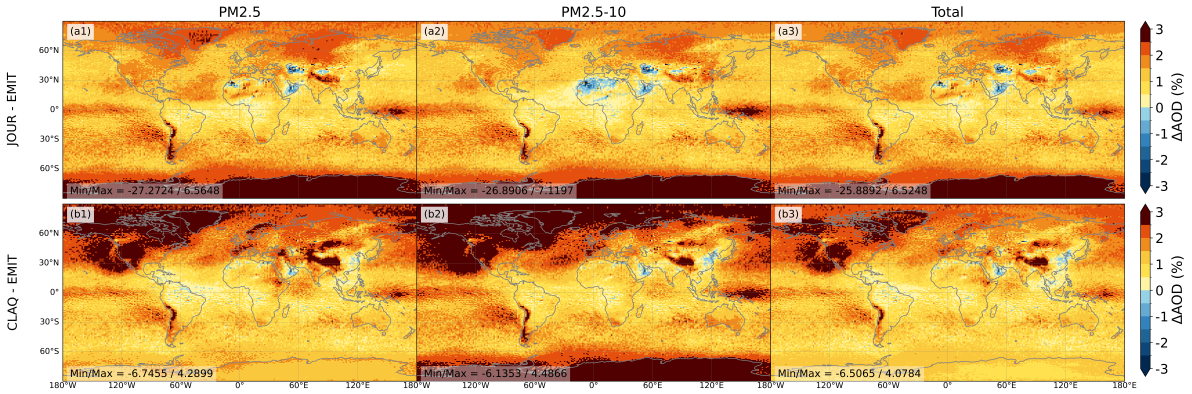

Figure C.7: Relative change (%) in AOD when using source-based mineral data from alternative mineral atlases (JOUR and CLAQ) compared to EMIT. *Total* refers to particles with $D < 20\mu m$

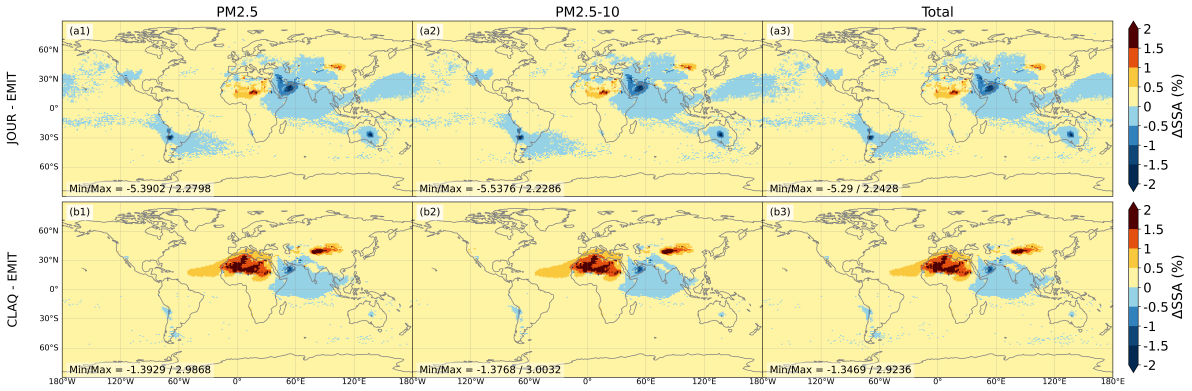

Figure C.8: Relative change (%) in SSA when using source-based mineral data from alternative mineral atlases (JOUR and CLAQ) compared to EMIT. *Total* refers to particles with $D < 20\mu m$

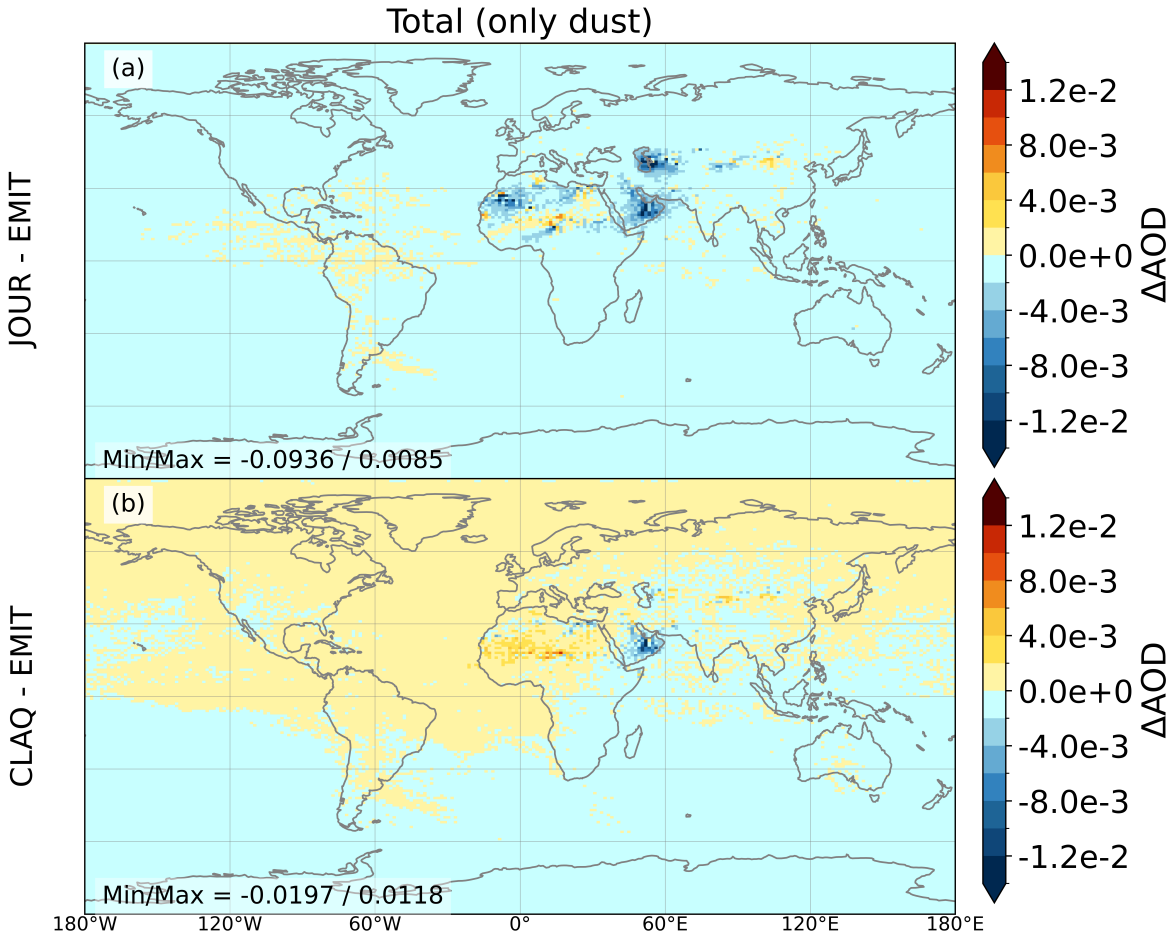

Figure C.9: Differences in AOD derived from dust bulk minerals (i.e. no condensables included) between simulations using Journet et al. (2014) (JOUR) and Claquin et al. (1999) (CLAQ) mineral datasets, compared with the case using EMIT. *Total* refers to particles with $D < 20\mu m$

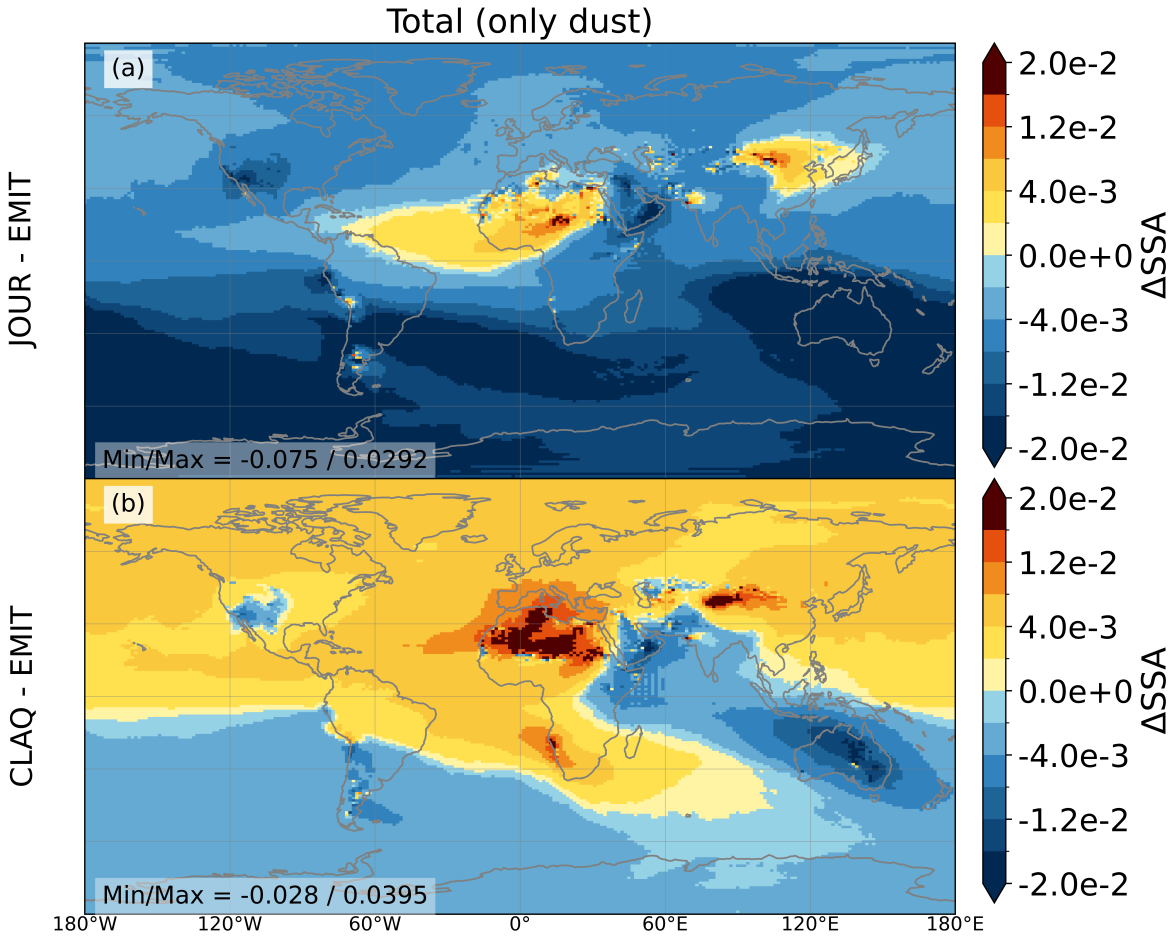

Figure C.10: Differences in SSA derived from dust bulk minerals (i.e. no condensables included) between simulations using Journet et al. (2014) (JOUR) and Claquin et al. (1999) (CLAQ) mineral datasets, compared with the case using EMIT. *Total* refers to particles with $D < 20\mu m$

References

AAPCA: State Air Trends & Successes: The StATS Report, https://cleanairact.org/wp-content/uploads/2025/05/AAPCA_2025_StATS_Report_FINAL_for-distribution.pdf, 2025.

Aas, W., Mortier, A., Bowersox, V., Cherian, R., Faluvegi, G., Fagerli, H., Hand, J., Klimont, Z., Galy-Lacaux, C., Lehmann, C. M. B., Myhre, C. L., Myhre, G., Olivié, D., Sato, K., Quaas, J., Rao, P. S. P., Schulz, M., Shindell, D., Skeie, R. B., Stein, A., Takemura, T., Tsyro, S., Vet, R., and Xu, X.: Global and regional trends of atmospheric sulfur, 9, 953, https://doi.org/10.1038/s41598-018-37304-0, publisher: Nature Publishing Group, 2019.

Adebiyi, A., Kok, J. F., Murray, B. J., Ryder, C. L., Stuut, J. B. W., Kahn, R. A., Knippertz, P., Formenti, P., Mahowald, N. M., García-Pando, C. P., Klose, M., Ansmann, A., Samset, B. H., Ito, A., Balkanski, Y., Biagio, C. D., Romanias, M. N., Huang, Y., and Meng, J.: A review of coarse mineral dust in the Earth system, 60, https://doi.org/10.1016/j.aeolia.2022.100849, 2023.

Adebiyi, A. A. and Kok, J. F.: Climate models miss most of the coarse dust in the atmosphere, 6, eaaz9507, https://doi.org/10.1126/sciadv.aaz9507, publisher: American Association for the Advancement of Science, 2020.

Al-Hosney, H. A. and Grassian, V. H.: Water, sulfur dioxide and nitric acid adsorption on calcium carbonate: A transmission and ATR-FTIR study, 7, 1266–1276, https://doi.org/10.1039/B417872F, publisher: The Royal Society of Chemistry, 2005.

Alari, A., Ranzani, O., Milà, C., Olmos, S., Basagaña, X., Dadvand, P., Duarte-Salles, T., Nieuwenhuijsen, M., and Tonne, C.: Long-term exposure to air pollution and lower respiratory infections in a large population-based adult cohort in Catalonia, 195, 109 230, https://doi.org/10.1016/j.envint.2024.109230, 2025.

Alexander, B., Park, R. J., Jacob, D. J., and Gong, S.: Transition metal-catalyzed oxidation of atmospheric sulfur: Global implications for the sulfur budget, 114, https://doi.org/10.1029/2008JD010486, _eprint: https://onlinelibrary.wiley.com/doi/pdf/10.1029/2008JD010486, 2009.

Amato, F., Alastuey, A., Karanasiou, A., Lucarelli, F., Nava, S., Calzolai, G., Severi, M., Becagli, S., Gianelle, V. L., Colombi, C., Alves, C., Custódio, D., Nunes, T., Cerqueira, M., Pio, C., Eleftheriadis, K., Diapouli, E., Reche, C., Minguillón, M. C., Manousakas, M.-I., Maggos, T., Vratolis, S., Harrison, R. M., and Querol, X.: AIRUSE-LIFE+: a harmonized PM speciation and source apportionment in five southern European cities, Atmospheric Chemistry and Physics, 16, 3289–3309, https://doi.org/10.5194/acp-16-3289-2016, 2016.

Amiri-Farahani, A., Allen, R. J., Neubauer, D., and Lohmann, U.: Impact of Saharan dust on North Atlantic marine stratocumulus clouds: importance of the semidirect effect, 17, 6305–6322, https://doi.org/10.5194/acp-17-6305-2017, publisher: Copernicus GmbH, 2017.

Ammann, M., Pöschl, U., and Rudich, Y.: Effects of reversible adsorption and Langmuir–Hinshelwood surface reactions on gas uptake by atmospheric particles, 5, 351–356, https://doi.org/10.1039/B208708A, 2003.

Ansari, A. S. and Pandis, S. N.: The effect of metastable equilibrium states on the partitioning of nitrate between the gas and aerosol phases, 34, 157–168, https://doi.org/10.1016/S1352-2310(99)00242-3, 2000.

Anuforom, A. C.: Spatial distribution and temporal variability of Harmattan dust haze in sub-Sahel West Africa, 41, 9079–9090, https://doi.org/10.1016/j.atmosenv.2007.08.003, 2007.

Aragnou, E., Watt, S., Nguyen Duc, H., Cheeseman, C., Riley, M., Leys, J., White, S., Salter, D., Azzi, M., Tzu-Chi Chang, L., Morgan, G., and Hannigan, I.: Dust Transport from Inland Australia and Its Impact on Air Quality and Health on the Eastern Coast of Australia during the February 2019 Dust Storm, 12, 141, https://doi.org/10.3390/atmos12020141, number: 2 Publisher: Multidisciplinary Digital Publishing Institute, 2021.

Arfin, T., Pillai, A. M., Mathew, N., Tirpude, A., Bang, R., and Mondal, P.: An overview of atmospheric aerosol and their effects on human health, 30, 125 347–125 369, https://doi.org/10.1007/s11356-023-29652-w, 2023.

Athanasopoulou, E., Tombrou, M., Pandis, S. N., and Russell, A. G.: The role of sea-salt emissions and heterogeneous chemistry in the air quality of polluted coastal areas, Atmospheric Chemistry and Physics, 8, 5755–5769, https://doi.org/10.5194/acp-8-5755-2008, 2008.

Badia, A., Jorba, O., Voulgarakis, A., Dabdub, D., García-Pando, C. P., Hilboll, A., Gonçalves, M., and Janjic, Z.: Description and evaluation of the Multiscale Online Nonhydrostatic AtmospheRe CHemistry model (NMMB-MONARCH) version 1.0: gas-phase chemistry at global scale, Geosci. Model Dev, 10, 609–638, https://doi.org/10.5194/gmd-10-609-2017, 2017.

Balkanski, Y., Schulz, M., Claquin, T., and Guibert, S.: Reevaluation of Mineral aerosol radiative forcings suggests a better agreement with satellite and AERONET data, 7, 81–95, https://doi.org/10.5194/acp-7-81-2007, 2007.

Banchelli, F., Garcia-Gasulla, M., Mantovani, F., Vinyals, J., Pocurull, J., Vicente, D., Eguzkitza, B., Galeazzo, F. C. C., Acosta, M. C., and Girona, S.: Introducing MareNostrum5: A European pre-exascale energy-efficient system designed to serve a broad spectrum of scientific workloads, 176, 108 125, https://doi.org/10.1016/j.future.2025.108125, 2026.

Barkan, J. and Alpert, P.: Synoptic analysis of a rare event of Saharan dust reaching the Arctic region, 65, 208–211, https://doi.org/10.1002/wea.503, _eprint: https://onlinelibrary.wiley.com/doi/pdf/10.1002/wea.503, 2010.

Bates, T. S., Quinn, P. K., Coffman, D. J., Covert, D. S., Miller, T. L., Johnson, J. E., Carmichael, G. R., Uno, I., Guazzotti, S. A., Sodeman, D. A., Prather, K. A., Rivera, M., Russell, L. M., and Merrill, J. T.: Marine boundary layer dust and pollutant transport associated with the passage of a frontal system over eastern Asia, 109, 2003JD004 094, https://doi.org/10.1029/2003JD004094, 2004.

Bauer, S. E. and Koch, D.: Impact of heterogeneous sulfate formation at mineral dust surfaces on aerosol loads and radiative forcing in the Goddard Institute for Space Studies general circulation model, 110, https://doi.org/10.1029/2005JD005870, _eprint: https://onlinelibrary.wiley.com/doi/pdf/10.1029/2005JD005870, 2005.

Bauer, S. E., Balkanski, Y., Schulz, M., Hauglustaine, D. A., and Dentener, F.: Global modeling of heterogeneous chemistry on mineral aerosol surfaces: Influence on tropospheric ozone chemistry and comparison to observations, Journal of Geophysical Research: Atmospheres, 109, 2304, https://doi.org/https://doi.org/10.1029/2003JD003868, 2004.

Bauer, S. E., Mishchenko, M. I., Lacis, A. A., Zhang, S., Perlwitz, J., and Metzger, S. M.: Do sulfate and nitrate coatings on mineral dust have important effects on radiative properties and climate modeling?, Journal of Geophysical Research: Atmospheres, 112, 6307, https://doi.org/10.1029/2005JD006977, 2007.

Bellouin, N., Rae, J., Jones, A., Johnson, C., Haywood, J., and Boucher, O.: Aerosol forcing in the Climate Model Intercomparison Project (CMIP5) simulations by HadGEM2-ES and the role of ammonium nitrate, Journal of Geophysical Research Atmospheres, 116, https://doi.org/10.1029/2011JD016074, 2011.

Bennett, C. M., McKendry, I. G., Kelly, S., Denike, K., and Koch, T.: Impact of the 1998 Gobi dust event on hospital admissions in the Lower Fraser Valley, British Columbia, 366, 918–925, https://doi.org/10.1016/j.scitotenv.2005.12.025, 2006.

Bergas-Massó, E., Gonçalves Ageitos, M., Myriokefalitakis, S., Miller, R. L., van Noije, T., Le Sager, P., Montané Pinto, G., and Pérez García-Pando, C.: Pre-Industrial, Present and Future Atmospheric Soluble Iron Deposition and the Role of Aerosol Acidity and Oxalate Under CMIP6 Emissions, 11, e2022EF003 353, https://doi.org/10.1029/2022EF003353, _eprint: https://onlinelibrary.wiley.com/doi/pdf/10.1029/2022EF003353, 2023.

Bergas-Massó, E., Ageitos, M. G., Myriokefalitakis, S., Miller, R. L., van Noije, T., Sager, P. L., Pinto, G. M., and García-Pando, C. P.: Pre-Industrial, Present and Future Atmospheric Soluble Iron Deposition and the Role of Aerosol Acidity and Oxalate Under CMIP6 Emissions, Earth's Future, 11, https://doi.org/10.1029/2022ef003353, 2023.

Betts, A. K. and Miller, M. J.: A new convective adjustment scheme. Part II: Single column tests using GATE wave, BOMEX, ATEX and arctic air-mass data sets, Quarterly Journal of the Royal Meteorological Society, 112, 693–709, https://doi.org/10.1002/QJ.49711247308, 1986.

Bian, H., Chin, M., Rodriguez, J. M., Yu, H., Penner, J. E., and Strahan, S.: Sensitivity of aerosol optical thickness and aerosol direct radiative effect to relative humidity, Atmospheric Chemistry and Physics, 9, 2375–2386, https://doi.org/10.5194/ACP-9-2375-2009, 2009.

Bian, H., Chin, M., Hauglustaine, D. A., Schulz, M., Myhre, G., Bauer, S. E., Lund, M. T., Karydis, V. A., Kucsera, T. L., Pan, X., Pozzer, A., Skeie, R. B., Steenrod, S. D., Sudo, K., Tsigaridis, K., Tsimpidi, A. P., and Tsyro, S. G.: Investigation of global particulate nitrate from the AeroCom phase III experiment, 17, 12 911–12 940, https://doi.org/10.5194/acp-17-12911-2017, publisher: Copernicus GmbH, 2017.

Binkowski, F. S. and Shankar, U.: The Regional Particulate Matter Model: 1. Model description and preliminary results, Journal of Geophysical Research: Atmospheres, 100, 26 191–26 209, https://doi.org/10.1029/95JD02093, 1995.

Bleam, W.: Clay Mineralogy and Chemistry, Soil and Environmental Chemistry, pp. 87–146, https://doi.org/10.1016/B978-0-12-804178-9.00003-3, 2017.

Blum, A. E.: Feldspars in Weathering, pp. 595–630, Springer Netherlands, Dordrecht, ISBN 978-94-011-1106-5, https://doi.org/10.1007/978-94-011-1106-5_15, 1994.

Bobbink, R. and Hicks, W. K.: Factors Affecting Nitrogen Deposition Impacts on Biodiversity: An Overview, in: Nitrogen Deposition, Critical Loads and Biodiversity, edited by Sutton, M. A., Mason, K. E., Sheppard, L. J., Sverdrup, H., Haeuber, R., and Hicks, W. K., pp. 127–138, Springer Netherlands, ISBN 978-94-007-7939-6, https://doi.org/10.1007/978-94-007-7939-6_14, 2014.

Boucher, O., Randall, D., Artaxo, P., Bretherton, C., Artaxo, P., Bretherton, C., Feingold, G., Forster, P., Kerminen, V.-M., Kondo, Y., Liao, H., Lohmann, U., Rasch, P., Satheesh, S., Sherwood, S., Stevens, B., and Zhang, X.-Y.: Clouds and Aerosols. In: Climate Change 2013: The Physical Science Basis. Contribution of Working Group I to the Fifth Assessment Report of the Intergovernmental Panel on Climate Change, pp. 571–657, https://doi.org/doi:10.1017/CBO9781107415324.016, 2013.

Bowdalo, D., Basart, S., Guevara, M., Jorba, O., Pérez García-Pando, C., Jaimes Palomera, M., Rivera Hernandez, O., Puchalski, M., Gay, D., Klausen, J., Moreno, S., Netcheva, S., and Tarasova, O.: GHOST: a globally harmonised dataset of surface atmospheric composition measurements, 16, 4417–4495, https://doi.org/10.5194/essd-16-4417-2024, publisher: Copernicus GmbH, 2024.

Brasseur, G. P. and Jacob, D. J.: Modeling of atmospheric chemistry, Cambridge University Press, 2017.

Breuning-Madsen, H. and Awadzi, T. W.: Harmattan dust deposition and particle size in Ghana, 63, 23–38, https://doi.org/10.1016/j.catena.2005.04.001, 2005.

Bristow, C. S., Hudson-Edwards, K. A., and Chappell, A.: Fertilizing the Amazon and equatorial Atlantic with West African dust, 37, https://doi.org/10.1029/2010GL043486, _eprint: https://onlinelibrary.wiley.com/doi/pdf/10.1029/2010GL043486, 2010.

Britannica, The Editors of Encyclopaedia: chlorite, https://www.britannica.com/science/chlorite-mineral, [Online; accessed March 11, 2024], 2018.

Brodrick, P., Okin, G., Ochoa, Francisco, T. D., Clark, R., Ehlmann, B., Keebler, A., Miller, R., Mohawald, N., Ginoux, P., Garcia-Pando, C., Goncalves, M., and Green, R.: EMIT L3 Aggregated Mineral Spectral Abundance and Uncertainty 0.5 Deg V002 [Data set], https://doi.org/10.5067/EMIT/EMITL3ASA.002, online; Accessed 2025-11-10, 2025.

Brodrick, P. G. et al.: Earth Surface Mineral Dust Source Investigation (EMIT) EMIT L2B Algorithm: Mineral Detection and Related Products at the Pixel Scale Theoretical Basis, Technical report, NASA Jet Propulsion Laboratory, California Institute of Technology, 2023.

Bullard, J. E., Baddock, M., Bradwell, T., Crusius, J., Darlington, E., Gaiero, D., Gassó, S., Gisladottir, G., Hodgkins, R., McCulloch, R., McKenna-Neuman, C., Mockford, T., Stewart, H., and Thorsteinsson, T.: High-latitude dust in the Earth system, 54, 447–485, https://doi.org/10.1002/2016RG000518, _eprint: https://onlinelibrary.wiley.com/doi/pdf/10.1002/2016RG000518, 2016.

Burkholder, J., Sander, S., Abbatt, J., Barker, J., Cappa, C., Crounse, J., Dibble, T., Huie, R., Kolb, C., Kurylo, M., Orkin, V., Percival, C., Wilmouth, D., and Wine, P.: Chemical kinetics and photochemical data for use in atmospheric studies; evaluation number 19, Pasadena, CA: Jet Propulsion Laboratory, National Aeronautics and Space Administration, 2020, https://doi.org/2014/49199, 2020.

Byun, D. W.: Dynamically Consistent Formulations in Meteorological and Air Quality Models for Multiscale Atmospheric Studies. Part I: Governing Equations in a Generalized Coordinate System, Journal of the Atmospheric Sciences, 56, 3789 – 3807, https://doi.org/10.1175/1520-0469(1999)056<3789:DCFIMA>2.0.CO;2, 1999.

Camargo, J. A. and Alonso, : Ecological and toxicological effects of inorganic nitrogen pollution in aquatic ecosystems: A global assessment, 32, 831–849, https://doi.org/10.1016/j.envint.2006.05.002, 2006.

Campbell, S. W., Evans, M. C., and Poor, N. D.: Predictions of size-resolved aerosol concentrations of ammonium, chloride and nitrate at a bayside site using EQUISOLV II, 36, 4299–4307, https://doi.org/10.1016/S1352-2310(02)00404-1, 2002.

Canals-Angerri, A., Hopke, P. K., Lara, R., Alastuey, A., Reche, C., Pérez, N., van Drooge, B. L., and Querol, X.: Changes in PM10 concentrations, composition, and source contributions in the last decades in urban and regional Barcelona, Urban Climate, 64, 102 677, https://doi.org/10.1016/j.uclim.2025.102677, 2025.

Cao, J., Xu, H., Xu, Q., Chen, B., and Kan, H.: Fine Particulate Matter Constituents and Cardiopulmonary Mortality in a Heavily Polluted Chinese City, 120, 373–378, https://doi.org/10.1289/ehp.1103671, publisher: Environmental Health Perspectives, 2012.

Capaldo, K. P., Pilinis, C., and Pandis, S. N.: A computationally efficient hybrid approach for dynamic gas/aerosol transfer in air quality models, Atmospheric Environment, 34, 3617–3627, https://doi.org/10.1016/s1352-2310(00)00092-3, 2000.

Cape, J. N., van der Eerden, L. J., Sheppard, L. J., Leith, I. D., and Sutton, M. A.: Evidence for changing the critical level for ammonia, 157, 1033–1037, https://doi.org/10.1016/j.envpol.2008.09.049, 2009.

Caquineau, S., Gaudichet, A., Gomes, L., and Legrand, M.: Mineralogy of Saharan dust transported over northwestern tropical Atlantic Ocean in relation to source regions, 107, AAC 4–1–AAC 4–12, https://doi.org/10.1029/2000JD000247, _eprint: https://onlinelibrary.wiley.com/doi/pdf/10.1029/2000JD000247, 2002.

Carey, C.: Nitrogen cycling in a changing world: Response of a California grassland to multiple global change factors, https://escholarship.org/uc/item/4ck8j7sw, 2014.

Carlos-Cuellar, S., Li, P., Christensen, A. P., Krueger, B. J., Burrichter, C., and Grassian, V. H.: Heterogeneous Uptake Kinetics of Volatile Organic Compounds on Oxide Surfaces Using a Knudsen Cell Reactor: Adsorption of Acetic Acid, Formaldehyde, and Methanol on -Fe2O3, -Al2O3, and SiO2, 107, 4250–4261, https://doi.org/10.1021/jp0267609, publisher: American Chemical Society, 2003.

Casquero-Vera, J. A., Pérez-Ramírez, D., Lyamani, H., Rejano, F., Casans, A., Titos, G., Olmo, F. J., Dada, L., Hakala, S., Hussein, T., Lehtipalo, K., Paasonen, P., Hyvärinen, A., Pérez, N., Querol, X., Rodríguez, S., Kalivitis, N., González, Y., Alghamdi, M. A., Kerminen, V.-M., Alastuey, A., Petäjä, T., and Alados-Arboledas, L.: Impact of desert dust on new particle formation events and the cloud condensation nuclei budget in dust-influenced areas, Atmospheric Chemistry and Physics, 23, 15 795–15 814, https://doi.org/10.5194/acp-23-15795-2023, 2023.

Chang, L.-T., Tang, C.-S., Pan, Y.-Z., and Chan, C.-C.: Association of Heart Rate Variability of the Elderly with Personal Exposure to PM1, PM1–2.5, and PM2.5–10, 79, 552–556, https://doi.org/10.1007/s00128-007-9233-4, 2007.

Charlson, R. and Heintzenberg, J.: Aerosol Forcing of Climate, 1995.

Chen, Q., Yin, Y., Jiang, H., Chu, Z., Xue, L., Shi, R., Zhang, X., and Chen, J.: The Roles of Mineral Dust as Cloud Condensation Nuclei and Ice Nuclei During the Evolution of a Hail Storm, Journal of Geophysical Research: Atmospheres, 124, 14 262–14 284, https://doi.org/10.1029/2019JD031403, _eprint: https://agupubs.onlinelibrary.wiley.com/doi/pdf/10.1029/2019JD031403, 2019.

Chin, M., Rood, R. B., Lin, S.-J., Müller, J.-F., and Thompson, A. M.: Atmospheric sulfur cycle simulated in the global model GOCART: Model description and global properties, 105, 24 671–24 687, https://doi.org/10.1029/2000JD900384, _eprint: https://onlinelibrary.wiley.com/doi/pdf/10.1029/2000JD900384, 2000.

Chin, M., Ginoux, P., Kinne, S., Torres, O., Holben, B. N., Duncan, B. N., Martin, R. V., Logan, J. A., Higurashi, A., and Nakajima, T.: Tropospheric Aerosol Optical Thickness from the GOCART Model and Comparisons with Satellite and Sun Photometer Measurements, Journal of the Atmospheric Sciences, 59, 461 – 483, https://doi.org/10.1175/1520-0469(2002)059<0461:TAOTFT>2.0.CO;2, 2002.

Chou, C., Formenti, P., Maille, M., Ausset, P., Helas, G., Harrison, M., and Osborne, S.: Size distribution, shape, and composition of mineral dust aerosols collected during the African Monsoon Multidisciplinary Analysis Special Observation Period 0: Dust and Biomass-Burning Experiment field campaign in Niger, January 2006, 113, https://doi.org/10.1029/2008JD009897, _eprint: https://onlinelibrary.wiley.com/doi/pdf/10.1029/2008JD009897, 2008.

Clappier, A., Thunis, P., Beekmann, M., Putaud, J. P., and de Meij, A.: Impact of SOx, NOx and NH3 emission reductions on PM2.5 concentrations across Europe: Hints for future measure development, Environment International, 156, 106 699, https://doi.org/10.1016/j.envint.2021.106699, 2021.

Claquin, T., Schulz, M., and Balkanski, Y. J.: Modeling the mineralogy of atmospheric dust sources, Journal of Geophysical Research: Atmospheres, 104, 22 243–22 256, https://doi.org/10.1029/1999JD900416, 1999.

Clark, R. N., Swayze, G. A., Livo, K. E., Brodrick, P. G., Noe Dobrea, E., Vijayarangan, S., Green, R. O., Wettergreen, D., Candela, A., Hendrix, A., Pérez García-Pando, C., Pearson, N. C., Lane, M. D., González-Romero, A., Querol, X., the EMIT, and teams, T.: Imaging Spectroscopy: Earth and Planetary Remote Sensing with the PSI Tetracorder and Expert Systems from Rovers to EMIT and Beyond, The Planetary Science Journal, 5, 276, https://doi.org/10.3847/PSJ/ad6c3a, 2024.

Cosentino, N. J., Gaiero, D. M., and Lambert, F.: Present-Day Patagonian Dust Emissions: Combining Surface Visibility, Mass Flux, and Reanalysis Data, Journal of Geophysical Research: Atmospheres, 126, e2020JD034 459, https://doi.org/10.1029/2020JD034459, _eprint: https://agupubs.onlinelibrary.wiley.com/doi/pdf/10.1029/2020JD034459, 2021.

Cowie, S. M., Knippertz, P., and Marsham, J. H.: Are vegetation-related roughness changes the cause of the recent decrease in dust emission from the Sahel?, 40, 1868–1872, https://doi.org/10.1002/grl.50273, _eprint: https://onlinelibrary.wiley.com/doi/pdf/10.1002/grl.50273, 2013.

Crowley, J. N., Ammann, M., Cox, R. A., Hynes, R. G., Jenkin, M. E., Mellouki, A., Rossi, M. J., Troe, J., and Wallington, T. J.: Atmospheric Chemistry and Physics Evaluated kinetic and photochemical data for atmospheric chemistry: Volume V-heterogeneous reactions on solid substrates, Atmos. Chem. Phys, 10, 9059–9223, https://doi.org/10.5194/acp-10-9059-2010, 2010.

Crowley, J. N., Ammann, M., Cox, R. A., Hynes, R. G., Jenkin, M. E., Mellouki, A., Rossi, M. J., Troe, J., and Wallington, T. J.: Sciences ess Atmospheric Chemistry and Physics Climate of the Past Geoscientific Instrumentation Methods and Data Systems "Evaluated kinetic and photochemical data for atmospheric chemistry: Volume V-heterogeneous reactions on solid substrates" published, Atmos. Chem. Phys, 13, 9059–9223, https://doi.org/10.5194/acp-13-7359-2013, 2013.

Dang, R., Jacob, D. J., Zhai, S., Coheur, P., Clarisse, L., Van Damme, M., Pendergrass, D. C., Choi, J.-s., Park, J.-s., Liu, Z., and Liao, H.: Diagnosing the Sensitivity of Particulate Nitrate to Precursor Emissions Using Satellite Observations of Ammonia and Nitrogen Dioxide, 50, e2023GL105 761, https://doi.org/10.1029/2023GL105761, _eprint: https://onlinelibrary.wiley.com/doi/pdf/10.1029/2023GL105761, 2023.

Dasgupta, P. K., Campbell, S. W., Al-Horr, R. S., Ullah, S. M., Li, J., Amalfitano, C., and Poor, N. D.: Conversion of sea salt aerosol to NaNO3 and the production of HCl: Analysis of temporal behavior of aerosol chloride/nitrate and gaseous HCl/HNO3 concentrations with AIM, Atmospheric Environment, 41, 4242–4257, https://doi.org/10.1016/j.atmosenv.2006.09.054, 2007.

Dassios, K. G. and Pandis, S. N.: The mass accommodation coefficient of ammonium nitrate aerosol, 33, 2993–3003, https://doi.org/10.1016/S1352-2310(99)00079-5, 1999.

De Deckker, P.: An evaluation of Australia as a major source of dust, Earth-Science Reviews, 194, 536–567, https://doi.org/10.1016/j.earscirev.2019.01.008, 2019.

de Reus, M., Dentener, F., Thomas, A., Borrmann, S., Ström, J., and Lelieveld, J.: Airborne observations of dust aerosol over the North Atlantic Ocean during ACE 2: Indications for heterogeneous ozone destruction, 105, 15 263–15 275, https://doi.org/10.1029/2000JD900164, _eprint: https://onlinelibrary.wiley.com/doi/pdf/10.1029/2000JD900164, 2000.

de Vries, W., Cellier, P., Erisman, J. W., and Sutton, M. A.: Assessment of nitrogen fluxes to air and water from site scale to continental scale: An overview, 159, 3143–3148, https://doi.org/10.1016/j.envpol.2011.08.047, 2011.

de Vries, W., Dobbertin, M. H., Solberg, S., van Dobben, H. F., and Schaub, M.: Impacts of acid deposition, ozone exposure and weather conditions on forest ecosystems in Europe: an overview, 380, 1–45, https://doi.org/10.1007/s11104-014-2056-2, 2014.

de Vries, W., Posch, M., Simpson, D., de Leeuw, F. A. A. M., van Grinsven, H. J. M., Schulte-Uebbing, L. F., Sutton, M. A., and Ros, G. H.: Trends and geographic variation in adverse impacts of nitrogen use in Europe on human health, climate, and ecosystems: A review, 253, 104 789, https://doi.org/10.1016/j.earscirev.2024.104789, 2024.

Denier van der Gon, H., Gauss, M., Granier, C., Arellano, S., Benedictow, A., Darras, S., Dellaert, S., Guevara, M., Jalkanen, J.-P., Krueger, K., Kuenen, J., Liaskoni, M., Liousse, C., Markova, J., Perez, A. P., Quack, B., Simpson, D., Sindelarova, K., and Soulie, A.: Documentation of CAMS emission inventory products, https://atmosphere.copernicus.eu/node/1054, 2023.

Denier van der Gon, H. a. C., Bergström, R., Fountoukis, C., Johansson, C., Pandis, S. N., Simpson, D., and Visschedijk, A. J. H.: Particulate emissions from residential wood combustion in Europe – revised estimates and an evaluation, 15, 6503–6519, https://doi.org/10.5194/acp-15-6503-2015, publisher: Copernicus GmbH, 2015.

Dentener, F. J. and Crutzen, P. J.: Reaction of N2O5 on tropospheric aerosols: Impact on the global distributions of NO , O3, and OH, 98, 7149–7163, https://doi.org/10.1029/92JD02979, _eprint: https://onlinelibrary.wiley.com/doi/pdf/10.1029/92JD02979, 1993.

Dentener, F. J., Carmichael, G. R., Zhang, Y., Lelieveld, J., and Crutzen, P. J.: Role of mineral aerosol as a reactive surface in the global troposphere, Journal of Geophysical Research Atmospheres, 101, 22 869–22 889, https://doi.org/10.1029/96jd01818, 1996.

Deshpande, A. G., Jones, M. R., van Dijk, N., Mullinger, N. J., Harvey, D., Nicoll, R., Toteva, G., Weerakoon, G., Nissanka, S., Weerakoon, B., Grenier, M., Iwanicka, A., Duarte, F., Stephens, A., Ellis, C. J., Vieno, M., Drewer, J., Wolseley, P. A., Nanayakkara, S., Prabhashwara, T., Bealey, W. J., Nemitz, E., and Sutton, M. A.: Estimation of ammonia deposition to forest ecosystems in Scotland and Sri Lanka using wind-controlled NH3 enhancement experiments, 320, 120 325, https://doi.org/10.1016/j.atmosenv.2023.120325, 2024.

Di Biagio, C., Formenti, P., Balkanski, Y., Caponi, L., Cazaunau, M., Pangui, E., Journet, E., Nowak, S., Andreae, M. O., Kandler, K., Saeed, T., Piketh, S., Seibert, D., Williams, E., and Doussin, J.-F.: Complex refractive indices and single-scattering albedo of global dust aerosols in the shortwave spectrum and relationship to size and iron content, 19, 15 503–15 531, https://doi.org/10.5194/acp-19-15503-2019, 2019.

Di Biagio, C., Balkanski, Y., Albani, S., Boucher, O., and Formenti, P.: Direct Radiative Effect by Mineral Dust Aerosols Constrained by New Microphysical and Spectral Optical Data, 47, e2019GL086 186, https://doi.org/10.1029/2019GL086186, _eprint: https://onlinelibrary.wiley.com/doi/pdf/10.1029/2019GL086186, 2020.

Dias, T., Clemente, A., Martins-Loução, M. A., Sheppard, L., Bobbink, R., and Cruz, C.: Ammonium as a Driving Force of Plant Diversity and Ecosystem Functioning: Observations Based on 5 Years' Manipulation of N Dose and Form in a Mediterranean Ecosystem, 9, e92 517, https://doi.org/10.1371/journal.pone.0092517, publisher: Public Library of Science, 2014.

Dise, N. B., Ashmore, M., Belyazid, S., Bleeker, A., Bobbink, R., de Vries, W., Erisman, J. W., Spranger, T., Stevens, C. J., and van den Berg, L.: Nitrogen as a threat to European terrestrial biodiversity, pp. 463–494, Cambridge University Press, ISBN 978-1-107-00612-6, https://doi.org/10.1017/CBO9780511976988.023, 2011.

Duan, X., Zheng, G., Chen, C., Zhang, Q., and He, K.: Driving factors of aerosol acidity: a new hierarchical quantitative analysis framework and its application in Changzhou, China, 25, 3919–3928, https://doi.org/10.5194/acp-25-3919-2025, publisher: Copernicus GmbH, 2025.

Dubovik, O., Holben, B., Eck, T. F., Smirnov, A., Kaufman, Y. J., King, M. D., Tanré, D., and Slutsker, I.: Variability of Absorption and Optical Properties of Key Aerosol Types Observed in Worldwide Locations, Journal of the Atmospheric Sciences, 59, 590–608, https://doi.org/10.1175/1520-0469(2002)059<0590:VOAAOP>2.0.CO;2, publisher: American Meteorological Society Section: Journal of the Atmospheric Sciences, 2002.

Edwards, T. M., Puglis, H. J., Kent, D. B., Durán, J. L., Bradshaw, L. M., and Farag, A. M.: Ammonia and aquatic ecosystems – A review of global sources, biogeochemical cycling, and effects on fish, 907, 167 911, https://doi.org/10.1016/j.scitotenv.2023.167911, 2024.

EEA: European Union emission inventory report 1990–2018 under the UNECE Convention on Long-Range Transboundary Air Pollution (EEA Report 05/2020), https://www.eea.europa.eu/en/analysis/publications/european-union-emission-inventory-report-1990-2018, 2020.

EEA: Air pollution in Europe: 2023 reporting status under the National Emission Reduction Commitments Directive, https://doi.org/10.2800/339055, 2023.

Ek, M. B., Mitchell, K. E., Lin, Y., Rogers, E., Grunmann, P., Koren, V., Gayno, G., and Tarpley, J. D.: Implementation of Noah land surface model advances in the National Centers for Environmental Prediction operational mesoscale Eta model, Journal of Geophysical Research: Atmospheres, 108, 8851, https://doi.org/10.1029/2002JD003296, 2003.

Emanuel, K. A. and Živković Rothman, M.: Development and Evaluation of a Convection Scheme for Use in Climate Models, Journal of the Atmospheric Sciences, 56, 1766 – 1782, https://doi.org/https://doi.org/10.1175/1520-0469(1999)056<1766:DAEOAC>2.0.CO;2, 1999.

Engelbrecht, J. P., McDonald, E. V., Gillies, J. A., Jayanty, R. K. M., Casuccio, G., and Gertler, A. W.: Characterizing Mineral Dusts and Other Aerosols from the Middle East—Part 1: Ambient Sampling, 21, 297–326, https://doi.org/10.1080/08958370802464273, publisher: Taylor & Francis _eprint: https://doi.org/10.1080/08958370802464273, 2009.

Escribano, J., Di Tomaso, E., Jorba, O., Klose, M., Gonçalves Ageitos, M., Macchia, F., Amiridis, V., Baars, H., Marinou, E., Proestakis, E., Urbanneck, C., Althausen, D., Bühl, J., Mamouri, R.-E., and Pérez García-Pando, C.: Assimilating spaceborne lidar dust extinction can improve dust forecasts, Atmospheric Chemistry and Physics, 22, 535–560, https://doi.org/10.5194/acp-22-535-2022, publisher: Copernicus GmbH, 2022.

Escribano, J., Di Tomaso, E., Jorba, O., Gonçalves Ageitos, M., Klose, M., Basart, S., and Pérez García-Pando, C.: Constraining spatio-temporal variations in dust emission at global scale with ensemble data assimilation of satellite optical depth retrievals, in: EGU General Assembly Conference Abstracts, EGU General Assembly Conference Abstracts, pp. EGU–9569, https://doi.org/10.5194/egusphere-egu23-9569, 2023.

Essington, M. E., Nelson, J. B., and Holden, W. L.: Gibbsite and Goethite Solubility, Soil Science Society of America Journal, 69, 996–1008, https://doi.org/10.2136/SSSAJ2004.0287, 2005.

Fagerli, H., Tsyro, S., Simpson, D., Schulz, M., Gauss, M., Jonson, J. E., Benedictow, A., Wind, P., Ágnes Nyíri, Steensen, B. M., Valiyaveetil, S., Aas, W., Hjellbrekke, A.-G., Solberg, S., Stebel, K., Tørseth, K., Yttri, K. E., Mareckova, K., Wankmüller, R., Pinterits, M., Ullrich, B., Posch, M., van der Gon, H. D., Alastuey, A., and Theys, N.: Transboundary particulate matter, photo-oxidants, acidifying and eutrophying components. EMEP Status Report 2015., https://emep.int/publ/reports/2015/EMEP_Status_Report_1_2015.pdf, 2015.

Fairlie, T. D., Jacob, D. J., Dibb, J. E., Alexander, B., Avery, M. A., van Donkelaar, A., and Zhang, L.: Impact of mineral dust on nitrate, sulfate, and ozone in transpacific Asian pollution plumes, Atmospheric Chemistry and Physics, 10, 3999–4012, https://doi.org/10.5194/acp-10-3999-2010, 2010.

Faloona, I.: Sulfur processing in the marine atmospheric boundary layer: A review and critical assessment of modeling uncertainties, 43, 2841–2854, https://doi.org/10.1016/j.atmosenv.2009.02.043, 2009.

Fang, T., Guo, H., Zeng, L., Verma, V., Nenes, A., and Weber, R. J.: Highly Acidic Ambient Particles, Soluble Metals, and Oxidative Potential: A Link between Sulfate and Aerosol Toxicity, 51, 2611–2620, https://doi.org/10.1021/acs.est.6b06151, publisher: American Chemical Society, 2017.

Fécan, F., Marticorena, B., and Bergametti, G.: Parametrization of the increase of the aeolian erosion threshold wind friction velocity due to soil moisture for arid and semi-arid areas, Annales Geophysicae, 17, 149–157, https://doi.org/10.1007/s00585-999-0149-7, 1999.

Feliciano, M. S., Pio, C. A., and Vermeulen, A. T.: Evaluation of SO2 dry deposition over short vegetation in Portugal, 35, 3633–3643, https://doi.org/10.1016/S1352-2310(00)00539-2, 2001.

Feng, Y. and Penner, J. E.: Global modeling of nitrate and ammonium: Interaction of aerosols and tropospheric chemistry, Journal of Geophysical Research Atmospheres, 112, 1–24, https://doi.org/10.1029/2005JD006404, 2007.

Fenter, F. F., Caloz, F., and Rossi, M. J.: Experimental evidence for the efficient "dry deposition" of nitric acid on calcite, Atmospheric Environment, 29, 3365–3372, https://doi.org/10.1016/1352-2310(95)00183-Y, 1995.

Fernández-Martínez, M., Corbera, J., Domene, X., Sayol, F., Sabater, F., and Preece, C.: Nitrate pollution reduces bryophyte diversity in Mediterranean springs, 705, 135 823, https://doi.org/10.1016/j.scitotenv.2019.135823, 2020.

Ferrier, B. S., Jin, Y., Lin, Y., Black, T., Rogers, E., and Dimego, G.: Implementation of a new grid-scale cloud and precipitation scheme in the NCEP Eta model, in: 15th Conf. on Numerical Weather Prediction, pp. 280–283, American Meteorological Society, 2002.

Foley, K. M., Roselle, S. J., Appel, K. W., Bhave, P. V., Pleim, J. E., Otte, T. L., Mathur, R., Sarwar, G., Young, J. O., Gilliam, R. C., Nolte, C. G., Kelly, J. T., Gilliland, A. B., and Bash, J. O.: Incremental testing of the Community Multiscale Air Quality (CMAQ) modeling system version 4.7, Geoscientific Model Development, 3, 205–226, https://doi.org/10.5194/gmd-3-205-2010, 2010.

Formenti, P., Schütz, L., Balkanski, Y., Desboeufs, K., Ebert, M., Kandler, K., Petzold, A., Scheuvens, D., Weinbruch, S., and Zhang, D.: Recent progress in understanding physical and chemical properties of African and Asian mineral dust, 11, 8231–8256, https://doi.org/10.5194/acp-11-8231-2011, publisher: Copernicus GmbH, 2011.

Formenti, P., Caquineau, S., Desboeufs, K., Klaver, A., Chevaillier, S., Journet, E., and Rajot, J. L.: Mapping the physico-chemical properties of mineral dust in western Africa: mineralogical composition, 14, 10 663–10 686, https://doi.org/10.5194/acp-14-10663-2014, publisher: Copernicus GmbH, 2014.

Fountoukis, C. and Nenes, A.: ISORROPIAII: A computationally efficient thermodynamic equilibrium model for K+-Ca2+-Mg2+-NH4+-Na+-SO42–NO3–Cl–H2O aerosols, 7, 4639–4659, https://doi.org/10.5194/acp-7-4639-2007, 2007.

Friedlander, S. K.: Smoke, Dust, and Haze: Fundamentals of Aerosol Dynamics (Topics in Chemical Engineering), https://books.google.com/books/about/Smoke_Dust_and_Haze.html?id=uxDcwAEACAAJ, 2000.

Fuchs, N. A. and Sutugin, A. G. A. G.: Highly dispersed aerosols,, Ann Arbor Science Publishers, ISBN 0250399962, 1970.

Fussell, J. C. and Kelly, F. J.: Mechanisms underlying the health effects of desert sand dust, 157, 106 790, https://doi.org/10.1016/j.envint.2021.106790, 2021.

Gebel, M. E., Finlayson-Pitts, B. J., and Ganske, J. A.: The uptake of SO2 on synthetic sea salt and some of its components, 27, 887–890, https://doi.org/10.1029/1999GL011152, _eprint: https://onlinelibrary.wiley.com/doi/pdf/10.1029/1999GL011152, 2000.

Gillette, D. A. and Passi, R.: Modeling dust emission caused by wind erosion, Journal of Geophysical Research: Atmospheres, 93, 14 233–14 242, https://doi.org/https://doi.org/10.1029/JD093iD11p14233, 1988.

Ginoux, P., Chin, M., Tegen, I., Prospero, J. M., Holben, B., Dubovik, O., and Lin, S. J.: Sources and distributions of dust aerosols simulated with the GOCART model, Journal of Geophysical Research Atmospheres, 106, 20 255–20 273, https://doi.org/10.1029/2000JD000053, 2001.

Ginoux, P., Garbuzov, D., and Hsu, N. C.: Identification of anthropogenic and natural dust sources using Moderate Resolution Imaging Spectroradiometer (MODIS) Deep Blue level 2 data, Journal of Geophysical Research: Atmospheres, 115, https://doi.org/10.1029/2009JD012398, _eprint: https://agupubs.onlinelibrary.wiley.com/doi/pdf/10.1029/2009JD012398, 2010.

Ginoux, P., Prospero, J. M., Gill, T. E., Hsu, N. C., and Zhao, M.: Global-scale attribution of anthropogenic and natural dust sources and their emission rates based on MODIS Deep Blue aerosol products, 50, https://doi.org/10.1029/2012RG000388, _eprint: https://onlinelibrary.wiley.com/doi/pdf/10.1029/2012RG000388, 2012.

Gliß, J., Mortier, A., Schulz, M., Andrews, E., Balkanski, Y., Bauer, S. E., Benedictow, A. M. K., Bian, H., Checa-Garcia, R., Chin, M., Ginoux, P., Griesfeller, J. J., Heckel, A., Kipling, Z., Kirkevåg, A., Kokkola, H., Laj, P., Le Sager, P., Lund, M. T., Lund Myhre, C., Matsui, H., Myhre, G., Neubauer, D., Van Noije, T., North, P., Olivié, D. J. L., Rémy, S., Sogacheva, L., Takemura, T., Tsigaridis, K., and Tsyro, S. G.: AeroCom phase III multi-model evaluation of the aerosol life cycle and optical properties using ground- and space-based remote sensing as well as surface in situ observations, 21, 87–128, https://doi.org/10.5194/acp-21-87-2021, 2021.

Gomes, C. S. F. and Silva, E. A. F.: Health Benefits and Risks of Minerals: Bioavailability, Bio-Essentiality, Toxicity, and Pathologies, in: Minerals latu sensu and Human Health: Benefits, Toxicity and Pathologies, edited by Gomes, C. and Rautureau, M., pp. 81–179, Springer International Publishing, ISBN 978-3-030-65706-2, https://doi.org/10.1007/978-3-030-65706-2_4, 2021.

Gomes, L. and Gillette, D. A.: A comparison of characteristics of aerosol from dust storms in Central Asia with soil-derived dust from other regions, 27, 2539–2544, https://doi.org/10.1016/0960-1686(93)90027-V, 1993.

Gonçalves Ageitos, M., Obiso, V., Miller, R. L., Jorba, O., Klose, M., Dawson, M., Balkanski, Y., Perlwitz, J., Basart, S., Di Tomaso, E., Escribano, J., Macchia, F., Montané, G., Mahowald, N. M., Green, R. O., Thompson, D. R., and Pérez García-Pando, C.: Modeling dust mineralogical composition: sensitivity to soil mineralogy atlases and their expected climate impacts, Atmospheric Chemistry and Physics, 23, 8623–8657, https://doi.org/10.5194/acp-23-8623-2023, 2023.

González-Romero, A., González-Flórez, C., Panta, A., Yus-Díez, J., Córdoba, P., Alastuey, A., Moreno, N., Hernández-Chiriboga, M., Kandler, K., Klose, M., Clark, R. N., Ehlmann, B. L., Greenberger, R. N., Keebler, A. M., Brodrick, P., Green, R., Ginoux, P., Querol, X., and Pérez García-Pando, C.: Characterization of the particle size distribution, mineralogy, and Fe mode of occurrence of dust-emitting sediments from the Mojave Desert, California, USA, 24, 9155–9176, https://doi.org/10.5194/acp-24-9155-2024, 2024a.

González-Romero, A., González-Flórez, C., Panta, A., Yus-Díez, J., Córdoba, P., Alastuey, A., Moreno, N., Kandler, K., Klose, M., Clark, R. N., Ehlmann, B. L., Greenberger, R. N., Keebler, A. M., Brodrick, P., Green, R. O., Querol, X., and Pérez García-Pando, C.: Probing Iceland's dust-emitting sediments: particle size distribution, mineralogy, cohesion, Fe mode of occurrence, and reflectance spectra signatures, 24, 6883–6910, https://doi.org/10.5194/acp-24-6883-2024, publisher: Copernicus GmbH, 2024b.

Gonçalves Ageitos, M., Obiso, V., Miller, R. L., Jorba, O., Klose, M., Dawson, M., Balkanski, Y., Perlwitz, J., Basart, S., Di Tomaso, E., Escribano, J., Macchia, F., Montané, G., Mahowald, N., Green, R. O., Thompson, D. R., and Pérez García-Pando, C.: Modeling dust mineralogical composition: sensitivity to soil mineralogy atlases and their expected climate impacts, pp. 8623–8657, https://doi.org/10.5194/acp-23-8623-2023, 2023.

Goodman, A. L.: A laboratory study of the heterogeneous reaction of nitric acid on calcium carbonate particles, Journal of Geophysical Research Atmospheres, 105, 29 053–29 064, https://doi.org/10.1029/2000JD900396, 2000.

Goodman, A. L., Bernard, E. T., and Grassian, V. H.: Spectroscopic study of nitric acid and water adsorption on oxide particles: Enhanced nitric acid uptake kinetics in the presence of adsorbed water, Journal of Physical Chemistry A, 105, 6443–6457, https://doi.org/10.1021/jp003722l, 2001.

Goss, K.-U.: Adsorption of Organic Vapors on Polar Mineral Surfaces and on a Bulk Water Surface: Development of an Empirical Predictive Model, https://doi.org/10.1021/es00053a017, archive Location: world Publisher: American Chemical Society, 2002a.

Goss, K. U.: Effects of temperature and relative humidity on the sorption of organic vapors on clay minerals, https://doi.org/10.1021/es00047a019, archive Location: world Publisher: American Chemical Society, 2002b.

Goss, K.-U. and Eisenreich, S. J.: Adsorption of VOCs from the Gas Phase to Different Minerals and a Mineral Mixture, 30, 2135–2142, https://doi.org/10.1021/es950508f, publisher: American Chemical Society, 1996.

Goudie, A. S.: Desert dust and human health disorders, 63, 101–113, https://doi.org/10.1016/j.envint.2013.10.011, 2014.

Goudie, A. S. and Middleton, N. J.: Saharan dust storms: nature and consequences, 56, 179–204, https://doi.org/10.1016/S0012-8252(01)00067-8, 2001.

Grahame, T. J. and Schlesinger, R. B.: Evaluating the Health Risk from Secondary Sulfates in Eastern North American Regional Ambient Air Particulate Matter, 17, 15–27, https://doi.org/10.1080/08958370590885672, publisher: Taylor & Francis _eprint: https://doi.org/10.1080/08958370590885672, 2005.

Grange, S. K., Sintermann, J., and Hueglin, C.: Meteorologically normalised long-term trends of atmospheric ammonia (NH3) in Switzerland/Liechtenstein and the explanatory role of gas-aerosol partitioning, Science of The Total Environment, 900, 165 844, https://doi.org/10.1016/j.scitotenv.2023.165844, 2023.

Green, R. O. and Thompson, D. R.: An Earth Science Imaging Spectroscopy Mission: The Earth Surface Mineral Dust Source Investigation (EMIT), in: IGARSS 2020 - 2020 IEEE International Geoscience and Remote Sensing Symposium, pp. 6262–6265, https://doi.org/10.1109/IGARSS39084.2020.9323741, ISSN: 2153-7003, 2020.

Green, R. O., Mahowald, N. M., Clark, R. N., Ehlmann, B. L., Ginoux, P. A., Kalashnikova, O. V., Miller, R. L., Okin, G., Painter, T. H., Pérez García-Pando, C., Realmuto, V. J., Swayze, G. A., Thompson, D. R., Middleton, E., Guanter, L., Ben Dor, E., and Phillips, B. R.: NASA's Earth Surface Mineral Dust Source Investigation, in: AGU Fall Meeting Abstracts, vol. 2018, pp. A24D–01, 2018.

Grennfelt, P. and Hultberg, H.: Effects of nitrogen deposition on the acidification of terrestrial and aquatic ecosystems, 30, 945–963, https://doi.org/10.1007/BF00303359, 1986.

Griffin, D. W.: Atmospheric Movement of Microorganisms in Clouds of Desert Dust and Implications for Human Health, 20, 459–477, https://doi.org/10.1128/CMR.00039-06, 2007.

Guenther, A., Karl, T., Harley, P., Wiedinmyer, C., Palmer, P. I., and Geron, C.: Estimates of global terrestrial isoprene emissions using MEGAN (Model of Emissions of Gases and Aerosols from Nature), Atmospheric Chemistry and Physics, 6, 3181–3210, https://doi.org/10.5194/ACP-6-3181-2006, 2006.

Guerschman, J. P., Scarth, P. F., McVicar, T. R., Renzullo, L. J., Malthus, T. J., Stewart, J. B., Rickards, J. E., and Trevithick, R.: Assessing the effects of site heterogeneity and soil properties when unmixing photosynthetic vegetation, non-photosynthetic vegetation and bare soil fractions from Landsat and MODIS data, Remote Sensing of Environment, 161, 12–26, https://doi.org/https://doi.org/10.1016/j.rse.2015.01.021, 2015.

Guerzoni, S. and Chester, R., eds.: The Impact of Desert Dust Across the Mediterranean, vol. 11 of *Environmental Science and Technology Library*, Springer Netherlands, ISBN 978-90-481-4764-9 978-94-017-3354-0, https://doi.org/10.1007/978-94-017-3354-0, 1996.

Guevara, M., Tena, C., Porquet, M., Jorba, O., and García-Pando, C. P.: HERMESv3, a stand-alone multi-scale atmospheric emission modelling framework-Part 1: Global and regional module, Geoscientific Model Development, 12, 1885–1907, https://doi.org/10.5194/GMD-12-1885-2019, 2019.

Guevara, M., Tena, C., Porquet, M., Jorba, O., and Pérez García-Pando, C.: HERMESv3, a stand-alone multi-scale atmospheric emission modelling framework–Part 2: The bottom–up module, Geoscientific Model Development (GMD), 13, 873–903, 2020.

Guevara, M., Jorba, O., Tena, C., Denier van der Gon, H., Kuenen, J., Elguindi, N., Darras, S., Granier, C., and Pérez García-Pando, C.: Copernicus Atmosphere Monitoring Service TEMPOral profiles (CAMS-TEMPO): global and European emission temporal profile maps for atmospheric chemistry modelling, Earth System Science Data, 13, 367–404, https://doi.org/10.5194/essd-13-367-2021, 2021.

Guimbaud, C., Arens, F., Gutzwiller, L., Gäggeler, H. W., and Ammann, M.: Uptake of HNO3 to deliquescent sea-salt particles: A study using the short-lived radioactive isotope tracer 13N, Atmospheric Chemistry and Physics, 2, 249–257, https://doi.org/10.5194/acp-2-249-2002, 2002.

Guo, H., Sullivan, A. P., Campuzano-Jost, P., Schroder, J. C., Lopez-Hilfiker, F. D., Dibb, J. E., Jimenez, J. L., Thornton, J. A., Brown, S. S., Nenes, A., and Weber, R. J.: Fine particle pH and the partitioning of nitric acid during winter in the northeastern United States, 121, 10,355–10,376, https://doi.org/10.1002/2016JD025311, _eprint: https://agupubs.onlinelibrary.wiley.com/doi/pdf/10.1002/2016JD025311.

Guo, H., Liu, J., Froyd, K. D., Roberts, J. M., Veres, P. R., Hayes, P. L., Jimenez, J. L., Nenes, A., and Weber, R. J.: Fine particle pH and gas–particle phase partitioning of inorganic species in Pasadena, California, during the 2010 CalNex campaign, 17, 5703–5719, https://doi.org/10.5194/acp-17-5703-2017, publisher: Copernicus GmbH, 2017.

Guo, H., Otjes, R., Schlag, P., Kiendler-Scharr, A., Nenes, A., and Weber, R. J.: Effectiveness of ammonia reduction on control of fine particle nitrate, Atmospheric Chemistry and Physics, 18, 12 241–12 256, https://doi.org/10.5194/ACP-18-12241-2018, 2018.

Guo, H., Gao, Z., and Xing, S.: Water–Rock Interactions, chap. 7, pp. 111–127, John Wiley Sons, Ltd, ISBN 9781119867371, https://doi.org/https://doi.org/10.1002/9781119867371.ch7, 2023.

Guo, P., Yang, L., Kong, D., and Zhao, H.: Differential effects of ammonium and nitrate addition on soil microbial biomass, enzymatic activities, and organic carbon in a temperate forest in North China, 481, 595–606, https://doi.org/10.1007/s11104-022-05663-3, 2022.

Hamer, M., Graham, R. C., Amrhein, C., and Bozhilov, K. N.: Dissolution of Ripidolite (Mg, Fe-Chlorite) in Organic and Inorganic Acid Solutions, 67, 654–661, https://doi.org/10.2136/sssaj2003.6540, _eprint: https://onlinelibrary.wiley.com/doi/pdf/10.2136/sssaj2003.6540, 2003.

Hamilton, D. S., Baker, A. R., Iwamoto, Y., Gassó, S., Bergas-Masso, E., Deutch, S., Dinasquet, J., Kondo, Y., Llort, J., Myriokefalitakis, S., Perron, M. M. G., Wegmann, A., and Yoon, J.-E.: An aerosol odyssey: Navigating nutrient flux changes to marine ecosystems, 11, 00 037, https://doi.org/10.1525/elementa.2023.00037, 2023.

Hand, J. L., Schichtel, B. A., Malm, W. C., and Pitchford, M.: Widespread reductions in sulfate across the United States since the early 1990s, 1527, 495–498, https://doi.org/10.1063/1.4803313, 2013.

Hanisch, F. and Crowley, J. N.: The heterogeneous reactivity of gaseous nitric acid on authentic mineral dust samples, and on individual mineral and clay mineral components, Physical Chemistry Chemical Physics, 3, 2474–2482, https://doi.org/10.1039/b101700o, 2001.

Hanisch, F. and Crowley, J. N.: Heterogeneous reactivity of NO and HNO3 on mineral dust in the presence of ozone, Physical Chemistry Chemical Physics, 5, 883–887, https://doi.org/10.1039/b211503d, 2003.

Hans Wedepohl, K.: The composition of the continental crust, 59, 1217–1232, https://doi.org/10.1016/0016-7037(95)00038-2, 1995.

Hansen, J., Sato, M., Ruedy, R., Nazarenko, L., Lacis, A., Schmidt, G. A., Russell, G., Aleinov, I., Bauer, M., Bauer, S., Bell, N., Cairns, B., Canuto, V., Chandler, M., Cheng, Y., Del Genio, A., Faluvegi, G., Fleming, E., Friend, A., Hall, T., Jackman, C., Kelley, M., Kiang, N. Y., Koch, D., Lean, J., Lerner, J., Lo, K., Menon, S., Miller, R. L., Minnis, P., Novakov, T., Oinas, V., Perlwitz, J. P., Perlwitz, J., Rind, D., Romanou, A., Shindell, D., Stone, P., Sun, S., Tausnev, N., Thresher, D., Wielicki, B., Wong, T., Yao, M., and Zhang, S.: Efficacy of climate forcings, Journal of Geophysical Research, 110, D18 104, https://doi.org/10.1029/2005JD005776, 2005.

Harrison, A. D., Lever, K., Sanchez-Marroquin, A., Holden, M. A., Whale, T. F., Tarn, M. D., McQuaid, J. B., and Murray, B. J.: The ice-nucleating ability of quartz immersed in water and its atmospheric importance compared to K-feldspar, 19, 11 343–11 361, https://doi.org/10.5194/acp-19-11343-2019, publisher: Copernicus GmbH, 2019.

Hauglustaine, D. A., Balkanski, Y., and Schulz, M.: A global model simulation of present and future nitrate aerosols and their direct radiative forcing of climate, Atmospheric Chemistry and Physics, 14, 11 031–11 063, https://doi.org/10.5194/acp-14-11031-2014, 2014.

Heald, C. L., Collett, J. L. J., Lee, T., Benedict, K. B., Schwandner, F. M., Li, Y., Clarisse, L., Hurtmans, D. R., Van Damme, M., Clerbaux, C., Coheur, P.-F., Philip, S., Martin, R. V., and Pye, H. O. T.: Atmospheric ammonia and particulate inorganic nitrogen over the United States, 12, 10 295–10 312, https://doi.org/10.5194/acp-12-10295-2012, publisher: Copernicus GmbH, 2012.

Heald, C. L., Ridley, D. A., Kroll, J. H., Barrett, S. R. H., Cady-Pereira, K. E., Alvarado, M. J., and Holmes, C. D.: Contrasting the direct radiative effect and direct radiative forcing of aerosols, Atmospheric Chemistry and Physics, 14, 5513–5527, https://doi.org/10.5194/acp-14-5513-2014, 2014.

Herich, H., Tritscher, T., Wiacek, A., Gysel, M., Weingartner, E., Lohmann, U., Baltensperger, U., and Cziczo, D. J.: Water uptake of clay and desert dust aerosol particles at sub- and supersaturated water vapor conditions, Physical Chemistry Chemical Physics, 11, 7804–7809, https://doi.org/10.1039/b901585j, 2009.

Hersbach, H., Bell, B., Berrisford, P., Biavati, G., Horányi, A., Muñoz Sabater, J., Nicolas, J., Peubey, C., Radu, R., Rozum, I., Schepers, D., Simmons, A., Soci, C., Dee, D., and Thépaut, J.-N.: ERA5 hourly data on single levels from 1940 to present, https://doi.org/10.24381/cds.adbb2d47, [Online; accessed 11 March 2024], 2023.

Hess, M., Koepke, P., and Schult, I.: Optical properties of aerosols and clouds: The software package OPAC, Bulletin of the American meteorological society, 79, 831–844, 1998.

Highwood, E. J., Northway, M. J., McMeeking, G. R., Morgan, W. T., Liu, D., Osborne, S., Bower, K., Coe, H., Ryder, C., and Williams, P.: Aerosol scattering and absorption during the EUCAARI-LONGREX flights of the Facility for Airborne Atmospheric Measurements (FAAM) BAe-146: can measurements and models agree?, 12, 7251–7267, https://doi.org/10.5194/acp-12-7251-2012, publisher: Copernicus GmbH, 2012.

Hobbs, P. V.: Introduction to Atmospheric Chemistry, Cambridge University Press, ISBN 978-0-521-77800-8, https://doi.org/10.1017/CBO9780511808913, 2000.

Hodzic, A. and Jimenez, J. L.: Model Development Modeling anthropogenically controlled secondary organic aerosols in a megacity: a simplified framework for global and climate models, Geosci. Model Dev, 4, 901–917, https://doi.org/10.5194/gmd-4-901-2011, 2011.

Hodzic, A., Bessagnet, B., and Vautard, R.: A model evaluation of coarse-mode nitrate heterogeneous formation on dust particles, Atmospheric Environment, 40, 4158–4171, https://doi.org/10.1016/j.atmosenv.2006.02.015, 2006.

Holben, B. N., Eck, T., Slutsker, I., Smirnov, A., Sinyuk, A., Schafer, J., Giles, D., and Dubovik, O.: AERONET's Version 2.0 quality assurance criteria, in: Remote Sensing of the Atmosphere and Clouds, vol. 6408, pp. 134–147, SPIE, 2006.

Hoyle, C. R., Fuchs, C., Järvinen, E., Saathoff, H., Dias, A., El Haddad, I., Gysel, M., Coburn, S. C., Tröstl, J., Bernhammer, A.-K., Bianchi, F., Breitenlechner, M., Corbin, J. C., Craven, J., Donahue, N. M., Duplissy, J., Ehrhart, S., Frege, C., Gordon, H., Höppel, N., Heinritzi, M., Kristensen, T. B., Molteni, U., Nichman, L., Pinterich, T., Prévôt, A. S. H., Simon, M., Slowik, J. G., Steiner, G., Tomé, A., Vogel, A. L., Volkamer, R., Wagner, A. C., Wagner, R., Wexler, A. S., Williamson, C., Winkler, P. M., Yan, C., Amorim, A., Dommen, J., Curtius, J., Gallagher, M. W., Flagan, R. C., Hansel, A., Kirkby, J., Kulmala, M., Möhler, O., Stratmann, F., Worsnop, D. R., and Baltensperger, U.: Aqueous phase oxidation of sulphur dioxide by ozone in cloud droplets, 16, 1693–1712, https://doi.org/10.5194/acp-16-1693-2016, 2016.

Hsu, N. C., Tsay, S.-C., King, M. D., and Herman, J. R.: Aerosol properties over bright-reflecting source regions, IEEE Transactions on Geoscience and Remote Sensing, 42, 557–569, https://doi.org/10.1109/TGRS.2004.824067, 2004.

Hsu, N. C., Lee, J., Sayer, A. M., Kim, W., Bettenhausen, C., and Tsay, S.-C.: VIIRS Deep Blue Aerosol Products Over Land: Extending the EOS Long-Term Aerosol Data Records, Journal of Geophysical Research: Atmospheres, 124, 4026–4053, https://doi.org/10.1029/2018JD029688, 2019.

Huang, J., Lin, B., Minnis, P., Wang, T., Wang, X., Hu, Y., Yi, Y., and Ayers, J. K.: Satellite-based assessment of possible dust aerosols semi-direct effect on cloud water path over East Asia, 33, https://doi.org/10.1029/2006GL026561, _eprint: https://onlinelibrary.wiley.com/doi/pdf/10.1029/2006GL026561, 2006.

Huang, J., Zhang, X., Ni, Y., Kong, Y., Shi, J., and Qi, J.: Characteristics of the long-term variations in sulfate–nitrate–ammonium aerosols in a coastal city in Northern China—Interpretability analysis from a machine learning perspective, 353, 121 245, https://doi.org/10.1016/j.atmosenv.2025.121245, 2025.

Huang, J. P., Liu, J. J., Chen, B., and Nasiri, S. L.: Detection of anthropogenic dust using CALIPSO lidar measurements, Atmospheric Chemistry and Physics, 15, 11 653–11 665, https://doi.org/10.5194/acp-15-11653-2015, publisher: Copernicus GmbH, 2015.

Huebert, B. J., Bates, T., Russell, P. B., Shi, G., Kim, Y. J., Kawamura, K., Carmichael, G., and Nakajima, T.: An overview of ACE-Asia: Strategies for quantifying the relationships between Asian aerosols and their climatic impacts, 108, https://doi.org/10.1029/2003JD003550, _eprint: https://onlinelibrary.wiley.com/doi/pdf/10.1029/2003JD003550, 2003.

Huggett, J.: Clay Minerals, Reference Module in Earth Systems and Environmental Sciences, https://doi.org/10.1016/B978-0-12-409548-9.09519-1, 2015.

Hulett, G. A. and Allen, L. E.: The solubility of gypsum, Journal of the American Chemical Society, 24, 667–679, https://doi.org/10.1021/JA02021A007/ASSET/JA02021A007.FP.PNG_V03, 1902.

Huneeus, N., Schulz, M., Balkanski, Y., Griesfeller, J., Prospero, J., Kinne, S., Bauer, S., Boucher, O., Chin, M., Dentener, F., Diehl, T., Easter, R., Fillmore, D., Ghan, S., Ginoux, P., Grini, A., Horowitz, L., Koch, D., Krol, M. C., Landing, W., Liu, X., Mahowald, N., Miller, R., Morcrette, J.-J., Myhre, G., Penner, J., Perlwitz, J., Stier, P., Takemura, T., and Zender, C. S.: Global dust model intercomparison in AeroCom phase I, 11, 7781–7816, https://doi.org/10.5194/acp-11-7781-2011, 2011.

Iacono, M. J., Delamere, J. S., Mlawer, E. J., Shephard, M. W., Clough, S. A., and Collins, W. D.: Radiative forcing by long-lived greenhouse gases: Calculations with the AER radiative transfer models, Journal of Geophysical Research: Atmospheres, 113, 13 103, https://doi.org/10.1029/2008JD009944, 2008.

IPCC: Climate Change 2021: The Physical Science Basis. Contribution of Working Group I to the Sixth Assessment Report of the Intergovernmental Panel on Climate Change, 2021.

Israelevich, P., Ganor, E., Alpert, P., Kishcha, P., and Stupp, A.: Predominant transport paths of Saharan dust over the Mediterranean Sea to Europe, 117, https://doi.org/10.1029/2011JD016482, _eprint: https://onlinelibrary.wiley.com/doi/pdf/10.1029/2011JD016482, 2012.

Jacob, D. J.: Heterogeneous chemistry and tropospheric ozone, 2000.

Jacob, D. J., Crawford, J. H., Kleb, M. M., Connors, V. S., Bendura, R. J., Raper, J. L., Sachse, G. W., Gille, J. C., Emmons, L., and Heald, C. L.: Transport and Chemical Evolution over the Pacific (TRACE-P) aircraft mission: Design, execution, and first results, 108, https://doi.org/10.1029/2002JD003276, _eprint: https://onlinelibrary.wiley.com/doi/pdf/10.1029/2002JD003276, 2003.

Jaeglé, L., Quinn, P. K., Bates, T. S., Alexander, B., and Lin, J. T.: Global distribution of sea salt aerosols: New constraints from in situ and remote sensing observations, Atmospheric Chemistry and Physics, 11, 3137–3157, https://doi.org/10.5194/ACP-11-3137-2011, 2011.

Jaffe, D., Snow, J., and Cooper, O.: The 2001 Asian dust events: Transport and impact on surface aerosol concentrations in the U.S., 84, 501–507, https://doi.org/10.1029/2003EO460001, _eprint: https://onlinelibrary.wiley.com/doi/pdf/10.1029/2003EO460001, 2003.

Jaffe, D., Tamura, S., and Harris, J.: Seasonal cycle and composition of background fine particles along the west coast of the US, 39, 297–306, https://doi.org/10.1016/j.atmosenv.2004.09.016, 2005.

Jang, M., Czoschke, N. M., Lee, S., and Kamens, R. M.: Heterogeneous Atmospheric Aerosol Production by Acid-Catalyzed Particle-Phase Reactions, 298, 814–817, https://doi.org/10.1126/science.1075798, publisher: American Association for the Advancement of Science, 2002.

Janjic, Z.: Nonlinear Advection Schemes and Energy Cascade on Semi-Staggered Grids, AMS, https://doi.org/https://doi.org/10.1175/1520-0493(1984)112<1234:NASAEC>2.0.CO;2, 1984.

Janjic, Z. and Gall, R.: Scientific Documentation of the NCEP Nonhydrostatic Multiscale Model on the B grid (NMMB). Part 1 Dynamics, http://www.ucar.edu/library/collections/technotes/technotes.jsp, 2012.

Janjic, Z. I.: The Mellor-Yamada level 2.5 turbulence closure scheme in the NCEP Eta Model, World Meteorological Organization-Publications-WMO TD, pp. 4–14, 1996.

Janjić, Z. I.: Comments on "Development and Evaluation of a Convection Scheme for Use in Climate Models", Journal of the Atmospheric Sciences, 57, 3686 – 3686, https://doi.org/https://doi.org/10.1175/1520-0469(2000)057<3686:CODAEO>2.0.CO;2, 2000.

Janjić, Z. I.: Nonsingular Implementation of the Mellor-Yamada Level 2.5 Scheme in the NCEP Meso model, NCEP Office Note; 437, https://repository.library.noaa.gov/view/noaa/11409, 2001.

Jones, A. C., Hill, A., Remy, S., Abraham, N. L., Dalvi, M., Hardacre, C., Hewitt, A. J., Johnson, B., Mulcahy, J. P., and Turnock, S. T.: Exploring the sensitivity of atmospheric nitrate concentrations to nitric acid uptake rate using the Met Office ' s Unified Model, 21, 1–48, https://doi.org/10.5194/acp-21-15901-2021, 2021.

Jonson, J. E., Fagerli, H., Scheuschner, T., and Tsyro, S.: Modelling changes in secondary inorganic aerosol formation and nitrogen deposition in Europe from 2005 to 2030, 22, 1311–1331, https://doi.org/10.5194/acp-22-1311-2022, publisher: Copernicus GmbH, 2022.

Jorba, O., Dabdub, D., Blaszczak-Boxe, C., Pérez, C., Janjic, Z., Baldasano, J. M., Spada, M., Badia, A., and Gonçalves, M.: Potential significance of photoexcited NO2 on global air quality with the NMMB/BSC chemical transport model, Journal of Geophysical Research: Atmospheres, 117, 13 301, https://doi.org/10.1029/2012JD017730, 2012.

Jordan, C., Talbot, R., and Keim, B.: Water-soluble nitrogen at the New Hampshire sea coast: HNO3, aerosols, precipitation, and fog, 105, 26 403–26 432, https://doi.org/10.1029/2000JD900298, 2000.

Jordan, C. E., Dibb, J. E., Anderson, B. E., and Fuelberg, H. E.: Uptake of nitrate and sulfate on dust aerosols during TRACE-P, 108, https://doi.org/10.1029/2002JD003101, _eprint: https://onlinelibrary.wiley.com/doi/pdf/10.1029/2002JD003101, 2003.

Journet, E., Balkanski, Y., and Harrison, S. P.: A new data set of soil mineralogy for dust-cycle modeling, Atmospheric Chemistry and Physics, 14, 3801–3816, https://doi.org/10.5194/ACP-14-3801-2014, 2014.

Kaiser, J., Heil, A., Andreae, M., Benedetti, A., Chubarova, N., Jones, L., Morcrette, J.-J., Razinger, M., Schultz, M., Suttie, M., et al.: Biomass burning emissions estimated with a global fire assimilation system based on observed fire radiative power, Biogeosciences, 9, 527–554, 2012.

Kakavas, S. and Pandis, S. N.: Effects of urban dust emissions on fine and coarse PM levels and composition, Atmospheric Environment, p. 118006, https://doi.org/10.1016/j.atmosenv.2020.118006, 2020.

Kakavas, S., Patoulias, D., Zakoura, M., Nenes, A., and Pandis, S. N.: Size-resolved aerosol pH over Europe during summer, 21, 799–811, https://doi.org/10.5194/acp-21-799-2021, publisher: Copernicus GmbH, 2021.

Kanakidou, M., Seinfeld, J. H., Pandis, S. N., Barnes, I., Dentener, F. J., Facchini, M. C., Van Dingenen, R., Ervens, B., Nenes, A., Nielsen, C. J., Swietlicki, E., Putaud, J. P., Balkanski, Y., Fuzzi, S., Horth, J., Moortgat, G. K., Winterhalter, R., Myhre, C. E. L., Tsigaridis, K., Vignati, E., Stephanou, E. G., and Wilson, J.: Organic aerosol and global climate modelling: a review, Atmospheric Chemistry and Physics, 5, 1053–1123, https://doi.org/10.5194/acp-5-1053-2005, 2005.

Kanakidou, M., Myriokefalitakis, S., and Tsigaridis, K.: Aerosols in atmospheric chemistry and biogeochemical cycles of nutrients, 13, 063 004, https://doi.org/10.1088/1748-9326/aabcdb, publisher: IOP Publishing, 2018.

Kandler, K., Benker, N., Bundke, U., Cuevas, E., Ebert, M., Knippertz, P., Rodríguez, S., Schütz, L., and Weinbruch, S.: Chemical composition and complex refractive index of Saharan Mineral Dust at Izaña, Tenerife (Spain) derived by electron microscopy, 41, 8058–8074, https://doi.org/10.1016/j.atmosenv.2007.06.047, 2007.

Kandler, K., Schneiders, K., Heuser, J., Waza, A., Aryasree, S., Althausen, D., Hofer, J., Abdullaev, S. F., and Makhmudov, A. N.: Differences and Similarities of Central Asian, African, and Arctic Dust Composition from a Single Particle Perspective, 11, 269, https://doi.org/10.3390/atmos11030269, number: 3 Publisher: Multidisciplinary Digital Publishing Institute, 2020.

Karydis, V. A., Tsimpidi, A. P., Lei, W., Molina, L. T., and Pandis, S. N.: Formation of semivolatile inorganic aerosols in the Mexico City Metropolitan Area during the MILAGRO campaign, Atmospheric Chemistry and Physics, 11, 13 305–13 323, https://doi.org/10.5194/ACP-11-13305-2011, 2011.

Karydis, V. A., Tsimpidi, A. P., Pozzer, A., Astitha, M., and Lelieveld, J.: Effects of mineral dust on global atmospheric nitrate concentrations, 16, 1491–1509, https://doi.org/10.5194/acp-16-1491-2016, publisher: Copernicus GmbH, 2016.

Karydis, V. A., Tsimpidi, A. P., Pozzer, A., and Lelieveld, J.: How alkaline compounds control atmospheric aerosol particle acidity, 21, 14 983–15 001, https://doi.org/10.5194/acp-21-14983-2021, 2021.

Kellogg, C. A. and Griffin, D. W.: Aerobiology and the global transport of desert dust, 21, 638–644, https://doi.org/10.1016/j.tree.2006.07.004, 2006.

Kelly, F. J. and Fussell, J. C.: Health Effects of Airborne Particles in Relation to Composition, Size and Source, https://doi.org/10.1039/9781782626589-00344, 2016.

Kelly, J. T., Chuang, C. C., and Wexler, A. S.: Influence of dust composition on cloud droplet formation, Atmospheric Environment, 41, 2904–2916, https://doi.org/https://doi.org/10.1016/j.atmosenv.2006.12.008, 2007.

Kim, D., Chin, M., Schuster, G., Yu, H., Takemura, T., Tuccella, P., Ginoux, P., Liu, X., Shi, Y., Matsui, H., Tsigaridis, K., Bauer, S. E., Kok, J. F., and Schulz, M.: Where Dust Comes From: Global Assessment of Dust Source Attributions With AeroCom Models, Journal of Geophysical Research: Atmospheres, 129, e2024JD041 377, https://doi.org/10.1029/2024JD041377, _eprint: https://agupubs.onlinelibrary.wiley.com/doi/pdf/10.1029/2024JD041377, 2024.

Kim, J. S. and Park, K.: Atmospheric aging of Asian dust particles during long range transport, 46, 913–924, https://doi.org/10.1080/02786826.2012.680984, 2012.

Kim, S.-Y., Peel, J. L., Hannigan, M. P., Dutton, S. J., Sheppard, L., Clark, M. L., and Vedal, S.: The Temporal Lag Structure of Short-term Associations of Fine Particulate Matter Chemical Constituents and Cardiovascular and Respiratory Hospitalizations, 120, 1094–1099, https://doi.org/10.1289/ehp.1104721, publisher: Environmental Health Perspectives, 2012.

Klingmüller, K., Karydis, V. A., Bacer, S., Stenchikov, G. L., and Lelieveld, J.: Weaker cooling by aerosols due to dust–pollution interactions, 20, 15 285–15 295, https://doi.org/10.5194/acp-20-15285-2020, publisher: Copernicus GmbH, 2020.

Klose, M., Gill, T. E., Etyemezian, V., Nikolich, G., Ghodsi Zadeh, Z., Webb, N. P., and Van Pelt, R. S.: Dust emission from crusted surfaces: Insights from field measurements and modelling, 40, 1–14, https://doi.org/10.1016/j.aeolia.2019.05.001, 2019.

Klose, M., Jorba, O., Gonçalves Ageitos, M., Escribano, J., Dawson, M. L., Obiso, V., Di Tomaso, E., Basart, S., Montané Pinto, G., Macchia, F., et al.: Mineral dust cycle in the Multiscale Online Nonhydrostatic AtmospheRe CHemistry model (MONARCH) version 2.0, Geoscientific Model Development, 14, 6403–6444, 2021.

Kok, J. F., Parteli, E. J. R., Michaels, T. I., and Karam, D. B.: The physics of wind-blown sand and dust, 75, 106 901, https://doi.org/10.1088/0034-4885/75/10/106901, publisher: IOP Publishing, 2012.

Kok, J. F., Ridley, D. A., Zhou, Q., Miller, R. L., Zhao, C., Heald, C. L., Ward, D. S., Albani, S., and Haustein, K.: Smaller desert dust cooling effect estimated from analysis of dust size and abundance, Nature Geoscience 2017 10:4, 10, 274–278, https://doi.org/10.1038/ngeo2912, 2017.

Kok, J. F., Ward, D. S., Mahowald, N. M., and Evan, A. T.: Global and regional importance of the direct dust-climate feedback, 9, 241, https://doi.org/10.1038/s41467-017-02620-y, publisher: Nature Publishing Group, 2018.

Kok, J. F., Adebiyi, A. A., Albani, S., Balkanski, Y., Checa-Garcia, R., Chin, M., Colarco, P. R., Hamilton, D. S., Huang, Y., Ito, A., Klose, M., Li, L., Mahowald, N. M., Miller, R. L., Obiso, V., Pérez García-Pando, C., Rocha-Lima, A., and Wan, J. S.: Contribution of the world's main dust source regions to the global cycle of desert dust, 21, 8169–8193, https://doi.org/10.5194/acp-21-8169-2021, 2021.

Kok, J. F., Storelvmo, T., Karydis, V. A., Adebiyi, A. A., Mahowald, N. M., Evan, A. T., He, C., and Leung, D. M.: Mineral dust aerosol impacts on global climate and climate change, https://doi.org/10.1038/S43017-022-00379-5, publisher: Springer Nature, 2023.

Kolb, C. E., Cox, R. A., Abbatt, J. P. D., Ammann, M., Davis, E. J., Donaldson, D. J., Garrett, B. C., George, C., Griffiths, P. T., Hanson, D. R., Kulmala, M., McFiggans, G., Pöschl, U., Riipinen, I., Rossi, M. J., Rudich, Y., Wagner, P. E., Winkler, P. M., Worsnop, D. R., and O' Dowd, C. D.: An overview of current issues in the uptake of atmospheric trace gases by aerosols and clouds, 10, 10 561–10 605, https://doi.org/10.5194/acp-10-10561-2010, 2010.

Konduracka, E. and Rostoff, P.: Links between chronic exposure to outdoor air pollution and cardiovascular diseases: a review, 20, 2971–2988, https://doi.org/10.1007/s10311-022-01450-9, 2022.

Krueger, B. J., Grassian, V. H., Laskin, A., and Cowin, J. P.: The transformation of solid atmospheric particles into liquid droplets through heterogeneous chemistry: Laboratory insights into the processing of calcium containing mineral dust aerosol in the troposphere, 30, 1148–1148, https://doi.org/10.1029/2002GL016563, publisher: John Wiley & Sons, Ltd, 2003.

Krueger, B. J., Grassian, V. H., Cowin, J. P., and Laskin, A.: Heterogeneous chemistry of individual mineral dust particles from different dust source regions: The importance of particle mineralogy, 38, 6253–6261, https://doi.org/10.1016/j.atmosenv.2004.07.010, 2004.

Krupa, S. V.: Effects of atmospheric ammonia (NH3) on terrestrial vegetation: a review, 124, 179–221, https://doi.org/10.1016/S0269-7491(02)00434-7, 2003.

Kuang, C., McMurry, P. H., McCormick, A. V., and Eisele, F. L.: Dependence of nucleation rates on sulfuric acid vapor concentration in diverse atmospheric locations, 113, https://doi.org/10.1029/2007JD009253, _eprint: https://onlinelibrary.wiley.com/doi/pdf/10.1029/2007JD009253, 2008.

Kulmala, M., Laaksonen, A., and Pirjola, L.: Parameterizations for sulfuric acid/water nucleation rates, 103, 8301–8307, https://doi.org/10.1029/97JD03718, 1998.

Kwon, H.-J., Cho, S.-H., Chun, Y., Lagarde, F., and Pershagen, G.: Effects of the Asian Dust Events on Daily Mortality in Seoul, Korea, 90, 1–5, https://doi.org/10.1006/enrs.2002.4377, 2002.

Kyrö, E.-M., Väänänen, R., Kerminen, V.-M., Virkkula, A., Petäjä, T., Asmi, A., Dal Maso, M., Nieminen, T., Juhola, S., Shcherbinin, A., Riipinen, I., Lehtipalo, K., Keronen, P., Aalto, P. P., Hari, P., and Kulmala, M.: Trends in new particle formation in eastern Lapland, Finland: effect of decreasing sulfur emissions from Kola Peninsula, 14, 4383–4396, https://doi.org/10.5194/acp-14-4383-2014, publisher: Copernicus GmbH, 2014.

Lajtha, K. and Jones, J.: Trends in cation, nitrogen, sulfate and hydrogen ion concentrations in precipitation in the United States and Europe from 1978 to 2010: a new look at an old problem, 116, 303–334, https://doi.org/10.1007/s10533-013-9860-2, 2013.

Lamsal, L. N., Martin, R. V., van Donkelaar, A., Celarier, E. A., Bucsela, E. J., Boersma, K. F., Dirksen, R., Luo, C., and Wang, Y.: Indirect validation of tropospheric nitrogen dioxide retrieved from the OMI satellite instrument: Insight into the seasonal variation of nitrogen oxides at northern midlatitudes, 115, https://doi.org/10.1029/2009JD013351, _eprint: https://onlinelibrary.wiley.com/doi/pdf/10.1029/2009JD013351, 2010.

Lana, A., Bell, T. G., Simó, R., Vallina, S. M., Ballabrera-Poy, J., Kettle, A. J., Dachs, J., Bopp, L., Saltzman, E. S., Stefels, J., Johnson, J. E., and Liss, P. S.: An updated climatology of surface dimethlysulfide concentrations and emission fluxes in the global ocean, Global Biogeochemical Cycles, 25, https://doi.org/https://doi.org/10.1029/2010GB003850, 2011.

Lanzl, C. A., Baltrusaitis, J., and Cwiertny, D. M.: Dissolution of Hematite Nanoparticle Aggregates: Influence of Primary Particle Size, Dissolution Mechanism, and Solution pH, 28, 15 797–15 808, https://doi.org/10.1021/la3022497, publisher: American Chemical Society, 2012.

Leoni, B., Patelli, M., Soler, V., and Nava, V.: Ammonium Transformation in 14 Lakes along a Trophic Gradient, 10, 265, https://doi.org/10.3390/w10030265, number: 3 Publisher: Multidisciplinary Digital Publishing Institute, 2018.

Levin, Z. and Cotton, W. R., eds.: Aerosol Pollution Impact on Precipitation, Springer Netherlands, Dordrecht, ISBN 978-1-4020-8689-2 978-1-4020-8690-8, https://doi.org/10.1007/978-1-4020-8690-8, 2009.

Levin, Z., Teller, A., Ganor, E., and Yin, Y.: On the interactions of mineral dust, sea-salt particles, and clouds: A measurement and modeling study from the Mediterranean Israeli Dust Experiment campaign, Journal of Geophysical Research: Atmospheres, 110, https://doi.org/10.1029/2005JD005810, _eprint: https://agupubs.onlinelibrary.wiley.com/doi/pdf/10.1029/2005JD005810, 2005.

Li, C., McLinden, C., Fioletov, V., Krotkov, N., Carn, S., Joiner, J., Streets, D., He, H., Ren, X., Li, Z., and Dickerson, R. R.: India Is Overtaking China as the World's Largest Emitter of Anthropogenic Sulfur Dioxide, 7, 14 304, https://doi.org/10.1038/s41598-017-14639-8, publisher: Nature Publishing Group, 2017.

Li, H. J., Zhu, T., Zhao, D. F., Zhang, Z. F., and Chen, Z. M.: Kinetics and mechanisms of heterogeneous reaction of NO_2 on $CaCO_3$ surfaces under dry and wet conditions, 10, 463–474, https://doi.org/10.5194/acp-10-463-2010, publisher: Copernicus GmbH, 2010.

Li, J., Wang, Z., Zhuang, G., Luo, G., Sun, Y., and Wang, Q.: Mixing of Asian mineral dust with anthropogenic pollutants over East Asia: A model case study of a super-duststorm in March 2010, Atmospheric Chemistry and Physics, 12, 7591–7607, https://doi.org/10.5194/acp-12-7591-2012, 2012.

Li, J., Dong, H., Zeng, L., Zhang, Y., Shao, M., Wang, Z., Sun, Y., and Fu, P.: Exploring possible missing sinks of nitrate and its precursors in current air quality models-A case simulation in Pearl River delta of China using an observation-based box model, Scientific Online Letters on the Atmosphere, 11, 124–128, https://doi.org/10.2151/sola.2015-029, 2015.

Li, L., Chen, Z. M., Zhang, Y. H., Zhu, T., Li, J. L., and Ding, J.: Kinetics and mechanism of heterogeneous oxidation of sulfur dioxide by ozone on surface of calcium carbonate, 6, 2453–2464, https://doi.org/10.5194/acp-6-2453-2006, publisher: Copernicus GmbH, 2006.

Li, L., Mahowald, N. M., Gonçalves Ageitos, M., Obiso, V., Miller, R. L., Pérez García-Pando, C., Di Biagio, C., Formenti, P., Brodrick, P. G., Clark, R. N., Green, R. O., Kokaly, R., Swayze, G., and Thompson, D. R.: Improved constraints on hematite refractive index for estimating climatic effects of dust aerosols, Communications Earth & Environment, 5, 295, https://doi.org/10.1038/s43247-024-01441-4, 2024a.

Li, L., Mahowald, N. M., Obiso, V., Kok, J. F., Miller, R. L., Liu, X., Gonçalves Ageitos, M., Pérez García-Pando, C., Leung, D. M., Ke, Z., Brodrick, P. G., Clark, R. N., Formenti, P., Di Biagio, C., Ginoux, P., Okin, G. S., Zhou, B., Thompson, D. R., and Green, R. O.: Dust Direct Radiative Effect Including Large Particles and Component Minerals, Geophysical Research Letters, 52, e2025GL119 383, https://doi.org/10.1029/2025GL119383, _eprint: https://agupubs.onlinelibrary.wiley.com/doi/pdf/10.1029/2025GL119383, 2025.

Li, W. J. and Shao, L. Y.: Observation of nitrate coatings on atmospheric mineral dust particles, Atmospheric Chemistry and Physics, 9, 1863–1871, https://doi.org/10.5194/acp-9-1863-2009, 2009.

Li, X., Yu, Z., Yue, M., Liu, Y., Huang, K., Chi, X., Nie, W., Ding, A., Dong, X., and Wang, M.: Impact of mineral dust photocatalytic heterogeneous chemistry on the formation of the sulfate and nitrate: A modelling study over East Asia, 316, 120 166, https://doi.org/10.1016/j.atmosenv.2023.120166, 2024b.

Li, Y., Schichtel, B. A., Walker, J. T., Schwede, D. B., Chen, X., Lehmann, C. M., Puchalski, M. A., Gay, D. A., and Collett, J. L.: Increasing importance of deposition of reduced nitrogen in the United States, Proceedings of the National Academy of Sciences of the United States of America, 113, 5874–5879, https://doi.org/10.1073/pnas.1525736113, 2016.

Liao, H. and Seinfeld, J. H.: Global impacts of gas-phase chemistry-aerosol interactions on direct radiative forcing by anthropogenic aerosols and ozone, 110, https://doi.org/10.1029/2005JD005907, _eprint: https://onlinelibrary.wiley.com/doi/pdf/10.1029/2005JD005907, 2005.

Liao, H., Adams, P. J., Chung, S. H., Seinfeld, J. H., Mickley, L. J., and Jacob, D. J.: Interactions between tropospheric chemistry and aerosols in a unified general circulation model, Journal of Geophysical Research: Atmospheres, 108, https://doi.org/10.1029/2001jd001260, 2003.

Liao, H., Seinfeld, J. H., Adams, P. J., and Mickley, L. J.: Global radiative forcing of coupled tropospheric ozone and aerosols in a unified general circulation model, 109, https://doi.org/10.1029/2003JD004456, _eprint: https://onlinelibrary.wiley.com/doi/pdf/10.1029/2003JD004456, 2004.

Likus-Cieślik, J. and Pietrzykowski, M.: Sulfur Contamination and Environmental Effects: A Case Study of Current SO2 Industrial Emission by Biomonitoring and Regional Post-mining hot-spots, 15, 82–96, https://doi.org/10.2174/1874070702115010082, 2021.

Lin, H., Tao, J., Du, Y., Liu, T., Qian, Z., Tian, L., Di, Q., Rutherford, S., Guo, L., Zeng, W., Xiao, J., Li, X., He, Z., Xu, Y., and Ma, W.: Particle size and chemical constituents of ambient particulate pollution associated with cardiovascular mortality in Guangzhou, China, 208, 758–766, https://doi.org/10.1016/j.envpol.2015.10.056, 2016.

Lippmann, M.: Toxicological and epidemiological studies of cardiovascular effects of ambient air fine particulate matter (PM2.5) and its chemical components: Coherence and public health implications, 44, 299–347, https://doi.org/10.3109/10408444.2013.861796, publisher: Taylor & Francis _eprint: https://doi.org/10.3109/10408444.2013.861796, 2014.

Lippmann, M., Ito, K., Hwang, J.-S., Maciejczyk, P., and Chen, L.-C.: Cardiovascular Effects of Nickel in Ambient Air, 114, 1662–1669, https://doi.org/10.1289/ehp.9150, publisher: Environmental Health Perspectives, 2006.

Liu, J., Wang, X., Wu, D., Wei, H., Li, Y., and Ji, M.: Historical footprints and future projections of global dust burden from bias-corrected CMIP6 models, 7, 1–12, https://doi.org/10.1038/s41612-023-00550-9, publisher: Nature Publishing Group, 2024.

Liu, L., Breitner, S., Schneider, A., Cyrys, J., Brüske, I., Franck, U., Schlink, U., Marian Leitte, A., Herbarth, O., Wiedensohler, A., Wehner, B., Pan, X., Wichmann, H.-E., and Peters, A.: Size-fractioned particulate air pollution and cardiovascular emergency room visits in Beijing, China, 121, 52–63, https://doi.org/10.1016/j.envres.2012.10.009, 2013.

Liu, L., Li, H., Zhang, H., Zhong, J., Bai, Y., Ge, M., Li, Z., Chen, Y., and Zhang, X.: The role of nitric acid in atmospheric new particle formation, Physical Chemistry Chemical Physics, 20, 17 406–17 414, https://doi.org/10.1039/C8CP02719F, publisher: The Royal Society of Chemistry, 2018.

Liu, L., Xu, W., Lu, X., Zhong, B., Guo, Y., Lu, X., Zhao, Y., He, W., Wang, S., Zhang, X., Liu, X., and Vitousek, P.: Exploring global changes in agricultural ammonia emissions and their contribution to nitrogen deposition since 1980, 119, e2121998 119, https://doi.org/10.1073/pnas.2121998119, publisher: Proceedings of the National Academy of Sciences, 2022a.

Liu, Q., Huang, Z., Hu, Z., Dong, Q., and Li, S.: Long-Range Transport and Evolution of Saharan Dust Over East Asia From 2007 to 2020, Journal of Geophysical Research: Atmospheres, 127, e2022JD036 974, https://doi.org/10.1029/2022JD036974, _eprint: https://onlinelibrary.wiley.com/doi/pdf/10.1029/2022JD036974, 2022b.

Liu, T. and Abbatt, J. P. D.: Oxidation of sulfur dioxide by nitrogen dioxide accelerated at the interface of deliquesced aerosol particles, Nature Chemistry 2021, pp. 1–5, https://doi.org/10.1038/s41557-021-00777-0, 2021.

Liu, Y., P., C. J., Wang, H., and Laskin, A.: Kinetic Study of Heterogeneous Reaction of Deliquesced NaCl Particles with Gaseous HNO 3, J. Phys. Chem. A, 111, 10 026–10 043, 2007.

Liu, Y., Gibson, E. R., Cain, J. P., Wang, H., Grassian, V. H., and Laskin, A.: Kinetics of heterogeneous reaction of CaCO3 particles with gaseous HNO3 over a wide range of humidity, Journal of Physical Chemistry A, 112, 1561–1571, https://doi.org/10.1021/jp076169h, 2008.

Liu, Y., Feng, Z., Zheng, F., Bao, X., Liu, P., Ge, Y., Zhao, Y., Jiang, T., Liao, Y., Zhang, Y., Fan, X., Yan, C., Chu, B., Wang, Y., Du, W., Cai, J., Bianchi, F., Petäjä, T., Mu, Y., He, H., and Kulmala, M.: Ammonium nitrate promotes sulfate formation through uptake kinetic regime, Atmospheric Chemistry and Physics, 21, 13 269–13 286, https://doi.org/10.5194/acp-21-13269-2021, 2021.

Liu, Y., Zhan, J., Zheng, F., Song, B., Zhang, Y., Ma, W., Hua, C., Xie, J., Bao, X., Yan, C., Bianchi, F., Petäjä, T., Ding, A., Song, Y., He, H., and Kulmala, M.: Dust emission reduction enhanced gas-to-particle conversion of ammonia in the North China Plain, Nature Communications, 13, https://doi.org/10.1038/s41467-022-34733-4, 2022c.

Lu, D., Li, H., Tian, M., Wang, G., Qin, X., Zhao, N., Huo, J., Yang, F., Lin, Y., Chen, J., Fu, Q., Duan, Y., Dong, X., Deng, C., Abdullaev, S. F., and Huang, K.: Secondary aerosol formation during a special dust transport event: impacts from unusually enhanced ozone and dust backflows over the ocean, Atmospheric Chemistry and Physics, 23, 13 853–13 868, https://doi.org/10.5194/acp-23-13853-2023, 2023.

Lu, F., Xu, D., Cheng, Y., Dong, S., Guo, C., Jiang, X., and Zheng, X.: Systematic review and meta-analysis of the adverse health effects of ambient PM2.5 and PM10 pollution in the Chinese population, 136, 196–204, https://doi.org/10.1016/j.envres.2014.06.029, 2015.

Luo, G., Yu, F., and Schwab, J.: Revised treatment of wet scavenging processes dramatically improves GEOS-Chem 12.0.0 simulations of surface nitric acid, nitrate, and ammonium over the United States, Geoscientific Model Development, 12, 3439–3447, https://doi.org/10.5194/gmd-12-3439-2019, 2019.

Lurmann, F. W., Wexler, A. S., Pandis, S. N., Musarra, S., Kumar, N., and Seinfeld, J. H.: Modelling urban and regional aerosols—II. Application to California's South Coast Air Basin, Atmospheric Environment, 31, 2695–2715, https://doi.org/10.1016/S1352-2310(97)00100-3, 1997.

Lv, Z., Ye, X., Huang, W., Yao, Y., Duan, Y., Lv, Z., Ye, X., Huang, W., Yao, Y., and Duan, Y.: Elucidating Decade-Long Trends and Diurnal Patterns in Aerosol Acidity in Shanghai, 15, https://doi.org/10.3390/atmos15081004, 2024.

Ma, Q., Zhong, C., Ma, J., Ye, C., Zhao, Y., Liu, Y., Zhang, P., Chen, T., Liu, C., Chu, B., and He, H.: Comprehensive Study about the Photolysis of Nitrates on Mineral Oxides, Environmental Science and Technology, 55, 8604–8612, https://doi.org/10.1021/ACS.EST.1C02182/SUPPL_FILE/ES1C02182_SI_001.PDF, 2021.

Maas, R. and Grennfelt, P.: Towards Cleaner Air. Scientific Assessment Report, 2016.

Mahowald, N., Albani, S., Kok, J. F., Engelstaeder, S., Scanza, R., Ward, D. S., and Flanner, M. G.: The size distribution of desert dust aerosols and its impact on the Earth system, 15, 53–71, https://doi.org/10.1016/j.aeolia.2013.09.002, publisher: Elsevier B.V., 2014.

Mahowald, N. M.: Anthropocene changes in desert area: Sensitivity to climate model predictions, 34, https://doi.org/10.1029/2007GL030472, _eprint: https://onlinelibrary.wiley.com/doi/pdf/10.1029/2007GL030472, 2007.

Mahowald, N. M. and Luo, C.: A less dusty future?, 30, https://doi.org/10.1029/2003GL017880, _eprint: https://onlinelibrary.wiley.com/doi/pdf/10.1029/2003GL017880, 2003.

Mahowald, N. M., Baker, A. R., Bergametti, G., Brooks, N., Duce, R. A., Jickells, T. D., Kubilay, N., Prospero, J. M., and Tegen, I.: Atmospheric global dust cycle and iron inputs to the ocean, 19, https://doi.org/10.1029/2004GB002402, _eprint: https://onlinelibrary.wiley.com/doi/pdf/10.1029/2004GB002402, 2005.

Mahowald, N. M., Kloster, S., Engelstaedter, S., Moore, J. K., Mukhopadhyay, S., McConnell, J. R., Albani, S., Doney, S. C., Bhattacharya, A., Curran, M. A. J., Flanner, M. G., Hoffman, F. M., Lawrence, D. M., Lindsay, K., Mayewski, P. A., Neff, J., Rothenberg, D., Thomas, E., Thornton, P. E., and Zender, C. S.: Observed 20th century desert dust variability: impact on climate and biogeochemistry, 10, 10 875–10 893, https://doi.org/10.5194/acp-10-10875-2010, 2010.

Mallone, S., Stafoggia, M., Faustini, A., Gobbi, G. P., Marconi, A., and Forastiere, F.: Saharan Dust and Associations between Particulate Matter and Daily Mortality in Rome, Italy, 119, 1409–1414, https://doi.org/10.1289/ehp.1003026, publisher: Environmental Health Perspectives, 2011.

Manisalidis, I., Stavropoulou, E., Stavropoulos, A., and Bezirtzoglou, E.: Environmental and Health Impacts of Air Pollution: A Review, 8, https://doi.org/10.3389/fpubh.2020.00014, publisher: Frontiers, 2020.

Manktelow, P. T., Mann, G. W., Carslaw, K. S., Spracklen, D. V., and Chipperfield, M. P.: Regional and global trends in sulfate aerosol since the 1980s, 34, https://doi.org/10.1029/2006GL028668, _eprint: https://onlinelibrary.wiley.com/doi/pdf/10.1029/2006GL028668, 2007.

Manubens-Gil, D., Vegas-Regidor, J., Matthews, D., and Shin, M.: Assesment report on autosubmit, cylc and ecflow, Technical report, 2016.

Markel, V. A.: Introduction to the Maxwell Garnett approximation: tutorial, Journal of the Optical Society of America A, 33, 1244, https://doi.org/10.1364/JOSAA.33.001244, 2016.

Marschner, P., ed.: Mineral Nutrition of Higher Plants, Academic Press, ISBN 978-0-12-384905-2, https://doi.org/10.1016/B978-0-12-384905-2.00030-3, 2012.

Marticorena, B. and Bergametti, G.: Modeling the atmospheric dust cycle: 1. Design of a soil-derived dust emission scheme, Journal of Geophysical Research: Atmospheres, 100, 16 415–16 430, https://doi.org/https://doi.org/10.1029/95JD00690, 1995.

Martin, L. R. and Good, T. W.: Catalyzed oxidation of sulfur dioxide in solution: The iron-manganese synergism, 25, 2395–2399, https://doi.org/10.1016/0960-1686(91)90113-L, 1991.

Martín, A., Corbera, J., Cano, O., Preece, C., Peñuelas, J., Sabater, F., and Fernández-Martínez, M.: The influence of nitrate pollution on elemental and isotopic composition of aquatic and semi-aquatic bryophytes, 190, 103 710, https://doi.org/10.1016/j.aquabot.2023.103710, 2024.

Mashburn, C. D., Frinak, E. K., and Tolbert, M. A.: Heterogeneous uptake of nitric acid on Na-montmorillonite clay as a function of relative humidity, Journal of Geophysical Research Atmospheres, 111, https://doi.org/10.1029/2005JD006525, 2006.

Masselot, P., Sera, F., Schneider, R., Kan, H., Lavigne, , Stafoggia, M., Tobias, A., Chen, H., Burnett, R. T., Schwartz, J., Zanobetti, A., Bell, M. L., Chen, B.-Y., Guo, Y.-L. L., Ragettli, M. S., Vicedo-Cabrera, A. M., Åström, C., Forsberg, B., Íñiguez, C., Garland, R. M., Scovronick, N., Madureira, J., Nunes, B., De La Cruz Valencia, C., Hurtado Diaz, M., Honda, Y., Hashizume, M., Ng, C. F. C.,

Samoli, E., Katsouyanni, K., Schneider, A., Breitner, S., Ryti, N. R., Jaakkola, J. J., Maasikmets, M., Orru, H., Guo, Y., Valdés Ortega, N., Matus Correa, P., Tong, S., and Gasparrini, A.: Differential Mortality Risks Associated With PM2.5 Components: A Multi-Country, Multi-City Study, Epidemiology, 33, 167–175, https://doi.org/10.1097/EDE.0000000000001455, 2022.

Matsumoto, K., Masuda, N., and Nakano, T.: Partitioning of atmospheric fixed nitrogen species among gas phase, fine particles, and coarse particles, 54, 49–58, https://doi.org/10.1016/j.jaerosci.2012.06.009, 2012.

McTainsh, G. H., Nickling, W. G., and Lynch, A. W.: Dust deposition and particle size in Mali, West Africa, 29, 307–322, https://doi.org/10.1016/S0341-8162(96)00075-6, 1997.

Meier, J., Wehner, B., Massling, A., Birmili, W., Nowak, A., Gnauk, T., Brüggemann, E., Herrmann, H., Min, H., and Wiedensohler, A.: Hygroscopic growth of urban aerosol particles in Beijing (China) during wintertime: A comparison of three experimental methods, Atmospheric Chemistry and Physics, 9, 6865–6880, https://doi.org/10.5194/ACP-9-6865-2009, 2009.

Mellon, C.: ISORROPIA v2.1 REFERENCE MANUAL, 2009.

Meng, J., Huang, Y., Leung, D. M., Li, L., Adebiyi, A. A., Ryder, C. L., Mahowald, N. M., and Kok, J. F.: Improved Parameterization for the Size Distribution of Emitted Dust Aerosols Reduces Model Underestimation of Super Coarse Dust, 49, e2021GL097287, https://doi.org/10.1029/2021GL097287, 2022.

Meng, Z. and Seinfeld, J. H.: Time scales to achieve atmospheric gas-aerosol equilibrium for volatile species, Atmospheric Environment, 30, 2889–2900, https://doi.org/10.1016/1352-2310(95)00493-9, 1996.

Menz, F. C. and Seip, H. M.: Acid rain in Europe and the United States: an update, 7, 253–265, https://doi.org/10.1016/j.envsci.2004.05.005, 2004.

Meskhidze, N., Chameides, W. L., Nenes, A., and Chen, G.: Iron mobilization in mineral dust: Can anthropogenic SO2 emissions affect ocean productivity?, 30, https://doi.org/10.1029/2003GL018035, _eprint: https://onlinelibrary.wiley.com/doi/pdf/10.1029/2003GL018035, 2003.

Metzger, S., Dentener, F., Pandis, S., and Lelieveld, J.: Gas/aerosol partitioning: 1. A computationally efficient model, 107, 4312, https://doi.org/10.1029/2001JD001102, 2002.

Metzger, S., Mihalopoulos, N., and Lelieveld, J.: Importance of mineral cations and organics in gas-aerosol partitioning of reactive nitrogen compounds: Case study based on MINOS results, Atmospheric Chemistry and Physics, 6, 2549–2567, https://doi.org/10.5194/acp-6-2549-2006, 2006.

Metzger, S. M.: Gas/Aerosol partitioning: a simplified method for global modeling, https://ui.adsabs.harvard.edu/abs/2000PhDT.....328M, publication Title: Ph.D. Thesis ADS Bibcode: 2000PhDT.....328M, 2000.

Mexico, G. R., Nakajima, T., Ramanathan, V., Ramaswamy, V., Artaxo, P., Berntsen, T., Betts, R., Fahey, D., Haywood, J., Lean, J., Lowe, D., Myhre, G., Nganga, J., Prinn, R., Raga, G., Schulz, M., Van, R., Solomon, C., Qin, D., Manning, M., Chen, Z., Marquis, M., and Averyt, K.: The Physical Science Basis. Contribution of Working Group I, 2007.

Miller, R. L., Knippertz, P., Pérez García-Pando, C., Perlwitz, J. P., and Tegen, I.: Impact of dust radiative forcing upon climate, pp. 327–357, Springer, Dordrecht, the Netherlands, https://doi.org/10.1007/978-94-017-8978-3_13, 2014.

Milousis, A., Tsimpidi, A. P., Tost, H., Pandis, S. N., Nenes, A., Kiendler-Scharr, A., and Karydis, V. A.: Implementation of the ISORROPIA-lite aerosol thermodynamics model into the EMAC chemistry climate model (based on MESSy v2.55): implications for aerosol composition and acidity, Geoscientific Model Development, 17, 1111–1131, https://doi.org/10.5194/gmd-17-1111-2024, 2024.

Milousis, A., Klingmüller, K., Tsimpidi, A., Kok, J., Kanakidou, M., Nenes, A., and Karydis, V.: Impact of mineral dust on the global nitrate aerosol direct and indirect radiative effect, 25, 1333–1351, https://doi.org/10.5194/acp-25-1333-2025, 2025.

Mindat.org: Chlorite Group, https://www.Mindat.org/min-1016.html, [Online; accessed March 11, 2024], a.

Mindat.org: Feldspar Group, https://www.Mindat.org/min-1624.html, [Online; accessed March 11, 2024], b.

Monin, A. S. and Obukhov, A. M.: Basic laws of turbulent mixing in the surface layer of the atmosphere, in: Tr. Akad. Nauk SSSR Geophiz. Inst, vol. 24, pp. 163–187, 1954.

Moosmüller, H., Engelbrecht, J. P., Skiba, M., Frey, G., Chakrabarty, R. K., and Arnott, W. P.: Single scattering albedo of fine mineral dust aerosols controlled by iron concentration, 117, https://onlinelibrary.wiley.com/doi/abs/10.1029/2011JD016909, publisher: John Wiley & Sons, Ltd, 2012.

Morgan, W. T., Allan, J. D., Bower, K. N., Highwood, E. J., Liu, D., McMeeking, G. R., Northway, M. J., Williams, P. I., Krejci, R., and Coe, H.: Airborne measurements of the spatial distribution of aerosol chemical composition across Europe and evolution of the organic fraction, 10, 4065–4083, https://doi.org/10.5194/acp-10-4065-2010, publisher: Copernicus GmbH, 2010.

Muller, P.: Glossary of terms used in physical organic chemistry (IUPAC Recommendations 1994), Pure and Applied Chemistry, 66, 1077–1184, https://doi.org/10.1351/pac199466051077, publisher: De Gruyter, 1994.

Muraleedharan, M. G., Herz-Thyhsen, R., Dewey, J. C., Kaszuba, J. P., and van Duin, A. C. T.: Understanding the chemistry of cation leaching in illite/water interfacial system using reactive molecular dynamics simulations and hydrothermal experiments, 186, 564–574, https://doi.org/10.1016/j.actamat.2019.12.059, 2020.

Myhre, G., Stordal, F., Berglen, T., Sundet, J., and Isaksen, I.: Uncertainties in the radiative forcing due to sulfate aerosols, 61, 485–498, https://doi.org/10.1175/1520-0469(2004)061<0485:UITRFD>2.0.CO;2, 2004.

Myhre, G., Grini, A., and Metzger, S.: Modelling of nitrate and ammonium-containing aerosols in presence of sea salt, Atmospheric Chemistry and Physics, 6, 4809–4821, https://doi.org/10.5194/acp-6-4809-2006, 2006.

Myriokefalitakis, S., Bergas-Massó, E., Gonçalves-Ageitos, M., Pérez García-Pando, C., Van Noije, T., Le Sager, P., Ito, A., Athanasopoulou, E., Nenes, A., Kanakidou, M., Krol, M. C., and Gerasopoulos, E.: Multiphase processes in the EC-Earth model and their relevance to the atmospheric oxalate, sulfate, and iron cycles, Geoscientific Model Development, 15, 3079–3120, https://doi.org/10.5194/gmd-15-3079-2022, 2022.

Möhler, O., Field, P. R., Connolly, P., Benz, S., Saathoff, H., Schnaiter, M., Wagner, R., Cotton, R., Krämer, M., Mangold, A., and Heymsfield, A. J.: Efficiency of the deposition mode ice nucleation on mineral dust particles, www.atmos-chem-phys.net/6/3007/2006/, 2006.

National Center for Biotechnology Information: PubChem Compound Summary for CID 14833, Hematite, https://pubchem.ncbi.nlm.nih.gov/compound/Hematite, [Online; accessed January 24, 2024], 2024a.

National Center for Biotechnology Information: PubChem Compound Summary for CID 92027383, Muscovite, https://pubchem.ncbi.nlm.nih.gov/compound/Muscovite, [Online; accessed January 24, 2024], 2024b.

National Center for Biotechnology Information. PubChem Compound Database: PubChem Compound Summary for CID 24928, Calcium Sulfate Dihydrate, https://pubchem.ncbi.nlm.nih.gov/compound/Calcium-Sulfate-Dihydrate, [Online; accessed January 24, 2024], 2024a.

National Center for Biotechnology Information. PubChem Compound Database: PubChem Compound Summary for CID 91502, Goethite (Fe(OH)O), https://pubchem.ncbi.nlm.nih.gov/compound/Goethite-_Fe_OH_O, [Online; accessed January 24, 2024], 2024b.

Navarro-Barboza, H., Pandolfi, M., Guevara, M., Enciso, S., Tena, C., Via, M., Yus-Díez, J., Reche, C., Pérez, N., Alastuey, A., Querol, X., and Jorba, O.: Uncertainties in source allocation of carbonaceous aerosols in a Mediterranean region, 183, 108 252, https://doi.org/10.1016/j.envint.2023.108252, 2024.

Nenes, A., Pandis, S. N., and Pilinis, C.: ISORROPIA: A New Thermodynamic Equilibrium Model for Multiphase Multicomponent Inorganic Aerosols, Aquatic Geochemistry 1998 4:1, 4, 123–152, https://doi.org/10.1023/A:1009604003981, 1998.

Nenes, A., Krom, M. D., Mihalopoulos, N., Van Cappellen, P., Shi, Z., Bougiatioti, A., Zarmpas, P., and Herut, B.: Atmospheric acidification of mineral aerosols: a source of bioavailable phosphorus for the oceans, 11, 6265–6272, https://doi.org/10.5194/acp-11-6265-2011, publisher: Copernicus GmbH, 2011.

Nenes, A., Pandis, S. N., Weber, R. J., and Russell, A.: Aerosol pH and liquid water content determine when particulate matter is sensitive to ammonia and nitrate availability, Atmospheric Chemistry and Physics, 20, 3249–3258, https://doi.org/10.5194/acp-20-3249-2020, 2020.

Nickovic, S., Vukovic, A., Vujadinovic, M., Djurdjevic, V., and Pejanovic, G.: Technical Note: High-resolution mineralogical database of dust-productive soils for atmospheric dust modeling, 12, 845–855, https://doi.org/10.5194/acp-12-845-2012, publisher: Copernicus GmbH, 2012.

Nutting, P.: The solution and colloidal dispersion of minerals in water on JSTOR, Washington Academy of Sciences, 22, 261–267, https://www.jstor.org/stable/24522222, 1932.

Nutting, P. G.: The action of some aqueous solutions on clays of the montmorillonite group, United States department of interior, pp. 219–235, 1941.

Oakes, M., Ingall, E. D., Lai, B., Shafer, M. M., Hays, M. D., Liu, Z. G., Russell, A. G., and Weber, R. J.: Iron Solubility Related to Particle Sulfur Content in Source Emission and Ambient Fine Particles, 46, 6637–6644, https://doi.org/10.1021/es300701c, publisher: American Chemical Society, 2012.

Obiso, V., Gonçalves Ageitos, M., Pérez García-Pando, C., Perlwitz, J. P., Schuster, G. L., Bauer, S. E., Di Biagio, C., Formenti, P., Tsigaridis, K., and Miller, R. L.: Observationally constrained regional variations of shortwave absorption by iron oxides emphasize the cooling effect of dust, 24, 5337–5367, https://doi.org/10.5194/acp-24-5337-2024, 2024.

Okin, G. S., Ochoa, F., Brodrick, P. G., Thompson, D. R., Keebler, A., Ehlmann, B. L., Mahowald, N., and Miller, R.: EMIT L3 Algorithm: Aggregated: Mineral Mass Fractions Theoretical Basis, Tech. Rep. 3, NASA Jet Propulsion Laboratory, 2025.

Pai, S., Heald, C., Pierce, J., Farina, S., Marais, E., Jimenez, J., Campuzano-Jost, P., Nault, B., Middlebrook, A., Coe, H., Shilling, J., Bahreini, R., Dingle, J., and Vu, K.: An evaluation of global organic aerosol schemes using airborne observations, An evaluation of global organic aerosol schemes using airborne observations, pp. 1–39, https://doi.org/10.5194/acp-2019-331, 2019.

Pan, D., Mauzerall, D. L., Wang, R., Guo, X., Puchalski, M., Guo, Y., Song, S., Tong, D., Sullivan, A. P., Schichtel, B. A., Collett, J. L., and Zondlo, M. A.: Regime shift in secondary inorganic aerosol formation and nitrogen deposition in the rural United States, 17, 617–623, https://doi.org/10.1038/s41561-024-01455-9, publisher: Nature Publishing Group, 2024.

Pan, X. L., Yan, P., Tang, J., Ma, J. Z., Wang, Z. F., Gbaguidi, A., and Sun, Y. L.: Observational study of influence of aerosol hygroscopic growth on scattering coefficient over rural area near Beijing megacity, Atmospheric Chemistry and Physics, 9, 7519–7530, https://doi.org/10.5194/ACP-9-7519-2009, 2009.

Pandis, S. N., Wexler, A. S., and Seinfeld, J. H.: Secondary organic aerosol formation and transport — II. Predicting the ambient secondary organic aerosol size distribution, Atmospheric Environment. Part A. General Topics, 27, 2403–2416, https://doi.org/10.1016/0960-1686(93)90408-Q, 1993.

Panta, A., Kandler, K., Alastuey, A., González-Flórez, C., González-Romero, A., Klose, M., Querol, X., Reche, C., Yus-Díez, J., and Pérez García-Pando, C.: Insights into the single-particle composition, size, mixing state, and aspect ratio of freshly emitted mineral dust from field measurements in the Moroccan Sahara using electron microscopy, Atmospheric Chemistry and Physics, 23, 3861–3885, https://doi.org/10.5194/acp-23-3861-2023, 2023.

Park, J. W., Lim, Y. H., Kyung, S. Y., An, C. H., Lee, S. P., Jeong, S. H., and Ju, Y.-S.: Effects of ambient particulate matter on peak expiratory flow rates and respiratory symptoms of asthmatics during Asian dust periods in Korea, 10, 470–476, https://doi.org/10.1111/j.1440-1843.2005.00728.x, _eprint: https://onlinelibrary.wiley.com/doi/pdf/10.1111/j.1440-1843.2005.00728.x, 2005.

Park, M., Joo, H. S., Lee, K., Jang, M., Kim, S. D., Kim, I., Borlaza, L. J. S., Lim, H., Shin, H., Chung, K. H., Choi, Y.-H., Park, S. G., Bae, M.-S., Lee, J., Song, H., and Park, K.: Differential toxicities of fine particulate matters from various sources, 8, 17 007, https://doi.org/10.1038/s41598-018-35398-0, publisher: Nature Publishing Group, 2018.

Parker, A. and Rae, J. E., eds.: Environmental Interactions of Clays, Springer, ISBN 978-3-642-08208-5 978-3-662-03651-8, https://doi.org/10.1007/978-3-662-03651-8, 1998.

Pathak, R. K., Wu, W. S., and Wang, T.: Summertime $PM_{2.5}$ ionic species in four major cities of China: nitrate formation in an ammonia-deficient atmosphere, 9, 1711–1722, https://doi.org/10.5194/acp-9-1711-2009, publisher: Copernicus GmbH, 2009.

Paulot, F., Ginoux, P., Cooke, W. F., Donner, L. J., Fan, S., Lin, M.-Y., Mao, J., Naik, V., and Horowitz, L. W.: Sensitivity of nitrate aerosols to ammonia emissions and to nitrate chemistry: implications for present and future nitrate optical depth, Atmos. Chem. Phys, 16, 1459–1477, https://doi.org/10.5194/acp-16-1459-2016, 2016.

Paulot, F., Fan, S., and Horowitz, L. W.: Contrasting seasonal responses of sulfate aerosols to declining SO2 emissions in the Eastern U.S.: Implications for the efficacy of SO2 emission controls, 44, 455–464, https://doi.org/10.1002/2016GL070695, _eprint: https://onlinelibrary.wiley.com/doi/pdf/10.1002/2016GL070695, 2017.

Pearce, I. S. K., Woodin, S. J., and Van Der Wal, R.: Physiological and growth responses of the montane bryophyte Racomitrium lanuginosum to atmospheric nitrogen deposition, 160, 145–155, https://doi.org/10.1046/j.1469-8137.2003.00875.x, _eprint: https://onlinelibrary.wiley.com/doi/pdf/10.1046/j.1469-8137.2003.00875.x, 2003.

Pendergrass, A. G., Knutti, R., Lehner, F., Deser, C., and Sanderson, B. M.: Precipitation variability increases in a warmer climate, 7, 17 966, https://doi.org/10.1038/s41598-017-17966-y, publisher: Nature Publishing Group, 2017.

Penuelas, J., Fernández-Martínez, M., Vallicrosa, H., Maspons, J., Zuccarini, P., Carnicer, J., Sanders, T. G. M., Krüger, I., Obersteiner, M., Janssens, I. A., Ciais, P., and Sardans, J.: Increasing atmospheric CO2 concentrations correlate with declining nutritional status of European forests, 3, 1–11, https://doi.org/10.1038/s42003-020-0839-y, publisher: Nature Publishing Group, 2020.

Perez, L., Tobias, A., Querol, X., Künzli, N., Pey, J., Alastuey, A., Viana, M., Valero, N., González-Cabré, M., and Sunyer, J.: Coarse Particles From Saharan Dust and Daily Mortality, 19, 800, https://doi.org/10.1097/EDE.0b013e31818131cf, 2008.

Perlwitz, J. P., Pérez García-Pando, C., and Miller, R. L.: Predicting the mineral composition of dust aerosols – Part 1: Representing key processes, Atmospheric Chemistry and Physics, 15, 11 593–11 627, https://doi.org/10.5194/acp-15-11593-2015, 2015a.

Perlwitz, J. P., Pérez García-Pando, C., and Miller, R. L.: Predicting the mineral composition of dust aerosols – Part 2: Model evaluation and identification of key processes with observations, Atmospheric Chemistry and Physics, 15, 11 629–11 652, https://doi.org/10.5194/acp-15-11629-2015, publisher: Copernicus GmbH, 2015b.

Pey, J., Querol, X., Alastuey, A., Forastiere, F., and Stafoggia, M.: African dust outbreaks over the Mediterranean Basin during 2001–2011: PM 10 concentrations, phenomenology and trends, and its relation with synoptic and mesoscale meteorology, Atmospheric Chemistry and Physics, 13, 1395–1410, 2013.

Phadnis, M. J. and Carmichael, G. R.: Numerical Investigation of the Influence of Mineral Dust on the Tropospheric Chemistry of East Asia, 36, 285–323, https://doi.org/10.1023/A:1006391626069, 2000.

Pinder, R. W., Adams, P. J., and Pandis, S. N.: Ammonia Emission Controls as a Cost-Effective Strategy for Reducing Atmospheric Particulate Matter in the Eastern United States, Environmental Science & Technology, 41, 380–386, https://doi.org/10.1021/es060379a, publisher: American Chemical Society, 2007.

Popovicheva, O. B., Persiantseva, N. M., Kireeva, E. D., Khokhlova, T. D., and Shonija, N. K.: Quantification of the Hygroscopic Effect of Soot Aging in the Atmosphere: Laboratory Simulations, 115, 298–306, https://doi.org/10.1021/jp109238x, publisher: American Chemical Society, 2011.

Pratte, P. and Rossi, M. J.: Nitric acid uptake on NaCl and sea salt aerosol at relative humidities in the range 2 . 8 to 25 1–22, https://doi.org/10.13140/2.1.2053.4562, 2006.

Prince, A. P., Kleiber, P., Grassian, V. H., and Young, M. A.: Heterogeneous interactions of calcite aerosol with sulfur dioxide and sulfur dioxide–nitric acid mixtures, Physical Chemistry Chemical Physics, 9, 3432–3439, https://doi.org/10.1039/B703296J, 2007.

Pringle, K. J., Tost, H., Message, S., Steil, B., Giannadaki, D., Nenes, A., Fountoukis, C., Stier, P., Vignati, E., and Lelieveld, J.: Description and evaluation of GMXe: A new aerosol submodel for global simulations (v1), 3, 391–412, https://doi.org/10.5194/gmd-3-391-2010, 2010.

Prospero, J. M. and Mayol-Bracero, O. L.: Understanding the Transport and Impact of African Dust on the Caribbean Basin, 94, 1329–1337, https://doi.org/10.1175/BAMS-D-12-00142.1, publisher: American Meteorological Society Section: Bulletin of the American Meteorological Society, 2013.

Prospero, J. M., Ginoux, P., Torres, O., Nicholson, S. E., and Gill, T. E.: Environmental characterization of global sources of atmospheric soil dust identified with the nimbus 7 total ozone mapping spectrometer (TOMS) absorbing aerosol product, https://doi.org/10.1029/2000RG000095, 2002.

Pye, H. O. T., Nenes, A., Alexander, B., Ault, A. P., Barth, M. C., Clegg, S. L., Collett Jr., J. L., Fahey, K. M., Hennigan, C. J., Herrmann, H., Kanakidou, M., Kelly, J. T., Ku, I.-T., McNeill, V. F., Riemer, N., Schaefer, T., Shi, G., Tilgner, A., Walker, J. T., Wang, T., Weber, R., Xing, J., Zaveri, R. A., and Zuend, A.: The acidity of atmospheric particles and clouds, Atmospheric Chemistry and Physics, 20, 4809–4888, https://doi.org/10.5194/acp-20-4809-2020, publisher: Copernicus GmbH, 2020.

Pye, K.: Chapter Three - DUST ENTRAINMENT, TRANSPORT AND DEPOSITION, in: Aeolian Dust and Dust Deposits, edited by Pye, K., pp. 29–62, Academic Press, ISBN 978-0-12-568690-7, https://doi.org/10.1016/B978-0-12-568690-7.50007-7, 1987.

Pérez, C., Haustein, K., Janjic, Z., Jorba, O., Huneeus, N., Baldasano, J. M., Black, T., Basart, S., Nickovic, S., Miller, R. L., Perlwitz, J. P., Schulz, M., and Thomson, M.: Atmospheric dust modeling from meso to global scales with the online NMMB/BSC-Dust model ndash; Part 1: Model description, annual simulations and evaluation, Atmospheric Chemistry and Physics, 11, 13 001–13 027, https://doi.org/10.5194/acp-11-13001-2011, 2011.

Pöschl, U.: Atmospheric Aerosols: Composition, Transformation, Climate and Health Effects, 44, 7520–7540, https://doi.org/10.1002/anie.200501122, _eprint: https://onlinelibrary.wiley.com/doi/pdf/10.1002/anie.200501122, 2005.

Querol, X., Alastuey, A., Puicercus, J., Mantilla, E., Ruiz, C. R., Lopez-Soler, A., Plana, F., and Juan, R.: Seasonal evolution of suspended particles around a large coal-fired power station: Chemical characterization, 32, 719–731, https://doi.org/10.1016/S1352-2310(97)00340-3, 1998.

Querol, X., Tobías, A., Pérez, N., Karanasiou, A., Amato, F., Stafoggia, M., Pérez García-Pando, C., Ginoux, P., Forastiere, F., Gumy, S., Mudu, P., and Alastuey, A.: Monitoring the impact of desert dust outbreaks for air quality for health studies, 130, 104 867, https://doi.org/10.1016/j.envint.2019.05.061, 2019.

Rad, U. v., Hinz, K., Sarnthein, M., and Seibold, E.: Geology of the Northwest African Continental Margin, Springer Science & Business Media, ISBN 978-3-642-68409-8, google-Books-ID: wg5JCAAAQBAJ, 2012.

Raupach, M. R., Gillette, D. A., and Leys, J. F.: The effect of roughness elements on wind erosion threshold, Journal of Geophysical Research: Atmospheres, 98, 3023–3029, https://doi.org/https://doi.org/10.1029/92JD01922, 1993.

Rea, D. K.: The paleoclimatic record provided by eolian deposition in the deep sea: The geologic history of wind, Reviews of Geophysics, 32, 159–195, https://doi.org/10.1029/93RG03257, 1994.

Reche, C., Pérez, N., Alastuey, A., Cots, N., Pérez, E., and Querol, X.: 2011–2020 trends of urban and regional ammonia in and around Barcelona, NE Spain, Chemosphere, 304, 135 347, https://doi.org/10.1016/j.chemosphere.2022.135347, 2022.

Reiss, R., Anderson, E. L., Cross, C. E., Hidy, G., Hoel, D., McClellan, R., and Moolgavkar, S.: Evidence of health impacts of sulfate-and nitrate-containing particles in ambient air, 19, 419–449, https://doi.org/10.1080/08958370601174941, 2007.

Resch, F., Sunnu, A., and Afeti, G.: Saharan dust flux and deposition rate near the Gulf of Guinea, 60, 98, https://doi.org/10.1111/j.1600-0889.2007.00286.x, 2008.

Riemer, N., Vogel, H., Vogel, B., Schell, B., Ackermann, I., Kessler, C., and Hass, H.: Impact of the heterogeneous hydrolysis of N2O5 on chemistry and nitrate aerosol formation in the lower troposphere under photosmog conditions, Journal of Geophysical Research: Atmospheres, 108, https://doi.org/https://doi.org/10.1029/2002JD002436, 2003.

Riemer, N., Ault, A. P., West, M., Craig, R. L., and Curtis, J. H.: Aerosol Mixing State: Measurements, Modeling, and Impacts, Reviews of Geophysics, 57, 187–249, https://doi.org/10.1029/2018RG000615, 2019.

Riipinen, I., Talvinen, S., Chassaing, A., Georgakaki, P., Li, X., García-Pando, C. P., Bergman, T., Kommula, S. M., Proske, U., Gkouvousis, A., Tsimpidi, A. P., Chatziparaschos, M., Neuberger, A., Karydis, V. A., Calderón, S. M., Romakkaniemi, S., Partridge, D. G., Khadir, T., Dada, L., Noije, T. v., Decesari, S., Seland, , Zieger, P., Bender, F., Carslaw, K., Cermak, J., Costa-Surós, M., Ageitos, M. G., Gramlich, Y., Haugvaldstad, O. W., Holopainen, E., Hoose, C., Jorba, O., Kakavas, S., Kanakidou, M., Kokkola, H., Krejci, R., Kühn, T., Kulmala, M., Sager, P. L., Makkonen, R., Manavi, S. E. I., Mentel, T. F., Milousis, A., Myriokefalitakis, S., Nenes, A., Nieminen, T., Pandis, S. N., Patoulias, D., Petäjä, T., Quaas, J., Regayre, L., Scholz, S. M. C., Schulz, M., Skyllakou,

K., Sousse, R., Stier, P., Thomas, M. A., Villinger, J. T., Virtanen, A., Wyser, K., and Ekman, A. M. L.: Treatment of Key Aerosol and Cloud Processes in Earth System Models – Recommendations from the FORCeS Project, 78, https://doi.org/10.16993/tellusb.1883, 2026.

Rodrıguez, S., Querol, X., Alastuey, A., Kallos, G., and Kakaliagou, O.: Saharan dust contributions to PM10 and TSP levels in Southern and Eastern Spain, Atmospheric Environment, 35, 2433–2447, 2001.

Rodriguez-Caballero, E., Stanelle, T., Egerer, S., Cheng, Y., Su, H., Canton, Y., Belnap, J., Andreae, M. O., Tegen, I., Reick, C. H., Pöschl, U., and Weber, B.: Global cycling and climate effects of aeolian dust controlled by biological soil crusts, 15, 458–463, https://doi.org/10.1038/s41561-022-00942-1, publisher: Nature Publishing Group, 2022.

Rodríguez, S., Alastuey, A., Alonso-Pérez, S., Querol, X., Cuevas, E., Abreu-Afonso, J., Viana, M., Pérez, N., Pandolfi, M., and De La Rosa, J.: Transport of desert dust mixed with North African industrial pollutants in the subtropical Saharan Air Layer, Atmospheric Chemistry and Physics, 11, 6663–6685, https://doi.org/10.5194/acp-11-6663-2011, 2011.

Roy, C. J. and Milton, D. K.: Airborne Transmission of Communicable Infection — The Elusive Pathway, 350, 1710–1712, https://doi.org/10.1056/NEJMp048051, publisher: Massachusetts Medical Society _eprint: https://www.nejm.org/doi/pdf/10.1056/NEJMp048051, 2004.

Ryder, C. L.: Radiative Effects of Increased Water Vapor in the Upper Saharan Air Layer Associated With Enhanced Dustiness, Journal of Geophysical Research: Atmospheres, 126, e2021JD034 696, https://doi.org/https://doi.org/10.1029/2021JD034696, e2021JD034696 2021JD034696, 2021.

Rémy, S., Kipling, Z., Flemming, J., Boucher, O., Nabat, P., Michou, M., Bozzo, A., Ades, M., Huijnen, V., Benedetti, A., Engelen, R., Peuch, V.-H., and Morcrette, J.-J.: Description and evaluation of the tropospheric aerosol scheme in the European Centre for Medium-Range Weather Forecasts (ECMWF) Integrated Forecasting System (IFS-AER, cycle 45R1), 12, 4627–4659, https://doi.org/10.5194/gmd-12-4627-2019, 2019.

Rémy, S., Kipling, Z., Huijnen, V., Flemming, J., Nabat, P., Michou, M., Ades, M., Engelen, R., and Peuch, V.-H.: Description and evaluation of the tropospheric aerosol scheme in the Integrated Forecasting System (IFS-AER, cycle 47R1) of ECMWF, 15, 4881–4912, https://doi.org/10.5194/gmd-15-4881-2022, 2022.

Rémy, S., Metzger, S., Huijnen, V., Williams, J. E., and Flemming, J.: An improved representation of aerosol in the ECMWF IFS-COMPO 49R1 through the integration of EQSAM4Climv12 – a first attempt at simulating aerosol acidity, 17, 7539–7567, https://doi.org/10.5194/gmd-17-7539-2024, 2024.

Saleh, T. A.: Environmental Concerns and the Importance of Desulfurization, https://doi.org/10.4018/978-1-7998-2146-5.ch008, archive Location: environmental-concerns-and-the-importance-of-desulfurization ISBN: 9781799821465 Publisher: IGI Global Scientific Publishing, 2020.

Samset, B. H., Stjern, C. W., Andrews, E., Kahn, R. A., Myhre, G., Schulz, M., and Schuster, G. L.: Aerosol Absorption: Progress Towards Global and Regional Constraints, 4, 65–83, https://doi.org/10.1007/s40641-018-0091-4, 2018.

Sand, M., Samset, B. H., Myhre, G., Gliß, J., Bauer, S. E., Bian, H., Chin, M., Checa-Garcia, R., Ginoux, P., Kipling, Z., et al.: Aerosol absorption in global models from AeroCom phase III, Atmospheric Chemistry and Physics, 21, 15 929–15 947, 2021.

Sartori, D., Macchia, S., and Gaion, A.: Did you consider ammonium? A possible confounding factor in evaluating the toxicity of marine sediments, 199, 116 021, https://doi.org/10.1016/j.marpolbul.2023.116021, 2024.

Sase, H.: Effects of Acidic Substances on Ecosystems, in: Handbook of Air Quality and Climate Change, edited by Akimoto, H. and Tanimoto, H., pp. 1–30, Springer Nature, ISBN 978-981-15-2527-8, https://doi.org/10.1007/978-981-15-2527-8_26-1, 2020.

Saul, T. D., Tolocka, M. P., and Johnston, M. V.: Reactive uptake of nitric acid onto sodium chloride aerosols across a wide range of relative humidities, Journal of Physical Chemistry A, 110, 7614–7620, https://doi.org/10.1021/jp060639a, 2006.

Sayer, A. M., Hsu, N. C., Lee, J., Kim, W. V., and Dutcher, S. T.: Validation, Stability, and Consistency of MODIS Collection 6.1 and VIIRS Version 1 Deep Blue Aerosol Data Over Land, Journal of Geophysical Research: Atmospheres, 124, 4658–4688, https://doi.org/10.1029/2018JD029598, 2019.

Scanza, R. A., Mahowald, N., Ghan, S., Zender, C. S., Kok, J. F., Liu, X., Zhang, Y., and Albani, S.: Modeling dust as component minerals in the Community Atmosphere Model: development of framework and impact on radiative forcing, Atmospheric Chemistry and Physics, 15, 537–561, https://doi.org/10.5194/acp-15-537-2015, 2015.

Scheuvens, D., Schütz, L., Kandler, K., Ebert, M., and Weinbruch, S.: Bulk composition of northern African dust and its source sediments — A compilation, 116, 170–194, https://doi.org/10.1016/j.earscirev.2012.08.005, 2013.

Schlesinger, R. B. and Cassee, F.: Atmospheric Secondary Inorganic Particulate Matter: The Toxicological Perspective as a Basis for Health Effects Risk Assessment, https://doi.org/10.1080/08958370304503, publisher: Taylor & Francis, 2003.

Schmidt, G. A., Kelley, M., Nazarenko, L., Ruedy, R., Russell, G. L., Aleinov, I., Bauer, M., Bauer, S. E., Bhat, M. K., Bleck, R., Canuto, V., Chen, Y.-H., Cheng, Y., Clune, T. L., Del Genio, A., de Fainchtein, R., Faluvegi, G., Hansen, J. E., Healy, R. J., Kiang, N. Y., Koch, D., Lacis, A. A., LeGrande, A. N., Lerner, J., Lo, K. K., Matthews, E. E., Menon, S., Miller, R. L., Oinas, V., Oloso, A. O., Perlwitz, J. P., Puma, M. J., Putman, W. M., Rind, D., Romanou, A., Sato, M., Shindell, D. T., Sun, S., Syed, R. A., Tausnev, N., Tsigaridis, K., Unger, N., Voulgarakis, A., Yao, M.-S., and Zhang, J.: Configuration and assessment of the GISS ModelE2 contributions to the CMIP5 archive, Journal of Advances in Modeling Earth Systems, 6, 141–184, https://doi.org/10.1002/2013MS000265, _eprint: https://agupubs.onlinelibrary.wiley.com/doi/pdf/10.1002/2013MS000265, 2014.

Schulze, D. G.: CLAY MINERALS, Encyclopedia of Soils in the Environment, 4, 246–254, https://doi.org/10.1016/B0-12-348530-4/00189-2, 2005.

Schuster, G. L., Dubovik, O., Arola, A., Eck, T. F., and Holben, B. N.: Remote sensing of soot carbon – Part 2: Understanding the absorption Ångström exponent, Atmospheric Chemistry and Physics, 16, 1587–1602, https://doi.org/10.5194/acp-16-1587-2016, 2016.

Schwartz, S. E.: Mass-Transport Considerations Pertinent to Aqueous Phase Reactions of Gases in Liquid-Water Clouds, in: Chemistry of Multiphase Atmospheric Systems, edited by Jaeschke, W., pp. 415–471, Springer Berlin Heidelberg, ISBN 978-3-642-70627-1, 1986.

Seaton, A. and Cherrie, J. W.: Quartz exposures and severe silicosis: a role for the hilar nodes, 55, 383–386, https://www.ncbi.nlm.nih.gov/pmc/articles/PMC1757591/, 1998.

Seemann, S.-L., Daskalakis, N., Qu, K., and Vrekoussis, M.: Combining the Emission Preprocessor HERMES with the Chemical Transport Model TM5-MP, 15, 469, https://doi.org/10.3390/atmos15040469, number: 4 Publisher: Multidisciplinary Digital Publishing Institute, 2024.

Segelstein, D. J.: The complex refractive index of water, Ph.D. thesis, University of Missouri–Kansas City, 1981.

Seinfeld, J. and Pandis, S.: Atmospheric Chemistry and Physics: From Air Pollution to Climate Change. 2nd Edition,, John Wiley & Sons, https://www.scirp.org/(S(i43dyn45teexjx455qlt3d2q))/reference/ReferencesPapers.aspx?ReferenceID=1345321, 2006.

Seinfeld, J. H.: TROPOSPHERIC CHEMISTRY AND COMPOSITION | Aerosols/Particles, in: Encyclopedia of Atmospheric Sciences (Second Edition), edited by North, G. R., Pyle, J., and Zhang, F., pp. 182–187, Academic Press, ISBN 978-0-12-382225-3, https://doi.org/10.1016/B978-0-12-382225-3.00438-2, 2015.

Seinfeld, J. H. and Pandis, S. N.: Atmospheric Chemistry and Physics: From Air Pollution to Climate Change, Environment: Science and Policy for Sustainable Development, 40, 26–26, https://doi.org/10.1080/00139157.1999.10544295, 1998.

Seisel, S., Börensen, C., Vogt, R., and Zellner, R.: Kinetics and mechanism of the uptake of N2O5 on mineral dust at 298 K, Atmospheric Chemistry and Physics, 5, 3423–3432, https://doi.org/10.5194/acp-5-3423-2005, 2005.

Semeniuk, K. and Dastoor, A.: Current state of atmospheric aerosol thermodynamics and mass transfer modeling: A review, Atmosphere, 11, 1–71, https://doi.org/10.3390/atmos11020156, 2020.

Shao, Y.: A model for mineral dust emission, 106, 20 239–20 254, https://doi.org/10.1029/2001JD900171, _eprint: https://onlinelibrary.wiley.com/doi/pdf/10.1029/2001JD900171, 2001.

Shao, Y., ed.: Dust Transport and Deposition, pp. 247–301, Springer Netherlands, ISBN 978-1-4020-8895-7, https://doi.org/10.1007/978-1-4020-8895-7_8, 2008a.

Shao, Y., ed.: Dust Emission, pp. 211–245, Springer Netherlands, ISBN 978-1-4020-8895-7, https://doi.org/10.1007/978-1-4020-8895-7_7, 2008b.

Shao, Y., Raupach, M. R., and Findlater, P. A.: Effect of saltation bombardment on the entrainment of dust by wind, 98, 12 719–12 726, https://doi.org/10.1029/93JD00396, _eprint: https://onlinelibrary.wiley.com/doi/pdf/10.1029/93JD00396, 1993.

Shao, Y., Wyrwoll, K.-H., Chappell, A., Huang, J., Lin, Z., McTainsh, G. H., Mikami, M., Tanaka, T. Y., Wang, X., and Yoon, S.: Dust cycle: An emerging core theme in Earth system science, 2, 181–204, https://doi.org/10.1016/j.aeolia.2011.02.001, 2011.

Sheppard, L. J., Leith, I. D., Mizunuma, T., Neil Cape, J., Crossley, A., Leeson, S., Sutton, M. A., van Dijk, N., and Fowler, D.: Dry deposition of ammonia gas drives species change faster than wet deposition of ammonium ions: evidence from a long-term field manipulation, 17, 3589–3607, https://doi.org/10.1111/j.1365-2486.2011.02478.x, _eprint: https://onlinelibrary.wiley.com/doi/pdf/10.1111/j.1365-2486.2011.02478.x, 2011.

Shi, L., Zhang, J., Yao, F., Zhang, D., and Guo, H.: Drivers to dust emissions over dust belt from 1980 to 2018 and their variation in two global warming phases, 767, 144 860, https://doi.org/10.1016/j.scitotenv.2020.144860, 2021.

Siefert, R. L., Webb, S. M., and Hoffmann, M. R.: Determination of photochemically available iron in ambient aerosols, 101, 14 441–14 449, https://doi.org/10.1029/96JD00857, _eprint: https://onlinelibrary.wiley.com/doi/pdf/10.1029/96JD00857, 1996.

Silvern, R. F., Jacob, D. J., Kim, P. S., Marais, E. A., Turner, J. R., Campuzano-Jost, P., and Jimenez, J. L.: Inconsistency of ammonium–sulfate aerosol ratios with thermodynamic models in the eastern US: a possible role of organic aerosol, 17, 5107–5118, https://doi.org/10.5194/acp-17-5107-2017, publisher: Copernicus GmbH, 2017.

Simpson, D., Benedictow, A., Berge, H., Bergström, R., Emberson, L. D., Fagerli, H., Flechard, C. R., Hayman, G. D., Gauss, M., Jonson, J. E., Jenkin, M. E., Nyúri, A., Richter, C., Semeena, V. S., Tsyro, S., Tuovinen, J. P., Valdebenito, A., and Wind, P.: The EMEP MSC-W chemical transport model ndash; Technical description, Atmospheric Chemistry and Physics, 12, 7825–7865, https://doi.org/10.5194/ACP-12-7825-2012, 2012.

Sinyuk, A., Holben, B. N., Eck, T. F., Giles, D. M., Slutsker, I., Korkin, S., Schafer, J. S., Smirnov, A., Sorokin, M., and Lyapustin, A.: The AERONET Version 3 aerosol retrieval algorithm, associated uncertainties and comparisons to Version 2, Atmospheric Measurement Techniques, 13, 3375–3411, https://doi.org/10.5194/amt-13-3375-2020, publisher: Copernicus GmbH, 2020.

Sokolik, I. N. and Toon, O. B.: Incorporation of mineralogical composition into models of the radiative properties of mineral aerosol from UV to IR wavelengths, 104, 9423–9444, https://doi.org/10.1029/1998JD200048, _eprint: https://onlinelibrary.wiley.com/doi/pdf/10.1029/1998JD200048, 1999.

Sokolik, I. N., Winker, D. M., Bergametti, G., Gillette, D. A., Carmichael, G., Kaufman, Y. J., Gomes, L., Schuetz, L., and Penner, J. E.: Introduction to special section: Outstanding problems in quantifying the radiative impacts of mineral dust, Journal of Geophysical Research: Atmospheres, 106, 18 015–18 027, https://doi.org/10.1029/2000JD900498, 2001.

Son, J.-Y., Lee, J.-T., Kim, K.-H., Jung, K., and Bell, M. L.: Characterization of Fine Particulate Matter and Associations between Particulate Chemical Constituents and Mortality in Seoul, Korea, 120, 872–878, https://doi.org/10.1289/ehp.1104316, publisher: Environmental Health Perspectives, 2012.

Song, C. H. and Carmichael, G. R.: The aging process of naturally emitted aerosol (sea-salt and mineral aerosol) during long range transport, 33, 2203–2218, https://doi.org/10.1016/S1352-2310(98)00301-X, 1999.

Song, C. H. and Carmichael, G. R.: A three-dimensional modeling investigation of the evolution processes of dust and sea-salt particles in east Asia, 106, 18 131–18 154, https://doi.org/10.1029/2000JD900352, _eprint: https://onlinelibrary.wiley.com/doi/pdf/10.1029/2000JD900352, 2001.

Song, C. H., Kim, C. M., Lee, Y. J., Carmichael, G. R., Lee, B. K., and Lee, D. S.: An evaluation of reaction probabilities of sulfate and nitrate precursors onto East Asian dust particles, J. Geophys. Res, 112, 18 206, https://doi.org/10.1029/2006JD008092, 2007.

Song, S., Gao, M., Xu, W., Shao, J., Shi, G., Wang, S., Wang, Y., Sun, Y., and McElroy, M. B.: Fine-particle pH for Beijing winter haze as inferred from different thermodynamic equilibrium models, Atmospheric Chemistry and Physics, 18, 7423–7438, https://doi.org/10.5194/acp-18-7423-2018, 2018.

Soulie, A., Granier, C., Darras, S., Zilbermann, N., Doumbia, T., Guevara, M., Jalkanen, J. P., Keita, S., Liousse, C., Crippa, M., Guizzardi, D., Hoesly, R., and Smith, S. J.: Global anthropogenic emissions (CAMS-GLOB-ANT) for the Copernicus Atmosphere Monitoring Service simulations of air quality forecasts and reanalyses, Earth System Science Data, 16, 2261–2279, https://doi.org/10.5194/ESSD-16-2261-2024, 2024.

Soussé Villa, R., Jorba, O., Gonçalves Ageitos, M., Bowdalo, D., Guevara, M., and Pérez García-Pando, C.: A comprehensive global modeling assessment of nitrate heterogeneous formation on desert dust, Atmospheric Chemistry and Physics, 25, 4719–4753, https://doi.org/10.5194/acp-25-4719-2025, 2025.

Spada, M.: Development and evaluation of an atmospheric aerosol module implemented within the NMMB/BSC-CTM, Ph.D. thesis, Universitat Politècnica de Catalunya, http://hdl.handle.net/2117/95991, 2015.

Spada, M., Jorba, O., Pérez García-Pando, C., Janjic, Z., and Baldasano, J. M.: Modeling and evaluation of the global sea-salt aerosol distribution: sensitivity to size-resolved and sea-surface temperature dependent emission schemes, 13, 11 735–11 755, https://doi.org/10.5194/acp-13-11735-2013, 2013.

Squizzato, S., Masiol, M., Brunelli, A., Pistollato, S., Tarabotti, E., Rampazzo, G., et al.: Factors determining the formation of secondary inorganic aerosol: a case study in the Po Valley (Italy), Atmospheric chemistry and physics, 13, 1927, 2013.

Stanelle, T., Bey, I., Raddatz, T., Reick, C., and Tegen, I.: Anthropogenically induced changes in twentieth century mineral dust burden and the associated impact on radiative forcing, 119, 13,526–13,546, https://doi.org/10.1002/2014JD022062, _eprint: https://onlinelibrary.wiley.com/doi/pdf/10.1002/2014JD022062, 2014.

Stockdale, A., Krom, M. D., Mortimer, R. J. G., Benning, L. G., Carslaw, K. S., Herbert, R. J., Shi, Z., Myriokefalitakis, S., Kanakidou, M., and Nenes, A.: Understanding the nature of atmospheric acid processing of mineral dusts in supplying bioavailable phosphorus to the oceans, 113, 14 639–14 644, https://doi.org/10.1073/pnas.1608136113, publisher: Proceedings of the National Academy of Sciences, 2016.

Stokes, R. H. and Robinson, R. A.: Interactions in Aqueous Nonelectrolyte Solutions. I. Solute-Solvent Equilibria, The Journal of Physical Chemistry, 70, 2126–2131, https://doi.org/10.1021/j100879a010, publisher: American Chemical Society, 1966.

Sulprizio, M.: Chemistry instability introduced by ISORROPIA v2.2, http://wiki.seas.harvard.edu/geos-chem/index.php/ISORROPIA_II#Chemistry_instability_introduced_by_ISORROPIA_v2.2, 2022.

Suman, A., Zanini, N., Vulpio, A., and Pinelli, M.: Apparatus and methods for the calibration and correction of a polydispersed dust feeding system applied in multiphase flow experiments, Experimental Thermal and Fluid Science, 151, 111 074, https://doi.org/https://doi.org/10.1016/j.expthermflusci.2023.111074, 2024.

Sun, F., Cui, Y., Su, J., Zhang, Y., Shi, X., Zhang, J., Liu, H., Xiao, Q., Lu, X., Zeng, Z.-C., Griffis, T. J., and Hu, C.: Spatial-temporal variations of atmospheric NH_3 concentration and its dry deposition across China based on one decade of satellite and ground-based observations, https://doi.org/10.5194/egusphere-2025-3090, 2025.

Sutton, M. A. and Howard, C. M.: Satellite pinpoints ammonia sources globally, 564, 49–50, https://doi.org/10.1038/d41586-018-07584-7, bandiera_abtest: a Cg_type: News And Views Publisher: Nature Publishing Group Subject_term: Environmental sciences, Biogeochemistry, 2018.

Sutton, M. A., van Dijk, N., Levy, P. E., Jones, M. R., Leith, I. D., Sheppard, L. J., Leeson, S., Sim Tang, Y., Stephens, A., Braban, C. F., Dragosits, U., Howard, C. M., Vieno, M., Fowler, D., Corbett, P., Naikoo, M. I., Munzi, S., Ellis, C. J., Chatterjee, S., Steadman, C. E., Móring, A., and Wolseley, P. A.: Alkaline air: changing perspectives on nitrogen and air pollution in an ammonia-rich world, 378, 20190 315, https://doi.org/10.1098/rsta.2019.0315, publisher: Royal Society, 2020.

Swarbrick, V. J., Simpson, G. L., Glibert, P. M., and Leavitt, P. R.: Differential stimulation and suppression of phytoplankton growth by ammonium enrichment in eutrophic hardwater lakes over 16 years, 64, S130–S149, https://doi.org/10.1002/lno.11093, _eprint: https://onlinelibrary.wiley.com/doi/pdf/10.1002/lno.11093, 2019.

Tabazadeh, A., Jacobson, M. Z., Singh, H. B., Toon, O. B., Lin, J. S., Chatfield, R. B., Thakur, A. N., Talbot, R. W., and Dibb, J. E.: Nitric acid scavenging by mineral and biomass burning aerosols, 25, 4185–4188, https://doi.org/10.1029/1998GL900062, _eprint: https://onlinelibrary.wiley.com/doi/pdf/10.1029/1998GL900062, 1998.

Tanaka, T. Y., Kurosaki, Y., Chiba, M., Matsumura, T., Nagai, T., Yamazaki, A., Uchiyama, A., Tsunematsu, N., and Kai, K.: Possible transcontinental dust transport from North Africa and the Middle East to East Asia, 39, 3901–3909, https://doi.org/10.1016/j.atmosenv.2005.03.034, 2005.

Tang, M., Huang, X., Lu, K., Ge, M., Li, Y., Cheng, P., Zhu, T., Ding, A., Zhang, Y., Gligorovski, S., Song, W., Ding, X., Bi, X., and Wang, X.: Heterogeneous reactions of mineral dust aerosol: Implications for tropospheric oxidation capacity, Atmospheric Chemistry and Physics, 17, 11 727–11 777, https://doi.org/10.5194/acp-17-11727-2017, 2017.

Textor, C., Schulz, M., Guibert, S., Kinne, S., Balkanski, Y., Bauer, S., Berntsen, T., Berglen, T., Boucher, O., Chin, M., Dentener, F., Diehl, T., Easter, R., Feichter, H., Fillmore, D., Ghan, S., Ginoux, P., Gong, S., Grini, A., Hendricks, J., Horowitz, L., Huang, P., Isaksen, I., Iversen, T., Kloster, S., Koch, D., Kirkevåg, A., Kristjansson, J. E., Krol, M., Lauer, A., Lamarque, J. F., Liu, X., Montanaro, V., Myhre, G., Penner, J., Pitari, G., Reddy, S., Seland, , Stier, P., Takemura, T., and Tie, X.: Analysis and quantification of the diversities of aerosol life cycles within AeroCom, Atmos. Chem. Phys, 6, 1777–1813, www.atmos-chem-phys.net/6/1777/2006/, 2006.

Thompson, D. R., Green, R. O., Bradley, C., Brodrick, P. G., Mahowald, N., Dor, E. B., Bennett, M., Bernas, M., Carmon, N., Chadwick, K. D., Clark, R. N., Coleman, R. W., Cox, E., Diaz, E., Eastwood, M. L., Eckert, R., Ehlmann, B. L., Ginoux, P., Ageitos, M. G., Grant, K., Guanter, L., Pearlshtien, D. H., Helmlinger, M., Herzog, H., Hoefen, T., Huang, Y., Keebler, A., Kalashnikova, O., Keymeulen, D., Kokaly, R., Klose, M., Li, L., Lundeen, S. R., Meyer, J., Middleton, E., Miller, R. L., Mouroulis, P., Oaida, B., Obiso, V., Ochoa, F., Olson-Duvall, W., Okin, G. S., Painter, T. H., Pérez García-Pando, C., Pollock, R., Realmuto, V., Shaw, L., Sullivan, P., Swayze, G., Thingvold, E., Thorpe, A. K., Vannan, S., Villarreal, C., Ung, C., Wilson, D. W., and Zandbergen, S.: On-orbit calibration and performance of the EMIT imaging spectrometer, Remote Sensing of Environment, 303, 113 986, https://doi.org/https://doi.org/10.1016/j.rse.2023.113986, 2024.

Tian, S., Pan, Y., Liu, Z., Wen, T., and Wang, Y.: Size-resolved aerosol chemical analysis of extreme haze pollution events during early 2013 in urban Beijing, China, Journal of Hazardous Materials, 279, 452–460, https://doi.org/10.1016/J.JHAZMAT.2014.07.023, 2014.

Tilgner, A., Schaefer, T., Alexander, B., Barth, M., Collett Jr., J. L., Fahey, K. M., Nenes, A., Pye, H. O. T., Herrmann, H., and McNeill, V. F.: Acidity and the multiphase chemistry of atmospheric aqueous particles and clouds, 21, 13 483–13 536, https://doi.org/10.5194/acp-21-13483-2021, publisher: Copernicus GmbH, 2021.

Tolocka, M. P., Saul, T. D., and Johnston, M. V.: Reactive uptake of nitric acid into aqueous sodium chloride droplets using real-time single-particle mass spectrometry, The Journal of Physical Chemistry A, 108, 2659–2665, 2004.

Tomlinson, G. H. I.: Air pollutants and forest decline, 17, 246A–256A, https://doi.org/10.1021/es00112a716, publisher: American Chemical Society, 1983.

Topping, D., Coe, H., McFiggans, G., Burgess, R., Allan, J., Alfarra, M. R., Bower, K., Choularton, T. W., Decesari, S., and Facchini, M. C.: Aerosol chemical characteristics from sampling conducted on the Island of Jeju, Korea during ACE Asia, 38, 2111–2123, https://doi.org/10.1016/j.atmosenv.2004.01.022, ISBN: 4416120036, 2004.

Trochkine, D., Iwasaka, Y., Matsuki, A., Yamada, M., Kim, Y.-S., Nagatani, T., Zhang, D., Shi, G.-Y., and Shen, Z.: Mineral aerosol particles collected in Dunhuang, China, and their comparison with chemically modified particles collected over Japan, 108, https://doi.org/10.1029/2002JD003268, _eprint: https://onlinelibrary.wiley.com/doi/pdf/10.1029/2002JD003268, 2003.

Trump, E. R., Fountoukis, C., Donahue, N. M., and Pandis, S. N.: Improvement of simulation of fine inorganic PM levels through better descriptions of coarse particle chemistry, Atmospheric Environment, 102, 274–281, https://doi.org/10.1016/j.atmosenv.2014.11.059, 2015.

Tsigaridis, K. and Kanakidou, M.: Secondary organic aerosol importance in the future atmosphere, Atmospheric Environment, 41, 4682–4692, https://doi.org/10.1016/J.ATMOSENV.2007.03.045, 2007.

Tsigaridis, K. and Kanakidou, M.: The Present and Future of Secondary Organic Aerosol Direct Forcing on Climate, Current Climate Change Reports, 4, 84–98, 2018.

Tsimpidi, A. P., Karydis, V. A., and Pandis, S. N.: Response of inorganic fine particulate matter to emission changes of sulfur dioxide and ammonia: the eastern United States as a case study, 57, 1489–1498, https://doi.org/10.3155/1047-3289.57.12.1489, 2007.

Tsimpidi, A. P., Karydis, V. A., and Pandis, S. N.: Response of fine particulate matter to emission changes of oxides of nitrogen and anthropogenic volatile organic compounds in the eastern United States, 58, 1463–1473, 2008.

Twohy, C. H., Kreidenweis, S. M., Eidhammer, T., Browell, E. V., Heymsfield, A. J., Bansemer, A. R., Anderson, B. E., Chen, G., Ismail, S., DeMott, P. J., and Van Den Heever, S. C.: Saharan dust particles nucleate droplets in eastern Atlantic clouds, Geophysical Research Letters, 36, https://doi.org/10.1029/2008GL035846, _eprint: https://agupubs.onlinelibrary.wiley.com/doi/pdf/10.1029/2008GL035846, 2009.

Ullerstam, M., Johnson, M. S., Vogt, R., and Ljungström, E.: DRIFTS and Knudsen cell study of the heterogeneous reactivity of SO_2 and NO_2 on mineral dust, 3, 2043–2051, https://doi.org/10.5194/acp-3-2043-2003, publisher: Copernicus GmbH, 2003.

UN: Assessment report on ammonia, https://unece.org/sites/default/files/2021-10/ECE_EB.AIR_2021_7-2113502E.pdf, 2021.

Underwood, G. M., Song, C. H., Phadnis, M., Carmichael, G. R., and Grassian, V. H.: Heterogeneous reactions of NO2 and HNO3 on oxides and mineral dust: A combined laboratory and modeling study, 106, 18 055–18 066, https://doi.org/10.1029/2000JD900552, _eprint: https://onlinelibrary.wiley.com/doi/pdf/10.1029/2000JD900552, 2001.

Uno, I., Eguchi, K., Yumimoto, K., Takemura, T., Shimizu, A., Uematsu, M., Liu, Z., Wang, Z., Hara, Y., and Sugimoto, N.: Asian dust transported one full circuit around the globe, 2, 557–560, https://doi.org/10.1038/ngeo583, publisher: Nature Publishing Group, 2009.

Uno, I., Osada, K., Yumimoto, K., Wang, Z., Itahashi, S., Pan, X., Hara, Y., Kanaya, Y., Yamamoto, S., and Fairlie, T. D.: Seasonal variation of fine-and coarse-mode nitrates and related aerosols over East Asia: synergetic observations and chemical transport model analysis, Atmos. Chem. Phys, 17, 14 181–14 197, https://doi.org/10.5194/acp-17-14181-2017, 2017a.

Uno, I., Yumimoto, K., Pan, X., Wang, Z., Osada, K., Itahashi, S., and Yamamoto, S.: Simultaneous dust and pollutant transport over East Asia: The Tripartite Environment Ministers Meeting March 2014 case study, 13, 47–52, https://doi.org/10.2151/sola.2017-009, 2017b.

Uno, I., Wang, Z., Itahashi, S., Yumimoto, K., Yamamura, Y., Yoshino, A., Takami, A., Hayasaki, M., and Kim, B.-G. G.: Paradigm shift in aerosol chemical composition over regions downwind of China, Scientific Reports, 10, 1–11, https://doi.org/10.1038/s41598-020-63592-6, 2020.

Usher, C. R., Al-Hosney, H., Carlos-Cuellar, S., and Grassian, V. H.: A laboratory study of the heterogeneous uptake and oxidation of sulfur dioxide on mineral dust particles, 107, https://doi.org/10.1029/2002JD002051, 2002.

Usher, C. R., Michel, A. E., and Grassian, V. H.: Reactions on Mineral Dust, Chemical Reviews, 103, 4883–4939, https://doi.org/10.1021/cr020657y, 2003.

van der Wal, R., Pearce, I. S. K., and Brooker, R. W.: Mosses and the struggle for light in a nitrogen-polluted world, 142, 159–168, https://doi.org/10.1007/s00442-004-1706-0, 2005.

Van Grinsven, H. J. M., Holland, M., Jacobsen, B. H., Klimont, Z., Sutton, M. a., and Jaap Willems, W.: Costs and Benefits of Nitrogen for Europe and Implications for Mitigation, 47, 3571–3579, https://doi.org/10.1021/es303804g, publisher: American Chemical Society, 2013.

van Vuuren, D. P., Edmonds, J., Kainuma, M., Riahi, K., Thomson, A., Hibbard, K., Hurtt, G. C., Kram, T., Krey, V., Lamarque, J.-F., Masui, T., Meinshausen, M., Nakicenovic, N., Smith, S. J., and Rose, S. K.: The representative concentration pathways: an overview, 109, 5, https://doi.org/10.1007/s10584-011-0148-z, 2011.

Varga, G., Kovács, J., and Újvári, G.: Analysis of Saharan dust intrusions into the Carpathian Basin (Central Europe) over the period of 1979–2011, 100, 333–342, https://doi.org/10.1016/j.gloplacha.2012.11.007, 2013.

Vasilakos, P., Russell, A., Weber, R., and Nenes, A.: Understanding nitrate formation in a world with less sulfate, Atmospheric Chemistry and Physics, 18, 12 765–12 775, https://doi.org/10.5194/ACP-18-12765-2018, 2018.

Vehkamäki, H., Kulmala, M., Napari, I., Lehtinen, K. E., Timmreck, C., Noppel, M., and Laaksonen, A.: An improved parameterization for sulfuric acid-water nucleation rates for tropospheric and stratospheric conditions, 107, AAC 3–10, https://doi.org/10.1029/2002JD002184, 2002.

Vet, R., Artz, R. S., Carou, S., Shaw, M., Ro, C.-U., Aas, W., Baker, A., Bowersox, V. C., Dentener, F., Galy-Lacaux, C., Hou, A., Pienaar, J. J., Gillett, R., Forti, M. C., Gromov, S., Hara, H., Khodzher, T., Mahowald, N. M., Nickovic, S., Rao, P. S. P., and Reid, N. W.: A global assessment of precipitation chemistry and deposition of sulfur, nitrogen, sea salt, base cations, organic acids, acidity and pH, and phosphorus, 93, 3–100, https://doi.org/10.1016/j.atmosenv.2013.10.060, 2014.

Vignati, E., Wilson, J., and Stier, P.: M7: An efficient size-resolved aerosol microphysics module for large-scale aerosol transport models, Journal of Geophysical Research D: Atmospheres, 109, 1–17, https://doi.org/10.1029/2003JD004485, 2004.

Vlasenko, A., Sjogren, S., Weingartner, E., Stemmler, K., Gäggeler, H. W., and Ammann, M.: Atmospheric Chemistry and Physics Effect of humidity on nitric acid uptake to mineral dust aerosol particles, Atmos. Chem. Phys, 6, https://doi.org/doi.org/10.5194/acp-6-2147-2006, 2006.

Vlasenko, A., Huthwelker, T., Gäggeler, H. W., and Ammann, M.: Kinetics of the heterogeneous reaction of nitric acid with mineral dust particles: An aerosol flowtube study, Physical Chemistry Chemical Physics, 11, 7921–7930, https://doi.org/10.1039/b904290n, 2009.

Walker, J. M., Philip, S., Martin, R. V., and Seinfeld, J. H.: Simulation of nitrate, sulfate, and ammonium aerosols over the United States, 12, 11 213–11 227, https://doi.org/10.5194/acp-12-11213-2012, 2012.

Walters, R.: Understanding Soil pH: Theory, Measurement, Application, https://agrosphere-international.net/Documents/DHC/Understanding%20pH.pdf, 2025.

Wang, A., Zhang, S., Liang, Z., Zeng, Z., Ma, Y., Zhang, Z., Yang, Y., He, Z., Yu, G., and Liang, Y.: Response of microbial communities to exogenous nitrate nitrogen input in black and odorous sediment, 248, 118 137, https://doi.org/10.1016/j.envres.2024.118137, 2024a.

Wang, C., Yan, Y., Niu, Y., Li, R., Xu, Y., Hu, D., Wu, J., and Peng, L.: Formation and driving factors of sulfate in PM2.5 at a high-level atmospheric SO2 city of Yangquan in China, 14, 491–501, https://doi.org/10.1007/s11869-020-00953-0, 2021.

Wang, H., Tian, X., Zhao, W., Li, J., Yu, H., Feng, Y., and Song, S.: Technical note: Influence of different averaging metrics and temporal resolutions on the aerosol pH calculated by thermodynamic modeling, Atmospheric Chemistry and Physics, 24, 6583–6592, https://doi.org/10.5194/acp-24-6583-2024, publisher: Copernicus GmbH, 2024b.

Wang, J., Wu, Z., Qiu, T., Man, R., Zong, T., Qiu, Y., Fang, W., Chen, S., Liang, D., Song, M., Ahn, J., Lee, J., and Hu, M.: Impacts of aerosol acidity and liquid water content on secondary inorganic aerosol pollution in East Asian megacities: Beijing and Seoul, 361, 121 479, https://doi.org/10.1016/j.atmosenv.2025.121479, 2025a.

Wang, L., Wang, F., Zhang, X., Du, Z., and Ming, J.: Long-term trends in water-soluble ions in aerosols at Urumqi Glacier No. 1: Evidence of increasing dust and alkalinity in Central Asia, 357, 121 314, https://doi.org/10.1016/j.atmosenv.2025.121314, 2025b.

Wang, M., Kong, W., Marten, R., He, X.-C., Chen, D., Pfeifer, J., Heitto, A., Kontkanen, J., Dada, L., Kürten, A., Yli-Juuti, T., Manninen, H. E., Amanatidis, S., Amorim, A., Baalbaki, R., Baccarini, A., Bell, D. M., Bertozzi, B., Bräkling, S., Brilke, S., Murillo, L. C., Chiu, R., Chu, B., De Menezes, L.-P., Duplissy, J., Finkenzeller, H., Carracedo, L. G., Granzin, M., Guida, R., Hansel, A., Hofbauer, V., Krechmer, J., Lehtipalo, K., Lamkaddam, H., Lampimäki, M., Lee, C. P., Makhmutov, V., Marie, G., Mathot, S., Mauldin, R. L., Mentler, B., Müller, T., Onnela, A., Partoll, E., Petäjä, T., Philippov, M., Pospisilova, V., Ranjithkumar, A., Rissanen, M., Rörup, B., Scholz, W., Shen, J., Simon, M., Sipilä, M., Steiner, G., Stolzenburg, D., Tham, Y. J., Tomé, A., Wagner, A. C., Wang, D. S., Wang, Y., Weber, S. K., Winkler, P. M., Wlasits, P. J., Wu, Y., Xiao, M., Ye, Q., Zauner-Wieczorek, M., Zhou, X., Volkamer, R., Riipinen, I., Dommen, J., Curtius, J., Baltensperger, U., Kulmala, M., Worsnop, D. R., Kirkby, J., Seinfeld, J. H., El-Haddad, I., Flagan, R. C., and Donahue, N. M.: Rapid growth of new atmospheric particles by nitric acid and ammonia condensation, 581, 184–189, https://doi.org/10.1038/s41586-020-2270-4, publisher: Nature Publishing Group, 2020.

Wang, R., Balkanski, Y., Boucher, O., Ciais, P., Schuster, G. L., Chevallier, F., Samset, B. H., Liu, J., Piao, S., Valari, M., et al.: Estimation of global black carbon direct radiative forcing and its uncertainty constrained by observations, Journal of Geophysical Research: Atmospheres, 121, 5948–5971, 2016.

Wang, X., Heald, C. L., Liu, J., Weber, R. J., Campuzano-Jost, P., Jimenez, J. L., Schwarz, J. P., and Perring, A. E.: Exploring the observational constraints on the simulation of brown carbon, AGUFM, 2018a.

Wang, Z., Pan, X., Uno, I., Li, J., Wang, Z., Chen, X., Fu, P., Yang, T., Kobayashi, H., Shimizu, A., Sugimoto, N., and Yamamoto, S.: Significant impacts of heterogeneous reactions on the chemical composition and mixing state of dust particles: A case study during dust events over northern China, Atmospheric Environment, 159, 83–91, https://doi.org/10.1016/j.atmosenv.2017.03.044, 2017.

Wang, Z., Zheng, F., Zhang, W., and Wang, S.: Analysis of SO2 Pollution Changes of Beijing-Tianjin-Hebei Region over China Based on OMI Observations from 2006 to 2017, 2018, 8746 068, https://doi.org/10.1155/2018/8746068, _eprint: https://onlinelibrary.wiley.com/doi/pdf/10.1155/2018/8746068, 2018b.

Wang, Z., Uno, I., Yumimoto, K., Pan, X., Chen, X., Li, J., Wang, Z., Shimizu, A., and Sugimoto, N.: Dust Heterogeneous Reactions during Long-Range Transport of a Severe Dust Storm in May 2017 over East Asia, 10, https://doi.org/10.3390/atmos10110680, 2019.

Wang, Z., Chen, S., Liu, C., Chen, Y., Gong, Y., and Cheng, S.: Dynamic Dust Source Regions and the Associated Natural and Anthropogenic Dust Emissions at the Global Scale, Frontiers in Earth Science, 10, https://doi.org/10.3389/feart.2022.802658, publisher: Frontiers, 2022.

Wang, Z. B., Hu, M., Pei, X. Y., Zhang, R. Y., Paasonen, P., Zheng, J., Yue, D. L., Wu, Z. J., Boy, M., and Wiedensohler, A.: Connection of organics to atmospheric new particle formation and growth at an urban site of Beijing, Atmospheric Environment, 103, 7–17, https://doi.org/10.1016/j.atmosenv.2014.11.069, 2015.

Warneck, P. and Williams, J.: Aqueous Phase Chemistry, in: The Atmospheric Chemist's Companion: Numerical Data for Use in the Atmospheric Sciences, edited by Warneck, P. and Williams, J., pp. 271–314, Springer Netherlands, ISBN 978-94-007-2275-0, https://doi.org/10.1007/978-94-007-2275-0_8, 2012.

Watanabe, S., Hajima, T., Sudo, K., Nagashima, T., Takemura, T., Okajima, H., Nozawa, T., Kawase, H., Abe, M., Yokohata, T., Ise, T., Sato, H., Kato, E., Takata, K., Emori, S., and Kawamiya, M.: MIROC-ESM 2010: model description and basic results of CMIP5-20c3m experiments, Geoscientific Model Development, 4, 845–872, https://doi.org/10.5194/gmd-4-845-2011, 2011.

Weast, R. C.: CRC Handbook of Chemistry and Physics, Cronus Books, 60 edn., https://www.abebooks.com/servlet/BookDetailsPL?bi=31210018960&searchurl=an%3Dweast%2Brobert%26sortby%3D17%26tn%3Dcrc%2Bhandbook%2Bchemistry%2Bphysics%2B60th&cm_sp=snippet-_-srp1-_-title1, 1980.

Weber, R. J., Guo, H., Russell, A. G., and Nenes, A.: High aerosol acidity despite declining atmospheric sulfate concentrations over the past 15 years, 9, 282–285, https://doi.org/10.1038/ngeo2665, publisher: Nature Publishing Group, 2016.

Webmineral: Albite Mineral Data, http://webmineral.com/data/Albite.shtml, [Online; accessed 11 March 2024], 2008a.

Webmineral: Anorthite Mineral Data, http://webmineral.com/data/Anorthite.shtml, [Online; accessed 11 March 2024], 2008b.

Webmineral: Calcite Mineral Data, http://webmineral.com/data/Calcite.shtml, [Online; accessed 11 March 2024], 2008c.

Webmineral: Gypsum Mineral Data, http://webmineral.com/data/Gypsum.shtml, [Online; accessed 11 March 2024], 2008d.

Webmineral: Orthoclase Mineral Data, http://webmineral.com/data/Orthoclase.shtml, [Online; accessed 11 March 2024], 2008e.

Webmineral: Illite Mineral Data, http://webmineral.com/data/Illite.shtml, [Online; accessed 20 October 2022], 2008f.

Wei, C.: Modeling the effects of heterogeneous reactions on atmospheric Modeling the effects of heterogeneous reactions on atmospheric chemistry and aerosol properties chemistry and aerosol properties, Ph.D. thesis, University of Iowa, https://doi.org/10.17077/etd.2xewzpnz, 2010.

Wei, H., Liu, W., Zhang, J., and Qin, Z.: Effects of simulated acid rain on soil fauna community composition and their ecological niches, 220, 460–468, https://doi.org/10.1016/j.envpol.2016.09.088, 2017.

Wesely, M.: Parameterization of surface resistances to gaseous dry deposition in regional-scale numerical models, Atmospheric Environment (1967), 23, 1293–1304, https://doi.org/https://doi.org/10.1016/0004-6981(89)90153-4, 1989.

Wexler, A. S. and Seinfeld, J. H.: The distribution of ammonium salts among a size and composition dispersed aerosol, 24, 1231–1246, https://doi.org/10.1016/0960-1686(90)90088-5, 1990.

Whitten, G. Z., Heo, G., Kimura, Y., McDonald-Buller, E., Allen, D. T., Carter, W. P., and Yarwood, G.: A new condensed toluene mechanism for Carbon Bond: CB05-TU, Atmospheric Environment, 44, 5346–5355, https://doi.org/10.1016/J.ATMOSENV.2009.12.029, 2010.

Wild, O., Zhu, X., and Prather, M. J.: Fast-J: Accurate simulation of in-and below-cloud photolysis in tropospheric chemical models, Journal of Atmospheric Chemistry, 37, 245–282, 2000.

Wolseley, P. A., James, P. W., Theobald, M. R., and Sutton, M. A.: Detecting changes in epiphytic lichen communities at sites affected by atmospheric ammonia from agricultural sources, 38, 161–176, https://doi.org/10.1017/S0024282905005487, 2006.

Wu, M., Wang, H., Lu, Z., Liu, X., Bian, H., Cohen, D., Feng, Y., Chin, M., Hauglustaine, D., Karydis, V., Lund, M., Myhre, G., Pozzer, A., Michael, S., Skeie, R., Tsimpidi, A., Tsyro, S., and Xie, S.: Observationally constrained analysis on the distribution of fine- and coarse-mode nitrate in global models, 25, 10 049–10 074, https://doi.org/10.5194/acp-25-10049-2025, 2025.

Wu, Y., Gu, B., Erisman, J. W., Reis, S., Fang, Y., Lu, X., and Zhang, X.: PM2.5 pollution is substantially affected by ammonia emissions in China, Environmental Pollution, 218, 86–94, https://doi.org/10.1016/j.envpol.2016.08.027, 2016.

Xu, L. and Penner, J.: Global simulations of nitrate and ammonium aerosols and their radiative effects., Atmospheric Chemistry & Physics Discussions, 12, 2012.

Yang, L.: Title Kaolinite dissolution and precipitation kinetics at 22oC and pH 4 Permalink https://escholarship.org/uc/item/0qz871kp Publication Date, https://escholarship.org/uc/item/0qz871kp, 2008.

Yang, W., Ma, Q., Liu, Y., Ma, J., Chu, B., Wang, L., and He, H.: Role of NH3 in the Heterogeneous Formation of Secondary Inorganic Aerosols on Mineral Oxides, Journal of Physical Chemistry A, 122, 6311–6320, https://doi.org/10.1021/acs.jpca.8b05130, 2018.

Yang, W., Ma, J., Yang, H., Li, F., and Han, C.: Photoenhanced sulfate formation by the heterogeneous uptake of SO_2 on non-photoactive mineral dust, 24, 6757–6768, https://doi.org/10.5194/acp-24-6757-2024, publisher: Copernicus GmbH, 2024.

Yarwood, G., Rao, S., Yocke, M., and Whitten, G. Z.: Updates to the carbon bond chemical mechanism: CB05 final report to the US EPA, RT-0400675, https://www.regulations.gov/document/EPA-HQ-OAR-2010-0162-3417, 2005.

Yu, Z., Jang, M., and Park, J.: Modeling atmospheric mineral aerosol chemistry to predict heterogeneous photooxidation of SO₂, 17, 10 001–10 017, https://doi.org/10.5194/acp-17-10001-2017, 2017.

Yue, Y., Cheng, J., Lee, K. S., Stocker, R., He, X., Yao, M., and Wang, J.: Effects of relative humidity on heterogeneous reaction of SO2 with CaCO3 particles and formation of CaSO4·2H2O crystal as secondary aerosol, Atmospheric Environment, 268, https://doi.org/10.1016/J.ATMOSENV.2021.118776, 2022.

Zakoura, M. and Pandis, S. N.: Overprediction of aerosol nitrate by chemical transport models: The role of grid resolution, 187, 390–400, https://doi.org/10.1016/j.atmosenv.2018.05.066, 2018.

Zaveri, R. A., Easter, R. C., Fast, J. D., and Peters, L. K.: Model for Simulating Aerosol Interactions and Chemistry (MOSAIC), Journal of Geophysical Research Atmospheres, 113, 1–29, https://doi.org/10.1029/2007JD008782, 2008.

Zdanovskii, A. B.: New methods of calculating solubilities of electrolytes in multi- component systems, Zh. Fiz. Khim, 22(12), 1478–1485, 1948.

Zhai, S., Jacob, D. J., Pendergrass, D. C., Colombi, N. K., Shah, V., Yang, L. H., Zhang, Q., Wang, S., Kim, H., Sun, Y., Choi, J.-S., Park, J.-S., Luo, G., Yu, F., Woo, J.-H., Kim, Y., Dibb, J. E., Lee, T., Han, J.-S., Anderson, B. E., Li, K., and Liao, H.: Coarse particulate matter air quality in East Asia: implications for fine particulate nitrate, 23, 4271–4281, https://doi.org/10.5194/acp-23-4271-2023, publisher: Copernicus GmbH, 2023.

Zhang, A., Wang, Y., Zhang, Y., Weber, R. J., Song, Y., Ke, Z., and Zou, Y.: Modeling global radiative effect of brown carbon: A larger heating source in the tropical free troposphere than black carbon, Atmospheric Chemistry & Physics Discussions, pp. 1–36, https://doi.org/https://doi.org/10.5194/acp-2019-594, 2020.

Zhang, J., Cheng, H., Wang, D., Zhu, Y., Yang, C., Shen, Y., Yu, J., Li, Y., Xu, S., Zhang, S., Song, X., Zhou, Y., Chen, J., Jiang, J., Fan, L., Wang, C., and Hao, K.: Chronic Exposure to PM2.5 Nitrate, Sulfate, and Ammonium Causes Respiratory System Impairments in Mice, 55, 3081–3090, https://doi.org/10.1021/acs.est.0c05814, 2021a.

Zhang, R., Wang, G., Guo, S., Zamora, M. L., Ying, Q., Lin, Y., Wang, W., Hu, M., and Wang, Y.: Formation of Urban Fine Particulate Matter, 115, 3803–3855, https://doi.org/10.1021/acs.chemrev.5b00067, publisher: American Chemical Society, 2015.

Zhang, X., Zhao, L., Tong, D. Q., Wu, G., Dan, M., and Teng, B.: A Systematic Review of Global Desert Dust and Associated Human Health Effects, 7, 158, https://doi.org/10.3390/atmos7120158, number: 12 Publisher: Multidisciplinary Digital Publishing Institute, 2016.

Zhang, X., Wang, Z., Cheng, M., Wu, X., Zhan, N., and Xu, J.: Long-term ambient SO2 concentration and its exposure risk across China inferred from OMI observations from 2005 to 2018, 247, 105 150, https://doi.org/10.1016/j.atmosres.2020.105150, 2021b.

Zhang, Y. and Carmichael, G. R.: The Role of Mineral Aerosol in Tropospheric Chemistry in East Asia—A Model Study, 38, 353–366, https://doi.org/10.1175/1520-0450(1999)038<0353:TROMAI>2.0.CO;2, publisher: American Meteorological Society Section: Journal of Applied Meteorology and Climatology, 1999.

Zhang, Y. and Muhammed, M.: Solubility of Calcium Sulfate Dihydrate in Nitric Acid Solutions Containing Calcium Nitrate and Phosphoric Acid, Journal of Chemical and Engineering Data, 34, 121–124, https://doi.org/10.1021/je00055a032, 1989.

Zhang, Y., Sunwoo, Y., Kotamarthi, V., and Carmichael, G. R.: Photochemical Oxidant Processes in the Presence of Dust: An Evaluation of the Impact of Dust on Particulate Nitrate and Ozone Formation, 33, 813–824, https://doi.org/10.1175/1520-0450(1994)033<0813:POPITP>2.0.CO;2, publisher: American Meteorological Society Section: Journal of Applied Meteorology and Climatology, 1994.

Zhang, Y., Lang, J., Cheng, S., Li, S., Zhou, Y., Chen, D., Zhang, H., and Wang, H.: Chemical composition and sources of PM1 and PM2. 5 in Beijing in autumn, Science of the Total Environment, 630, 72–82, 2018.

Zhao, C., Niu, M., Song, S., Li, J., Su, Z., Wang, Y., Gao, Q., and Wang, H.: Serum metabolomics analysis of mice that received repeated airway exposure to a water-soluble PM2.5 extract, 168, 102–109, https://doi.org/10.1016/j.ecoenv.2018.10.068, 2019.

Zhao, F., Hawkesford, M., and McGrath, S.: Sulphur Assimilation and Effects on Yield and Quality of Wheat, 30, 1–17, https://doi.org/10.1006/jcrs.1998.0241, 1999.

Zhao, P., Chen, Y., and Su, J.: Size-resolved carbonaceous components and water-soluble ions measurements of ambient aerosol in Beijing, Journal of Environmental Sciences, 54, 298–313, https://doi.org/10.1016/J.JES.2016.08.027, 2017.

Zheng, B., Tong, D., Li, M., Liu, F., Hong, C., Geng, G., Li, H., Li, X., Peng, L., Qi, J., Yan, L., Zhang, Y., Zhao, H., Zheng, Y., He, K., and Zhang, Q.: Trends in China's anthropogenic emissions since 2010 as the consequence of clean air actions, 18, 14 095–14 111, https://doi.org/10.5194/acp-18-14095-2018, publisher: Copernicus GmbH, 2018.

Zhu, S., Butler, T., Sander, R., Ma, J., and Lawrence, M. G.: Impact of dust on tropospheric chemistry over polluted regions: a case study of the Beijing megacity, 10, 3855–3873, https://doi.org/10.5194/acp-10-3855-2010, 2010.

Zhu, X., Prospero, J. M., Savoie, D. L., Millero, F. J., Zika, R. G., and Saltzman, E. S.: Photoreduction of iron(III) in marine mineral aerosol solutions, 98, 9039–9046, https://doi.org/10.1029/93JD00202, _eprint: https://onlinelibrary.wiley.com/doi/pdf/10.1029/93JD00202, 1993.

Zilitinkevich, S. S.: Bulk characteristics of turbulence in the atmospheric planetary boundary layer, vol. 167, Trudy GGO, 1965.

Zimmermann, F., Weinbruch, S., Schütz, L., Hofmann, H., Ebert, M., Kandler, K., and Worringen, A.: Ice nucleation properties of the most abundant mineral dust phases, 113, https://doi.org/10.1029/2008JD010655, _eprint: https://onlinelibrary.wiley.com/doi/pdf/10.1029/2008JD010655, 2008.

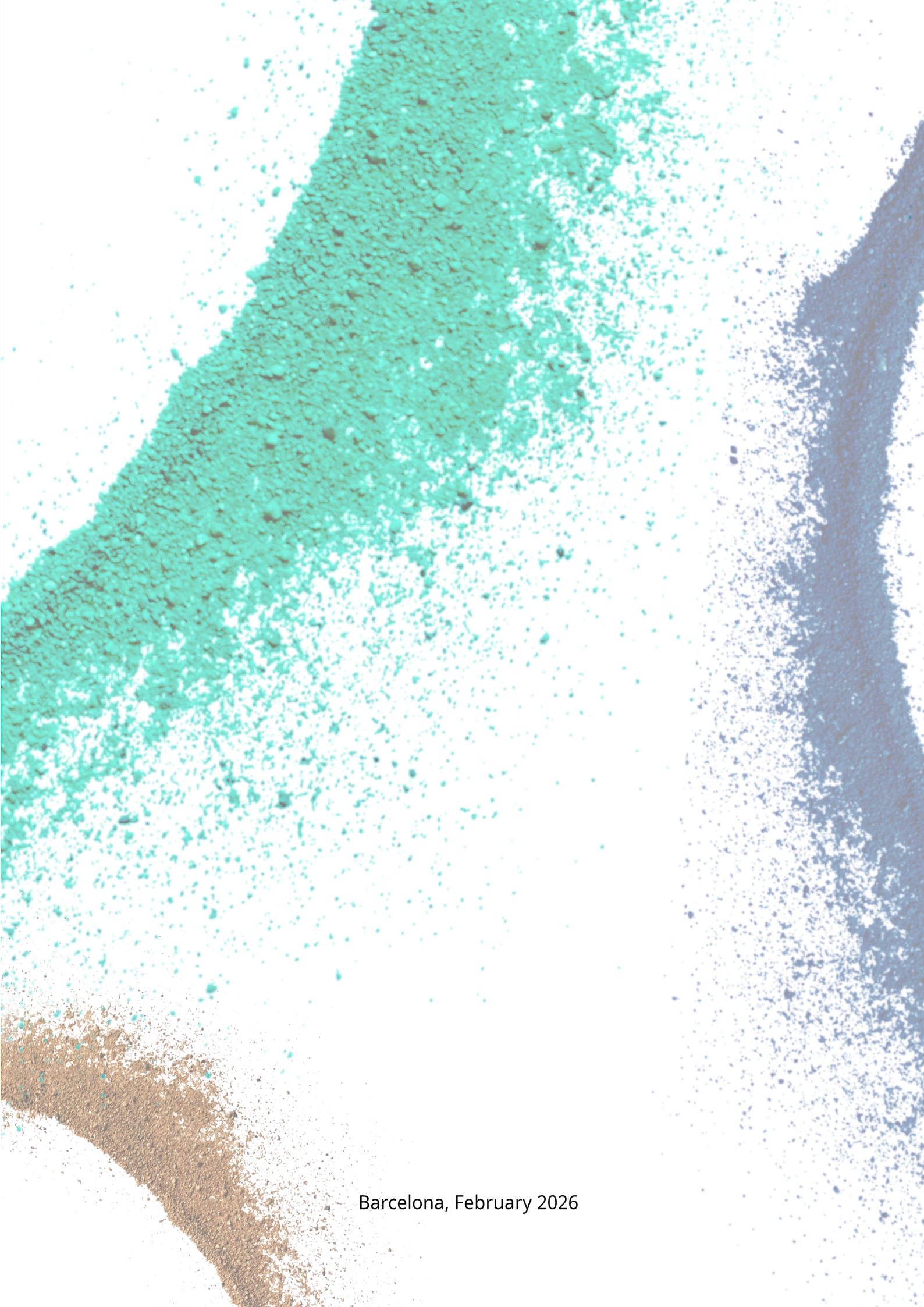

Barcelona, February 2026